CRANFIELD UNIVERSITY

2001

Nicholas Stone

RAMAN SPECTROSCOPY OF BIOLOGICAL TISSUE FOR APPLICATION IN OPTICAL DIAGNOSIS OF MALIGNANCY

Department of Environmental and Ordinance Systems

&

Cranfield Postgraduate Medical School

PhD Thesis

CRANFIELD UNIVERSITY

Department of Environmental and Ordinance Systems,
The Royal Military College of Science

&

Cranfield Postgraduate Medical School

PhD Thesis

Academic Year 2000/2001

Nicholas Stone **BSc(Hons), MSc(Dist), MSc(Dist), Grad. Dip. IPSM(Merit)**

RAMAN SPECTROSCOPY OF BIOLOGICAL TISSUE FOR APPLICATION IN OPTICAL DIAGNOSIS OF MALIGNANCY

Supervisors: Dr. S. R. Ahmad & Prof. H. Barr

September 2001

This thesis is submitted in partial fulfilment of the requirements for the degree of Doctor of Philosophy.

Abstract

The utilisation of near-infrared Raman spectroscopy for the discrimination of cancers and pre-cancers from normal tissue in the aero-digestive tract has been evaluated. A commercially available Raman microspectrometer has been modified to provide optimum throughput, sensitivity and fluorescence suppression for epithelial tissue measurements. Laser excitation at 830nm was demonstrated to be optimum. High quality (S/N ratio 15-20) NIR-Raman spectra have been acquired from oesophageal and laryngeal tissues in time scales under 30 seconds.

Pathological groupings covering the full range of normal and neoplastic tissues in the organs of interest have been studied. Both fresh (snap frozen) and formalin fixed tissue samples were investigated, firstly to indicate whether tissue-types can be distinguished in vivo and secondly to demonstrate the use of Raman spectroscopy as a tool for classification in the pathology lab.

Results using multivariate statistical techniques to distinguish between spectra from specimens exhibiting different tissue pathologies have been extremely promising. Cross-validation of the spectral predictive models has shown that three groups of larynx tissue can be separated with sensitivities and specificities of between 86 and 90% and 87 and 95% respectively. Oesophageal prediction models have demonstrated sensitivities and specificities of 84 to 97% and 93 to 98% respectively for a three-group consensus model and 73 to 100% and 92 to 100% for an eight-group consensus model.

Epithelial tissues including stomach, tonsil, endometrium, bladder and prostate have been studied to identify further tissues where Raman spectroscopy may be employed for detection of disease. Spectra were similar to those obtained from oesophagus and larynx, although sufficiently different for distinct discriminant models to be required. This work has demonstrated the generic nature of Raman spectroscopy for the detection and classification of cancers and pre-cancerous lesions in many tissues. The evidence provided by this study indicates that utilisation of Raman spectroscopy for non-invasive detection and classification of disease is a distinct possibility. Potential difficulties in the transferability from in vitro to in vivo have been evaluated and no significant barriers have been observed. However, further in vivo probe development and optimisation will be required before 'optical biopsy' with Raman spectroscopy can become a reality.

Acknowledgments

This work was funded in part by The Winfield Hospital, Gloucester and MedLINK and involved a collaboration between Gloucestershire Royal Hospital, Renishaw plc. (Spectroscopy Division), Bristol University Interface Analysis Centre and KEYMED (Olympus). MedLINK funding was provided by the Department of Health and EPSRC matched by the commercial partners.

Dr Rafi Ahmad deserves a great deal of thanks for his perseverance and patience as the prime supervisor of this part-time PhD carried out at various sites in the UK and Australia. He has kept me on track throughout and even though there have sometimes been long gaps between communications, he has still closely followed the ups and downs of my investigations. He has an excellent grasp of vibrational spectroscopy and has taught me to believe in myself as an independent scientist.

Prof Hugh Barr has been an inspiration. He is the most interested and knowledgeable clinician I have ever had the pleasure of working with. As a physical scientist employed in the biomedical field it is virtually impossible to achieve significant research without the enthusiasm of a senior clinician. This has been made very easy by Hugh and his boundless energy has rubbed off onto others helping us to form important collaborations.

Catherine Kendall has been closely involved with this project, especially with the extremely important process of collecting and keeping track of tissue samples, diagnoses and consent forms. Without Catherine's organisational skills things would have been much more difficult. Moreover, the opportunity of having a group (Catherine and Janelle) to discuss ideas with has certainly benefited my thought processes, although probably slowed my rate of progress.

My time spent in Australia at the Queensland University of Technology as a Visiting Academic proved invaluable. Edeline, Jan and Llew were very welcoming and helped me get up to speed in the practical aspects of the art of chemometrics and vibrational spectroscopy of biological tissues. They were especially helpful, supporting me whilst there was no laboratory equipment available to perform experiments in the UK.

The author would like to thank the histology department at Gloucestershire Royal Hospital and especially Richard Allison for all their help and support with this project and others involving large amounts of tissue collection and storage. Professor Neil Shepherd also deserves gratitude for all his work defining the pathologies of our samples. He has always been willing to discuss and explain complex histology to further the understanding that I could not have achieved without him. Prof Karel Goboes and Dr Brian Warren were also kind contributors to the consensus of histopathological opinion on the tissue samples used in this study.

Most of all I would like to thank my wife Megan for her patience and love to help me through the long days of writing up whilst working fulltime. We have almost 'lost' two years of weekends to this exercise. Apologies for all the DIY you had to do alone on our new house, while I wrote or pondered over this thesis.

Finally, I would like to thank my friends and family, firstly for not asking every time I saw them when I was going to finish (well not quite every time), but also for still wanting to spend time with me even if I haven't communicated with them over the last 12 to 18 months.

In memory of my Grandmother,

Evelyn Wadley for her love, support and work ethic.

She followed my progress with enthusiasm and would have been most proud of me.

Nan passed away just before this thesis was submitted for evaluation.

Contents

List of Figures

List of Tables

1. Introduction

1.1 Background

The incidence of all forms of cancer is much greater than many people realise. There were over 219,000 new cases of cancer reported in England and Wales in 1993 alone.[1] Moreover as many as one in three people in the UK will be struck down by the disease in their lifetime. Malignancy is more commonly found in older members of the community; with only six percent of all cancers in males and nine percent in females occurring in those aged under 45 years. The peak age group for presenting with cancer is between 70 and 74 years for both males and females.[1] Furthermore, with the mean age of the population increasing the number of cases is likely to rise markedly. Table 1.1 displays the survival rates for the four most common cancers in England and Wales for cases first diagnosed between 1991 and 1993.

	Cancer	Number of natients	One-vear survival (%)	Five-vear survival (%)
Men	**Lung**	60,300	19.8	5.0
	Prostate	41,877	79.3	48.9
	Colon	22,164	64.0	41.6
	Rectum	16,807	68.7	39.2
Women	**Breast**	83,912	91.8	73.7
	Lung	29,052	19.8	5.0
	Colon	24,239	60.9	40.2
	Rectum	12,281	69.4	42.5

Table 1.1: Cancer survival rates for the four most common cancers in men and women, at one and five years for patients diagnosed during 1991-1993 and followed up to 31 December 1998.[2]

The primary requirement for successful treatment of any malignancy is early detection. Although the pathogenesis of most malignancies is not fully understood, some cancers are known to develop through a pre-malignant state. Current methods of detecting early malignancies rely upon surveillance of at risk populations or diagnostic investigations following presentation with suspicious symptoms. By the time symptoms are present tumours are usually of a significant size, and it is often too late to facilitate a full cure.

Over the last century there have been myriad of technological breakthroughs leading to improvements in medical diagnosis and therapy. These include the use of X-rays, magnetic resonance imaging (MRI), computer assisted tomography (CT), ultrasound, radio-isotope imaging, and endoscopy for diagnosis; and radiotherapy, chemotherapy, laser surgery and photodynamic therapy (PDT) for treatment. Most diagnostic techniques measure the changes in architecture and morphology of tissue that follow initiation of the disease process. Nuclear Medicine and selected areas of MRI are able to provide some functionality. However with Nuclear Medicine resolution is of the order of cms and MRI the order of mms. Therefore it is apparent that using current medical technology, the detection of malignant change at a cellular level (where a successful treatment is most likely) will rely upon the removal of tissue samples to enable microscopic histopathological analysis.

The 'gold standard' for detection of malignancies and pre-malignancies is excisional biopsy followed by histopathological analysis. This technique relies upon sectioning tissue less than one cell thick (<10 microns) and staining with haematoxylin and eosin (H & E). This provides some functional information in addition to the morphology of the tissue that can be viewed under a conventional light microscope. The principle of histology has changed little since its conception in the 19th century.[3]

In the analysis of pre-cancerous lesions there are often high levels of discrepancy between pathologists, due to the subjective nature of histological analysis. The variation in histopathological grading poses a significant problem in the classification of many pre-malignant abnormalities. Melville et al (1989)[4] compared the grading of dysplasia in ulcerative colitis by five pathologists. Overall agreement between any two pathologists ranged from 42% to 65%. Discrepancies in the diagnosis increased with the severity of the dysplasia. Jensen et al (1995)[5] showed similar discrepancies with the grading of severity of dysplasia in 194 slides of colorectal adenomas by 3 experienced pathologists. Reid et al (1988)[6] showed that there is a substantial observer variation in the diagnosis of dysplasia in Barrett's oesophagus due to the subjective nature of histopathological analysis. The study involved the comparison of 71 sections from the oesophagus classified into one of 5 groups: negative for dysplasia, indefinite for dysplasia, low grade dysplasia, high grade dysplasia, and intra-mucosal carcinoma. The resulting agreement in classification by 8 gastrointestinal pathologists was between 58% and 61% over all groups. Blackwell et al (1995) showed agreement, in classification of laryngeal dysplasia, of only 54% between 2 pathologists studying a group of 148 laryngeal biopsies.[7]

A further problem associated with the gold standard involves the targeting of biopsy samples from microscopic abnormal lesions. It is often the case with many pre-cancerous lesions that they will be too small to be detected by endoscopy alone. Therefore a random tissue selection procedure is usually employed. This can lead to a high probablitiy of missing abnormal tissue by random biopsy. Van Sandick et al (1998)[8] followed 16 patients undergoing surveillance for Barrett's oesophagus, a condition whereby the risk of developing oesophageal adenocarcinoma is increased many-fold. The patients underwent regular surveillance endoscopy over a number of years up until surgical resection was required, due to the development of high-grade dysplasia (essentially a localised cancerous lesion) or adenocarcinoma. Biopsies were obtained from all four quadrants of the oesophagus, every 2cm along the visible length of the Barrett's mucosa. Each biopsy was sectioned at three different levels and stained with haematoxylin and eosin. The histological findings, shown in Figure 1.1, indicate either the sampling procedure is missing areas of abnormality, from one endoscopic procedure to the next, or dysplastic lesions are regressing and then reoccurring. The latter is thought to be unlikely.

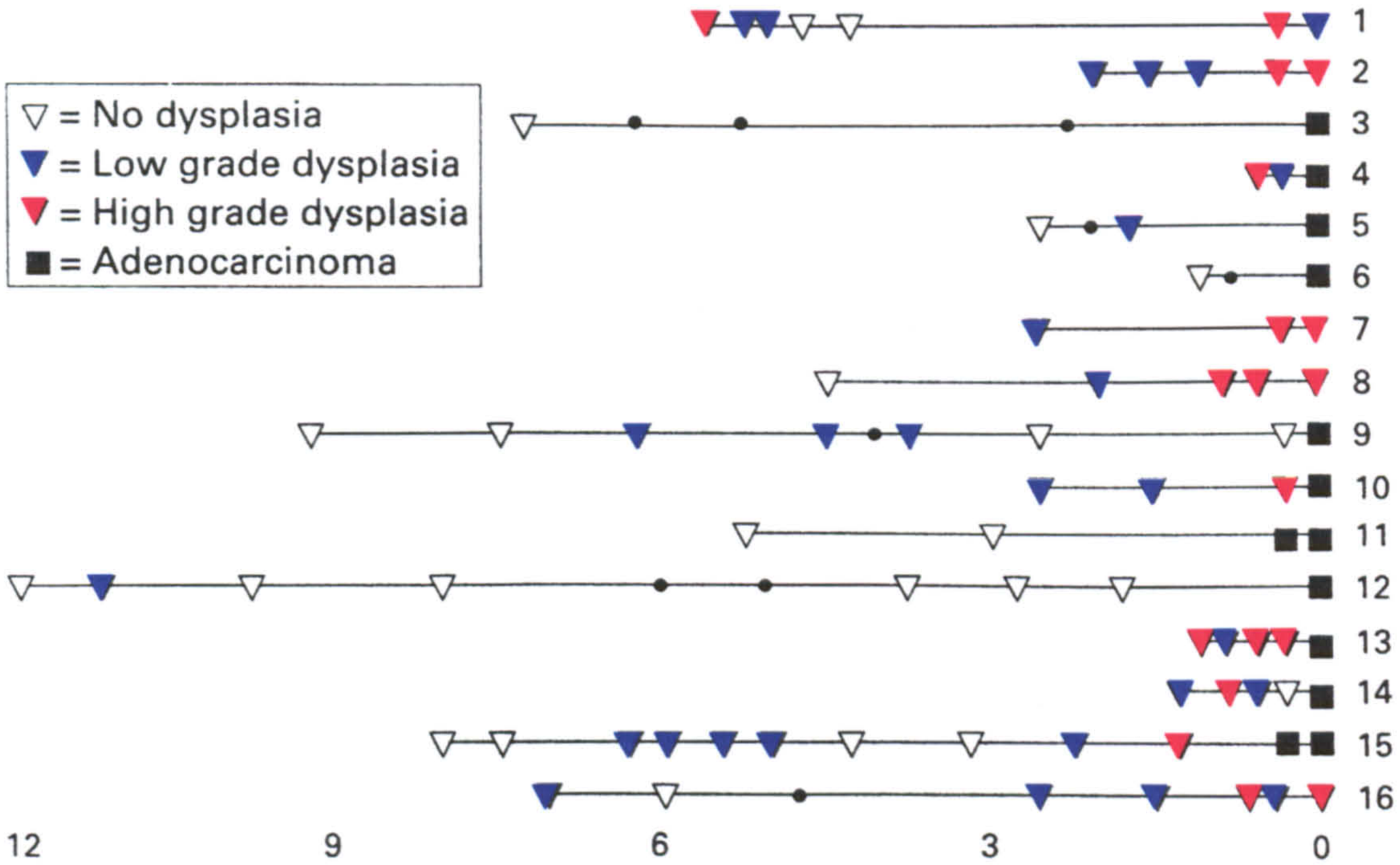

Figure 1.1: duration and frequency of endoscopic surveillance with accompanying histological findings in 16 patients undergoing surveillance of Barrett's oesophagus. Black dots represent endoscopic examinations at which no biopsy specimens were obtained. Modified and reproduced courtesy of van Sandick et al (1998).[8]

Biochemical changes within tissue may either initiate disease or occur as the result of the disease process. The qualitative analysis of such changes provides important clues in the search for a specific diagnosis and the quantitative analysis of biochemical abnormalities is important in measuring the extent of the disease process, designing therapy and evaluating the efficacy of treatment. The conventional method for detection of malignancy using histopathological examination of biopsy samples relies upon the subjective assessment of tissue architecture, which is likely to demonstrate abnormal changes at a later stage than would analysis of biochemistry. Furthermore, histopathological analysis requires tissue to be removed with possibly undesirable consequences. Evidently, the development of a rapid, non-invasive, qualitative histochemical analysis technique, enabling objective biochemical analysis of tissue, would be of great value. This may be possible with a variety of optical techniques.

Over the past few years a number of groups have been working towards real-time, non-invasive techniques that utilise light to study abnormalities in tissue.[9] Recent technological developments have made it possible to obtain significant amounts of

biochemical or architectural data from extremely complex biological tissue in very short time scales (milliseconds to seconds). Optical diagnosis relies upon measurement of the interaction of light photons with the constituents of biological tissue. The resultant data can provide an evaluation of histochemistry or morphology. This information can aid with the deduction of the pathological state of the tissue, and hence lead to a diagnosis.

Light can interact with tissue in a number of ways, including elastic and inelastic scattering; reflection off boundary layers; and absorption, leading to fluorescence and phosphorescence. All of these can be utilised in some way to measure abnormal changes in tissue. Many authors have used the term 'Optical Biopsy' when describing these techniques. Optical biopsy is a misnomer because no tissue is removed in the analysis, however it does help to convey to the lay person the general principle of using light to detect cancerous transformations in tissue.

Initial optical biopsy systems, utilising tissue fluorescence, have been used as an adjunct to current investigative techniques, mainly to improve targeting of blind biopsy.[10,11,12,13] Future prospects utilising molecular-specific techniques may enable complete replacement of biopsy with objective optical detection providing a real-time, highly sensitive and specific measurement of the tissue histological state. However until its efficacy is proven it is most likely that optical detection will be used as a complimentary technique to improve targeting of biopsy selection.

The clinical requirements for an objective, non-invasive real time probe for the accurate and repeatable measurement of tissue pathological state are overwhelming. There is a clinical need for optical diagnosis in a number of important areas:

1. Situations where sampling errors severely restrict the effectiveness of excisional biopsy, such as the high failure rates associated with blind biopsies, whereby the clinician has to randomly select sites for sample collection. This method is used to screen for pre-malignant conditions such as ulcerative colitis and Barrett's oesophagus.
2. Where conventional excisional biopsy is potentially hazardous, examples of vulnerable regions include the central nervous system, vascular system and articular cartilage.
3. An immediate diagnosis during an investigative procedure would eliminate the need for many secondary procedures by enabling treatment to take place directly following diagnosis. This is especially useful with the development of treatments utilising light energy, such as photo-dynamic therapy and laser ablation. This is likely to improve patient outcomes and decrease waiting times by reducing the number of costly procedures required.
4. Tumour margins could be identified during surgical resection, thus enabling a more accurately targeted resection to be performed.
5. A surgeon with any doubt over a diagnosis could cross-validate a previous diagnosis prior to excision of an organ or lesion using a non-invasive optical probe.

The objective of the present research is to evaluate the potential for Raman spectroscopy, a highly specific optical analysis technique, to achieve the capability of in vivo detection of early malignant changes. Initial work has been carried out to optimise a Raman microspectrometer for tissue measurements; to target potential malignancies with a clinical need for diagnostic improvements; and to build and test spectral libraries and prediction algorithms for the various tissue types and pathologies. The extent of this thesis does not extend to cover in vivo measurements. However, the discussions outline the likely work required for successful implementation of an in vivo Raman probe for early detection of malignancy.

1.2 Raman Spectroscopy

Recently it has been suggested that Raman spectroscopy has the potential to identify markers associated with malignant change.[14,15,16] This may lead to its use as a diagnostic tool for the study of the evolution of pre-cancerous and cancerous lesions in vivo. The direct detection of biochemical tissue constituents via vibrational spectroscopy may provide a new methodology for non-invasive detection of disease, together with new information for classifying, grading and evaluating the progression of malignant neoplasms.

Raman spectroscopy is the analysis of inelastic scattered photons following monochromatic laser excitation. It provides information about both the chemical and morphological structure of tissue in near real time[17] and can be used as a non-invasive optical method of tissue characterisation. Most biological molecules are Raman active with their own characteristic spectral fingerprint. Proteins, nucleic acids, cell membranes, single cells and tissues can all be studied. The Raman spectrum is a plot of scattered intensity, as a function of energy difference between the incident and scattered photons. The loss (or gain) in photon energies corresponds to the difference in the final and initial vibrational energy levels of molecules participating in the interaction. The observed peaks (bands) in the Raman spectrum are relatively narrow, easy to resolve and sensitive to molecular structure, conformation and environment.

Generally biological tissues are inhomogeneous in composition and highly scattering; the full analysis of Raman signals thus requires an understanding of tissue optical parameters and photon propagation in turbid media. Raman signals are inherently weak and, in addition, early diagnosis of disease requires detection of tissue molecular constituents present in low concentrations. This is accentuated by the fact that lasers with high intensity cannot be used to observe weak signals from tissues because of the potential for sample damage. Thirdly, the complex nature of tissue composition results in absorption of light throughout the entire uv-visible region, and subsequent intense fluorescence emission strongly interferes with weak Raman signals.

Fluorescence is one of the primary obstacles encountered in the Raman spectroscopy of biological tissue. A fairly recent development has been the use of near infrared (NIR) laser excitation and dispersive spectrometers to allow rapid detection of spectra with low background fluorescence. NIR radiation generally does not induce electronic absorption in tissue chromophores, consequently fluorescence is weak relative to the Raman signal. Holographic notch filters are used to filter the elastic (Rayleigh) scattered light from the

signal.[18] In combination with a single monochromator the throughput of the system is increased compared with the triple monochromators commonly used previously. The development of charge coupled device (CCD) detectors and solid state semiconductor lasers has enabled the development of portable NIR Raman systems that produce spectra with high signal to noise in short integration times.[16] Compatibility with fibre optics and the development of new probes is making in vivo diagnostics with Raman spectroscopy a real possibility.

Raman spectroscopy has shown a great deal of potential for biomedical diagnosis of malignancy in localised sites. Techniques using ultraviolet, visible and near-infrared wavelengths of light have shown repeatable differences between Raman spectra from normal and malignant tissue.[19,14,20] There appears to be little Raman work published on the upper aero-digestive tract.[21] This region includes the naso-pharynx, larynx and oesophagus; where an increasing number of invasive adenocarcinomas are being found, often at a stage where the chance of successful treatment is unlikely. Raman spectroscopy has the potential to detect pre-malignant lesions, such as dysplasia in Barrett's oesophagus and squamous dysplasia in the larynx. Use of Raman spectroscopy in vivo would potentially enhance targeting of the biopsy forceps to sites of abnormality, and thus would improve the probability of detection of abnormalities over the random biopsy currently employed for detection of pre-malignancies. A substantial amount of research is required to evaluate the sensitivity and specificity of this technique for diagnosis and to correlate specific Raman spectral features with histopathological data.

1.3 Biology of Specific Malignancies

The following sub-sections outline the current understanding of the pathogenesis of two particular cancers of the aero-digestive tract that have been studied in this work. The cancers have been selected for this study because they develop into invasive malignancies via a pre-malignant step. It must be noted that not all patients with pre-malignant abnormalities will go on to develop invasive cancers, but the probability that this will occur can be increased by more than 100-fold.[22,23]

1.3.1 Adenocarcinoma of the Oesophagus

The oesophagus is a muscular, flexible tube that transports food and liquid from the laryngopharynx (throat) to the stomach. It lies posterior to the trachea and is about 25cm long. It is made up of a number of different layers of cells, in common with other parts of the gastrointestinal tract, mucosa, sub-mucosa, muscularis and the serosa. See Figure 1.2. The inner surface, or mucosa, of a normal oesophagus is lined with stratified squamous epithelial cells, which form a smooth surface to aid the passage of food boluses and protect against wear-and-tear. The oesophagus secretes mucus and transports food to the stomach by the action or peristalsis. It does not produce digestive enzymes or carry out absorption of nutrients. At the lower end of the oesophagus there is a narrowing of the lumen or sphincter, which controls the entrance to the stomach. If the sphincter fails to close after the food has entered the stomach, the stomach contents can enter the distal (lower) portion of the oesophagus. This is called gastro-oesophageal reflux. Hydrochloric

acid and bile acid from the stomach can irritate the oesophageal mucosa and cause a burning sensation.

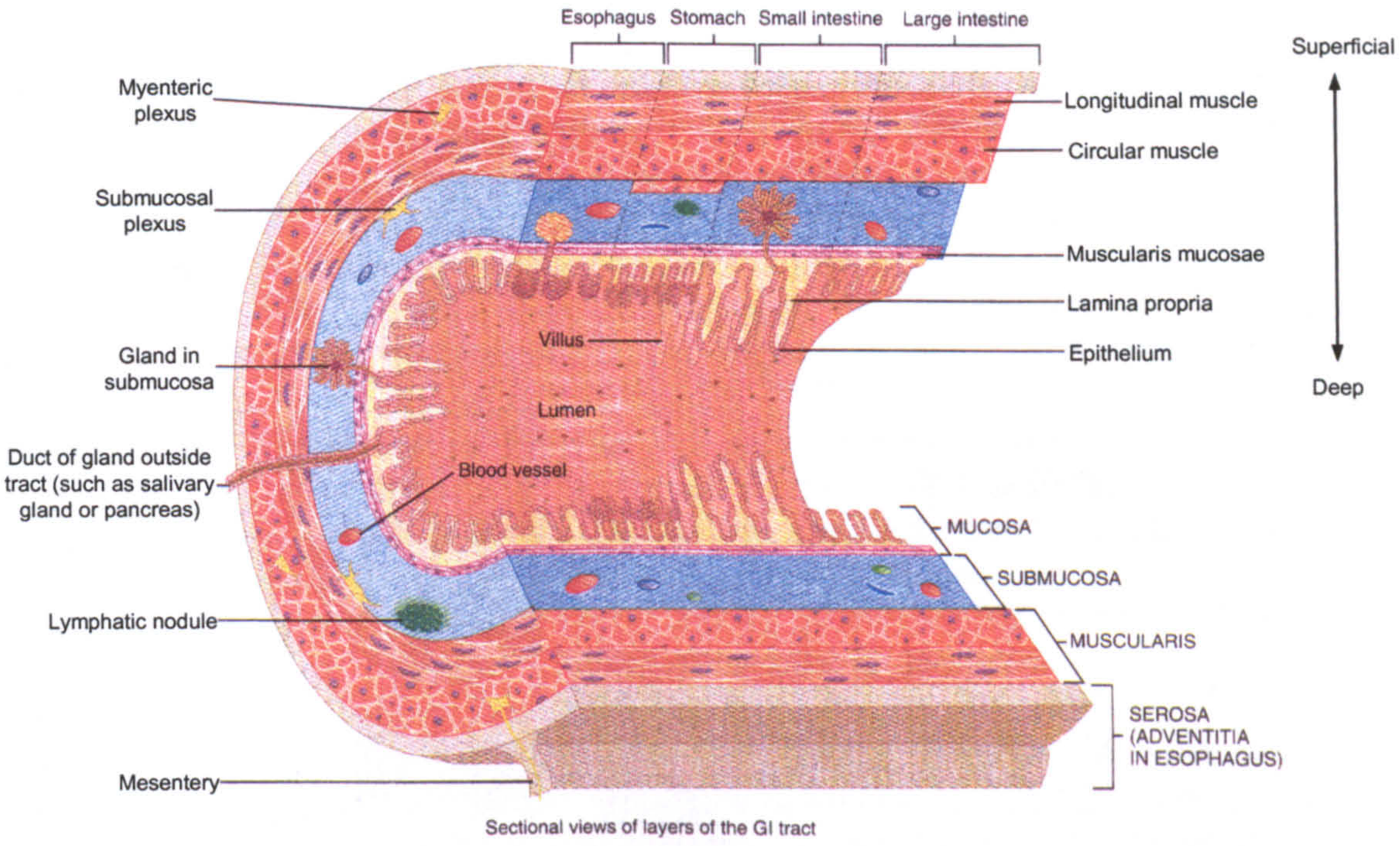

Figure 1.2: composite of various sections of the gastrointestinal tract seen in a three-dimensional drawing depicting the various layers and related structures. Reproduced from Tortora and Grabowski (1996).[24]

Long periods of exposure to these irritants in gastro-oesophageal reflux can lead to a change in the cells lining the oesophagus, whereby the squamous epithelium lining the distal oesophagus is replaced by columnar epithelium.[25] This is called Barrett's oesophagus and is a metaplastic condition in which the cells are essentially normal but they do not belong in that location. Prospective studies have shown the prevalence of columnar lined oesophagus in patients exhibiting reflux was between 11 and 12%.[26,27] Morphologically the columnar epithelium of Barrett's Oesophagus can resemble the mucosa of the gastric fundus, cardia, antrum, or intestine. Parietal cells are present in the gastric fundic-type epithelium[28] and these have been found to produce acid in the oesophagus.[29] This epithelium also has chief cells which contain and secrete pepsinogens. The columnar-lined mucosa is more likely to be resistant to the effects of reflux than squamous-lined mucosa.

Barrett's oesophagus is associated with an increased risk of oesophageal adenocarcinoma.[30,31,32,33,34] In recent prospective studies, Robertson et al[49] reported an incidence of 1786 cases of Barrett's associated carcinoma per 100,000 population per year and Hameeteman et al[35] reported 1920 cases per 100,000 per year. The estimated risk of adenocarcinoma in Barrett's oesophagus has been shown to be between 30 and 350 times greater than that found in the average population, depending on the figures

used.[35,22,23] Adenocarcinomas occurring in Barrett's oesophagus make up between 54 and 68% of all oesophageal cancers[36,37] and the rate of incidence is rising more rapidly than for any other cancer.[38,39] These carcinomas typically occur in older (mean age 57 years),[40] male (male:female ratio = 5.5:1),[40] white patients.[32,41]

Dysplasia is the most frequently used marker of increased cancer risk in Barrett's oesophagus. It is an abnormal change in the maturation and development that can occur in all three types of Barrett's epithelia. However, it is more commonly seen in areas of intestinal metaplasia (IM) and it is unlikely that oesophageal adenocarcinoma occurs except in patients with IM.[42,43,44] Follow-up studies in patients with Barrett's oesophagus have shown that only patients with dysplasia progress to adenocarcinoma.[45] A number of studies have shown over 50% of patients operated on for high grade dysplasia will be found to have invasive carcinoma.[44,46,47] Circumstantial evidence suggests that dysplasia may not only be a marker for carcinoma, but may in itself be the early carcinomatous change that can progress to invasive carcinoma.[33] All grades of dysplasia appear to have the potential to give rise to invasive carcinoma and epithelial changes need not go through a recognisable carcinoma in situ phase before being associated with invasion.[33] Although the circumstantial evidence for the dysplasia to carcinoma sequence is strong, the progression of dysplasia to carcinoma is still unproven and the time course unknown.[48] Therefore, the potential benefits of removing an oesophagus exhibiting dysplasia must be weighed against the relatively high mortality associated with oesophagectomy (5 to 15%)[33] and the poor outcome in patients who present with invasive adenocarcinoma of the oesophagus (23% survival at 1 year and 7% survival at 5 years in the England and Wales between 1986 and 1990).[2]

Robertson et al recommended that patients with Barrett's oesophagus be screened by endoscopy and biopsy to detect and monitor the presence and progress of dysplasia.[49] It has therefore become common practice to place patients with Barrett's oesophagus in a cancer surveillance programme. The goal of surveillance is either prevention of carcinoma or the detection of carcinoma in an early and potentially curable phase. The current regime used for surveillance endoscopy in most UK hospitals involves the selection of biopsy samples from all 4 quadrants every 2cm along the entire Barrett's epithelium. Since the mortality and morbidity of oesophagectomy is high confirmation of a diagnosis of high-grade dysplasia is usually required before moving on to resect the organ. (A negative result is viewed with caution and initial samples are usually re-examined. Since dysplasia is considered neoplastic, it is unlikely to ever resolve spontaneously. Therefore, once true dysplasia has been identified all follow up negatives are likely to be the result of sampling error.[48]) Dysplasia is relatively rare in patients with Barrett's oesophagus but data suggest that when biopsy specimens are positive for high-grade dysplasia, there is a high probability that infiltrating carcinoma will already be present.[50,51]

Histopathology is currently the gold standard for diagnosis of dysplastic changes in the oesophagus. However it can be limited by the subjective nature of biopsy interpretation and targetting,[6] especially in the grading of dysplasia, which has no set limits to progression (i.e. follows a continuum). Most patients with Barrett's oesophagus will not

develop dysplasia or adenocarcinoma.[45,52] Reliable methods for identifying those patients with Barrett's oesophagus who will progress to carcinoma do not exist at present. Therefore, techniques that enable a greater understanding of the biological processes leading to carcinogenesis will be extremely valuable.

1.3.2 Squamous Cell Carcinoma of the Larynx

The larynx is the organ used for speech. It is the passage-way that links the laryngopharynx with the trachea. The wall of the larynx is made up of nine pieces of cartilage that influence the positions and tensions of the vocal folds (Figure 1.3). The epiglottis is a large piece of elastic cartilage covered with epithelium that acts as a trap door preventing swallowed foods and liquids from entering the trachea. The larynx rises during swallowing allowing the free edge of the epiglottis to close a lid over the glottis. The glottis is made up of a pair of folds of mucous membrane – these are the true vocal cords – and the space between them, the rima glottidis. The paired arytenoid cartilages attach to the vocal folds and intrinsic pharyngeal muscles. Contracting these muscles stretches the vocal cords out into the airway so that the rima glottidis is narrowed. If air is directed at the vocal folds they are forced to vibrate and set up sound waves in the column of air in the pharynx, nose and mouth. The pitch of the sound produced is controlled by adjusting the tension on the vocal cords.

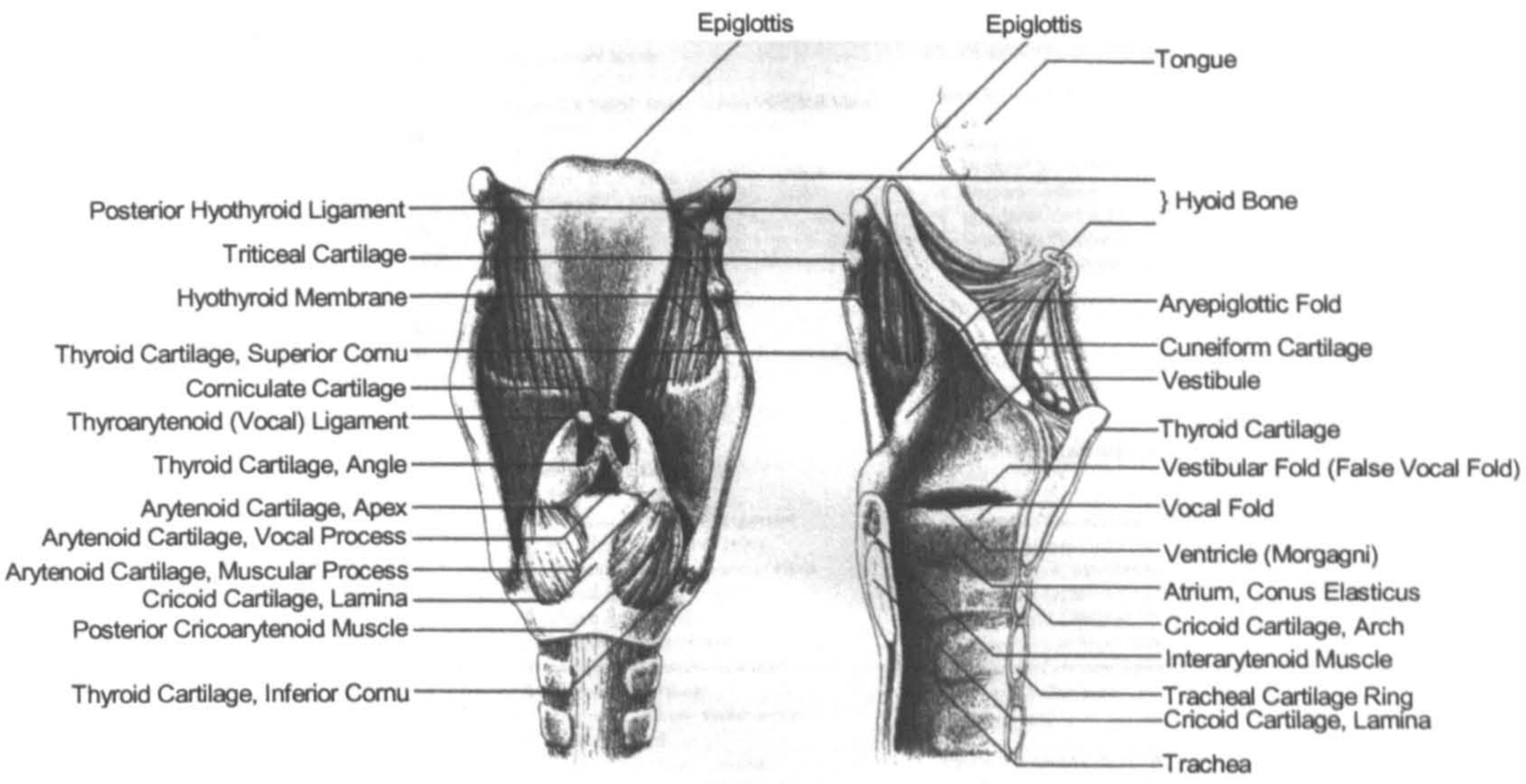

Figure 1.3: Larynx (posterior and sagittal views). Reproduced from Palmer (1993).[53]

The mucous membrane of the larynx forms two pairs of folds: a superior pair called the ventricular folds (false vocal cords) and an inferior pair called simply the vocal cords (true vocal cords). The mucous membrane of the vocal folds is lined by nonkeratinized stratified squamous epithelium. Irritants such as cigarette smoke, alcohol, or respiratory infection can cause an inflammation of the vocal folds (laryngitis), causing hoarseness by interfering with the contraction of the folds or by causing them to swell so that they cannot vibrate freely. It has been suggested as long ago as 1960 that chronic laryngitis may be a pre-cursor to carcinoma of the larynx.[54,55]

Cancer of the larynx is one of the more common malignancies with over 2000 new cases per year in England and Wales. Incident rates are about 8 per 100,000 per year with about 80% of cases in men. About 45% of laryngeal tumours diagnosed during the 1980s arose in the glottis (endolarynx), including the vocal cords, and about 16% in the supraglottis (epilarynx) and four in five of these tumours were squamous carcinomas. The incidence of laryngeal cancer has progressively risen over the last 25 years, with the most significant increase occurring in women.[56] It has been estimated that there has been no overall improvement in the mortality from laryngeal cancer over the last three decades; those cancers diagnosed during 1986-90 in England and Wales having a relative survival of 84% at one year and 64% at five years for men and 78% at one year and 59% at five years for women.[57] Delayed diagnosis leading to loco-regional failure and a high incidence of second primary malignancy in long-term survivors are the two main reasons for this poor outcome.[58] In addition, laryngeal cancer has one of the greatest effects on quality of life of any cancer, causing devastating lifestyle changes and resulting in permanent cosmetic and psychosocial disability.

The vast majority of laryngeal cancers originate in the epithelial surface. The standard method of detection is by inspection of the organ with endoscopy and removal of a sample of tissue for histopathological analysis. This can be time consuming, costly and due to the random nature of biopsy selection stands a chance of missing any abnormal cells in the organ. In addition repeated biopsy procedures increase the risk of affecting the quality of the voice. The transformation from the normal state to carcinoma in the larynx involves an intermediate step, whereby the cells in the squamous epithelial layer begin to grow and mature abnormally. This state is called squamous dysplasia. It is known that lesions exhibiting mild dysplasia have a lower potential for malignant degeneration than those with severe dysplasia.[7,59,60,61] Table 1.2 shows the frequency of progression to invasive carcinoma in patients undergoing laryngeal biopsies displaying various degrees of dysplasia. If the tumour can be visually detected at endoscopy it may already be too late to initiate a full cure. Recently, contact endoscopy has been proposed as a means of avoiding these problems by directly visualising the mucosa under high magnification following application of a tissue stain (methylene blue)[10]. However, this remains very qualitative, time-consuming and can only, of necessity, detect abnormalities in the most superficial layers of cells.

Study	Grade 1	Grade 2	Grade 3
Crissman (1979)[61]	0/52	0/26	3/16
Hellquist et al (1982)[59]	2/98	3/24	9/39
Silamniku et al (1989)[60]	33/808	4/23	25/90
Blackwell et al (1995)[7]	3/32	5/15	5/18
Total	**38/990 (3.8%)**	**12/88 (13.6%)**	**42/163 (25.8%)**

Table 1.2: Frequency of progression to invasive carcinoma in patients undergoing laryngeal biopsies displaying various degrees of dysplasia.

The development of an automated diagnostic method allowing detection of pre-malignant and malignant lesions earlier, at a cellular level, would facilitate faster, more effective patient management and potentially further reduce mortality.

2. Medical and Biological Applications of Raman Spectroscopy: A Critical Review of Relevant Literature

A brief discussion of Raman spectroscopy as a tool for non-invasive, real-time optical diagnosis of early cancers was carried out in the Introduction to this thesis. This chapter is intended to expand on the area and to critically review the published literature for evaluation of the current state of play in this exciting new field. It has been explained that Raman spectroscopy is a technique that utilises the molecular specific inelastic scattering of light photons to interrogate biological tissues. By measuring the change in energy of the collected photons from those of the illuminating photons, the vibrational energy levels of the molecules present in the sample may be deduced. Raman spectroscopy is a complementary technique to infrared (IR) absorption spectroscopy; which is also utilised to measure vibrational molecular states. However, in biochemical applications the presence of water makes the use of IR spectroscopy difficult, whereas the Raman scattering signal of water is weak compared to other molecular species present in tissue.

There are a variety of techniques employing light to analyse and/or image tissue structure or biochemistry. They include fluorescence spectroscopy[11,62,63] and fluorescence imaging;[12,64,13,65] elastic scattering spectroscopy;[66,67] optical coherence tomography;[68,69] and infrared absorption spectroscopy.[70,71,72,73,74] Optical techniques for medical diagnosis have been reviewed in great detail by numerous authors[9,75] including this one[17,76] (refer to Appendix 5 for copies of relevant publications by the author). Further discussion of these alternative approaches is beyond the scope of this thesis, other than to name and reference the key players in various areas.

Optical spectroscopic methods have the potential for providing real-time histopathological information and biochemical imaging of lesions. Unlike fluorescence (and elastic scattering) spectra, whose features are broad, Raman spectral features are sharp and molecular specific, thus providing an opportunity for extracting quantitative molecular information about tissue composition. Mahadevan et al (1995)[77] compared fluorescence and Raman spectroscopies for diagnosis of cervical precancers. Of 36 cervical biopsies that were measured, 19 were normal and 17 samples exhibited various abnormalities. It was demonstrated that multivariate analysis using a number of Raman peak intensities was capable of discriminating between precancers and cancers, and other tissues with 88% sensitivity and 100% specificity.* This is in contrast to fluorescence spectroscopy which when coupled with a principal component analysis routine was only able to separate cancers and precancers from other tissue with 80% sensitivity and 67% specificity. These results indicate the problems associated with fluorescence spectroscopy for medical diagnosis. It was observed that samples of benign lesions such as

---

* Sensitivity and specificity are used in medicine as measures of the ability of a test to correctly make a diagnosis. The sensitivity is the ratio of the number of true positive results to the sum of the true positives and false negatives, i.e. the ratio of correct to incorrect results for a particular condition. The specificity is a measure of the ability of the test to discriminate between two or more conditions. This is calculated by the ratio of true negatives to the sum of the true negatives and false positives. This is explained in greater detail in Appendix 3.

inflammation and metaplasia were commonly diagnosed falsely as precancers. It is the specificity of Raman spectroscopy, with each peak being specific to a particular molecular vibrational mode, which makes it such a valuable tool for medicine.

There is little understanding of the pathogenesis of most cancers, although it is known that those originating in different tissues in the body will have distinct developmental pathways. Therefore it is necessary to measure and characterise these changes before a technique can be used for diagnosis or detection of a particular disease. For example normal and neoplastic colon tissues have distinct biochemical features that can be exploited with Raman spectroscopy. Measurements of excised human colon carcinoma with ^{13}Carbon nuclear magnetic resonance (NMR) have revealed that tumours exhibit decreased triacyglycerols, increased phospholipids, decreased saturation of lipids and increased lactate compared to adjacent normal tissue.[78] Raman spectroscopy has been proposed for early cancer diagnosis by a number of authors.[16,79,80,81] It has shown potential for early diagnosis of malignancy in a variety of organs (breast,[82,20] brain,[83] cervix,[84] oesophagus,[21] skin,[85] and colon[86]) by identifying markers associated with malignant change. Most biological molecules are Raman active with their own characteristic fingerprints, thus the use of Raman spectroscopy for studying the evolution of pre-cancerous and cancerous lesions has been suggested as a valuable tool. The in vivo detection of biochemical tissue constituents using vibrational spectroscopy has been considered by the authors to have the potential to provide a new methodology for non-invasive detection of disease, together with new information for classifying, grading and evaluating the progression of malignant neoplasms.

The use of Raman spectroscopy to investigate tissue biochemistry has only been made possible in recent years by technological improvements in laser sources, spectrometer design and the evolution of high sensitivity multichannel detectors. A brief summary of these important developments is given in Section 2.1. The exploitation of medical applications of Raman spectroscopy has followed rapidly behind the pioneering work that has shown the potential of this technique (see Section 2.2). Further developments towards practical exploitation of biomedical Raman spectroscopy are outlined in Section 2.3 and a brief discussion of the future pitfalls and prospects for its utilisation for detection and classification of cancers and pre-cancers in vivo and in vitro is given in Section 2.4.

2.1 Instrumentation Developments

When C.V. Raman first observed Raman scattering, in 1928, he used a very simple system; whereby sunlight was filtered and focussed onto a sample of liquid. Detection of the scattered radiation was achieved using a number of filters and polarisers placed between the sample and the eye of the observer.[87] The basic concept of a Raman spectroscope has remained the same (see Figure 2.1) as technological developments have made individual components more sophisticated. It was the development of the laser in 1960 by Maiman[88] that enabled this technique to really become a practical tool in the spectroscopist's arsenal. Due to the relative weakness of Raman scattering compared to that of other interactions of light with matter, a Raman system must utilise a high intensity, monochromatic radiation source as well as a highly sensitive detector coupled to a high resolution wavelength dispersive element having high noise rejection factor.

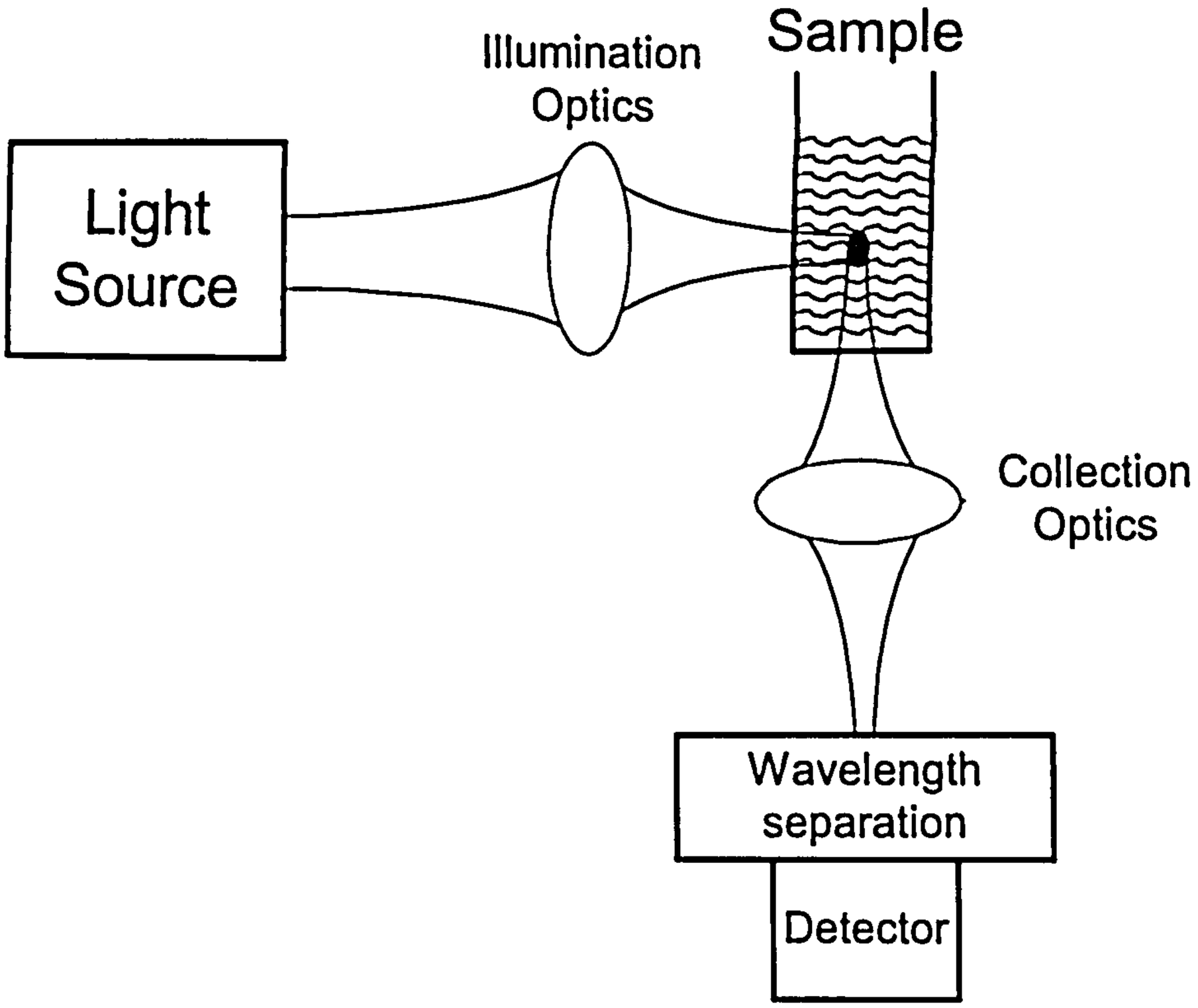

Figure 2.1, schematic diagram of apparatus to measure Raman scattering in a liquid sample, with a 90 degree collection geometry.

Early attempts to measure the Raman spectra of biological tissues were limited by two factors: (1) the inherent high fluorescence of these samples and (2) instrument sensitivity, which necessitated long integration times and high power densities to achieve spectra with good signal-to-noise ratios. The early Raman spectra of biological samples were excited with visible lasers; mainly with the Argon laser lines.[89,90] Detection of the Raman scattered light involved the use of a monochromator to frequency disperse the collected light and a photomultiplier tube to detect the intensity of the photons in the frequency range of interest.

Visible Raman spectroscopy was superseded by the development of interferometers enabling the use of Fourier transform Raman spectroscopy. This technique employs infra-red excitation light, thereby reducing the tissue fluorescence contribution, because excitation of fluorophores is less likely with lower energy photons. The majority of tissue fluorophores have electronic absorption levels substantially higher in energy than that provided by an IR photon. After modulation by the interferometer, the filtered Raman scattered light is usually detected by means of a high sensitivity indium-gallium-arsenide (InGaAs) detector. The Fourier transform IR-Raman technique produces spectra with adequate signal-to-noise-ratios (SNR), with moderately high incident power densities. However acquisition times of about 30 minutes are required to obtain the spectra of highly fluorescent tissues.[20,91]

The development of diode lasers and CCD cameras, sensitive in the near infra-red (NIR), has made it possible to measure Raman spectra of biological tissue with NIR excitation. The major advantage of this technique is that NIR radiation does not generally induce electronic

absorption, but it does have a greater cross-section for Raman scattering than IR photons. Therefore most materials, including biological tissue, exhibit extremely weak fluorescence, with NIR excitation, in comparison to that accompanying visible-excited Raman and adequate signal-to-noise ratios (SNR) can be achieved with relatively short integration times of much less than a minute.[92,93]

The advent of holographic notch filters has also played a major part in improving the practicality of Raman spectroscopy for medicine. The largest component of scattered light from tissue is the elastically (Rayleigh) scattered light. This must be filtered or suppressed prior to measurement. Early designs used triple monochromators to achieve this. However, the throughput of this type of system is very low, necessitating long acquisition times or high laser powers. However, with a holographic Rayleigh rejection filter only a single monochromator is required to separate the Raman spectra into its component energies. Hence a greater throughput is achieved and much shorter acquisition times or reduced laser powers are possible.

The choice of the optimal excitation wavelength for measuring biological tissue must be balanced between the λ^{-4} dependence of the Raman cross-section and the fact that at higher photon energies, greater fluorescence signal is induced. The optimum range generally falls between 750 and 850nm.[94] Nevertheless, despite the relatively high SNR, the resulting tissue Raman spectra still contain some fluorescence background. A challenge in achieving a useful tissue Raman signal is the accurate subtraction of the fluorescence signal. This is vital because in most Raman techniques the fluorescence and weaker Raman signals lie in the same spectral region.

An alternative strategy for overcoming fluorescence interference in Raman spectra is to resonantly excite high-lying electronic states with ultraviolet light, a process known as UV resonance Raman (UVRR) spectroscopy. In biological materials, quenching and non-radiative relaxation from these states often eliminates fluorescence or causes it to occur at much longer wavelengths, so that Raman spectra can be obtained without interference.[86] The principle advantage of UVRR in biomedical applications is that by selecting the appropriate excitation wavelength, to correspond to an absorption peak of a chemical group of interest, Raman bands of disease markers can be enhanced by several orders of magnitude. This enables distinct Raman peaks of low concentration constituents to be observed in the midst of overlapping contributions from more abundant tissue components. Wavelengths in the range 200-260nm selectively enhance the Raman signal from aromatic amino acids and purine and pyrimidine bases of nucleic acids and proteins.[86] Hence, disease markers present in low concentration can be potentially observed. For example nucleic acids make up <5% of the dry weight of tissue, therefore enhancement is required to produce a signal large enough to be seen above the large protein/lipid background. The use of UVRR and NIR-Raman methods are complementary. UV light exhibits shallow penetration in tissue (20-50μm), providing the ability to sample superficial lesions, such as dysplasia. NIR light has a relatively small extinction coefficient and hence penetrates deeply into tissues, providing the opportunity to sample large volumes and probe subsurface details.

Further technological developments lead by Hendra (1988)[95] have resulted in optical fibre probes for in situ Raman spectral measurements. Initially 514.5nm illumination and a

triple monochromator was used, however low Raman signals from tissue and high background from the probes have restricted their use in medicine and biology. Recently a number of groups have been working towards an in vivo fibre probe using near-infrared illumination, thus reducing the fibre background signals with the longer wavelength and by the introduction of filters into the probe head (refer to Section 2.4).

2.2 Pioneering Research

The advancement of laser technology enabled Raman spectroscopy to begin a renaissance in the late 1960s. As the sensitivity of systems using visible excitation wavelengths improved the study of biological samples became possible. In the 1970s pioneering work was carried out by Lord and Yu (1970)[96] by undertaking the first laser excited (632.8nm) Raman spectroscopic measurement of native protein from lysozyme. Hartman et al (1973)[97] took a further step forward by measuring the Raman spectra of intact RNA viruses. The spectra were of high enough quality for many peaks, assignable to RNA and intracellular proteins, to be resolved.

The majority of the work carried out in the 1970s involved the characterisation of Raman spectra from biological molecules and simple cellular components and tissues, excited with visible wavelength lasers. An excellent text outlining the findings of this work has been written by Carey (1982)[98] and more recently by Miura and Thomas (1995).[99] Mitochondria were studied using resonance Raman between the wavelengths of 442-568nm, enabling the identification of cytochromes within the organelle.[100] The first tissue samples to be investigated with Raman spectroscopy were very simple and exhibited strong Raman bands. Examples of these are teeth[101,102] and eye lenses.[103]

However, the first study to indicate the promise of Raman spectroscopy as a method for medical diagnosis was carried out by Larsson and Hellgren (1974).[104] Measurements were made of combined Raman and fluorescence spectra of human blood plasma from patients with various cancers, viral hepatitis and sepsis to evaluate differences between spectra from patients with disease. An argon ion laser was used to excite samples in a borosilicate capillary tube. Healthy plasma exhibited some Raman spectral peaks attributable to resonance enhanced carotenoids and aromatic amino acid side chains. However, all patients with advanced carcinomas showed a massive increase in fluorescence background and the sharp bands in healthy plasma were not visible. This technique was able to distinguish between all diseased and healthy plasma samples, whereas the conventional method of erythrocyte sedimentation rate was positive for disease in only 32 of 53 disease cases. Nevertheless, it must be noted that although the technique used was sensitive to disease, a positive result, i.e. high fluorescence was not specific to any particular illness. Another group, Plouvier and Huong (1984),[105] used ultraviolet resonance (UVRR) Raman spectroscopy to identify blue chromophores observed in blood from patients with cancer and leukemia. The source of the particles is still unknown.

Further instrumental developments in the 1970s by Delhaye and Dhamelincourt (1975)[106] and others lead to the coupling of a dispersion Raman spectrometer with a microscope to enable study of microscopic heterogeneity within samples for the first time. This was

vital for the further development of Raman spectroscopy in the study of biological tissues, cells and constituents with the dimensions of the order of microns to tens of microns. Abraham and Etz (1979)[107] were the first group to utilise this technique for the pathological analysis of human tissue. An argon ion laser emitting 514.5nm light was used to excite a deparaffinated section from a lymph node near to the site of a silicone finger joint replacement. It enabled silicone inclusions to be visualised and identified in tissue for the first time. Other groups have used the same techniques to study inclusions in silicosis lung tissue[108] and to provide microanalysis of gallstones, thus providing information on stone constituents.[109]

All of the studies described above have exploited Raman spectroscopy to identify the presence of a foreign material within human tissue. These so called 'inclusions' usually exhibit strong and distinctly different Raman scattering from normal tissue. It was not until Raman spectroscopy showed the potential to elucidate very subtle changes in biochemistry, that precede or accompany pathological changes, that the interest of the medical community was captured. These developments have lead to the prospect of making use of Raman spectroscopy to monitor all kinds of diseases, from those such as diabetes, whereby glucose levels in cells are unstable, to precancerous and cancerous changes, whereby the cell biochemistry undergoes subtle changes leading to neoplasia and cellular invasion. Early work demonstrating the use of Raman spectroscopy has been used to monitor physiological changes in contracting muscle cells[110] and oxygenation of red blood cells.[111]

It was not until the late 1980s and early 1990s that the Raman spectra obtained from biological tissues were of sufficient quality to enable identification of complex components within the tissues that induce or accompany the disease processes. This generally became a possibility with the development of FT-Raman systems enabling measurements of Raman spectra with near-infrared light (1064nm), thus markedly reducing the fluorescence background and hence the shot noise that tended to obscure weaker Raman peaks. In addition, dispersion spectrometers were being developed for use in the near-infrared (750-850nm) with sensitive multichannel detectors, thus reducing acquisition times. In 1989 McCreery and coworkers constructed a dispersive NIR Raman spectrometer utilising a diode laser source (783nm), single-stage imaging spectrograph and electronically cooled CCD detector.[112] They suggested that the new system offered better sensitivity than FT-Raman spectrometers.[113] Moreover, with the development of a confocal Raman microspectrometer the field of investigation open to Raman spectroscopy has been significantly extended. Microscopically small intact biological objects such as single cells and chromosome bands can now be studied.[114,115]

2.3 In Vitro Analysis of Cancerous and Pre-cancerous Tissues

The prospect of utilising Raman spectroscopy for the detection of cancer has been studied by a number of authors. Improvements in system sensitivity and source wavelength selection has lead to the realisation that Raman spectroscopy has the capability of distinguishing the extremely subtle changes that occur when normal tissues become pre-cancerous. It is at this stage of the disease process that treatment will be most successful. Early work on evaluating the differences between cancerous and normal tissue from various

organs did not begin until the 1990s. The first groups used FT-Raman systems to study breast[20] and gynaecological tumours[15] and in 1993 Alfano et al filed for a US Patent for cancer detection with Raman spectroscopy.[116] By the end of the 1990s a small number groups had initiated work on assessing the potential for Raman detection of cancer in a few different human tissues. This was essential to increase the understanding of various processes that cells undergo whilst progressing towards cancer and to enable the potential of Raman to be assessed for detection of each cancer type. The present work will focus on developing diagnostic algorithms for in vivo and in vitro cancer detection based on differences in spectral data from normal and cancerous cells and tissues. The most significant work in a number of cancer areas is outlined in the sub-sections below.

2.3.1 Breast Cancers

The differences in Raman scattering properties of normal and cancerous breast tissues were first observed using near-IR excitation with 1064nm laser light.[20] Although the results were encouraging the S/N ratios of the spectra in this study were poor and unacceptably long data acquisition times of 10 to 30 minutes were required for signal retrieval. In a later study, excitation at visible wavelengths (514.5 and 633nm) and detection with a more efficient spectrometer system provided much better S/N ratios in a comparative data averaging time.[14] However, more recent studies using a laser at longer wavelengths (784nm[117] and 830nm[81,82]) and single monochromator dispersion systems were found to be more efficient than those of the above works. A significantly lower tissue background signal was achieved than at visible wavelengths. It was also shown by varying excitation wavelengths that spectra of different tissue components could be relatively enhanced.[118,119] For example between 782 and 830nm spectra exhibited mainly lipid peaks in normal breast samples, whereas between 488 and 515nm spectra consisted largely of enhanced carotenoid peaks. However, it was noted that the maximum for fluorescence from breast tissue occurred with 530nm excitation.[119] These studies indicated that the noise contributed by the background tissue fluorescence was minimum at a specific excitation wavelength somewhere between 633 and 1064nm.

An alternative approach has utilised ultra-violet-resonance-Raman (UVRR).[19] Although the use of UV light is unlikely to be accepted for in vivo medical diagnosis, because of mutagenic effects, it has shown promise in the fact that enhancement of particular vibrational bands especially DNA can be achieved with 257.3nm light.[19] UVRR spectra of normal and malignant breast tissue have been measured with 4-5mW of 257.3nm light in 10 to 20 minutes. Tissue spectra consisted of mainly DNA and protein bands. The concentrations of the nucleic acids relative to the cell proteins were shown to increase in malignant cells.

More extensive studies involving greater sample numbers and optimised excitation / spectrometer configurations have enabled acquisition of high quality spectra with integration times as short as 10s.[94,120] Improvements in spectral quality made it possible to distinguish between pathology types using empirical peak area ratio measurements and by exploiting the changes in relative concentrations of lipids and proteins in the samples.[81,117] Empirical methods of analysis, utilising information in individual peaks or peak ratios, have yielded some separation between pathology types, but changes in biochemistry accompanying the

disease process are very complex. Therefore, multivariate analysis, which involves more of the information in the spectra, has been used to exploit this. However, until spectral S/N ratios improved to rival those observed in infrared absorption spectroscopy (where chemometrics or multivariate analysis was first used) it was not feasible to use these complex methods. A very recent study, utilising 830nm excited tissue spectra integrated for 100s, calculated four diagnostically significant principal components* for entry into a discrimination algorithm. The resulting model correctly classified 14/15 normal, 13/15 benign, and 31/31 malignant specimens.[82] These results appear impressive, however, it must be noted that this model was not tested using new data or cross-validation methods. Hence, the discriminant algorithm was used to predict the classification of the tissue sample from a spectrum that had actually been used to create the calibration. Therefore the performance of the algorithm would be expected to be significantly worse for the classification of new samples.

2.3.2 Gynaecological Cancers

The early work investigating the Raman scattering properties at different stages of the disease process in gynaecological tissue utilised near-IR (1064nm) laser light and an FT-Raman spectrometer. Some empirical analysis was possible by using peak intensity ratios to demonstrate the ability to distinguish between normal, benign and malignant cervical tumour tissue.[15] However, long integration times were required and poor SNR spectra were obtained. Improvements in instrumentation were required to enabled high quality spectra to be measured at 789nm using a prototype fibre probe.[77,84] These spectra (measured in 15 minutes) were of sufficient quality to be studied with multivariate analysis. The spectra were compared with the histological results from two board-certified pathologists. It was shown that analysis using a number of Raman peak intensities was capable of discriminating between precancers (and cancers) and other tissues with 88% sensitivity and 100% specificity.[84] In terms of medical significance, this work was an important progression because it investigated the facility of Raman spectroscopy to distinguish precancerous and cancerous tissue from normal tissue. It is the precancerous lesions that have the most significance medically because they are most likely to be treated successfully. It must however be noted that biopsies with mixed pathology were included in the analysis, but spectroscopic results were correlated with the most severe pathological diagnosis. This experimental methodology is unlikely to produce an accurate representation of the changes in inelastic scattering properties with pathology because heterogeneous tissue samples with mixed pathologies have been studied.

The alternative approach of UVRR spectroscopy for the study of normal and malignant cervical tissue has been studied using 257.3nm light.[19] Spectral differences between normal and malignant tissue have been demonstrated to represent changes in the concentrations of nucleic acids relative to cell proteins. Mutagenic effects are likely to prevent the use of this technology in vivo.

---

* A brief description of principal components and other multivariate statistical analysis methods can be found in Appendix 3.

Ovarian tissue has been studied very recently by utilising NIR excitation at 785nm to produce high quality spectra of ex-frozen ovarian tissue in 30 seconds. A prototype fibre-probe was employed to collect the spectra.[121] Principal component analysis was performed and the diagnostically significant principal components were selected using a two-tailed Student t-test. They were entered into a Fisher's linear discriminant analysis algorithm. The resulting separation in the two groups (normal and endometriosis, and cystic and cancerous) was achieved with 93% sensitivity and 87% specificity.[121] Nevertheless, histopathological analysis was not performed on the samples, as a result comparisons made between tissue pathology and spectra are not particularly convincing.

2.3.3 Colon Cancers

The most extensive investigations into UVRR for the analysis of tissue pathology has been carried out in colon tissue by a number of workers to provide resonance enhancement of colon tissue constituents.[86,122,93] It has been shown that at 240nm proteins and aromatic amino acid peaks are observed; and at 250nm selective excitation of nucleic acids is achieved.[122,93] The Raman cross-section of nucleic acids were calculated and demonstrated to be one hundred times greater with 250nm excitation than at 239.6nm.[86] A more recent study involving 100 samples utilised 251nm excitation to produce spectra with a SNR of 20 in integration times of 100s.[123] This study enabled analysis and understanding of biochemical processes in the colon to be improved by modelling tissue spectra from the spectra of 8 likely constituents. The major contributors to colon spectra at this wavelength were found to be guanosine, tryptophan and lipids.[123] UVRR has been performed on both bulk and microtomed specimen with similar results.[124] Once again promise has been shown for understanding of the disease process, but in vivo use of UV-illumination is unlikely to be accepted.

Conventional approaches to Raman spectroscopy of colon tissue have utilised visible excitation at 406.7nm and a triple monochromator system,[118] or NIR excitation at 830nm with a single monochromator system.[81] The signal-to-noise ratios of the NIR spectra were significantly better than those observed with visible excitation and this was possible in shorter integration times. The NIR spectra were made up mainly of protein bands, however by calculating difference spectra between normal and cancerous tissue it was shown to be possible to distinguish an increase in the nucleic acid peaks (at 1662, 1576, 1458, 1340cm^{-1}) and a decrease in lipid peaks in cancerous colonic mucosa.[81]

2.3.4 Hepatic Cancers

The liver is a vital organ and any disease affecting its function can be life threatening. However, it is also fairly rugged and can recover in time from various assaults. It is this property that allows resection of areas of liver with a hot wire during keyhole surgery, causing little effect on the function of the remaining healthy tissue. Consequently, reliable non-invasive detection of abnormal lesions in the liver during laparoscopy would allow immediate removal of abnormal areas, thus reducing the need for secondary procedures. Preliminary work on the evaluation of Raman spectroscopy for the discrimination of liver pathologies has shown promise, although much more work needs to be done. Early work on Raman spectroscopy of human and rabbit livers utilised FT-

Raman technology.[125] This required huge integration times of between 1-4 hours to enable discrimination between normal and cirrotic liver by utilising shifts from protein to lipid dominated spectra respectively. Some promise has been shown in the study of normal and malignant hepatocytes (liver cells), in both cultured cells and human liver cells, using visible illumination (632.8nm) and a dispersion spectrometer.[126] It was shown that discrimination between the samples was possible by using the ratio of the intensities at 1182 and 1156cm^{-1}. It was found to be around 0.73 for normal liver, 1.16 for cirrhotic liver, and 1.3 for cancer. Although the results indicate some promise, it must be noted that only three tissue samples and a few cell cultures were studied.

2.3.5 Skin and Adipose Cancers

Initial work on the skin utilised FT-Raman spectroscopy with 1064nm laser light to distinguish between benign and malignant skin lesions. An average of 250 scans taking a total of 10 minutes were required to provide adequate signal-to-noise ratios.[127,85,128,129] However, the spectra were of sufficient quality for artificial neural networks to successfully discriminate between the data from normal and basal cell carcinoma tissue. Models were tested using leave-one-out cross-validation. Alternatively, peak-area-ratio analysis employing the peaks between 1290-1360 and 1220-1290cm^{-1} was shown to give mean values of 0.67 for normal skin and 1.37 for BCC.[127] Study of malignant melanomas with the same technology resulted in spectra with pretty poor SNRs, although it was indicated that differences in protein conformation, observed by changes in the amide I, amide III and C-C backbone peaks, accompanies changes to malignant melanoma.[128] A significant improvement was demonstrated by measuring tissue samples with NIR excitation (850nm) and a dispersion microspectrometer. Equivalent SNRs were achieved with only a 60 second acquisition time.[130]

A small percentage of malignancies develop in adipose tissue (the fat layer usually underlying the skin) and detection relies upon presentation of symptoms and biopsy. A single study has demonstrated the facility of a near-infrared (830nm) dispersion system to measure adequate quality spectra of human adipose tissue in short timescales (15-60s).[93] Spectra from normal adipose tissue and liposarcoma have been compared and liposarcoma samples were shown to contain increased polyunsaturated lipids, indicated by the discrimination ratio I_{1442}/I_{1667}, which describes lipid CH bend to lipid C=C stretch peak intensity ratios.[93]

2.3.6 Brain Disease

The first Raman spectra of human brain tissues and tumours were measured with a NIR (1064nm) FT-Raman system.[83] Acceptable quality spectra were obtained following spectral accumulation for 120-150 minutes. Raman spectra from the following tissue types were compared: normal grey and white matter, gliomas (grade II and III), acoustic neurinomas (so called because they lead to hearing loss, due to their proximity to the auditory nerve), and central neurocytomas. Distinct differences representing biochemical changes in the tissue were observed.[83]

Further study of the brain for diagnosis of degenerative diseases such as Alzheimer's, Parkinson's and Creutzfeldt-Jacob disease (CJD) with Raman spectroscopy compared both

FT-Raman and visible excitation/dispersion systems.[131] However, it was only possible to measure Raman spectra with 1064nm illumination and the resulting spectra were only of sufficient quality to display significant differences between grey and white brain matter. Samples were destroyed by thermal damage from the laser source in any attempt to acquire spectra with visible illumination.[131] However, recent work utilising NIR (830nm) has enabled spectra of adequate quality for discrimination between Alzheimer's and normal tissue to be acquired in 80 seconds. Mean spectra for each sample were used in a principal component analysis. Two principal components provided discrimination between the normal and abnormal samples with significance of greater than 99.9%.

2.3.7 Malignancies of the Upper Aero-digestive Tract

Although the upper aero-digestive tract includes the tongue, soft and hard palates, pharynx, epiglottis, larynx, oesophagus, stomach and trachea, to date Raman work has been published solely on the oesophagus (and the stomach). However, an increasing number of investigators are evaluating alternative optical techniques for detection of epithelial cancers in this region. The hollow organs enable access to endoscopic investigation and hence potentially Raman spectroscopic analysis.

The pathogenesis of oesophageal adenocarcinoma is very complex. The small body of work investigating the application of Raman spectroscopy for the detection of early cancerous changes in the oesophagus has not fully taken this into account. In section 1.3.1 it was explained that there are potentially at least nine histopathologically different tissues present in a cancerous oesophagus. Although some important preliminary work has been carried out to indicate that Raman spectra can be used to discriminate between normal and cancerous tissue in the oesophagus it will also be necessary to distinguish between all the other pathologies also likely to be present. Following the lessons learned measuring Raman spectra from other tissues, the first spectra of oesophageal tissue were measured with a NIR (850nm) dispersion microspectrometer.[132] Spectra were measured from only three pathological groups of snap-frozen oesophageal mucosa (normal, Barrett's and adenocarcinoma). Spectra were acquired in 15 seconds with 100mW of laser light and five were averaged to achieve good quality, repeatable spectra. Difference spectra have identified glycogen content to be the most significant variance between normal and Barrett's oesophagus. Multivariate analysis was carried out using a factorial discriminant analysis (FDA) model (i.e. principal component analysis followed by linear discriminant analysis). Good separation with pathology was achieved, with 78/79 normal, 117/120 Barrett's and 112/115 adenocarcinoma spectra correctly classified.[133]

Further work utilising 785nm laser excitation and a dispersion spectrometer indicated the possibility of measuring spectra of sufficient quality for multivariate analysis within 30 seconds. A model constructed from 260 spectra was able to differentiate dysplasia from intestinal metaplasia with 77% sensitivity and 93% specificity, using artificial neural networks.[134] Using principal components to separate the same data enabled discrimination between squamous mucosa (normal) and Barrett's or dysplastic tissue, but not discrimination between Barrett's and dysplastic tissue, which is the most clinically significant for the detection of early cancerous changes. It was noted that 250mW focussed

to a 500μm spot did not produce a detectable temperature (<1°C) rise in the biopsy samples in one minute.[134]

2.3.8 Thyroid Cancers

Raman spectroscopy of the thyroid has been investigated recently by only one group. Visible Raman spectroscopy (632.8nm) was used to study microtomed sections of human thyroid tumours.[135] Thyroid tissue from 30 patients (3 carcinomas, 16 adenomas, 11 nodules/goiters) was collected, sectioned and Raman mapped using an automated microscope stage. Spectra were acquired in 30 seconds and the spectra were used to calculate a principal components algorithm that enabled the spectral data to be separated into two groups (papillary and follicular carcinomas; and micro- and macro-adenomas). However, nodular tissue is present in both groups.

2.4 Conclusions

The use of near-infrared (785-860nm) dispersion spectrometers for the measurement of biological samples have been shown to offer spectra with the lowest background fluorescence and highest S/N ratios in the shortest timescales, for most tissue types. Further work is required to identify optimum wavelengths for excitation within this range for each individual tissue. Spectrometer efficiencies are still improving with the inclusion of novel filters and improvements in detector sensitivity in the NIR range. In addition, illumination intensities can potentially be increased to reduce acquisition times.

Small sample numbers and the lack of a thorough understanding of the shortcomings of histopathological analysis have restricted the accuracy of all of the tissue Raman studies published to date. The investigations have been limited to measuring spectral differences between two or three particular pathology types. Unfortunately the medical reality is more complex. Although the early work has proved valuable in demonstrating differences in Raman scattering properties that accompany pathological change, an immense amount of work is required to make this a functional tool. Samples covering the full spectrum of disease in each organ will need to be used to train spectral diagnostic models.

The work of calibrating a spectroscopic diagnostic model with the current 'gold-standard' of histopathological analysis requires a great deal of collaboration with expert pathologists. Discrepancies in tissue classification can be as high as 50% from one pathologist to the next.[6] Therefore it is vital that a number of pathologists with expertise in the disease of interest work together to provide a consensus of opinion on the tissue samples used to train and test the spectral models. In addition, tissue samples are commonly heterogeneous. To enable a precise calibration of a spectral diagnostic algorithm it is essential that only tissue samples with a single pathology are included for measurement. Currently these important steps have not been undertaken by anyone.

Many technical problems must be solved to enable routine use of Raman spectroscopy as an in vivo clinical tool (see Annex I). The use of fibre-optic systems (see Annex II) based upon near-infrared diode laser illumination, filtered probes and a single spectrometer/CCD detector arrangement appears to be the most promising, although radical new designs may be necessary to eradicate the silica Raman signal. With quick integration times, due to high

sensitivity and low tissue fluorescence background signal the NIR system appears to offer the greatest benefits for use in a clinical environment. Current in vivo probe designs tend to sample from the first few 100μms. However, NIR photons are highly scattered in tissue, therefore with improved understanding of photon migration in tissue, imaging of subsurface lesions may become possible.

Studies to date have not shown any significant thermal damage to tissue from high intensity laser illumination for in vivo work (see Annex III). Nevertheless, further studies into the effects of the excitation light on the probed tissue must be carried out prior to routine in vivo work. The effect of temperature rises on the tissue or photochemical reactions caused by the light may have unforeseen consequences.

In the long term it may be possible to use Raman spectroscopy to provide automated diagnosis for a number of conditions. This could be achieved by utilising the differences in spectral features with diagnostic algorithms. The simplest algorithms are based on empirically identified diagnostic features. These differences may be variations in intensity, intensity ratios and the number and location of peaks. However, it is minute changes in spectral shape that may indicate clinically significant biochemical changes that precede or accompany disease processes. Therefore high quality spectra will be required to enable use of multivariate techniques that analyse all the data in a spectrum and thus be more likely to provide the information required for detection of disease. There are a number of multivariate statistical techniques that are being evaluated for discrimination between diseased states and microbiological taxonomy. They include principal component analysis, cluster analysis, linear discriminant analysis and artificial neural networks. A large volume of texts discuss these techniques, although they have not been commonly used for spectral analysis (Appendix 3 discusses these further).

The greatest obstacle to automated medical diagnosis will most likely be the transferability of Raman spectra acquired with different systems. If automated diagnostic algorithms are to be used, it must be possible to purchase an off the shelf spectral library and sort algorithm for a particular disease or tissue type. However this implies the need for spectra from all systems to be corrected to achieve the ideal that is used for calibration of these classification models.

In summary, there is such a small body of work in the area of Raman spectroscopic detection of cancer and pre-cancers, that all contributions will be valuable to improve the understanding of biochemical processes that precede and accompany disease. Moreover much of the published work has demonstrated proof-of-principle and little more at this stage.

Annex I: Raman Spectroscopy for In Vivo Cancer Diagnostics

The employment of Raman spectroscopy in situ for the study of most tissues necessitates the use of fibre optics to deliver and return the signal from the tissue site. There have been a number of fibre probes designs considered.[136] The most popular configuration uses a central excitation fibre surrounded by 6 collection fibres. The total diameter, using 200μm diameter core fibres, is usually a few mm. A small reduction in size would allow the fibre probe to be inserted into a 1mm biopsy needle. Therefore percutaneous assessment of tissues is theoretically possible by utilising the needle probe to sample at depth in tissue, no more invasively than current needle biopsy techniques.

The major problem associated with Raman-fibre probes is that Raman signals are generated by the fibres themselves. The signal is proportional to the length of the fibre and to the excitation light intensity. It can have magnitudes equal to and often greater than that of the sample under study.[137] Fibre signal is generated in the delivery fibre by the excitation light. In addition, a background signal is also generated in the collection fibres by the elastically scattered excitation light returning along the collection fibre. A practical probe design must prevent unwanted signal generated in the delivery fibre from illuminating the sample as well as preventing light elastically scattered by the tissue from entering the collection fibres and generating unwanted signal. Practical examples use holographic notch filters to reject the Rayleigh scattered light from the tissue and a narrow band-pass filter to exclude the silica Raman before the excitation light illuminates the tissue.

An alternative mathematical technique has been proposed to remove the silica Raman interference.[117] This involves acquiring a spectrum of air, by employing the same apparatus as that used on tissue, and subtracting this from the tissue spectra. Although this will compensate for some of the probe signal, less backscattered light will enter the collection fibres with the air measurement, thus reducing the signal contribution in the correction spectrum. In addition shot noise (following the relationship $N \pm \sqrt{N}$, were N is number of counts) will be much greater if the fluorescence is removed post-detection and hence the weaker tissue Raman peaks will be obscured.

Annex II: In Vivo Raman Experiments with Fibre-Probes

The earliest in vivo measurements with a Raman fibre-probe were carried out on a rat, using an FT-Raman spectrometer to measure the signal from leg muscle.[136] The fibres probes utilised were shown to degrade the SNR by 5-10 times relative to measurements with a normal FT-spectrometer. A lower background signal from the silica fibres was observed with 1064nm illumination than at shorter wavelengths. Therefore a more simple probe design is possible for FT-Raman measurements, but the integration times required for adequate spectra have been shown in the above sections to be restrictively long for in vivo work (tens of minutes to hours).

The first practical Raman in vivo probe for human use utilised a multi-fibre design coupled to a NIR-dispersion spectrometer.[138] The device was tested on human skin with 785nm excitation light from a diode laser. The fibre-probe consisited of six collection fibres (NA 0.22) surrounding a single illumination fibre, with no internal filters

incorporated into the probe head. Evaluation of the effect of different fibres in the probe for reduction of fluorescence background was performed. It was shown that Low-OH silica fibres demonstrated the lowest contribution to the signal.[138] In the spectra of muscle and adipose tissue, measured ex vivo in 3 minutes, the silica Raman signal was shown to be 2-5 times greater than the tissue signal in the 900-1700cm^{-1} wavenumber range. Use of background subtraction was able to yield a poor quality tissue spectrum. In vivo measurements with the same probe and spectrometer indicated that spectra measured in 30 seconds from human skin, buccal cheek epithelium, fingernail and teeth were possible.[138] Similar unfiltered probes have been used to measure atherosclerotic plaques with 830nm laser excitation.[139] However, due to the highly scattering nature of the lesions, following subtraction of the fibre-background, acceptable spectra could be acquired in a matter of seconds. In vivo Raman spectra measured from atherosclerotic plaque in femoral arteries during surgery, integrated in 3 seconds was sufficient to identify the strong peak at 960cm^{-1}, attributable to hydroxyapatite.[139] The presence of this peak is clinically significant in that it demonstrates the presence of a calcified atherosclerotic plaque. Nevertheless, use of filterless-fibre-probes make it very difficult to measure normal tissue Raman spectra in acceptable timescales for in vivo use. A demonstration of the difficulty of employing a filter-less fibre probe was given by measuring pure cholesterol. With 350mW of 830nm laser light at the sample, and a 10 second integration time, the background from the silica fibres at 1000cm^{-1} was more than 30 times greater than the Raman signal from the cholesterol.[139]

A recent extensive study measured Raman spectra of biomedical samples using various fibre probe designs incorporating: single fibres, bifurcated fibres, and filtered fibres.[140] All configurations used 2mW of 830nm light from a laser diode passed through a narrow bandpass filter, to remove the spontaneous radiation, coupled to the fibre probes using a lens. The output of the collection fibre/s was passed through a holographic notch filter and imaged onto the spectrometer slit, a single dispersion grating and CCD detector integrated the spectral signal distribution. It was shown that use of a single fibre (400µm diameter, 2 ft long) for transmission and collection produced benzene spectra totally swamped with the fibre background signal in integration times of 5 seconds. A bifurcated probe design with no internal filters employing a single illumination fibre and 6 collection fibres produced adequate benzene spectra but spectra from a chicken fat, a strong biological Raman scatterer, was swamped by the fibre background (greater than 10 times the Raman signal from the tissue).[140] An improved probe design, incorporating a narrow bandpass filter at the exit of the illumination fibre with the illumination fibre surrounded by 16x200µm collection fibres, was evaluated. Spectra of chicken fat measured with the narrow bandpass filtered-probe enabled tissue Raman peaks to be observed, however the spectrum also included silica Raman peaks. It was thus concluded that a narrow bandpass filter was required in the excitation tip and a notch or long pass filter was required to remove the elastically scattered signal from the tissue to reduce silica Raman signal induced in the collection fibre.[140]

Filtered probes have been shown to significantly improve the SNR and remove fluorescence background, although the silica Raman signal has remained. The highest collection efficiency can theoretically be achieved when a single fibre is used for both illumination and collection, giving a complete overlap between illumination and collection light cones.

However, multiple collection fibres reduce silica Raman signal, but have worse collection efficiency at short probe-sample distances.[80] All of the recent work on in vivo fibre-probes for Raman spectroscopy has involved the development of multi-fibre, internally filtered, designs.[80,84,79,141,142]

Improvements in signal efficiency, background reduction and miniaturisation have been the key aims of the most recent studies. A fairly large 12mm diameter fibre-probe, made up of a single 200μm illumination fibre and seven 100μm collection fibres, was used to measure cervical tissue in vivo.[143] The excitation beam was filtered in the tip of the probe with a bandpass filter and the collected light was passed through holographic notch filters to remove the signal at the laser wavelength prior to launch along the collection fibres. With NIR (789nm) excitation light, the time required for an acceptable spectrum to be acquired was 90 seconds.[143] Even with the filtered probe, silica Raman bands were still observed in the tissue spectra, thus obscuring tissue Raman bands below 900cm^{-1}. However, in vivo spectra were shown to exhibit similar peak-intensity-ratios to those that have been used for discrimination between normal and cancerous cervical tissue during in vitro experiments.[84]

A similar probe design incorporating filters and beam steering optics to improve the collection efficiency[80,141] was successfully tested on rat palate and rat oesophagus, with 785nm illumination.[79] This improvement in collection efficiency enabled spectra to be obtained in 10 to 50 seconds. Subtraction of probe background was still a necessity, to elucidate the tissue Raman scattering peaks. In addition, the large size of the probe tip (4cm) was shown to be a problem for the transfer of this method to endoscopic investigation.

Further miniaturisation enabled a 3m long bifurcated fibre-optic probe with a central delivery fibre (low OH-silica 400μm core and silica cladding), 7 collection fibres (300μm core), incorporating bandpass and longpass filters, to be used to measure in vivo Raman spectra during routine gastro-intestinal endoscopy.[142] The fibre-probe was passed through the biopsy channel of the endoscope and placed in contact with the tissue surface. 100mW of NIR laser light (785nm) was used to excite the Raman spectra and a sampling depth of 500μm was achieved. Spectra were integrated for 5 seconds, whilst a shutter blocked the white light from the endoscope. Normal and diseased sites in oesophagus, stomach and colon were biopsied and sent for histopathological analysis following Raman measurement. Effects of probe tip pressure on the tissue were found to be insignificant. A sampling depth of approximately 100μm was achieved. Even in areas where blood was seen to be pooling, measured spectra were uncontaminated so long as the fibre tip in contact with the mucosal surface. Limited sample numbers (400 spectra from 20 patients) were used and no spectral correlation with pathology was performed.[142] Even when utilising filtered probes, the Raman tissue peaks below 1100cm^{-1} were obscured by background signal from the silica fibres. The resulting spectra were pretty noisy showing only the largest four to five peaks.[134]

Finally the most recent modifications to the multi-fibre probe design have lead to in vivo Raman measurements in the coronary arteries of sheep and lambs.[144] A side firing probe design was used to measure Raman spectra with 830nm illumination in 10 to 30 seconds. Spectra with good SNRs were obtained when the probe was in contact with the artery wall. Positioning was achieved by trial and error, therefore a method of giving repeatable

contact will require development. The in vivo Raman spectra were of sufficient quality to define molecular composition of the examined sites.[144] However, during earlier discussions it was pointed out that atherosclerotic plaques exhibit high Raman scattering cross-sections, therefore further improvements in signal levels will be required to achieve in vivo diagnosis of cancerous tissues.

Annex III: Effect of Intense Laser Radiation on Human Tissue

A concern with any Raman technique applied to tissue is the possibility of radiation damage. CCD spectrometers are sufficiently sensitive that laser powers of a few milliwatts generate useful spectra. However, safety limits for exposure of living tissue to laser light are not fully established and will vary for tissue type, wavelength and spot size. It is clear that radiation damage will have to be evaluated if a Raman technique is to be used in vivo.

To achieve a practical Raman signal from tissue it appears that higher intensities of light, than those set by the *British Standard: Radiation safety of laser products*,[145] will be necessary. (This document is currently being updated, so these limits may change in the near future. Additionally it must be noted that these limits are not set for medical exposure but for exposure limits for operators or bystanders.) The British Standard (BS4803) defines a maximum permissible exposure (MPE) as the exposure causing minimum injury that can be observed clinically. Experimental values are provided for eyes and skin. Therefore making the assumption that the tissue being sampled has similar properties as skin, we may compare the exposure to that of the MPE for skin at that wavelength and exposure time. For example Alfano et al (1991)[20] used IR FT Raman spectroscopy to study breast tissue in vitro with 10 $W.cm^{-2}$ for 4-5 minutes. Redd et al (1993)[14] used 0.4-1.0 $W.cm^{-2}$ of 514.5nm light, for a number of minutes to acquire adequate Raman spectra of tissue samples. The MPE to skin for light 400-1400nm for 10 to 30000 seconds is 0.2 $W.cm^{-2}$. Therefore both authors used exposures between five and fifty times the MPE.

All of the studies into Raman spectral measurements of biological tissue that have published illumination intensity data have exceeded the MPE limit. A number of qualitative studies have been carried out to assess the effect of these high intensities on tissue. Mahadevan-Jansen et al (1996)[16] investigated the thermal effects of laser exposures in excess of 0.3 $W.cm^{-2}$ at 789nm. A simulation calculated a rise of 5.6 °C per minute for a laser intensity of 12.73 $W.cm^{-2}$, which is by no means a high intensity for the excitation of Raman scattering in tissue. However it must be noted, the above simulation did not account for the substantial cooling of tissue afforded by blood flow. A study by Shim et al (2000)[134] demonstrated this effect by carrying out in vivo temperature measurements during laser illumination of oesophageal tissue. Laser powers of 250mW of 830nm light were focussed to a 500µm spot. It was shown that no detectable temperature rise (<1°C) occurred in the tissue in 1 minute. Shim and Wilson (1996)[146] evaluated laser heating of tissue with laser powers of 450, 250, 100mW with a 1064nm, Nd:YAG laser source, focussed to a 0.5mm spot size. A thermocouple was placed on the tissue, 1mm from the beam edge, spectra were acquired for 30 minutes at each illumination power. Following measurement the samples were sectioned and histologically analysed for damage to cell viability. For adipose, muscle and liver tissues there was no evidence of heat damage after exposure with

450mW of laser radiation for 30 minutes. In addition, there were no spectral changes observed over the 30 minutes with any laser power. Temperature rises measured for 450mW of laser power with the tissue soaked in PBS (more representative of intracellular fluid) were between 2.3 and 6.7°C, and in dry tissue samples between 2.3 and 26°C. Darker tissues such as lung and liver absorbed a great deal of energy, whereas most others exhibited little absorption.

In vitro measurements on porcine aorta using a multi-fibre probe to illuminate the tissue with 100mW of 830nmlight resulted in a 2°C temperature rise over several minutes.[144] Thus for short periods of illumination with NIR laser light, thermal damage should not occur in most tissues. However, it has been demonstrated that damage thresholds are wavelength dependent.[114] Sample degradation measured in single intact lymphocytes, with a confocal Raman microspectrometer using a x63 water immersion objective (NA 1.2) to focus 10mW of laser power into a 0.5µm spot (5MW cm^{-2}) for wavelengths of 514.5, 633, 660nm. At 514.5 nm, degradation occurred at 0.5-20mW, with visible paling combined with a gradual reduction in Raman signal. Whereas for 660 and 632.8nm, no degradation was observed for under 20mW, although above this level cell death is also caused.

Ultraviolet light has been used fairly extensively to excite the Raman bands of a number of biological substances in vitro. However the ideal application of Raman spectroscopy in medicine is for direct detection of malignancy in vivo, where the use of high-energy photons may cause mutagenic effects. The key parameter is the photon dose required for ultraviolet resonance Raman spectral data acquisition compared to that which causes a significant number of mutagenic alterations in the cells. There is little information available on this at present. Therefore the use of UVRR to study tissue in vivo is unlikely to be accepted until further understanding of the disruptive effect of ultraviolet light on nucleic acids can be achieved. However, the technique has been shown to be valuable in the study of ex vivo tissues, due to the enhancement of Raman scattering in constituents such as DNA that are present in the tissue in lower concentrations than proteins and lipids that dominate the non-resonant spectra. A review on the damaging effects of ultra-violet and visible light on DNA has been presented by Coohill et al (1987).[147]

3. Theory of Raman Scattering

3.1 Introduction

If a monochromatic beam of photons passes through a transparent medium, i.e. where photons of the incident energy will not be absorbed, a fraction will be scattered in all directions. The scattered photons will consist almost entirely of radiation of the incident frequency, ν. This is Rayleigh scattering, an elastic process, whereby no energy is lost from the interacting photon. In addition, a small number of photons will emerge with discrete frequencies above and below that of the incident beam ($\nu \pm \Delta\nu_i$). It is the process that leads to these discrete shifts that is referred to as Raman scattering. These shifts, or Raman frequencies, are independent of the exciting frequency, ν, and are characteristic of the species of molecule giving rise to the scattering.[148] In effect these frequencies represent the vibrational frequencies of the molecules.

Study of vibrational frequencies in tissue samples using infra-red absorption spectroscopy is not always possible due to strong absorption by water and other species. Raman spectroscopy complements infra-red spectroscopy using ultra-violet, visible, or near infra-red excitation. Therefore Raman spectroscopy can be used to probe the vibrational energy levels of molecules within many biological (and non-biological) samples. A Raman spectrum is a plot of scattered intensity as a function of energy difference between the incident and scattered photons. The unit of photon energy (E) is expressed in wavenumbers, the inverse of wavelength (λ) in units of cm^{-1} for convenience, such that;

$$E = h \cdot \nu = \frac{h \cdot c}{\lambda}. \qquad (3.1)$$

Where h is Planck's constant, c is the velocity of light and ν is the frequency of the radiation field. The loss, or gain, in photon energies corresponds to the difference in the final and initial vibrational energy levels of molecules participating in the interaction. A typical Raman peak is spectrally narrow, easy to resolve and sensitive to molecular structure and the surrounding environment. Vibrational spectroscopy techniques can thus provide specific histochemical information from biological tissue, unparalleled by other optical methods. Both vibrational absorption and scattering methods are promising for biomedical applications.

The Raman effect can be induced by light of all frequencies. However, the cross-section for an inelastic scattering process is proportional to λ_{in}^{-4}, where λ_{in} is the wavelength of the incident photon. For example photons of 300nm wavelength have a cross-section of scattering sixteen times greater than photons at 600nm; assuming that there are no resonance effects, which may occur for incident photons having energy near an electronic absorption line of the molecule.

The energy loss (or gain) of the scattered photon is constant for a particular molecular species no matter what frequency of excitation is used. As an example of this, the C=C stretching vibration of the benzene molecule always produces a Raman peak downshifted by 1612 cm^{-1} independent of the frequency of the excitation light.[86] In practice the environment

of the molecular species is important, as local perturbations of the electric fields around it will tend to slightly shift the vibrational energy levels.

The main factors that determine the choice of excitation wavelength for tissue spectroscopy are:

1. The depth of penetration of the light through tissue.
2. The intensity of the induced fluorescence signal at that wavelength, as this can swamp the weaker Raman signal.
3. The availability of an intense source and a sensitive detector at the wavelength selected.

Raman scattering is an inherently weak process. The intensity of the Raman signal is typically 10^{-9} to 10^{-6} of the Rayleigh background.[149] For this reason it is difficult to observe without intense monochromatic excitation and a sensitive detector. There are various methodologies that may be utilised to obtain Raman spectra. The best technique depends upon the application.

It must be noted that the Raman effect occurs without photon absorption by the molecule, but rather the molecule is perturbed by the photon and it is induced to undergo a vibrational or rotational transition. Hence the interaction process between the photon and molecule is very fast, of the order of picoseconds (10^{-12} s), whereas the time for absorption and fluorescence is of the order of nanoseconds (10^{-9} s).[150]

3.2 Classical Theory

When light is incident upon a molecule, it's varying electric field,

$$\underline{E}_{in}(t) = \underline{E}_o \sin(2\pi\nu_{in}t), \qquad (3.2)$$

induces an oscillating dipole, which re-emits (scatters) the light at the frequency of the dipole oscillation. An assumption is made that the entire molecule is within a homogeneous incident electric field and that the incident light is monochromatic, with frequency ν_{in}. In practice the time-varying dipole moment, $\underline{p}(t)$, will consist of many different harmonic frequency components, each of which can be described by the following equation:

$$\underline{p}(t) = \underline{p}_o \sin(2\pi\nu_{sc}t) \qquad (3.3)$$

where ν_{sc} is the frequency (in Hertz) of the scattered light and $\underline{p}_o$ is the maximum induced dipole moment for a given frequency component. The induced dipole moment can be approximated by

$$\underline{p}(t) = \alpha\underline{E}_{in}(t) \qquad (3.4)$$

where α is the polarisability of the molecule. The polarisability describes the ease with which molecular orbits can be distorted by the presence of an external electric field. An oscillating dipole will radiate light in all directions at all frequency components of the dipole oscillation; the component of scattered light due to dipole oscillations at $\nu_{sc} = \nu_{in}$ is called Rayleigh scatter.

If a molecule undergoes some internal motion whilst oscillating in an electric field, such as vibration or rotation that periodically changes the polarisability, then the oscillating dipole will have the vibrational or rotational oscillation superimposed on it. For example, we can write an expression for the time-dependent nature of the polarisability by performing a Taylor expansion about the equilibrium position of the atoms, Q_0, expressed in normal coordinates, giving us

$$\alpha = \alpha_o + \left(\frac{\partial \alpha}{\partial Q}\right)_0 Q + \frac{1}{2}\left(\frac{\partial^2 \alpha}{\partial Q^2}\right)_0 Q^2 + \ldots \qquad (3.5)$$

where α_o is the polarisability at rest and $(\partial\alpha/\partial Q)_0$, known as the derived polarisability, represents the rate of change of polarisability with respect to Q, the displacement from the equilibrium position of the vibrational mode ($Q = Q_0 \sin(2\pi\nu_{vib}t)$). If we consider the vibrational frequency ν_{vib} that changes the polarisability, and neglect higher powers of Q, for small displacements along the normal coordinate, expression (3.5) becomes

$$\alpha = \alpha_0 + \left(\frac{\partial \alpha}{\partial Q}\right)_0 Q_0 \sin(2\pi\nu_{vib}t) \qquad (3.6)$$

Inserting (3.2) and (3.6) into expression (3.4) gives us

$$\underline{p}(t) = \alpha \underline{E}_{in}(t) = \left(\alpha_0 + \left(\frac{\partial \alpha}{\partial Q}\right)_0 Q_0 \sin(2\pi\nu_{vib}t)\right) \bullet (\underline{E}_o \sin(2\pi\nu_{in}t)).$$

Using the trigonometric expression

$$\sin A \sin B = \frac{1}{2}\{\cos(A-B) - \cos(A+B)\}$$

leads to

$$\underline{p}(t) = \underline{\alpha}_o \underline{E}_o \sin(2\pi\nu_{in}t) + \frac{1}{2}\left(\frac{\partial \alpha}{\partial Q}\right)_0 Q_0 \underline{E}_o \{\cos 2\pi(\nu_{in} - \nu_{vib})t - \cos 2\pi(\nu_{in} + \nu_{vib})t\}. \qquad (3.7)$$

Thus from expression (3.7) it can be seen that an oscillating dipole will have frequency components equal to $\nu_{in} \pm \nu_{vib}$ as well as the exciting frequency ν_{in}. If the vibrational mode of the molecule does not alter the polarisability of the molecule then $(\partial\alpha/\partial Q)_0 = 0$. Hence the components of the dipole moment, in expression (3.7), are reduced to those containing only the frequency of the incident radiation, ν_{in}. Therefore, for a rotational or vibrational mode to be Raman active it must cause some change in a component of the molecular polarisability.

3.2.1 Tensor Character of Polarisability

Scatter from isotropic molecules is characterised by the fact that the direction of $\underline{p}$ and $\underline{E}_{in}$ are always parallel and the magnitude of $\underline{p}$ is independent of the orientation of the

molecule and $\underline{E}_{in}$. However, when light is incident on a stationary anisotropic molecule, in general the induced dipole moment, $\underline{p}$, will not be aligned with $\underline{E}_{in}$. If we let E_x, E_y, E_z be the components of the electric field vector relative to a cartesian coordinate system and consider a fixed, non-rotating molecule, then the components of the induced dipole moment can be written as follows

$$\begin{aligned} P_x &= \alpha_{xx}E_x+\alpha_{xy}E_y+\alpha_{xz}E_z \\ P_y &= \alpha_{yx}E_x+\alpha_{yy}E_y+\alpha_{yz}E_z \\ P_z &= \alpha_{zx}E_x+\alpha_{zy}E_y+\alpha_{zz}E_z. \end{aligned} \qquad (3.8)$$

It can be seen from these expressions that an incident electric field parallel to one cartesian axis can induce a dipole moment along a perpendicular axis, so long as the relevant polarisability is non-zero.

Thus the polarisability tensor α_{ij} is defined by an array of nine components $\begin{pmatrix} \alpha_{xx} & \alpha_{xy} & \alpha_{xz} \\ \alpha_{yx} & \alpha_{yy} & \alpha_{yz} \\ \alpha_{zx} & \alpha_{zy} & \alpha_{zz} \end{pmatrix}$, where the first subscript denotes the direction of the induced dipole, and the second the direction of the applied electric field.

Thus $(\partial\alpha/\partial Q)_{ij}$, the derived-polarisability tensor, the first-order term component of the polarisability tensor, will give rise to the inelastic Raman scattering. It should be noted that since a non-linear molecule of atoms has 3n-6 normal coordinates, there will also be 3n-6 derived-polarisability terms, with each normal mode of Raman active vibration arising from the corresponding derived-polarisability tensor.

3.3 Quantum Theory

In the quantum mechanical concept molecules gain or lose sums of energy only in accordance with the laws of quantum physics. Thus, a molecule's change in energy, ΔE, on excitation with $h\nu_{in}$ must be equivalent to the difference in energy between two of its allowed states. ΔE must represent a change in the vibrational and/or rotational energy of the molecule. During the interaction if the molecule gains ΔE, the photon is scattered with energy ($h\nu_{in}$-ΔE), this is called Stokes radiation. If the molecule loses ΔE, the photon is scattered with energy ($h\nu_{in}$+ΔE), this is called anti-Stokes radiation.

At room temperature the number of molecules in an excited vibrational state will be low. This can be shown by using Boltzmann's equation.

$$\frac{N_v}{N_0} = \exp\left(-\frac{E_v}{kT}\right) \qquad (3.9)$$

Where N_v/N_0 is the fraction of molecules in the vibrational state; E_v is the energy of the vibrational state; k is Boltzmann's constant and T is the absolute temperature. For example the C=C stretch oscillation (1612 cm^{-1} shift) of a benzene ring requires 1.99×10^{-20} Joules of energy to excite the oscillation from the ground state. Using equation (3.9)

the fraction of benzene molecules in the excited vibrational state at 20°C is 0.0078. Hence it is obvious that, at room temperature, incident photons are much less likely to encounter molecules in an excited state. Therefore the likelyhood of Stokes' radiation, whereby the molecule captures a portion of the incident photon's energy is that much greater than the alternative anti-Stokes, since the anti-Stokes' radiation can only occur if the molecule is in an excited vibrational or rotational state.

Soon after C.V. Raman's experimental discovery of the inelastic scattering of photons,[87] Placzek,[151] Dirac[152] and others developed classical, semi-classical and quantum-mechanical theoretical approaches. The full treatment of light scattering using quantum mechanics would require the incident radiation and the scattering molecule to be considered as quantum particles. This would call for the introduction of relativistic effects on the particles, which is beyond the scope of this thesis. A close approximation can be achieved if the incident electromagnetic wave is treated as a perturbation of the wavefunction of the scattering molecule. The perturbation due to the incident radiation produces a time-dependent virtual state. An expression can be derived for the polarisability of the molecule from the second-order perturbation theory. This method is based upon the Kramers-Heisenberg dispersion theory[153] and Dirac's second-order time-dependent perturbation theory.[152] It is generally known as the 'sum-over-states' method because the contributions to the Raman scattering intensity, arising from the coupling between the initial, intermediate and final states, are summed over all possible intermediate states. The following section outlines the derivation of an expression for the intensity of scattered light by a system of N molecules based upon the 'sum-over-states' method.

3.3.1 Perturbation Theory

In the quantum-mechanical description of the scattering of light photons we are interested in the change in the vibrational energy levels, and hence the wave functions, which will occur when the molecule is placed within an external electric field. The fields produced by the incident radiation are usually small in comparison with the internal Coulomb fields in the molecule. Therefore the effect of the external field may be regarded as a small correction to the wave function. This correction is usually referred to as a perturbation.

Firstly we will begin by looking at the interaction between an individual molecule and the electric field of the incident electro-magnetic radiation. If the linear dimensions of the molecule are much smaller than the wavelength of the incident radiation, the phase change within the molecule may be neglected. Hence the field inside the molecule may be taken to be $\underline{E} = \underline{E}_0 \cos(\omega t)$ and is the same at all points inside the molecule at a given time t, where $\omega = 2\pi\nu_{in}$ is the frequency of the incident radiation and $\underline{E}_0$ is the maximum electric field vector of the incident radiation.

Let the molecule be in an energy state E_n before the light wave is in effect 'switched on'. The corresponding wave function describing this state is $\Psi_n^0(\underline{r},t)$. When the light field is 'switched on', the state of the molecule is modified. If we suppose that this new state is

described by $\Psi_n(\underline{r},t)$ and this function must satisfy the time-dependent Schrödinger equation

$$i\hbar\frac{\partial\Psi_n}{\partial t} = H^0\Psi_n + W\Psi_n \qquad (3.10)$$

where H^0 is the total energy operator for the system in the absence of the light wave and W is the perturbation due to this wave, described simply as;

$$W(\underline{r},t) = e(\underline{E}_0.\underline{r})\cos(\omega t) \qquad (3.11)$$

which is in effect the potential energy of an electron in the oscillating electric field $\underline{E}$; at a position, $\underline{r}$, relative to the nucleus; where e is the electric charge of an electron. ψ_n can be expanded as:

$$\Psi_n(\underline{r},t) = \psi_n^0(\underline{r})e^{-i\omega_n t} + U_n(\underline{r})e^{-i(\omega_n-\omega)t} + V_n(\underline{r})e^{-i(\omega_n+\omega)t} \qquad (3.12)$$

where $\omega_n = E_n/\hbar$ and U_n and V_n are the required corrections to the state function, Ψ_n^0, for the undisturbed system, to account for the effects of the electric field on the system. In an undisturbed system

$$H^0\Psi_n^0 = E_n\Psi_n^0. \qquad (3.13)$$

Combining expressions (3.12), (3.11) and (3.10) and, as a first approximation, neglecting the products $W.U_n$ and $W.V_n$, since these terms are proportional to $|\underline{E}_o^2|$ and therefore correspond to the second-order electric field approximation leads to

$$\hbar(\omega_n-\omega)U_n e^{i\omega t} + \hbar(\omega_n+\omega)V_n e^{-i\omega t} = H^0U_n e^{i\omega t} + H^0V_n e^{-i\omega t} + e(\underline{E}_0.\underline{r})\frac{e^{i\omega t}+e^{-i\omega t}}{2}\psi_n^0.$$

By equating the coefficients of corresponding terms of $e^{i\omega t}$ and $e^{-i\omega t}$ we obtain the following equations for U_n and V_n

$$\hbar(\omega_n-\omega)U_n = H^0U_n + \frac{e(\underline{E}_0.\underline{r})}{2}\psi_n^0 \qquad (3.14a)$$

$$\hbar(\omega_n+\omega)V_n = H^0V_n + \frac{e(\underline{E}_0.\underline{r})}{2}\psi_n^0. \qquad (3.14b)$$

These equations can be solved by expanding U_n and V_n in terms of the orthogonal functions ψ_n^0.

$$U_n = \sum_l A_{nl}\psi_l^0 \qquad (3.15a)$$

$$V_n = \sum_l B_{nl}\psi_l^0 \qquad (3.15b)$$

By substituting expressions (3.15a) and (3.15b) into (3.14a) and (3.14b) respectively and remembering that for an undisturbed system $H^0\Psi_n^0 = E_n\Psi_n^0$, we have

$$\hbar \sum_l A_{nl}(\omega_n - \omega_l - \omega)\psi_l^0 = \frac{e(\underline{E}_0.\underline{r})}{2}\psi_n^0 \qquad (3.16a)$$

$$\hbar \sum_l B_{nl}(\omega_n - \omega_l + \omega)\psi_l^0 = \frac{e(\underline{E}_0.\underline{r})}{2}\psi_n^0. \qquad (3.16b)$$

By multiplying both sides of these equations by ψ_k^{0*} and integrating over all space, bearing in mind that ψ_k^{0*} and ψ_l^0 are orthogonal, we have

$$\hbar(\omega_n - \omega_k - \omega)A_{nk} = \frac{e}{2}\int \psi_k^{0*}(\underline{E}_0.\underline{r})\psi_n^0 d\tau \qquad (3.17a)$$

$$\hbar(\omega_n - \omega_k + \omega)B_{nk} = \frac{e}{2}\int \psi_k^{0*}(\underline{E}_0.\underline{r})\psi_n^0 d\tau\,. \qquad (3.17b)$$

The quantum-mechanical expression for the dipole moment, $\underline{D}_{kn}$, induced by the field $\underline{E}(t)$ that corresponds to the transition from state k to state n is expressed as:

$$\underline{D}_{kn} = -e\int \Psi_k^{0*}(\underline{r},t).\underline{r}.\Psi_n^0(\underline{r},t)d\tau\,. \qquad (3.18)$$

so that we may rewrite equations (3.17a) and (3.17b) as

$$A_{nk} = -\frac{\underline{E}_0.\underline{D}_{kn}}{2\hbar(\omega_{nk} - \omega)} \qquad (3.19a)$$

$$B_{nk} = -\frac{\underline{E}_0 D_{kn}}{2\hbar(\omega_{nk} + \omega)} \qquad (3.19b)$$

where $\omega_{nk} = (\omega_n - \omega_k)$ is the transition frequency between energy states n and k.

It must be noted that the above expressions are only valid for frequencies of incident radiation that are not too close to one of the natural frequencies of the molecule, ω_{nk}. It is possible to take into account Raman scattering that occurs at or near resonance by introducing a damping constant into the denominator, which describes the finite lifetime of each molecular state. However, the quantum-mechanical treatment for resonance Raman is beyond the scope of this chapter, it is explained further in a number of texts.[148,154]

If we substitute the above expressions for A_{nk} and B_{nk} into (3.15a) and (3.15b) and the expressions for U_n and V_n into (3.12) we can obtain an approximation for the wave function of the system when the incident radiation is 'switched on'.

$$\Psi_n(\underline{r},t) = \psi_n^0(\underline{r})e^{-i\omega_n t} - \frac{e^{-i(\omega_n-\omega)t}}{2\hbar}\sum_k \frac{\underline{E}_0.\underline{D}_{kn}}{\omega_{nk} - \omega}\psi_k^0(\underline{r}) - \frac{e^{-i(\omega_n+\omega)t}}{2\hbar}\sum_k \frac{\underline{E}_0.\underline{D}_{kn}}{\omega_{nk} + \omega}\psi_k^0(\underline{r}) \qquad (3.20)$$

If we now calculate the dipole moment $\underline{p}_{nn}(t)$, which is induced by the field $\underline{E}$ in the state Ψ_n^0, the electric dipole moment of the new state $\Psi_n(\underline{r},t)$ is given by

$$\underline{p}_{nn} = -e\int \Psi_n^*(\underline{r},t)\underline{r}.\Psi_n(\underline{r},t)dv = -e\iint \left|\Psi_n(\underline{r},t)\right|^2 .\underline{r}.d\tau\,. \qquad (3.21)$$

The square of the modulus of the wave function can be approximated to within first-order terms in $\underline{E}_0$ as

$$\begin{aligned}\left|\Psi_n(\underline{r},t)\right|^2 = \left|\psi_n^0\right|^2 &- \frac{e^{i\omega t}}{2\hbar}\sum_k \frac{\underline{E}_0.\underline{D}_{kn}}{\omega_{nk}-\omega}\psi_n^{0*}\psi_k^0 - \frac{e^{-i\omega t}}{2\hbar}\sum_k \frac{\underline{E}_0.\underline{D}_{kn}}{\omega_{nk}+\omega}\psi_n^{0*}\psi_k^0 - \\ &- \frac{e^{-i\omega t}}{2\hbar}\sum_k \frac{\underline{E}_0.\underline{D}_{kn}^*}{\omega_{nk}-\omega}\psi_k^{0*}\psi_n^0 - \frac{e^{i\omega t}}{2\hbar}\sum_k \frac{\underline{E}_0.\underline{D}_{kn}^*}{\omega_{nk}+\omega}\psi_k^{0*}\psi_n^0 .\end{aligned} \qquad (3.22)$$

Therefore by substituting into (3.21) and using expression (3.18) to simplify we obtain

$$\begin{aligned}\underline{p}_{nn}(t) = \underline{D}_{nn} &- \frac{e^{i\omega t}}{2\hbar}\sum_k \left\{\frac{(\underline{E}_0.\underline{D}_{kn})\underline{D}_{kn}^*}{\omega_{nk}-\omega} + \frac{(\underline{E}_0.\underline{D}_{kn}^*)\underline{D}_{kn}}{\omega_{nk}+\omega}\right\} - \\ &- \frac{e^{-i\omega t}}{2\hbar}\sum_k \left\{\frac{(\underline{E}_0.\underline{D}_{kn})\underline{D}_{kn}^*}{\omega_{nk}+\omega} + \frac{(\underline{E}_0.\underline{D}_{kn}^*)\underline{D}_{kn}}{\omega_{nk}-\omega}\right\}.\end{aligned} \qquad (3.23)$$

We can see from expression (3.23) that the electric-dipole moment $\underline{p}_{nn}(t)$ is made up of two components: a time independent dipole moment $\underline{D}_{nn}$ and the induced dipole moment, which depends linearly on the electric field strength. $\underline{D}_{nn}$ is the mean electric dipole moment of the atom or molecule in the state n. The induced dipole moment is a periodic function of time and has a frequency equal to the frequency of the incident radiation ω. The phase of the oscillating dipole moment is directly related to the phase of the electric field vector in the incident radiation. This moment represents coherent scattering or Rayleigh scattering.

To describe an inelastic scattering process using the above terminology it is necessary to consider the additional dipole moment, $\underline{p}_{mn}$, that is induced by incident radiation in a quantum mechanical system during its transition from state m to another state n. This can be described by developing expression (3.21)

$$\underline{P}_{mn}(t) = -e\int \Psi_m^*(\underline{r},t)\underline{r}.\Psi_n(\underline{r},t)dv \qquad (3.24)$$

State $\Psi_n(\underline{r},t)$ results from $\psi_n^0(\underline{r})\exp(-i\omega_n t)$ under the influence of the incident radiation and state $\Psi_m(\underline{r},t)$ results from $\psi_m^0(\underline{r})\exp(-i\omega_m t)$ under the influence of the same radiation. By substituting into (3.20) we obtain

$$\Psi_n(\underline{r},t) = \psi_n^0(\underline{r})e^{-i\omega_n t} - \frac{e^{-i(\omega_n-\omega)t}}{2\hbar}\sum_k \frac{\underline{E}_0.\underline{D}_{kn}}{\omega_{nk}-\omega}\psi_k^0(\underline{r}) - \frac{e^{-i(\omega_n+\omega)t}}{2\hbar}\sum_k \frac{\underline{E}_0.\underline{D}_{kn}}{\omega_{nk}+\omega}\psi_k^0(\underline{r}) \qquad (3.25a)$$

and

$$\Psi_m^*(\underline{r},t)=\psi_m^0(\underline{r})e^{i\omega_m t}-\frac{e^{i(\omega_m-\omega)t}}{2\hbar}\sum_k\frac{\underline{E}_0.\underline{D}_{km}}{\omega_{mk}-\omega}\psi_k^0(\underline{r})-\frac{e^{i(\omega_m+\omega)t}}{2\hbar}\sum_k\frac{\underline{E}_0.\underline{D}_{km}}{\omega_{mk}+\omega}\psi_k^0(\underline{r})$$

(3.25b)

These can then be inserted into (3.24) to provide us with the following expression

$$\underline{P}_{mn}(t)=\underline{D}_{mn}e^{i\omega_{mn}t}+\underline{D}_{mn}^{(+)}e^{i(\omega_{mn}+\omega)t}+\underline{D}_{mn}^{(-)}e^{i(\omega_{mn}-\omega)t} \qquad (3.26)$$

where
$$\underline{D}_{mn}^{(+)}=-\frac{1}{2\hbar}\sum_k\left\{\frac{(\underline{E}_0.\underline{D}_{kn})\underline{D}_{mk}}{\omega_{nk}-\omega}+\frac{(\underline{E}_0.\underline{D}_{mk})\underline{D}_{kn}}{\omega_{mk}+\omega}\right\} \qquad (3.27a)$$

$$\underline{D}_{mn}^{(-)}=-\frac{1}{2\hbar}\sum_k\left\{\frac{(\underline{E}_0.\underline{D}_{kn})\underline{D}_{mk}}{\omega_{nk}+\omega}+\frac{(\underline{E}_0.\underline{D}_{mk})\underline{D}_{kn}}{\omega_{mk}-\omega}\right\} \qquad (3.27b)$$

The dipole moment $\underline{D}_{mn}$ is a periodic function of time with a frequency ω_{mn}, there are two further dipole moments induced by the incident radiation for which the frequencies are given by $\omega=\omega_{mn}\pm\omega$. The dipole moment $\underline{D}_{mn}$ determines the emission and absorption of radiation for the transitions $E_m \Leftrightarrow E_n$. The additional dipole moments $\underline{D}_{mn}^{(+)}$ and $\underline{D}_{mn}^{(-)}$ are responsible for the inelastic scattering of the incident radiation. The change in frequency is given by the sum or the difference of the frequency of the incident radiation, ω, and one of the natural frequencies $\omega_{mn}=\frac{E_m-E_n}{\hbar}$ of the system. In order to determine the intensity of the scattered radiation, it is necessary to use the correspondence principle, which states that an atom or molecule emits and absorbs radiation as if it were a set of classical oscillators.

From equation (3.26) we can see that we have three oscillators to take into account: $\underline{D}_{mn}e^{i\omega_{mn}t}$, $\underline{D}_{mn}^{(+)}e^{i(\omega_{mn}+\omega)t}$, $\underline{D}_{mn}^{(-)}e^{i(\omega_{mn}-\omega)t}$.

Blokhintsev (1964)[155] showed that using Einstein's equation for the probability of absorption per second of a photon with energy, $\hbar\omega_{mn}=(E_m-E_n)$, it is possible to derive an expression for the radiation emitted per second into a solid angle dΩ as a result of the transition $m \rightarrow n$. By taking into account θ_{mn} the angle between the dipole vector $\underline{D}_{mn}$ and the direction of propagation of the incident radiation and integrating over the total solid angle Ω an expression for the total radiation emitted per second can be obtained

$$\frac{dE}{dt}=\frac{\omega_{mn}^4}{32\pi^2\varepsilon_0 c^3}\left|\underline{D}_{mn}\right|^2. \qquad (3.28)$$

This expression can be modified to yield the following equations for the scattering intensity at the frequencies $\omega'=\omega_{mn}+\omega$ and $\omega''=\omega_{mn}-\omega$

Anti-stokes scattering:
$$\frac{dE'}{dt} = \frac{(\omega_{mn} + \omega)^4}{32\pi^2 \varepsilon_0 c^3} \left| \underline{D}_{mn}^{(+)} \right|^2 \qquad (3.29a)$$

Stokes scattering:
$$\frac{dE''}{dt} = \frac{(\omega_{mn} - \omega)^4}{32\pi^2 \varepsilon_0 c^3} \left| \underline{D}_{mn}^{(-)} \right|^2 \qquad (3.29b)$$

In order to determine the absolute intensity of the scattered radiation at the frequencies ω' and ω'', equation (3.29a) must be multiplied by the number of atoms, N_m in the excited state m (see Figure 3.1), and equation (3.29b) by the number of atoms, N_n in the lower energy state n.

Anti-Stokes scattering intensity:
$$I' = N_m \frac{(\omega_{mn} + \omega)^4}{32\pi^2 \varepsilon_0 c^3} \left| \underline{D}_{mn}^{(+)} \right|^2 \qquad (3.30a)$$

Stokes scattering intensity:
$$I'' = N_n \frac{(\omega_{mn} - \omega)^4}{32\pi^2 \varepsilon_0 c^3} \left| \underline{D}_{mn}^{(-)} \right|^2 \qquad (3.30b)$$

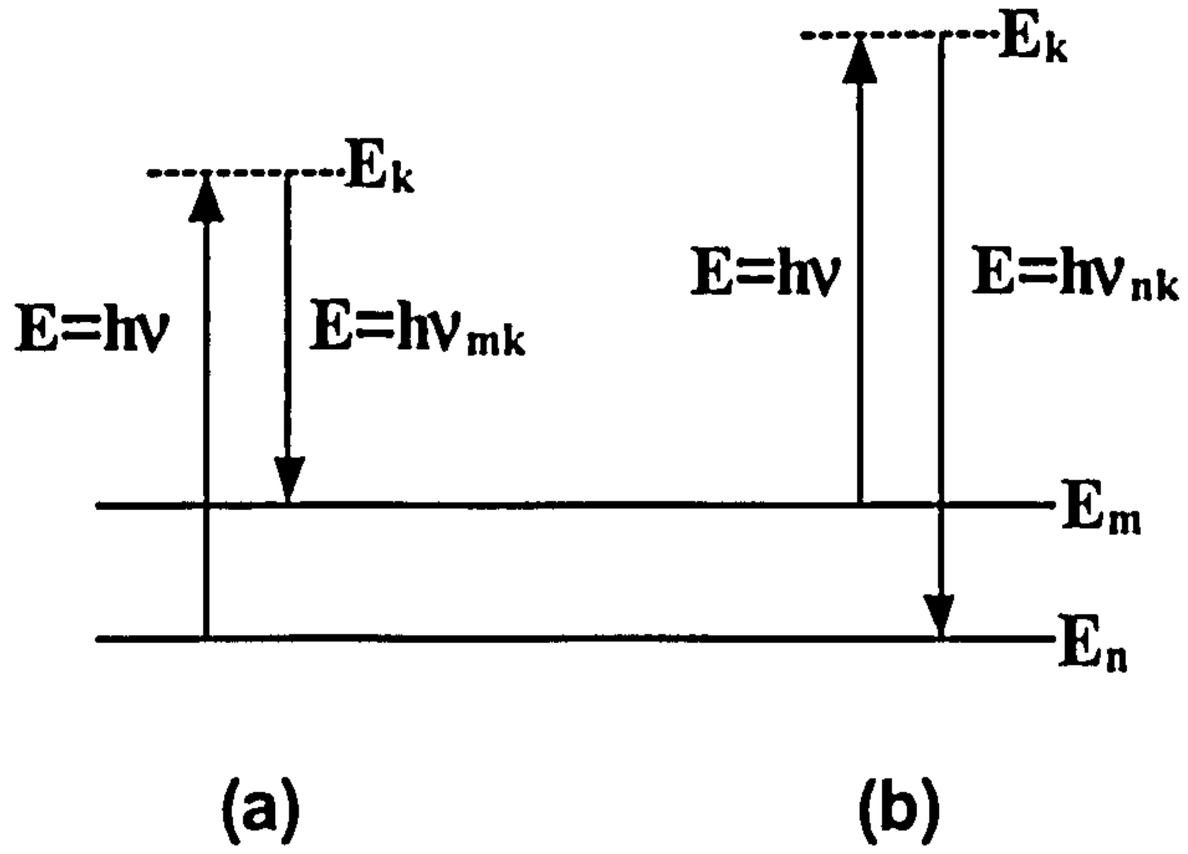

Figure 3.1 Diagram showing the energy states of a system involved in Stokes (a) and anti-Stokes Raman scattering (b).

Finally, the above expressions can be developed to yield a description of the scattering intensity in terms of the intensity of the incident light, I_0, and the molecular polarisability, α. The time-averaged value of the magnitude of the Pointing vector[156,157]

$$\langle \underline{S} \rangle = I_0 = \frac{c\varepsilon_o}{2} \left| \underline{E}_0 \right|^2 \qquad (3.31)$$

gives us the irradiance or energy per unit area per unit time incident upon the scattering molecule. By manipulating (3.27a) and (3.27b) we can obtain

$$\underline{D}_{mn}^{(+)} = \frac{|\underline{E}_0|}{2} \bullet \left(-\frac{1}{h} \sum_k \left\{ \frac{\underline{D}_{kn} \cdot \underline{D}_{mk}}{\nu_{nk} - \nu} + \frac{\underline{D}_{mk} \cdot \underline{D}_{kn}}{\nu_{mk} + \nu} \right\} \right) \qquad (3.32a)$$

$$\underline{D}_{mn}^{(-)} = \frac{|\underline{E}_0|}{2} \bullet \left(-\frac{1}{h} \sum_k \left\{ \frac{\underline{D}_{kn} \cdot \underline{D}_{mk}}{\nu_{nk} + \nu} + \frac{\underline{D}_{mk} \cdot \underline{D}_{kn}}{\nu_{mk} - \nu} \right\} \right) \qquad (3.32b).$$

The components within the round-brackets in equations (3.32) are in effect components of the polarisability tensor of the molecule, which can be written in the more general form, to take into account all orientations of the molecules,

$$(\alpha_{ij})_{mn} = -\frac{1}{h} \sum_k \left\{ \frac{(D_i)_{kn}(D_j)_{mk}}{\nu_{nk} - \nu} + \frac{(D_i)_{mk}(D_j)_{kn}}{\nu_{mk} + \nu} \right\} \qquad (3.33)$$

where the i^{th} element represents the direction of the induced dipole moment and j^{th} element represents the direction of the incident electric vector.

Therefore by substituting (3.33) into (3.32) summing over all orientations of the scattering molecules and then combining with (3.31) we can develop expressions (3.30a) and (3.30b) to give us

anti-Stokes scattering intensity: $I' = \frac{\pi^2}{4c^4\varepsilon_0^2} \cdot N_m \cdot I_0 \cdot (\nu_{mn} + \nu)^4 \cdot \sum_{ij} \left| (\alpha_{ij})_{mn} \right|^2$ (3.34a)

Stokes scattering intensity: $I'' = \frac{\pi^2}{4c^4\varepsilon_0^2} \cdot N_n \cdot I_0 \cdot (\nu_{mn} - \nu)^4 \cdot \sum_{ij} \left| (\alpha_{ij})_{mn} \right|^2$ (3.34b).

These expressions can be reduced to

$$\sigma'_{mn} = \frac{I'}{I_0 \cdot N_m} = K \cdot (\nu_{mn} + \nu)^4 \cdot \sum_{ij} \left| (\alpha_{ij})_{mn} \right|^2 \qquad (3.35a)$$

$$\sigma''_{mn} = \frac{I''}{I_0 \cdot N_n} = K \cdot (\nu_{mn} - \nu)^4 \cdot \sum_{ij} \left| (\alpha_{ij})_{mn} \right|^2 \qquad (3.35b)$$

to give us expressions for the cross sections for Raman scattering, σ, in terms of the scattered intensity per molecule, per incident irradiance, for a given vibrational mode. K is a constant. In the situation where the excitation energy of the photons is far from that required to excite electronic absorption, as in the case of using near-infrared light, e.g. $\nu_{nk} >> \nu$, then the polarisability tensor is approximately independent of the frequency (equation 3.33). This allows us to understand the relationship between the Raman scattering intensity and the frequency of the incident light using the remaining function of ν in expressions 3.35. For individual vibrational modes the frequency dependence of the scattering intensity will vary slightly.

Rearranging expression (3.35)

$$\frac{\sigma_{mn}}{K \cdot \left(\sum_{ij} \left| (\alpha_{ij})_{mn} \right|^2 \right)} = K' = (\nu_{mn} \pm \nu)^4 \qquad (3.36)$$

which gives us an expression for a new factor of proportionality, K' and

$$\ln K' = 4 \ln(\nu_{mn} \pm \nu) \qquad (3.37)$$

when $\nu >> \nu_{mn}$ (for $\nu_{mn} \approx 0$), becomes a linear relationship and σ_{mn} is proportional to λ^{-4}. Log-log plots of the relative scattering cross-section for two Raman lines with widely different values of ν_{mn} are shown in Figure 3.2. Deviation from the ideal λ^{-4} dependency of the scattering cross-section is shown to be greater for larger values of ν_{mn}. For higher frequencies of laser excitation, where energies approach those to excite electronic absorption Albrecht[158,159] has provided an expression for the scattering cross-section taking into account the dependency of the polarisability tensor on the incident frequency (not included here).

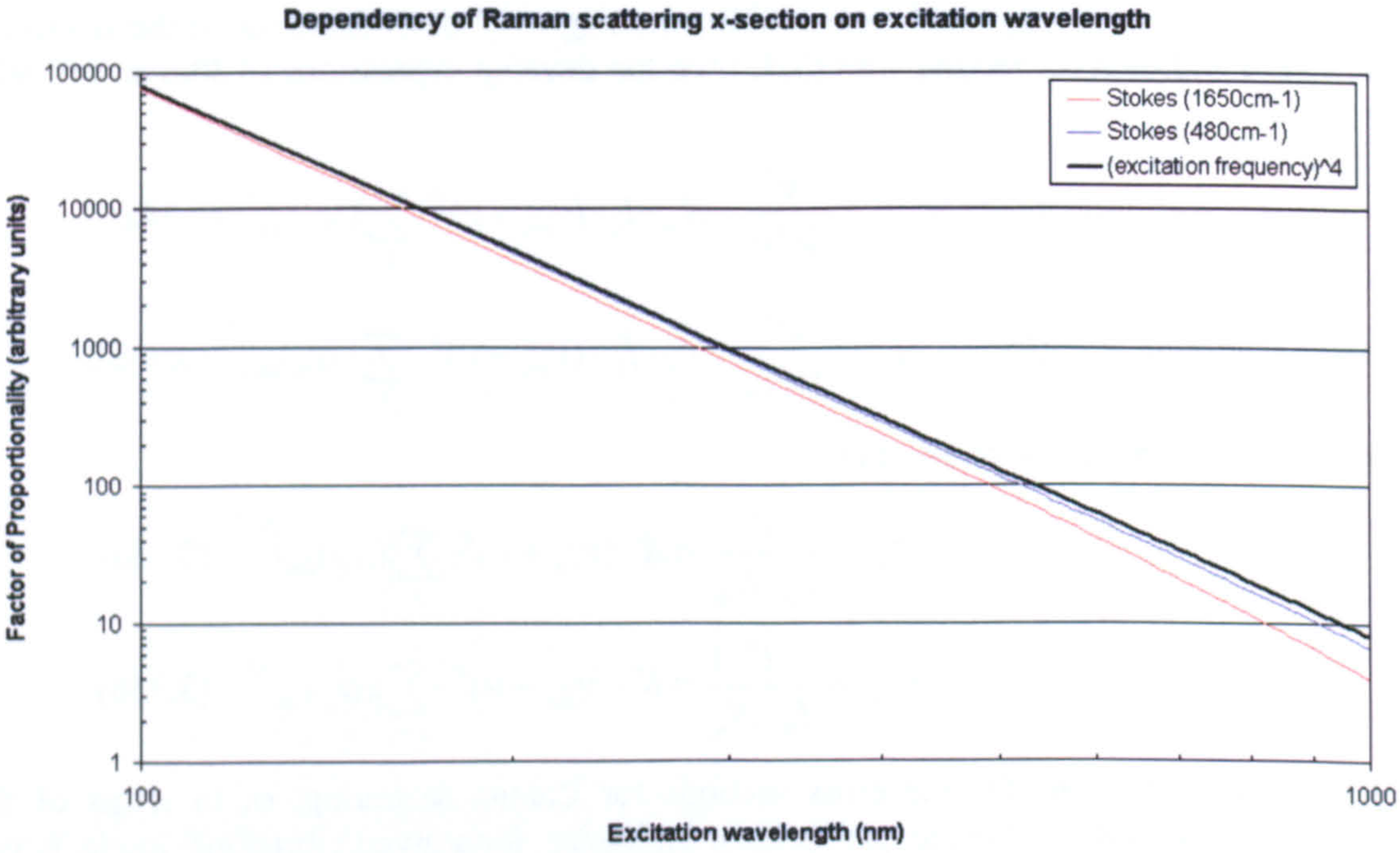

Figure 3.2: Log-log plot of the relationship between Raman scattering cross-sections and excitation wavelength for two Raman scattering peaks. The relationship depends upon the fourth power of the sum or the difference of the excitation frequency and the vibrational frequency of the peak. See equations 3.36.

4. Materials and Methods

4.1 Materials

The biological tissues studied in this work were selected because they exhibited the characteristic that the development of cancer in these tissues passes through an intermediate neoplastic (abnormal) step, which may be detected to allow treatment prior to invasion of deeper tissues.

4.1.1 Larynx Tissue

Thirty-five patients participated in this preliminary study. Their ages ranged from 18 to 79 years of age, with a median of 53 years of age. Informed consent was obtained from each patient and the study was approved by the United Kingdom South and West Local Research Ethics Committee.

Forty-one biopsy specimens ($3x3x3mm^3$) were collected during routine surgical procedures (microlaryngoscopy) and snap frozen in liquid nitrogen. Histological sections were cut from each of the samples using a freezing-microtome (Figure 4.1) and stained with haematoxylin and eosin (H&E). The remaining biopsy blocks were stored at -85^0C until spectroscopic studies could be carried out. The larynx sections were classified by a pathologist as normal squamous epithelium; squamous dysplasia and squamous cell carcinoma. The procedure used for this histopathological classification is explained in Appendix 1. For the purpose of this study, with limited numbers of samples, mild, moderate and severe dysplasia were grouped together.[160] Only homogenous samples with clearly defined pathologies were used in this investigation and those with mixed or indeterminate pathologies were discarded. Twenty-five samples were retained for analysis with Raman spectroscopy, including fourteen histologically normal samples, five exhibiting dysplasia and six with squamous cell carcinoma. Prior to carrying out spectral measurements, the specimens were passively warmed to room temperature and rinsed with phosphate buffered isotonic saline solution (pH 7.4).

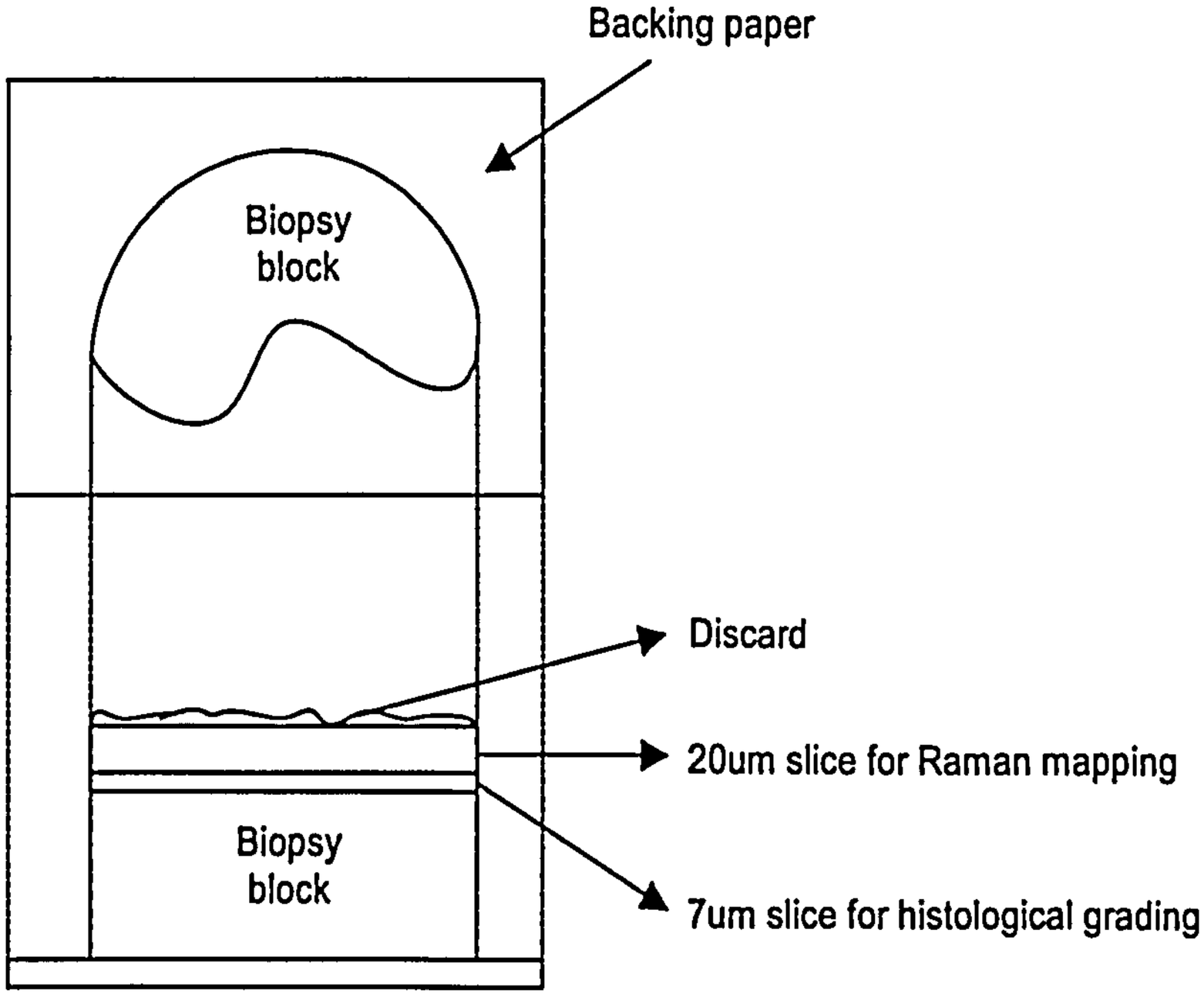

Figure 4.1 Orientation of biopsy block for sectioning with a freezing microtome. Samples were laid on acetate paper prior to being snap frozen.

4.1.2 Oesophagus Tissue

Jumbo biopsy samples have been harvested from patients undergoing endoscopic surveillance for dysplasia in Barrett's oesophagus. During the endoscopic procedure routine biopsy samples were removed at all four quadrants, every 2 cm in the region of Barrett's metaplasia in addition to areas exhibiting a suspicious appearance, such as ulceration or polyp. The patients involved in this study have provided written consent for a small number of additional biopsies to be taken from normal squamous epithelial mucosa as well as areas of columnar epithelium (Barrett's mucosa). Ethical approval for this procedure has been given by the Gloucestershire Local Research Ethics Committee.

4.1.2.1 Snap frozen tissue

Tissue samples were removed from the biopsy forceps and orientated on acetate paper (as shown in Figure 4.1) to enable a depth cross-section through the tissue to be seen. The mounted sample was then placed in a 2ml criovial (BDH) and dropped in liquid nitrogen. Histological sections were cut from each of the samples using a freezing-microtome (Figure 4.1) and stained with haematoxylin and eosin (H&E). The use of the acetate backing paper made it possible to stick the sample to the microtome using only water and thus give no chemical contamination to the tissue sample.

The H & E stained sections were sent for histopathological analysis by between one and three gastrointestinal registry pathologists. Samples were histopathologically graded following the procedures outlined in Appendix 2; those samples demonstrating mixed

pathologies were rejected. The remaining biopsy blocks were stored at –85^{0}C until spectroscopic studies could be carried out. 89 homogeneous samples, collected from 45 patients, exhibiting 9 different pathological states in the oesophagus were retained for study with Raman spectroscopy. Prior to carrying out spectral measurements, the specimens were passively warmed to room temperature. No other sample pre-treatment was performed.

4.1.2.2 Formalin fixed tissue

Following the above protocol for sample collection and histopathological analysis, a random selection of homogeneous samples were placed in a buffered 10% formalin solution. 42 oesophageal biopsy samples from 19 patients were used in this study. 22 samples were stored for 18 months at room temperature, in individual criovials containing fixative solution, and a further 20 samples were stored for 2-3 weeks prior to measurement. This allowed comparison of the effects of storage time on the Raman spectra and the facility of Raman spectroscopy of formalin fixed tissue to discriminate between pathology.

4.1.3 Other Tissues

The following tissues were also collected to evaluate whether NIR Raman spectroscopy could be used in future work to study the pathogenesis of early malignant changes and detect abnormal lesions in vivo. Small numbers of these samples have been harvested, snap frozen, microtomed, histopathologically analysed and measured.

1. Stomach.
2. Tonsil.
3. Endometrium.
4. Bladder.
5. Prostate.

4.2 System Configuration and Characterisation

A custom Raman spectrometer has been developed, from a commercially available Renishaw System 1000 microspectrometer, to facilitate the measurement of high signal-to-noise Raman spectra from biological tissue in short time-scales. A schematic of the customised Renishaw spectrometer is shown in figure 4.2. The following section will outline the system configuration and process of optimisation.

A high power tuneable laser source was coupled to the spectrometer and a Leica DML polarised light microscope. Diffraction gratings (G1 and G2 in Figure 4.2) were required to reject the spontaneous emission from the laser. A backscattering sample geometry was used with a laser line rejection filter restricting entry to a single monochromator and CCD array detector. For stability, the whole apparatus was rigidly bolted in position on a 3m x 1m x 10cm thick Melles-Griot optical bench.

The laboratory system was particularly large and required three-phase power and mains water cooling. Should the technique of Raman spectroscopy evolve to be used within a hospital environment, it would be necessary to miniaturise the system to fit upon a small trolley. In addition the system would have to run off 240V mains electricity with no external water cooling. This would be possible with the use of a single wavelength semiconductor laser; a miniaturised single monochromator and CCD detector; fibre-optic light delivery and collection; and laptop PC control. However, as an initial step towards this goal it was necessary to have the most flexible system available, with the ability to precisely visualise where in the tissue sample the spectra were being acquired.

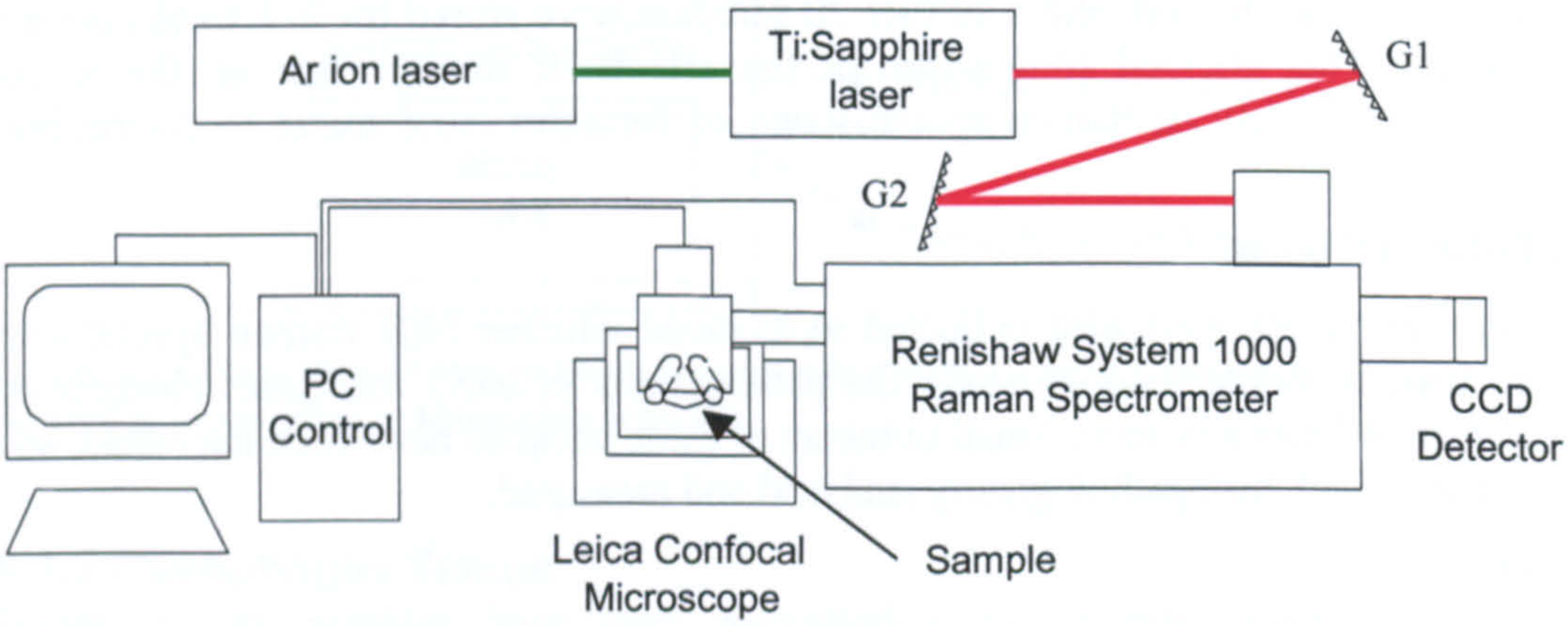

Figure 4.2: Schematic diagram of customised Raman system. G1 and G2 are diffraction gratings used to reject spontaneous emission from the Ti:sapphire laser.

The basic components of the Renishaw System 1000 spectrometer are shown in figure 4.3. They are labelled alphabetically to indicate the order that the incident light follows through the system. A is a steering mirror used to direct the laser light entering the spectrometer along the horizontal axis. B is a beam expander, usually used to fill the aperture of the microscope objective. This component was removed from the custom system used for this work, because use of the x80 ultra-long-working-distance lens for illumination and collection at the sample made the beam expander redundant (due to the tiny lens aperture). C is a further beam steering mirror to direct the laser light at the laser-line rejection apparatus. D/F, the laser-line rejection apparatus, reflects light at the wavelength of the laser line and allows light of energy with greater than 150cm^{-1} shift to pass through. Hence excitation light is reflected off the surface of the filter and directed to the microscope E. Following illumination of the sample, the collected light is redirected horizontally at the laser-line rejection filter. Light with the laser wavelength is reflected off-axis and the rest of the collected light is allowed to pass through to the focussing lens G. Lens G focuses the collected light on to the monochromator entry slit H. The slit H is used to reject scattered light from the out-of-focus sample volume. This improves spatial resolution and removes the fluorescence contribution from the out-of-focus sample volume. I is a beam expanding

lens. Component J is a prism mirror with two reflective surfaces that direct the light to the grating K and collect the dispersed light from grating K. The grating disperses the collected light into its constituent wavelengths. It is mounted upon a precision rotational stage to allow selection of the spectral range for detection. L is the CCD focussing lens and M is a Renishaw built CCD array detector sensitive in the near-infrared region.

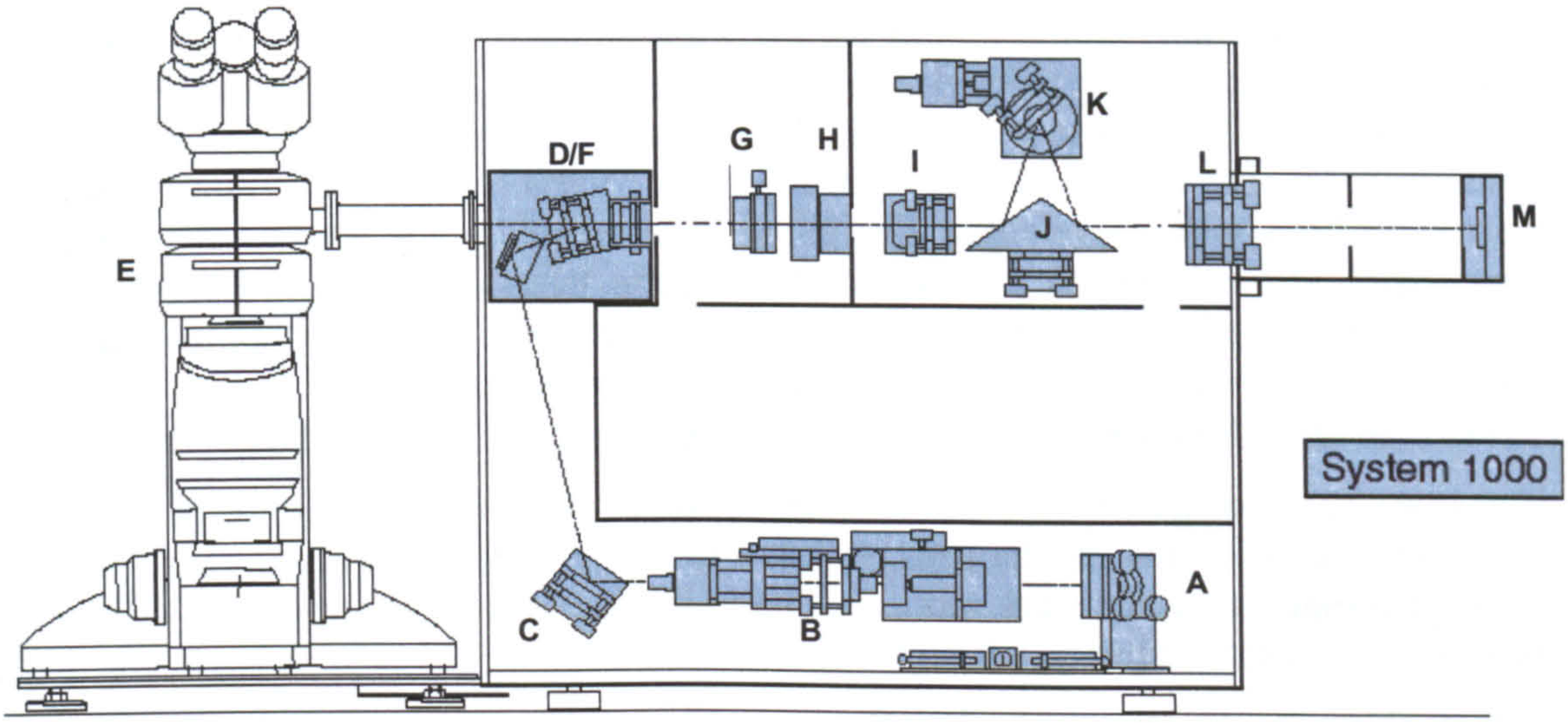

Figure 4.3: Internal diagram of Renishaw System 1000 microspectrometer. Labels indicate the sequence that the incident light follows through the system (reproduced by kind permission of Renishaw spectrometer division).

To enable a greater understanding of the transfer of energy through the system to a sample on the microscope stage, the laser power has been measured following each component. The losses at a few selected components is shown in Table 4.1; it can be seen from this data that the greatest loss of light energy occurs between the laser line rejection filter (on first pass) and the objective lens. The majority of this loss is due to the relatively small aperture at the back of the x80 ultra-long-working-distance lens and the large size of the laser spot in this plane. This can be observed by comparing the x80 objective throughput/loss with that using the x20 objective, in brackets in Table 4.1.

System component (after)	Power measured / mW	Loss / dB
Ti:Sapphire Laser head*	506.7	-
Plasma rejection gratings (G1 & G2)*	388.1	0.12
Mirror (A)§	353.3	0.04
Mirror (C)§	330.7	0.03
Laser line rejection filter (D)§	181.0	0.26
X80 ULWD objective (E)§	61.4	0.47
[X20 objective (E)§	113.3	0.20]
Laser line rejection filter (F)§	0.0064 (Raman)	-

Table 4.1: displaying the laser power losses at each significant component in the Raman spectrometer system. Components labelled with a '*' can be found in Figure 4.2 and those labelled with a '§'can be found in Figure 4.3.

The remainder of the System Configuration section is separated into sub-sections focussing on key individual components in the system.

4.2.1 Excitation Source Selection

The Raman excitation source chosen for the work outlined in this thesis was a Spectra-Physics Ti:Sapphire laser (Model 3900S), pumped with a Spectra-Physics Argon ion laser (Stabilite® 2017). The pump laser produced up to six Watts of laser power using all emission lines. The combined laser system provided a stable high power monochromatic source of light with wavelength flexibility; thus enabling selection of the optimum wavelength of excitation to produce Raman spectra with low fluorescence and a high signal to noise ratio. The range of tuneability is between 750 and 950nm, with peak power at 790nm. The linewidth is less than 40GHz and the power is stable to less than a 3% drift in any 2 hour period after warm-up for less than ±3°C temperature change.[161]

The laser was configured with a double set of Melles Griot® diffraction gratings (1200 lines mm^{-1}) to reject the spontaneous emission from the Ti:Sapphire laser. These gratings were positioned to enable the monochromatic radiation to be directed onto the entry mirror of the spectrometer (see figure 4.2).

Selection of the optimum wavelength was achieved following measurement of tissue Raman spectra at selected wavelengths across the visible and NIR range. These wavelengths were chosen to correspond to available holographic notch filters for rejection of specular reflection, diffuse reflection and Rayleigh scattering at the laser wavelength. A Renishaw system 1000 microspectrometer was used for all measurements, with the entrance slit set to 100μm and incorporating a 1200 lines mm^{-1} diffraction grating. Spectra of normal squamous mucosa from the oesophagus were acquired with excitation wavelengths of 514.5, 633, 785, 830, and 860nm. Laser powers were 32mW at the sample through a x80 objective for measurements at 785nm, 830nm and 860nm; and spectra were integrated for 30 seconds. Spectra acquired at 514.5 and 633nm were integrated for 300 seconds with 8mW of power through a x50 objective at the sample. The power density used in the acquisition of spectra in the NIR was approximately ten times that for the 514.5 and 633nm (visible) measurements. Therefore the use of a longer integration times for the visible wavelength Raman measurements enabled spectra with equivalent 'power density × integration time' products to be acquired, thus facilitating a more enlightening comparison between spectra at different wavelengths. The resulting raw spectra are shown in Figure 4.4, with the exception of that acquired at 514.5nm which demonstrated no visible Raman peaks within a large fluorescence background. Table 4.2 displays the signal-to-noise ratios (SNR) of the measured spectra at selected peak positions in the spectra (Figure 4.4). The SNRs were calculated by measuring the baseline corrected peak intensity and dividing it by the mean amplitude of the noise across the peak of interest.

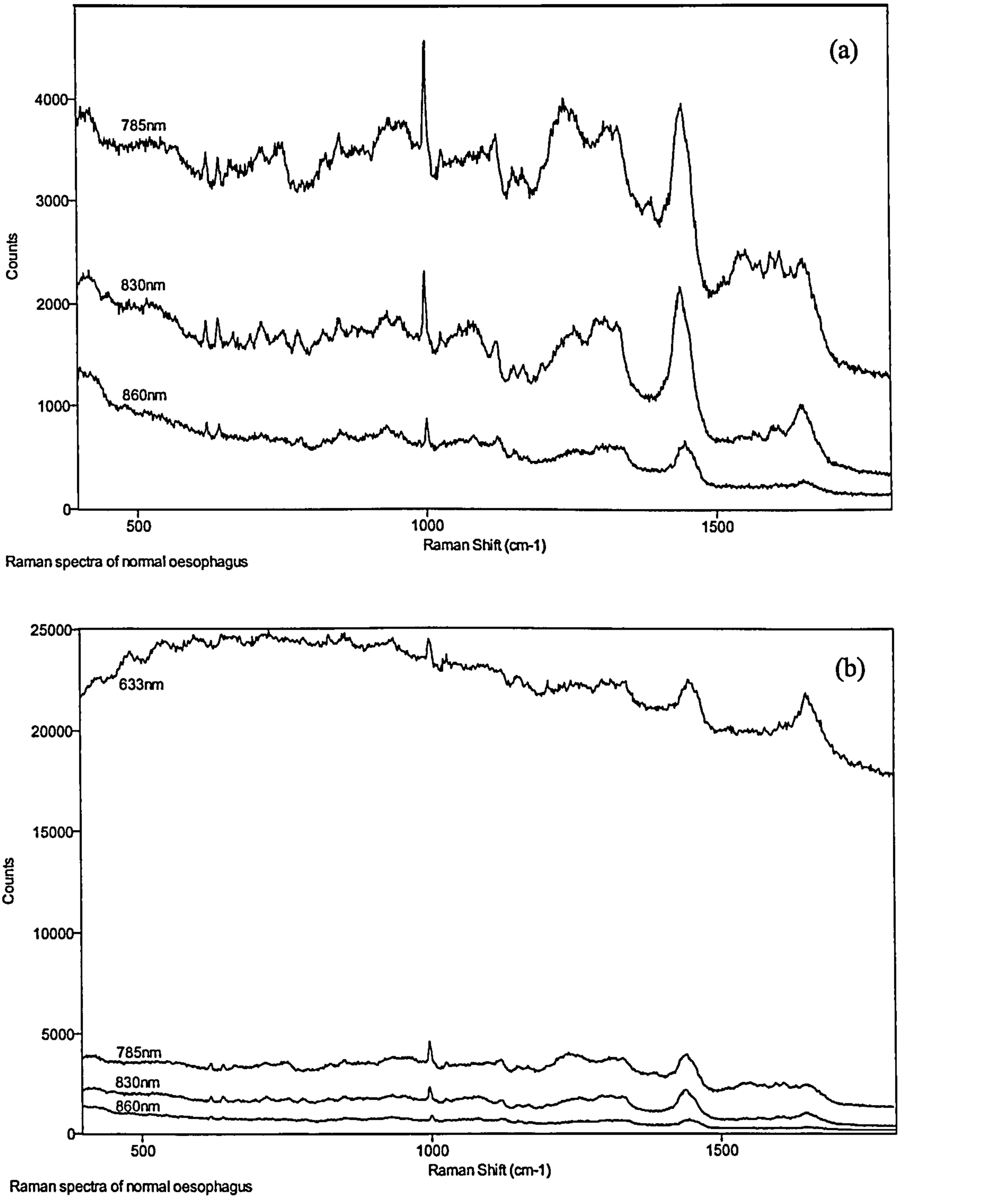

Figure 4.4: Plots showing differences in raw Raman spectra of normal squamous mucosa (oesophagus) at various excitation wavelengths. Spectra (a) at 785, 830, and 860nm were recorded for an integration time of 30s with 32mW of power at the sample, and the spectrum (b) at 633nm was measured in 300s with 8mW at the sample, other spectra are included in the same intensity scale.

Wavelength / nm	Signal-to-Noise Ratio (at wavenumber shift)					
	620 cm^{-1}	850 cm^{-1}	900 cm^{-1}	1250 cm^{-1}	1445 cm^{-1}	1650 cm^{-1}
633	1.4	1.6	3.9	4.0	9.8	7.2
785	4.6	4.3	5.6	9.7	10.5	10.4
830	15.1	6.8	10.9	15.0	18.5	11.0
860	2.5	2.3	4.3	3.0	8.4	2.4

Table 4.2: Comparison between signal-noise-ratios of Raman spectral peaks from normal oesophagus tissue at various wavelengths.

The choice of the optimal excitation wavelength for measuring biological tissue must be balanced between the λ^{-4} dependence of the Raman cross-section and the fact that at higher photon energies, greater fluorescence signal is induced. The optimum range generally falls between 750 and 850nm. Nevertheless, despite the relatively high S/N, the resulting tissue Raman spectra still contain a fluorescence background. A challenge in achieving a useful tissue Raman signal is the accurate subtraction of the fluorescence signal. This is vital because in most Raman techniques the fluorescence and weaker Raman signals lie in the same spectral region. Among the techniques available to minimise the fluorescence contribution to the Raman spectrum, the best method for the current analysis appears to be selection of the optimum wavelength of excitation to minimise fluorescence in the first place. From the spectra shown in Figure 4.4 it is evident that spectra acquired excitation wavelengths between 785nm and 830nm are optimum. The excitation wavelength of 830nm was shown to optimally balance the trade–off between the λ^{-4} Raman cross-section dependence, and the reducing fluorescence and detector sensitivities with increasing wavelength. Anecdotally, spectra acquired at 830nm also had much greater repeatability in terms of background fluorescence. At 785nm fluorescence was common enough to cause complete saturation of the detector with up to 30% of spectra due severe fluorescence, and large backgrounds due to moderate fluorescence in around 30% of spectra. At 633nm it was usually necessary to photobleach the chromophores prior to measurement, otherwise it was almost impossible to distinguish the Raman signal from the Shot noise. At 830nm about 1% of spectra were affected by severe fluorescence.

4.2.1.1 Stability of laser output characteristics

The Ti:sapphire laser warm up characteristics and long term temperature stability at 830nm were measured following power-up of the Argon ion pump laser. The laboratory was heated with a central-heating radiator and cooled with a Fujitsu Superwave unidirectional (cooling only) air conditioning unit.

The power output stability was measured during the first two hours after switching on the laser. A calibrated Newport photodiode (detector 818-SL) fitted with neutral density filter (OD3) coupled to a Newport optical power meter (model 840) was used to measure the laser power every 15 seconds. The ambient temperature was measured with a calibrated thermometer at one minute intervals. Figure 4.5 shows a plot of the laser power output

and ambient temperature versus time from power-up. The laser power can be seen to change drastically in the first 30 minutes from switching on. It then tends to stabilise and cycle ±0.1% over 5 minute time scales, combined with a gradual drift in power of up to 0.5% below the average over a period of a couple of hours. It can also be seen that the laboratory temperature changed rapidly in the first 30 minutes, followed by a more gradual rise to an equilibrium temperature. Thus it can be concluded that heat dissipation from the laser raises the ambient temperature.

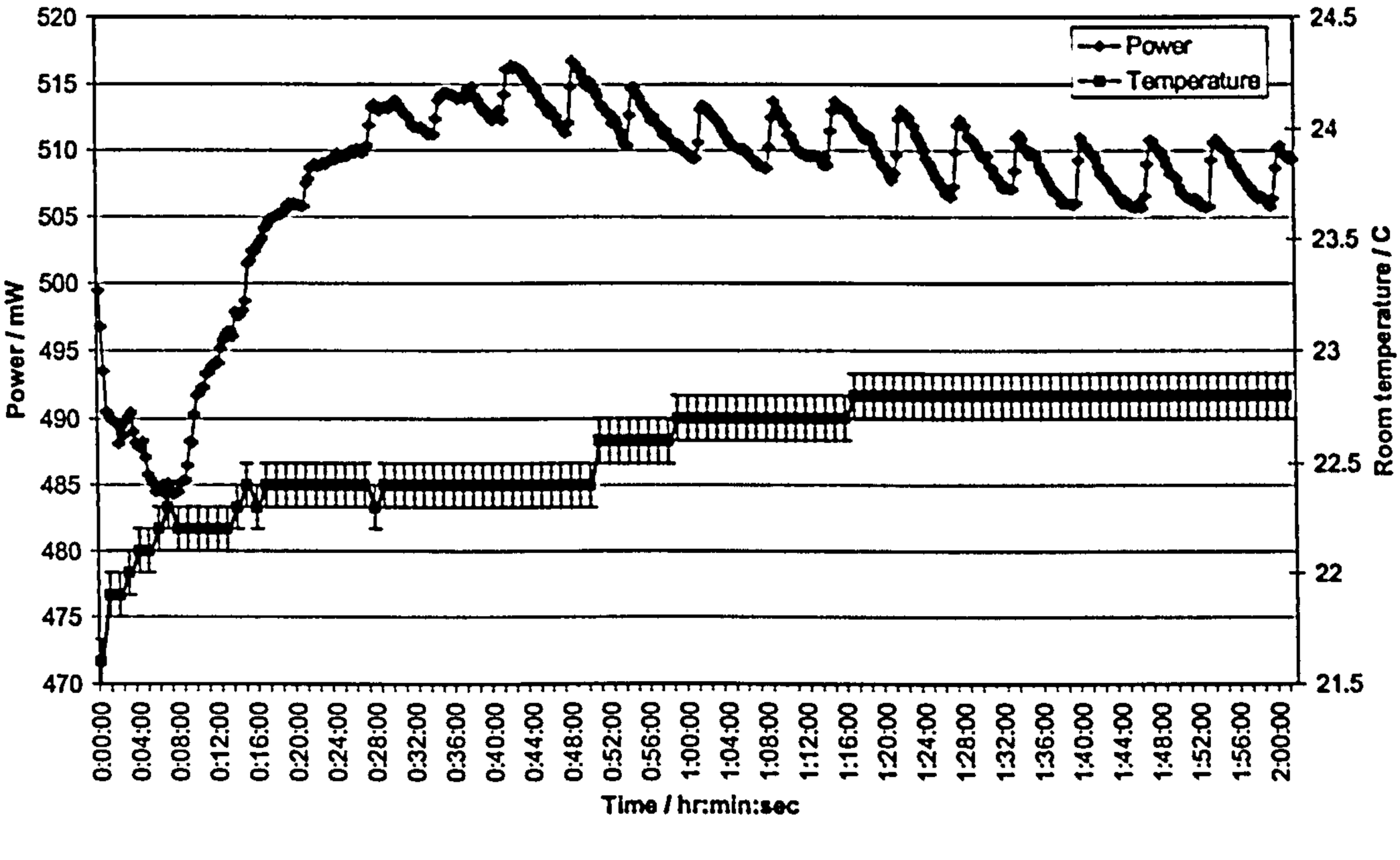

Figure 4.5: Plot of Ti:sapphire laser output power at 830nm versus time and ambient temperature versus time.

The wavelength stability of the Ti:sapphire laser at 830nm was evaluated by measuring the Raman spectrum of crystalline sulphur every minute over the warm up period and beyond. The power levels were set to those required for measurement of Raman spectra of biological tissue (500mW in this case). Air conditioning was set to #7 on a scale of one to ten. Spectra were acquired for 1 second. Figure 4.6 shows a typical crystalline sulphur spectrum measured at 830nm, with power at the sample of approximately 32mW. The wavenumber position of the sulphur peaks was mapped across the acquired spectra by utilising an Array Basic® program written for GRAMS/32® (Galactic®). The resulting wavenumber positions, for the 219-220cm^{-1} sulphur peak were plotted individually against time to enable visualisation of the wavenumber drift in the laser output (Figure 4.7).

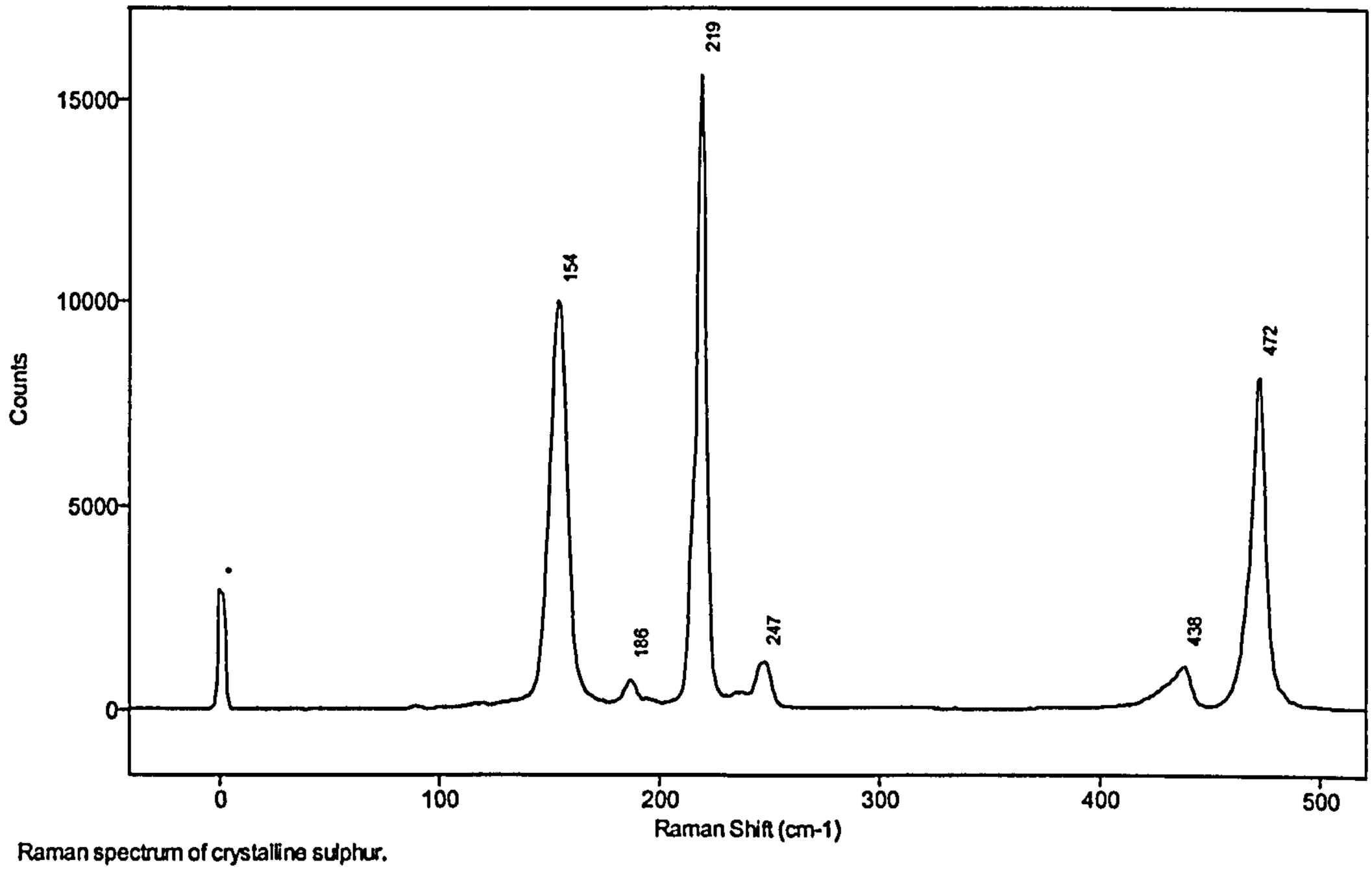

Raman spectrum of crystalline sulphur.

Figure 4.6: A typical Raman spectrum from crystalline sulphur measured at 830nm, in 1 second, with 32mW incident laser power.

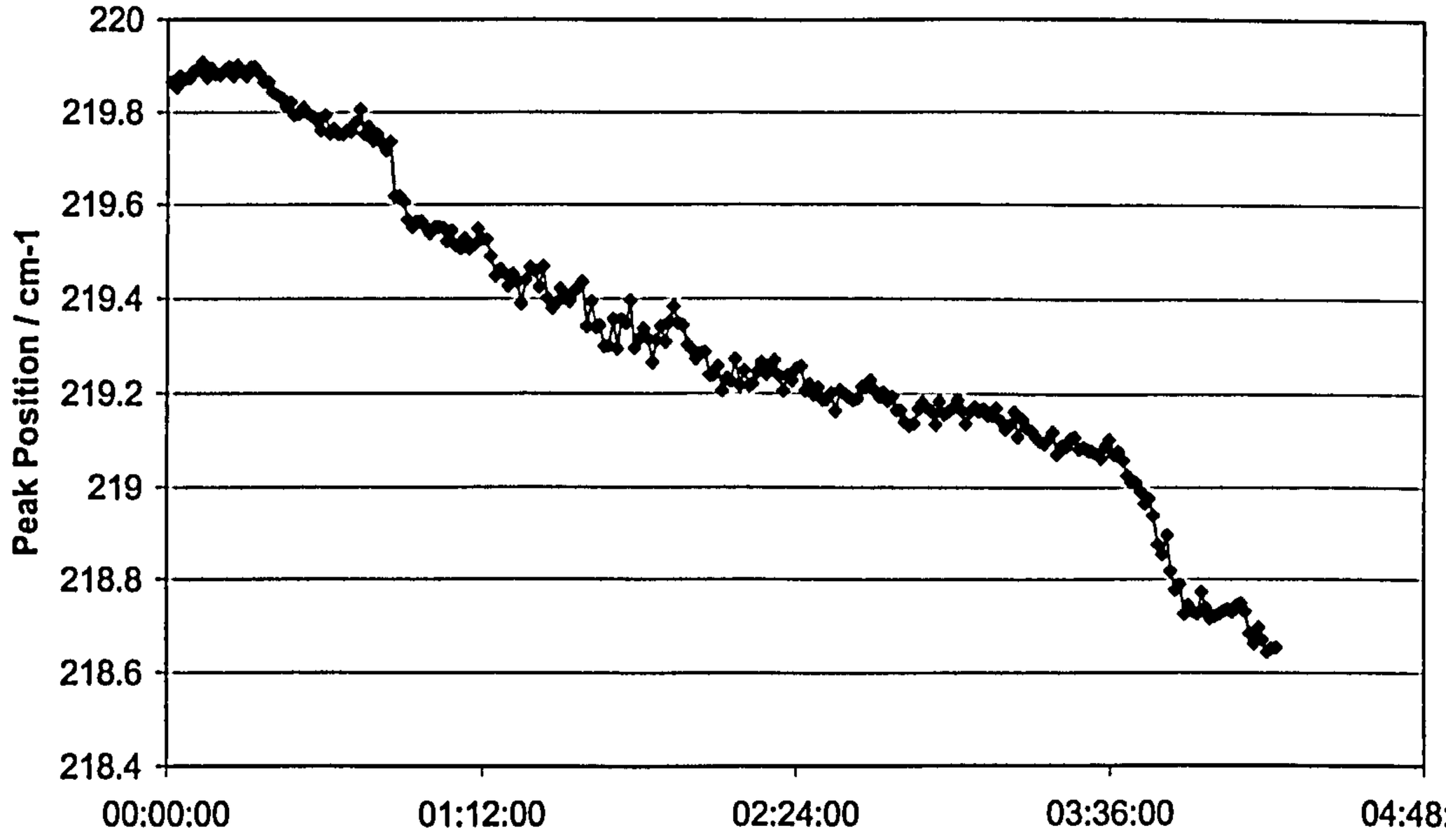

Figure 4.7: Plot of peak wavenumber position of sulphur line at around 219-220cm^{-1} versus time to enable visualisation of the laser wavelength drift.

Further adjustments were made to the laboratory and experimental apparatus to improve the temperature and mechanical stability of the system:

1. The temperature stability of the laboratory was improved by installing a two-way feedback loop temperature control system. This relied upon the air conditioning unit to cool the room and a thermostatically controlled fan heater to heat the room. This produced ambient temperature of 23.5°C ± 1°C over a period of days.
2. The cooling water flow was reduced to the minimum required to prevent automatic shutdown of the argon ion laser. This reduced the internal vibrations caused by turbulent flow through the system.
3. The locking bolts for the focussing mirror and the Ti:sapphire rod were tightened to prevent any unwanted translations caused by vibration.
4. The aperture of the argon ion laser was reduced to provide single mode TEM_{00} output (aperture position #5).
5. The Ti:sapphire laser was realigned and peaked for 830nm.
6. The Raman spectrometer was realigned, with Raman signal maximised.

Following the apparatus optimisation outlined above, the warm up characteristics of the laser were measured again by taking consecutive sulphur spectra at one minute intervals. The position of the 219-220cm^{-1} peak is plotted out in Figure 4.8.

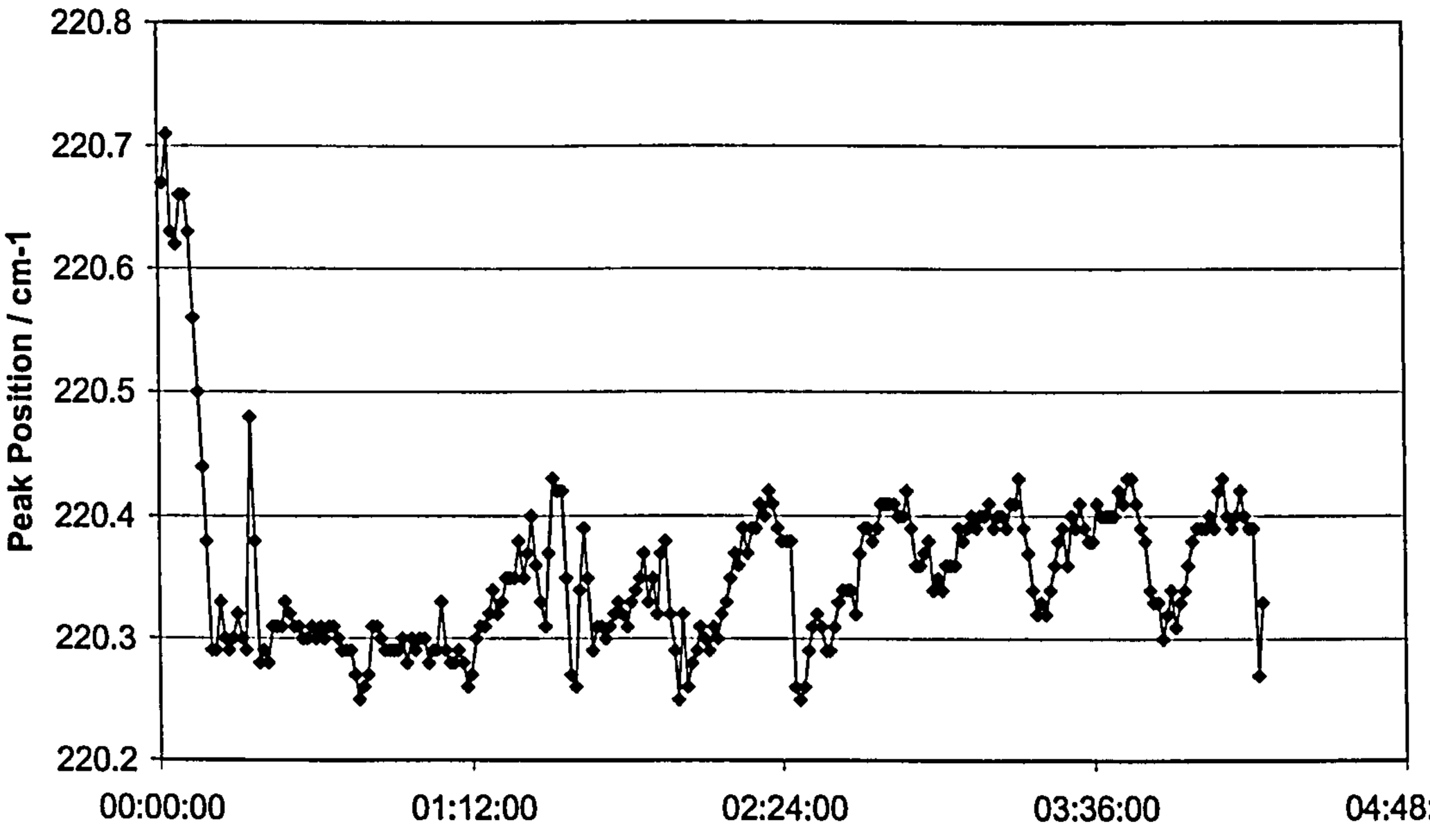

Figure 4.8: Plot of peak wavenumber position of sulphur line at 219-220cm^{-1} versus time to enable visualisation of the laser wavelength drift, showing improved wavelength stability following apparatus improvements.

Prior to installation of the two-way temperature stabilisation of the laboratory, the laser output drifted by between 1 to 2 cm^{-1} per hour. Following the improvements outlined above, the laser output was found to be stable to ± 0.15 cm^{-1} over many hours (up to 24), provided that the laser had been warmed up for in excess of one hour.

4.2.2 Sample Presentation Configuration

The sample presentation configuration includes the illumination and collection geometry, the orientation of the sample and the container or backing substrate holding the sample. The use of a microscope for illumination and collection of scattered light dictated the use of a 180° backscattering geometry. This relies upon fairly complex optical system design, but the overlapping axes of laser and collection optics significantly simplify alignment of illumination and collection volumes. The excitation beam is introduced into the system via a beam splitter. A schematic diagram of the sample presentation configuration is shown in Figure 4.9. The following section outlines the assessment of the important features to achieve high quality spectra from an accurately defined position in the tissue sample.

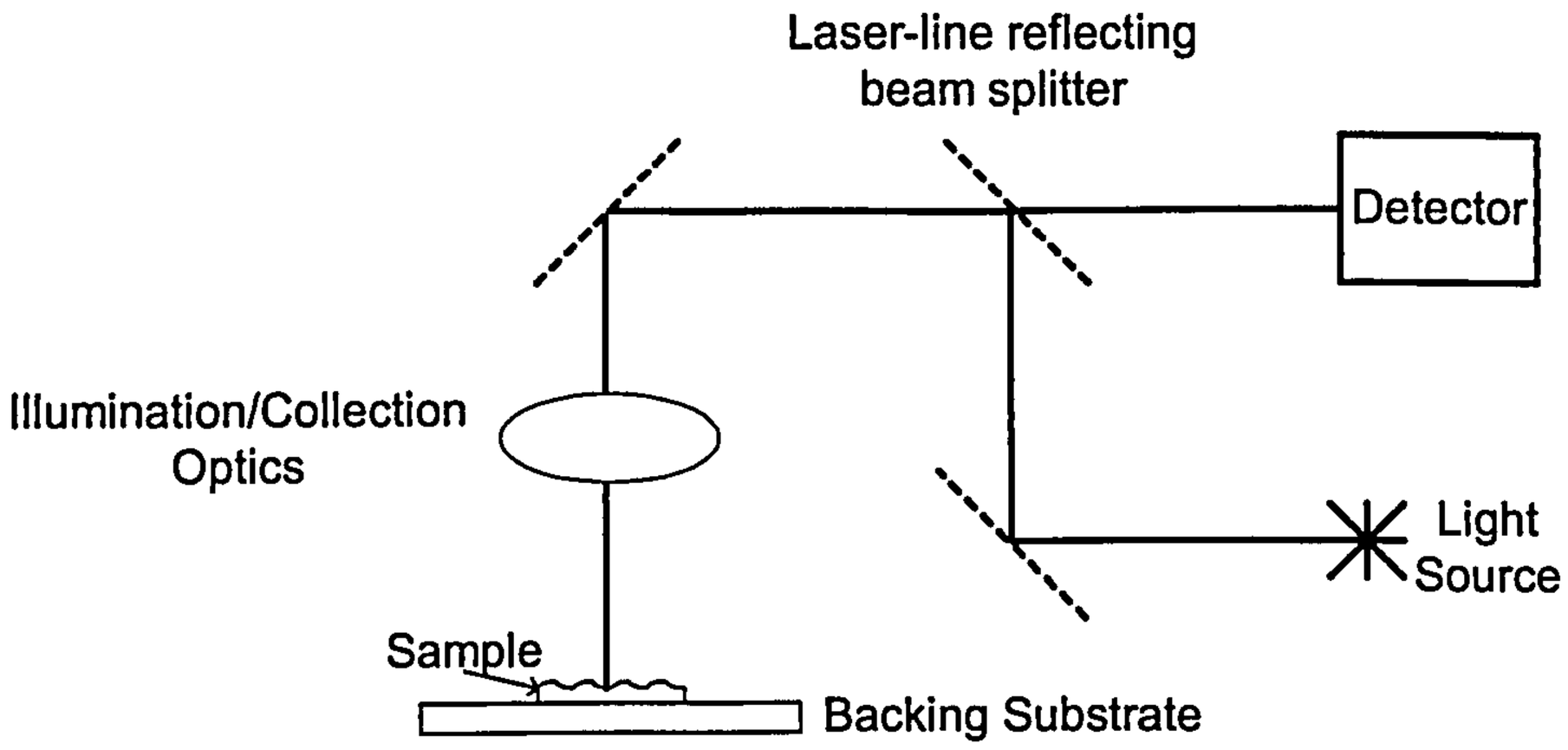

Figure 4.9: Schematic diagram of the 180° backscattering geometry employed to measure tissue Raman spectra.

4.2.2.1 Illumination/Collection Optics

Optimum selection from the available objectives for the Leica DML polarised light microscope was made by evaluating the relative power density achievable; the collection efficiency; the practical working distance and the contribution to the signal from fluorescence and Raman scattering in the optics. The objectives that were available are listed in Table 4.3, with the inclusion of important specifications for illumination and collection efficiency calculations.

The simplest method of increasing the Raman scattering signal is to raise the power density of the excitation beam. However, this may cause sample damage especially in biological samples. Therefore, once fluorescence is minimised by wavelength selection, then maximising collection and detection efficiency must be a priority for tissue Raman measurements.

The collection efficiency of Raman scattered photons is described by the fraction of the (4π steradian) solid angle around the sample volume that subtends the collection optics. If an assumption is made that the Raman scattering intensity is independent of direction, we can study the effect of lens characteristics upon the collection efficiency. The example of two typical objectives used for Raman scattering collection is outlined below.

The solid angle collected by an optic is described by

$$\Omega = 2\pi(1-\cos\theta) \qquad (4.1)$$

where the angle θ is the maximum angle of collection from the optical axis of the lens. See Figure 4.10.

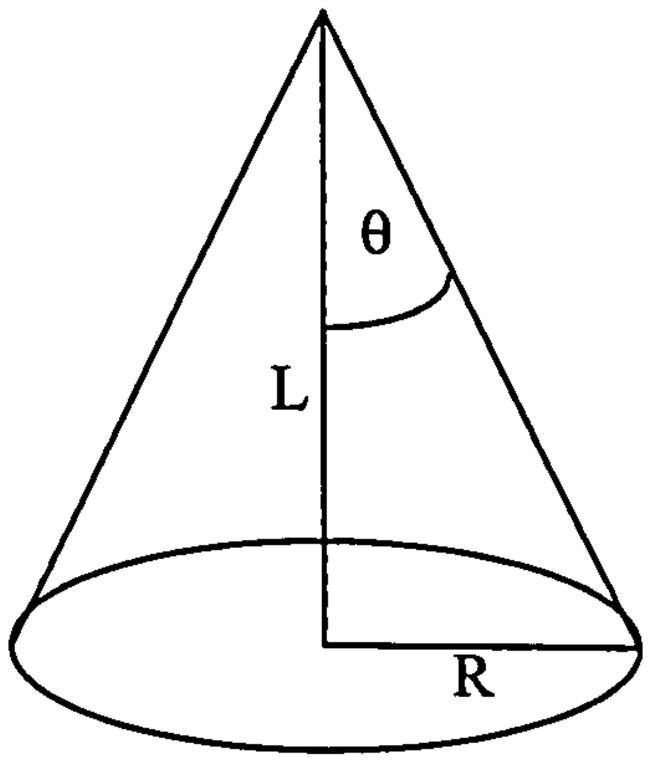

Figure 4.10: Line drawing enabling visualisation of the collection angle of a typical microscope objective. The angle θ is the maximum angle of collection of the lens, the length R is the radius of the collection area at the distance L away from the lens aperture.

A commonly used lens specification is the 'NA' or numerical aperture. This effectively describes the collection angle of the lens and follows the relation

$$N.A. = n_0 \sin\theta \qquad (4.2)$$

where n_0 is the refractive index of the material surrounding the outer surface of the lens, e.g. most commonly this is air (n_0=1). If we look at the following example of two typical microscope objectives it is possible to gain an understanding of their relative collection efficiencies. A x20 objective with a N.A. of 0.4, has a maximum collection angle, θ, of 23.6°. This relates to a solid angle Ω (equation 4.1) equal to 0.52 steradians and hence a collection efficiency of 4.2%; whereas a x80 objective with a N.A. of 0.75, has a maximum collection angle, θ, of 48.6°. This relates to a solid angle Ω equal to 2.13 steradians and hence a collection efficiency of 16.9%. There are obvious advantages to collecting a greater fraction of scattered photons from the sample, but there are other factors to consider. Generally a lens with a large numerical aperture will have a shorter practical working distance. In addition lenses with larger numerical apertures will have a shorter depth-of-field. Therefore using a lens with a large numerical aperture will enable spectra to be acquired from more accurately specified sample volumes.

Lens (manufacturer/ magnification)		Fabrication	Numerical Aperture (NA)	Collection Angle (degrees)	Collection Efficiency (%)	Power Density* (KW/cm^2)
Leica	x5	NPLAN	0.12	6.89	0.36	2.7
Leica	x20	NPLAN	0.4	23.58	4.17	42.4
Leica	x50	NPLAN	0.75	48.59	16.93	256.3
Olympus	x20	MDPLAN	0.4	23.58	4.17	42.4
Olympus	x80	MIRPLAN	0.75	48.59	16.93	679.1

Table 4.3: A list of the available microscope objectives with the important specifications for use in illumination of the tissue sample and collection of Raman signal from the sample. * The power density is calculated for a power at the sample of 32mW.

The contribution to the Raman signal of the objective lenses in the beam path was evaluated by measuring spectra with the laser spot focussed on a clean chromium surface. Spectra were acquired for either 10 or 30 seconds with a laser power of 10 or 32mW at the sample. Raman spectra of biological tissue will include unwanted contributions from any fluorescence or Raman scattering that occurs within the optics. Figures 4.11, 4.12, and 4.13 show the resulting spectral contributions from the various microscope objectives available at 785, 830, and 860nm respectively. It must be noted that it is not a trivial process to subtract the noise signal from a Raman spectrum, because the level of contribution will depend upon the amount of light scattering and reflecting back from the sample. Therefore the goal must be to reduce this contribution to a minimum. Variations in relative signal levels from one objective to the next are likely to be due to variable fluorescence excitation bands in the assorted compound optics found within each objective.

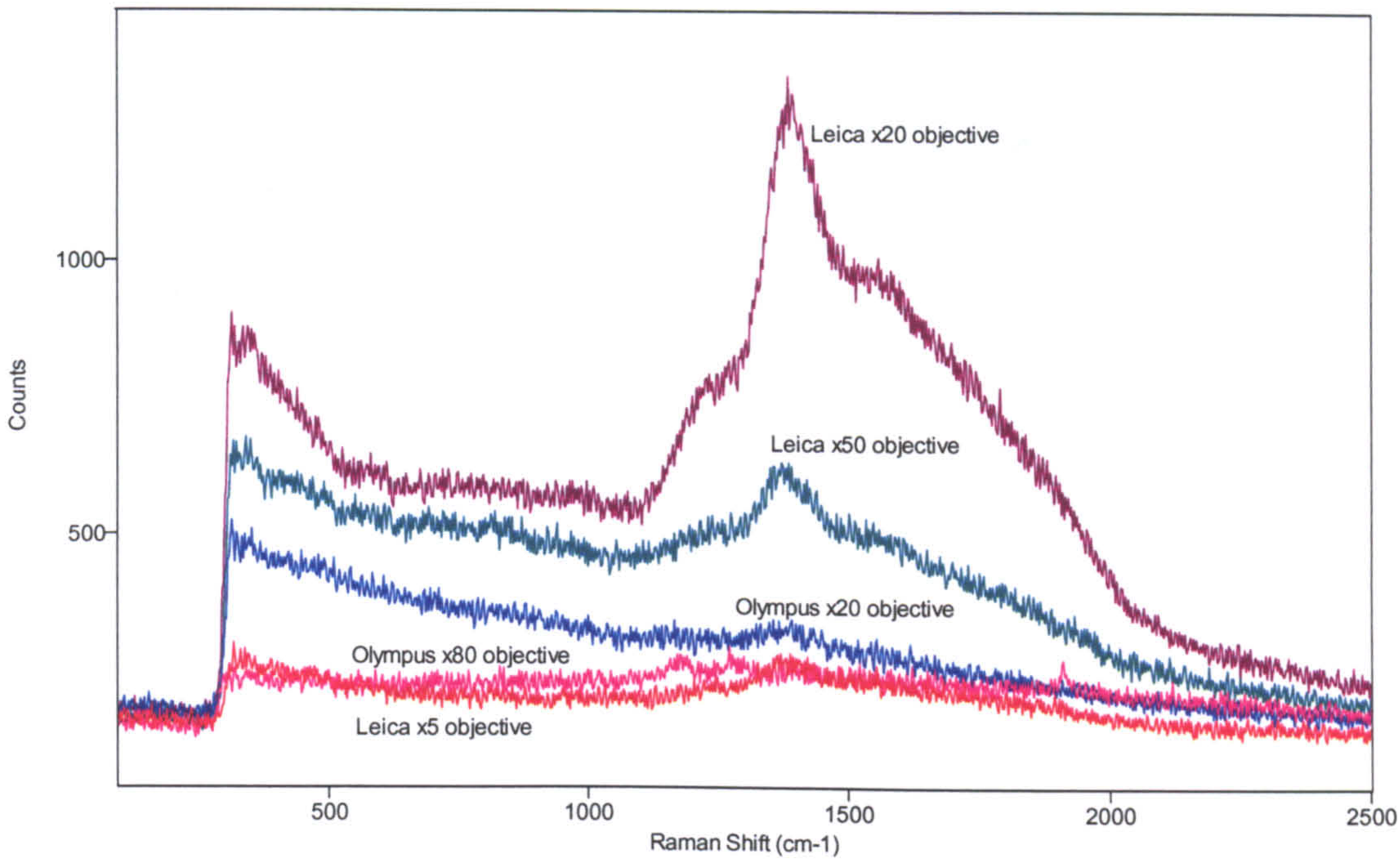

Figure 4.11: A comparision of spectral contributions from different illumination/collection optics. The spectra were excited from a clean chromium surface at 785nm excitation (10mW) and with an integration time of 10s.

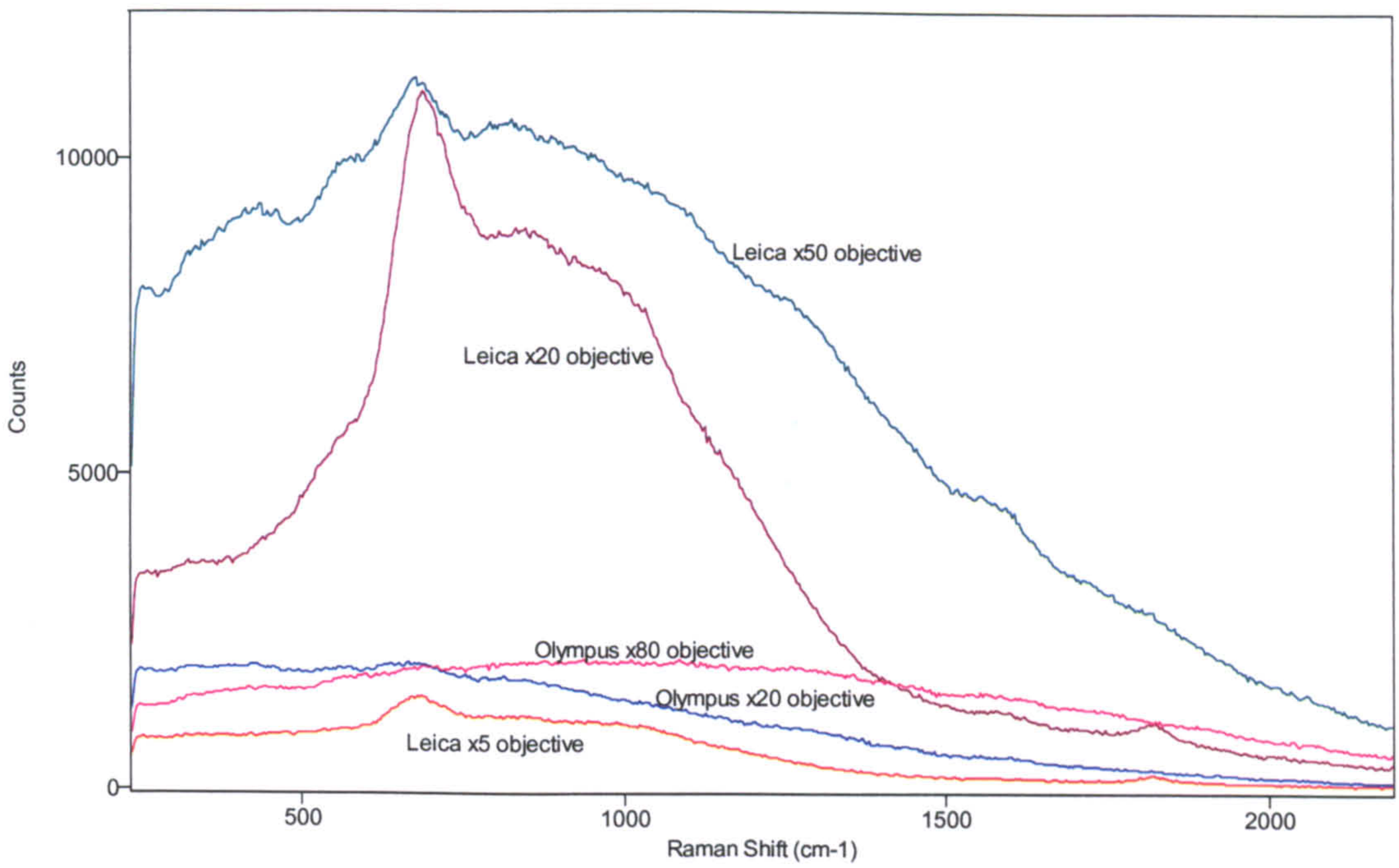

Figure 4.12: A comparision of spectral contributions from different illumination/collection optics. The spectra were excited from a clean chromium surface at 830nm excitation (32mW) and with an integration time of 30s.

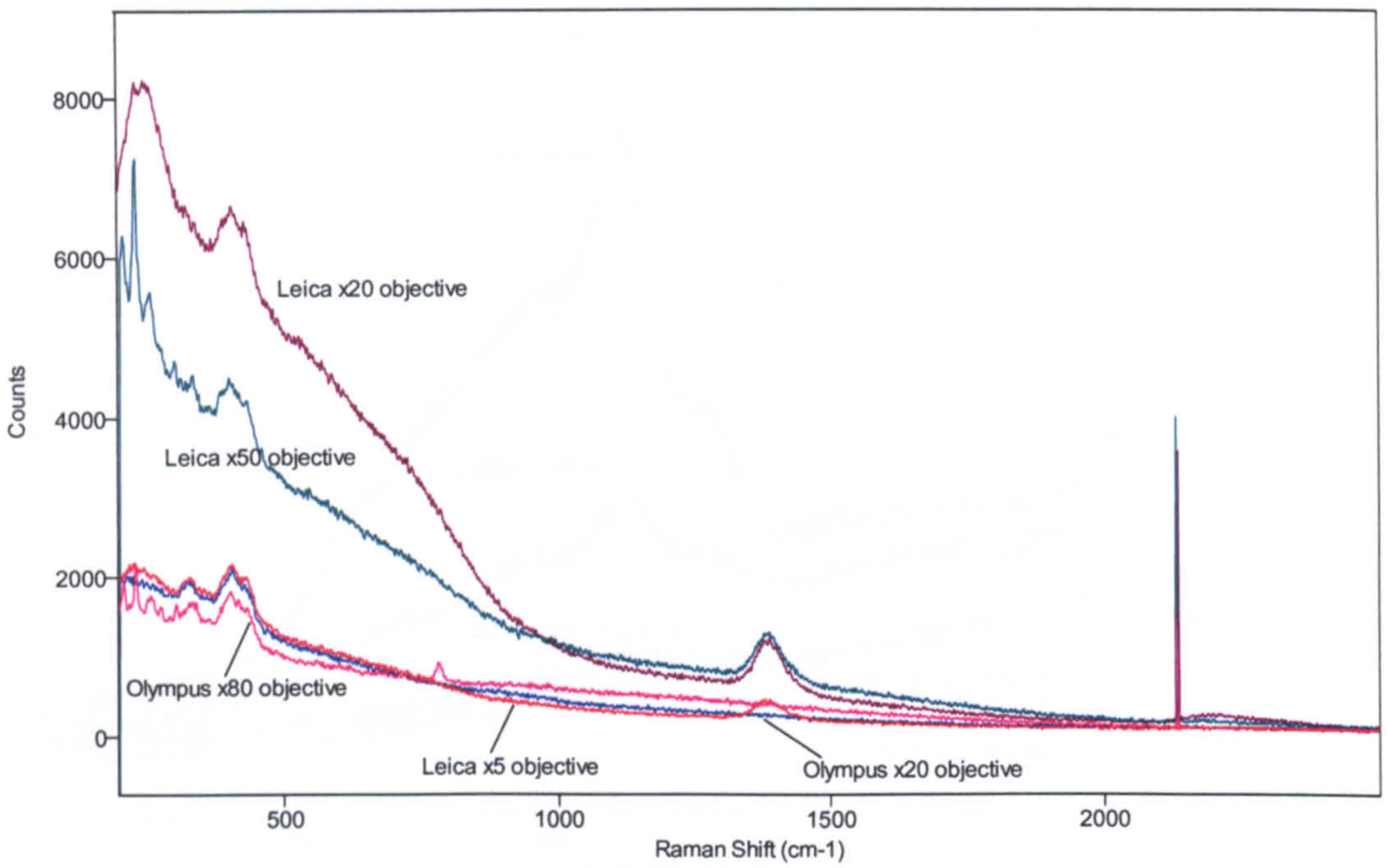

Figure 4.13: A comparision of spectral contributions from different illumination/collection optics. The spectra were excited from a clean chromium surface at 860nm excitation (32mW) and with an integration time of 30s.

The effect of power density on the signal-to-noise ratio of tissue Raman spectra was assessed very simply by using a x80 objective, to produce a fixed elliptical laser spot of diameters 2 and 3μm (short and long axes respectively) at the focus, and changing the laser illumination power. The resulting spectra can be seen in Figure 4.14. The S/N ratios of the spectra versus power density are tabulated in Table 4.4.

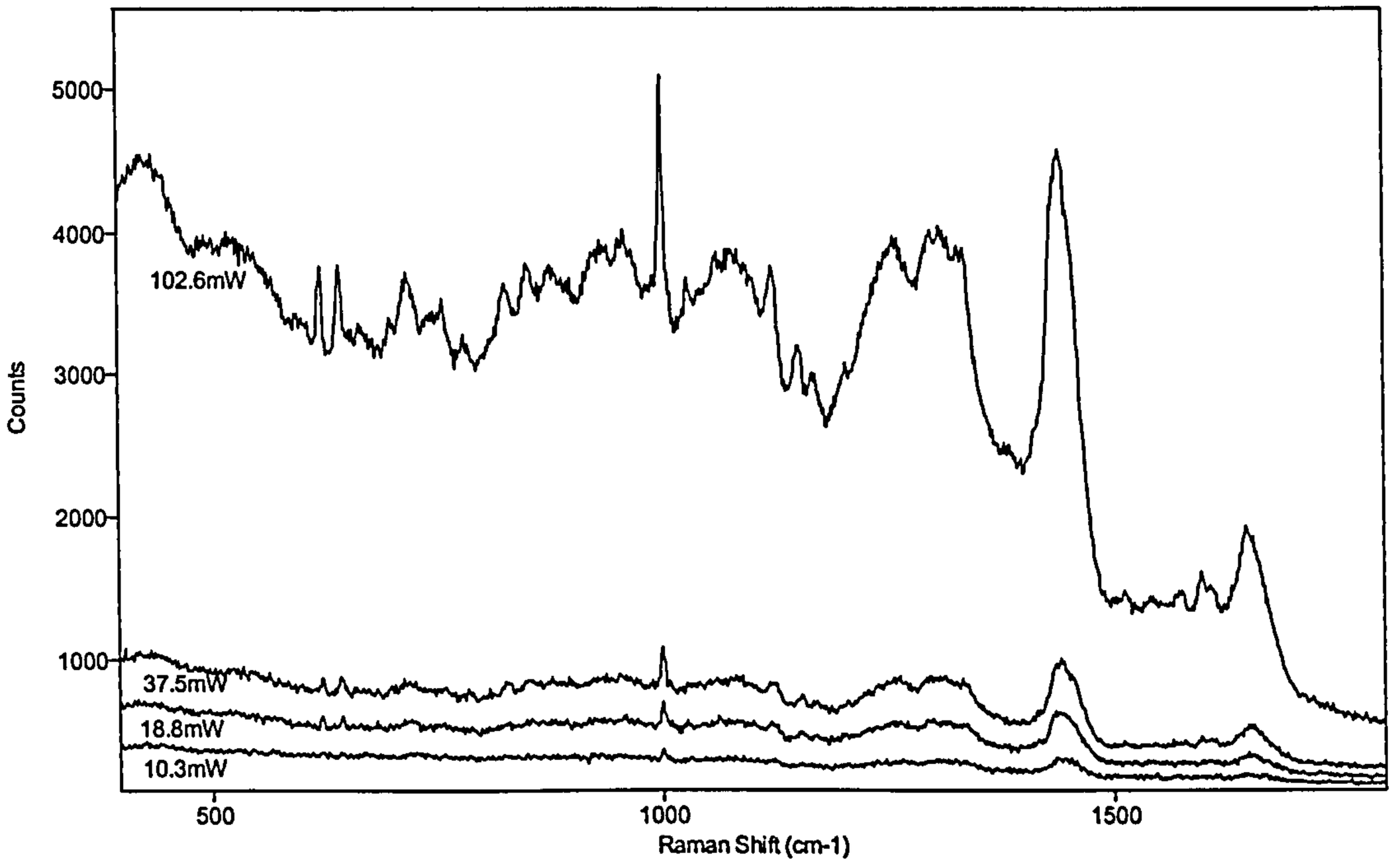

Figure 4.14: Raman spectra of oesophagus tissue (with low grade dysplasia) showing the effect of power density on the signal-to-noise ratio. Spectra were acquired in 30 seconds using a x80 objective.

Power / mW	Power density KW/cm^2	S/N Ratio
10.3	218.6	3.8
18.8	398.9	7.5
37.5	795.8	17.0
102.6	2177.2	63.0

Table 4.4: Signal-to-noise (S/N) ratio versus power density for oesophagus spectra measured at 830nm, in 30 seconds with a x80 objective. The S/N ratio was calculated for the 1445cm^{-1} peak.

The selection of the optimum microscope objective for measurement of tissue Raman spectra in the NIR has involved assessment of many characteristics. The x80, MIRPLAN, ultra-long-working-distance lens provides the greatest collection efficiency; the smallest spot size and hence the greatest power density; the lowest background contributions to the Raman signal; and the greatest practical working distance of any of the available objectives.

4.2.2.2 Backing Substrates

Tissue samples were mounted on a backing substrate prior to being positioned under the microspectrometer. Selection of the correct substrate was critical for thin tissue samples where the fluorescence or Raman signal from the substrate could exceed that from the sample. Signal contributions from a number of commonly available substrates were assessed by illuminating them with 60 mW of 830nm laser light and collecting the scattered light for 10 seconds. Figure 4.15 shows the signal contribution from uv-grade quartz, uv-grade calcium fluoride, glass slide and stainless steel. All the materials tested show some inherent Raman or fluorescence signal, however if the sample to be measured has spectral information at a different wavenumber position, then little interference should result. Calcium fluoride appears to be the ideal backing substrate for biological tissue measurements, with only one strong Raman peak at 323cm^{-1}. The fingerprint region for most tissue Raman bands lie within the region 400 to 1800 wavenumbers.

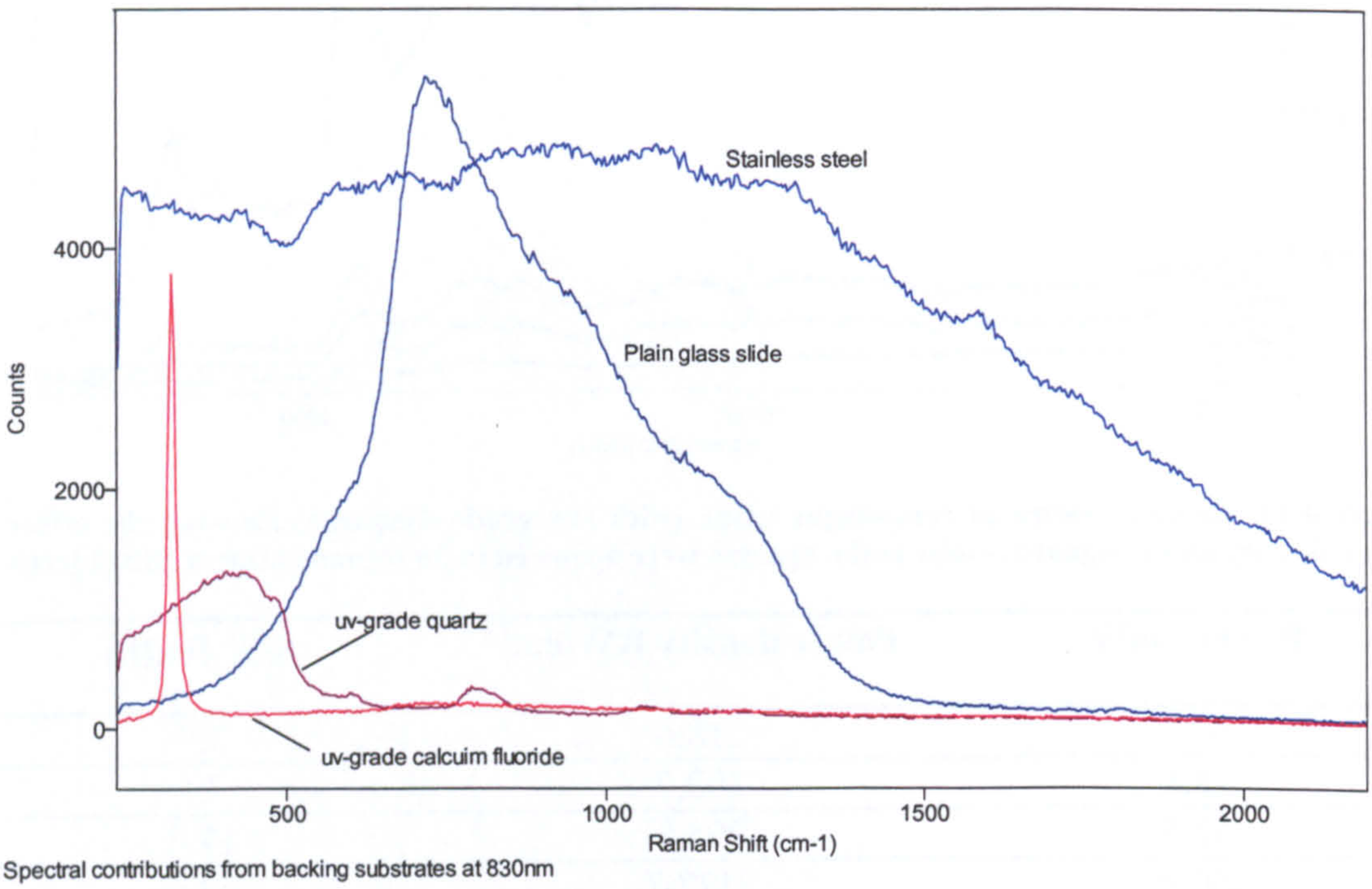

Spectral contributions from backing substrates at 830nm

Figure 4.15 spectral contributions from some typical backing substrates at 830nm, with 32mW laser power at the sample, x80 objective, T=10s.

4.2.3 Spectrometer Configuration

The spectrometer used in this work utilises a single dispersion grating coupled to a charge coupled device (CCD) array detector. This offers a system with the advantage of higher signal throughput, and one that can use higher numerical aperture collection optics that facilitate high collection and detection efficiencies. However, a single grating gives poor stray light rejection. The elastic scattered light (at the laser wavelength) can equal 10^{-1} to 10^{-5} of the laser intensity at the sample. This is many orders of magnitude greater than the

Raman signal. Hence the first priority of a spectrometer must be to reject or separate out the signal at the laser frequency.

The additional stray light rejection required by the single monochromator was achieved using band rejection or notch filters, with the region of rejection covering the laser wavelength. Dielectric notch filters constructed of alternating layers of high- and low-refractive index materials have been used initially by spectroscopists. However, they have been replaced for most applications with holographic notch filters. Holographic notch filters (HNF) are constructed from a gelatin film encapsulated in glass, with a refractive index profile varying sinusoidally with depth fixed in the gelatin. The rejection band can be varied in wavelength by varying the period of the oscillations in refractive index. HNFs have been constructed to reject wavelengths ranging from the UV to the NIR,[162] with optical densities in the rejection region of greater than 6. The attenuation band of a holographic notch filter shifts to shorter wavelength as the angle between the incident light and the normal to the surface increases.[163] In addition, the notch-filter performance degrades and becomes polarisation dependent as this angle increases. The transmission region has a very smooth profile, in contrast to dielectric interference filters, and low Raman shifts of the order of 50 to 100cm^{-1} can be observed using holographic filters. They are currently the most common laser line rejection filters for single monochromator Raman spectrometers.

The main disadvantage of the monochromator-notch filter combination is that a different filter is required for each wavelength, thus the flexible tuneability of triple monochromators is hard to achieve without multiple notch filters.

4.2.3.1 Laser-line Rejection Filter

A comparison was made between a pair of holographic notch filters (HNF)[a] and a pair of oxide layer edge filters[b] for the optimum rejection of Rayleigh scattered light from the Raman spectrum. A Renishaw System 1000 spectrometer fitted with a 1200 lines per mm dispersion grating was used to take the spectral measurements with each notch filter pair fitted in turn. The laser line rejection filters were mounted as a pair on a Renishaw EASYchange replacement unit. This simplified the alignment procedure when interchanging filters either for different wavelengths or in this case to compare filter technologies.

A white light spectrum from a tungsten-filament lamp was measured in each configuration to show the spectral attenuation characteristics of each filter set. The source was used to illuminate a barium fluoride (BaF2) disc placed under the x80 objective on the microscope (see Figure 4.15). The BaF_2 disc causes the light to be almost completely diffusely scattered. This reduced the effects of beam geometry on the results. The measured spectra are shown in Figure 4.17 for comparison. It is evident that the HNF set has a smoother transmission curve than the oxide layer edge filter set, and in addition, it can be used to measure anti-Stokes scattering.

---

[a] Kaiser, OD > 5 x 2, 65% transmission for the pair, cut-off ≈ 100cm^{-1}.
[b] Renishaw, OD > 5 x 2, 85% transmission for the pair, cut-off ≈ 150cm^{-1}.

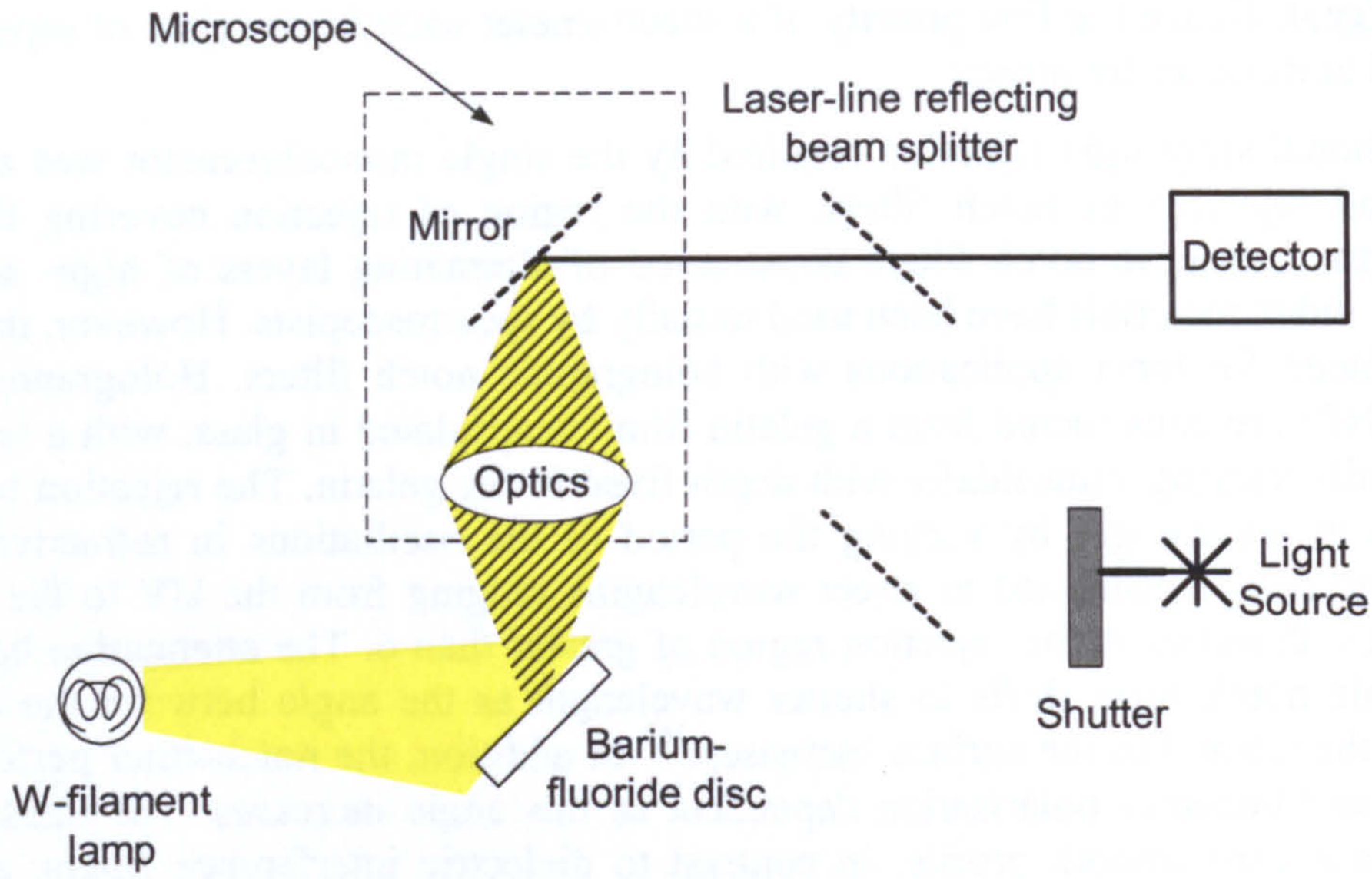

Figure 4.16: Illumination geometry for measurement of system energy sensitivity using a tungsten-filament lamp source with a known spectral profile.

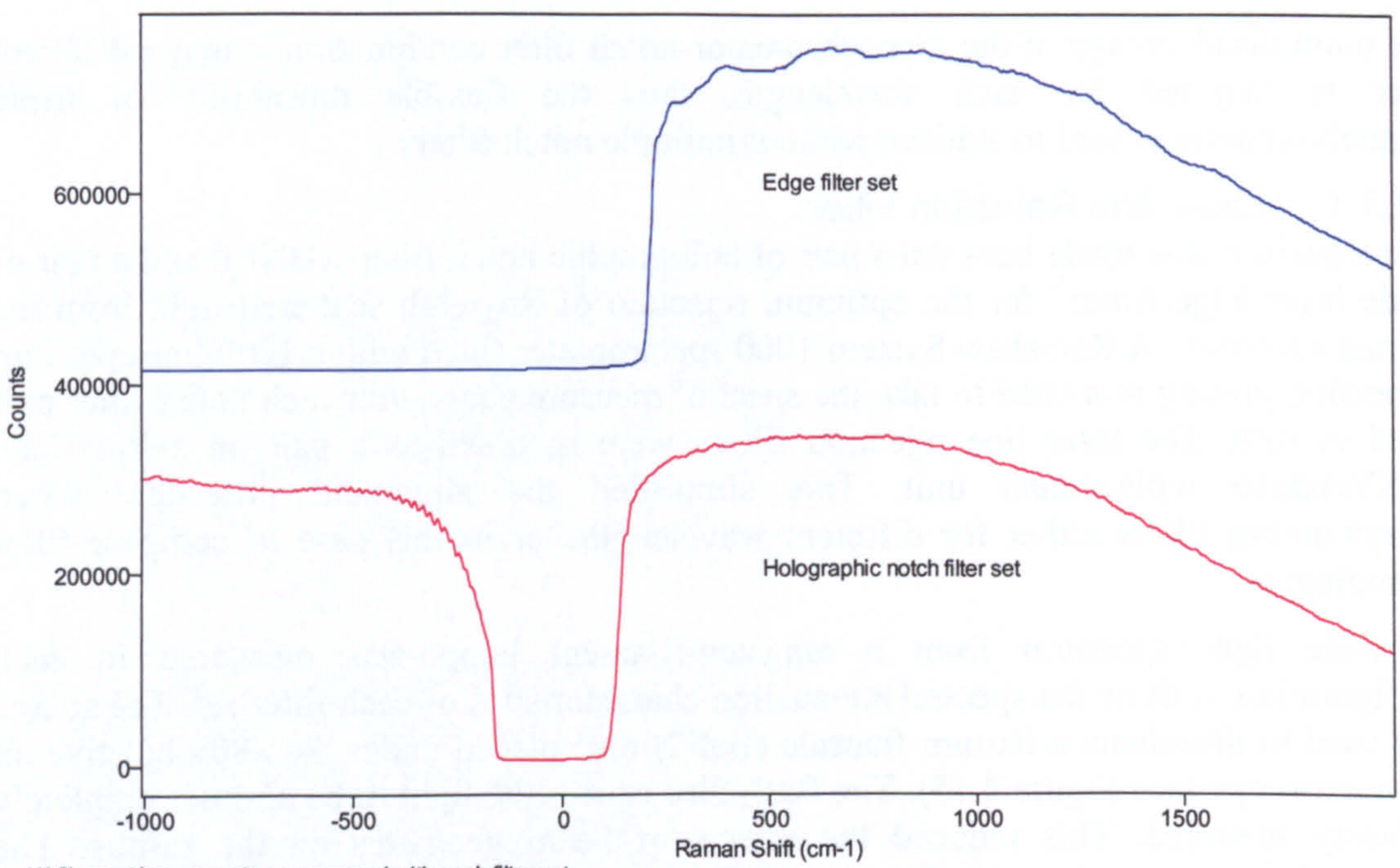

Figure 4.17: Comparison of white light spectra measured with the spectrometer fitted either with an edge filter set or a holographic notch filter set. Spectra were acquired for 60 seconds. The y-axis has arbritary units of intensity, whereas the x-axis represents the spectral energy in cm^{-1} relative to 830nm ($0cm^{-1}$).

Additionally, the laser-line rejection filters were evaluated by measuring spectra of crystalline sulphur at 830nm. The spectra were acquired for 1 second with a laser power of approximately 10mW at the sample. They are displayed in Figure 4.18. It can be seen that the Raman scattering measurements from sulphur using the two different rejection filter pairs at 830nm produce distinctly different spectra. The oxide edge filter set has a cut-off that extends further into the Stoke's Raman spectrum than the HNFs. In addition the edge filters suppress the anti-Stokes signal. However, the HNFs have a lower optical density at the laser line frequency.

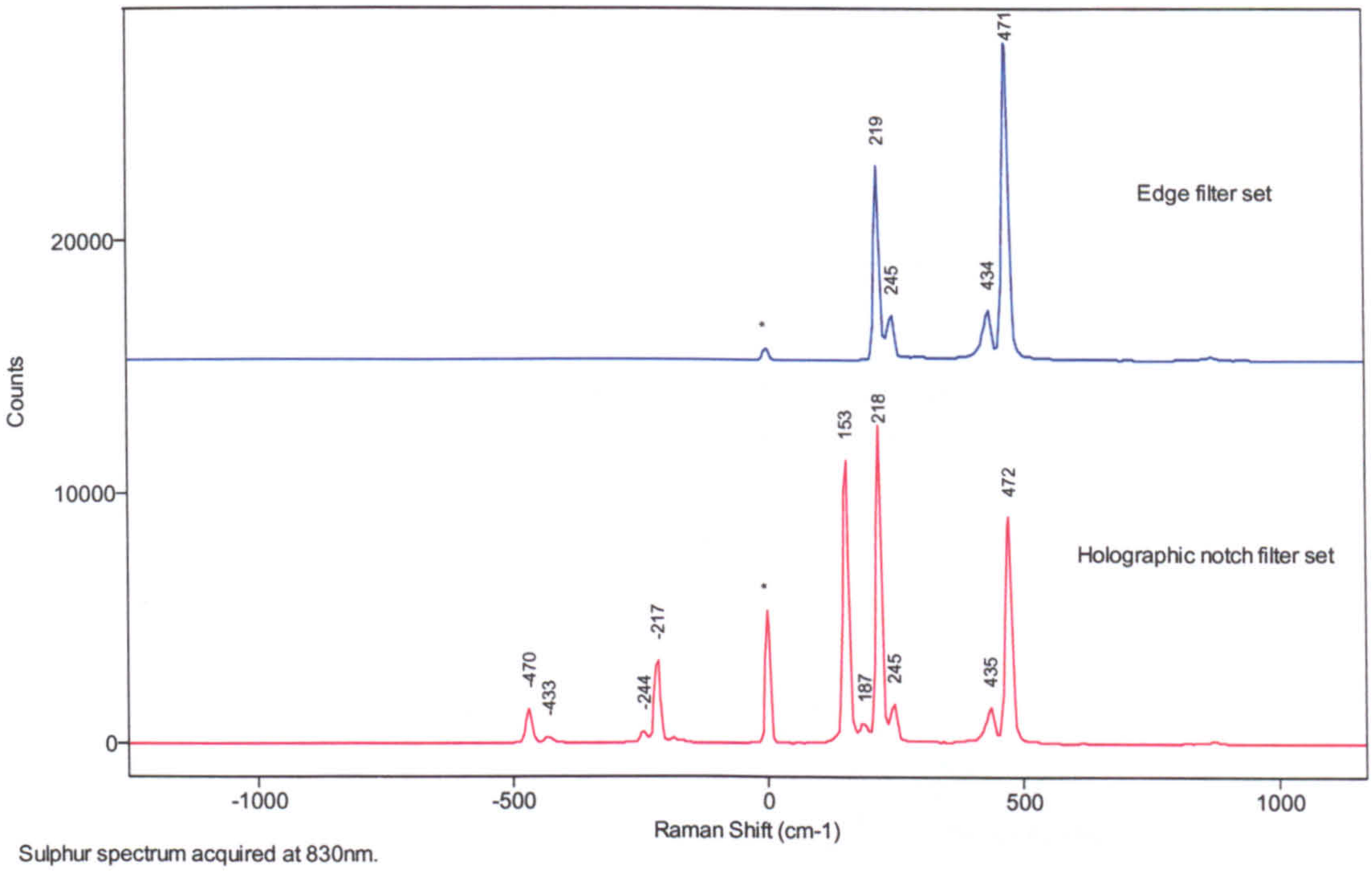

Figure 4.18: Comparison of sulphur spectra measured at 830nm, with a spectrometer fitted either with edge filter or holographic notch filter sets.

4.2.3.2 Dispersive Grating

The choice of grating for use with the custom spectrometer involved the consideration of three significant factors: the spectral range achievable without moving the grating; the signal-to-noise ratio of measured tissue spectra; and the spectral resolution. Two holographic diffraction gratings were evaluated: a 1200 lines per mm grating[c] and a 300 lines per mm grating.[d] For each grating Raman spectra of normal oesophageal mucosa were acquired in static mode (fixed grating position) to enable the spectral range and S/N ratio to be measured. The sample was illuminated with 32mW of 830nm light and spectra were integrated for 1, 10 and 30 seconds. The resulting spectra are shown in Figures 4.19 and 4.20 for comparison. Table 4.5 outlines the data on the factors described above.

---

[c] Optometrics, 1200 lines per mm, blazed at 1.0μm, gold coated holographic grating.
[d] Manufacturer confidential, 300 lines per mm, blazed at 1.0μm, custom gold grating.

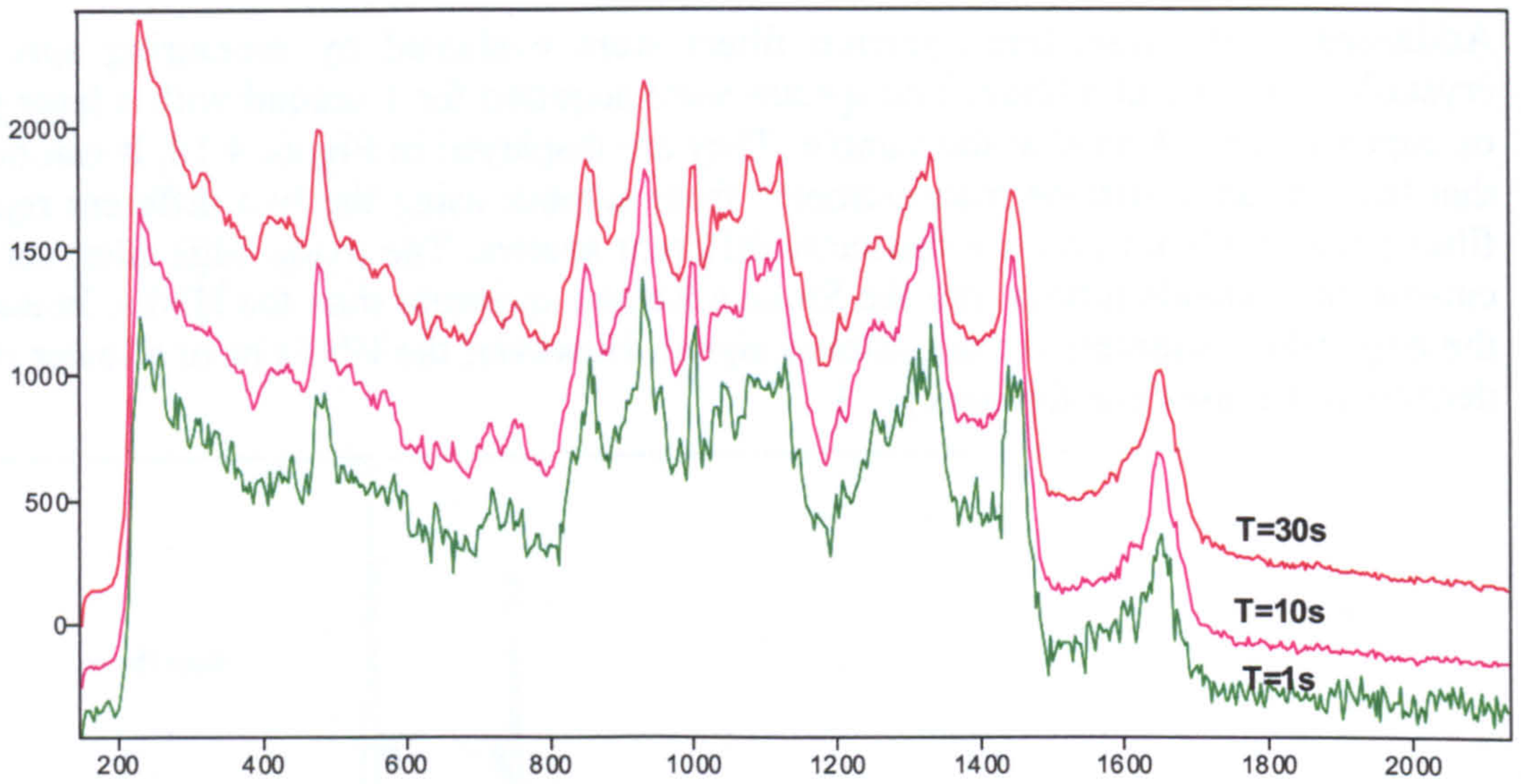

Figure 4.19: Comparison of Raman spectra from normal oesophageal mucosa acquired at various integration times using a 300 lines mm^{-1} grating coupled to a CCD array detector. Arbitrary intensity units.

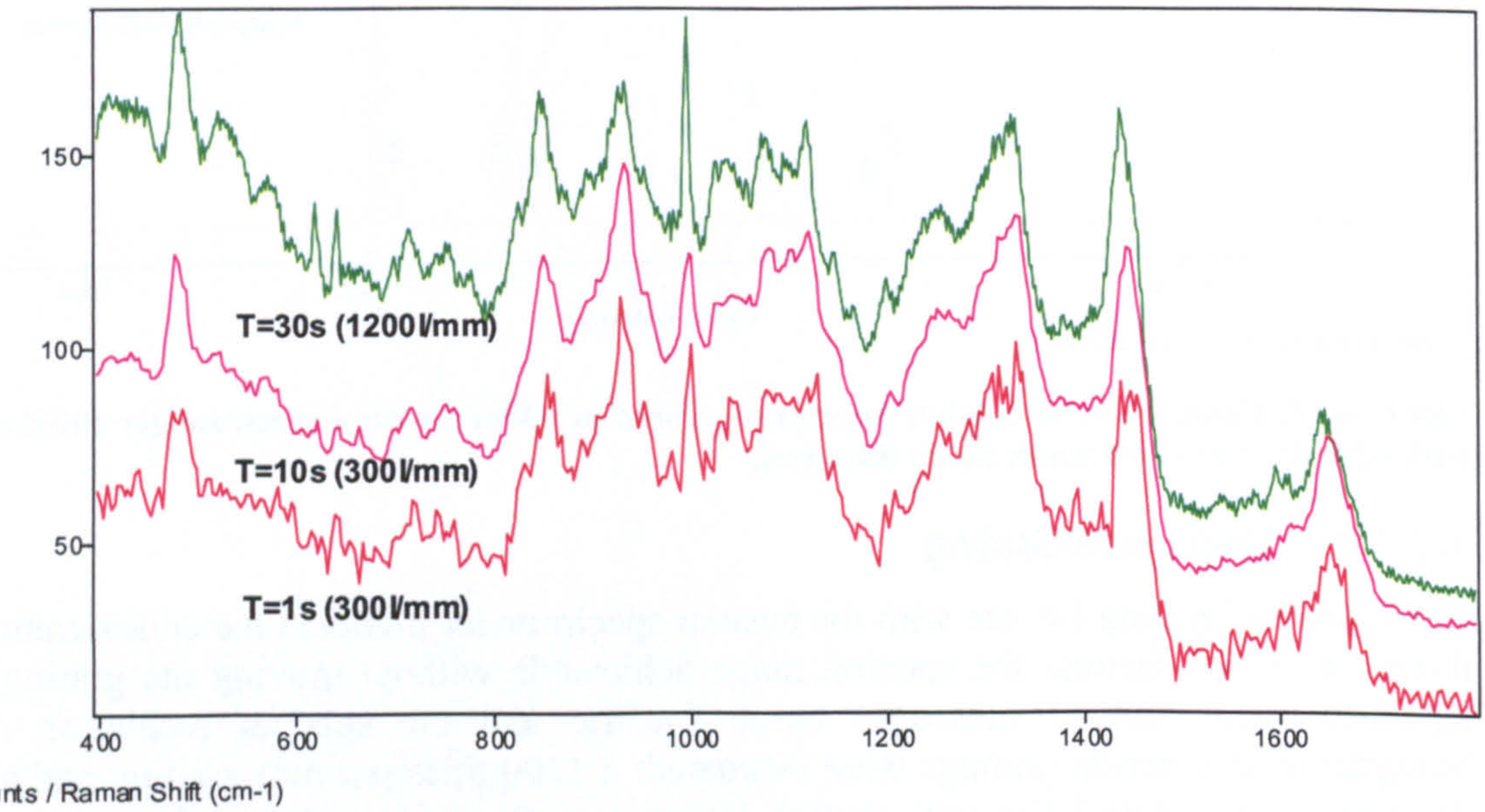

Figure 4.20: Comparison of Raman spectra from normal oesophageal mucosa acquired using 1200 lines mm^{-1} or 300 lines mm^{-1} gratings coupled to a CCD array detector. Arbitrary intensity units.

Grating Manufacturer	Line density (mm^{-1})	Spectral Range (cm^{-1})	Spectral Resolution (cm^{-1})	S/N ratio
Kaiser	1200	560	3	≈5
Confidential	300	1980	12	≈20

Table 4.5: Dispersion gratings used for tissue Raman measurement. The table includes line density, spectral range achievable in system without rotating the grating, spectral resolution at the configuration used and signal to noise ratio in spectra of normal oesophagus tissue measured with the same parameters in 30s.

For rapid spectral acquisition times and greater wavelength repeatability it was necessary to measure spectra without rotating the dispersion grating. This has been made possible because of the use of CCD array detectors which allowed a significant portion of the Raman spectral component wavelengths to be measured simultaneously, with each detector element measuring a separate component of the spectral range.

The dispersion from a grating is wavelength dependent and the Raman bands become narrower (in nm) as the illumination wavelength decreases. The dispersion was chosen to yield the required spectral coverage on the detector. A spectrograph for uv-light may use a high density grating (e.g. 3600 lines/mm) whereas for NIR a coarse grating (e.g. 300 lines/mm) may be adequate. For multichannel systems, the spectral range must fit onto the detector with a dimension of between 12 and 25mm. Hence the dispersion required must be low. For example in the Renishaw system 1000, the CCD detector has an active length of 12.7 mm in the spectral dispersion dimension. The CCD is made up of a 384x576 pixel array, with individual element size of 22μm. A 300 lines per mm grating was used to disperse Raman scattered light, using an 830nm source, to approximately $155cm^{-1}$ mm^{-1} across the CCD, giving a full spectral range of approximately 1980 cm^{-1}. The mean spectral dispersion per channel is $3.44cm^{-1}$. Use of gratings with a greater dispersion will result in a shorter spectral range projected upon the CCD. However, this will lead to improved spectral resolution.

A further advantage found in systems measuring the full Raman spectrum simultaneously can be observed when analysing a time varying sample. The sample can degrade during a scan, bubbles may pass across the collection volume, and the sample may pass in and out of the focus. In all of these cases if all parts of the spectrum are being acquired simultaneously, as in the case of the spectrometer coupled to a CCD array detector, the relative peak heights of bands in the spectrum will be unaffected. Whereas in systems compiling Raman spectra from sequential discrete measurements any change to the signal returning from the sample will affect the relative Raman band intensity. Moreover, greater accuracy in frequency repeatability is achieved with fixed grating systems than with scanning monochromators.

In array detector systems, increasing the spectral range of the measurement that can be achieved requires a reduction in the dispersion of the signal across the array and hence a reduction in the resolution of the spectrum. Alternatively the grating can be scanned to move the dispersed light across the array. Sequential sections of the spectrum can be acquired and then attached together. Discontinuities caused by wavelength calibration errors, energy sensitivity variations, or a time varying background can occur at the edges

of the segments. These discontinuities can be reduced or removed by using scanning multichannel techniques to combine spectral segments that have a large amount of overlap, thereby averaging out variations between segments. Further detail on this technique can be found in a number of texts.[164,165,166,167]

Although there is a reduction in spectral resolution caused by lowering the number density of lines on the dispersion grating; the signal-to-noise ratio is seen to markedly improve (Table 4.5).

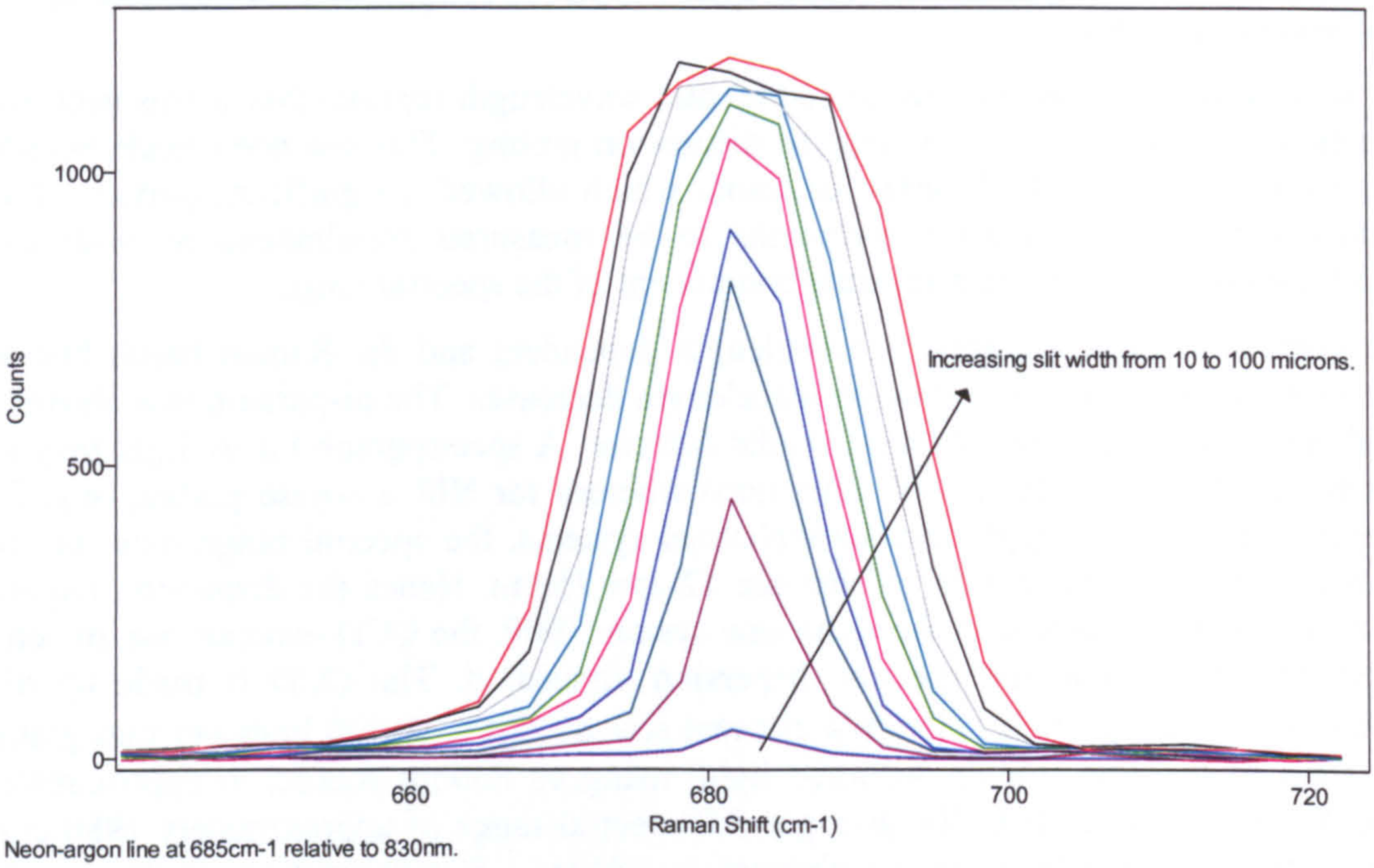

Figure 4.21: Spectra of neon-argon lamp source versus spectrometer entrance slit width. Spectrometer configuration includes a 300 lines mm^{-1} grating and an edge-filter for laser line rejection.

The apparent linewidth of narrow Ne-Ar atomic emission lines have been measured using the 300 lines per mm grating, an entrance slit and a CCD detector. The entrance slit width of the monochromator was adjusted sequentially from 10 to 100 μm. Spectra were acquired for 0.1s at each slit width, for a fixed grating angle. A plot showing a single spectral region centred on a selected peak from the resulting spectra is shown in Figure 4.21; the Raman shift is calculated relative to 830nm. A plot of the full-width-half-maximum (FWHM) of four of the neon-argon lines versus slit width is shown in Figure 4.22. This plot demonstrates that the apparent linewidth increases with increasing slit width, and hence the effective resolution of the system decreases. A balance was made between the stray light rejection of the monochromator entrance slit and the effective resolution of the system to provide sufficient signal to reach the detector. All subsequent measurements (unless stated otherwise) have been measured with a 50μm slit for the 300 lines mm^{-1} grating and with a 100μm slit for the 1200 lines mm^{-1} grating.

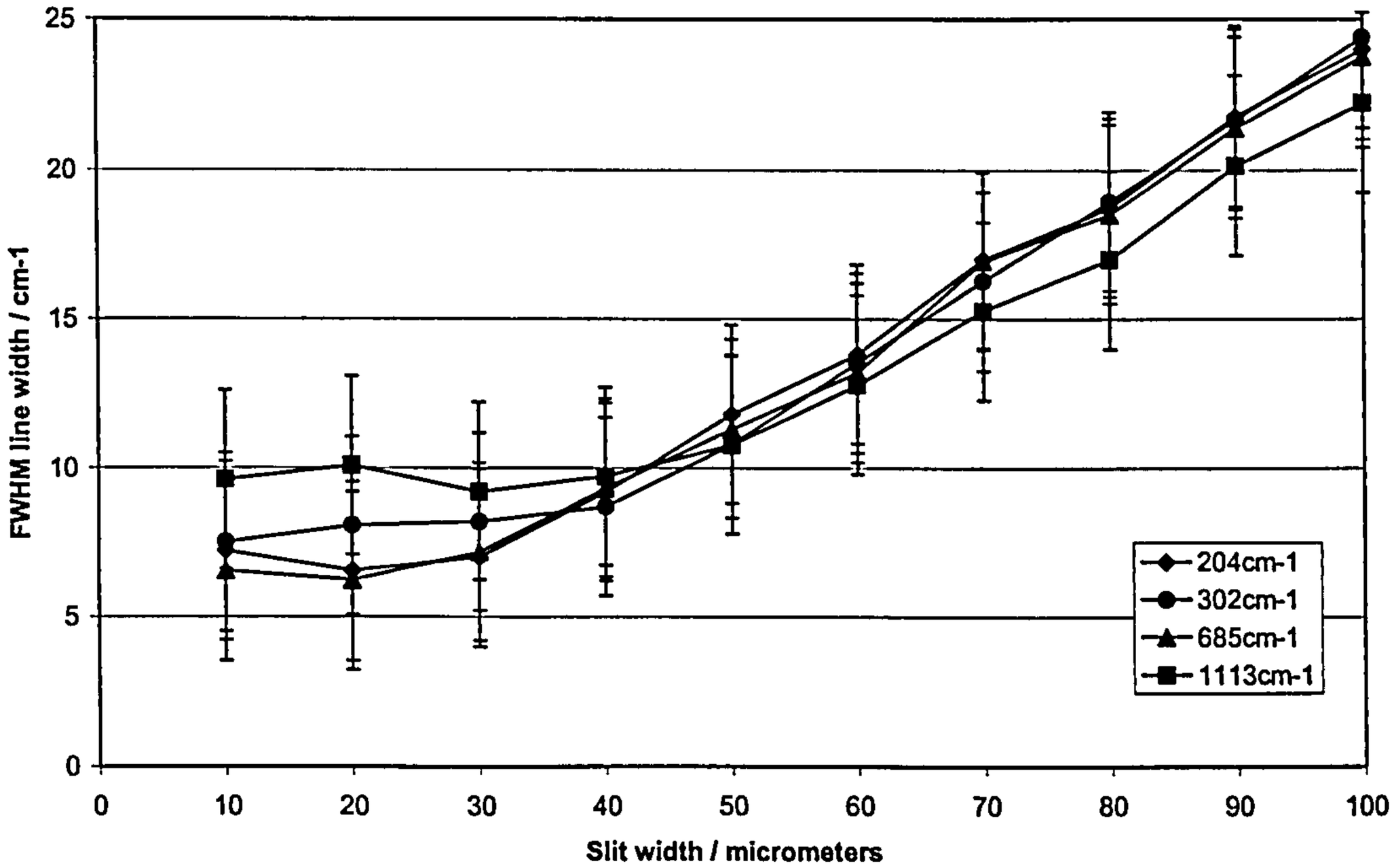

Figure 4.22: The full-width-half-maximum of neon-argon lines measured with the Renishaw system 1000, with a variable entrance slit width. Error bars display wavenumbers per pixel dispersion on CCD. Spectrometer configuration includes a 300 lines mm^{-1} grating and an edge-filter for laser line rejection.

4.2.3.3 Detection

A deep depletion charge-coupled-device (CCD) detector (Renishaw RenCam), comprising of an array of 576x384 detector elements was used to measure the dispersed light from the holographic grating. Thermal noise in the CCD was minimised (≈ 0.05 photoelectrons per pixel per second) by cooling the silicon wafer down to –70°C with a 4-layer Peltier cooler.

Silicon charge coupled device (CCD) arrays are the detectors of choice for most Raman scattering measurements where wavelengths are below 1000nm. CCDs are manufactured from monolithic silicon wafers into a rectangular array of photosensitive elements or pixels arranged in horizontal rows and vertical columns. Most available devices have been developed for imaging and not spectroscopy. This is evident in their aspect ratios of typically 1:1 (512x512 pixels) or 3:2 (576x378 pixels). Charge from the absorbed light is produced by the photoelectric effect and stored in a capacitor. The stored charge is proportional to the number of photons striking the pixel. In spectroscopic applications the spectral or wavelength direction typically corresponds to the vertical columns and the row pixels are usually summed horizontally, providing intensity at each wavelength (see figure 4.23). Charges can be electronically summed on the chip, a process called binning. Adjacent rows and column elements can be binned to improve signal-to-noise ratio, because the electronic summing is effectively noiseless. However when these are binned

in the wavelength dependent direction the achievable spectral resolution will be reduced; so a trade off must be made depending on experimental requirements. There is a finite limit to the number of photoelectrons that can be stored within a pixel; exceeding this limit causes overflow into adjacent pixels. Raman peak distortions and intensity non-linearities will result.

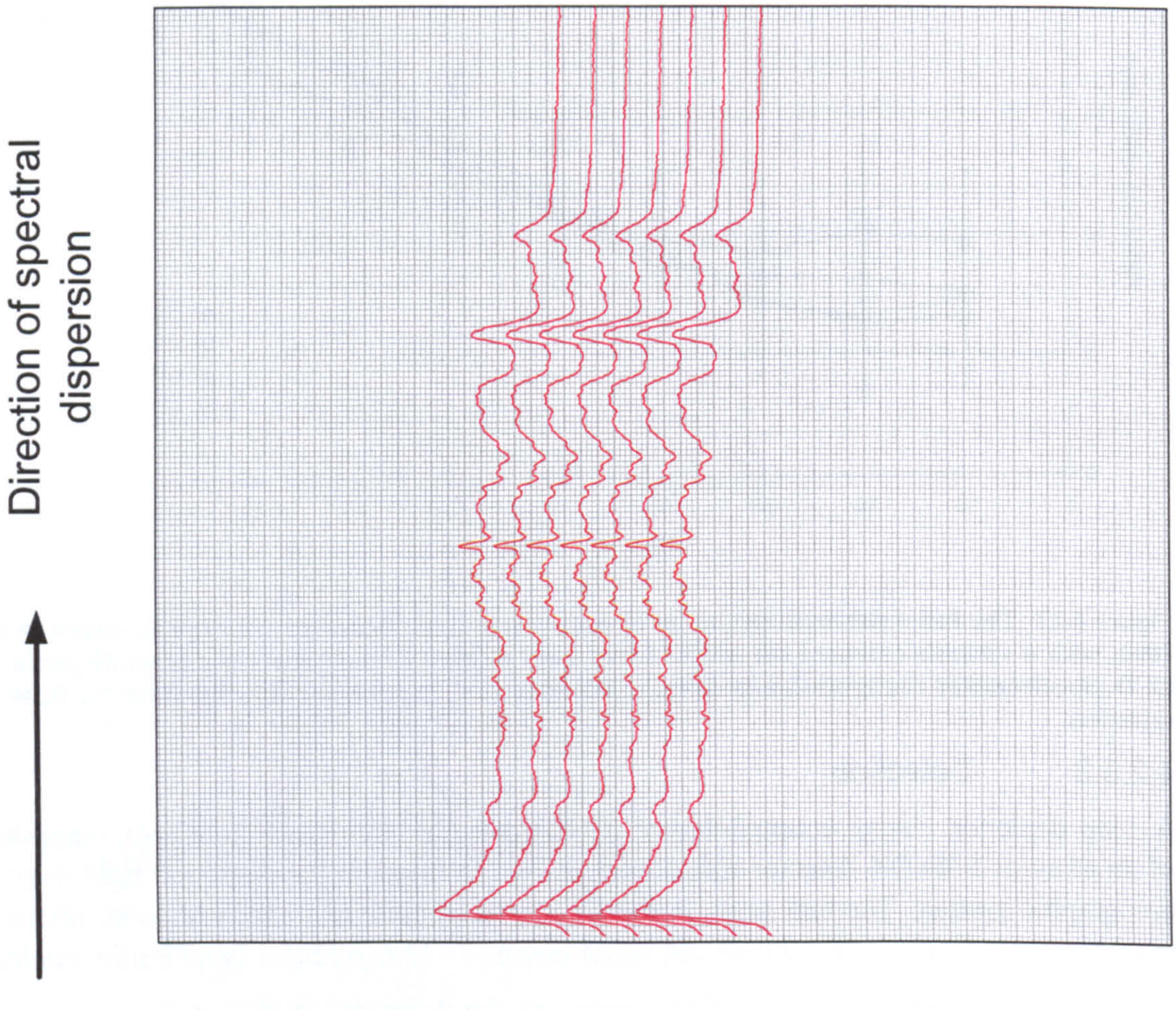

Figure 4.23: diagram of spectra projected onto the CCD pixel array to show the spectral variation in the vertical direction and the intensities can be summed in the horizontal direction.

The stored charges are measured sequentially by being moved across the pixels of the CCD to a single charge sensitive amplifier, whose output is digitised to enable computer storage and manipulation. The time required to readout all the stored charge on a 576x384 pixel CCD, at a digitising rate of 100kHz would be 2.22 seconds. It would also require substantial storage space for a 16-bit digitising accuracy (512kBytes). However,

for spectroscopy a reduced band of pixels, e.g. 20 wide in the intensity direction and 576 high in the energy dispersion direction can be used. The readout can be adjusted accordingly to digitise only the required pixels and discard the remainder. Therefore for a 576x20 pixel array at 100kHz digitisation rate, readout takes approximately 0.1 seconds. Binning the pixels prior to digitisation can also reduce the readout time and in addition reduce the read noise (see 4.2.6.4).

The CCD dark current resulting from thermally produced electrons has been measured to evaluate its impact on tissue Raman spectra (typically acquired in 30 seconds). The measurement was obtained by closing the shutter to the CCD and integrating the counts for 30 seconds. The average of 10 dark current measurements was made and the resulting spectrum is shown in Figure 4.24. The mean dark current was found to be 4.2 ± 3.2 counts in 30 seconds. Towards the edge of the CCD it can be seen that the dark current is substantially higher, due to the temperature gradient from the centre to the edge of the wafer.

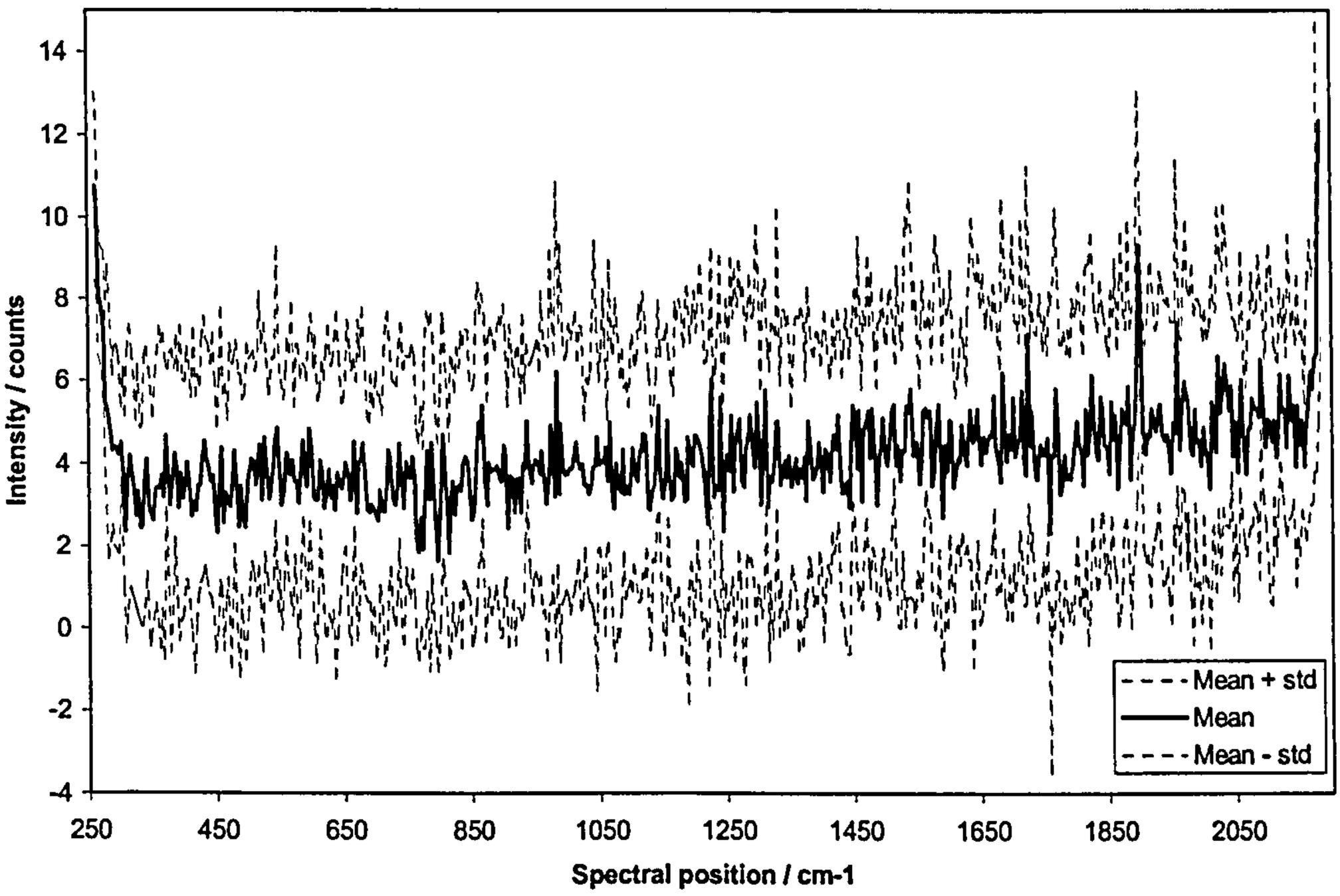

Figure 4.24: Mean dark current in 30 seconds (taken by averaging ten 30 second measurements). The upper and lower curves show the variation in the dark current in the form of the mean plus or minus one standard deviation.

The relative individual pixel sensitivity was measured by moving the narrow silicon Raman peak at 520.4cm^{-1} across the detector array, one pixel at a time (by rotating the dispersion grating) and measuring a spectrum. The time of acquisition was 1 second and the laser power was 18mW at 830nm. The intensity of the silicon peak measured sequentially by each detector element in the array was plotted against position on the wavelength axis on the detector. This plot is show in Figure 4.25 to enable visualisation

of the variability in sensitivity present in the detector. The mean intensity for the silicon peak was 17753.78 counts ± 8.4% for one standard deviation.

In summary CCD detectors have very low dark noise (typically 5 electrons per pixel per hour)[168], low readout noise (4-7 electrons at 50kHz)[168] and better quantum efficiency than the photocathodes of intensifiers or photomultipliers. Quantum efficiencies as high as 90% can be achieved from the visible to the near-IR, out to wavelengths of around 1100nm. There are other detectors (indium gallium arsenide, germanium and indium antimonide single-element and linear arrays) with quantum efficiencies around 70% from 1000 to 2000nm, in the spectral region where there is very little tissue fluorescence. However these devices exhibit levels of readout noise three to four orders of magnitude greater than that of silicon-based CCDs at 1000nm, resulting in measurements limited by detector noise as opposed to shot noise.

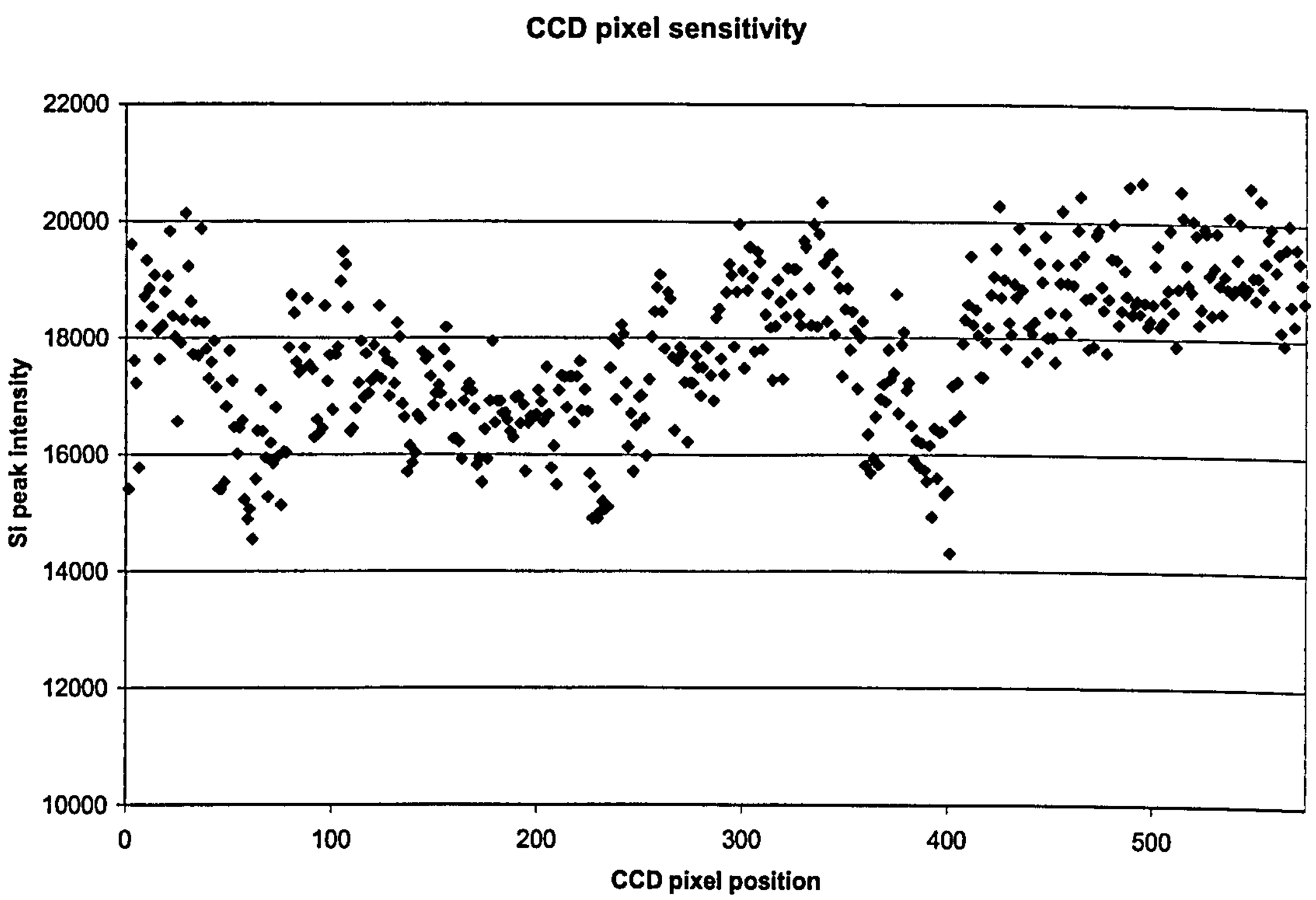

Figure 4.25: Plot of the relative silicon peak scattering intensity versus CCD pixel position, demonstrating the variability of sensitivity between detector elements.

4.2.4 System Calibration

4.2.4.1 Calibration of ordinate (wave number shift)

Wavenumber calibration of the Renishaw Raman system 1000 microspectrometer was achieved using a Neon-Argon standard lamp source. A number of the atomic emission lines were chosen to calibrate the ordinate of the spectrometer. They were selected to cover the spectral range required and to be sufficiently resolvable for the system to measure them accurately without any confusion from nearby lines. A part of the emission

spectrum acquired from the neon-argon lamp is shown in Figure 4.26. The absolute positions of these lines were defined in a text file (or line file). The line file used for the Neon-Argon lamp to calibrate the spectrometer in the 830nm region is displayed in Table 4.6. Calibration was carried out over the absolute wavenumber range of 10000 to 12100 cm^{-1}. The emission from the lamp was aligned with the Olympus x20 objective (N.A. 0.4) and the spectrometer was used to acquire a spectrum for 10 seconds (or less) at each spectral position. The grating was rotated to shift the spectrum in steps of 25 cm^{-1} and the measurement was repeated across the range. The entrance slit for the monochromator was closed down to between 10 and 20μm. Renishaw WIRE software was used to measure the spectrum of the lamp (or any Raman scattering source) and to fit the measured peak positions to the absolute spectral positions in the line file.

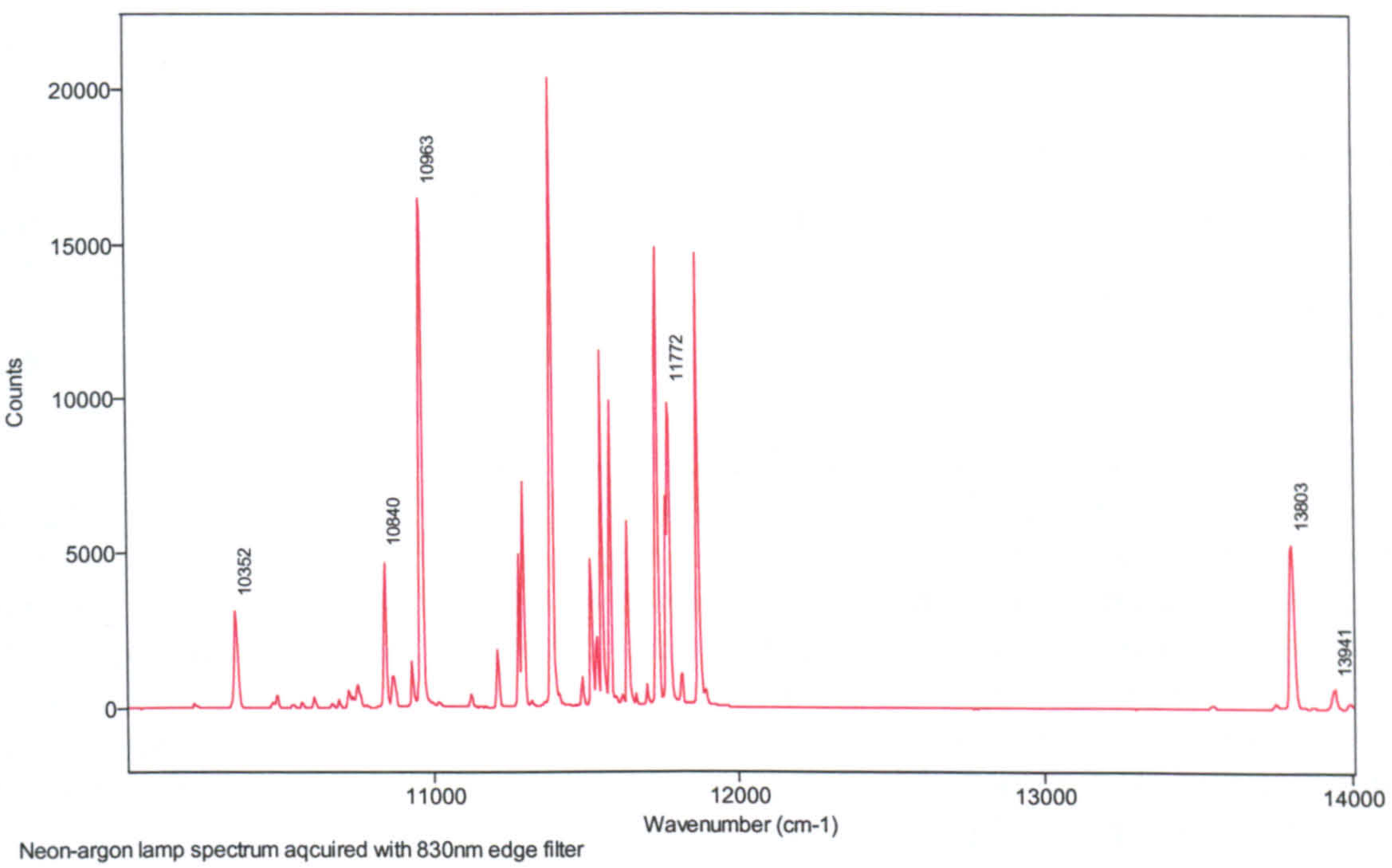

Figure 4.26: Neon-argon discharge lamp source spectrum used for calibration of energy-shift axis. Spectrum acquired with Renishaw system 1000 configured for 830nm excitation, with edge filter fitted for laser line rejection. Some discharge lines are suppressed by the laser line rejection filter.

Wavenumber (in air)	Intensity (counts)
13939.35	2500
13802.30	30300
12581.50	7840
11936.58	3500
11771.13	7440
10961.35	3500
10840.70	440
10354.34	300

Table 4.6: Neon-argon emission lines chosen for calibration of the Renishaw System 1000 at 830nm.

Optimum calibration with the holographic notch filter set and a 300 lines per mm grating configuration was achieved with an average error of approximately 0.4 cm^{-1} and a range of 1.573 to –1.237 cm^{-1}. For the edge filter optimum calibration with the 300 lines per mm grating was achieved with an average error of approximately 0.56 cm^{-1} and a range of 2.182 to –1.949 cm^{-1}.

Long-term drift of calibration was evaluated, for the system configured with 300 lines / mm grating and an edge filter laser line rejection filter set, by measuring daily Raman spectra of a standard of cyclohexane. This enabled shifts in peak positions caused by changes in calibration to be monitored. Spectra were measured with 32mW of 830nm laser light focussed through a uv-grade quartz cuvette contining spectroscopy-grade cyclohexane (Sigma). Integration times of 30 seconds were used. Figure 4.27 displays the relative drift of the seven most significant peaks in the Raman spectra of cyclohexane versus date of measurement. The last few measurments showed a reduction in relative drift. This was achieved by reducing the slit width from 20 to 10μm during calibration with the neon-argon lamp.

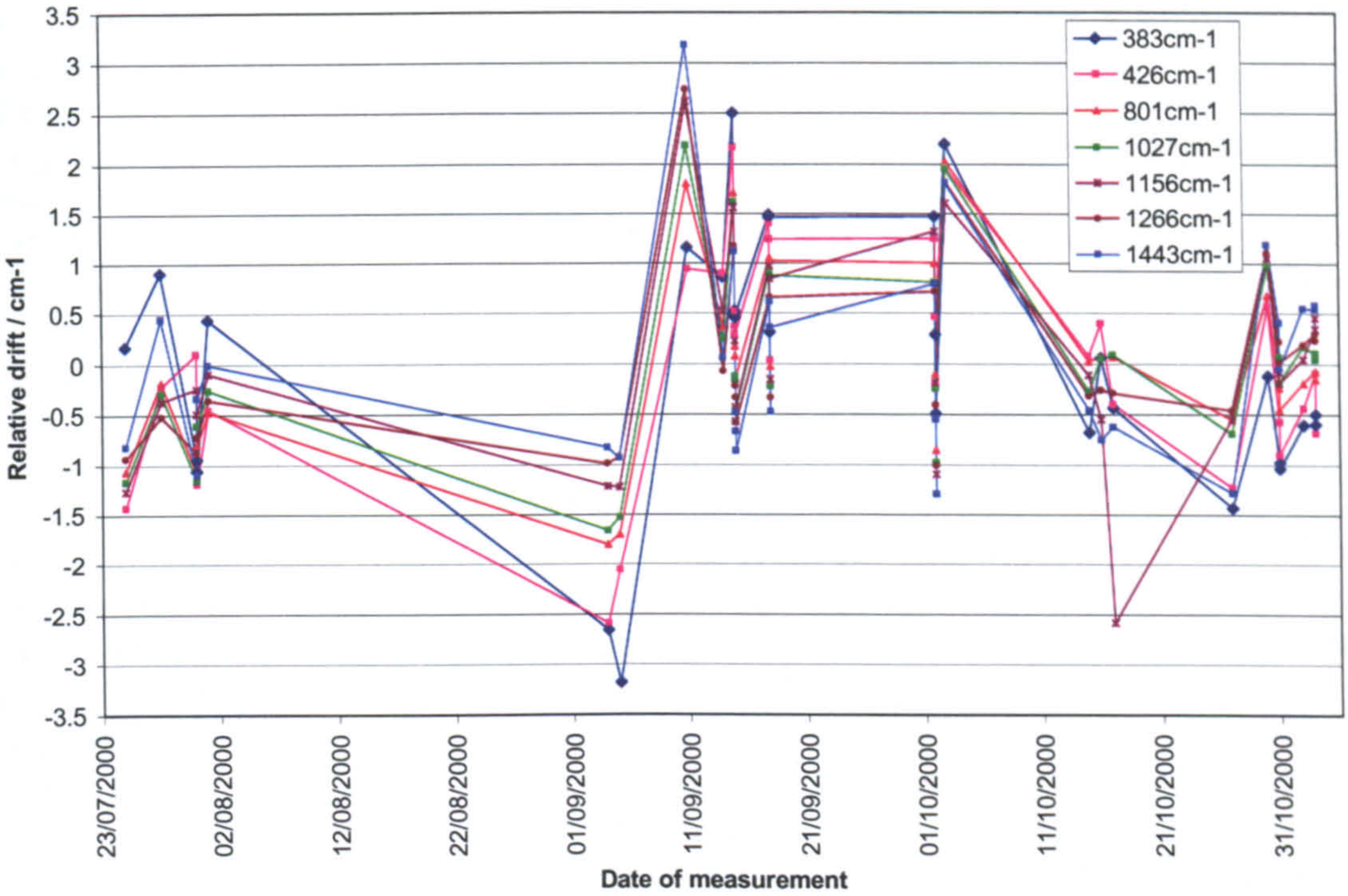

Figure 4.27: Plot of variation in wavenumber position of cyclohexane peaks (relative to mean values) versus date of measurement.

Currently there is little agreement in the literature over wavelength calibration procedures.[169] The typical approach relies upon one of two types of standard sources: either a wavelength standard using atomic emission lines from a gas discharge lamp; or a Raman shift standard derived from standard samples. A spectrum is acquired and in the case of CCD spectrometers, whereby the Raman shift is not linearly dispersed across the detector array, the spectral lines from the standard must be fit using a polynomial function. It is not usually possible to calibrate the intensity axis using the same standard, because the instrument response can severely distort the relative intensities for standard samples measured with different lasers or spectrometers.

The calibration procedure utilising atomic emission lines involves the measurement of the standard spectrum using the spectrometer. The position of the measured lines is then corrected to the true values using a second or third order polynomial. The advantages to this method are the high density of atomic lines across the Raman spectral range; the availability of accurate wavelength tables for line positions; and the repeatability and stability of the source. The main disadvantage with this method is the absolute nature of the emission lines used. If the laser wavelength for Raman excitation is changed and a new calibration is required then a different set of emission lines will be required for each of the laser wavelengths used. If the laser wavelength is not accurately known (±0.01 nm), as in the case of tuneable lasers, then it too must be measured against the atomic line standard.

The Raman shift method relies upon acquiring spectra of Raman shift standards under the same conditions as the experimental sample spectra. The raw Raman shift is adjusted using a second or third order polynomial to the known standard shift frequencies. The positional geometry of the standard can affect the wavelength accuracy. It is important to reproduce the sample configuration for experimental samples and standards. The benefit of using this method is that accurate calibration of the Raman shift can be achieved without accurate knowledge of the laser wavelength. There are increasing numbers of Raman shift standards published in the literature[170,171] using common materials. The greatest inconvenience with using this method is caused by the low density of Raman peaks across the spectral range. It is therefore necessary to use a large set of standards to cover the required spectral range. The shift range between 1800 and 2700 cm^{-1} has a deficiency of peaks for most standards.

4.2.4.2 Calibration of abscisa (intensity) / energy sensitivity correction

A major obstacle that prevents the acceptance of Raman spectroscopy in many fields is the problem associated with widely varying instrumental response. Spectrometers vary in transmission efficiency and detector quantum efficiency with wavelength, thus distorting the true spectrum of intensity against Raman shift. The vast majority of published Raman spectra remain uncorrected for instrumental response and are subject to large variations in relative peak intensities when obtained on different instruments. These variations tend to complicate comparison between spectra from different instruments and different sources, thus making library searches very complex indeed. Determination of Raman cross-sections requires an absolute measure of scattering intensity, so response function corrections are essential.

The majority of the change in instrument sensitivity varies slowly with wavelength. This is mainly caused by the gradual change in quantum efficiency of the detector across the spectral range. A smaller contribution to the response function originates from etaloning in the CCD, modal interference in optical filters, and variation in the CCD pixel sensitivity (Figure 4.25). This can cause a rapid oscillation in the sensitivity of a Raman instrument with changing wavelength.

The energy transfer function of the system was evaluated by measuring the slowly varying spectrum of a tungsten-filament lamp. The lamp source has been calibrated against a secondary standard by the National Physical Laboratory (NPL) and the user is provided with a spectrum of absolute intensities versus wavelength at a fixed distance from the source. Using the illumination geometry shown in Figure 4.16 to measure the white light spectrum using the Raman spectrometer it was possible to calculate the energy transfer function of the system by dividing the absolute spectrum of the lamp (Fig 4.28) by the measured spectrum. This transfer function can then be used to correct measured spectra for the energy dependent sensitivity of the system by multiplying the function by the measured spectrum. Figure 4.29 shows the absolute and measured spectra of the lamp and the calculated energy sensitivity function. These are given as an example and the process has been repeated at regular intervals when spectrometer configuration changes have been made.

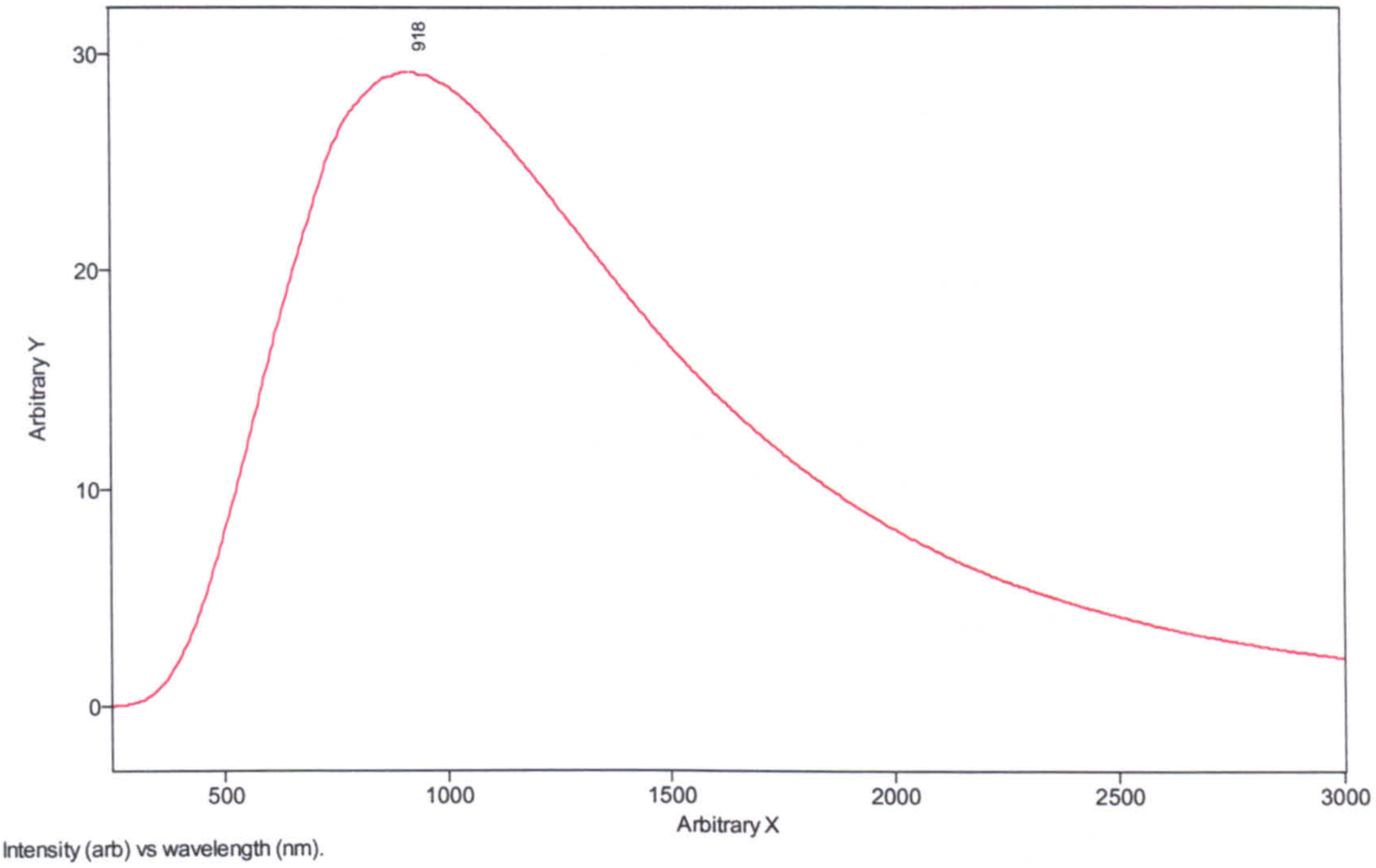

Figure 4.28: Absolute spectrum from an NPL calibrated, tungsten-filament lamp source, powered with a constant current supply.

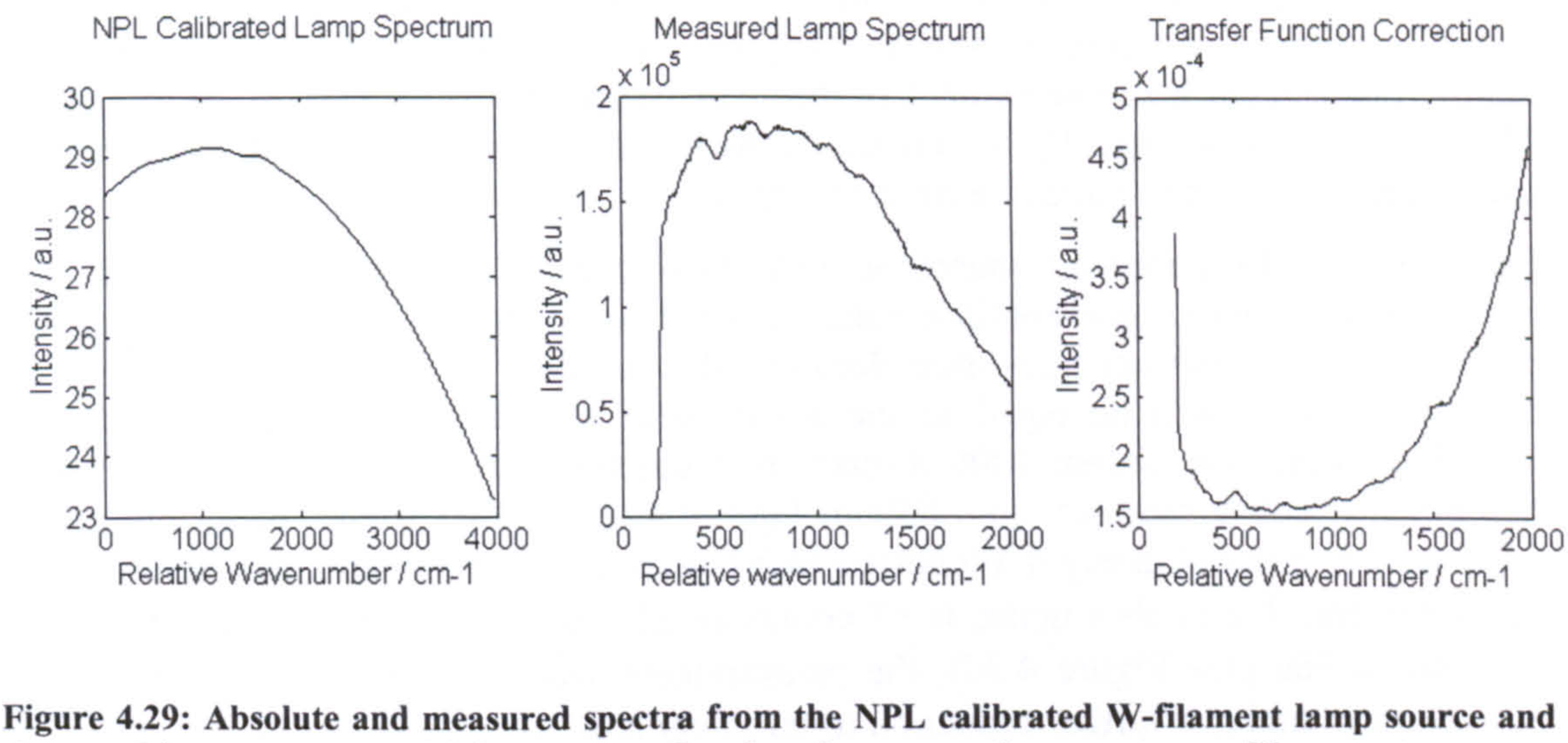

Figure 4.29: Absolute and measured spectra from the NPL calibrated W-filament lamp source and the resulting energy sensitivity or transfer function correction spectrum. The spectrum was measured with the 1200 lines per mm grating and the HNF pair configured for laser line rejection.

A typical Raman spectrum of normal oesophagus tissue at 830nm has been corrected for system energy sensitivity by multiplying the spectrum by the transfer function. The raw and corrected spectra are shown in Figure 4.30 for comparison.

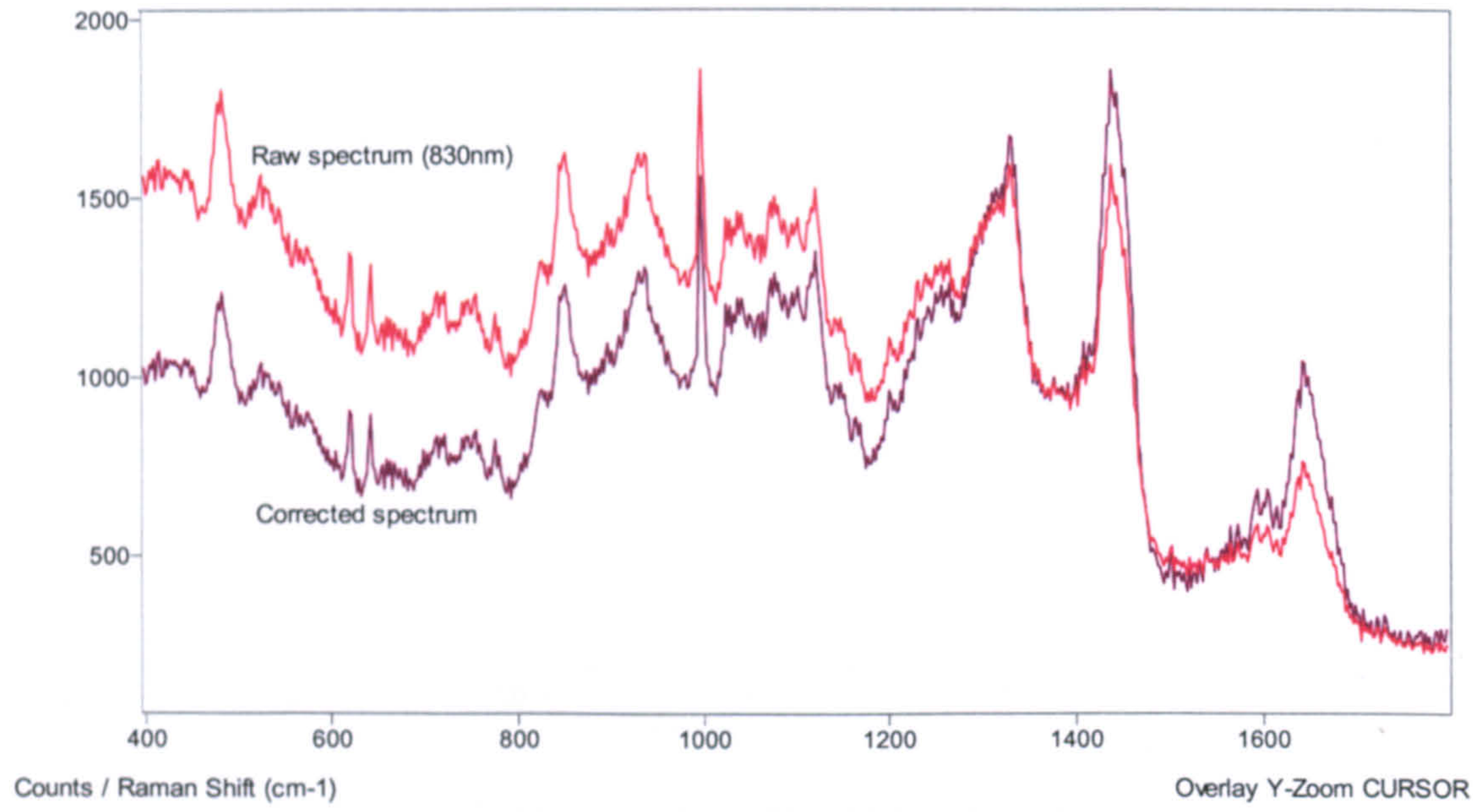

Figure 4.30: The effect of energy sensitivity correction on an 830nm Raman spectrum of normal oesophageal mucosa. The correction tends to flatten out the spectrum.

4.2.6 Appraisal of Noise Contributions

Raman spectroscopy for the measurement of biochemical changes in tissue depends as much upon the signal-to-noise (S/N) ratio as the magnitude of the measured Raman signal alone. The S/N ratio is a useful measure describing the quality of the spectrum, its inverse is the relative precision of the measurement, or the relative standard deviation from the true signal. This section aims to quantify the contributions to the Raman spectrum of each common component of noise or source of erroneous signal.

Shot noise is the dominant source of noise in dispersive Raman measurements. It is caused by the random probabalistic nature of light and matter. If the intensity of light is measured with a perfect noise-free detector, the standard deviation of the number of detected photons will be equal to the square root of detected photons.[172] Using the optimised Renishaw system 1000 Raman spectrometer to measure Raman scattering in oesophagus biopsy samples, with 830nm light, the strong C-H stretch band intensity at 1455 cm^{-1} is approximately 4500 counts in 30 seconds. Therefore the uncertainty of the measurement, due to shot noise, is 67 counts or ±1.5%. If the time of acquisition were reduced to 10s (see Figure 4.30), the measurement would yield 1500 ± 39 counts or ±2.6% uncertainty; a further reduction to an integration time of 1s would give 150 ± 12 counts or ±8% uncertainty. This example shows the effect of reducing acquisition time leads to a reduction in the signal to noise ratio and the certainty of the measurement.

It must be noted that the shot noise will not only originate from the Raman scattering signal but also background signal such as stray light and fluorescence signal. Therefore even if these signals can be subtracted the shot noise contribution will remain superimposed on the measurement, sometimes completely obscuring the Raman spectrum. For example if the fluorescence background induced in a sample produces 1000 counts per second at a particular wavenumber of a Raman scattering band that produces 100 counts per second, then the combined signal at the band position will be 1100 counts ± 33 counts from shot noise. Following subtraction of the fluorescence signal of 1000 counts we are left with the Raman band intensity of 100 photons ± 33 photons or ± 33% uncertainty.

Laser-induced fluorescence is the most common source of background light encountered in Raman spectroscopy. Fluorescence spectral features are usually much broader than Raman bands, and often look like a slowly changing baseline in the Raman spectrum. Some fluorophores can have fluorescence cross-sections 10^{10} times larger than typical Raman scattering cross-sections. Therefore even at tiny concentrations they can produce a fluorescence background stronger than the Raman spectrum of the bulk material. At 830 nm tissue fluorescence background contributes around 100 counts per second, whereas the Raman signal can be between 5 and 50 counts per second.

The effects of variation in pixel sensitivity and thermal noise across the CCD detector have been measured in section 4.2.3.3. Both of these phenomena will superimpose a fixed pattern noise on the Raman spectrum. The effects of these can be reduced by binning several illuminated pixels in the intensity direction; or can be corrected by collecting a spectrum of light that changes slowly with wavelength and dividing the Raman spectrum by the source spectrum. (This procedure has been outlined in 4.2.4.2.) CCDs have an inherently low dark noise that will depend upon the pixel location, as there will be a temperature gradient from the centre to the edge of the chip, yielding fixed pattern noise plus random noise. The Renishaw CCD detector was cooled to –70°C to reduce thermal noise contributions to a minimum.

The contribution to the signal from the CCD (Renishaw RenCam) readout noise is approximately 7 electrons per readout. Read noise is a random noise and therefore increases with the square root of the number of readouts per channel. In the case where an active region of 576x20 pixels was being used, when reading out 20 pixels separately then the read noise would be around 32 electrons per wavenumber channel (this equates to approximately 6 counts with the Renishaw system in high gain mode). However, if the 20 pixels are binned and digitised together the read noise would be about 7 electrons per channel.

Cosmic rays passing through the photosensitive region can produce thousands of photoelectrons. This effect results in a very strong sharp signal in the Raman spectrum. Quantification of spike noise is difficult due to the random nature of its occurrence. However, it is usually quite obvious to the observer when a spectrum of biological tissue contains a contribution from spike noise. These spikes can be erased from the spectrum or the whole spectrum can be discarded.

The effect of ambient lighting, another source of fixed pattern noise, on tissue Raman spectra acquired at 830nm was evaluated. Spectra of oesophageal biopsy samples were measured with either no ambient light in the laboratory; the overhead fluorescent light; or the tungsten-filament stand-lamp. Spectra were integrated for 30 seconds with a laser power of 32mW focussed on the sample with an Olympus x80 MIRPLAN ultra-long-working-distance lens. Figure 4.31 shows the resulting spectra. There appears to be little visible difference between them. It is therefore concluded that normal sources of ambient lighting have little effect on the tissue spectra at 830nm.

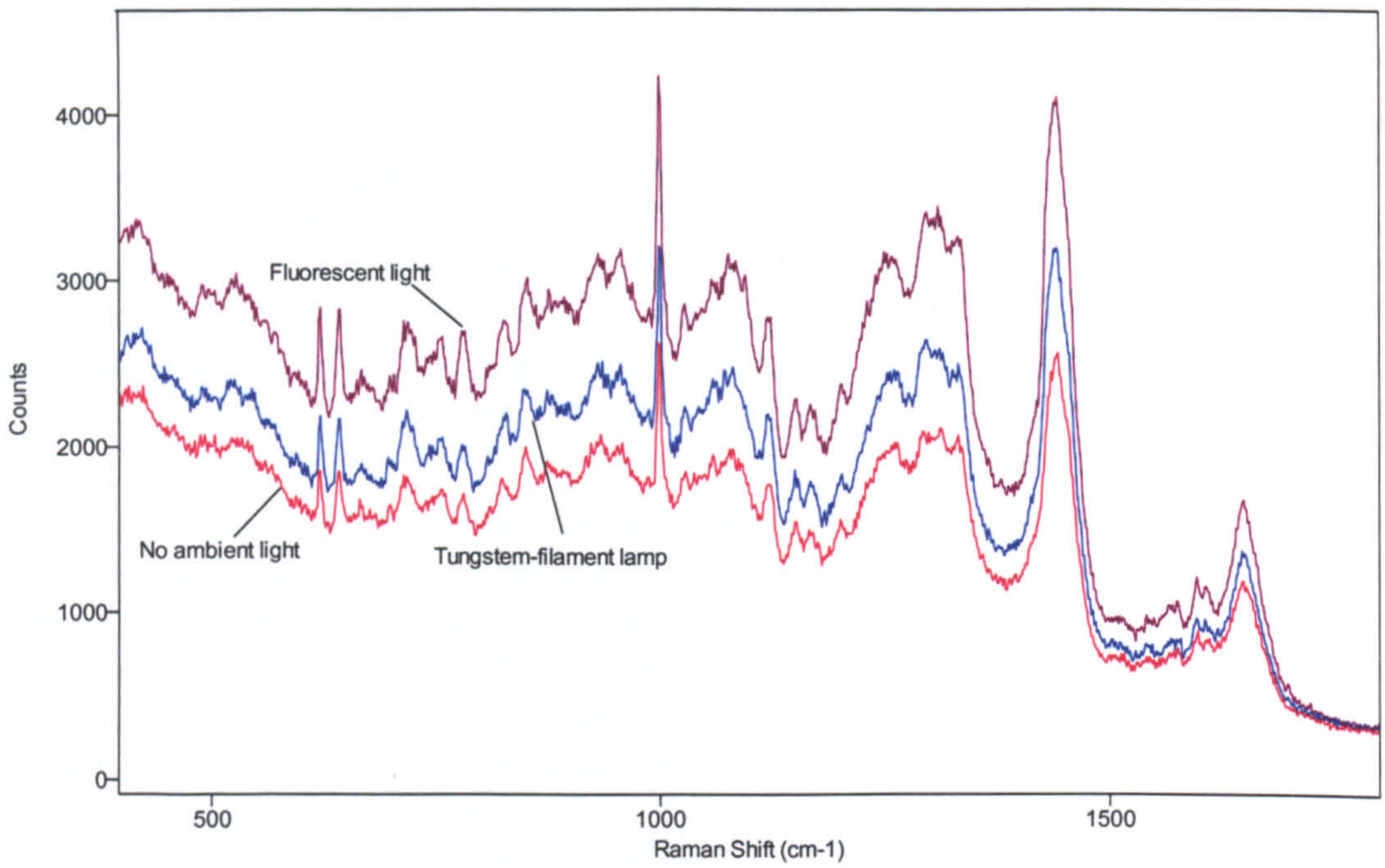

Figure 4.31: Oesophagus spectra measured at 830nm with different configurations of ambient lighting.

Source noise is caused by fluctuations in the irradiance of the incident light, which inherently causes fluctuations in the Raman scattering. Simultaneous measurement of all spectral components across the CCD array reduces the effect of this noise in an individual spectrum. However, comparison of one spectrum to the next for quantification of biochemical changes is complicated by source noise. The fluctuation in intensity and wavelength of the Ti:sapphire source has been quantified in section 4.2.1.1.

An often neglected source of fixed pattern noise is that caused by instrument alignment and calibration errors. Unwanted information about the performance of the Raman instrument is added to the Raman spectrum. Calibration drift errors have been assessed in section 4.2.4.1.

In summary, a typical Raman spectrum of fresh tissue, measured at 830nm for 30 seconds with a laser power of 32mW at the sample, will include a C-H stretch peak at 1445cm^{-1}. If the intensity at this peak is for example 4500 counts (see Figure 4.30) then a contribution of 67 counts will be due to Shot noise (4.2.6.1). The total signal of 4500 counts is made up of approximately 3000 counts of fluorescence signal and 1500 counts

of inelastic scattering signal. The contributions from fixed pattern noise sources have been minimised by multiplying the spectra by correction files. Read out noise contributes about 6 counts and the dark current or thermal noise in the CCD contributes approximately 4 counts in the 30s integration time. Hence measurement repeatability due to quantifiable noise contributions is approximately ±5% for the 1445cm^{-1} peak measured in 30 seconds. This can be converted to a quantifiable S/N ratio of 20. The theoretical noise contributions agree well with the measured S/N ratio at 830nm of 18.5 (see Table 4.2).

4.3 Experimental Methods

4.3.1 Detection of Early Malignant Changes in the Larynx

The goal of this study was to assess the feasibility of using NIR Raman spectroscopy for the early diagnosis of laryngeal malignancy originating in the squamous epithelial layer. Samples were collected, stored and histopathologically analysed following the procedure explained in section 4.1.1. Samples exhibiting mixed pathologies were rejected from this study. Raman spectra of normal larynx, dysplastic larynx and squamous cell carcinoma of the larynx were characterised in order to determine the potential of Raman spectroscopy to differentiate samples of distinct pathologies. The Raman scattering measurements were carried out in vitro with a customised Renishaw System 1000 Raman micro-spectrometer. The Ti:sapphire laser was tuned to provide an excitation wavelength of 830nm and a holographic notch filter pair (Kaiser) was used to reject unwanted light of the laser wavelength collected by the system. A 1200 lines per mm holographic dispersion grating (Optometrics) was used to separate the collected light into its spectral components. To enable measurement of the full fingerprint region of the tissue Raman spectra (400 to 1800cm^{-1}) with this grating it was necessary to scan the spectrum across the CCD using 'extended scan mode'. Otherwise the system configuration used for this experiment has been outlined in detail in section 4.2.

Twenty-five laryngeal biopsy samples were measured. They were orientated so that the incident laser beam illuminated the epithelial surface, with a similar geometry to that that would be used in vivo. Tissue samples were held in position on the microscope stage between two calcium fluoride slides (see Figure 4.32). A x80 ultra-long-working-distance lens was used to focus the laser beam (power at sample of 32 ± 1.1 mW) to a spot size of 2μm on the tissue surface and collect the scattered photons in non-confocal mode. The entry slit to the monochromator was set to 100μm. A minimum of five spectra were acquired from each sample (mean number = 7.96, range 5 to 12). The scattered Raman signal was integrated for 30 seconds and measured over a spectral range of 400-1800 cm^{-1} with respect to the excitation frequency.

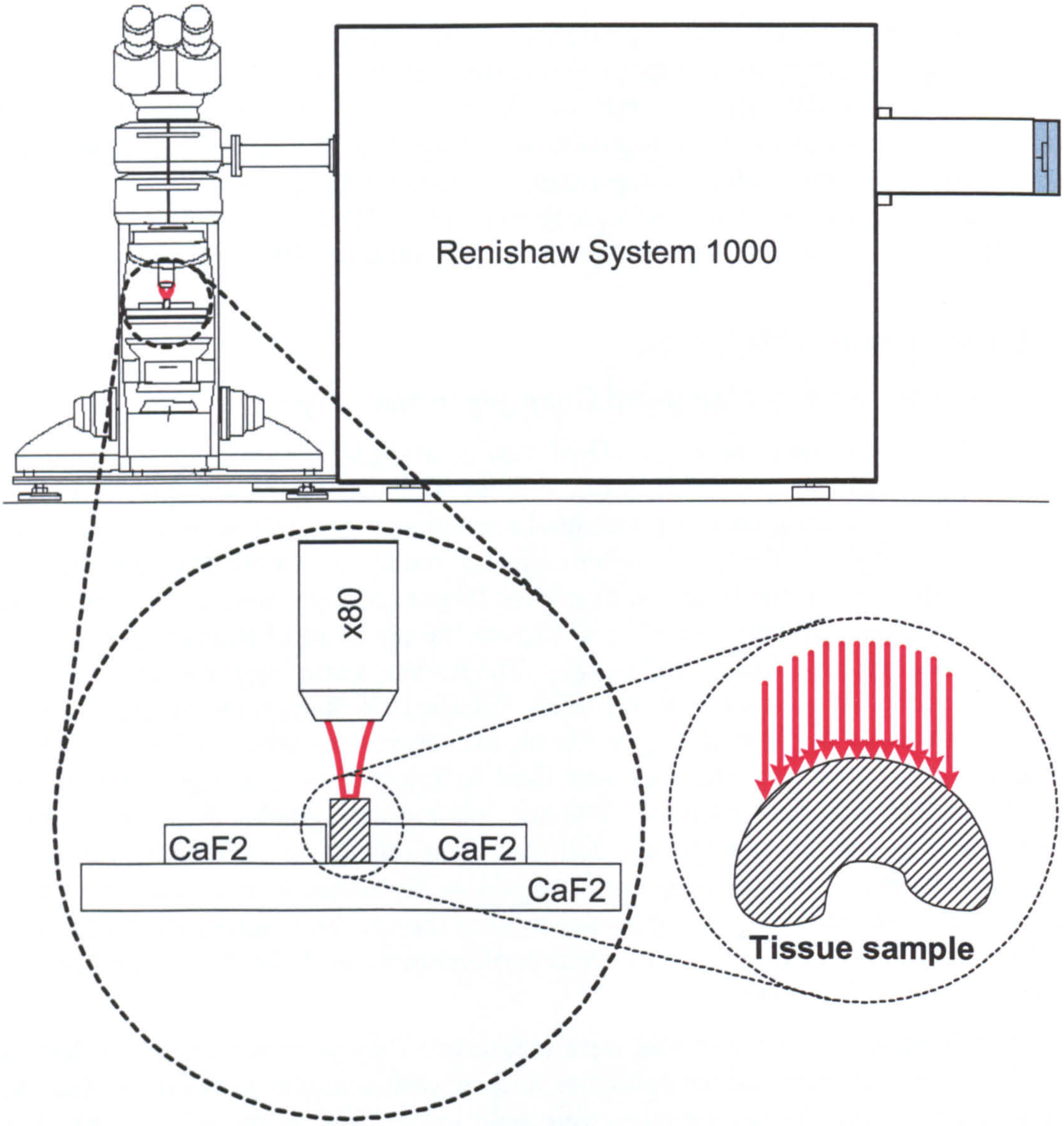

Figure 4.32: Schematic diagram of the Raman microspectrometer used to measure inelastic scattering from biopsy samples.

The Raman spectrometer was calibrated for wavenumber shift using a neon-argon lamp standard and Renishaw WIRE software (refer to Section 4.2.4.1). Tissue spectra were corrected for the energy dependent response of the system by multiplying the measured tissue spectrum by the energy transfer function measured using a tungsten-filament lamp with a spectral output calibrated by the National Physical Laboratory, UK (refer to Section 4.2.4.2). No further manipulation of the tissue spectra was performed prior to analysis. Intra-sample repeatability was evaluated and mean spectra for each tissue pathology were obtained. Any correlation between Raman spectral variations and histopathology was assessed using empirical and multivariate data analysis techniques. This involved the evaluation of absolute peak intensities or peak intensity ratios to look

for any correlations with pathology; in addition to developing multivariate classification models using principal component analysis and linear discriminant analysis methods.

4.3.2 Detection of Early Malignant Changes in Barrett's Oesophagus

The goal of this study was to assess the feasibility of using NIR Raman spectroscopy to detect early malignant changes in the oesophagus and to study the pathogenesis of adenocarcinoma in Barrett's oesophagus. Raman spectra of 9 histopathological groups (normal, cardiac Barrett's, fundic Barrett's, intestinal metaplasia, low grade dysplasia, high grade dysplasia, adenocarcinoma, squamous dysplasia, and squamous cell carcinoma), defined in Appendix 2, were measured in order to determine the potential of Raman spectroscopy to discriminate between samples of distinct pathologies. Samples were collected, stored and histopathologically analysed following the procedure explained in section 4.1.2. Samples exhibiting mixed pathologies were rejected from this study.

The Raman scattering measurements were obtained in vitro with a customised Renishaw System 1000 Raman micro-spectrometer. The Ti:sapphire laser was tuned to provide an excitation wavelength of 828nm and an edge filter pair (manufacturer confidential) was used to reject unwanted light of the laser wavelength collected by the system. A 300 lines per mm holographic dispersion grating (manufacturer confidential) was used to separate the collected light into its spectral components. This enabled measurement of the full fingerprint region of the tissue Raman spectra (400 to 1800cm^{-1}) without the need to move the grating. However a compromise in spectral resolution has been made. The procedure of optimisation of the system configuration for use in this experiment has been outlined in Section 4.2.

Eighty-nine oesophageal biopsy samples were measured. Tissue samples were orientated in the in vivo geometry (tissue surface facing the laser beam) and placed between two calcium fluoride slides (Figure 4.32). A x80 ultra-long-working-distance lens was used to focus the laser beam (power at sample of 31 ± 0.8 mW) to a spot size of 2-3 μm on the tissue surface and to collect the scattered photons in non-confocal mode. The entry slit to the monochromator was set to 50μm. A minimum of 10 spectra were acquired from each sample (mean number = 14, range 10 to 20). The scattered Raman signal was integrated for 30 seconds and measured over a spectral range of 200-2100 cm^{-1} with respect to the excitation frequency. All other experimental procedures and data analysis methodologies were the same as those for the larynx samples, as described above.

4.3.3 Detection of Early Malignant Changes in Formalin Fixed Tissue (Barrett's Oesophagus)

Raman spectroscopy for the evaluation of histopathology on formalin fixed tissue is likely to provide a more flexible pathological tool than that using fresh or snap frozen tissue. The aim of this study was to assess the use of NIR Raman spectroscopy to measure histopathological state in formalin fixed oesophagus tissue. Raman spectra of eight histopathological groups (normal, cardiac Barrett's, fundic Barrett's, intestinal metaplasia, low grade dysplasia, high grade dysplasia, adenocarcinoma, and squamous dysplasia), defined in Appendix 2, were measured in order to determine the potential of

Raman spectroscopy to discriminate between samples of different pathologies. Samples were collected, sectioned, stored and histopathologically analysed following the procedure explained in section 4.1.2.2. Samples exhibiting mixed pathologies were rejected from this study. Approximately half of the samples were stored for 18 months in 10% formalin (phosphate buffered) and the remainder stored for 2 to 3 weeks in the same fixative solution. This enabled an assessment of the effect of storage time on the achievable spectral discrimination between pathological types.

The Raman scattering measurements were obtained using the procedure outlined in section 4.3.2 Forty-three oesophageal biopsy samples were measured. A minimum of 7 spectra were acquired from each sample (mean number = 9.7, range 7 to 15). The scattered Raman signal was integrated for 30 seconds and measured over a spectral range of 200-2100 cm^{-1} with respect to the excitation frequency. Raman spectra were corrected for energy sensitivity of the system. However, no further manipulation of the tissue spectra was performed prior to analysis. Intra-sample repeatability was evaluated and mean spectra for each tissue pathology were obtained. Any correlation between Raman spectral variations and histopathology was assessed using empirical and multivariate data analysis techniques, as described above for the larynx samples. In addition, any correlation between tissue Raman spectra with time of storage in the formalin has been evaluated.

4.3.4 Monitoring of Temperature Dependence of Raman Spectra

The temperature dependence of tissue Raman spectra has been measured between 10 and 50°C to enable evaluation of differences between measurements made at laboratory temperatures and those to be made in vivo. Five normal oesophagus biopsy samples were used in this experiment. They were collected, stored and prepared following the procedure laid out in 4.1.2. A Linkram THMS600 hot/cold stage, that allowed accurate (±0.1°C) temperature selection in a stable nitrogen atmosphere, was used to vary the temperature of the tissue samples in steps of 10°C over the range 10 to 50°C. The stage temperature was governed by a remote control unit (Linkram TMS93) and temperatures were reached by using a feedback loop with resistive heating and liquid nitrogen cooling. Samples were allowed to equilibrate for five minutes at each new temperature prior to measurement with the Raman microspectrometer. Figure 4.33 shows the geometry of the tissue sample within the hot/cold stage.

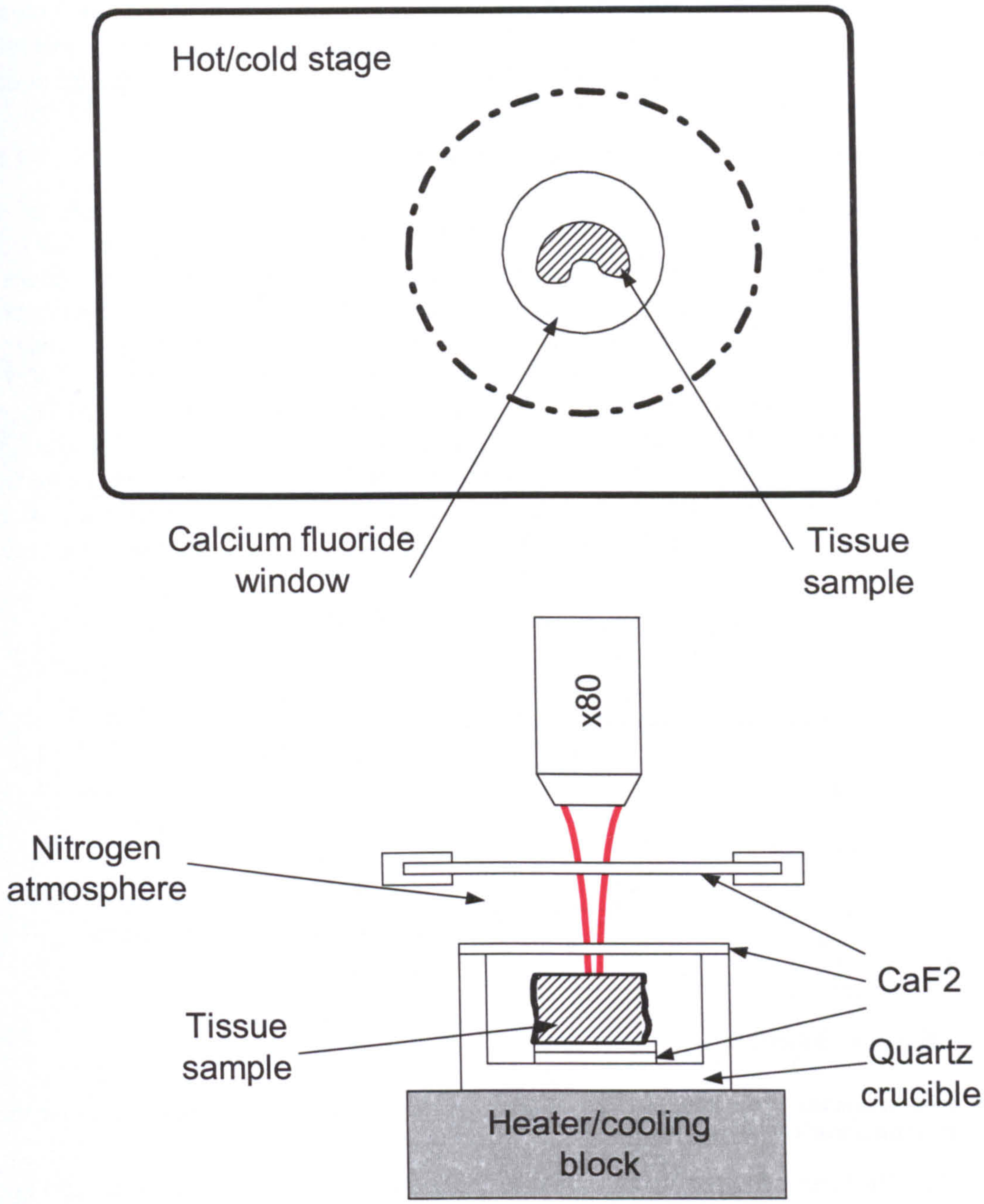

Figure 4.33: Schematic diagram showing tissue sample position in hot/cold stage.

Static spectra centred at 1150cm^{-1} were acquired by focussing the 828nm, 32mW, laser spot through the calcium fluoride windows and onto the surface of the tissue sample. It must be noted that reflections from refractive index boundaries substantially reduced signal levels compared with those achieved with direct illumination of the surface of the tissue. Therefore the collected signal was integrated for 60 seconds to provide adequate signal-to-noise ratio for analysis. The Olympus x80 ultra-long-working-distance

microscope objective was used in conjunction with a small monochromator slit size (20μm), and a band 4 pixels wide on the CCD detector, thus minimising the contributions to the signal from materials found outside the focal volume. The resulting spectra at each temperature were compared to evaluate observable differences.

4.3.5 Raman Depolarisation Ratio Measurements

A schematic diagram outlining the optical illumination and collection path of the microspectrometer is shown in Figure 4.34. It includes polarisers (Oriel, gelatine) that were used to enable evaluation of the depolarisation of the Raman vibrational modes in the tissue, and a half-wave plate (Oriel, 850nm) to enable an evaluation of the effect of illumination polarisation direction. These polarisation selection components can be rotated into or out of the beam. The polarisation from the Ti:sapphire laser was >100:1 in the horizontal direction. The arrows in the beam path show the direction of the electric vector component of the incident laser light. Rotating the half-waveplate into the laser beam caused the rotation of the polarisation of the incident light to >100:1 in the vertical direction. The polarisers were used to analyse the direction of the polarisation of the collected Raman scattered signal, by rotating them into the collection path one at a time.

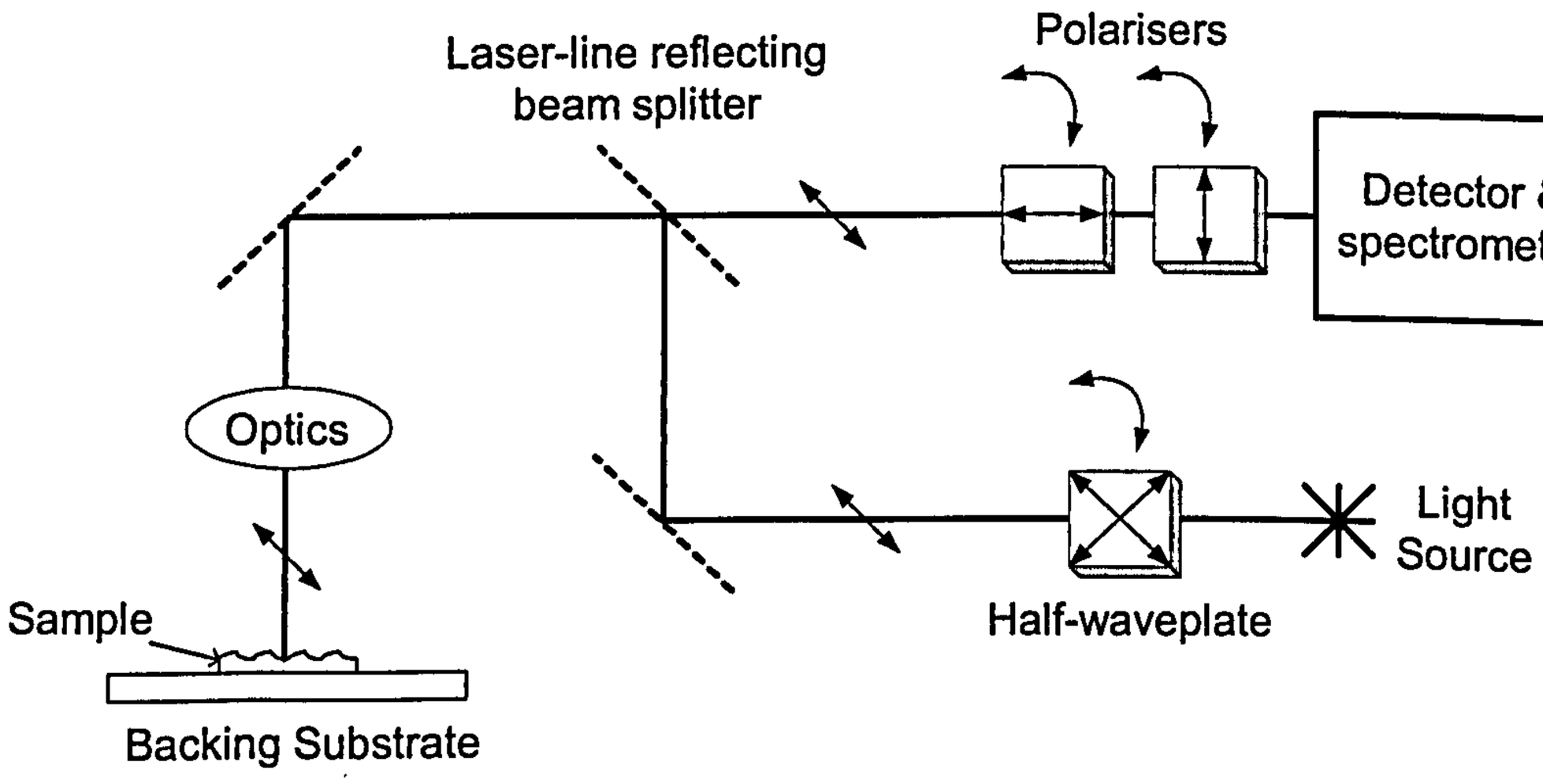

Figure 4.34: Schematic of the illumination and collection optical path of the microspectrometer used for polarisation sensitivity measurements.

Raman spectra were acquired using 32mW of 828nm laser light focussed to a 2μm spot using a x80 objective. The Raman scattered signal was integrated for 30 seconds for each position of the polarisation components: all out of the beam; horizontal polariser in, vertical polariser out; vertical polariser in, horizontal polariser out; and a repeat of the above with the half-waveplate in the incident beam path. This was repeated for a number of positions on the tissue. The resulting spectra were used to calculate the depolarisation ratio of each Raman peak.

4.3.6 Monitoring Effects of Sampling Depth

An investigation was made into the dependency on the depth of measurement beneath the mucosal surface of Raman spectra of oesophagus tissue. This was to enable evaluation of the possible effects of changing the depth of focus used to measure in vivo / in vitro tissue Raman spectra and to evaluate the possible contributions from underlying tissue layers. 20μm thick sections of snap frozen oesophageal biopsy samples were cut by freezing microtome during preparation of samples for histopathological analysis. They were placed on a calcium fluoride slide, orientated to show a cross-section through the tissue layers and positioned under the microscope. The sample was aligned using white light illumination through the x5 objective. A photograph was taken of the tissue showing the start position for mapping at 0,0 (Figure 4.35). The objective was changed to the Olympus x80 ultra-long-working-distance lens and used in conjunction with a small monochromator slit size (20μm), and a band 4 pixels wide on the CCD detector, thus minimising the contributions to the signal from materials found outside the focal volume. Spectra were measured at 830nm, with 32mW of laser power for 60 seconds at positions ranging from y=0 to –750μm and x=0 to 100μm by moving the laser spot in a raster pattern across the sample in steps of 10μm. This was achieved by translating the PC-controlled XYZ motorised stage. The y-direction represented depth beneath the mucosal surface. Spectra were saved for future analysis.

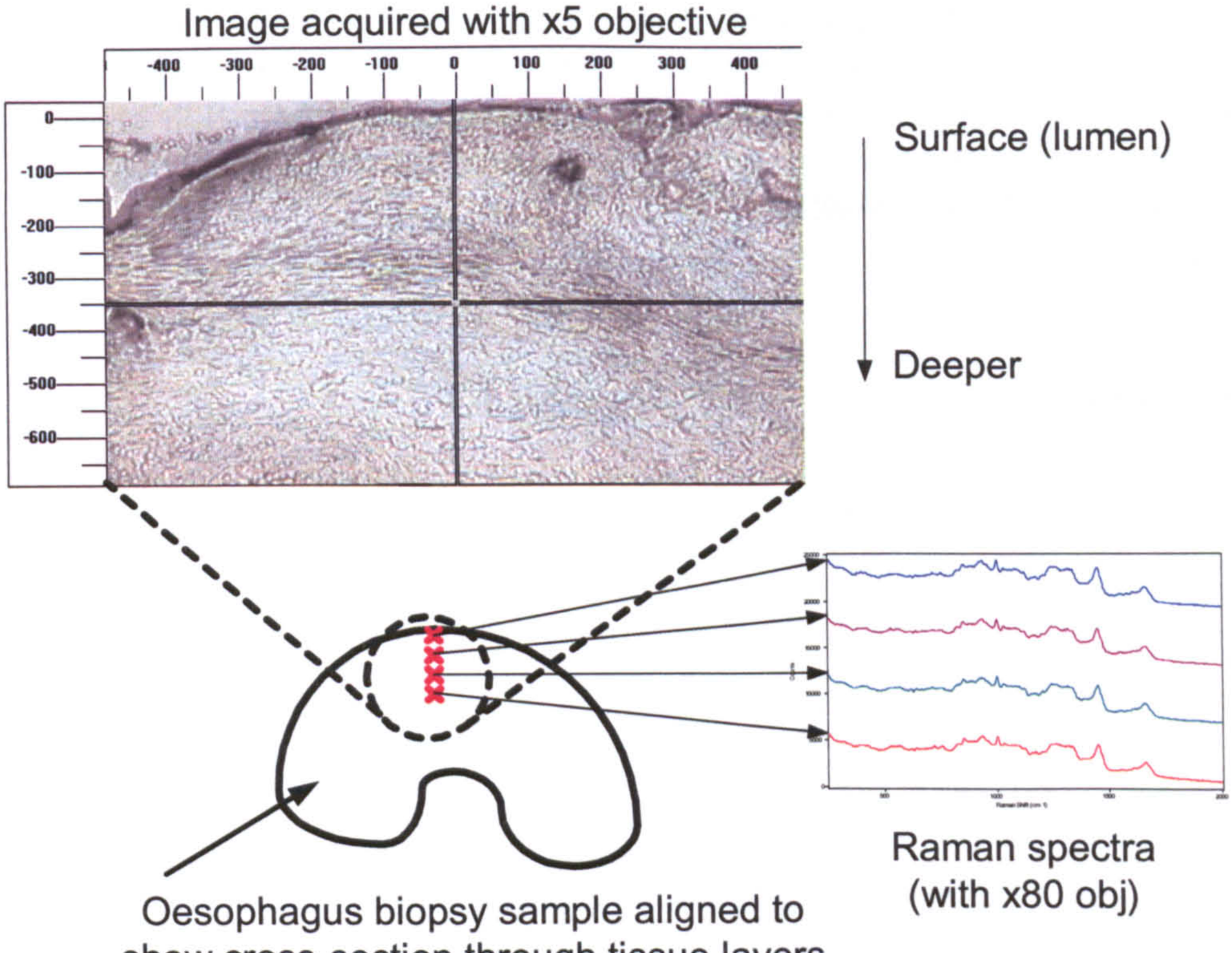

Figure 4.35: Schematic of spectral mapping to look at the differences between Raman spectra from the surface and deeper tissue layers in the oesophagus.

4.3.7 Confounding Factors

The effect of contamination on tissue Raman spectra from materials found in the in vivo environment have been evaluated. Raman spectra of these materials were measured using the customised Renishaw microspectrometer (outlined 4.2) with 828nm laser light focussed onto the sample by the x80 objective. Integration of the collected signal was carried out for 30 seconds with laser power levels of 32mW.

The contaminants investigated were:

1. Mucus
2. Bile
3. Blood
4. Coffee and spittle
5. Endoscope lubricant.

The intensity levels of the resulting contaminant spectra were compared with those tissue Raman spectra obtained with the same measurement configuration (4.3.2).

4.3.8 Other Biological Tissues

Additional biological tissues were studied to assess the potential for future exploitation of Raman spectroscopy for detection of abnormalities. Raman spectra of these tissues were measured using the customised Renishaw microspectrometer (outlined 4.2) with 828nm laser light focussed onto the sample by the x80 objective. Integration of the collected signal was carried out for 30 seconds with laser power levels of 32mW. The tissues evaluated included the following:

1. Stomach.
2. Tonsil.
3. Endometrium.
4. Bladder
5. Prostate.

5. Results and Analysis

This chapter has been compiled to outline the results obtained from NIR-Raman spectral measurements of various epithelial tissues. The possibility of spectrally discriminating between tissues originating from different stages of carcinogenesis has been evaluated by following a logical process of spectral analysis to extract as much clinically relevant data from the spectra as possible. The first sub-section (5.1) describes the results obtained from the laryngeal tissue experiments. The pathogenesis from normal squamous mucosa to squamous cell carcinoma in the larynx follows a simple path. This is in contrast with that occuring in tissues that initially undergo a metaplastic step. The development of oesophageal adenocarcinoma is an example of this more complex pathogenesis. The results of the work on Raman spectral classification of both fresh (snap frozen) and formalin fixed oesophageal tissues are outlined in the second and third sub-sections of this chapter (5.2 and 5.3). Results from experiments to evaluate likely differences between in vivo and in vitro classification models have been outlined in sub-section 5.4. Finally investigations involving other tissues are briefly outlined in sub-section 5.5.

5.1 Larynx

5.1.1 Raw Spectral Data

Following the procedures outlined in section 4.3.1 Raman spectra obtained from laryngeal tissue have been grouped according to the histopathological grading of the sample by a Consultant Pathologist at Gloucestershire Royal Hospital. This was carried out according to the classification protocol outlined in Appendix 1. Spectra were obtained from 25 homogeneous samples of larynx mucosal tissue (14 normal, 5 dysplastic, 6 squamous cell carcinoma (SCC)). A laser beam operating at 32 ± 1.1mW and 830nm was focussed down to a spot size of 2-3 μm across. An acquisition time of 30s was required to achieve acceptable signal to noise when using the 1200 lines per mm grating. The grating dispersed the spectrum over a larger collection area than that provided by the CCD therefore an extended scan was required to fit the spectra onto the CCD. Both 1 and 3 pixel binning was used for the larynx spectral measurements. Due to ongoing optimisation of the spectrometer configuration, interpolation and shift correction of the spectra were required during analysis. This helped reduce the effects of the varying S/N ratio and resolution from one spectrum to the next. Each spectrum was corrected for the wavelength sensitivity of the system by multiplying the spectrum by a correction file created using the procedure outlined in section 4.2.4.2. All spectra shown in this section have been calibrated for wavelength shift using a standard Neon-Argon source.

A plot of the mean of 200 spectra from normal, dysplastic and cancerous specimens is shown in Figure 5.1. The plot shows the intensity of the collected (Stokes) signal versus wavenumber shift relative to the 830 nm excitation source. The greater the wavenumber, the further the peak is shifted from the excitation wavelength. The most significant peaks in the spectrum have been labelled with the corresponding wavenumber shift. Tentative peak assignments have been made from extensive study of the literature. These are tabulated in Table 5.1. Further peak assignments have been compiled in Appendix 4.

The spectra of normal laryngeal specimens have shown little inter- and intra-sample variability. Figure 5.2 shows 100 NIR-Raman spectra obtained from ten normal larynx tissue specimens, with the mean spectrum displayed in green. Visual inspection of the spectra show the peak shapes and positions to be repeatable, although overall spectral intensities can vary by 15% about the mean spectrum for each sample. The Raman spectra from normal laryngeal epithelial tissues were dominated by several peaks (see Table 5.1 and Figure 5.1). They have contributions from a myriad of constituents including proteins, lipids, carbohydrates and nucleic acids. Many of the spectral peaks overlap and thus make a full understanding of the biochemistry very difficult to achieve. Amide I (at 1655 cm^{-1}) and amide III (at 1240-1265 cm^{-1}) bands originate from vibrations in the peptide modes of the proteins and reflect the secondary structure of the proteins, arranged in three dimensions as α-helix, β-pleated sheet, β-turn or random coil structures. The position of these two peaks indicated that the majority of proteins in the normal larynx are in the α-helix conformation. The intense peak at 1336 cm^{-1} can be attributed to both collagen and nucleic acids (DNA) and more specifically to the purine bases guanine and adenine (see Table 5.1 and Appendix 4).

The repeatability of the wavenumber position was evaluated by measuring the position of the phenylalanine peak (at around 1000 cm^{-1}) for each spectrum. The resulting wavenumber position for each spectrum in the data set (in order of acquisition) is plotted in Figure 5.3. The mean position was 1001.7 ± 3.25 cm^{-1}. It can be seen from the plot, by the step tooth pattern, that consecutive spectra tend to have similar phenylalanine (PHE) peak positions. A following set of spectra from a different day may have a completely different wavenumber position for the PHE peak. This indicates that the calibration of the spectrometer wavenumber position from one day to the next was not completely stable. It has been shown in section 4.2.1.1 that the laser wavelength stability and laser pointing stability were poor. Improvements were made to stabilise the laser, but these were carried out following the work described in this section. To compensate for the varying wavenumber position, spectra were shifted to align all PHE peaks to 1001.5 cm^{-1}.

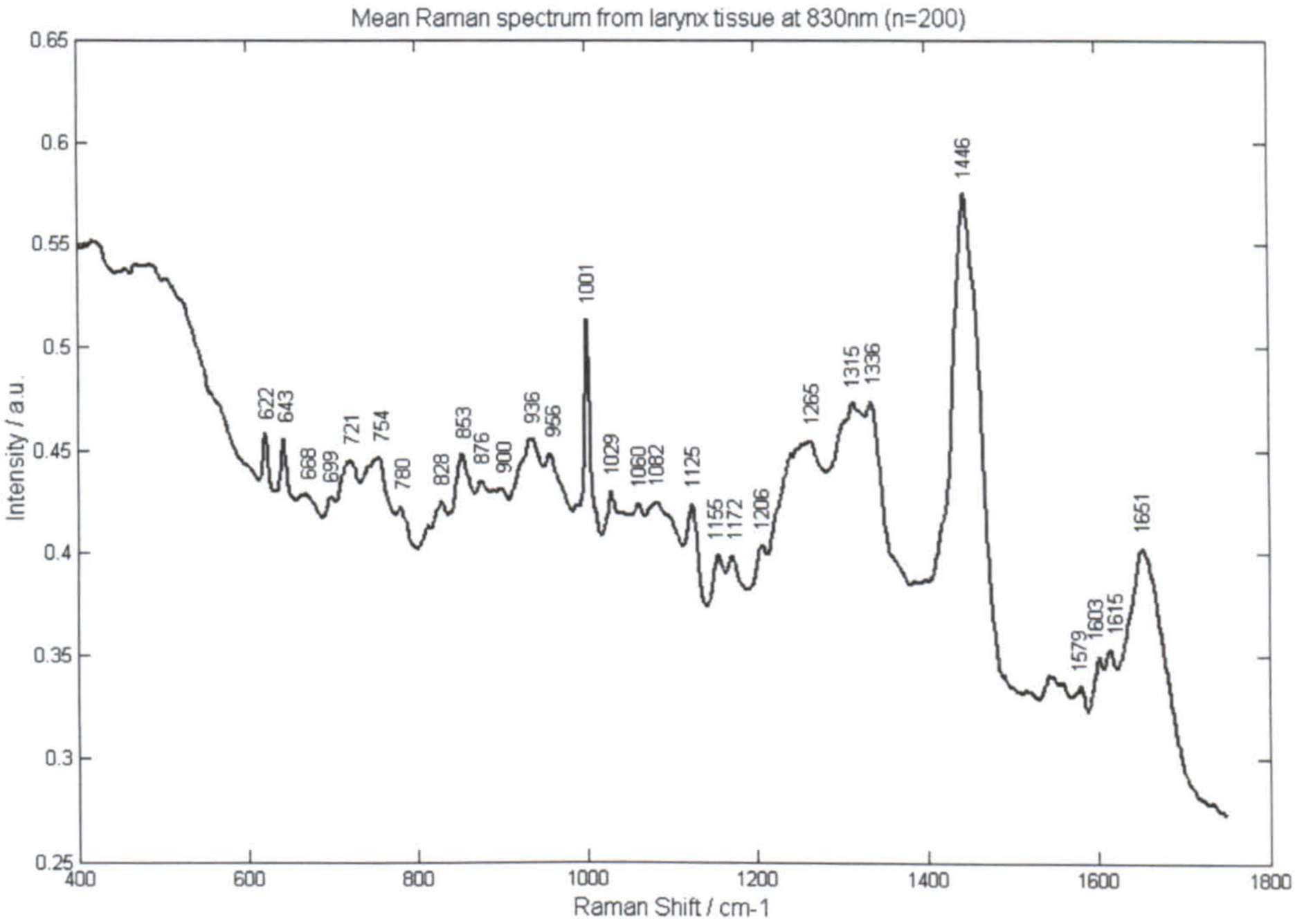

Figure 5.1: Mean Raman spectrum acquired from normal, dysplastic and cancerous laryngeal tissue with an 830nm excitation source. T=30s.

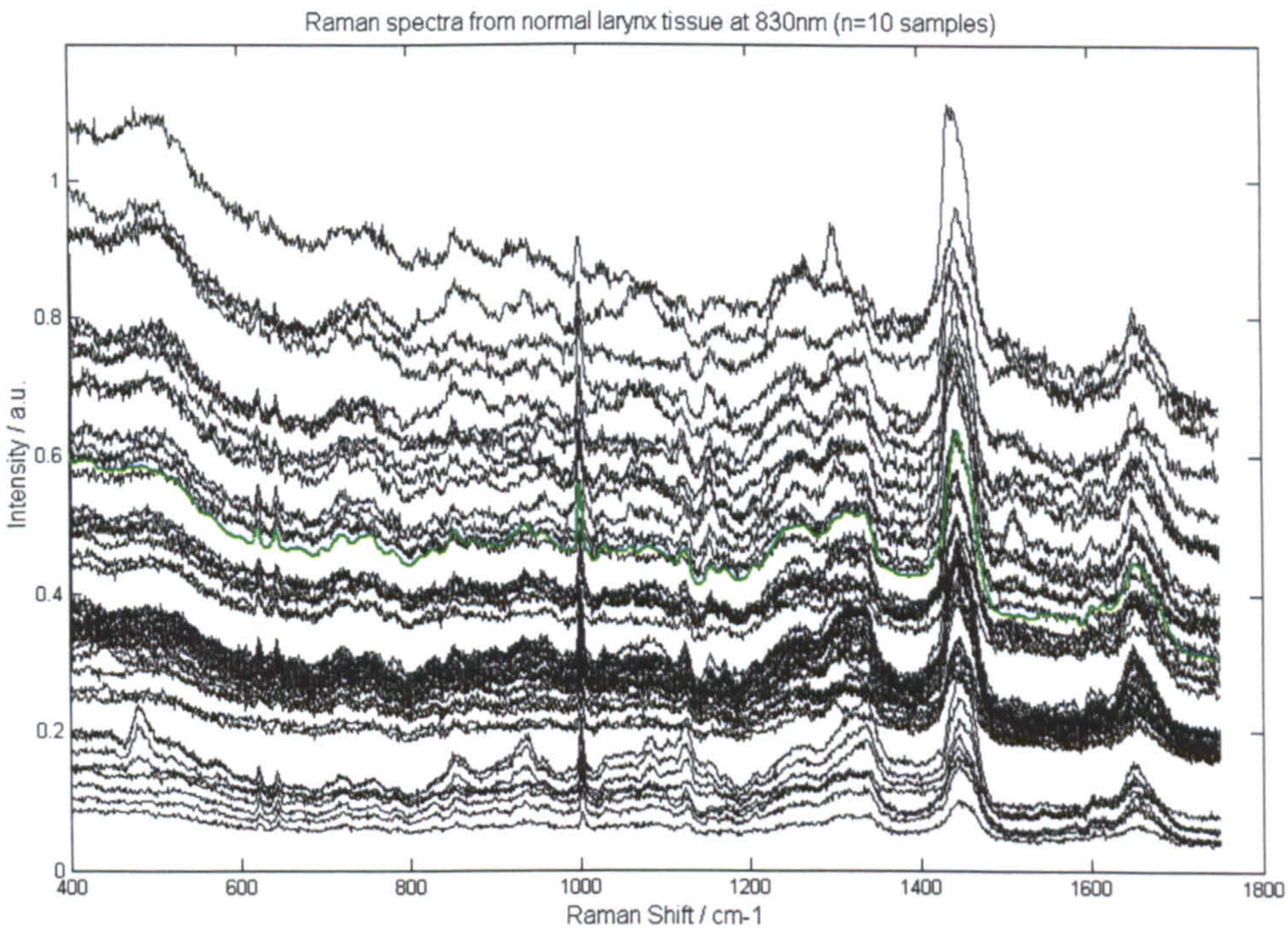

Figure 5.2: 100 Raman spectra from 10 normal larynx specimens, mean spectrum plotted in green.

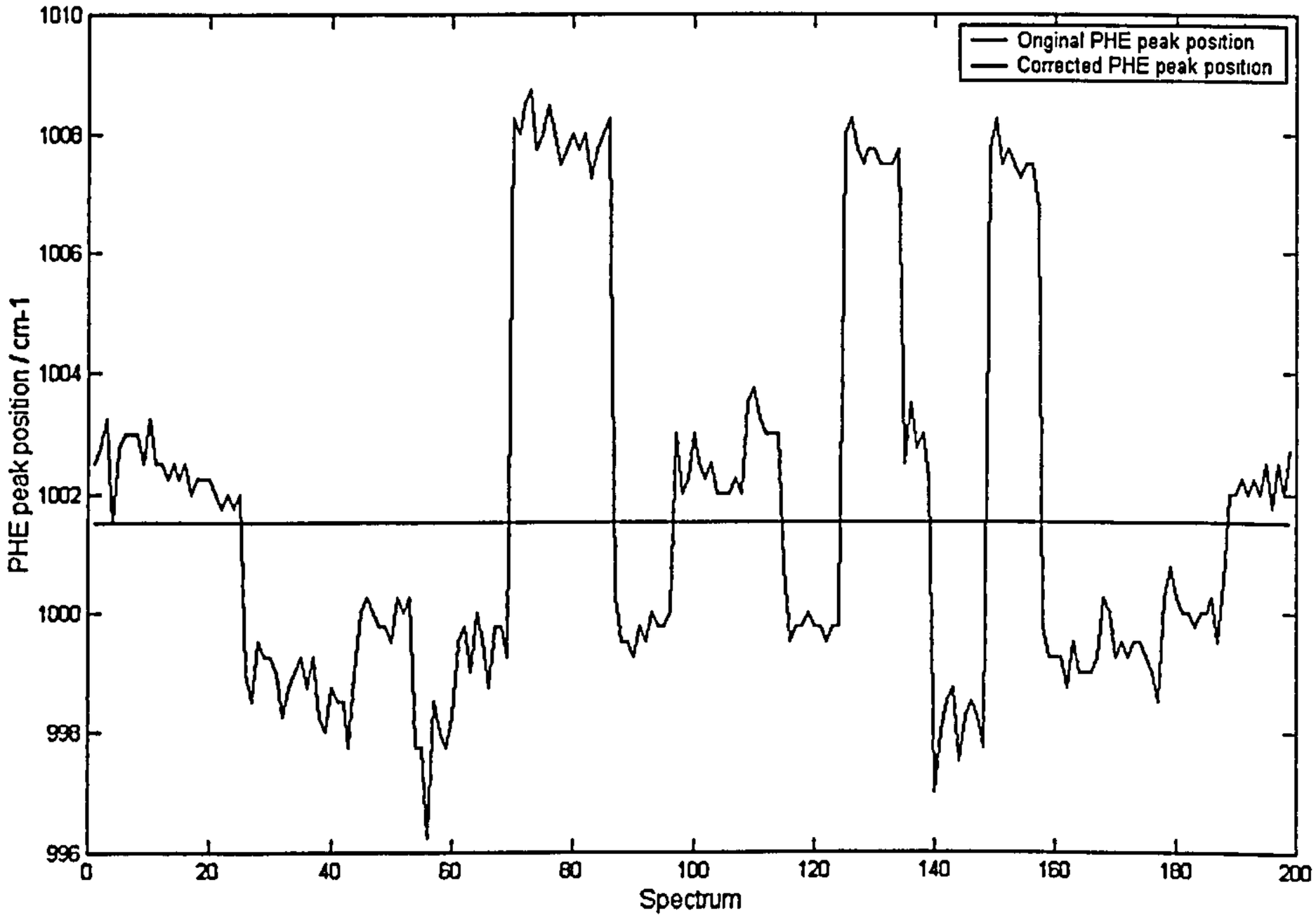

Figure 5.3: Plot of the wavenumber position of a peak assigned to phenylalanine versus acquired spectrum.

Table 5.1: Major vibrational modes identified in normal laryngeal samples.

Peak position (cm^{-1})	Major assignments
622	C-C twisting mode of phenylalanine
643	C-C twisting mode of tyrosine
668	C-S stretching mode of cystine
721	=C-H in-plane bending mode
754	Symmetric breathing of tryptophan
780	Unassigned
828	Out of plane ring breathing mode of tyrosine
853	Ring breathing mode of tyrosine and C-C stretch of proline ring
876	C-C stretch of hydroxyproline
900	C-C stretching mode of proteins (α-helix conformation)
920	C-C stretch of proline ring
936	C-C stretching mode of proline and valine (α-helix conformation)
1001	Symmetric ring breathing mode of phenylalanine
1029	C-H in-plane bending mode of phenylalanine
1048	Unassigned
1082	C-N stretching mode of proteins (and lipid mode to lesser degree)
1125	C-N stretching mode of proteins
1155	C-N stretching mode of proteins (also carotenoid mode)
1172	C-H in-plane bending mode of tyrosine
1206	Tryptophan and phenylalanine $\nu(C\text{-}C_6H_5)$ mode
1228	PO_2 antisymmetric stretching mode of polynucleotide chain (DNA)
1240-1265	Amide III (C-N stretching mode of proteins, indicating mainly α-helix conformation)
1315	CH_3CH_2 twisting mode of collagen
1336	CH_3CH_2 wagging mode of collagen and polynucleotide chain (DNA-purine bases)
1386	Unassigned
1446	CH_2 bending mode of proteins and lipids
1560	Tryptophan
1579	C=C bending mode of phenylalanine
1603	C=C in-plane bending mode of phenylalanine
1615	C=C stretching mode of tryptophan
1651	Amide I (C=O stretching mode of proteins, α-helix conformation)

5.1.2 Empirical Spectral Analysis

The spectra acquired from samples belonging to each of three pathological groups were collected together and mean spectra were calculated. A plot of the mean spectra normalised to the intensity at 1446 cm^{-1} is shown in Figure 5.4. From this plot it can be seen that the differences observed in the spectra from specimens at different stages of the cancer development process are very subtle. On first glance the spectra appear almost identical. However a closer study reveals miniscule changes in peak heights from one group to the next. One method of emphasising the variation between the spectra from each pathological group is to calculate difference spectra. Figures 5.5 to 5.7 display the resulting spectra obtained from taking the difference between mean normalised (and baseline subtracted) spectra from each of the groups in turn. The peaks in the difference plot with intensity greater than zero represent tissue constituents in excess in that pathology group. Conversely, those with a negative relative intensity have a lower concentration of that constituent relative to that found in the spectrum of the subtracted group.

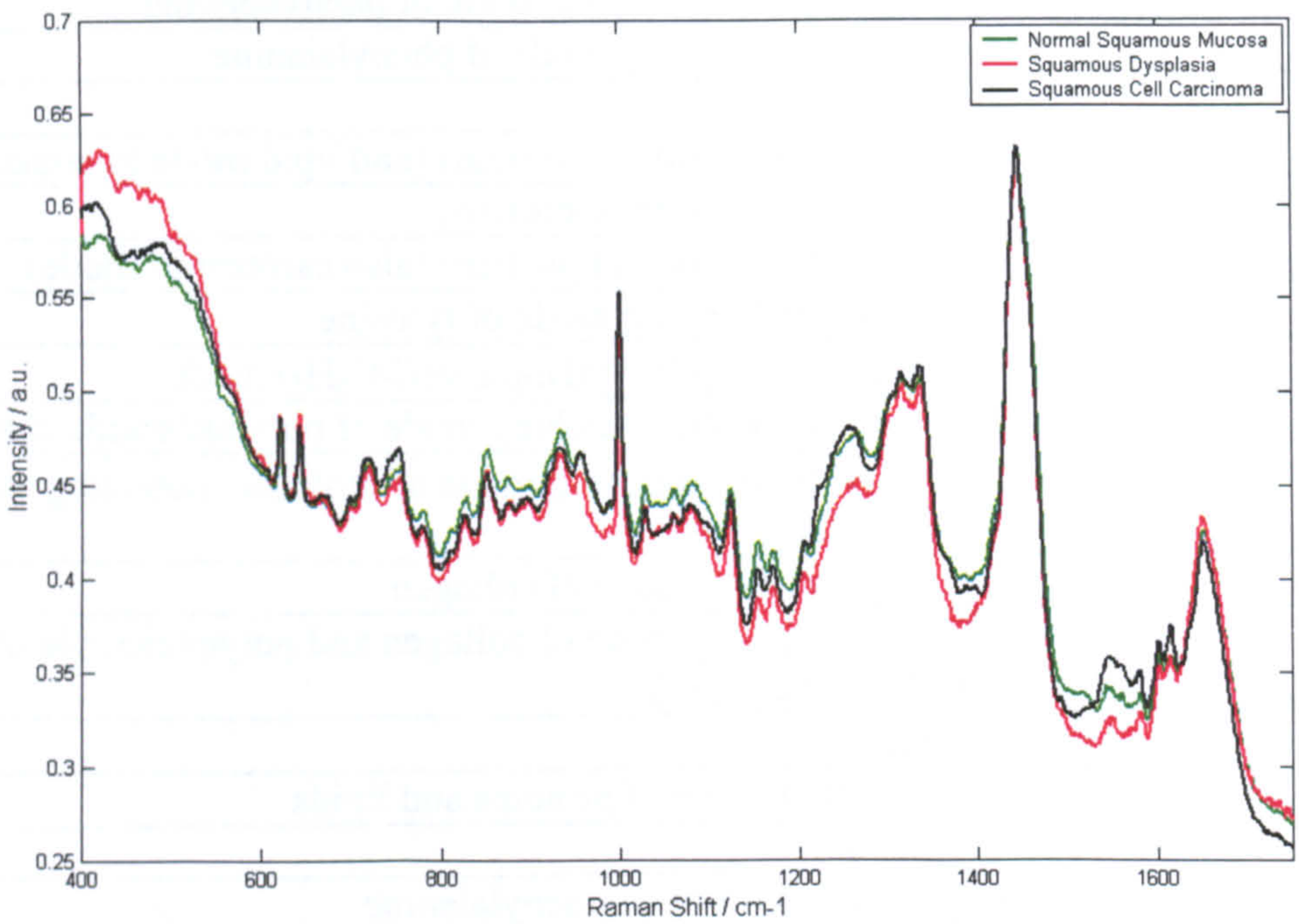

Figure 5.4: Mean Raman spectra from each laryngeal histopathological group, normalised to the peak intensity at 1446cm^{-1}.

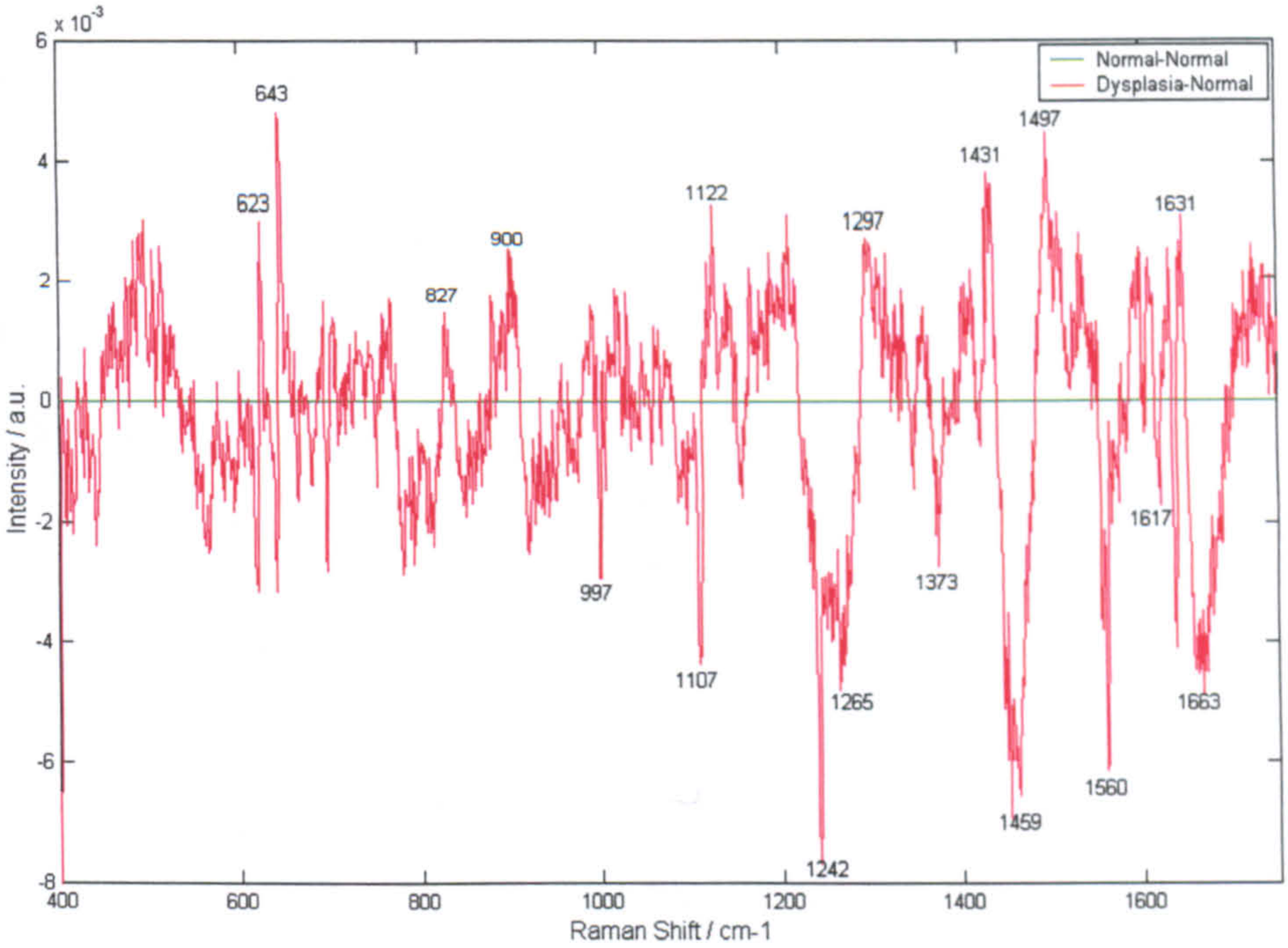

Figure 5.5: Mean normalised (and baseline corrected) Raman spectrum of dysplastic larynx tissue, with the mean normalized (and baseline corrected) spectrum of normal tissue subtracted.

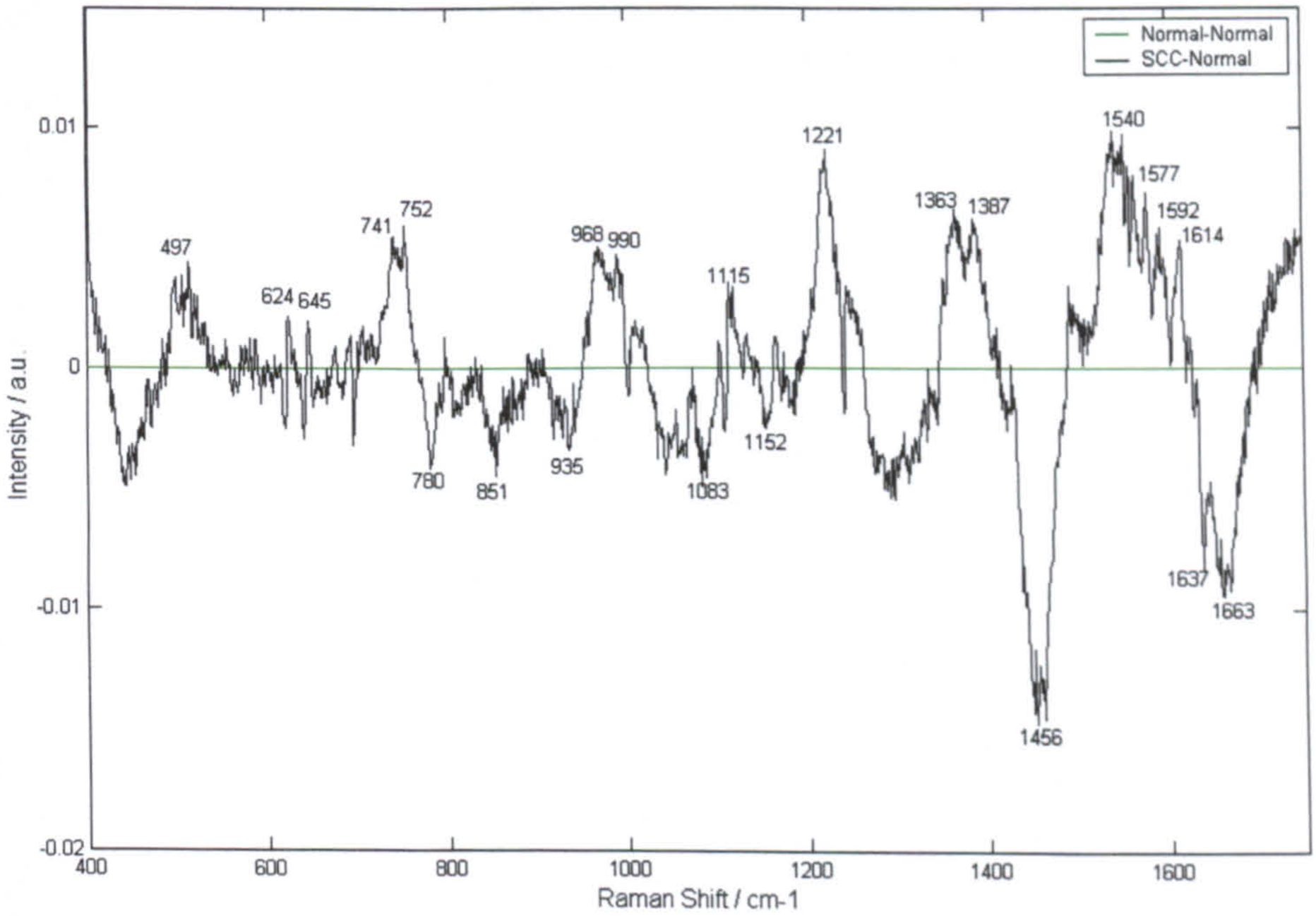

Figure 5.6: Mean normalised (and baseline corrected) Raman spectrum of cancerous larynx tissue with the mean normalized (and baseline corrected) normal tissue spectrum subtracted.

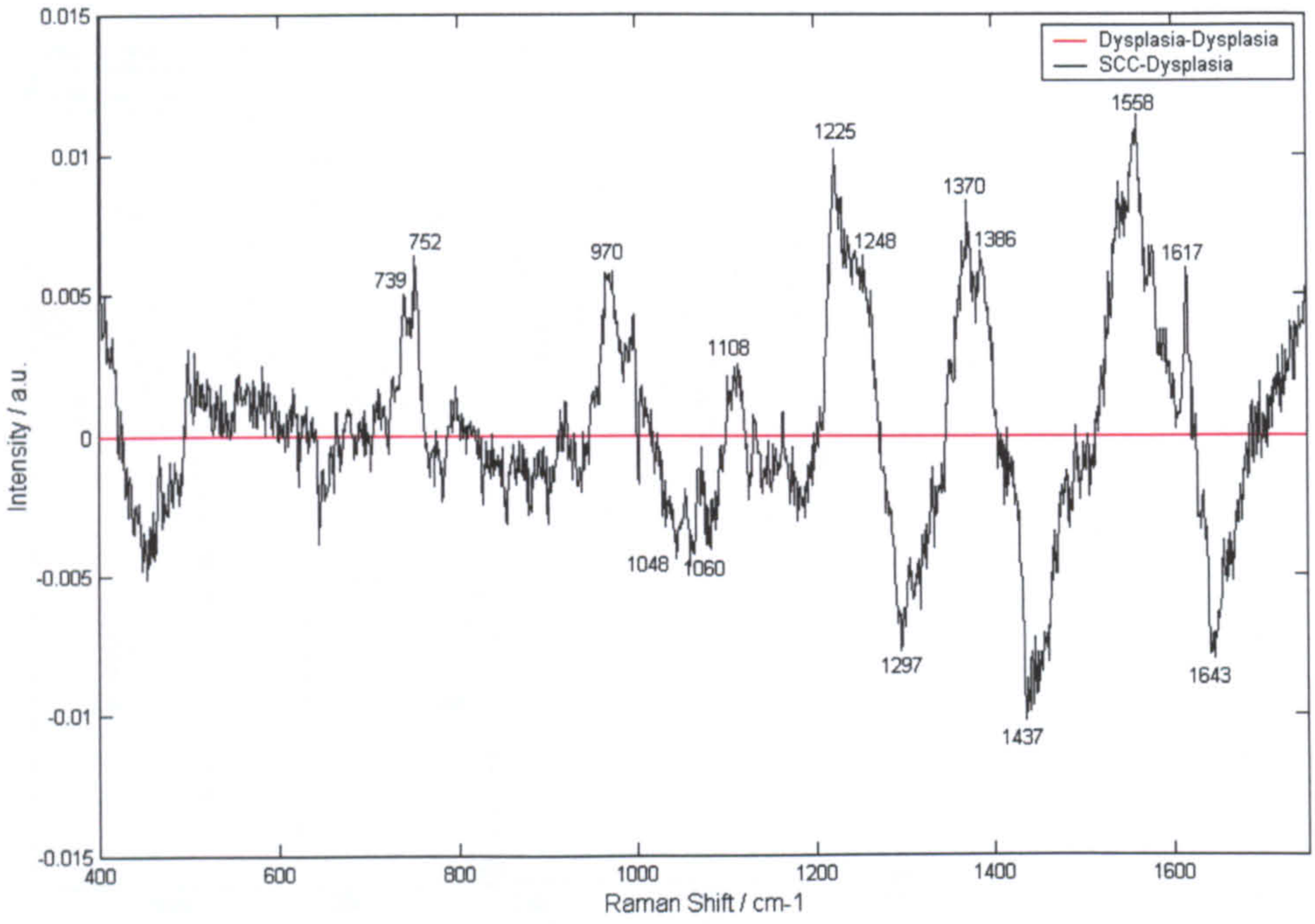

Figure 5.7: Mean normalised (and baseline corrected) Raman spectrum from cancerous larynx tissue with the mean normalised (and baseline corrected) spectrum from dysplastic tissue subtracted.

Study of the above difference spectra provides evidence for constituents in excess in certain pathology types and in deficit in others. Table 5.2 outlines the likely constituents that exhibit the greatest variation between the pathological groups.

	Dysplastic vs Normal		SCC vs Normal		SCC vs Dysplasia	
	Peak	Tentative Assignment	Peak	Tentative Assignment	Peak	Tentative Assignment
Excess	623	Phenylalanine (PHE)	497	?	739	Phospholipid (P-O-P)
	643	Tyrosine (TYR)	624	PHE	752	Thymine
	827	DNA (O-P-O stretch)	645	TYR	970	Hydoxyapatite
	900	DNA backbone	741	Phospholipid (P-O-P)	1108	Protein (C-C) stretch
	1122	Lipid (C-C stretch)	752	Thymine	1225	Heme/Am. III:β-sheet
	1297	Lipid (CH_2 deform.)	968	Hydroxyapatite	1248	PO^2- pl/na or
	1431	Lipid (CH_2)	990	?	1370	unordered
	1497	?	1115	Skeletal C-C unordered	1386	Porphyrins
	1631	?	1221	Heme/Am.III:β-sheet	1558	TRP / Porphyrins
			1250	PO^2-	1617	Nucleic Acids
			1363	Guanine/TRP/heme		
			1387	?		
			1540	TYR		
			1577	Nucleic acids (G/A)		
			1592	Nucleic acids (G/A)		
			1614	TYR/PHE/nuc acids		
Deficit	997	?	780	Nucleotide?	1048	Lactic acid ?
	1107	Skeletal protein(C-C)	851	Glycogen/C-C collagen	1060	? Lipid
	1242	Am. III: unordered	935	Glycogen/C-C collagen	?	Lipid (C-C)
	1265	Am. III: α-helix	1083	C-C Carotenoids	1297	CH_2 Lipid
	1373	Porphyrins	1152	CH_2 lipid / α-helix	1437	CH_2 Lipid
	1459	CH_2/CH_3 protein/lipid	1456	CH_2/CH_3 protein/lipid	1643	Am. I: α-helix
	1560	Tryptophan /	1663	? Am. I: α-helix		
	1617	Porphyrins				
	1663	Am. I: α-helix				

Table 5.2: Peaks from difference spectra between normal, dysplastic and cancerous larynx spectra, with tentative peak assignments. (? signifies no data available on peak.)

5.1.2.1 Analysis of clinical significance of individual peak intensities

A full analysis of the clinical significance of 32 selected peak intensities from the un-normalised spectra was carried out using analysis of variance (ANOVA).[173] The spectral intensities were compiled into an $n \times m$ matrix, representing n spectra and m peak intensity values. An algorithm written in the MATLAB computing environment, as a modification of a published formula,[174] was used to calculate the significance of these individual intensities for discrimination between the three pathological groups of interest. A selection of peaks with the corresponding ANOVA F-value (see below and Appendix 3 for further explanation) is shown in Table 5.3. This method of analysis tests the hypothesis that means from two or more samples are equal (drawn from populations with the same mean). This technique expands on the tests for two means, such as the t-test. The F-value is calculated from the sum of the squares of the variance from the mean peak intensity between and within pathology groups. The larger the F-value the greater the effective grouping with pathology. F_{crit} is the cut-off value for 99.9% significance, 7.19 in this case. The p-value is the probability that the intensities for all pathologies are statistically the same, i.e. that they do not correlate with histopathology of the sample. It

can be seen from the values in Table 5.3 that none of the individual peak intensities have a statistically significant (to 99.9%) difference between the groups.

Peak	Mean peak intensity			ANOVA, F-value
	Normal Larynx	Dysplastic Larynx	Cancerous Larynx	
I_{643}	0.453±0.403	0.328±0.509	0.560±0.616	3.1
I_{754}	0.446±0.412	0.317±0.521	0.548±0.601	3.1
I_{853}	0.457±0.419	0.317±0.525	0.530±0.570	4.0
I_{936}	0.465±0.422	0.322±0.532	0.537±0.553	4.5
I_{1155}	0.408±0.367	0.285±0.511	0.468±0.495	4.2
I_{1265}	0.463±0.407	0.321±0.544	0.540±0.536	4.3
I_{1446}	0.587±0.470	0.415±0.627	0.675±0.614	5.1
I_{1651}	0.396±0.319	0.316±0.597	0.485±0.572	4.0

Table 5.3: Selected peak intensities, with their corresponding mean and standard deviation values for each group. ANOVA F-values are included to indicate significance of peak for spectral group separation.

5.1.2.2 Analysis of clinical significance of peak intensity ratios

A more rigorous technique, better able to take into account variations in overall spectral intensity from one measurement to the next is the calculation of peak intensity ratios. In simple chemical solutions it is possible to select peaks that represent known molecular vibrations found in constituents of interest. While in principle this is possible with biological samples, practical difficulties and a lack of understanding of the complex biochemical processes occurring in tissue make this challenging. Therefore a process of testing all 32 selected peaks ratioed against one another was carried out by initially calculating an $n \times (m \times m)$ matrix containing the data for n spectra in each row, and each column representing the set of data for each peak ratio. Analysis of variance (ANOVA) was then used to evaluate the peak ratios demonstrating the most significant differences between groups. Considering that 1024 peak ratios were analysed (for clarity and sensible use of space) a selection have been recorded in Table 5.4, with the relevant mean and standard deviation ratios for each group. ANOVA F-values are recorded to provide information on the ability of each peak ratio to discriminate between pathology groups in the larynx. The critical F-value for 99.9% significance for this data set is 7.19. Peak ratio measurements with an F-value of greater than the critical value provide a high statistical significance (>> 99.9%) for measurement of group membership. However, it must be noted biological tissue is very complex in nature and although the mean and variance of the peak ratios indicate that discrimination is possible, in practice, sample variability makes it extremely difficult to achieve discrimination with only one peak ratio. The measurements of standard deviations from the mean values indicate the variability from one sample to the next.

Peak Ratio	Mean peak intensity ratio value			ANOVA, F-value
	Normal Larynx	Dysplastic Larynx	Cancerous Larynx	
I_{721}/I_{754}	1.006±0.028	1.020±0.032	0.983±0.031	12.57
I_{754}/I_{780}	0.953±0.036	0.942±0.035	0.906±0.041	33.46
I_{828}/I_{754}	1.035±0.038	1.035±0.061	1.076±0.045	38.15
I_{936}/I_{956}	1.029±0.044	1.018±0.027	1.007±0.036	7.10
I_{1155}/I_{1172}	1.017±0.046	0.982±0.034	0.996±0.028	3.29
I_{1265}/I_{1336}	0.944±0.084	0.897±0.070	0.927±0.068	1.07
I_{1315}/I_{1336}	1.001±0.031	0.998±0.029	0.994±0.027	1.17
I_{1603}/I_{1615}	0.997±0.028	1.005±0.057	0.968±0.026	18.28

Table 5.4: Selected peak intensity ratios, from normalised spectra, with their corresponding mean and standard deviation values for each group. ANOVA F-values are included to indicate significance of ratio for spectral group separation.

5.1.3 Multivariate Spectral Analysis

The use of multivariate analysis techniques enables more of the data included within the spectra to be utilised. A summary explanation is provided in Appendix 3. Principal components analysis (PCA) was performed to reduce the data to a linear combination of 25 orthogonal variables. These variables were used in a linear discriminant model for the prediction of sample pathology.

PCA was performed on the tissue spectra using a singular value decomposition (SVD) algorithm in the PLS-Toolbox (Eigenvector®) running in the MATLAB® environment. Of the 211 spectra acquired, 12 were discarded due to extremely poor signal to noise ratios or an unusually large fluorescence background. The remaining spectra were compiled into a training data set and a variety of pre-processing routines were performed upon it. Initially the spectra were interpolated to a regular number of points per wavenumber (the Renishaw system 1000 has a variable spacing due to the polynomial calibration fit of wavenumber per pixel across the CCD chip). The position of the phenylalanine (PHE) peak at around 1000 cm^{-1} was measured for each spectrum to evaluate system drift from one measurement to the next. Spectra were corrected for this drift by shifting the x-axis so that the PHE peak was at exactly 1001.5 cm^{-1} (Figure 5.3). In the first instance unfiltered spectra were used to build a discrimination model. Then pre-processing based upon Savitsky-Golay filters were applied to optimise the models for maximum group separation.

Following pre-processing the spectra were mean-centred; this involved calculating the average spectrum of all the spectra in the data set and subtracting this result from every spectrum. Principal component analysis was used to describe the resulting spectra as a sum of a small orthogonal set (25) of linear combinations of the original variables. Figures 5.8 a, b and c show plots of the PCs from the unfiltered data set. These principal

components described over 99.9% of the variance from the mean spectrum across the data set.

Table 5.5 lists each PC with the corresponding percentage variance described by it. Multiple ANOVA was used to identify the most diagnostically significant PCs, i.e. those that show a significant difference in value for normal, dysplastic and cancerous larynx. In addition a Wilks'-Lambda test has been performed on the data (Table 5.5). The larger the ANOVA F-value and the smaller the Wilks' Λ-value, the greater the discriminating power of the particular principal component.

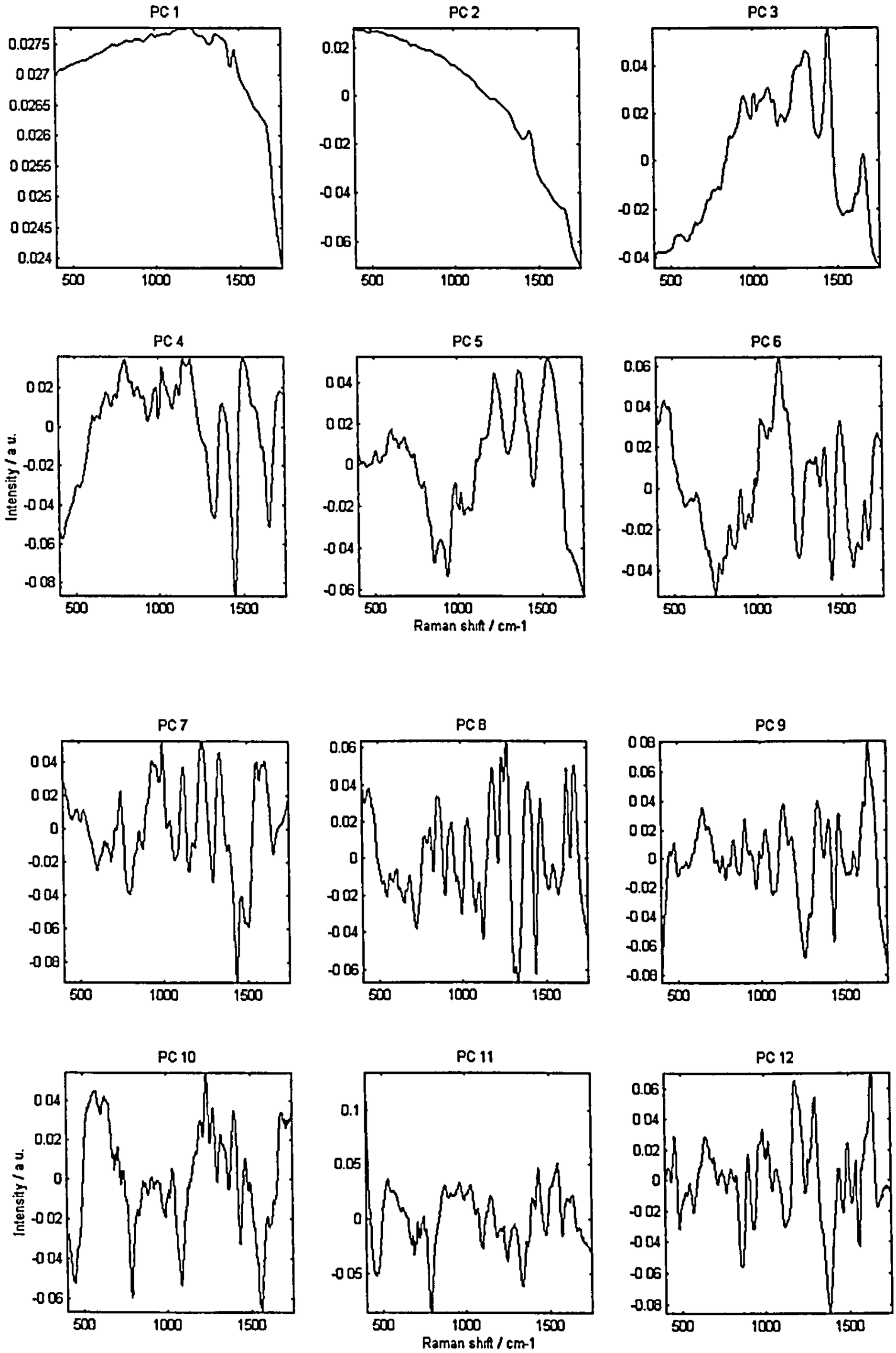

Figure 5.8(a): Principal components 1 to 12 representing the first 99.98% of the variance of the data set from the mean spectrum.

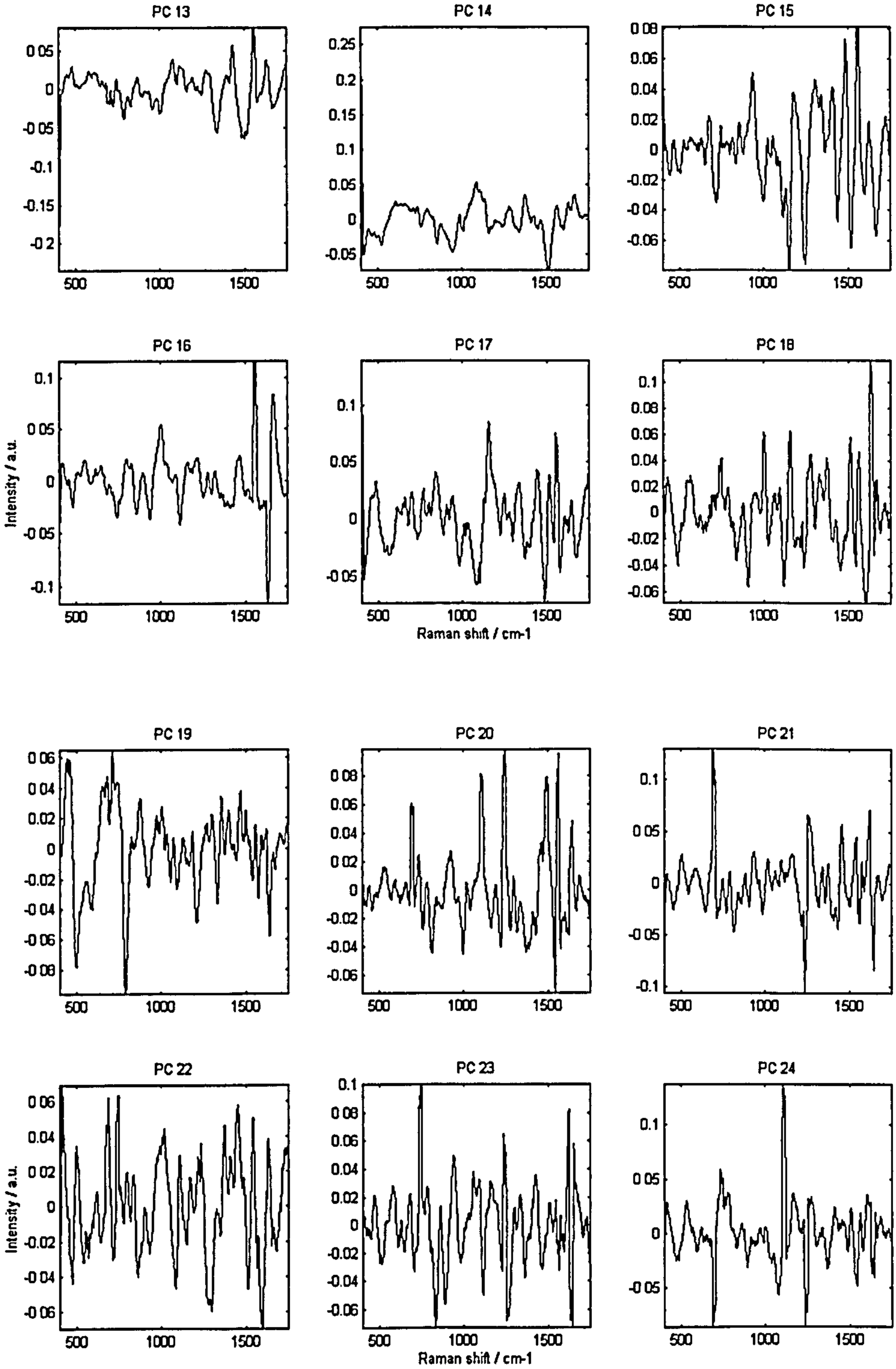

Figure 5.8(b): Principal components 13 to 24 representing 0.02% of the variance of the data set from the mean spectrum.

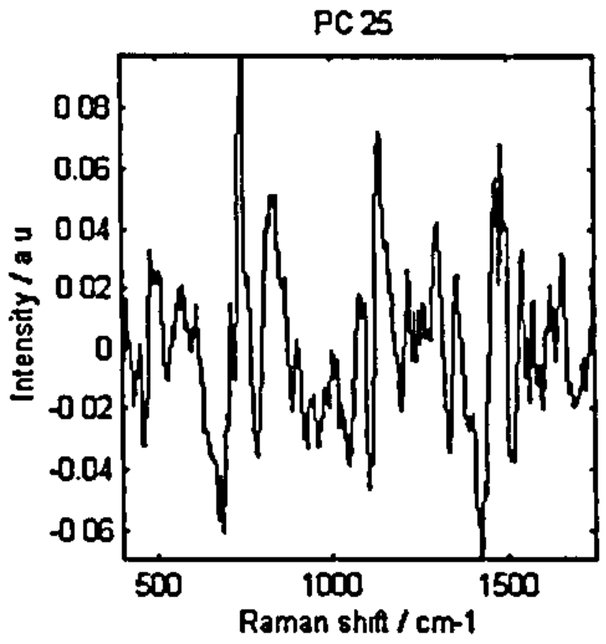

Figure 5.8(c): Principal component 25 representing 0.004% of the variance of the data set from the mean spectrum.

Principal Component	% Variance	Cumulative % Variance	Wilks' Lambda	F-Value	Significance = (100-p)
1	95.52	95.52	.970	3.029	.051
2	3.64	99.16	.999	.066	.936
3	0.60	99.75	.984	1.551	.215
4	0.15	99.90	.996	.404	.668
5	**0.03**	**99.93**	**.910**	**9.690**	**.000**
6	**0.02**	**99.95**	**.922**	**8.299**	**.000**
7	**0.01**	**99.96**	**.918**	**8.785**	**.000**
8	0.01	99.96	.954	4.697	.010
9	0.00	99.97	.981	1.912	.150
10	0.00	99.97	.995	.541	.583
11	0.00	99.97	.996	.404	.668
12	0.00	99.98	.970	3.027	.051
13	0.00	99.98	.969	3.118	.046
14	**0.00**	**99.98**	**.899**	**10.975**	**.000**
15	0.00	99.98	.992	.778	.461
16	0.00	99.98	.990	1.035	.357
17	0.00	99.99	.970	2.997	.052
18	0.00	99.99	.989	1.043	.354
19	0.00	99.99	.988	1.195	.305
20	0.00	99.99	.975	2.521	.083

Table 5.5: Displays the first 20 PCs with the corresponding variance of the data set described, with statistical significance test results for evaluation of group discrimination power. PCs with greater than 99.9% significance of discrimination between pathological groups are printed in bold.

5.1.3.1 Principal Component Discrimination

Individual PCs were selected with greater than 99.9% significance of discrimination between groups. The weights of principal components 5,6,7 and 14 were plotted in Figure 5.9. It can be seen that without any manipulation some clustering occurs within these PC between pathological groups.

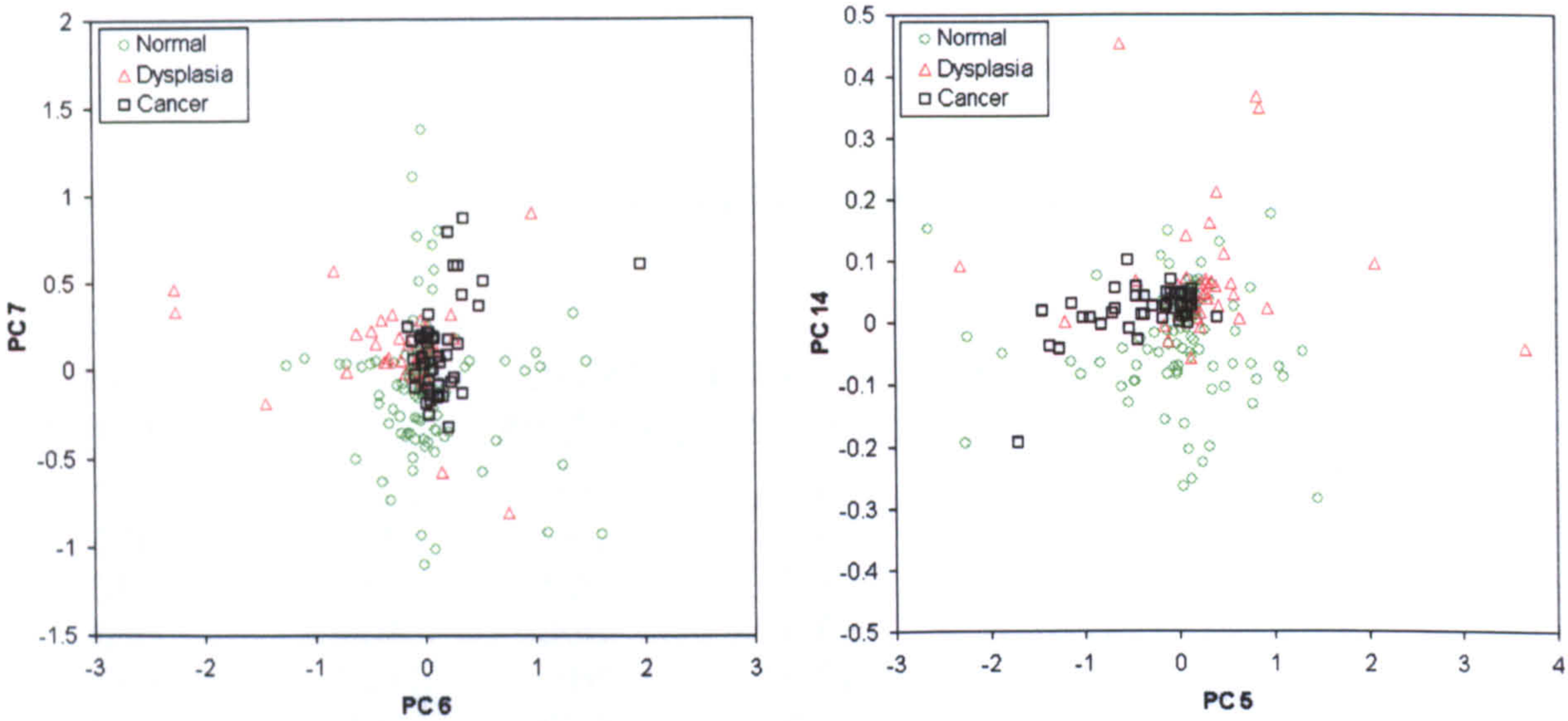

Figure 5.9: Scatter plots of principal component weights from PC6 versus PC7 and PC5 versus PC14. Symbols represent different larynx pathological states of specimens measured.

Note that the significant principal components describe only a small fraction (0.61%) of the total percentage variance in the data from larynx tissue. This indicates that changes in histochemistry, that accompany pathological changes in the tissue, produce quite subtle modifications to the Raman spectra obtained.

5.1.3.2 Three-group Linear Discriminant Model

The first 25 PCs (describing almost 100% of the total variance from the mean) were used to calculate two linear discriminant (LD) functions that maximised the variance in the data between the pathological groups and minimised the variance between members of the same pathological group. This was achieved by using a linear combination of the PCs to construct (n-1) discriminant functions to maximally separate n groups. A diagram outlining the steps taken to construct a linear discriminant model is shown in Figure 5.10 and Appendix 3. In this particular case two functions were required to separate three groups. The two LD functions (Figure 5.11) were combined to produce a diagnostic prediction model. The weights of the discriminant functions for each spectrum were plotted against each other in a scatter plot to enable visualisation of group separation. This is displayed in Figure 5.12. The prediction accuracy of the model was tested using a cross-validation procedure, whereby each measurement was held back in turn whilst all the others were used to calculate the discriminant functions. The held back measurement

then had its corresponding pathology forecast by the model. This continued until the pathologies of all the tissue samples measured with Raman spectroscopy had been predicted. The accuracy of these forecasts was compared to the 'gold standard' histopathological findings. Table 5.6 displays the resulting predictions versus histopathological grading and Table 5.7 displays the sensitivities and specificities of the test for each group.

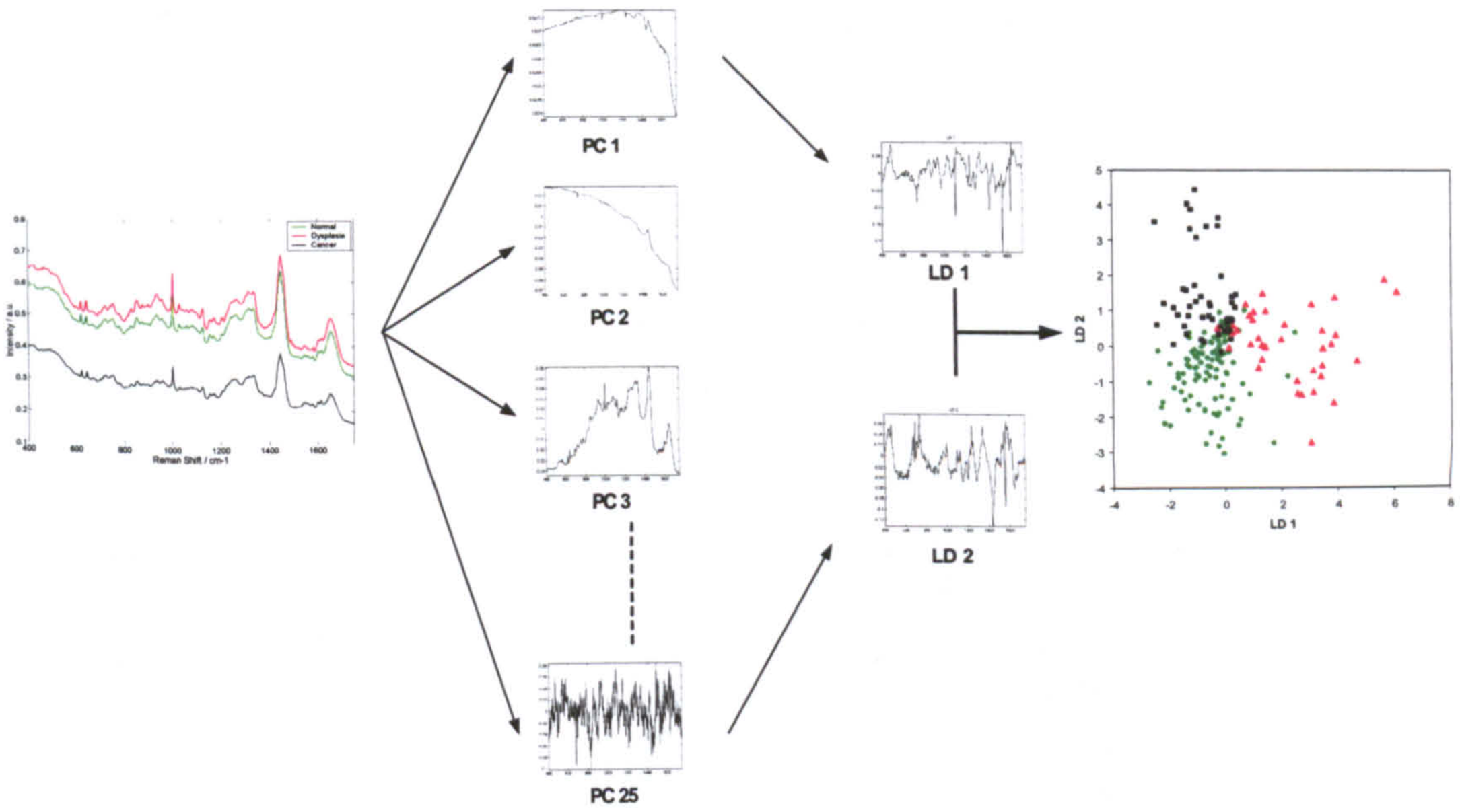

Figure 5.10: Diagram representing the steps of construction of a linear discrimiant model to separate 3 groups of specimens. 1. Calculate principal components from mean centred spectral data. 2. Select clinically significant PCs to calculate (n-1) linear discrimiant functions to maximally separate the groups.

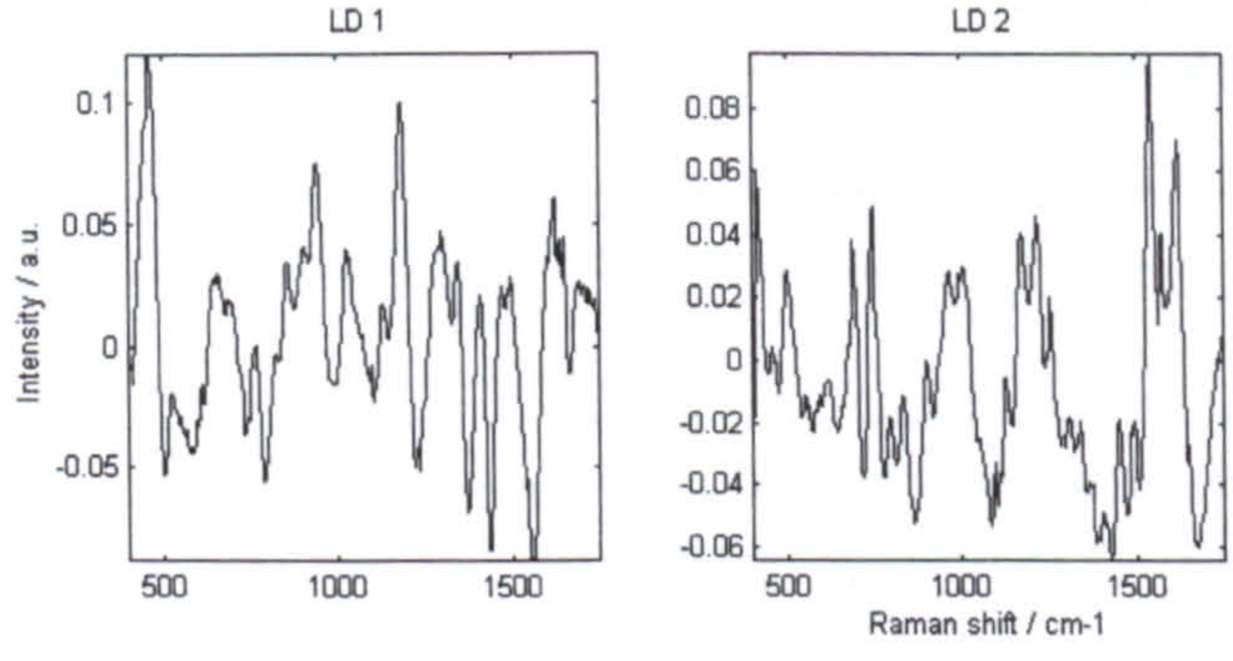

Figure 5.11: The two linear discrimiant functions required to maximally separate the specimens into three clinically significant pathology groups.

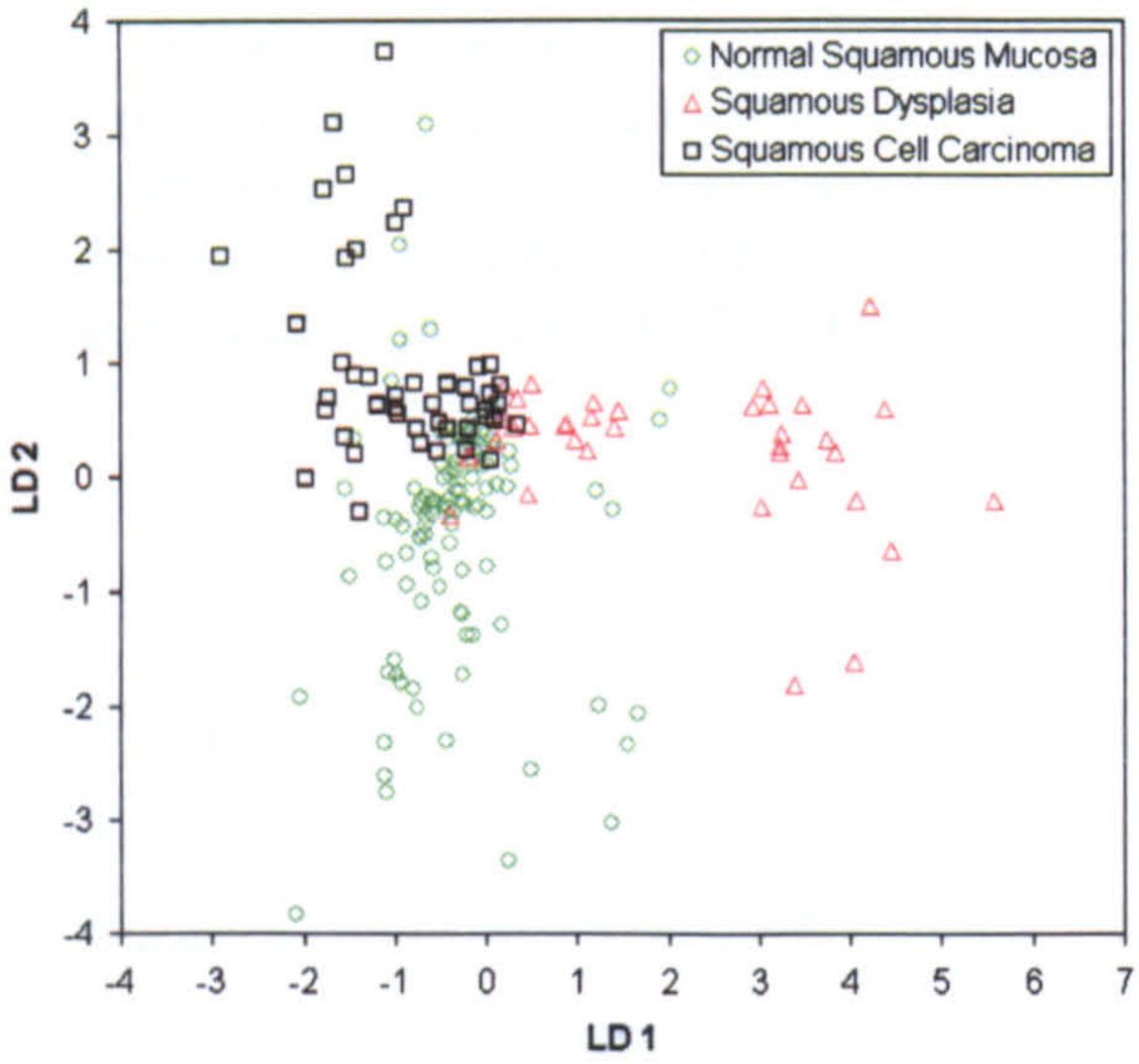

Figure 5.12: Plot of linear discriminant function weights for each spectrum, when tested against the model using a cross-validation process.

			Raman Predicted Group Membership			
		Classification	Normal	Dysplasia	Carcinoma	Total
Histopathology	No.	Normal	**81**	4	27	112
		Dysplasia	7	**29**	2	38
		Carcinoma	3	0	**46**	49
	%	Normal	**72**	4	24	100.0
		Dysplasia	18	**76**	5	100.0
		Carcinoma	6	0	**94**	100.0

Table 5.6: Cross-validation classification results obtained using the discriminant functions calculated from the first 25 principal components of the larynx spectra. Each case was classified by the functions derived from all cases other than that case. 78.4 % of cross-validated grouped cases are correctly classified using this method.

	Normal	Dysplasia	Carcinoma
Sensitivity	72%	76%	93%
Specificity	89%	96%	81%

Table 5.7: Sensitivity and specificity of Raman spectroscopy as a diagnostic test to classify pathology in the larynx, calculated from the cross-validation classification results obtained from the linear discriminant model.

5.1.3.3 Linear Discriminant Model Optimisation

Model optimisation was achieved by applying pre-processing functions such as 1st and 2nd derivative Savitsky-Golay filters, prior to calculation of PCs and linear discriminant functions. First and second derivative pre-processing filters removed influences from the overall signal level (baseline) and linear background slope respectively. A range of filters were applied and results were evaluated. A 95-point Savitsky-Golay fourth-order

polynomial, second-derivative function was shown to markedly improve the resulting discriminating power of the three-group larynx model. The resulting PCs and analysis are outlined below. Table 5.8 lists each PC with the corresponding percentage variance described by it. Multiple ANOVA and Wilks'-Lambda were used to identify the most diagnostically significant principal components, i.e. those that show a significant difference in value for normal, dysplastic and cancerous larynx. The larger the F-value and the smaller the Λ-value, the greater the discriminating power of the spectral principal component. The first 25 PCs (describing almost 100% of the total variance from the mean) were used to calculate two linear discriminant (LD) functions that maximised the variance in the data between the pathological groups and minimised the variance between members of the same pathological group. The weights of the discriminant functions have been plotted together to enable visualisation of group clustering (Figure 5.13). The prediction accuracy of the model was tested using a cross-validation procedure. The held back measurement then had its corresponding pathology forecast by the model. This continued until the pathologies of all the tissue samples measured with Raman spectroscopy had been predicted. The accuracy of these forecasts were compared to the 'gold standard' histopathological results. Tables 5.9 and 5.10 display the breakdown of the resulting prediction accuracy of the optimised model.

Principal Component	% Variance	Cumulative % Variance	Wilks' Lambda	F-Value	Significance = (100-p)
1	47.91	47.91	.964	3.637	.028
2	12.87	60.78	.989	1.136	.323
3	6.81	67.59	.934	6.954	.001
4	**4.74**	**72.33**	**.784**	**26.990**	**.000**
5	3.89	76.22	.955	4.605	.011
6	2.53	78.75	.997	.300	.741
7	2.37	81.12	.995	.503	.605
8	2.13	83.25	.996	.417	.659
9	**1.88**	**85.13**	**.923**	**8.178**	**.000**
10	1.67	86.80	.983	1.675	.190
11	1.62	88.42	.982	1.840	.161
12	1.26	89.68	.988	1.216	.299
13	1.22	90.90	.951	5.067	.007
14	0.98	91.88	.978	2.208	.113
15	0.86	92.74	.965	3.590	.029
16	0.78	93.52	.975	2.509	.084
17	0.66	94.18	.998	.154	.857
18	0.54	94.71	.996	.349	.705
19	0.51	95.23	1.000	.004	.996
20	**0.49**	**95.71**	**.883**	**13.048**	**.000**

Table 5.8: The first 20 PCs (from the optimised model) with the corresponding variance of the data set described, with statistical significance test results for evaluation of group discrimination power. PCs with greater than 99.9% significance of discrimination between pathological groups are printed in bold.

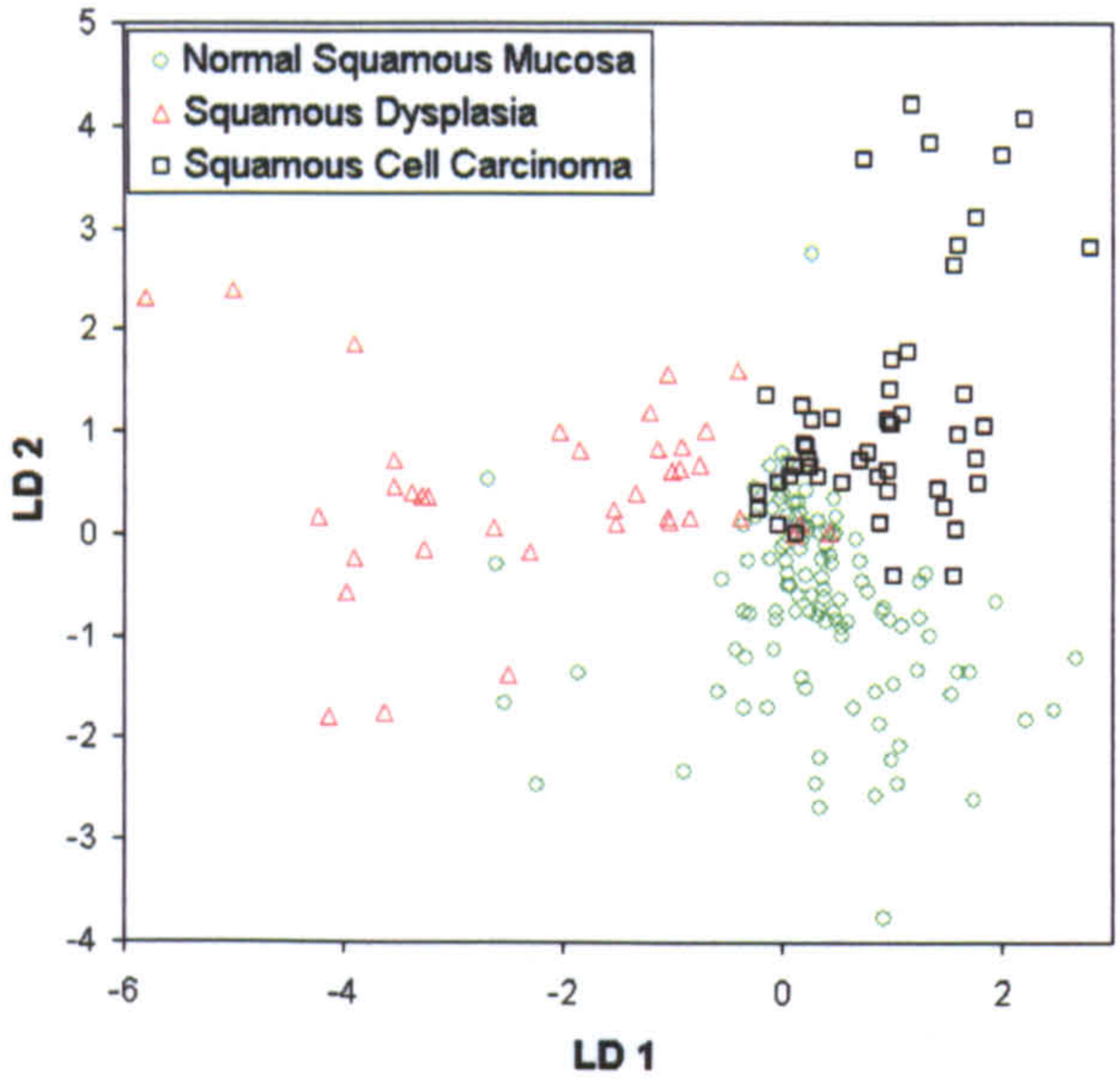

Figure 5.13: Plot of linear discriminant function weights for each spectrum, when tested against the optimised model using a cross-validation process.

Histopathology	Classification	Raman Predicted Group Membership: Normal	Dysplasia	Carcinoma	Total
No.	Normal	**100**	5	7	112
	Dysplasia	4	**34**	0	38
	Carcinoma	7	0	**42**	49
%	Normal	**89**	5	6	100.0
	Dysplasia	10	**90**	5	100.0
	Carcinoma	14	0	**86**	100.0

Table 5.9: Cross-validation classification results obtained using the discriminant functions calculated from the first 25 principal components of the larynx spectra. Each case was classified by the functions derived from all cases other than that case. 88.4 % of cross-validated grouped cases are correctly classified using this method.

	Normal	Dysplasia	Carcinoma
Sensitivity	89%	90%	86%
Specificity	87%	93%	95%

Table 5.10: Sensitivity and specificity of Raman spectroscopy as a diagnostic test to classify pathology in the larynx, calculated from the cross-validation classification results obtained from the linear discriminant model.

5.2 Oesophagus

The complexity of the carcinogenesis of oesophageal adenocarcinoma has been discussed earlier. Due to the difficulty in achieving a reliable diagnosis with tissue histopathology from one pathologist, it was necessary to work with a panel of three gastro-intestinal registry pathologists. This increased the complexity of the analysis required. Large sample numbers were collected, but it can be seen from Table 5.11 and Figure 5.14 that many were discarded prior to analysis. Figure 5.14 is a schematic diagram of the process of histopathological analysis of 150 oesophageal biopsy samples. Firstly all the samples were histopathologically analysed by each pathologist in turn, then either a majority or consensus of opinion of the histopathological state in each specimen was taken. Any samples without this agreement were discarded from the model. Further detail on histopathological analysis of the oesophagus tissue is provided in Appendix 2. Grey circles represent unknown or mixed pathology samples; green circles are normal tissue, blue circles are fundic Barrett's (FB), cyan circles are cardiac Barrett's (CB), purple circles are intestinal metaplasia (IM), pink circles are low-grade dysplasia (LGD), red circles are high-grade dysplasia (HGD), black circles are adenocarcinoma, yellow circles are squamous dysplasia, orange circles are squamous cell carcinoma (SCC).

From 150 biopsy samples, between 80 and 90 samples were homogeneous (depending on pathologist), therefore following majority selection there were 80 samples remaining and following consensus selection there were only 50 samples remaining. Either by looking at the colour coded biopsy symbols in Figure 5.14 or following the numbers in Table 5.11 it can be seen that there is little disagreement in normal samples, but significant disagreement in pre-malignant (or dysplastic) specimens.

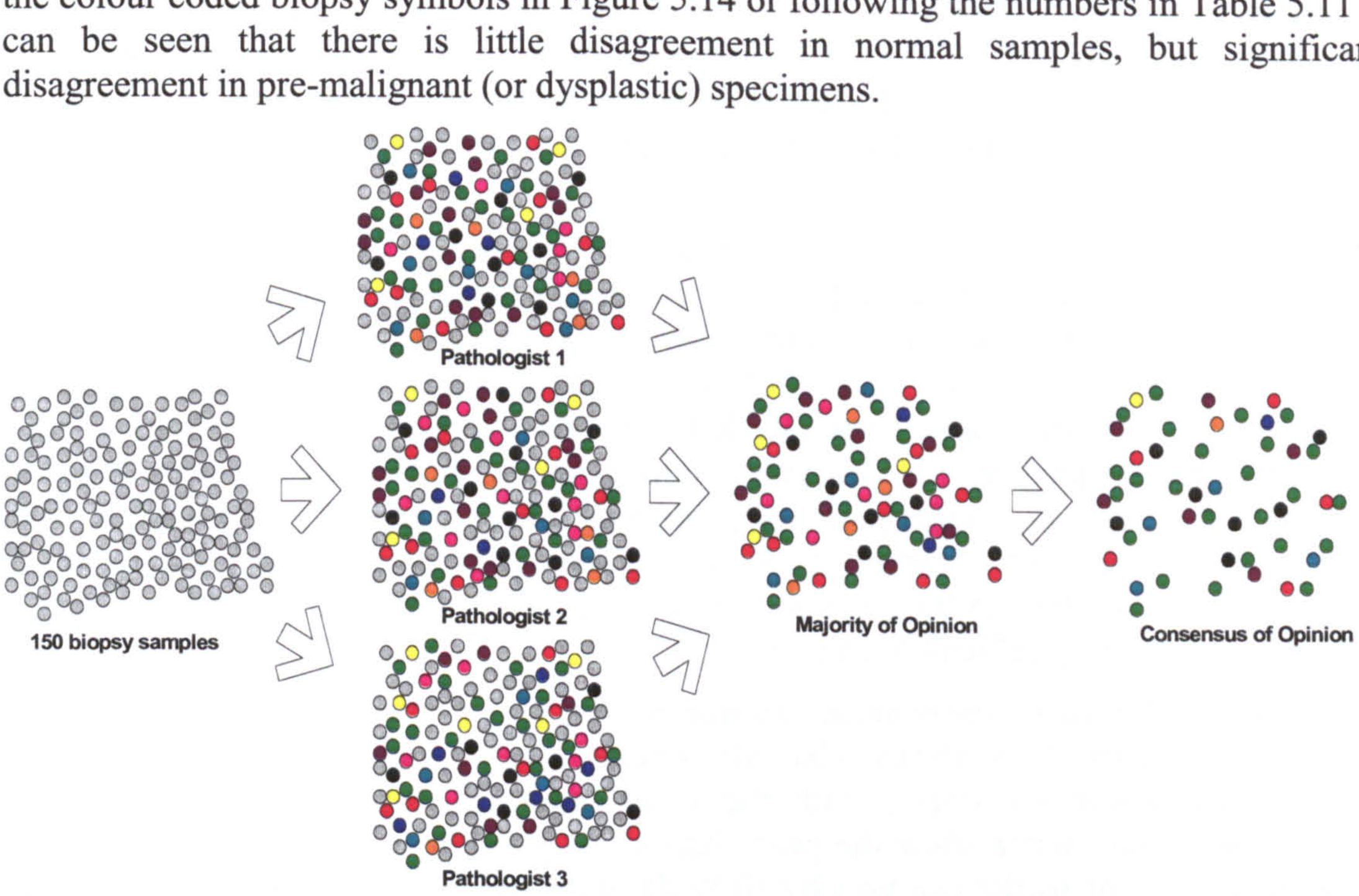

Figure 5.14: Schematic diagram outlining the process of histopathological analysis by three consultant pathologists to achieve a consensus result for comparison with spectral measurements.

	Reject	Normal	CB	FB	IM	LGD	HGD	Adeno	Sq Dys	SCC
Pathologist 1	1	27	4	8	13	5	11	9	4	5
Pathologist 2	1	25	2	5	13	10	11	11	4	5
Pathologist 3	8	28	7	5	7	8	10	7	6	1
Majority	7	27	2	6	11	8	10	8	4	4
Consensus	37	25	1	4	6	0	5	7	1	1

Table 5.11: Breakdown of results from individual pathologists and corresponding majority and consensus results for each pathology group in the oesophagus. Values are the number of samples classified to that group.

5.2.1 Raw Spectral Data

Raman spectra obtained from oesophagus tissue (following the procedures outlined in section 4.3.2) have been grouped according to the histopathological grading of the sample performed by a panel of three consultant pathologists. Spectra were obtained from 87 homogeneous samples (one pathologist's grading) of oesophageal mucosal tissue (25 normal, 2 cardiac Barrett's, 5 fundic Barrett's, 13 intestinal metaplasia, 10 low-grade dysplasia, 11 high-grade dysplasia, 11 adenocarcinoma, 4 squamous dysplasia and 5 squamous cell carcinoma). Laser light of 830nm, 31 ± 0.8mW, was focussed to a spot 2-3 μm across. An acquisition time of 30s was used to achieve excellent signal to noise when using the 300 lines per mm grating. The grating dispersed the whole spectrum over the collection area of the CCD, therefore the grating was not required to move during measurements. No pixel binning was used for the oesophageal spectral measurements. Each spectrum was corrected for the wavelength sensitivity of the system by multiplying the spectrum by a correction file created using the procedure outlined in section 4.2.4.2. All spectra shown in this section have been calibrated for wavelength shift using a standard Neon-Argon source.

A plot of the mean of 1200 spectra from normal, metaplastic, dysplastic and cancerous oesophagus specimens is shown in Figure 5.15. The plot shows the intensity of the collected (Stokes) signal versus wavenumber shift relative to the 830nm excitation source. The larger the wavenumber the greater the shift from the excitation wavelength. The most significant peaks in the spectrum have been labelled with the corresponding wavenumber shift. Tentative peak assignments have been made from extensive study of the literature. These are tabulated in Table 5.12. Further peak assignments have been compiled in Appendix 4. They have contributions from a myriad of constituents including proteins, lipids, carbohydrates and nucleic acids. Many of the spectral peaks overlap and thus make a full understanding of the biochemistry very difficult to achieve.

The spectra of normal oesophageal specimens have shown little inter- and intra-sample variability. Figure 5.16 shows 100 NIR-Raman spectra obtained from ten normal oesophageal tissue specimens, with the mean spectrum displayed in green. Visual inspection of the spectra show the peak shapes and positions to be repeatable, although overall spectral intensities can vary by 10 % about the mean spectrum for each individual sample. Wavenumber repeatability was evaluated by measuring the position of the PHE

peak at around 1000 cm^{-1}. Results have been plotted in Figure 5.17. The mean position of the PHE peak was shown to be 1001.8 ± 1.12 cm^{-1}.

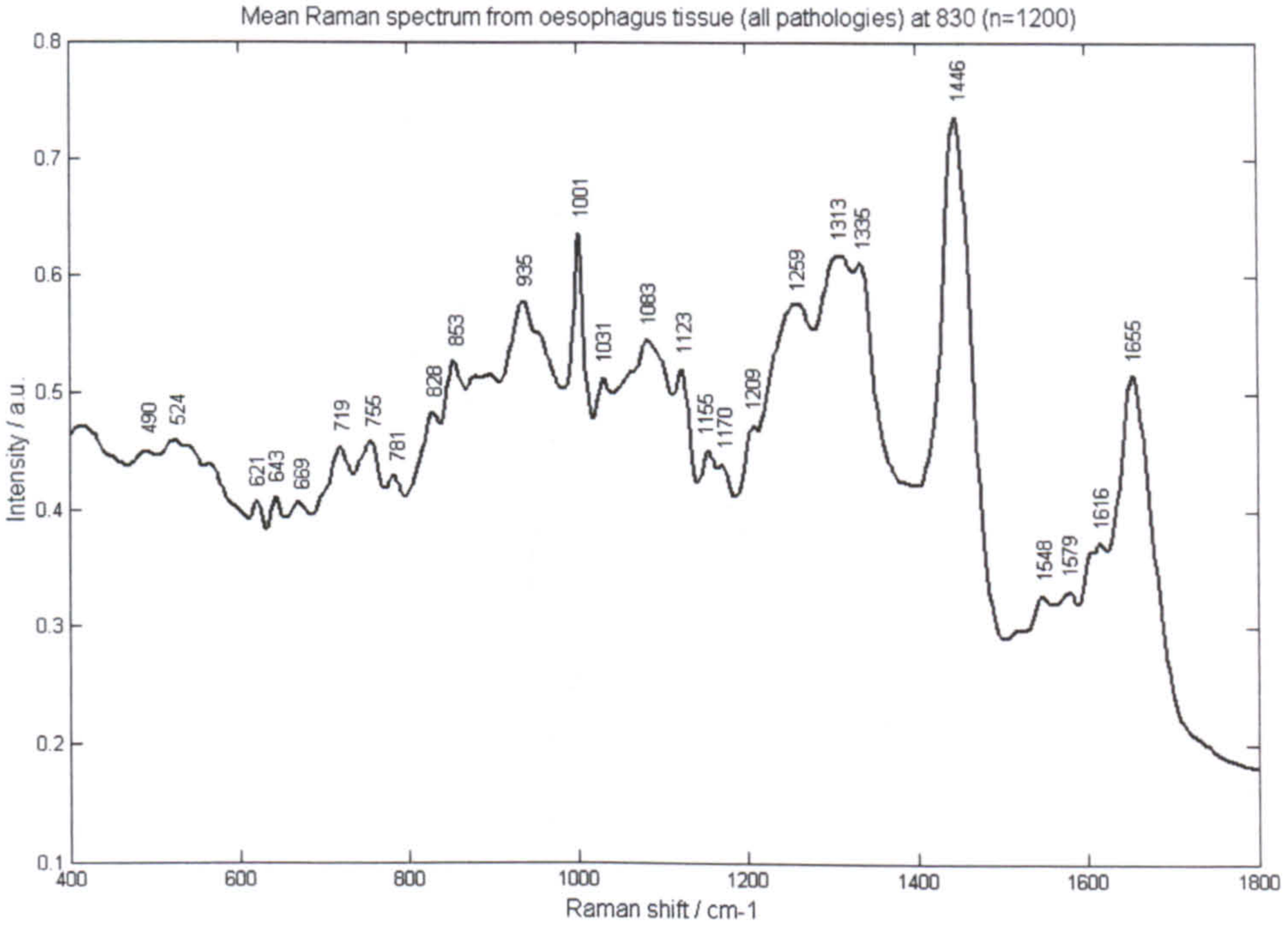

Figure 5.15: Mean Raman spectrum acquired from normal, metaplastic, dysplastic and cancerous oesophageal tissue with an 830nm excitation source. T=30s.

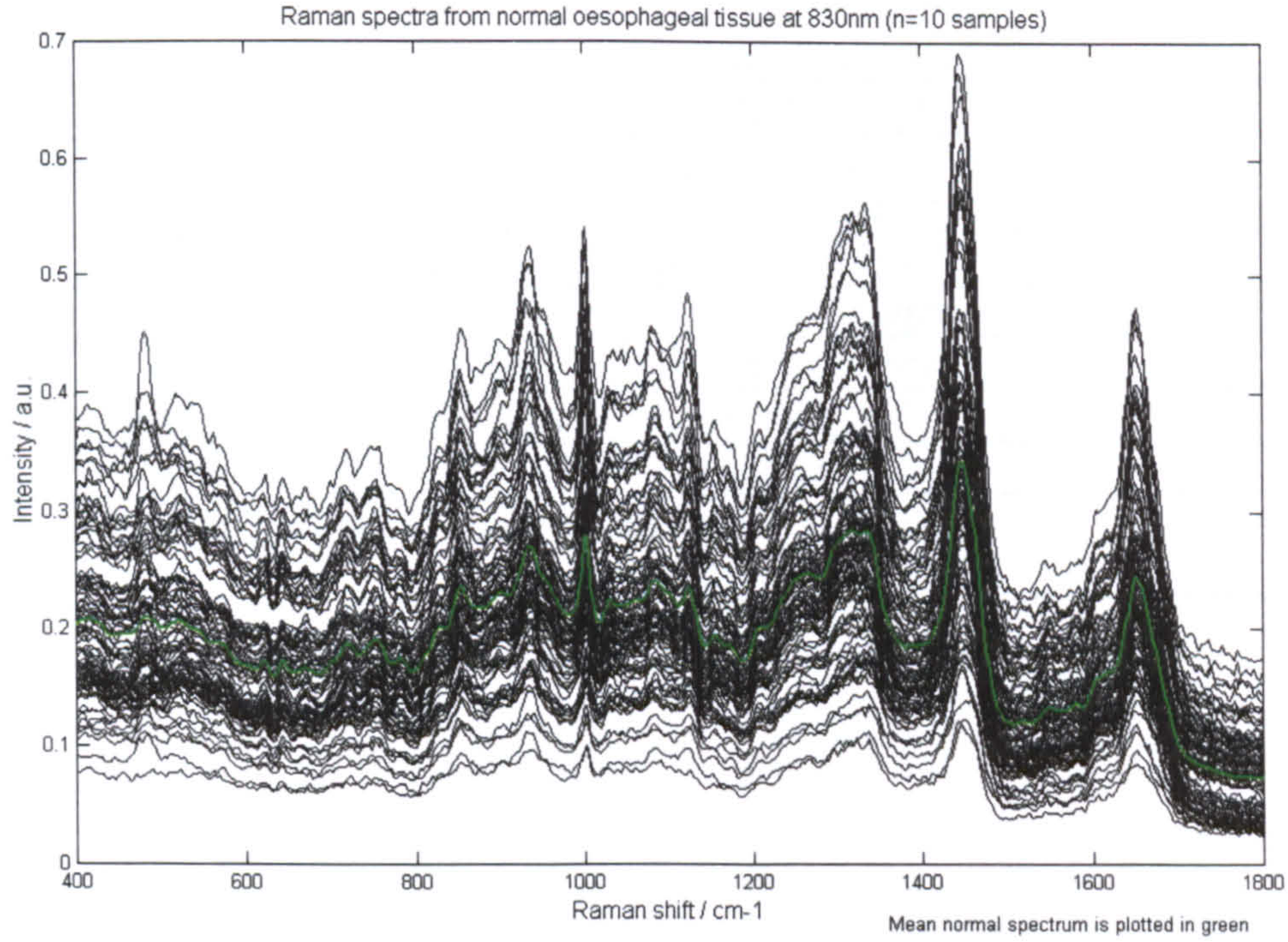

Figure 5.16: 100 Raman spectra from 10 normal oesophagus specimens, mean spectrum in green.

Table 5.12: Major vibrational modes identified in oesophageal samples.

Peak position (cm^{-1})	Major assignments
490	Glycogen
524	S-S disulfide stretch in proteins
621	C-C twisting mode of phenylalanine
643	C-C twisting mode of tyrosine
669	C-S stretching mode of cystine
719	C-N (membrane phospholipid head) / nucleotide peak
755	Symmetric breathing of tryptophan
781	Cytosine / uracil ring breathing (nucleotide)
828	Out of plane ring breathing tyrosine / O-P-O stretch DNA
853	Ring breathing mode of tyrosine and C-C stretch of proline ring
920	C-C stretch of proline ring / glucose / lactic acid
935	C-C stretching mode of proline and valine and protein backbone (α-helix conformation) / glycogen
1001	Symmetric ring breathing mode of phenylalanine
1031	C-H in-plane bending mode of phenylalanine
1083	C-N stretching mode of proteins (and lipid mode to lesser degree)
1123	C-C stretching mode of lipids / protein C-N stretch
1155	C-C (& C-N) stretching of proteins (also carotenoids)
1170	C-H in-plane bending mode of tyrosine
1209	Tryptophan and phenylalanine $\nu(C\text{-}C_6H_5)$ mode
1240-1265	Amide III (C-N stretching mode of proteins, indicating mainly α-helix conformation)
1313	CH_3CH_2 twisting mode of collagen / lipids
1335	CH_3CH_2 wagging mode of collagen and polynucleotide chain (DNA-purine bases)
1446	CH_2 bending mode of proteins and lipids
1548	Tryptophan
1579	Pyrimidine ring (nucleic acids) and heme protein
1603	C=C in-plane bending mode of phenylalanine and tyrosine
1616	C=C stretching mode of tyrosine and tryptophan
1655	Amide I (C=O stretching mode of proteins, α-helix conformation) / C=C lipid stretch

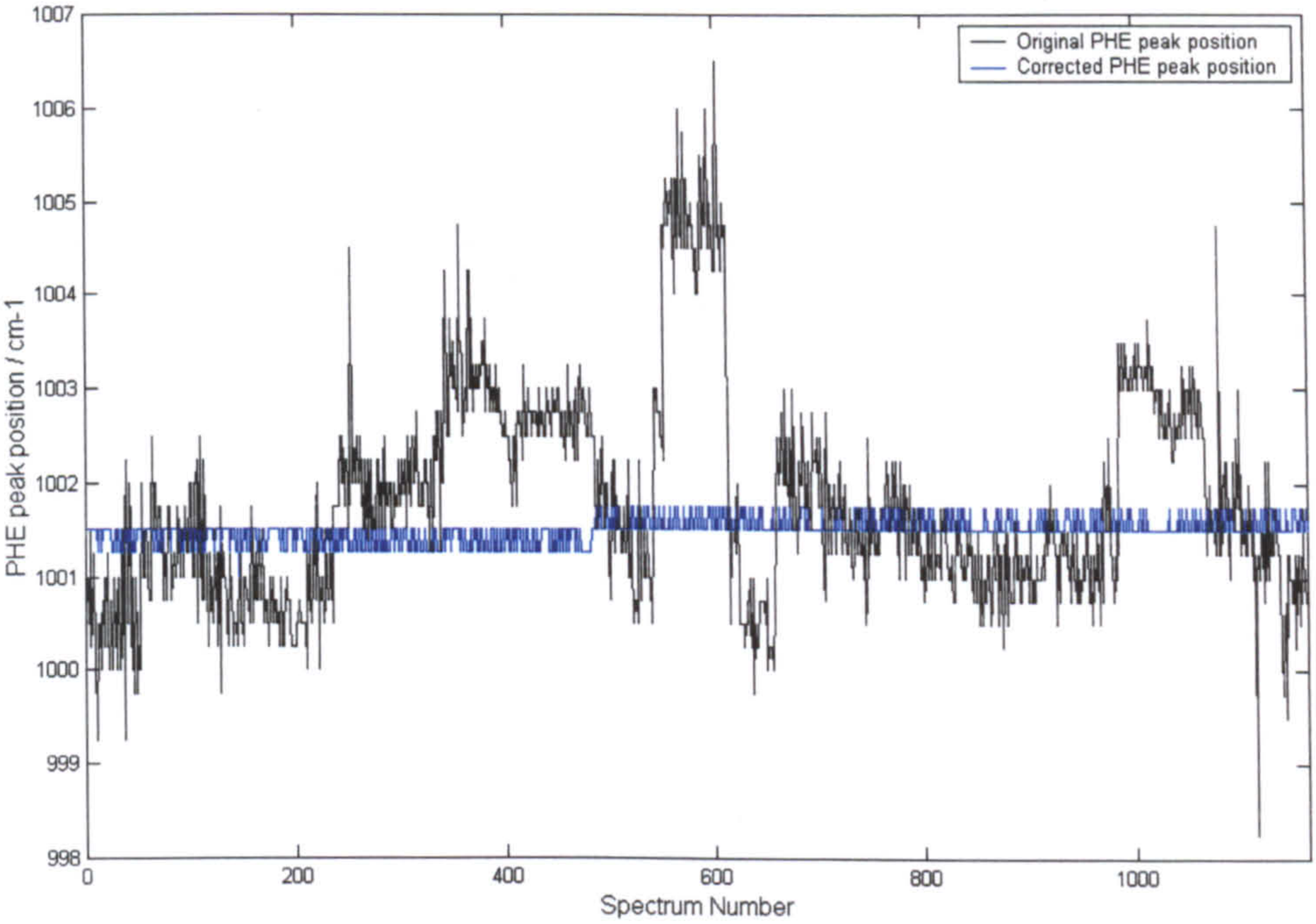

Figure 5.17: Plot of the wavenumber position of a peak assigned to phenylalanine versus acquired spectrum.

5.2.2 Empirical Spectral Analysis

The spectra acquired from samples belonging to each of nine pathological groups were collected together and mean spectra were calculated. A plot of the mean un-normalised spectra from each group is shown in Figure 5.18. From this plot it can be seen that the differences observed in the spectra from specimens at different stages of the cancer development process are very subtle. On first glance the spectra appear very similar, only very subtle variations in peak heights and positions can be seen from one group to the next.

Initially an evaluation of NIR-Raman spectroscopy for separation of specimens into three clinically significant groups, as would be required for biopsy targeting was carried out. Empirical analysis was performed on spectra compiled into three groups: normal tissue, metaplastic (Barrett's) tissue, and cancerous and pre-cancerous tissue in the third group. One method of emphasising the variation between the spectra from the three pathological groups is to calculate difference spectra. Figures 5.19 to 5.21 display the resulting difference spectra obtained from taking the difference between mean normalised and baseline subtracted spectra from each of the groups in turn.

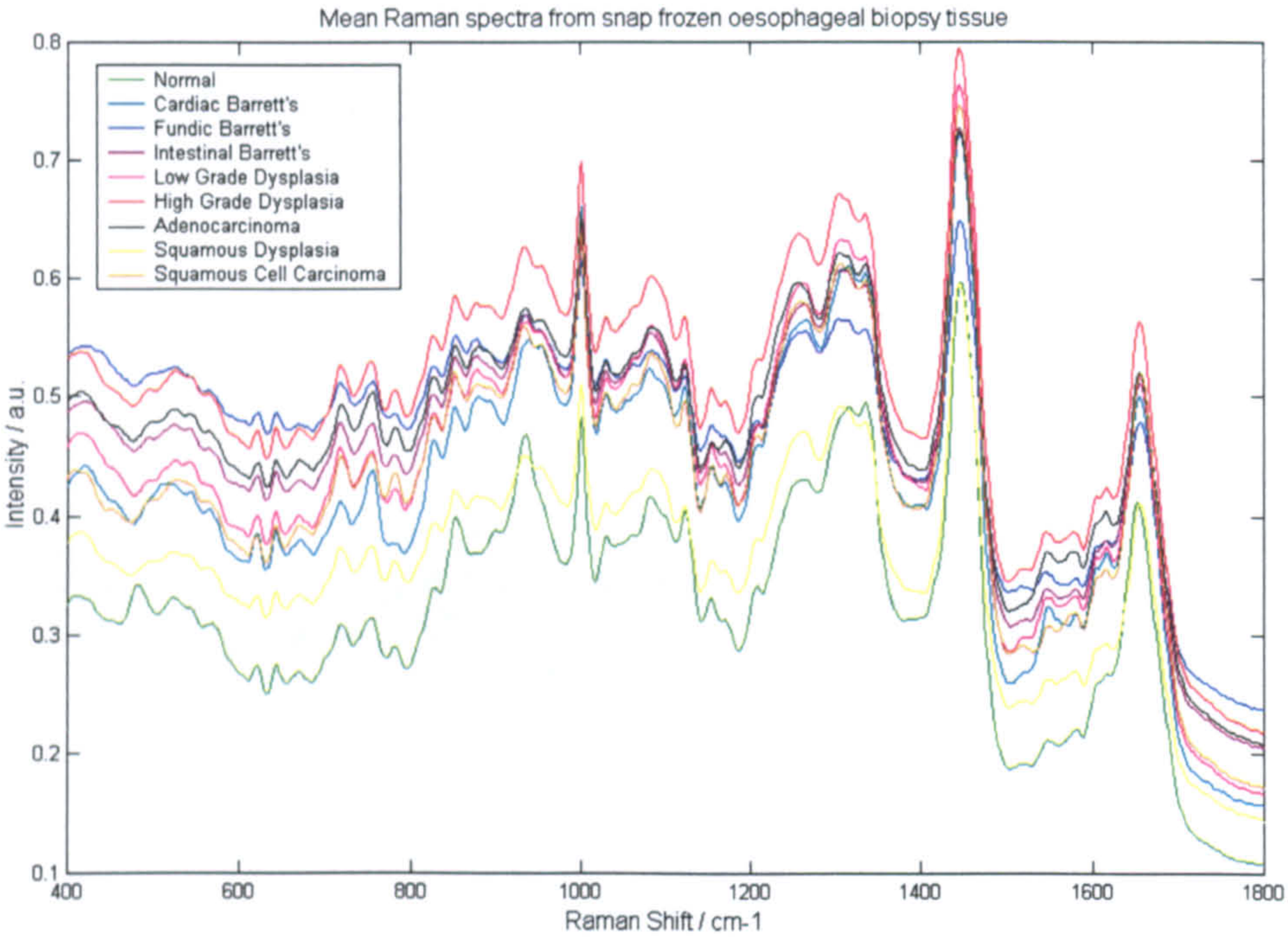

Figure 5.18: Mean Raman spectra from each oesophageal histopathological group.

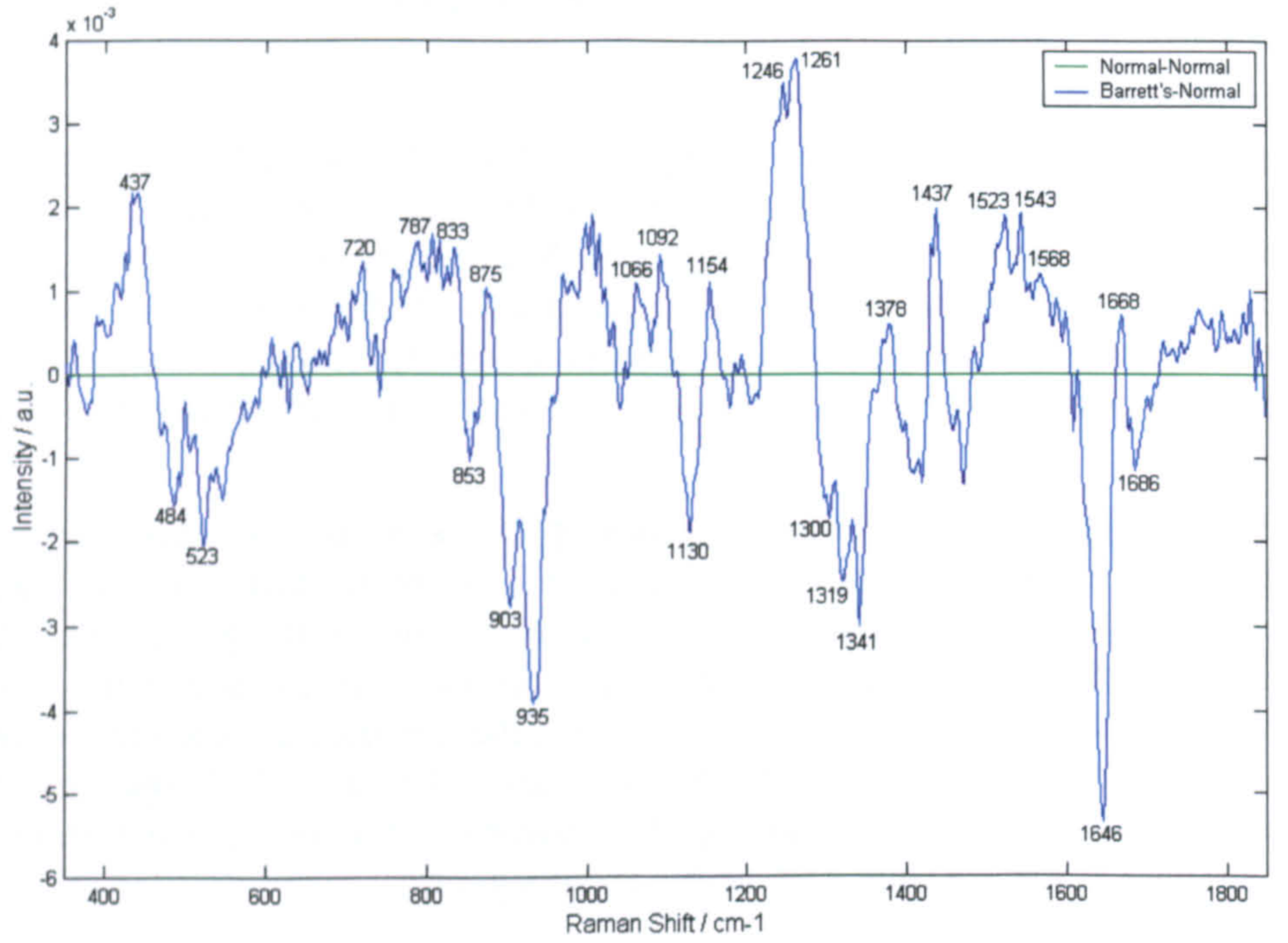

Figure 5.19: Mean normalised (and baseline corrected) Raman spectrum of Barrett's oesophageal tissue, with the mean normalized (and baseline corrected) spectrum of normal tissue subtracted.

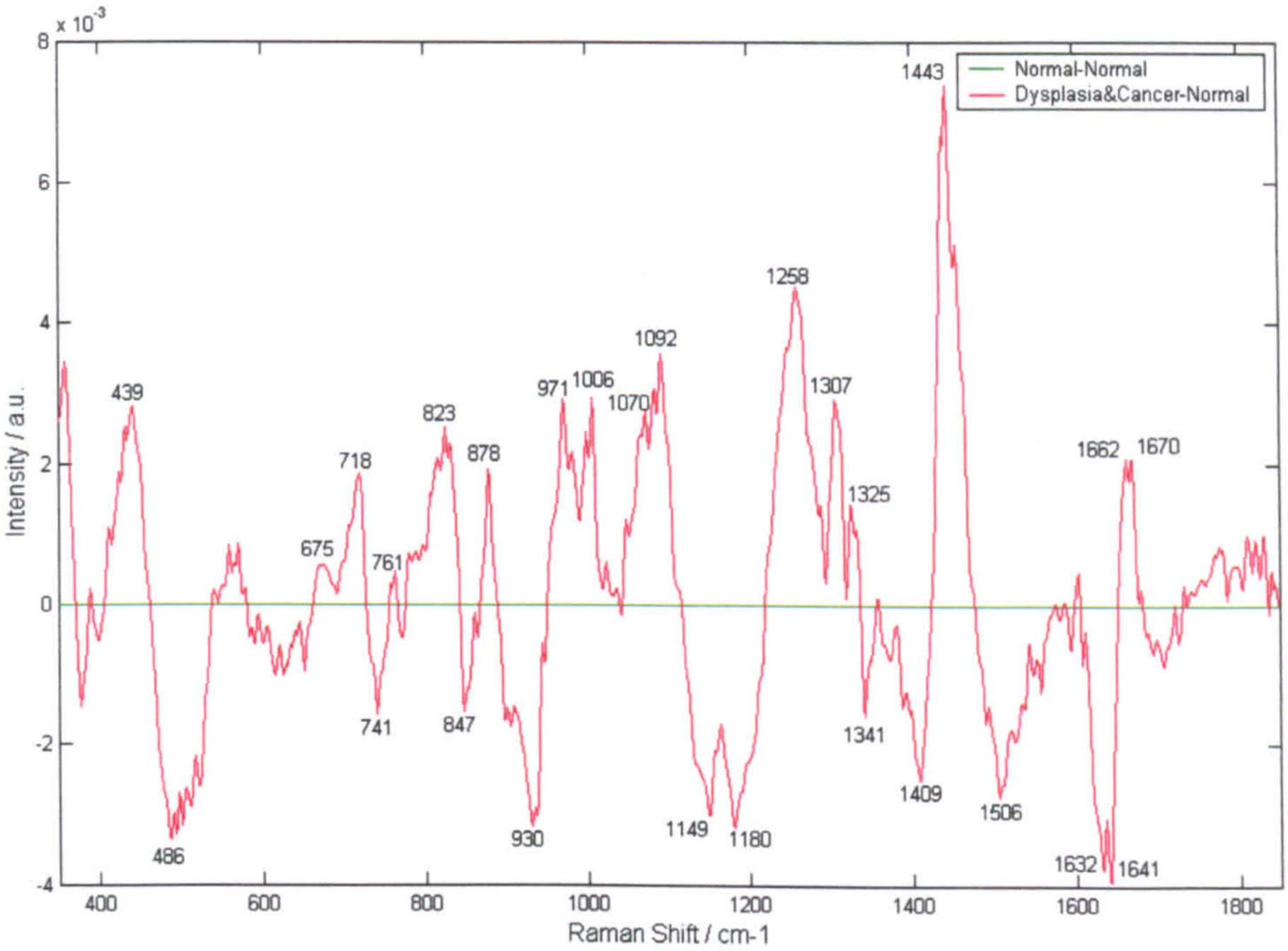

Figure 5.20: Mean normalised (and baseline corrected) Raman spectrum of dysplastic and cancerous oesophageal tissue with the mean (and baseline corrected) normalized normal tissue spectrum subtracted.

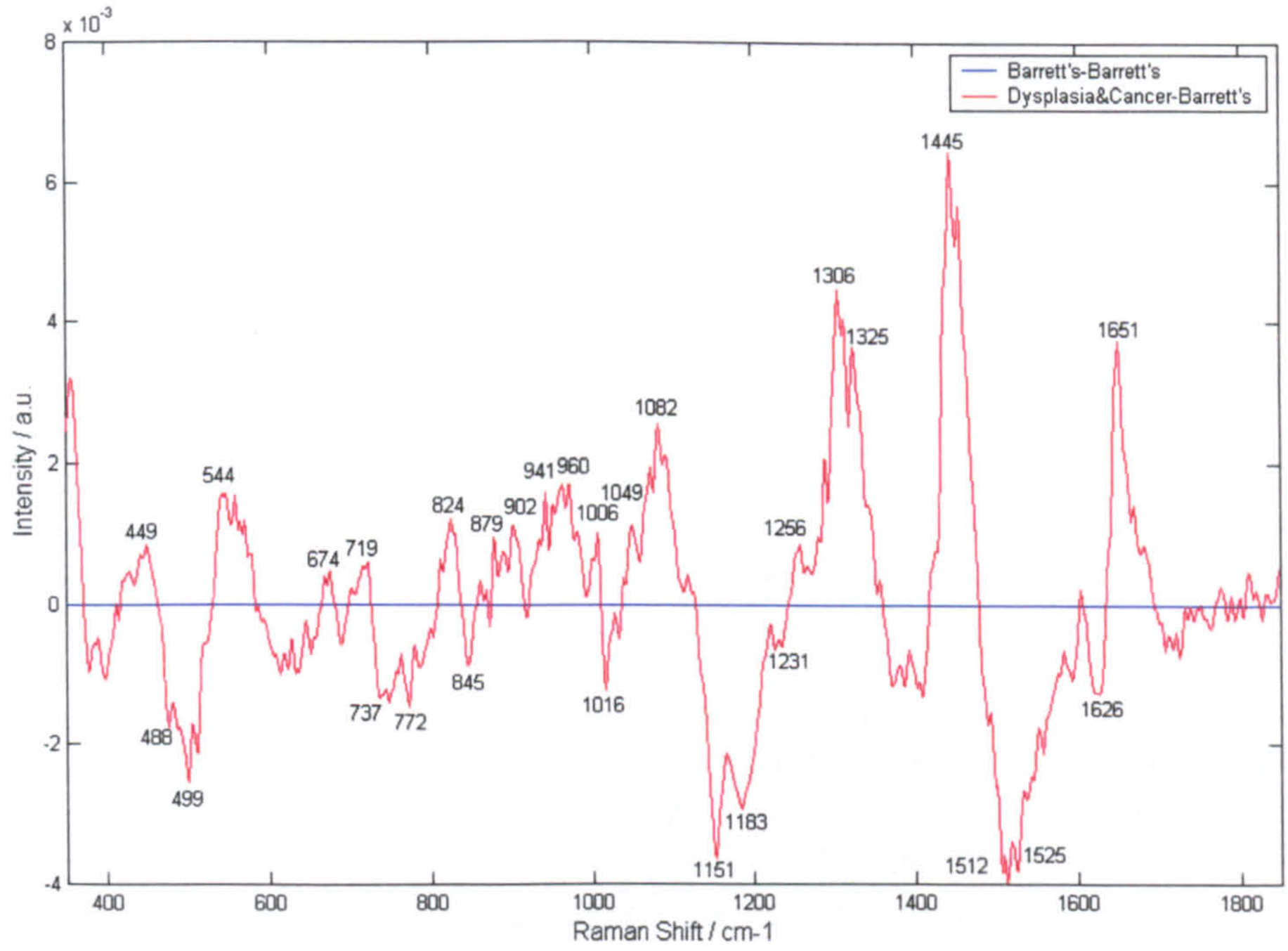

Figure 5.21: Mean normalised (and baseline corrected) Raman spectrum from dysplastic and cancerous oesophageal tissue with the mean normalized (and baseline corrected) spectrum from Barrett's oesophagus tissue subtracted.

Study of the above difference spectra provides evidence for constituents in excess in certain pathology types and in deficit in others. Table 5.13 outlines the likely constituents that exhibit the greatest variation between the pathological groups.

	Barrett's vs Normal		Dysplasia & Cancer vs Normal		Dysplasia & Cancer vs Barrett's	
	Peak	Tentative Assignment	Peak	Tentative Assignment	Peak	Tentative Assignment
Excess	437	Ribose	439	Ribose	449	Ribose ?
	720	Nucleotide/Phospholipid	675	Thymine / guanine	544	Protein (S-S)
	787	Cytosine/thymine/uracil	718	Nucleotide/phospholipid	674	Thymine / guanine
	833	DNA (O-P-O)	761	?	719	Nucleotide/phospholipid
	875	?	823	DNA (O-P-O)	824	DNA (O-P-O)
	1066	Protein (C-C stretch)	878	?	879	?
	1092	DNA (PO^2_-)	971	Hydroxyapatite	902	?
	1154	Carotenoids (C-C)	1006	Urea? / PHE	941	Proline/valine (C-C str)
	1246	Am. III: unordered	1070	Protein (C-C stretch)	960	Hydroxyapatite
	1261	Am. I: α-helix	1092	DNA (PO^2_-)	1006	Urea / PHE
	1378	T/A/G bases	1258	Am. III: α-helix	1049	?
	1437	CH_2/CH_3 lipid?	1307	Lipid / A/T	1070	Protein (C-C stretch)
	1523	Carotenoids (C=C)	1325	Nucleic acids	1082	Nuclear acids / lipid
	1543	?	1443	CH_2/CH_3 mainly lipid?	1256	Am. III: α-helix
	1568	?	1662	Am. I: unordered	1306	Lipid
	1668	Am. I: α-helix	1670	Am. I: α-helix	1325	Nuclear acids
					1445	CH_2/CH_3 mainly lipid?
					1651	Lipid (C=C)
Deficit	484	Glycogen	486	Glycogen	488	Glycogen
	523	Protein (S-S)	?	Protein (S-S)	499	Protein (S-S)
	853	TYR / carbohydrates	741	?	737	?
	903	Glycogen?	847	TYR / carbohydrates	772	Cytosine / Thymine
	935	Protein(C-C)/glycogen	?	Glycogen	845	TYR / carbohydrate
	1130	Glucose/ (C-C)lip/prot	930	Protein (C-C) / TRP	1016	TRP
	1300	CH_2 lipid	1130	Glucose/ (C-C) lip/prot	1151	Carotenoid (C-C)
	1319	CH_2 lipid	1149	Carotenoid (C-C)	1183	Carotenoid / TYR
	1341	TRP / lipid	1180	Carotenoid / TYR	1231	Am. III: β-sheet
	1646	Lipid (C=C)	1341	Lipid	1512	Carotenoid (C=C)
	1686	Am. I: β-sheet	1409	?	1525	?
			1506	PHE	1626	?
			?	Carotenoid (C=C)		
			1632	?		
			1641	Am. I: ?? / lipid (C=C)		

Table 5.13: Peaks from difference spectra between normal, Barrett's and dysplastic and cancerous oesophagus spectra, with tentative peak assignments. (? signifies no data available for peaks)

5.2.2.1 Analysis of clinical significance of individual peak intensities

A full analysis of the clinical significance of 29 selected peak intensities from un-normalised spectra was carried out using analysis of variance (ANOVA), following the procedure outlined in Section 5.1.2.1. A selection of peaks with the corresponding ANOVA F-value is shown in Table 5.14. This method of analysis tests the hypothesis that means from two or more samples are equal (drawn from populations with the same mean). The larger the F-value the greater the effective grouping with pathology. F_{crit} is the cut-off value for 99.9% significance. The p-value is the probability that the intensities

for all pathologies are statistically the same, i.e. that they do not correlate with histopathology of the sample.

Peak	Mean peak intensity			ANOVA, F-value
	Normal Oesophagus	Barrett's Oesophagus	Dysplasia & Cancer	
I_{480}	0.328±0.165	0.483±0.300	0.337±0.123	0.1
I_{755}	0.295±0.172	0.512±0.313	0.373±0.142	0.3
I_{853}	0.378±0.212	0.570±0.325	0.424±0.164	0.6
I_{935}	0.446±0.253	0.608±0.340	0.458±0.178	0.6
I_{1001}	0.458±0.276	0.685±0.375	0.519±0.214	1.1
I_{1259}	0.407±0.249	0.628±0.353	0.482±0.196	1.2
I_{1446}	0.568±0.348	0.783±0.407	0.626±0.271	2.3
I_{1655}	0.389±0.237	0.553±0.296	0.429±0.178	2.0

Table 5.14: Selected peak intensities, with their corresponding mean and standard deviation values for each group. ANOVA F-values are included to indicate significance of peak for spectral group separation. $F_{crit} = 7.05$.

5.2.2.2 Analysis of clinical significance of peak intensity ratios

A more rigorous technique, better able to take into account variations in overall spectral intensity from one measurement to the next is the calculation of peak intensity ratios. A process of testing all 29 selected peaks ratioed against one another was carried out by initially calculating an n x (m x m) matrix containing the data for n spectra in each row, and each column representing the set of data for each peak ratio. Analysis of variance (ANOVA) was then used to evaluate the peak ratios demonstrating the most significant differences between groups. A selection of the most significant peak ratios have been recorded in Table 5.15, with the relevant mean and standard deviation ratios for each group. ANOVA F-values are recorded to provide information on the ability of each peak ratio to discriminate between pathology groups in the larynx. The critical F-value for 99.9% significance for this data set is 7.05. Peak ratio measurements with an F-value of greater than the critical value provide a high statistical significance for measurement of group membership. The measurements of standard deviations from the mean values indicate the variability from one sample to the next.

Peak Ratio	Mean peak intensity ratio value			ANOVA, F-value
	Normal Oesophagus	Barrett's Oesophagus	Dysplasia and Cancer	
I_{643}/I_{1616}	0.949±0.085	0.887±0.096	0.927±0.094	14.95
I_{1548}/I_{669}	1.345±0.207	1.261±0.104	1.241±0.133	24.12
I_{935}/I_{1655}	0.860±0.094	0.912±0.063	0.929±0.069	18.81
I_{755}/I_{480}	1.197±0.334	0.946±0.054	0.916±0.073	10.48
I_{1155}/I_{1170}	0.932±0.065	0.975±0.029	0.978±0.049	11.87
I_{1259}/I_{1335}	1.185±0.105	1.034±0.046	1.033±0.040	4.07
I_{1335}/I_{1655}	0.817±0.086	0.854±0.041	0.862±0.040	14.40
I_{1616}/I_{755}	1.191±0.087	1.248±0.086	1.238±0.079	18.71

Table 5.15: Selected peak intensity ratios, from normalised spectra, with their corresponding mean and standard deviation values for each group. ANOVA F-values are included to indicate significance of ratio for spectral group separation. F_{crit}=7.05.

5.2.3 Multivariate Spectral Analysis

The use of Raman spectroscopy to assist biopsy targeting is likely to require simple decisions between either normal or abnormal tissues, therefore three- and four-group models would be likely to be used in this area. However, full classification of the pathological state of the tissue in the oesophagus, either in the laboratory or in vivo, would require the discrimination between a minimum of nine groups. The ability of multivariate statistical techniques to separate the specimens into pathological groups was assessed for different scenarios and for both majority and consensus pathology results.

Principal component analysis was performed on the oesophagus spectra using singular value decomposition (SVD) in PLS-Toolbox (Eigenvector) running in the MATLAB® environment. Of the 1225 spectra acquired, 36 were discarded due to extremely poor signal to noise ratios or an unusually large fluorescence background. The remaining spectra were compiled into a training data set and some sort of pre-processing was performed upon it. Initially the spectra were interpolated to a regular number of points per wavenumber (the Renishaw system 1000 has a variable spacing due to the polynomial calibration fit of wavenumber per pixel across the CCD chip). The position of the phenylalanine (PHE) peak at around 1000 cm^{-1} was measured for each spectrum to evaluate system drift from one measurement to the next. Due to improvements in stability since laryngeal spectral measurements were taken, it was not necessary to correct spectra for spectrometer drift. In the first instance unfiltered spectra were used to build a discrimination model. Then pre-processing based upon Savitsky-Golay filters were applied to optimise the models for maximum group separation.

Following pre-processing the spectra were mean-centred; this involved calculating the average spectrum of all the spectra in the data set and subtracting this result from every spectrum. Principal component analysis was used to describe the resulting spectra as a sum of a small orthogonal set (25) of linear combinations of the original variables.

Figures 5.22 a, b and c show plots of the PCs. These principal components described over 99.9% of the variance from the mean spectrum across the data set. Each PC can represent a single constituent or combination of constituents that vary colinearly between samples. The most identifiable of these is PC 3, in this case it represents the glycogen component of the oesophageal Raman spectra. Glycogen is the energy store within epithelial cells. Those cells rapidly dividing will use up this reserve and hence have lower concentrations and corresponding Raman scattering intensities.

Figure 5.22(a): Principal components 1 to 12 representing the first 99.98% of the variance of the data set from the mean spectrum.

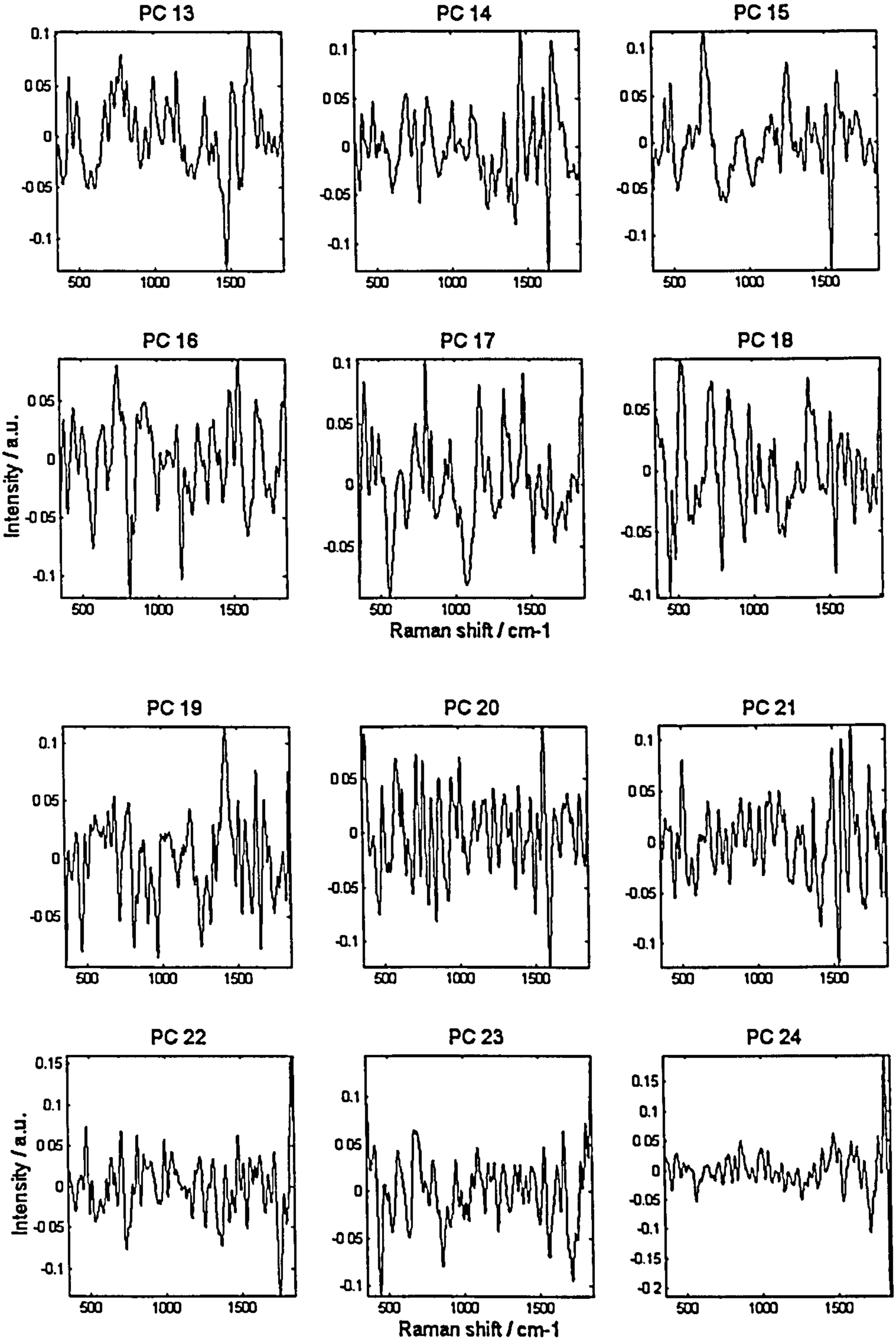

Figure 5.22(b): Principal components 13 to 24 representing 0.02% of the variance of the data set from the mean spectrum.

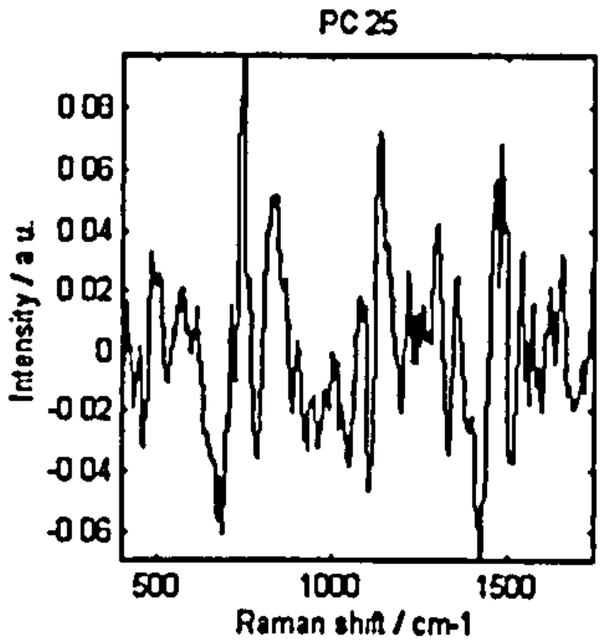

Figure 5.22(c): Principal component 25 representing 0.004% of the variance of the data set from the mean spectrum.

Table 5.16 lists each PC with the corresponding percentage variance described by it. Multiple ANOVA was used to identify the most diagnostically significant principal components, i.e. those that show a significant difference in value for normal, Barrett's, dysplastic and cancerous oesophagus. In addition a Wilks'-Lambda test has been performed on the data (Table 5.16).

Principal Component	% Variance	Cumulative % Variance	Wilks' Lambda	F-Value	Significance = (100-p)
1	**95.98**	**95.98**	**.864**	**48.162**	**.000**
2	**2.94**	**98.92**	**.907**	**31.474**	**.000**
3	**0.46**	**99.38**	**.969**	**9.686**	**.000**
4	**0.27**	**99.65**	**.926**	**24.500**	**.000**
5	**0.16**	**99.80**	**.864**	**48.377**	**.000**
6	**0.05**	**99.85**	**.734**	**111.044**	**.000**
7	**0.03**	**99.88**	**.850**	**54.212**	**.000**
8	**0.02**	**99.90**	**.971**	**9.235**	**.000**
9	0.02	99.91	.980	6.394	.002
10	**0.01**	**99.93**	**.974**	**8.111**	**.000**
11	0.01	99.94	.984	4.840	.008
12	**0.01**	**99.95**	**.917**	**27.699**	**.000**
13	0.01	99.95	.988	3.855	.022
14	0.00	99.96	.996	1.142	.320
15	0.00	99.96	.986	4.307	.014
16	0.00	99.96	.999	.456	.634
17	0.00	99.96	.995	1.440	.238
18	0.00	99.96	.992	2.585	.076
19	0.00	99.96	.994	1.986	.138
20	0.00	99.97	.999	.307	.736

Table 5.16: Displays the first 20 PCs with the corresponding variance of the data set described, with statistical significance test results for evaluation of group discrimination power. PCs with greater than 99.9% significance of discrimination between pathological groups are printed in bold.

5.2.3.1 Principal Component Discrimination

Individual PCs were selected with greater than 99.9% significance of discrimination between groups. The weights of principal components 1, 6, 4 and 5 were plotted in Figure 5.23. It can be seen that without any manipulation some clustering occurs within these PCs between pathological groups.

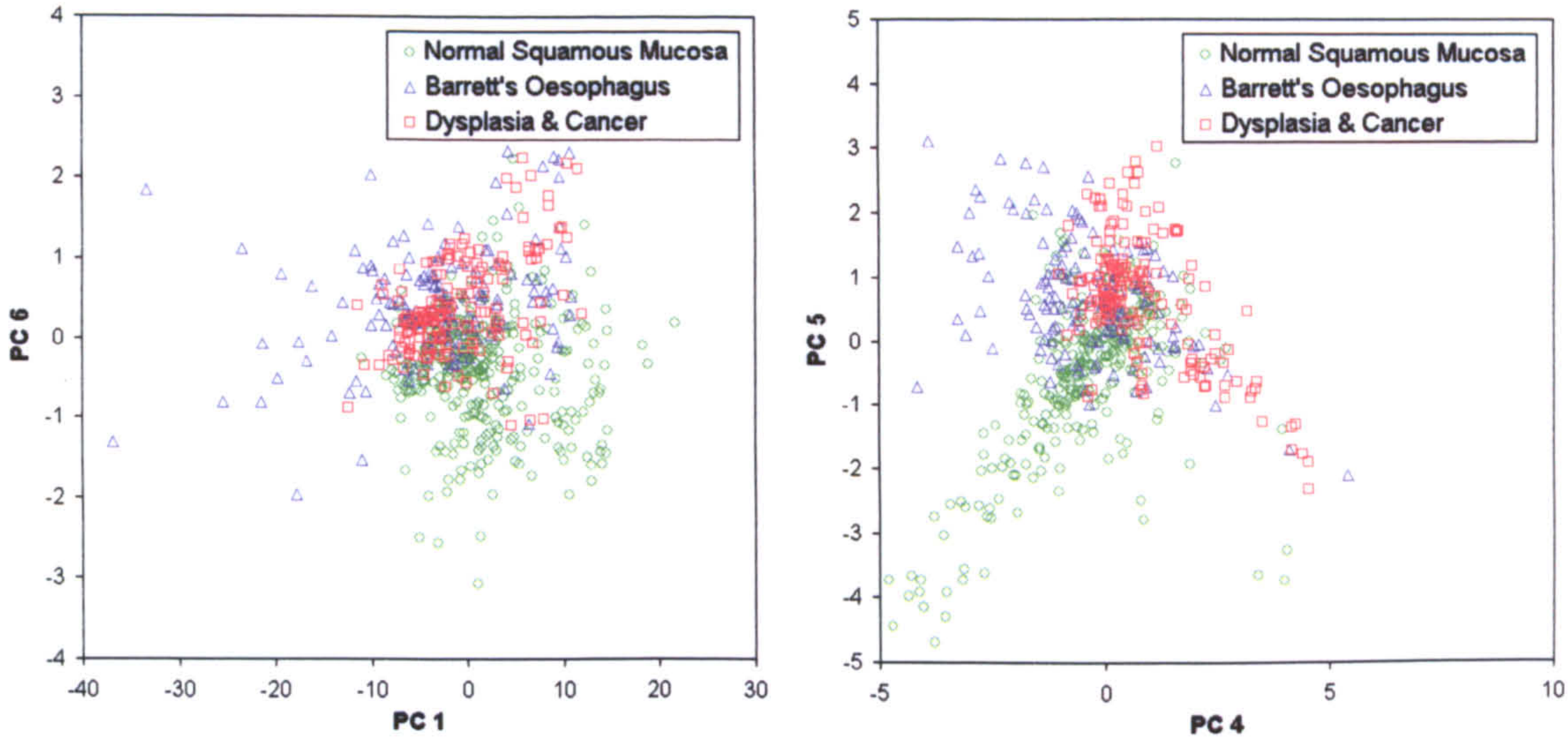

Figure 5.23: Scatter plots of principal component weights from PC1 versus PC6 and PC4 versus PC5. Symbols represent different oesophageal pathological states of specimens measured.

5.2.3.2 Three-group Linear Discriminant Consensus Model

The specimens were separated into three clinically significant pathology groups: Normal oesophagus, Barrett's oesophagus (Cardiac, Fundic and Intestinal Metaplasia together), and dysplasia and cancer (LGD, HGD and adenocarcinoma together).

The first 25 PCs (describing almost 100% of the total variance from the mean) were used to calculate two linear discriminant (LD) functions that maximised the variance in the data between the pathological groups and minimised the variance between members of the same pathological group. A diagram outlining the steps taken to construct a linear discriminant model is shown in Figure 5.24. The two LD functions (Figure 5.25) were combined to produce a diagnostic prediction model. The prediction accuracy of the model was tested using a cross-validation procedure, whereby each spectrum was held back in turn whilst all the others were used to calculate the discriminant functions. The weights of the linear discriminant functions for each spectrum were plotted against each other in a scatter plot to enable visualisation of group separation. This is displayed in Figure 5.26. The held back spectrum had its corresponding pathology forecast by the model. This continued until the pathologies of all the tissue samples measured with Raman spectroscopy had been predicted. The accuracy of these forecasts was compared to the 'gold standard' histopathological findings. Table 5.17 displays the resulting predictions versus histopathological grading and Table 5.18 displays the sensitivities and specificities of the test for each group.

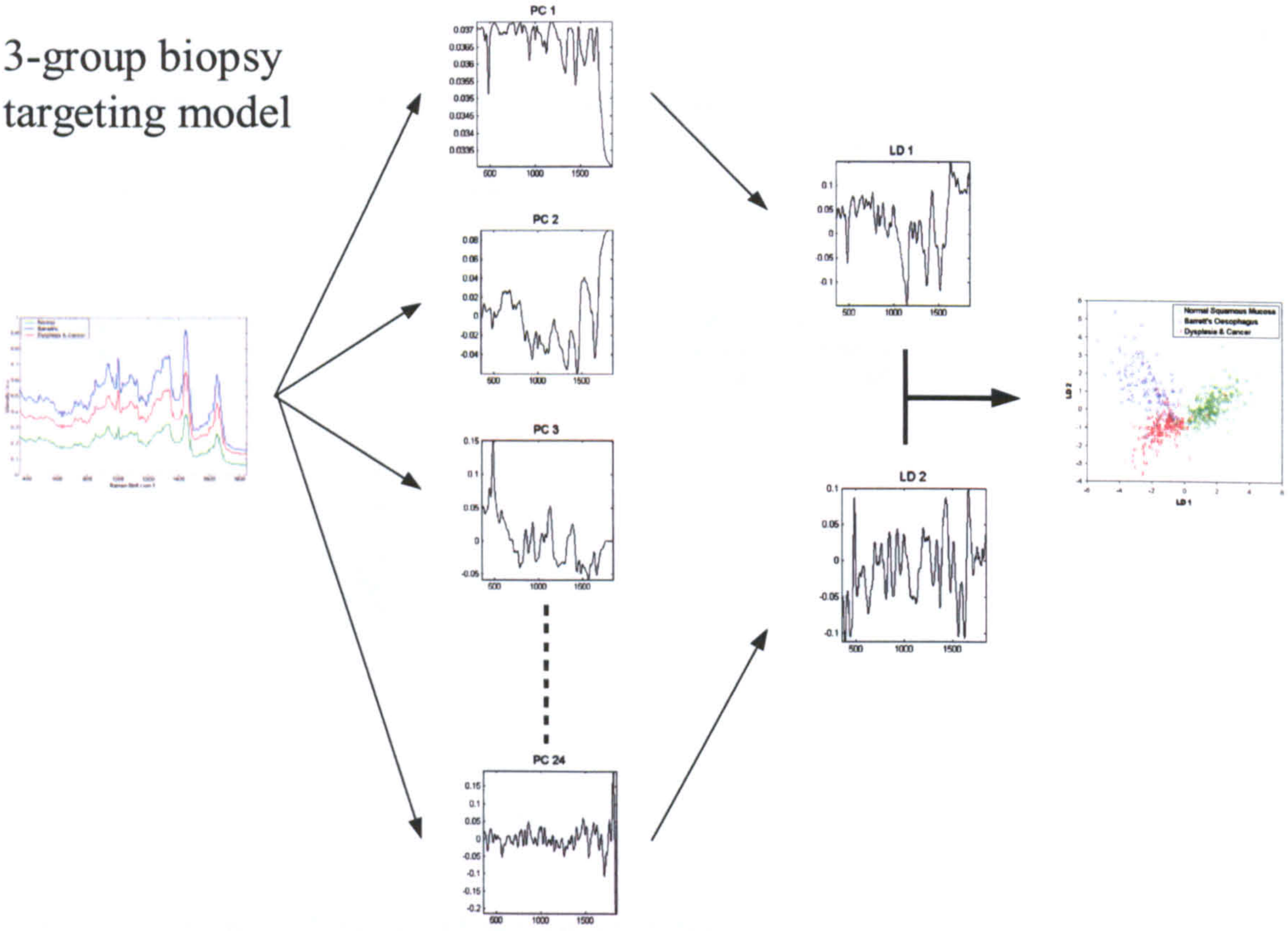

Figure 5.24: Diagram representing the steps of construction of a linear discrimiant model to separate 3 groups of specimens. 1. Calculate principal components from mean centred spectral data. 2. Select clinically significant PCs to calculate (n-1) linear discrimiant functions to maximally separate the groups.

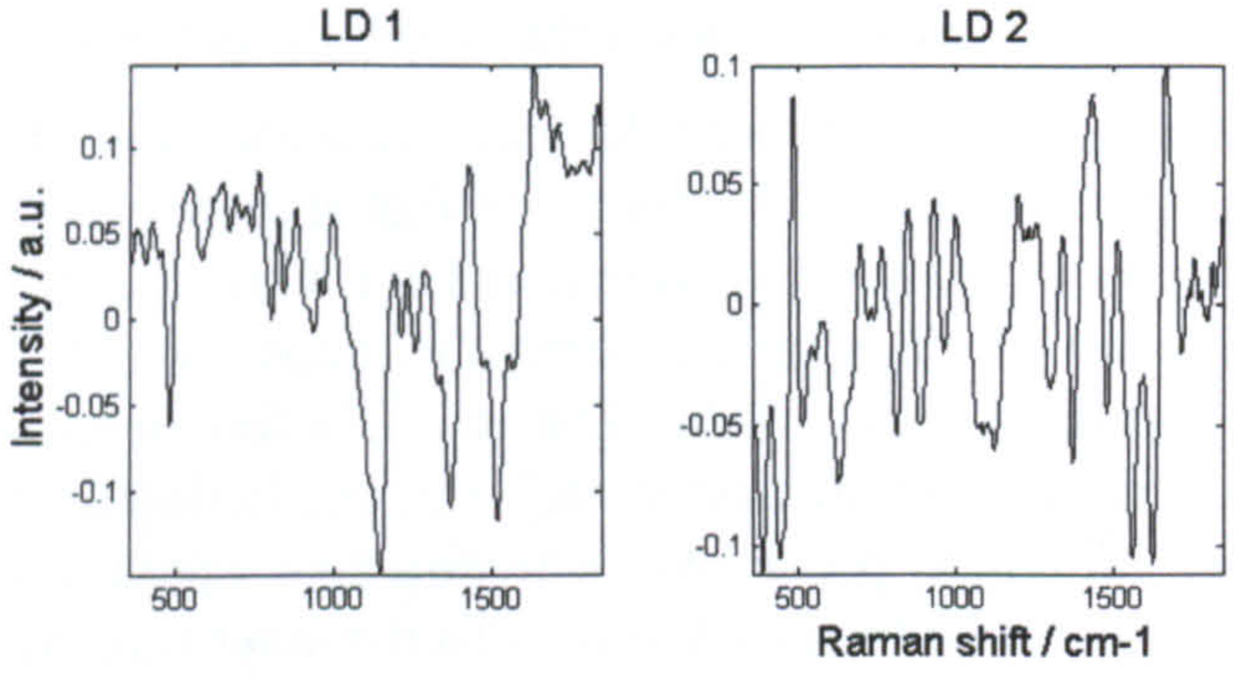

Figure 5.25: The two linear discrimiant functions required to maximally separate the three clinically significant oesophageal pathology groups.

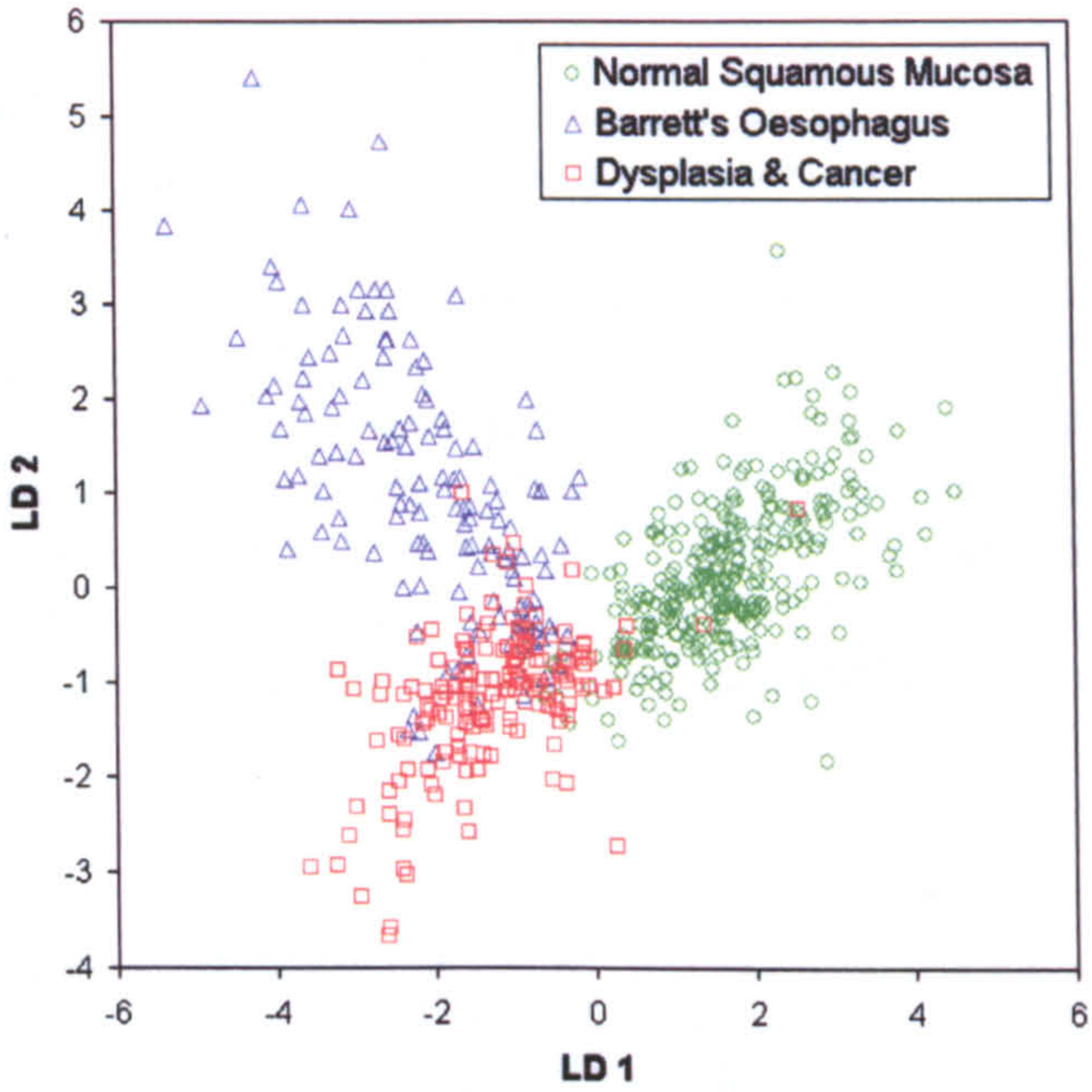

Figure 5.26: Plot of linear discriminant function weights for each spectrum, when tested against the model using a cross-validation process.

Histopathology	Classification	Raman Predicted Group Membership: Normal	Barrett's	Dysplasia & Cancer	Total
No.	Normal	**301**	1	8	310
	Barrett's	0	**122**	23	145
	Dys & Cancer	3	7	**152**	162
%	Normal	**97**	0	3	100.0
	Barrett's	0	**84**	16	100.0
	Dys & Cancer	2	4	**94**	100.0

Table 5.17: Cross-validation classification results obtained using the discriminant functions calculated from the first 25 principal components of the oesophagus spectra. Each case was classified by the functions derived from all cases other than that case. 93.2% of cross-validated grouped cases are correctly classified using this method.

	Normal	Barrett's	Dysplasia & Cancer
Sensitivity	97%	84%	94%
Specificity	99%	98%	93%

Table 5.18: Sensitivity and specificity of Raman spectroscopy as a diagnostic test to classify pathology in the oesophagus, calculated from the cross-validation classification results obtained from the linear discriminant model.

5.2.3.3 Four-group Linear Discriminant Consensus Model

The specimens were separated into four clinically significant pathology groups: Normal oesophagus, Barrett's oesophagus (Cardiac, Fundic and Intestinal Metaplasia together), Dysplasia, and Adenocarcinoma. The same process was followed, as that in the previous section, to construct and test a spectral discriminant model. However this time three linear discriminant functions were required to optimally separate four groups. These are shown in Figure 5.27. The weights of the functions were plotted in against one another in Figure 5.28 for each spectrum in the model. Pathological group separation can be seen from these plots. Cross-validation of the models enabled the prediction ability to be tested. Results of this are shown in Tables 5.19 and 5.20 and Figure 5.29. The bar chart in Figure 5.29 was included to enable visualisation of the cross-over between group prediction within the model. Colour coding of each group is consistent throughout the figures.

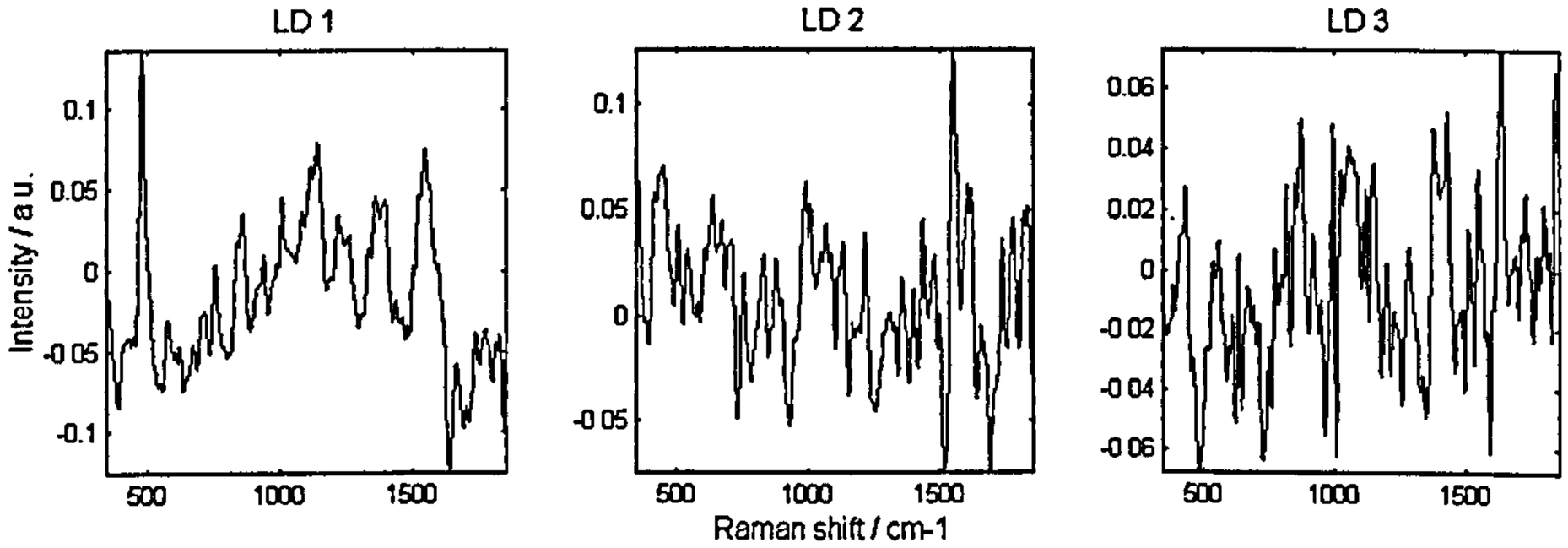

Figure 5.27: Three linear discriminant functions required to maximally separate four pathology groups from an unfiltered spectral data set.

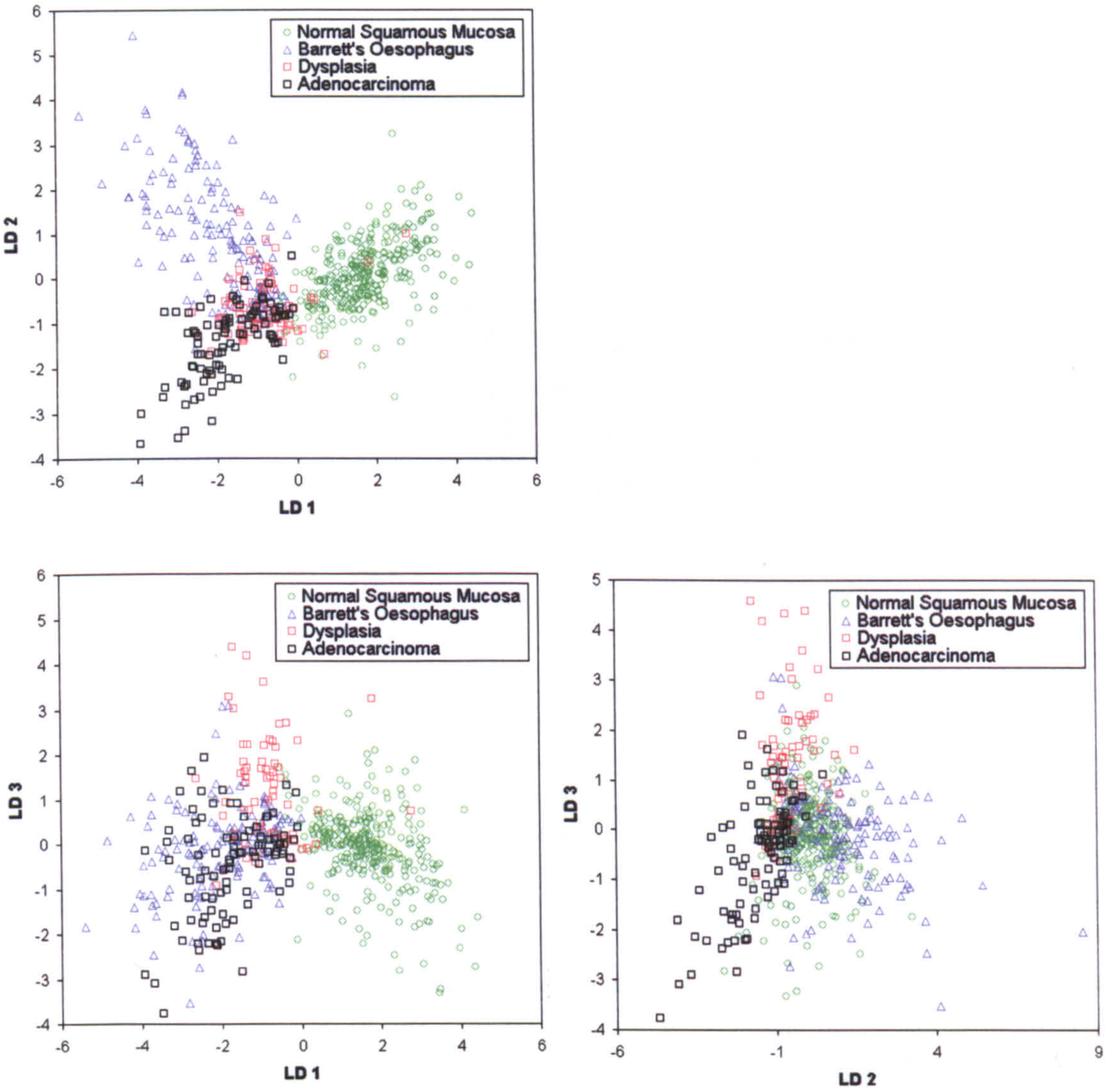

Figure 5.28: Plots of linear discriminant weights demonstrating clustering of pathology groups.

Histopathology	Classification	Raman Predicted Group Membership: Normal	Barrett's	Dysplasia	Cancer	Total
No.	Normal	**295**	0	13	2	310
	Barrett's	1	**111**	26	7	145
	Dysplasia	1	2	**56**	9	68
	Cancer	1	1	25	**67**	94
%	Normal	**95**	0	4	1	100
	Barrett's	1	**77**	18	5	100
	Dysplasia	1	3	**82**	13	100
	Cancer	1	1	27	**71**	100

Table 5.19: Cross-validation classification results obtained using the discriminant functions calculated from 25 PCs of the oesophagus spectra. Each case was classified by the functions derived from all cases other than that case. 85.7 % of cross-validated grouped cases are correctly classified using this method.

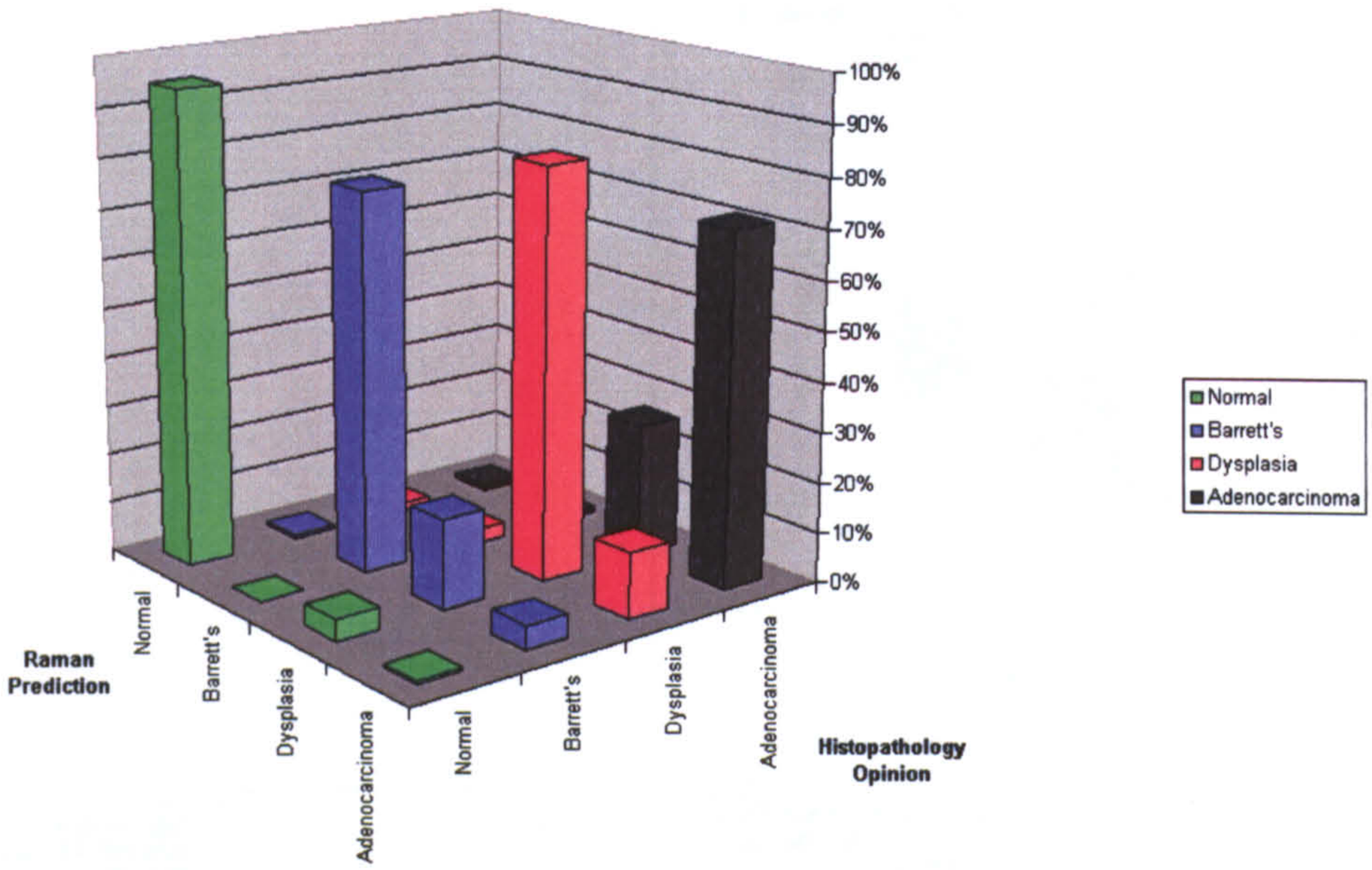

Figure 5.29: Bar chart of prediction power of the consensus four-group discriminant model.

	Normal	Barrett's	Dysplasia	Adenocarcinoma
Sensitivity	95%	77%	82%	71%
Specificity	99%	99%	88%	97%

Table 5.20: Sensitivity and specificity of Raman spectroscopy as a diagnostic test to classify pathology in the oesophagus, calculated from the cross-validation classification results obtained from the linear discriminant model.

5.2.3.4 Eight-group Linear Discriminant Consensus Model

The specimens were separated into eight clinically significant pathology groups: Normal oesophagus, cardiac Barrett's, fundic Barrett's, intestinal metaplasia, high grade dysplasia, adenocarcinoma, squamous dysplasia and squamous cell carcinoma. The same process was followed as that section 5.2.3.2, to construct and test a spectral discriminant model. However this time seven linear discriminant functions were required to optimally separate the eight groups. These are shown in Figure 5.30. The weights of the functions were plotted against one another in Figure 5.31 for each spectrum in the model. Pathological group separation can be seen from these plots, although full separation could only be visualised if one could plot and study seven-dimensional space. Cross-validation of the model enabled the prediction ability to be tested. Results of this are shown in Tables 5.21 and 5.22 and Figure 5.32. The bar chart in Figure 5.32 was included to enable visualisation of the cross-over between group prediction within in the model. Colour coding of each group is consistent throughout the figures.

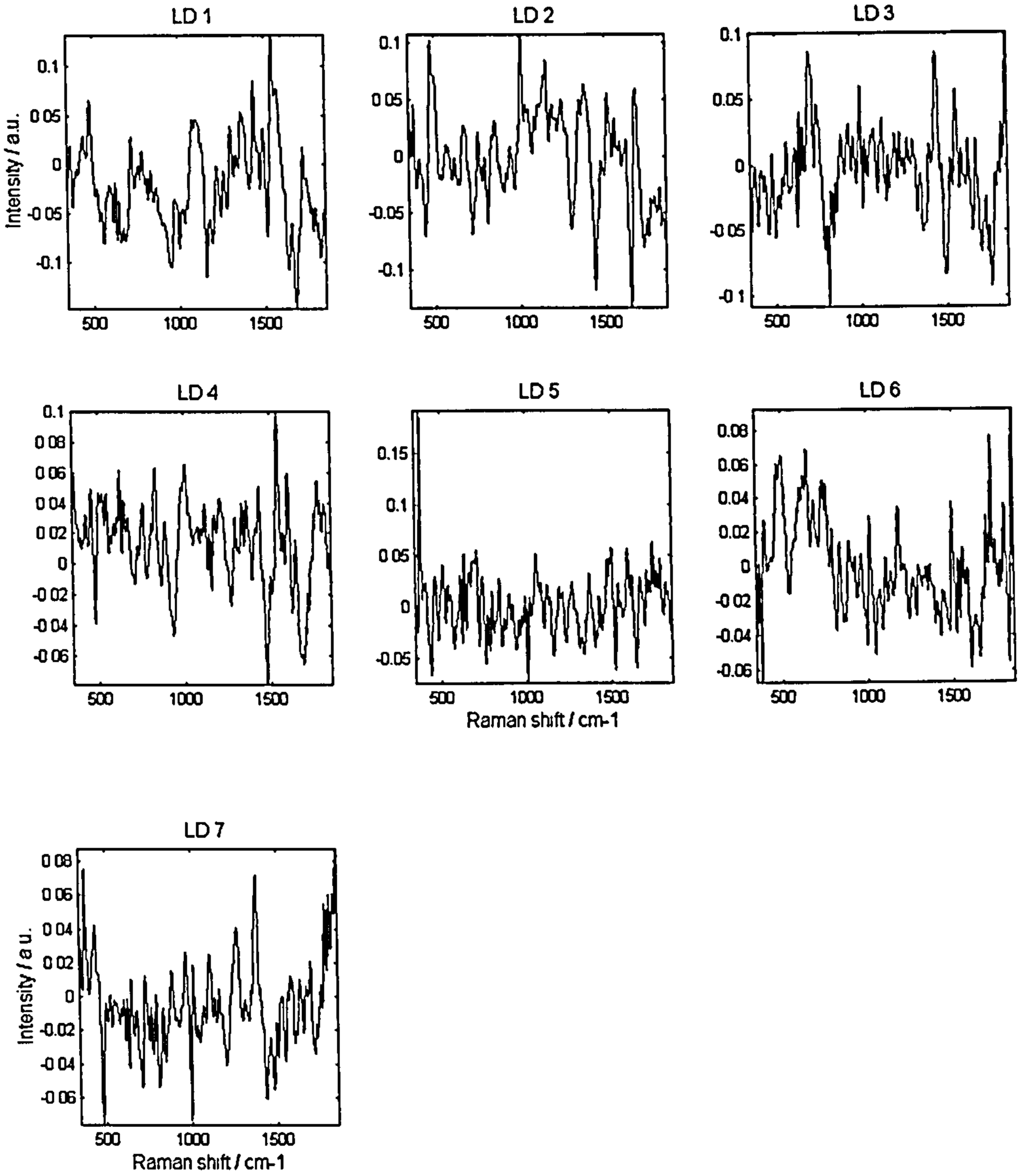

Figure 5.30: Seven linear discriminant functions required to maximally separate eight pathology groups from an unfiltered spectral data set.

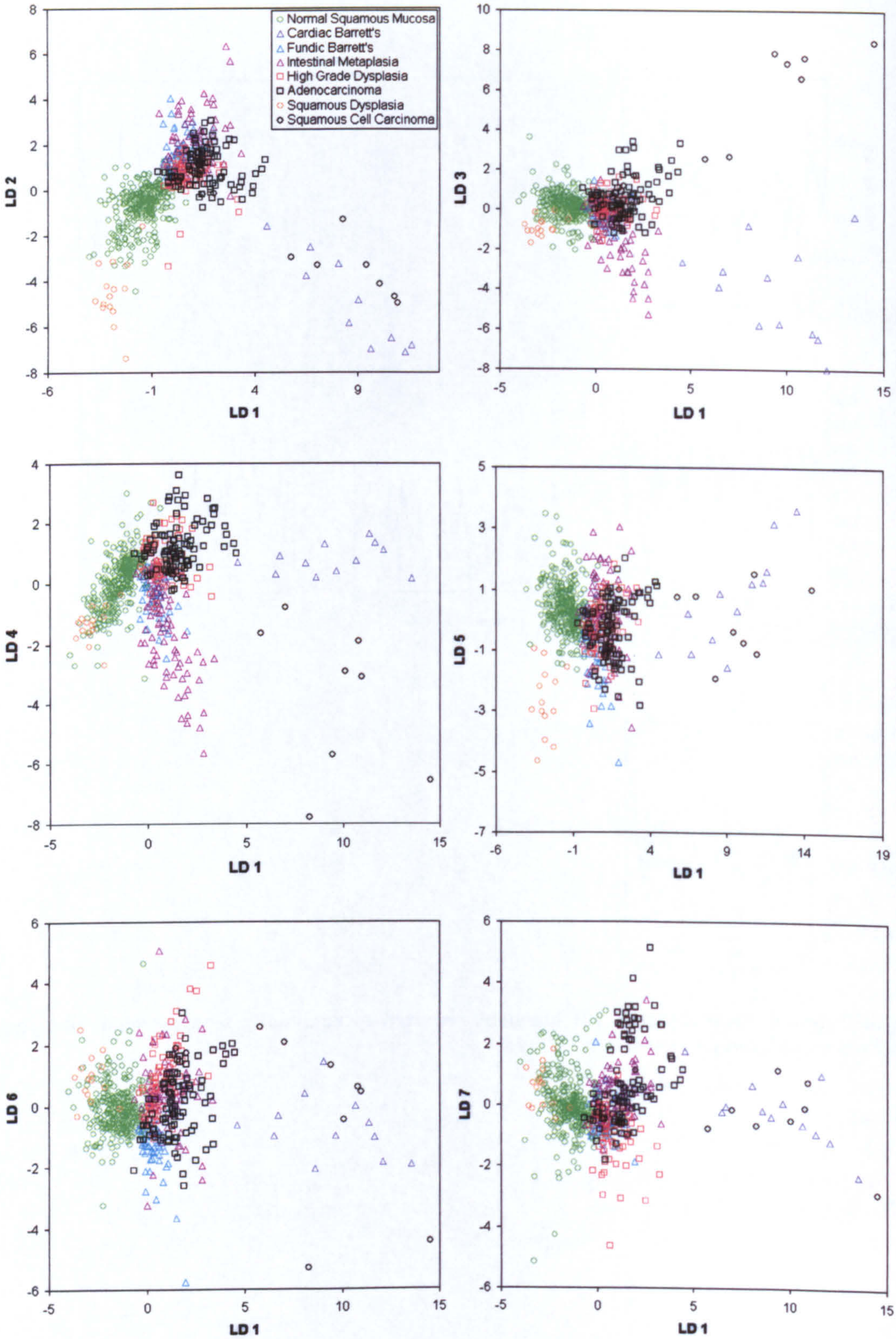

Figure 5.31: Two-dimensional scatter plots to enable visualisation of seven dimensional spectral discrimination model.

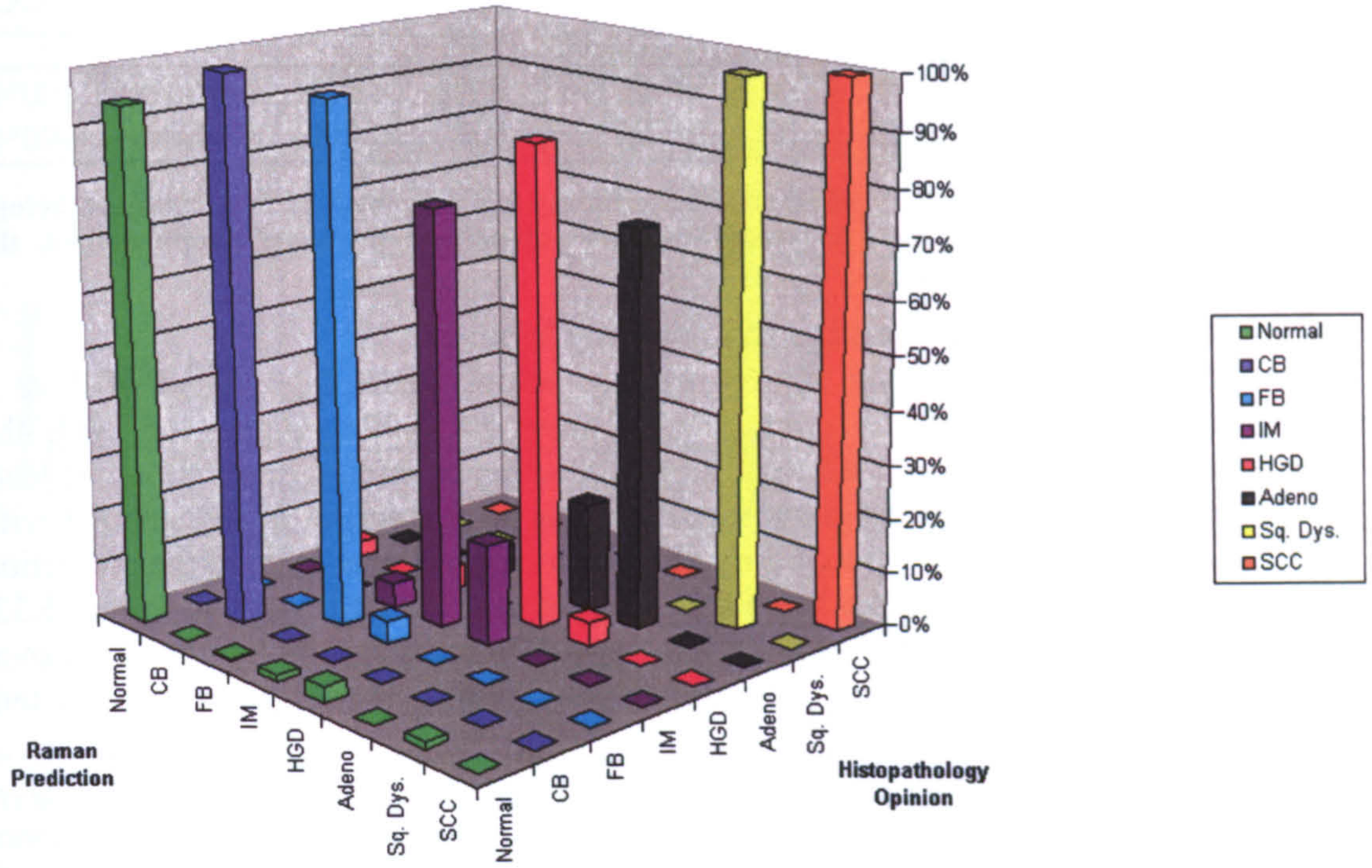

Figure 5.32: Bar chart of prediction power of the consensus eight-group discriminant model.

	Classification		Raman Predicted Group Membership								Total
			Normal	CB	FB	IM	HGD	Adeno	Sq. Dys	SCC	
Histopathology	No.	Normal	**292**	0	1	4	9	0	4	0	310
		CB	0	**12**	0	0	0	0	0	0	12
		FB	0	0	**45**	2	0	0	0	0	47
		IM	0	0	4	**66**	16	0	0	0	86
		HGD	2	0	3	0	**60**	3	0	0	68
		Adeno	0	0	5	1	19	**69**	0	0	94
		Sq. Dys.	0	0	0	0	0	0	**15**	0	15
		SCC	0	0	0	0	0	0	0	**10**	10
	%	Normal	**94**	0	0	1	3	0	1	0	100
		CB	0	**100**	0	0	0	0	0	0	100
		FB	0	0	**96**	4	0	0	0	0	100
		IM	0	0	5	**77**	19	0	0	0	100
		HGD	3	0	4	0	**88**	4	0	0	100
		Adeno	0	0	5	1	20	**73**	0	0	100
		Sq. Dys.	0	0	0	0	0	0	**100**	0	100
		SCC	0	0	0	0	0	0	0	**100**	100

Table 5.21: Cross-validation classification results obtained using the discriminant functions calculated from the first 25 principal components of the oesophagus spectra. Each case was classified by the functions derived from all cases other than that case. 88.6% of cross-validated grouped cases are correctly classified using this method.

	Normal	CB	FB	IM	HGD	Adeno	Sq. Dys.	SCC
Sensitivity	94%	100%	96%	77%	88%	73%	100%	100%
Specificity	99%	100%	98%	99%	92%	99%	99%	100%

Table 5.22: Sensitivity and specificity of Raman spectroscopy as a diagnostic test to classify pathology in the oesophagus, calculated from the cross-validation classification results obtained from the unfiltered linear discriminant model.

5.2.3.5 Nine-group Linear Discriminant Majority Model

The results of a model utilising the majority pathology result (agreement of 2 or 3 pathologists) on each specimen are outlined below to enable comparison with the consensus models. This has also allowed the introduction of an additional group of low-grade dysplasia. In the consensus groupings, there was no agreement on any samples with a low-grade dysplasia classification. Cross-validation of the model enabled the prediction ability to be assessed. Results of this are shown in Tables 5.23 and 5.24 and Figure 5.33. The bar chart in Figure 5.33 was included to enable visualisation of the cross-over between group prediction within in the model. Colour coding of each group is consistent throughout the figures.

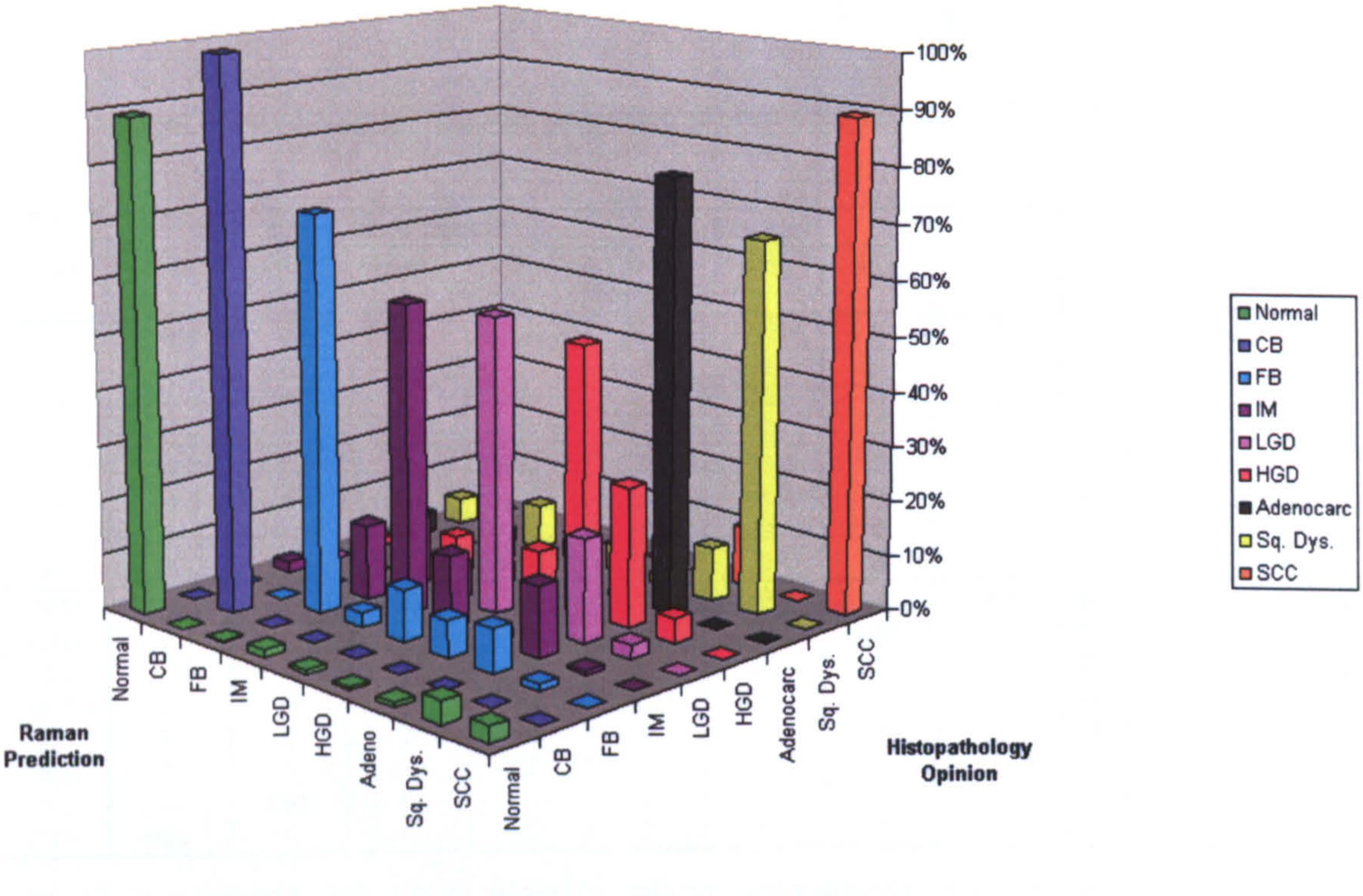

Figure 5.33: Bar chart of prediction power of the majority nine-group discriminant model.

	Classification		Raman Predicted Group Membership									Total
			Normal	CB	FB	IM	LGD	HGD	Adeno	Sq. Dys	SCC	
Histopathology	No.	Normal	303	0	1	5	2	2	3	14	10	340
		CB	0	24	0	0	0	0	0	0	0	24
		FB	0	0	54	2	7	5	6	1	0	75
		IM	3	0	21	87	20	3	20	1	0	155
		LGD	0	0	15	8	67	8	23	3	0	124
		HGD	2	0	9	5	12	66	34	6	0	134
		Adeno	4	0	6	0	12	1	85	0	0	108
		Sq. Dys.	3	0	5	2	3	1	6	42	0	62
		SCC	0	0	0	0	0	0	5	0	41	46
	%	Normal	89	0	0	1	1	1	1	4	3	100
		CB	0	100	0	0	0	0	0	0	0	100
		FB	0	0	72	3	9	7	8	1	0	100
		IM	2	0	14	56	13	2	13	1	0	100
		LGD	0	0	12	6	54	6	19	2	0	100
		HGD	1	0	7	4	9	49	25	4	0	100
		Adeno	4	0	6	0	11	1	79	0	0	100
		Sq. Dys.	5	0	8	3	5	2	10	68	0	100
		SCC	0	0	0	0	0	0	11	0	89	100

Table 5.23: Cross-validation classification results obtained using the discriminant functions calculated from the first 25 principal components of the oesophagus spectra. Each case was classified by the functions derived from all cases other than that case. 72.0% of cross-validated grouped cases are correctly classified using this method.

	Normal	CB	FB	IM	LGD	HGD	Adeno	Sq. Dys.	SCC
Sensitivity	89%	100%	72%	56%	54%	49%	79%	68%	89%
Specificity	98%	100%	94%	98%	94%	98%	90%	98%	99%

Table 5.24: Sensitivity and specificity of Raman spectroscopy as a diagnostic test to classify pathology in the oesophagus, calculated from the cross-validation classification results obtained from the unfiltered linear discriminant model.

5.2.3.6 Linear Discriminant Model Optimisation

Model optimisation was achieved by applying pre-processing functions such as 1st and 2nd derivative Savitsky-Golay filters, prior to calculation of PCs and linear discriminant functions. First and second derivative pre-processing filters removed influences from the overall signal level (baseline) and linear background slope respectively. A range of filters were applied and results were evaluated by comparing the discriminantion achieved with each model.

Optimised consensus model

A 95-point Savitsky-Golay third-order polynomial, second-derivative function was shown to improve the power of the eight-group consensus model to discriminate the clinically significant group of adenocarcinoma. The first 25 PCs (describing almost 100% of the total variance from the mean) were used to calculate two linear discriminant (LD) functions that maximised the variance in the data between the pathological groups and minimised the variance between members of the same pathological group.

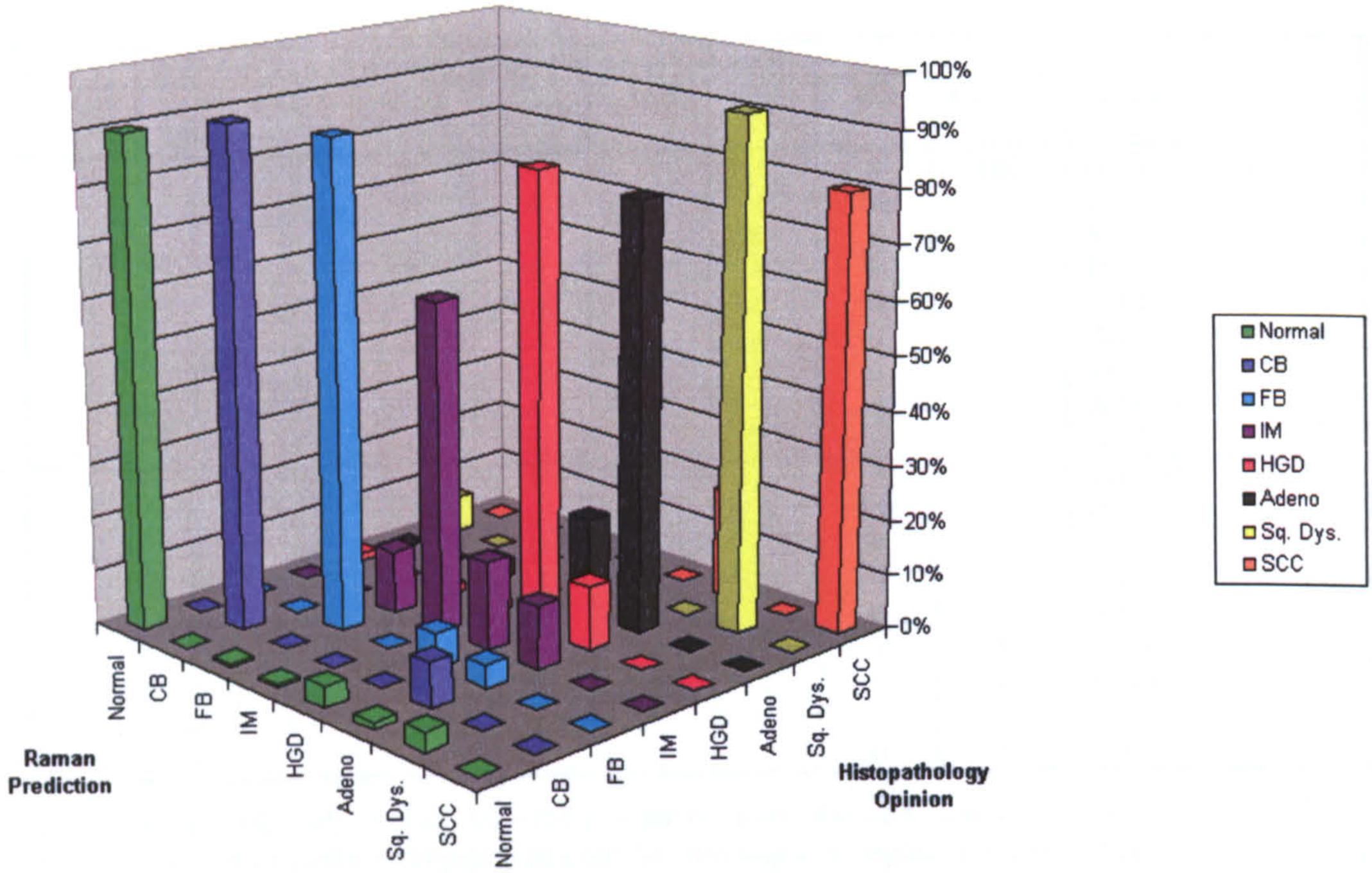

Figure 5.34: Bar chart of prediction power of the optimised consensus eight-group discriminant model.

	Normal	CB	FB	IM	HGD	Adeno	Sq. Dys.	SCC
Sensitivity	90%	92%	89%	60%	84%	79%	93%	80%
Specificity	99%	100%	97%	99%	92%	95%	98%	100%

Table 5.25: Sensitivity and specificity of Raman spectroscopy as a diagnostic test to classify pathology in the oesophagus, calculated from the cross-validation classification results obtained from the optimised pre-filtered linear discriminant consensus model.

Optimised Majority model

A Savitsky-Golay 2nd order polynomial, 11-point smooth provided optimum classification results for the nine-group majority prediction model. The prediction accuracy of the model was tested using a cross-validation procedure. Table 5.26 and Figure 5.35 display the breakdown of the resulting prediction accuracy of the optimised model.

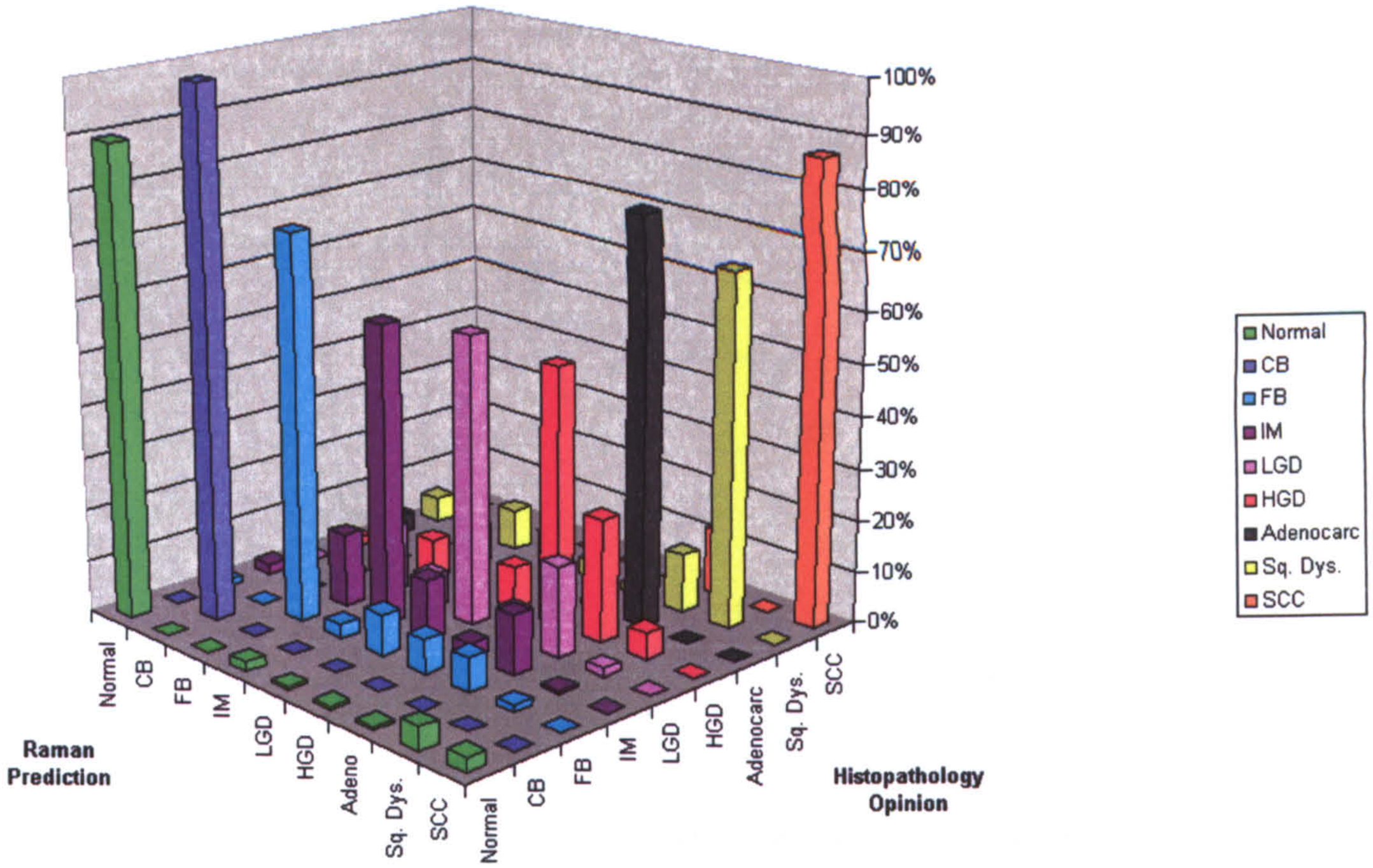

Figure 5.35: Bar chart of prediction power of the optimised majority nine-group discriminant model.

	Normal	CB	FB	IM	LGD	HGD	Adeno	Sq. Dys.	SCC
Sensitivity	89%	100%	73%	57%	56%	50%	77%	68%	87%
Specificity	98%	100%	94%	97%	95%	98%	90%	97%	99%

Table 5.26: Sensitivity and specificity of Raman spectroscopy as a diagnostic test to classify pathology in the oesophagus, calculated from the cross-validation classification results obtained from the optimised pre-filtered linear discriminant majority model.

5.2.3.7 Testing Ability of Model to Discriminate Spectra With Reduced SNR

An evaluation of the quality of the spectra required for prediction using the consensus eight-group model was made by projection of a set of test spectra onto the spectral discriminant model. The test spectra were acquired in 30 seconds, as were the model spectra, and they were downgraded by adding/subtracting increasing levels of random noise. The intention was to simulate the reduction in SNR that would accompany spectral acquisition in shorter timescales. These would be required for in vivo medical diagnosis. Due to the small sample numbers available only 10 adenocarcinoma spectra were measured for testing the model. With no imposed signal degradation 100 percent of the spectra were correctly predicted by the consensus 8-group model. Figures 5.36 and 5.37 show one test spectrum with 1% and 25% of random noise added, respectively. The spectrum with 25% noise is similar to those obtained in 1-2 seconds with the optimised spectrometer system. The results obtained from testing the consensus eight-group model were plotted (Figure 5.38) for spectra with noise added over the range from 0-50%.

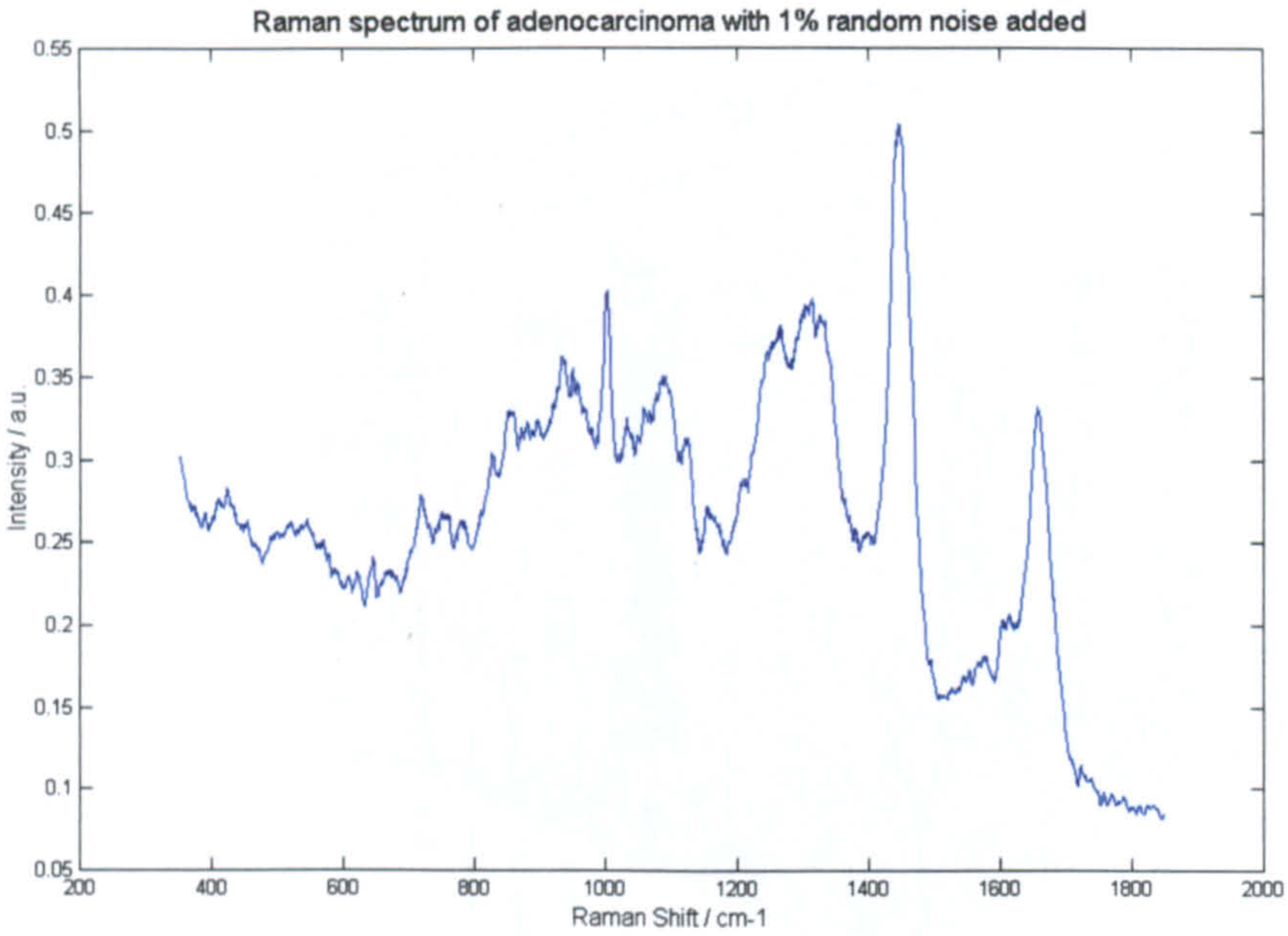

Figure 5.36: Plot of Raman spectrum from adenocarcinoma of the oesophagus measured in 30s, with 1% random noise added.

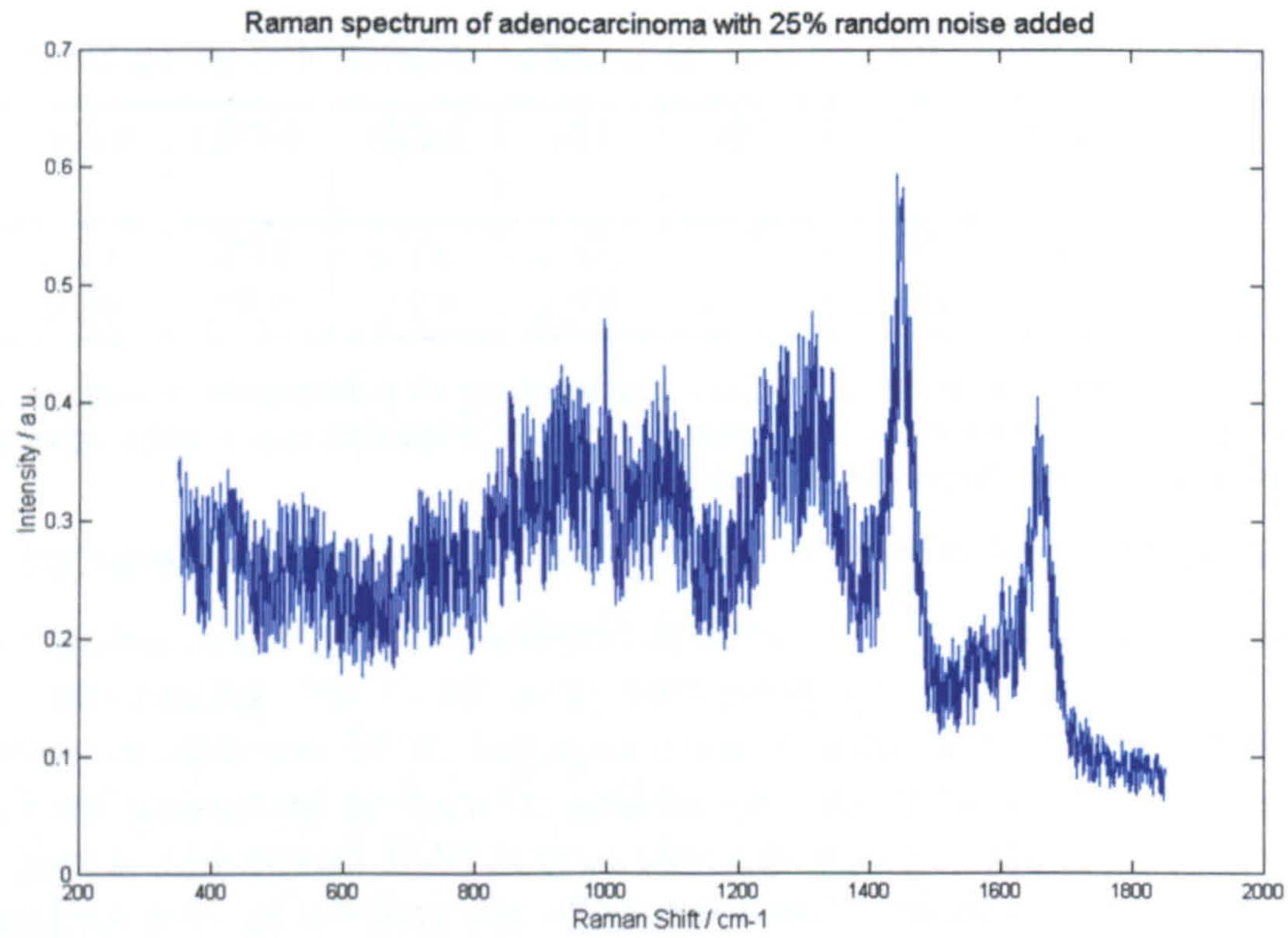

Figure 5.36: Plot of Raman spectrum from adenocarcinoma of the oesophagus measured in 30s, with 25% random noise added.

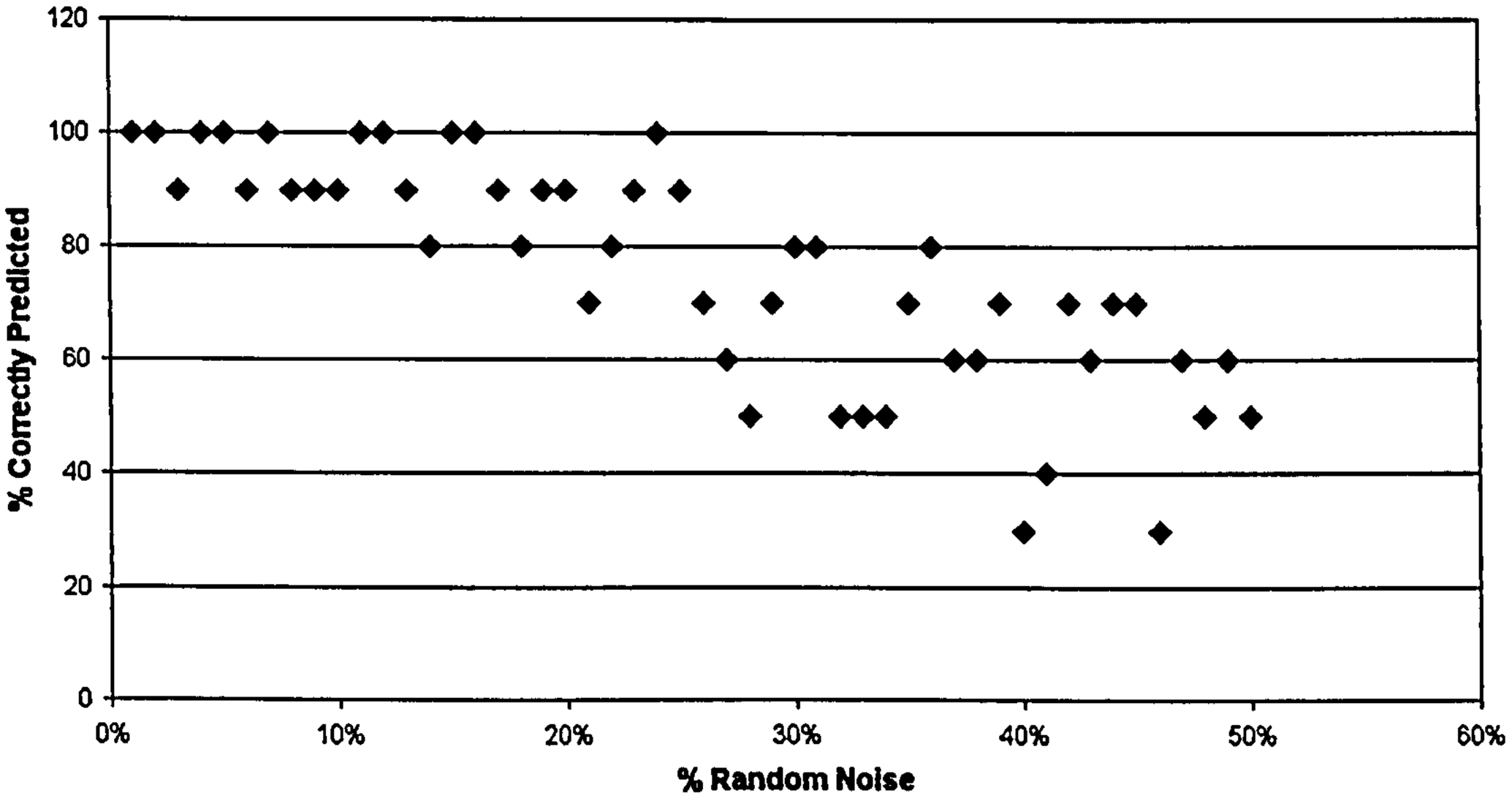

Figure 5.37: Plot of percentage of samples correctly predicted versus the percentage of random noise added to the test spectra.

5.3 Formalin fixed oesophagus models

Formalin fixation is the most common method used in collection and preparation of biopsy tissue for histopathological analysis. An evaluation of Raman spectral discrimination of formalin fixed oesophageal tissue has been carried out to assess its function as a pathologist's tool in the laboratory. Sample collection procedures have been outlined in section 4.1.2.2, and the Raman spectral acquisition parameters described in section 4.3.3. It must be noted that at this time the samples used in this study were histopathologically graded by only one consultant gastro-intestinal pathologist. Thus results will be expected to be less accurate than those that could be achieved with a consensus of pathological opinion, utilised in the previous section.

A plot of the mean of 418 spectra from normal, metaplastic, dysplastic and cancerous formalin fixed oesophagus specimens is shown in Figure 5.38. The plot shows the intensity of the collected (Stokes) signal versus wavenumber shift relative to the 830nm excitation source. The greater the wavenumber the greater the shift from the excitation wavelength. The most significant peaks in the spectrum have been labelled with the corresponding wavenumber shift. Tentative peak assignments have been made from extensive study of the literature. These have been compiled in Appendix 4.

The spectra of normal oesophageal specimens have shown little inter- and intra-sample variability. Figure 5.39 shows 100 NIR-Raman spectra obtained from ten normal oesophageal tissue specimens, with the mean spectrum displayed in green. Visual inspection of the spectra show the peak shapes and positions to be repeatable, although overall spectral intensities can vary by 10-15 % about the mean spectrum for each individual sample. Wavenumber repeatability was evaluated by measuring the position of

the PHE peak at around 1000 cm^{-1}. Results have been plotted in Figure 5.40. Mean PHE peak position was found to be 1002.2 ± 3.61 cm^{-1}.

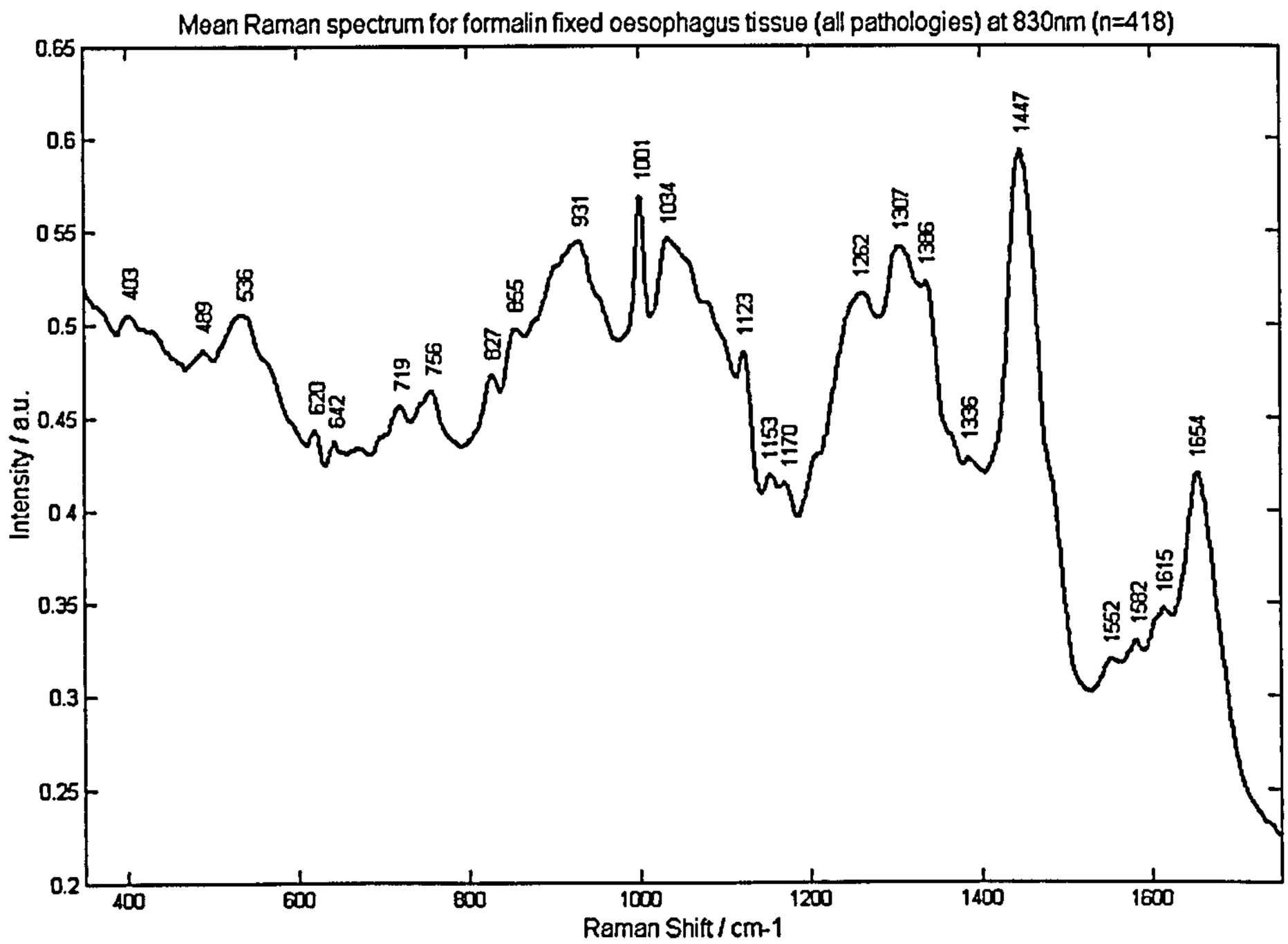

Figure 5.38: Mean Raman spectrum acquired from homogeneous formalin fixed oesophageal tissue samples, exhibiting eight different clinically significant pathologies, with an 830nm excitation source. T=30s.

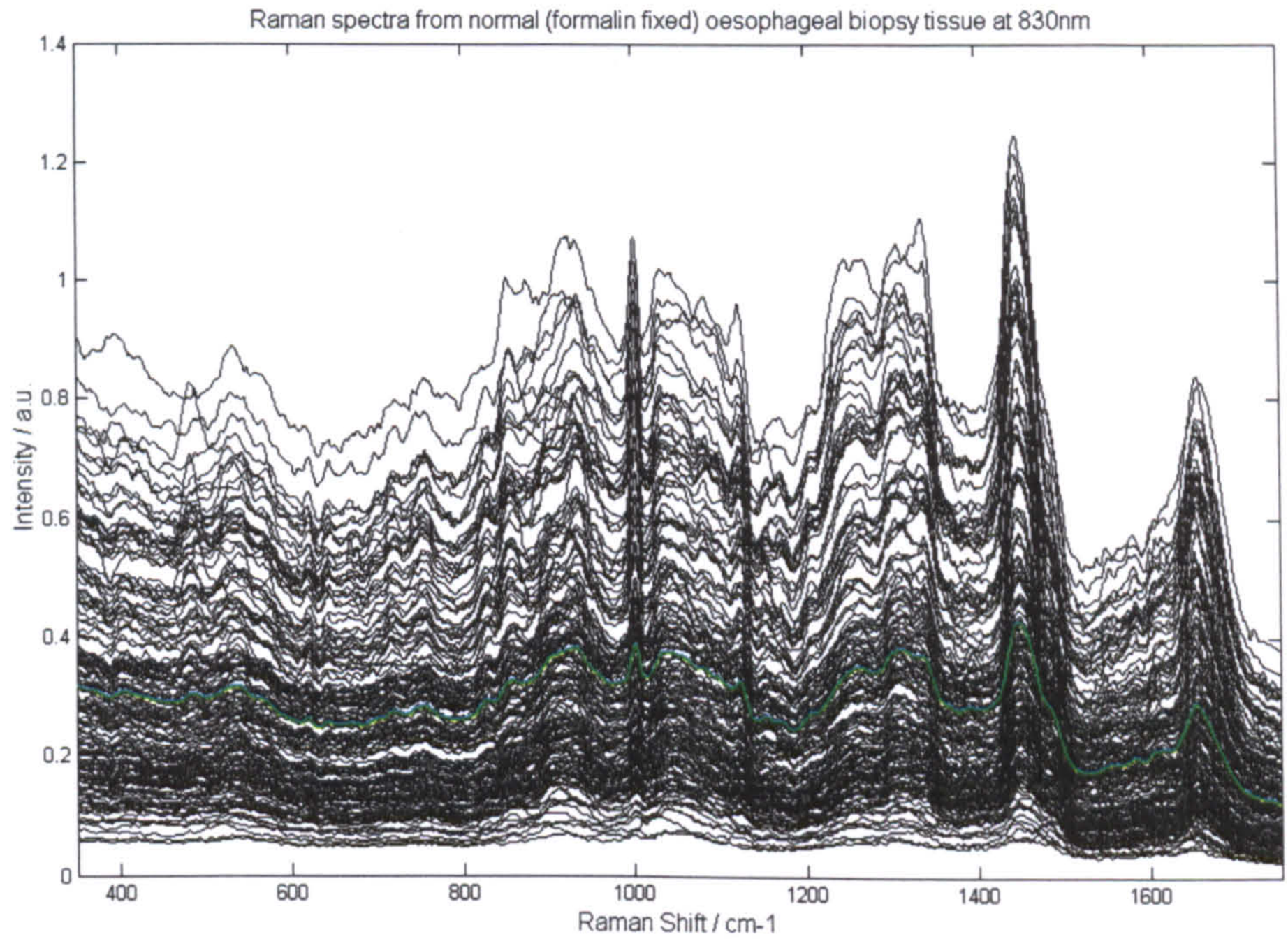

Figure 5.39: 100 Raman spectra from 10 formalin fixed normal oesophagus specimens, mean spectrum in green.

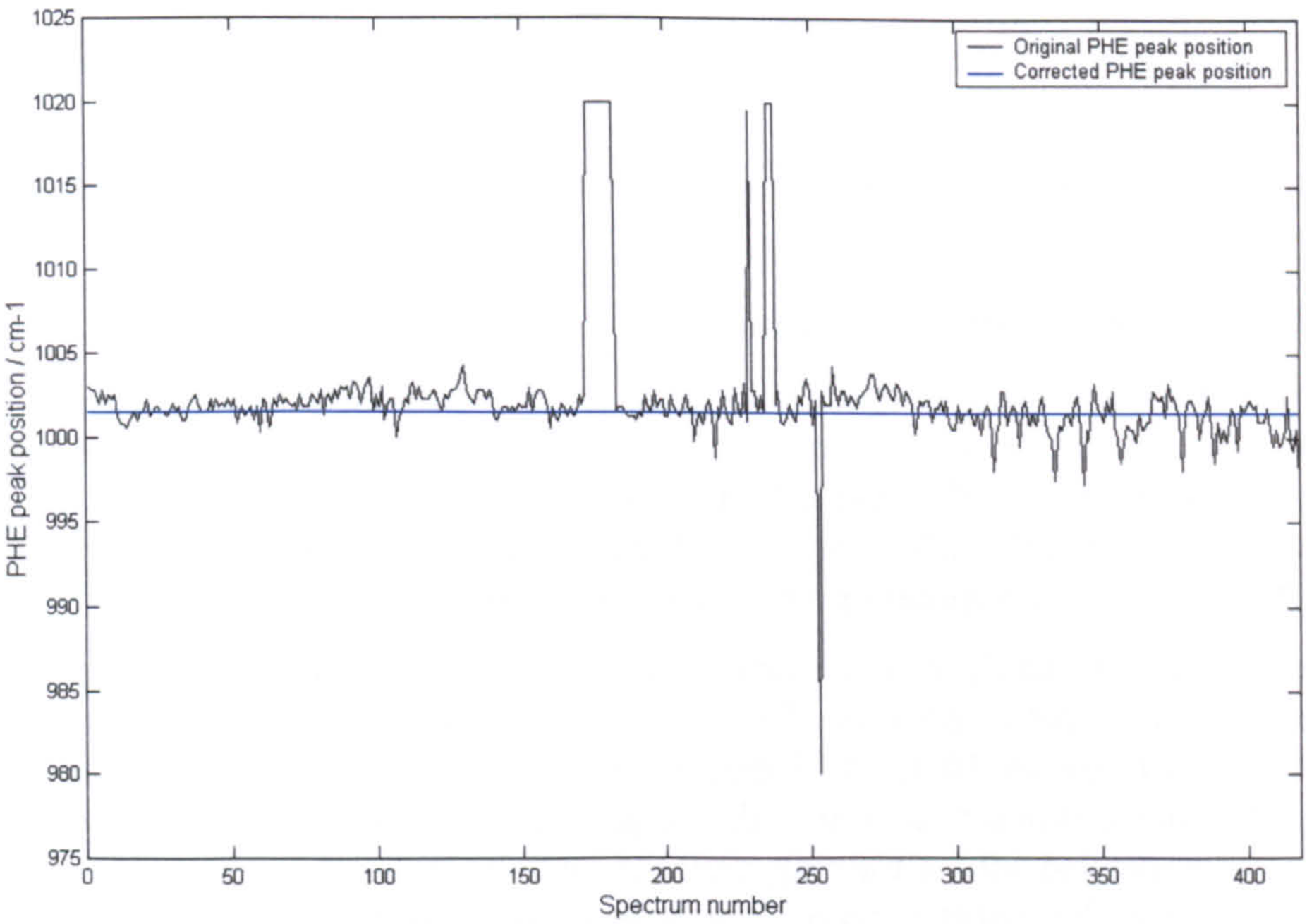

Figure 5.40: Plot of the wavenumber position of a peak assigned to phenylalanine versus acquired spectrum.

To evaluate the effect of formalin on tissue spectra a Raman spectrum of the formalin fixative, used to fix and store a sample of oesophagus, was acquired and shown in Figure 5.41. By studying Figures 5.41 and 5.38, a spectrum of normal oesophagus soaked in formalin, the contributions of the formalin can be assessed. Moreover, the protein cross-links caused by the fixation process will likely cause shifts in the Raman peak positions compared with those in fresh samples.

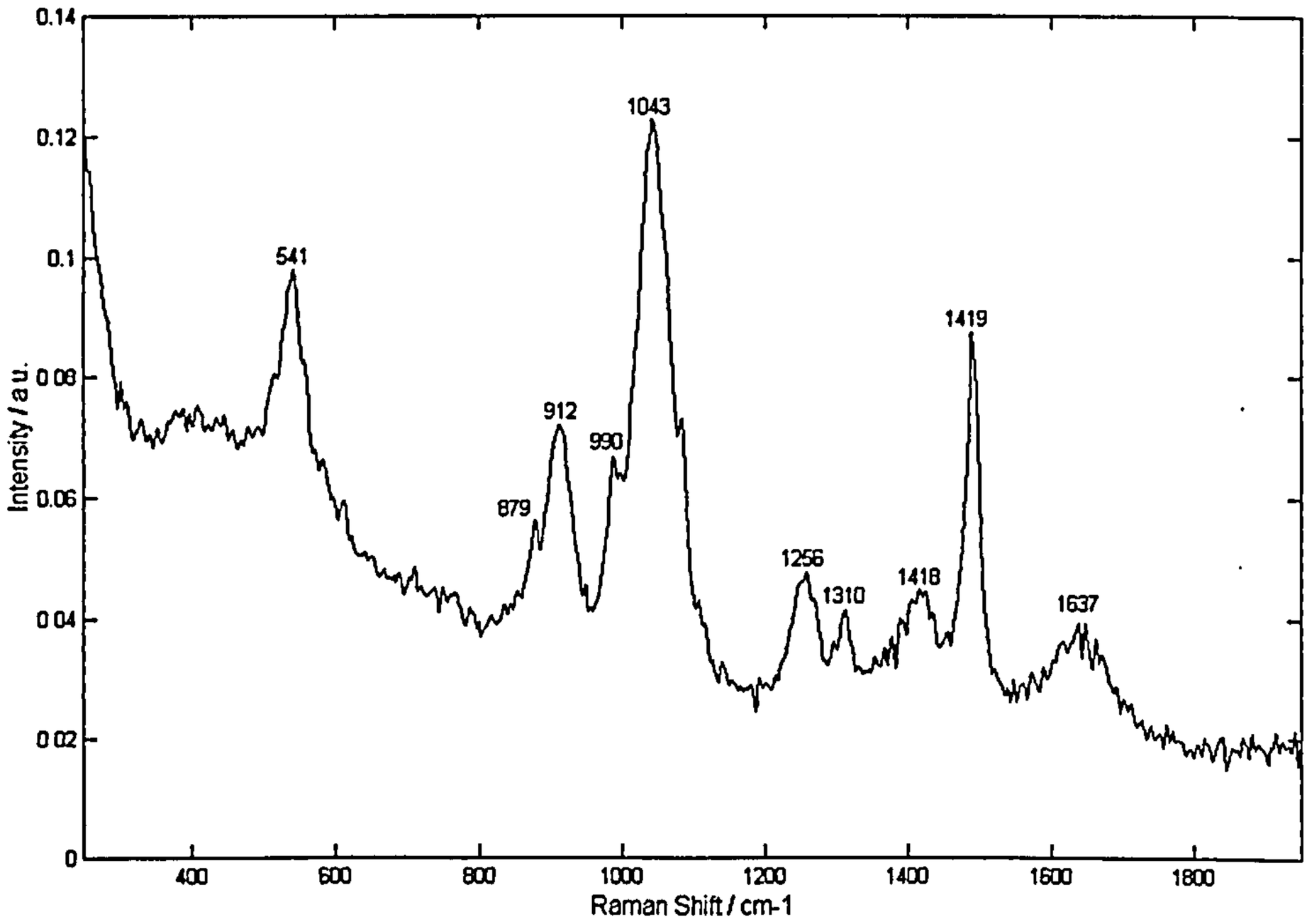

Figure 5.41: Plot of Raman spectrum of formalin fixative used to fix and store oesophagus samples.

5.3.2 Multivariate Spectral Analysis

The spectra acquired from samples belonging to each of eight pathological groups were collected together and mean spectra were calculated. A plot of the mean spectra from each group normalised to the intensity at 1445 cm^{-1} is shown in Figure 5.42. From this plot it can be seen that the differences observed in the spectra from specimens at different stages of the cancer development process are very subtle.

Principal component analysis was performed on the formalin fixed oesophagus spectra using singular value decomposition (SVD) in PLS-Toolbox (Eigenvector®) running in the MATLAB® environment. Of the 418 spectra acquired, 7 were discarded due to extremely poor signal to noise ratios or an unusually large fluorescence background. The remaining spectra were compiled into a training data set and some pre-processing was performed upon it. Initially the spectra were interpolated to a regular number of points per wavenumber (the Renishaw system 1000 has a variable spacing due to the polynomial calibration fit of wavenumber per pixel across the CCD chip). The position of the phenylalanine (PHE) peak at around 1000 cm^{-1} was measured for each spectrum to

evaluate system drift from one measurement to the next. This value was used to correct spectra for spectrometer drift. In the first instance unfiltered spectra were used to build a discrimination model. Then pre-processing based upon Savitsky-Golay filtering was applied to optimise the models for maximum group separation.

Following pre-processing the spectra were mean-centred; this involved calculating the average spectrum of all the spectra in the data set and subtracting this result from every spectrum. Principal component analysis was used to describe the resulting spectra as a sum of a small orthogonal set (25) of linear combinations of the original variables. Figures 5.43 a, b and c show plots of the PCs. These principal components described over 99.9% of the variance from the mean spectrum across the data set. PC 4 can be seen to exhibit mainly formalin peaks and PC 7 mainly glycogen peaks. Table 5.27 lists each PC with the corresponding percentage variance described by it. Multiple ANOVA was used to identify the most diagnostically significant principal components, i.e. those that show a significant difference in value for normal, Barrett's, dysplastic and cancerous oesophagus. In addition a Wilks'-Lambda test has been performed on the data (Table 5.27).

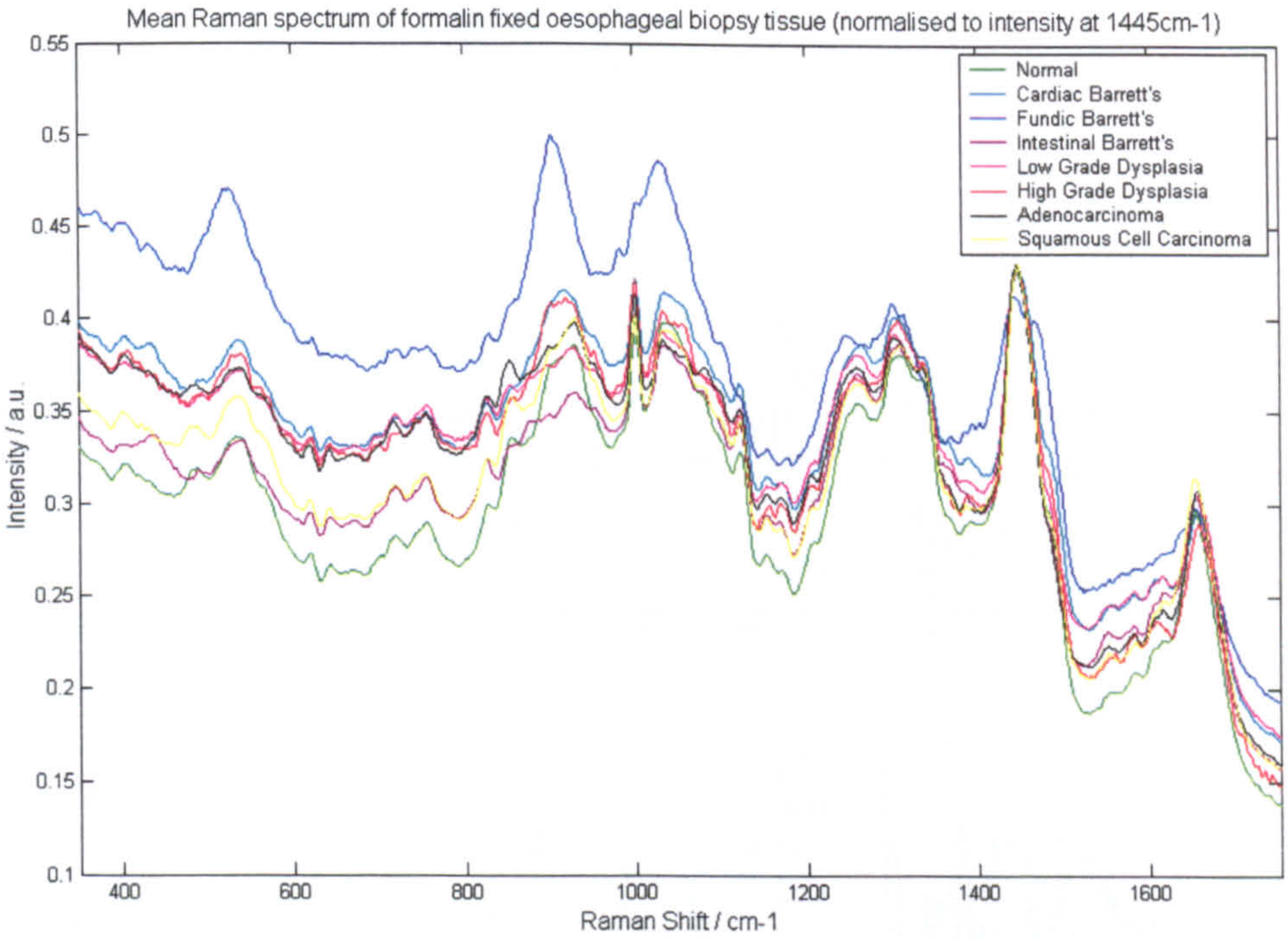

Figure 5.42: Mean Raman spectra normalized to the intensity at 1445 cm^{-1} from each formalin fixed oesophageal histopathological group.

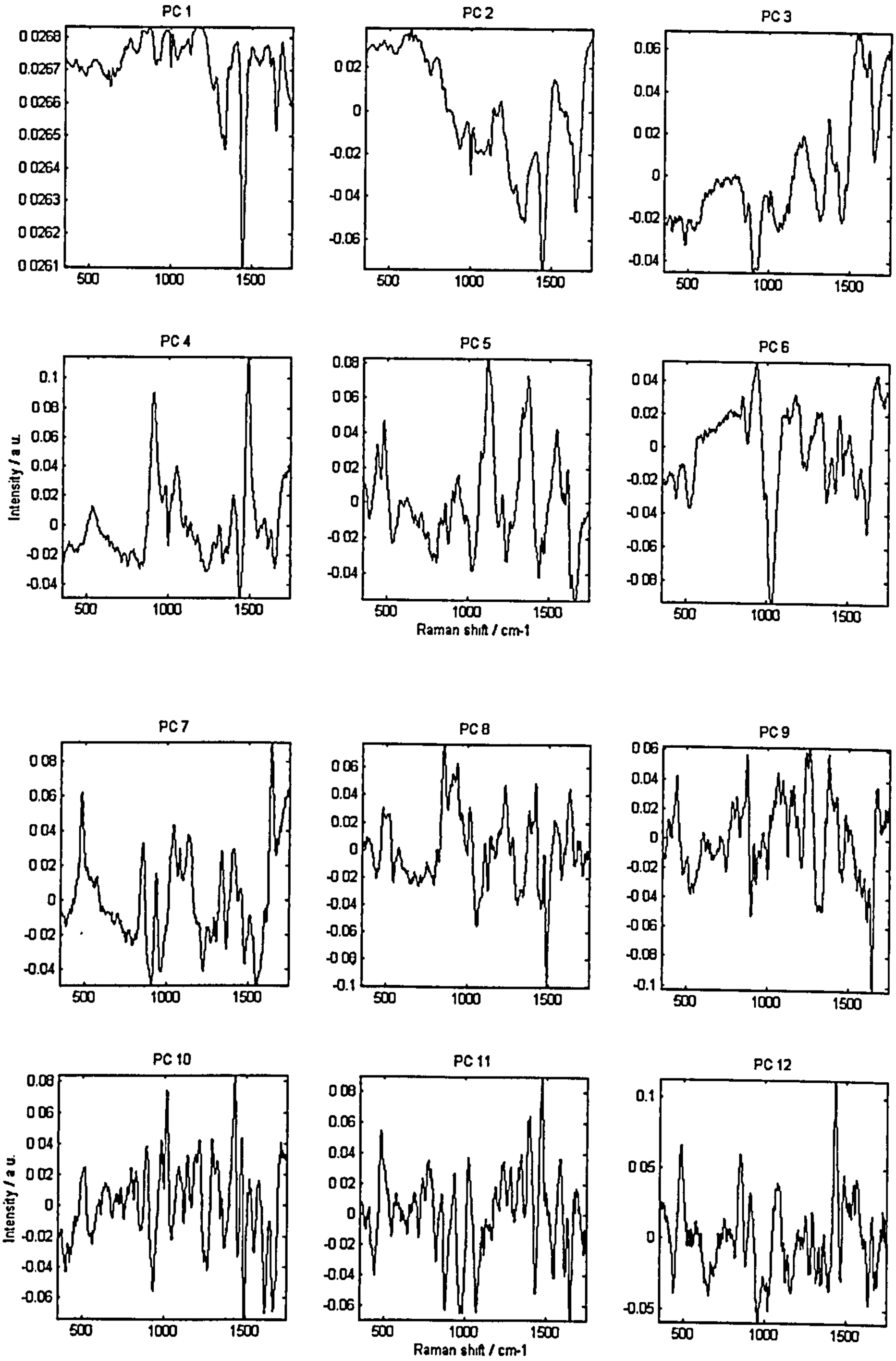

Figure 5.43(a): Principal components 1 to 12 representing the first 99.98% of the variance of the data set from the mean spectrum.

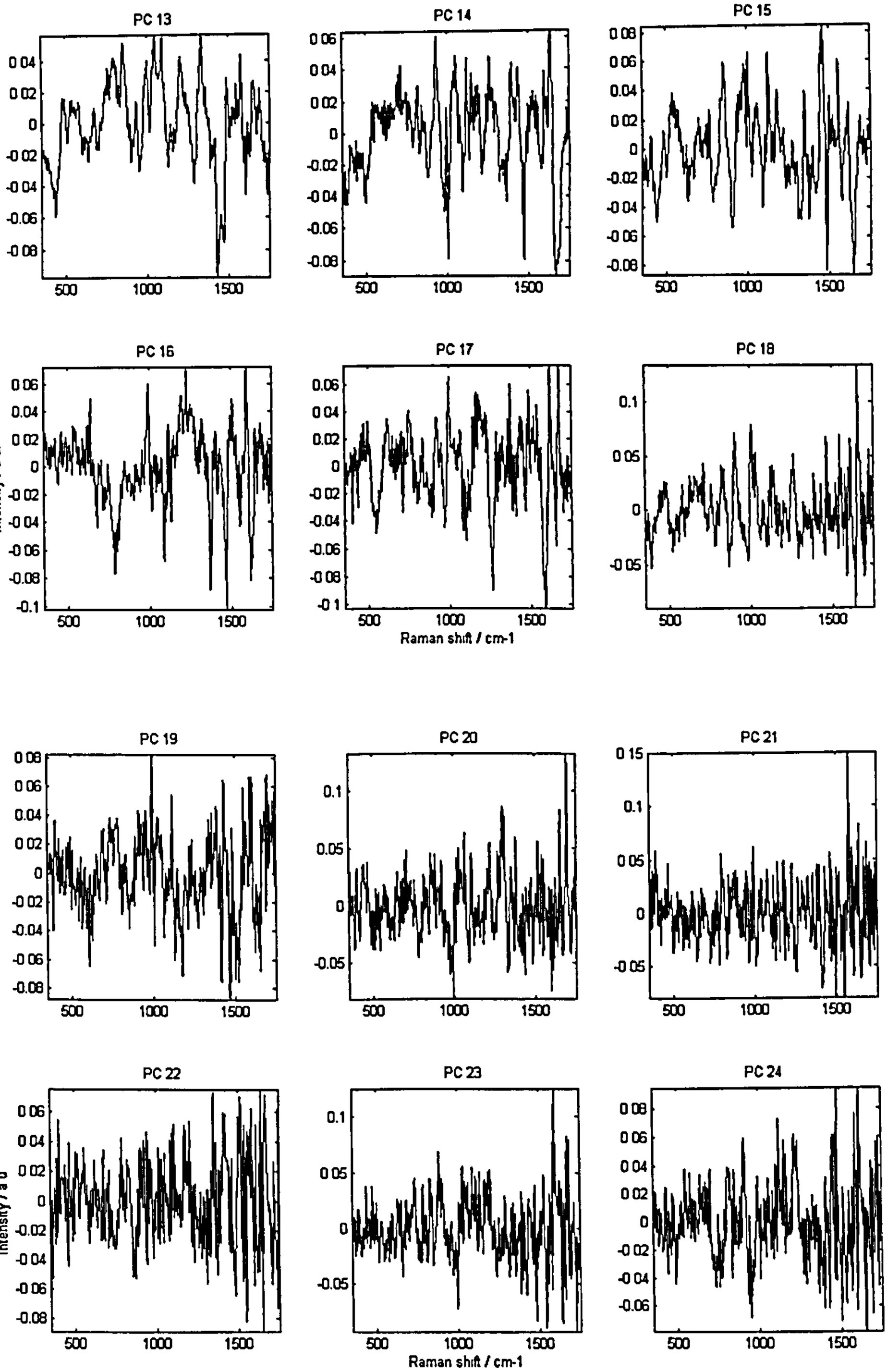

Figure 5.43(b): Principal components 13 to 24 representing 0.02% of the variance of the data set from the mean spectrum.

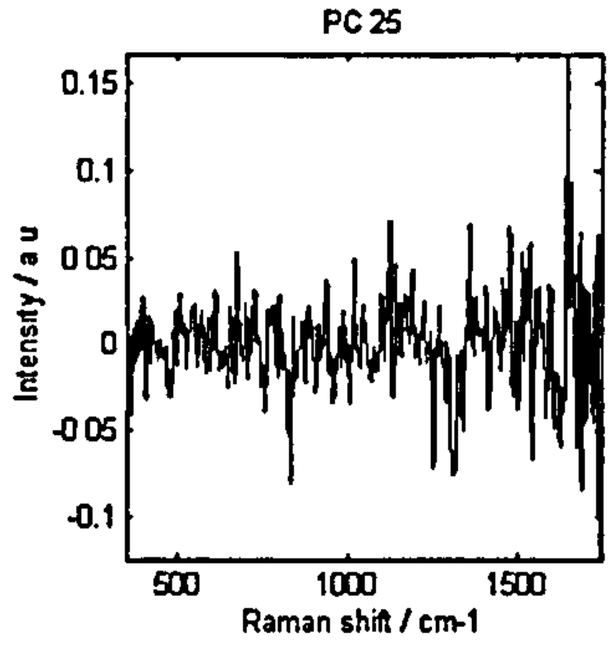

Figure 5.43(c): Principal component 25 representing 0.004% of the variance of the data set from the mean spectrum.

Principal Component	% Variance	Cumulative % Variance	Wilks' Lambda	F-Value	Significance = (100-p)
1	**99.08**	**99.08**	**.820**	**12.815**	**.000**
2	**0.68**	**99.76**	**.792**	**15.383**	**.000**
3	**0.11**	**99.88**	**.848**	**10.498**	**.000**
4	**0.03**	**99.91**	**.896**	**6.814**	**.000**
5	**0.02**	**99.93**	**.828**	**12.205**	**.000**
6	**0.02**	**99.95**	**.916**	**5.394**	**.000**
7	**0.02**	**99.97**	**.797**	**14.873**	**.000**
8	**0.01**	**99.97**	**.825**	**12.435**	**.000**
9	**0.00**	**99.98**	**.933**	**4.194**	**.000**
10	**0.00**	**99.98**	**.763**	**18.242**	**.000**
11	**0.00**	**99.99**	**.829**	**12.040**	**.000**
12	**0.00**	**99.99**	**.932**	**4.263**	**.000**
13	**0.00**	**99.99**	**.866**	**9.067**	**.000**
14	0.00	99.99	.962	2.326	.025
15	**0.00**	**99.99**	**.867**	**8.990**	**.000**
16	0.00	99.99	.954	2.847	.007
17	**0.00**	**99.99**	**.912**	**5.621**	**.000**
18	**0.00**	**99.99**	**.917**	**5.313**	**.000**
19	0.00	99.99	.982	1.076	.378
20	0.00	99.99	.962	2.302	.026

Table 5.27: Displays the first 20 PCs with the corresponding variance of the data set described, with statistical significance test results for evaluation of group discrimination power. PCs with greater than 99.9% significance of discrimination between pathological groups are printed in bold.

The specimens were separated into eight clinically significant pathology groups: Normal oesophagus, cardiac Barrett's (CB), fundic Barrett's (CB), intestinal metaplasia (IM), low-grade dysplasia (LGD), high-grade dysplasia (HGD), adenocarcinoma, and squamous dysplasia. The same process was followed as that in section 5.2.3.2, to

construct and test a spectral discriminant model. However this time seven linear discriminant functions were required to optimally separate the eight groups. These are shown in Figure 5.44. The weights of the functions were plotted against one another in Figure 5.45 for each spectrum in the model. Pathological group separation can be seen from these plots, although full separation would only be visualised if one could plot and study seven-dimensional space. Cross-validation of the model enabled the prediction efficiency to be tested. Results are shown in Table 5.28 and the bar chart in Figure 5.46 was included to enable visualisation of the cross-over between group prediction within in the model. Colour coding of each group is consistent throughout the figures.

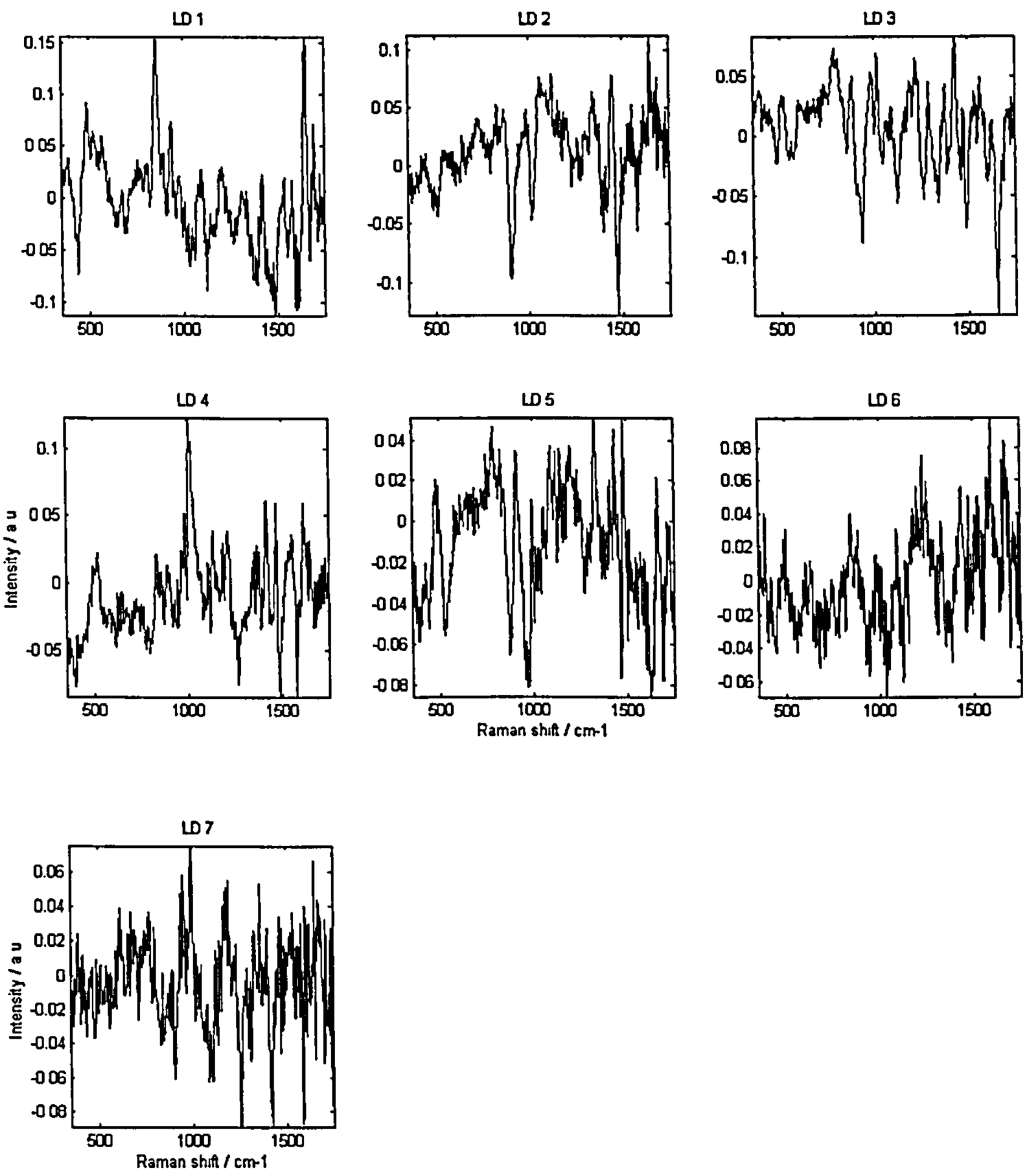

Figure 5.44: The seven linear discrimiant functions required to maximally separate the eight clinically significant oesophageal pathology groups using the formalin fixed sample spectral data.

	Normal	CB	FB	IM	LGD	HGD	Adeno	Sq Dys
Sensitivity	82%	81%	86%	75%	80%	100%	93%	80%
Specificity	92%	100%	97%	99%	94%	98%	99%	98%

Table 5.28: Sensitivity and specificity of Raman spectroscopy as a diagnostic test to classify pathology in the oesophagus, calculated from the cross-validation classification results obtained from the linear discriminant model. (Unfiltered model)

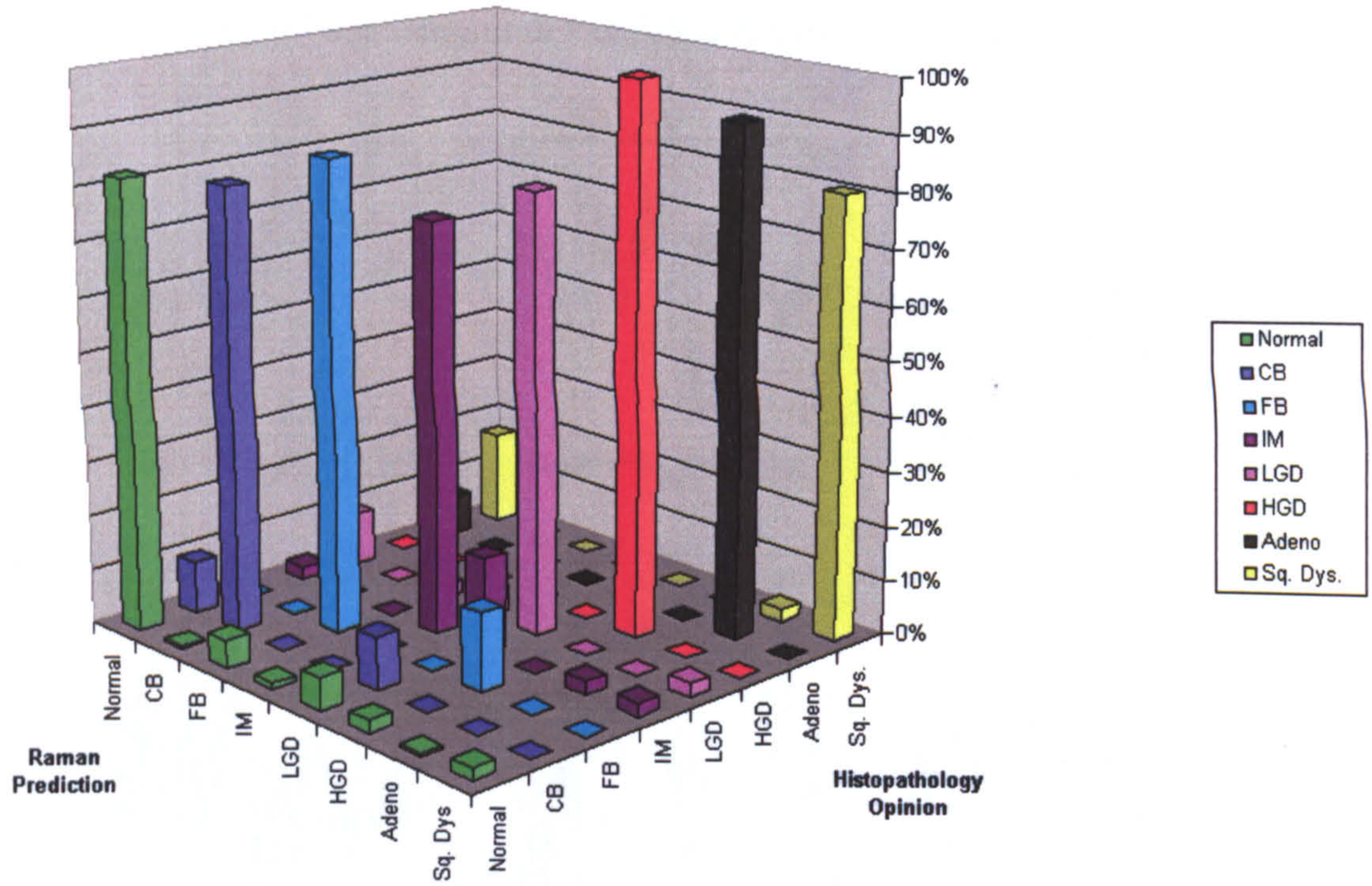

Figure 5.45: Bar chart of prediction efficiency of un-optimised discriminant model tested with cross-validation.

Model Optimisation

Model optimisation was achieved by applying pre-processing functions such as 1st and 2nd derivative Savitsky-Golay filters, prior to calculation of PCs and linear discriminant functions. First and second derivative pre-processing filters removed influences from the overall signal level (baseline). A zeroth derivative, third-order polynomial, 11-point smooth provided optimum separation of the pathological groups. A seven-dimensional linear discriminant model was tested using cross-validation and the results are outlined below. Table 5.29 displays the sensitivities and specificities achieved using the optimised model and Figure 5.46 displays a bar chart of the resulting model predictions.

	Normal	CB	FB	IM	LGD	HGD	Adeno	Sq Dys
Sensitivity	76%	85%	100%	80%	88%	100%	100%	88%
Specificity	99%	98%	98%	98%	94%	100%	99%	96%

Table 5.29: Sensitivity and specificity of Raman spectroscopy as a diagnostic test to classify pathology in the oesophagus, calculated from the cross-validation classification results obtained from the linear discriminant model. (Model optimised with pre-filtered spectra.)

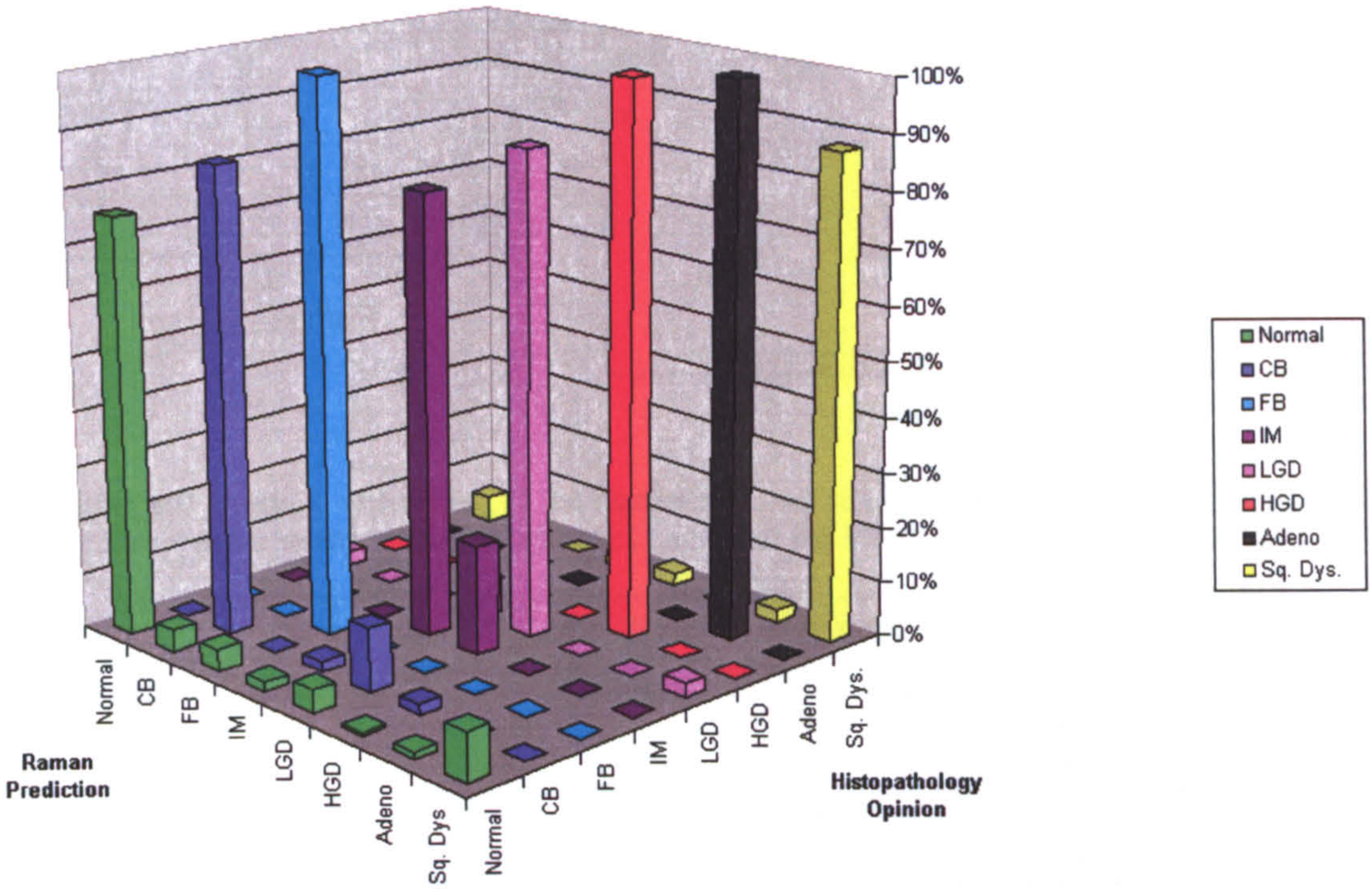

Figure 5.46: Bar chart of prediction efficiency of optimised discriminant model tested with cross-validation.

Effect of Time Stored in Formalin on Raman Classification of Pathology

The principal components calculated to separate the pathological groups for formalin fixed oesophagus tissue were found to also include information on the time of sample storage in formalin. Approximately one third of the samples were stored for a number of weeks and the other two-thirds were stored for between 12 and 18 months. A single linear discriminant function was constructed from a linear combination of the PCs used in the un-optimised model. The linear discriminant function and the weights of the function for each spectrum are plotted in Figure 5.47. Table 5.30 demonstrates the separation of the spectra into the two groups of specimens dependent upon the time in formalin.

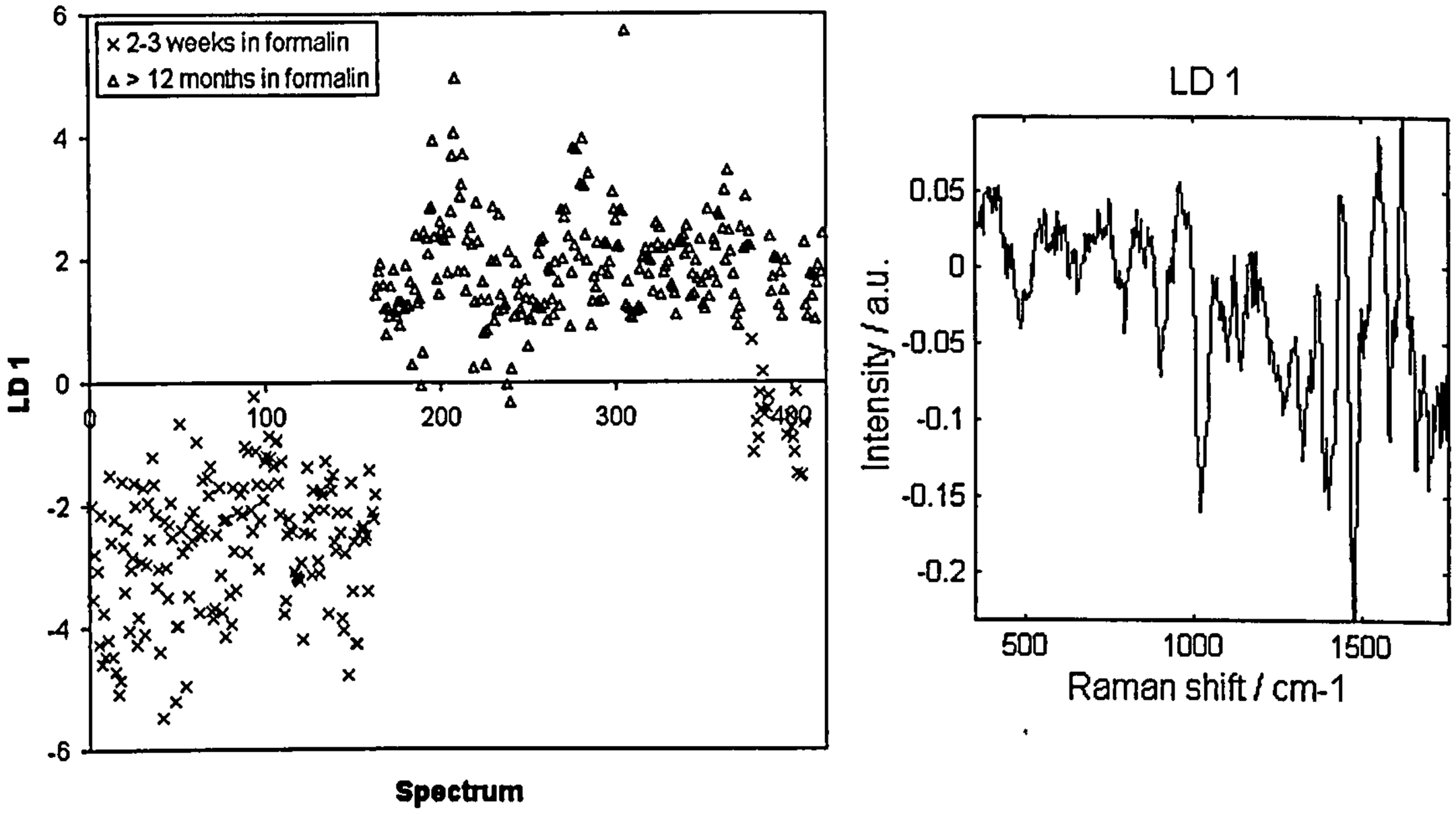

Figure 5.47: Plot of linear discriminant function calculated to maximally separate the samples by length of time in formalin. One set were left for over 12 months, the other set for a few weeks.

Time in formalin		Predicted Group Membership 2-3 Weeks	>12 months	Total
No.	2-3 Weeks	180	2	182
	>12 Months	3	233	236
%	2-3 Weeks	99	1	100.0
	>12 Months	1	99	100.0

Table 5.30: Displays resulting length of time in formalin prediction model results.

5.4 Appraisal of Factors Likely to Influence Transfer of In Vitro Raman Classification Models to In Vivo Spectral Discrimination

The effect of a number of factors likely to influence the transfer of in vitro Raman classification models to use for in vivo spectral discrimination have been studied. Firstly the temperature dependence of the tissue Raman spectra over the range from room temperature to body temperatures has been assessed. In addition, the polarisation dependence of the tissue Raman spectra has been evaluated. The most significant differences likely to be observed in vivo are from contamination of the tissue spectra by so called confounding factors, such as: blood, bile and gastric juices, spittle, mucus and endoscope lubricant.

5.4.1 Temperature Dependence of Tissue Raman Spectra

The temperature dependence of Raman spectra of oesophageal mucosa was measured over the range 10 to 50°C, following the procedure outlined in section 4.3.4. The most significant region for medical spectroscopy is between room and body temperatures. Figure 5.48 shows a plot of Raman spectra at 20, 30 and 40°C. The most significant changes over the investigated range appear to be increasing background luminescence with increased temperature.

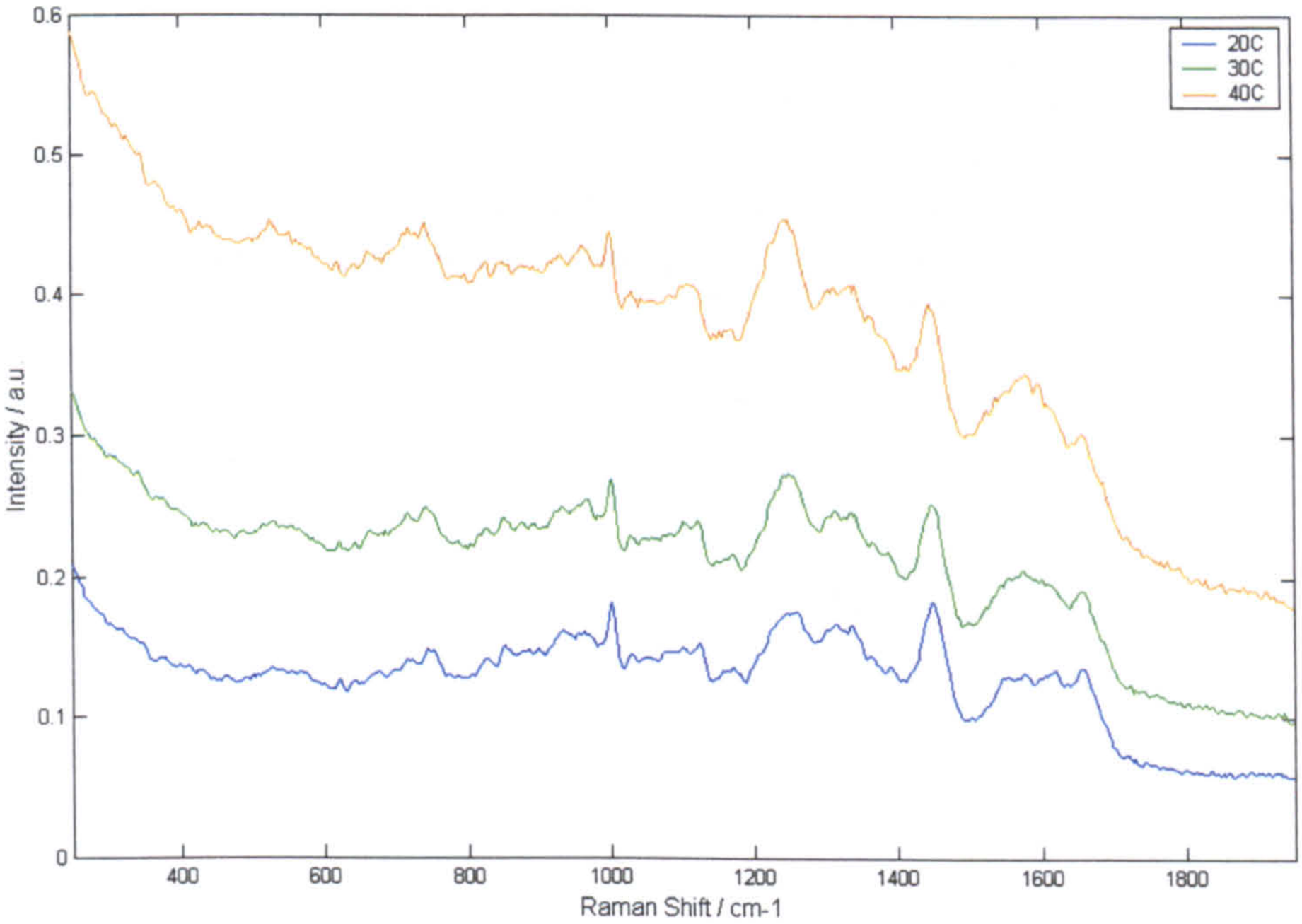

Figure 5.48: Plot of Raman spectra from a sample of oesophagus tissue at 20, 30 and 40°C.

5.4.2 Polarisation Sensitivity of Tissue Raman Spectra

Section 4.3.5 outlines the procedures carried out to study the polarisation sensitivity of oesophageal Raman spectra. The polarisation of the inelastic scattered light has been analysed and in addition the effect of the polarisation of the laser illumination has been evaluated. From a single point on the sample, three spectra were acquired without a polariser in the collection path, three spectra were acquired with a polariser parallel and three with a polariser perpendicular to the polarisation axis of the laser illumination. Figure 5.49 displays the mean resulting spectra. A depolarisation ratio has been calculated directly between the parallel and perpendicular polarisation spectra (Figure 5.50), without any corrections for the polarisation orientation sensitivity of the spectrometer grating. When the analysing polariser was parallel to the illumination polarisation axis, most of the Raman peaks remained in the spectrum. However, when the polariser was perpendicular to the illumination polarisation axis, a significant number of Raman peaks were removed from the spectrum. Theoretically the most symmetric

vibrational modes produce the most polarised inelastically scattered light. Therefore the spectral peaks corresponding to these vibrational modes will be the most sensitive to the introduction of a polariser aligned perpendicular to the incident laser polarisation. Further study of this data can be used to assist in the identification of peaks for assignment to vibrational modes.

An evaluation of the sensitivity of the spectra to illumination polarisation geometry was made by employing a half-wave plate to rotate the polarisation of the laser beam prior to sample illumination. The above procedure was then repeated in the analyser/collection path. The resulting spectra are displayed in Figure 5.51. The half-wave plate was shown to rotate the polarisation orientation by 90° and to reduce the illumination intensity to 80% of the incident irradiance. From Figure 5.51 it can be seen that the signal is decreased to significantly less than 80% of the scattering signal in Figure 5.49. This is likely to be due to the polarisation sensitivity of the optics in the spectrometer. Nevertheless, it can be seen that the spectral shapes are repeated when the laser illumination polarisation is rotated by 90°.

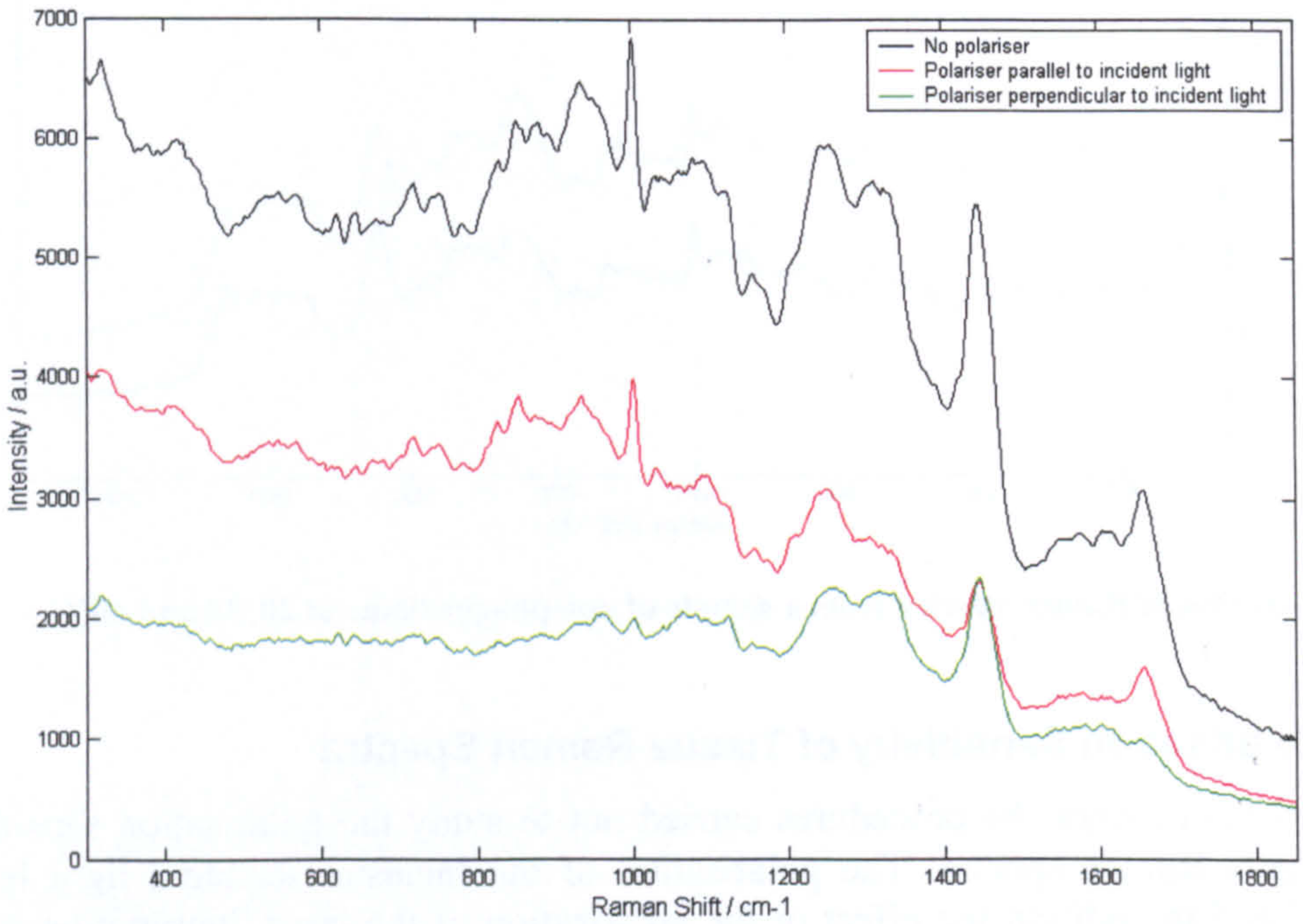

Figure 5.49: Mean Raman spectra of normal oesophageal mucosa with polarisation selection in the collection path.

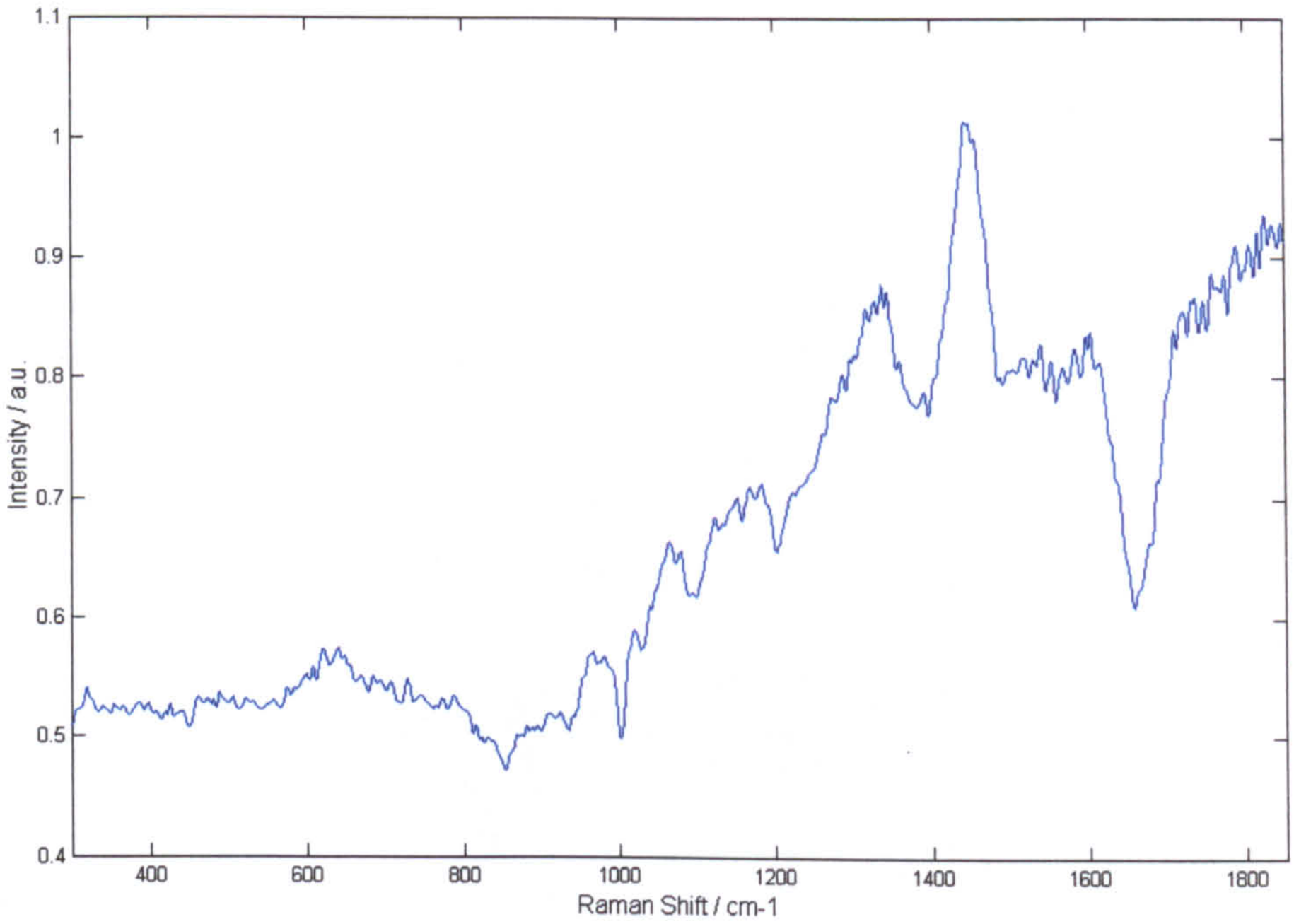

Figure 5.50: Plot of depolarisation ratio of normal oesophageal mucosa, uncorrected for system polarisation sensitivity.

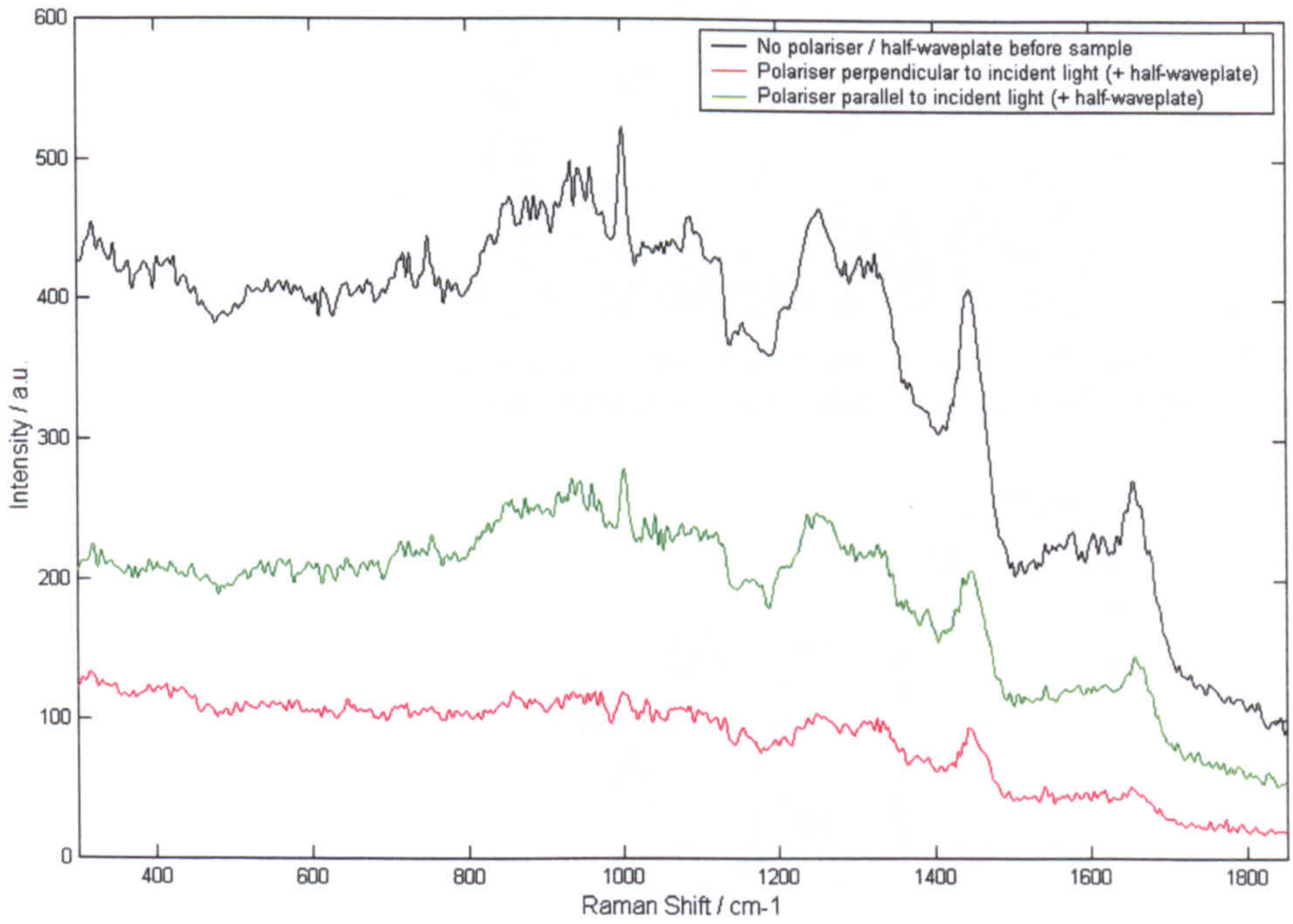

Figure 5.51: Mean Raman spectra of normal oesophageal mucosa with illumination polarisation rotated 90 degrees relative to the previous measurements and polarisation selection in the collection path.

5.4.3 Significance of Depth of Collection Volume in Oesophageal Tissue

Section 4.3.6 describes the experimental procedures employed to measure the variation of the Raman spectra from oesophageal tissue with depth, by mapping transverse sections. Figure 5.52a shows the resulting Raman false colour map superimposed upon the white light image of a normal oesophageal sample from the microscope camera. Each coloured pixel represents an individual Raman measurement. Multivariate analysis using principal components on each of the pixels has been carried out. The weights of the first three PCs (Figure 5.52b) have been combined to construct the false colour image. This has been repeated for a Barrett's oesophagus tissue section (Figures 5.53a and b). The false colour images emphasise differences in cellular layers of the tissue, which have been discriminated by the differing biochemistry of the cells and surrounding stroma.

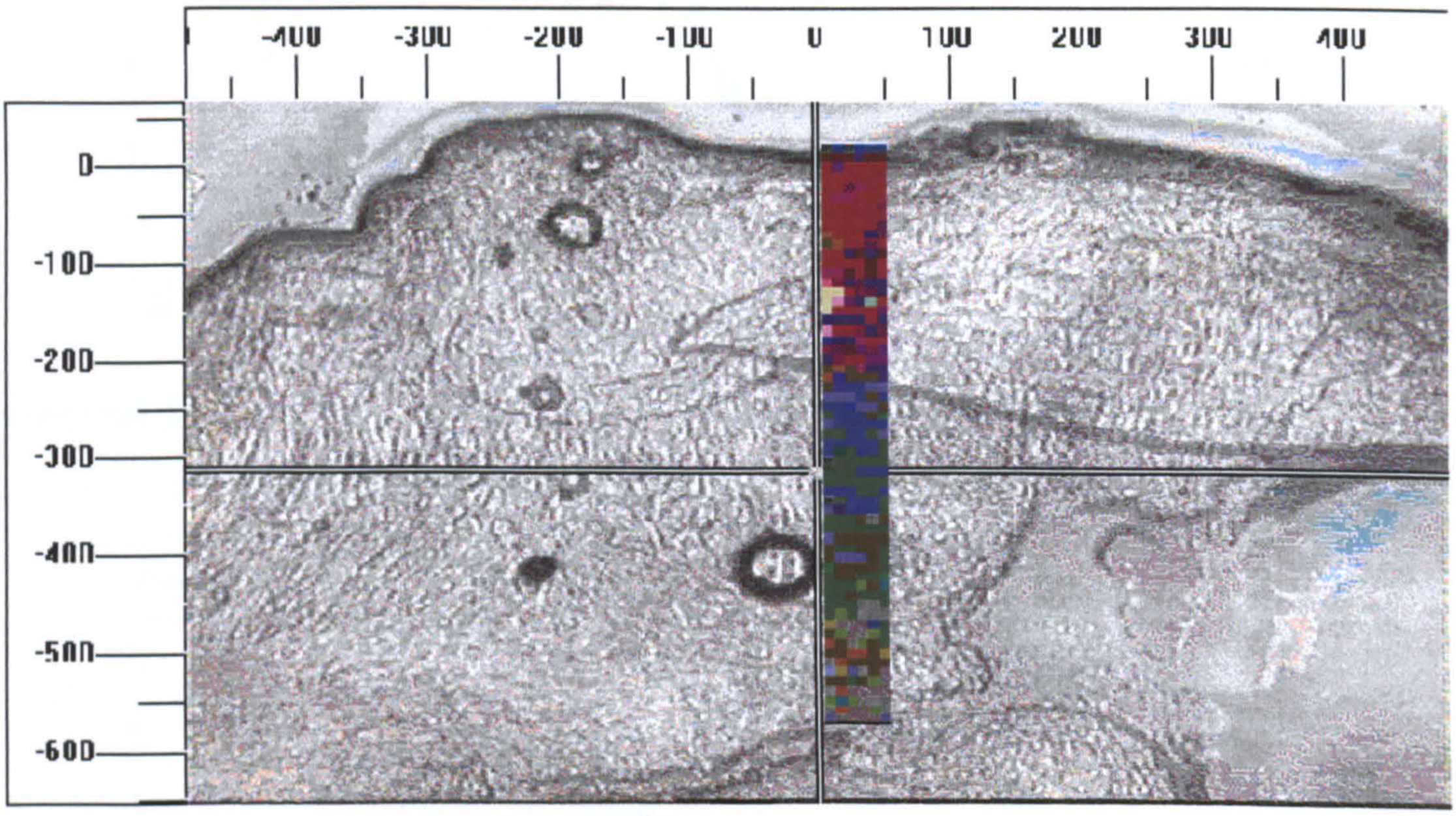

Figure 5.52a Raman false colour map superimposed upon the white light image of a normal oesophageal sample. Each pixel is made up of the combined weights of the first 3 PCs.

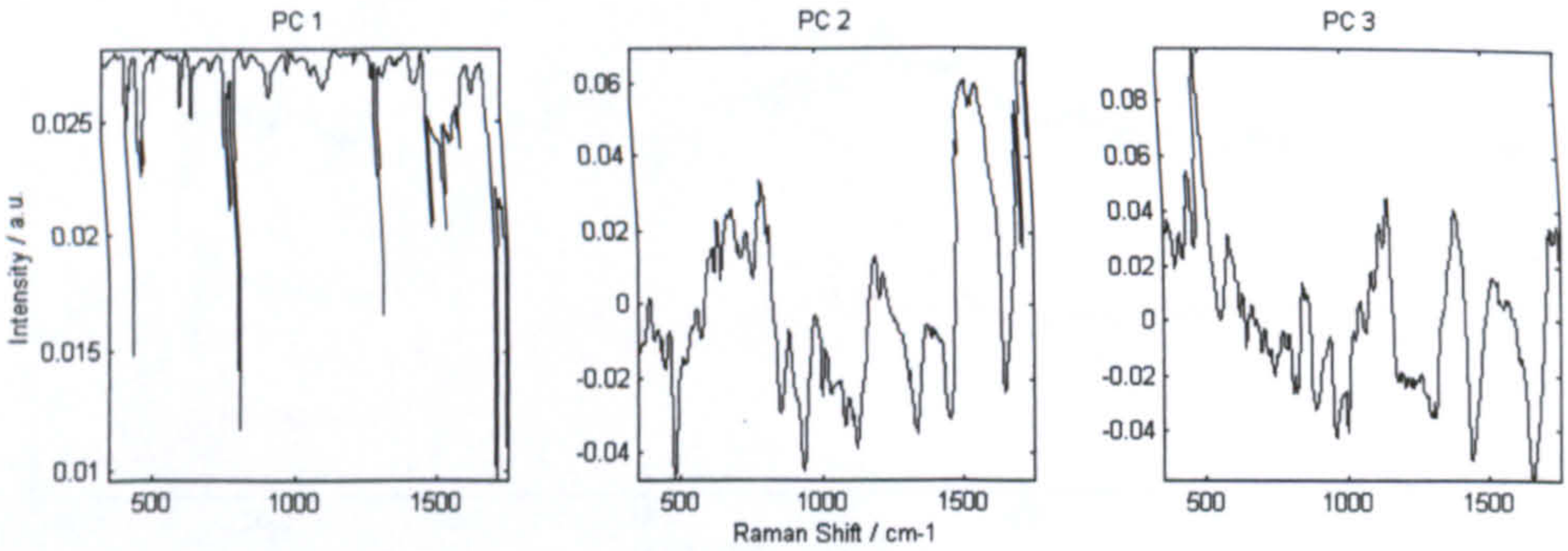

Figure 5.52b The PC loadings used to construct the false colour map image. Each PC represents the reducing variance from the mean.

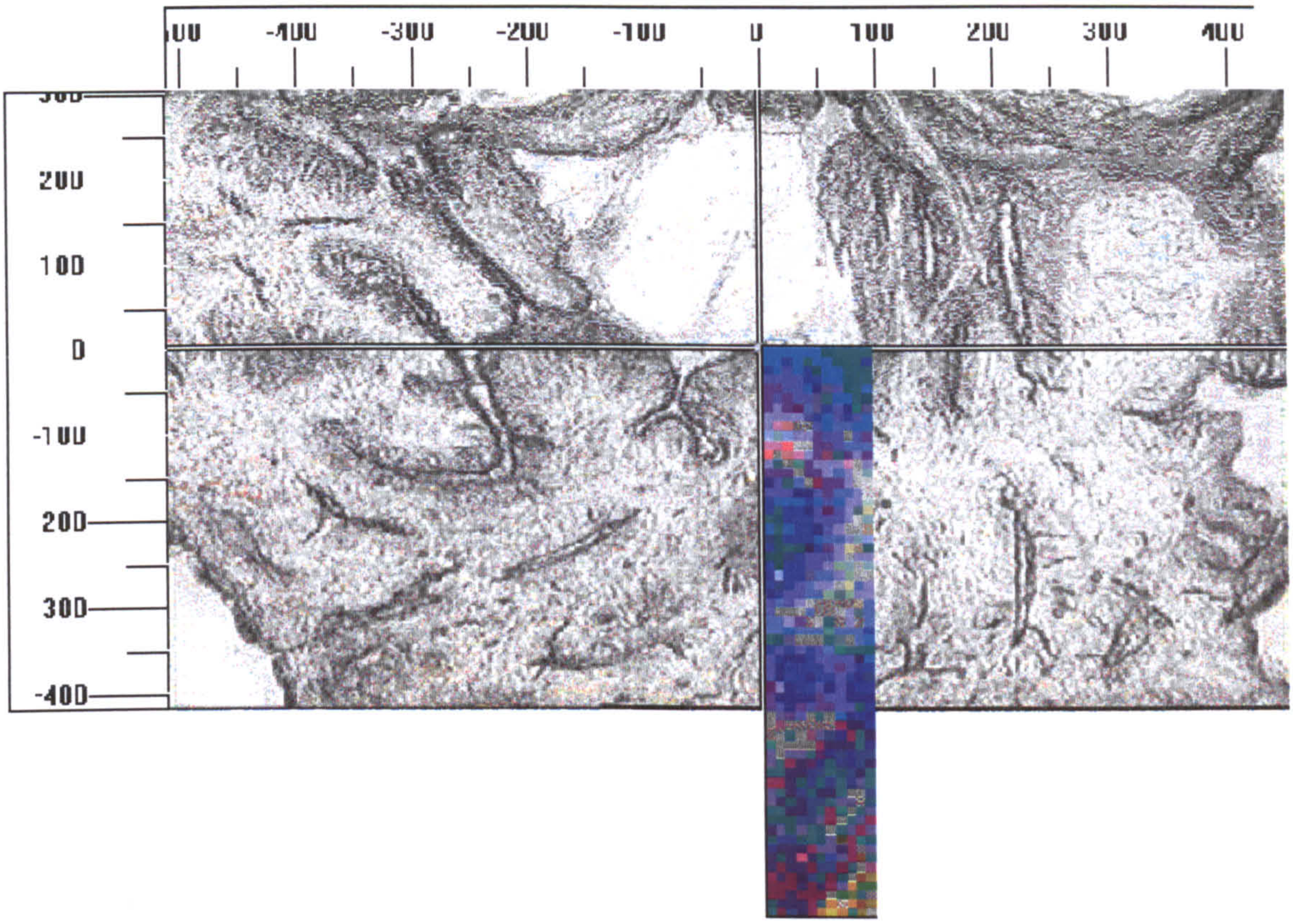

Figure 5.53a Raman false colour map superimposed upon the white light image of a Barrett's oesophagus sample.

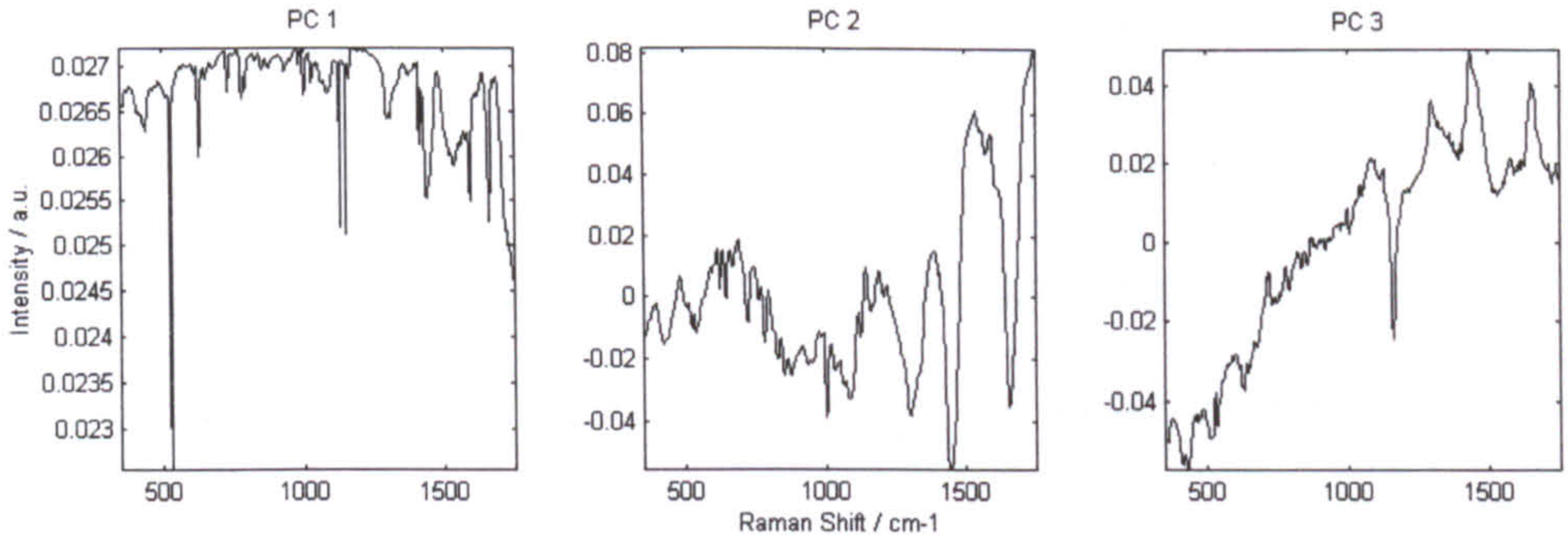

Figure 5.53b shows the PC loadings used to construct the false colour map image. Each PC represents the reducing variance from the mean.

5.4.4 Confounding Factors

A selection of contaminants likely to affect Raman spectra of oesophageal tissue measured in vivo have been measured with the same spectrometer configuration as that used to measure the oesophagus spectra. See section 4.3.7 for details. The spectra have all been corrected for energy sensitivity of the system, and the relative intensity levels indicate the likely effect they will have on any spectra measured in their presence. An

average oesophagus spectrum has been included for comparison of relative intensity levels and peak positions. Figure 5.54 displays these spectra.

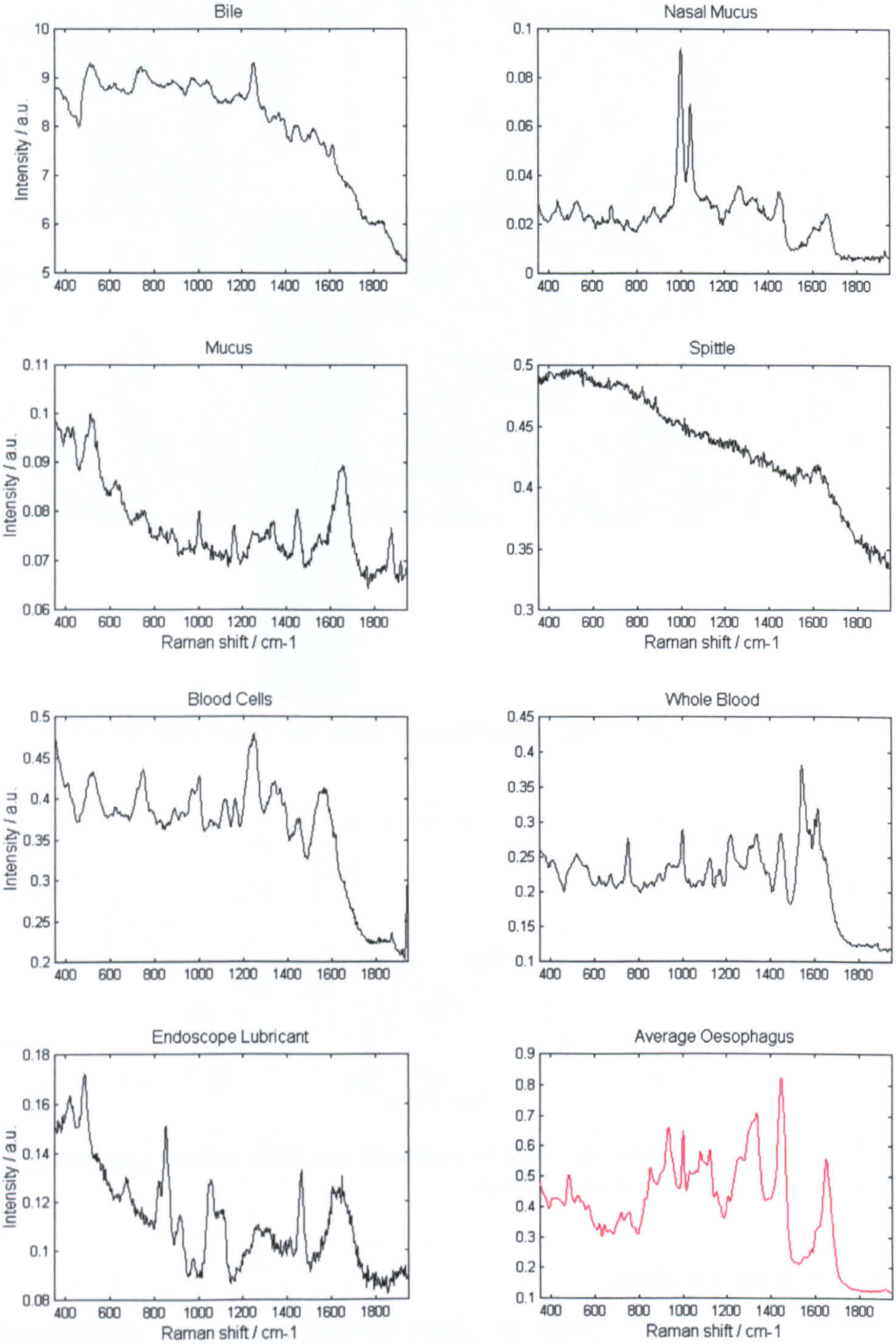

Figure 5.54: Raman spectra of possible contaminants of in vivo oesophagus spectra, measured in 30 seconds and corrected for energy sensitivity. Average oesophagus spectrum is included for comparison (in red).

It can be seen from the spectra of potential contaminants that there are a number of these that exhibit sharp Raman scattering spectra, that may interfere with tissue Raman spectra. However, if one looks at the relative intensities, it is only the bile that has a significantly higher signal strength than the tissue. This appears to be mainly due to a luminescent background. The sample measured was of pure human bile, extracted from the bile duct. By the time it reaches the gastro-oesophageal junction it is likely to be markedly diluted. It must also be noted that all the tissue in this study has been measured without pre-washing of the samples, therefore it is likely that most contaminants will already be present on the tissue surface.

5.5 Other Biological Tissues of Interest

A selection of other biological tissues where Raman spectroscopy will be likely to contribute to the detection and classification of cancers have been studied. Spectra of some of these are shown in Figure 5.55. Raman spectra of these tissues were measured using the customised Renishaw microspectrometer (outlined 4.2) with 828nm laser light focussed onto the sample by the x80 objective. Integration of the collected signal was carried out for 30 seconds with laser power levels of 32mW. The tissues evaluated included the following:

1. Stomach.
2. Tonsil.
3. Endometrium.
4. Bladder.
5. Prostate.

It can be seen that the epithelial spectra are visually similar, although subtle differences are present that would allow identification and potentially classification of pathology types in much the same way as those demonstrated for larynx and oesophagus tissues.

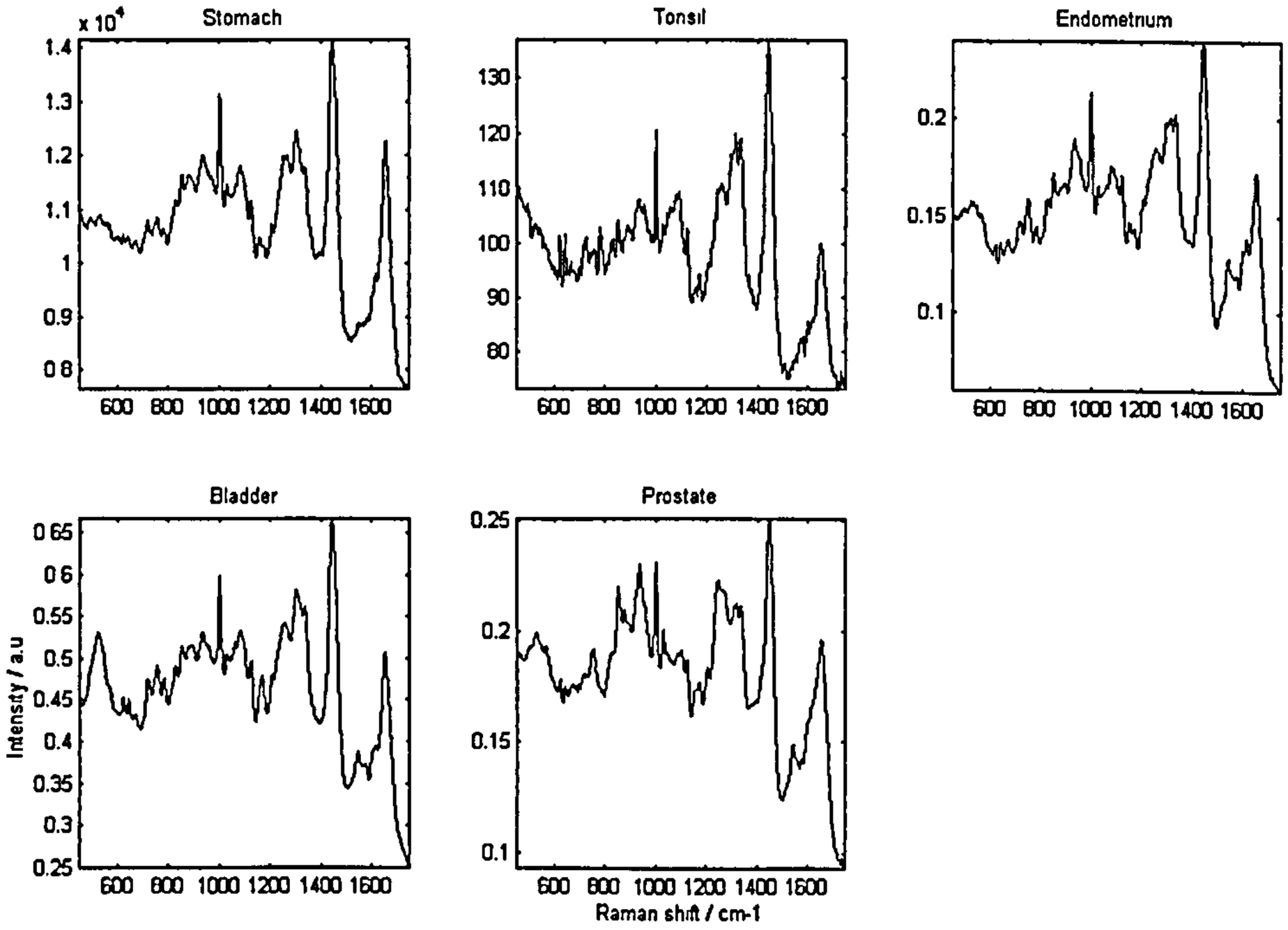

Figure 5.55: Raman spectra of other epithelial tissues with potential application for Raman spectroscopic diagnostics.

5.6 Summary of Results

A commercially available Raman microspectrometer (Renishaw System 1000) has been customized to provide optimum signal-to-noise ratio spectra in the shortest timescales, with the minimum fluorescence background signal contribution from the tissue fluorophors. The optimisation evolved throughout the early period of experimentation. In the ideal world this would not have happened. However, time constraints and difficulty in obtaining tissue samples has meant that in the earlier larynx work spectra were measured with various spectrometer configurations and therefore spectra obtained have included fixed pattern noise from the spectrometer in addition to the tissue signal.

The optimisation process has involved selection of the ideal excitation wavelength in the range available (514.5nm to 860nm). It has been demonstrated that the use of 830nm laser light produces the highest S/N ratio tissue spectra by providing a compromise between high sensitivity in the CCD detector (reducing with increasing wavelength), low tissue fluorescence (reducing with increasing wavelength), and the ν^4 dependence of the Raman cross-section. The most significant factor within the range of detector sensitivity is the background fluorescence, because high fluorescence can easily swamp weak Raman signals causing them to be obscured by shot noise levels (see section 4.2.6). Moreover, there has been no visible degradation observed in the spectral intensity when using 830nm excitation. However, when using 633nm excitation fluorescence bleaching is observed in a matter of seconds.

5.6.1 Raman Detection of Cancers and Pre-cancers in the Larynx

This study was the first to demonstrate the feasibility of using Raman spectroscopy to measure and discriminate the pathological state of laryngeal tissue. The resulting sensitivities and specificities that have been achieved with the use of multivariate linear discriminant models indicate a high degree of discrimination is possible, even between samples exhibiting only very subtle morphological changes, such as between normal squamous mucosa and squamous dysplasia; and squamous dysplasia and squamous cell carcinoma.

The samples were snap-frozen to ideally preserve the nature and freshness of the tissue without introduction of any impurities likely to cause uncharacteristic spectral variations. In addition the spectra were acquired using an illumination/collection geometry similar to that that would be used for in vivo measurements. Thus confirming the feasibility of using Raman spectroscopy for in vivo tissue surface analysis by coupling a fibre probe to the spectrometer.

Good inter- and intra- sample Raman spectral repeatability has been demonstrated. Thus negating the need for measurement of normal tissue as a baseline from each individual prior to diagnosis. There is some baseline variability that is likely to be due to a combination of microscopic tissue heterogeneity, a variable focus and variable laser powers. Wavenumber repeatability was demonstrated by calculating the standard deviation from the mean position. This was shown to be ± 3.25 cm^{-1} over all 200 spectra. This variation was likely to be due to significant drift in laser pointing and wavelength stability. Shift correction has been used to compensate prior to analysis.

The spectra obtained are highly complex in nature, consisting of a superposition of Raman scattering peaks from a myriad of tissue constituents. There are many discrepancies in the literature regarding the assignment of each peak. It is likely that most will be made up of scattering from many biological molecules co-added, thus peak shapes and positions may vary. Moreover, system resolution of 3-4 cm^{-1} will introduce some discrepancies.

All spectra from laryngeal mucosal tissue are inherently similar. Any differences between the spectra from one pathological group to the next have required complex analytical procedures to exploit the subtle variations. Initially empirical peak analysis was evaluated. Difference spectra calculated between normalised spectra from normal, dysplastic and cancerous larynx enabled the more obvious variations in the Raman scattering properties from one group to the next to be assessed. The magnitude of the variation between spectra could be quantified by comparing the magnitude of the peaks and troughs in the difference spectra with the intensity levels shown in the individual mean spectra. The dysplasia versus normal difference spectrum represented about 1% variation from the mean spectrum. The SCC versus normal and SCC versus dysplasia difference spectra represented approximately 2% of the variation from the mean. These values indicated the small differences from one pathological group to the next.

Utilisation of tentative peak assignments for significant positive and negative peaks in the difference spectra has enabled some sense to be made of the biochemical changes that accompany the progress towards cancer in laryngeal mucosal tissue. Dysplastic tissue has been shown (tentatively) to exhibit greater DNA, lipid, phenylalanine and tyrosine peaks; but lower protein backbone, unordered proteins, α-helix proteins, porphyrins, and tryptophan than normal tissue. Squamous cell carcinoma has been shown to demonstrate increased nucleic acids and DNA, hydroxyapatite, tryptophan, and β-sheet proteins and less glycogen, carotenoids, lipid and α-helix proteins than either normal or dysplastic larynx tissue. This tends to corroborate known biochemical changes leading to tumour develoment. These include, increased nuclear/cytoplasmic ratio, protein conformation changes and tissue calcification.

The histopathology grades have been developed by pathologists utilising architectural and morphological differences to recognise from experience when a tissue has undergone a change likely to be clinically significant. However, cells are undergoing a continuum of change from normal to squamous dysplasia to cancer, and therefore distinguishing between samples, either histologically or spectroscopically will be difficult.

The variation of peak intensities from one spectrum to the next has been shown to be larger than the subtle variation that represents the pathological changes within the tissue. The analysis of variance from the mean of 32 peak intensities from 200 un-normalised spectra was performed. None of the peaks were shown to vary with pathological group to the 99.9% significance level. Moreover, standard deviations from the mean peak intensity values were shown to be equivalent to the magnitude of the mean values. One method utilised to overcome this variation from one spectrum to the next has been peak intensity ratio analysis. The 32 selected peaks were ratioed with one another to produce 1024 peak ratio values for each spectrum. Analysis of variance from the mean (ANOVA) was performed on all of the values to evaluate significant differences between pathological groups. F-values were shown to vary from 38.15 for I_{828}/I_{754} to 1.07 for I_{1265}/I_{1336}. These represent significance levels of varying from one group to the next of greater than 99.9999% and 65.5% respectively.

Standard deviations of peak ratios are approximately 5% of the mean values, indicating significantly less variation than that demonstrated by peak analysis alone. Significant differences in the peak ratios with pathology groups have been demonstrated. Although, pathological changes are the result of highly complex biochemical processes unlikely to be fully described by only two molecular vibrational modes. Multivariate analysis has enabled the most clinically significant variations from the mean spectra of the data set to be utilised for discrimination between the sample groups. Initially principal components were calculated from spectra that had been shift-corrected, interpolated to one point per wavenumber and mean centred. Each principal component described ever decreasing levels of variance from the mean spectrum of the data set. A linear combination of enough of the PCs would enable reconstruction of the original mean centred spectrum. Four principal components (5, 6, 7 and 14) were shown to exhibit greater than 99.9% significance of discrimination between the three pathological groups. The four significant PCs described only 0.61% of the total variance from the mean, indicating that subtle

modifications in biochemistry precede and accompany significant pathological changes to the tissue. However, by plotting the weights of the PCs in scatter plots it could be seen that there was a good level of clustering but some overlap from one group to the next.

The application of linear discriminant analysis has enabled the group separation to be maximised by the construction of two functions from linear combinations of PCs to maximise the variance between groups and minimise the variance within groups. Two functions are necessary for discrimination between three groups. The model constructed from unfiltered spectra when tested with a cross-validation procedure correctly predicted 78.4% of the spectra, with sensitivities ranging from 72 to 93% and specificities of 81 to 96%. From scatter plots of the linear discriminant function weights it could be seen that group clustering was achieved successfully, although some groups appeared to cluster into two sub-groups. This is likely to be due to the evolving spectrometer configuration that was employed for measurements of larynx spectra. Raman spectra have been acquired with different resolutions, S/N ratios, calibration protocols and laser stabilities. The use of a smoothing function to pre-process the data has been shown to reduce the effect of these variations in the model.

Model optimisation has involved the use of smoothing filters, likely to remove any subtle fluctuations in peak positions. In addition the use of 1st and 2nd derivative functions would remove background offset and linear functions from the spectra prior to analysis, thus reducing the intersample variability from the sampling conditions. Optimisation of the linear discriminant (LD) model for the larynx tissue data was achieved by building multiple models with all the spectra pre-processed with Savitsky-Golay filters ranging from zeroth to second derivative, first- to fifth-order polynomial functions with widths from 7 to 105 points. The resulting discrimination was seen to vary with filter widths and type. It was possible to maximise the number of correctly predicted spectra for normal, dysplastic, or cancerous groups, or for a combination. In the case of optimisation for maximum number of samples correctly predicted from all groups, a 95-point, fourth-order polynomial, second-derivative filter, applied prior to analysis, provided an optimum separation for all three groups of 88.4% correctly classified. The scatter plots of the resulting LD weights have less overlap and sensitivities have improved to between 86 to 90% and 87 to 95 % specificity; although the sensitivity for cancer detection has been shown to drop from 93 to 86%. This reduced the large number of false positives seen in the un-optimised model, but has introduced a few more false negatives, which will be likely to be more important to patient outcomes.

5.6.2 Raman Detection of Cancers and Pre-Cancers in the Oesophagus

Published studies have indicated high levels of discrepancy between even highly experienced histopathologists in the classification of oesophageal pre-cancerous lesions (see Chapters 1 and 2). Three expert gastrointestinal-registry histopathologists were used to judge the pathological state of all the samples used in this work. Spectral models were trained with majority and consensus data to evaluate the importance of a full agreement on the functionality of a Raman spectral diagnostic technique. Under normal circumstances a pathologist would classify a tissue sample by the highest or most clinically significant grade in a mixed sample. In this study the pathologists were given

the task of describing all the grades present in the tissue. Heterogeneous samples were discarded to remove the possibility of introducing errors from measuring different areas of the samples from those defined by the pathologist. Those samples with a discrepancy of opinion were discarded using majority or consensus selection rules.

The results obtained in this study have been the first to demonstrate the feasibility of using Raman spectroscopy to measure and discriminate between large numbers (n=9) of pathological groups in oesophageal tissue and the first investigation to carry out a rigorous histopathological analysis protocol. The resulting sensitivities and specificities that have been achieved with the use of multivariate linear discriminant models indicate a high degree of discrimination is possible, even between samples exhibiting only very subtle morphological changes, such as between Barrett's oesophagus (intestinal metaplasia) and low-grade and high-grade dysplasias.

Two separate studies were undertaken, the first with samples snap-frozen, and the second with the samples formalin fixed. Snap-freezing preserved the nature and freshness of the tissue without the introduction of any impurities likely to cause uncharacteristic spectral variations. Formalin is the fixative of choice for most excisional biopsies. However it is known to introduce cross-links between proteins and is thus likely to introduce changes to Raman tissue spectra, in addition to the contribution from the formalin solution itself. All the spectra were acquired in a geometry similar to that that would be used for in vivo measurements. Both studies were complimentary in that the facility of Raman spectroscopy to distinguish between diseased states in both fresh (live) tissue and fixed tissue in the pathology laboratory has been evaluated. The same spectrometer configuration was used throughout, 31mW of 830nm laser light was focussed on the tissue surface with a x80 ultra-long-working-distance lens. A monochromator with a 50μm entrance slit and 300 lines per mm grating was used to disperse the collected light. An integration time of 30 seconds was used for acquisition of high quality spectra (SNR >15). Use of a low dispersion grating has allowed the full spectral range of the tissue fingerprint region (200-2100 cm^{-1}) to be acquired with a static, and hence more repeatable grating position.

5.6.2.1 Snap-frozen tissue

Initial discussion will focus on the snap-frozen oesophageal tissue models. Good inter- and intra- sample spectral repeatability has been demonstrated, thus negating the need for measurement of normal tissue as a baseline from each individual prior to diagnosis. There has been no visible degradation observed in the spectral intensity when using 830nm excitation. There is some baseline variability that is likely to be due to a combination of microscopic tissue heterogeneity, variable focus and variable laser powers. Wave number repeatability was demonstrated by calculating the standard deviation from the mean position. This was shown to be ± 1.12 cm^{-1} over all 1200 spectra. This variation was likely to be due to a drift in laser pointing and wave length stability. Shift correction has not been used on the spectra prior to analysis.

The spectra obtained are highly complex in nature, consisting of a superposition of Raman scattering peaks from a myriad of tissue constituents. There are many

discrepancies in the literature regarding the assignment of each peak. It is likely that most will be made up of scattering from many biological molecules co-added, thus peak shapes and positions may vary. Moreover, a system resolution of around 10-12 cm^{-1} (for the 300 lines per mm grating and 50 μm slit configuration) will introduce some discrepancies.

All spectra from oesophageal mucosal tissue are inherently similar. Complex analytical procedures have been necessary to exploit the subtle variations between the spectra from each pathological group. Initially empirical peak analysis was evaluated for samples included in the three-group consensus model (normal, Barrett's and dysplasia and cancer combined). Difference spectra between mean normalised spectra from normal, Barrett's, and dysplastic and cancerous oesophagus enabled the more obvious differences between the Raman scattering properties from one group to the next to be assessed. The magnitude of the variation between spectra could be quantified by comparing the magnitude of the peaks and troughs in the difference spectra with the intensity levels shown in the individual mean spectra. The Barrett's versus normal difference spectrum represents about 1% variation from the mean spectrum. The dysplasia and cancer versus normal and dysplasia and cancer versus Barrett's represent approximately 2% of the variation from the mean. These values indicate the small differences from one pathological group to the next.

Utilisation of tentative peak assignments for significant positive and negative peaks in the difference spectra has enabled some sense to be made of the biochemical changes that accompany the progress towards adenocarcinoma in oesophageal tissue. Dysplastic and cancerous tissues have been shown (tentatively) to exhibit greater DNA, hydroxyapatite, urea/phenylalanine, α-helix and unordered proteins, but lower glycogen, carbohydrates, protein disulphide bonding, and carotenoids than normal tissue. This tends to corroborate known biochemical changes leading to tumour develoment such as increased energy consumption from cell division, increased nuclear/cytoplasmic ratio, protein conformation changes and tissue calcification. The histopathological groupings developed by pathologists utilise architectural and morphological differences to recognise from collective experience when a tissue has undergone a change likely to be clinically significant. However, cells are undergoing a continuum of change from Barrett's mucosa to dysplasia to adenocarcinoma, and therefore full separation, either histologically or spectroscopically will be difficult.

The variation of each peak intensity across the spectral dataset has been shown to be larger than the subtle variation that represents the pathological changes within tissue. The analysis of variance from the mean of 29 peak intensities from 617 un-normalised spectra was performed. None of the peaks were shown to vary with pathological group to the 99.9% significance level. Moreover, standard deviations from the mean peak intensity values were shown to be equivalent to approximately 30% of the magnitude of the mean values. One method utilised to overcome this variation from one spectrum to the next has been peak intensity ratio analysis. The 29 selected peaks were ratioed with one another to produce 841 peak ratio values for each spectrum. Analysis of variance from the mean (ANOVA) was performed on all of the values to evaluate significant differences between pathological groups. F-values were shown to vary from 24.12 for I_{1548}/I_{669} to 4.07 for

I_{1259}/I_{1335}. These represent greater than 99.9999% and 98.25% significance of variation between pathology groups.

Standard deviations of peak ratios from the mean values average approximately 7%, indicating significantly less variation than that demonstrated by peak analysis alone. Although significant differences in peak ratios have been demonstrated, pathological changes are the result of highly complex biochemical processes unlikely to be described by a pair of Raman peaks representing two molecular vibrational modes.

Multivariate analysis has enabled the most significant variations from the mean spectra of the data set to be utilised for discrimination between the sample groups. Initially principal components were calculated from spectra that had been interpolated to one point per wavenumber and mean centred. Ten principal components (1, 2, 3, 4, 5, 6, 7, 8, 10 and 12) were shown to exhibit greater than 99.9% significance of discrimination between the eight pathological groups designated from a consensus of opinion of three pathologists. The most significant PC (6) described only 0.05% of the total variance from the mean, indicating that subtle modifications in biochemistry precede and accompany significant pathological changes to the tissue. A plot of the weights of the PCs demonstrated that there was a good level of clustering but some overlap from one group to the next.

Although most principal components are made up of a complex combination of tissue components. PC3 can be seen to represent glycogen, which is known to be the main energy source found in human cells. Normal cells will have this in abundance and in deficit in abnormal cells. This appears to be demonstrated in both difference spectra and principal component analyses.

A collection of models have been assembled to discriminate between the three or four significant groups required for biopsy targeting in the oesophagus, and to discriminate between the eight or nine significant groups required for full classification of oesophageal tissue pathology. Models constructed from spectra classified with consensus and majority histopathogy have been compared.

In the three-group consensus model the application of linear discriminant analysis has enabled the group separation to be maximised. This was achieved by the construction of two functions from linear combinations of the PCs to maximise the variance between groups and minimise the variance within groups. Two functions were necessary for discrimination between three groups, and three functions for discrimination between four groups, and so on. The three-group consensus discriminant model (constructed from unfiltered spectra) when tested with a cross-validation procedure correctly predicted 93.2% of the spectra. Sensitivities of 97, 84 and 97% and specificities of 99, 98, and 93% were achieved for groups of normal, Barrett's and neoplasia (dysplasia and cancer) respectively. From scatter plots of the linear discriminant function weights it could be seen that group clustering was achieved extremely successfully.

The four-group consensus discriminant model (constructed from unfiltered spectra) when tested with a cross-validation procedure correctly predicted 85.7% of the spectra. Sensitivities of 95, 77, 82 and 71% and specificities of 99, 99, 88 and 97% were achieved for groups of normal, Barrett's, dysplasia and cancer respectively. From the two-

dimensional scatter plots of the linear discriminant function weights it is difficult to fully visualise the model distribution in three dimensions. Nevertheless it could be seen that group clustering was achieved relatively successfully.

The eight-group consensus discriminant model (constructed from unfiltered spectra) when tested with a cross-validation procedure correctly predicted 88.6% of the spectra. Sensitivities ranging from 73 to 100% and specificities ranging from 92 to 100% were achieved for groups including normal, cardiac Barrett's, fundic Barrett's, intestinal metaplasia, high-grade Barrett's dysplasia, adenocarcinoma, squamous dysplasia and squamous cell carcinoma. From the two-dimensional scatter plots of the linear discriminant function weights it is extremely difficult to fully visualise the model distribution in seven dimensions. Nevertheless it could be seen that group clustering was achieved relatively successfully. The bar chart plot of the discrimination power of the model indicates that the greatest cross-over between groups occurred between the intestinal metaplasia, high-grade dysplasia and adenocarcinoma groups. It is these that cause the pathologists the greatest difficulty in classification. The cross-over is likely to be due in part to both the difficulty in pathological discrimination between these groups and the fact that abnormal development of the epithelial tissue follows a continuum with many biochemical similarities.

The nine-group majority discriminant model (constructed from unfiltered spectra) when tested with a cross-validation procedure correctly predicted 72.0% of the spectra. Sensitivities ranging from 49 to 100% and specificities ranging from 94 to 100% were achieved for groups including normal, cardiac Barrett's, fundic Barrett's, intestinal metaplasia, low-grade and high-grade Barrett's dysplasia, adenocarcinoma, squamous dysplasia and squamous cell carcinoma. From the two-dimensional scatter plots of the linear discriminant function weights it is extremely difficult to fully visualise the model distribution in eight dimensions. Nevertheless it could be seen that some group clustering was achieved, but significantly worse than in the consensus model. The bar chart plot of the discrimination power of the model indicates that once again the greatest cross-over between groups occurs between the intestinal metaplasia, high-grade dysplasia and adenocarcinoma groups. However, in the case of the majority model the cross-over is significant between these groups. This is almost exclusively due to discrepancies in pathological classification. These were introduced by including samples with an agreement of only two out of the three pathologists.

Optimisation of the LD model for the oesophagus tissue data was achieved by building multiple models with all the spectra pre-processed with Savitsky-Golay filters ranging from zeroth to second derivative, first to fifth polynomial functions over 7 to 105 points. The resulting discrimination was seen to fluctuate with filter widths and type. It was possible to maximise the correctly predicted spectra for any pathological grouping, or for a combination. A 95-point Savitsky-Golay third-order polynomial, second-derivative function was shown to improve the power of the eight-group consensus model to discriminate the clinically significant group of adenocarcinoma. An improvement of 73% to 79% sensitivity for adenocarcinoma was achieved. This reduced the number of false negatives seen in the un-optimised model, but has introduced a few more false positives.

A simplistic evaluation of the effect of testing new data acquired in shorter integration times, or lower laser powers, has been performed by testing the model with degraded spectra. Varying levels of random noise have been added to the new spectra prior to projection onto the trained model. The resulting spectral prediction was compared with consensus pathology opinion. Noise levels of less than 30% of the signal, equivalent to those that would be achieved within 1-30 seconds with the present system, lead to 75-100% correct prediction of the test spectra. This indicates that so long as the training data is of high quality then repeatable prediction is possible with new spectra measured with significantly lower S/N ratios.

5.6.2.2 Formalin fixed tissue

The majority of biopsy samples collected for histopathological analysis are formalin fixed immediately following excision. This provides stablilisation of tissue properties until analysis can be performed. To enable evaluation of the use of Raman spectroscopy as a tool to aid histopathological analysis or as an automated sorting tool to remove non-clinically interesting samples, it was important to establish whether spectra obtained from formalin fixed tissue could be used for discrimination between pathology types.

Due to time constraints only the pathological results from one gastrointestinal-registry pathologist were used to train the spectral models. This has inherently introduced errors due to the discrepancies known to exist between pathologists, however as a proof-of-principle study it still proves valid. The results obtained demonstrate the feasibility of using Raman spectroscopy to measure and discriminate between eight pathological groups in formalin fixed oesophageal tissue.

Good inter- and intra- sample spectral repeatability has been demonstrated. Thus negating the need for measurement of normal tissue as a baseline from each individual prior to diagnosis. There has been no visible degradation observed in the spectral intensity when using 830nm excitation. There is some baseline variability that is likely to be due to a combination of microscopic tissue heterogeneity, variable focus and variable laser powers. Wave number repeatability was demonstrated by calculating the standard deviation from the mean position. This was shown to be ± 3.61 cm^{-1} over all 418 spectra. This variation was likely to be due to significant drift in laser pointing and wave length stability. Shift correction was used on the spectra prior to analysis.

Multivariate analysis has enabled the most significant variations from the mean spectra of the data set to be utilised for discrimination between the sample groups. Initially principal components were calculated from spectra that had been shift-corrected, interpolated to one point per wavenumber and mean centred. 16 principal components were shown to exhibit greater than 99.9% significance of discrimination between the eight pathological groups designated from a consensus of opinion of three pathologists. The most significant PC (10) described less than 0.01% of the total variance from the mean, indicating that subtle modifications in biochemistry accompany significant pathological changes to the tissue. A plot of the weights of the PCs demonstrated that there was a good level of clustering but some overlap from one group to the next.

The eight-group discriminant model (constructed from unfiltered spectra) when tested with a cross-validation procedure correctly predicted 82.5% of the spectra. Sensitivities ranging from 75 to 100% and specificities ranging from 94 to 100% were achieved for groups including normal, cardiac Barrett's, fundic Barrett's, intestinal metaplasia, low-grade Barrett's dysplasia, high-grade Barrett's dysplasia, adenocarcinoma, and squamous dysplasia. From the two-dimensional scatter plots of the linear discriminant function weights it is extremely difficult to fully visualise the model distribution in seven dimensions. Nevertheless it could be seen that group clustering was achieved relatively successfully. The bar chart plot of the discrimination power of the model indicates that the greatest cross-over between groups occurred between the intestinal metaplasia and low-grade dysplasia groups. It is these that cause the pathologists the greatest difficulty in classification. The cross-over is likely to be due in part to both the difficulty in pathological discrimination between these groups and the fact that the progress through these groups follow a continuum with many biochemical similarities.

Optimisation of the LD model for the oesophagus tissue data was achieved by building multiple models with all the spectra pre-processed with Savitsky-Golay filters ranging from zeroth to second derivative, first to fifth polynomial functions over 7 to 105 points. The resulting discrimination was seen to fluctuate with filter widths and type. It was possible to maximise the correctly predicted spectra for any pathological grouping, or for a combination. In the case of optimisation for maximum number of samples correctly predicted from all groups, an 11-point, third-order polynomial, zeroth-derivative filter provided an optimum separation of all three groups of 83.7% correctly classified. The scatter plots of the resulting LD weights have less overlap and sensitivities have improved to between 76 to 100% and 94 to 100 % specificity; although the sensitivity for the clinically important grades of LGD, HGD, adeno, sq dys, were all shown to increase from 80%, 100%, 93% and 80% to 88%, 100%, 100% and 88% respectively. Thus reductions in false negatives have been achieved.

The spectra were also shown to contain information on the length of time they had been stored in formalin, although this didn't effect the diagnostic algorithms. Using multivariate analysis 98.8% of spectra were correctly predicted for time in formalin. However, it is not being suggested that a linear model could accurately predict time in formalin, just whether the sample has been immersed for short or long timescales (either a few weeks or many months).

5.6.3 Factors Likely to Affect Transfer from In Vitro to In Vivo Detection

The effect on tissue Raman spectra of changing between body- and ambient-temperatures has been demonstrated to change the background fluorescence levels. Nevertheless, Raman scattering peaks are not seen to vary over this temperature range. It is this fact that should allow translation of spectra measured at room temperature to diagnostic algorithms destined for use with in vivo measurements.

The evaluation of the potential effects of contaminants on oesophageal spectra has demonstrated that substances present in the lumen of the oesophagus exhibit some degree of Raman scattering, although these tend to be present in low concentrations. The tissue

spectra measured to date from unwashed biopsy samples have not been unduly affected by these contaminants. Although, the strengths of the signals indicate that they should not be ignored from analyses altogether. Furthermore, the effects of blood flow in tissue cannot be practically quantified in vitro. This will have to be evaluated during further work carried out in vivo.

Measurement of the sensitivity of the epithelial Raman spectra to polarisation has shown that the orientation of the polarisation of the laser illumination does not significantly effect the tissue spectra. However the spectrometer is polarisation sensitive so rotation of the illumination polarisation will require correction to maintain the same spectral intensity. The polarisation of the inelastic scattering from oesophageal tissue has been evaluated by use of a pair of analysers in the collection path. Measurement of the spectrum perpendicular to the illumination polarisation axis tends to significantly suppress many of the Raman peaks, most especially those spectral peaks corresponding to symmetric vibrational modes. The technique of polarisation analysis of scattered light may potentially be used as a tool to improve discrimination between normal and diseased tissues. Further work will be necessary to assess the facility of polarisation analysis for increased discrimination between pathology type.

The effect of measuring spectra from bulk tissue versus small samples was evaluated by measuring spectra from both biopsy material and larger resected tissue samples. Tiny sample volumes of the order 200 μm^3 were used throughout this study. No visible differences between the spectra were observed. Although it appears that the depth of field of the measurement is small enough to remove likely contamination to the spectra from deeper tissue, it is possible that more important diagnostic information may be found at greater depth. Moreover, it may be necessary to increase the sampling volume, by increasing the spot size, to enable averaging over more cells.

Further analysis of the different oesophageal tissues at greater depth has been carried out by mapping transverse frozen sections. Multivariate image analysis was used to demonstrate the variation in chemical constituents from the surface of squamous and Barrett's mucosa to deeper tissue layers. Further work is required with models built from measurement of larger sample volumes and larger depths before the ideal configuration can be fully understood. A study by Ackroyd et al. (1999) showed that the mean depth of columnar epithelium in 100 cases of Barrett's oesophagus was 0.5 ± 0.004mm (range 0.39-0.59mm) compared with a mean depth of squamous epithelium in normal oesophagus of 0.49 ± 0.03mm (range 0.42-0.58mm).[175]

Raman spectra of other epithelial tissues have been measured. The spectra obtained from stomach, bladder, prostate, endometrium and tonsil are relatively similar. However, subtle differences are visible and further analysis by construction of large sample number multivariate models are expected to demonstrate high levels of discrimination between normal, pre-cancerous and cancerous tissue.

6. Discussion of Results

The primary objective of this study has been to provide an appraisal of the potential use of Raman spectroscopy for both in vitro classification and in vivo detection of early malignant changes in the aero-digestive tract.

This study was:

- The first to demonstrate the feasibility of using Raman spectroscopy to measure and discriminate the pathological grade of laryngeal tissue.
- The first to demonstrate the feasibility of using Raman spectroscopy to measure and discriminate between large numbers (9) of pathological groups in oesophageal tissue.
- The first to demonstrate the feasibility of using Raman spectroscopy to measure and discriminate between eight pathological groups in formalin fixed oesophageal tissue.
- The first to follow rigorous sample handling and histopathological analysis protocols. This included the precise orientation of samples prior to snap freezing; and discarding any samples likely to cause errors either from mixed pathology samples, or from discrepancies in histopathology opinion.

A NIR dispersion Raman spectrometer has been optimised for measurement of the inelastic scattering properties of tissue. A wavelength of 830nm was demonstrated to be the ideal for both oesophageal and laryngeal tissue. Incident laser powers of around 30mW were adequate when utilising a x80 ultra-long-working-distance objective (N.A. 0.75) for illumination and collection of scattered light. A 300 lines per mm, single grating monochromator coupled to a deep-depletion CCD detector provided excellent throughput and high signal to noise ratio spectra in timescales of seconds. An oxide layer edge filter set provided the required high stray light rejection.

Raman spectra of epithelial tissues have been measured in vitro with S/N ratios of 15 to 20 in an integration time of 30 seconds. Following illumination with a power density of 1.6kW mm^{-2} of 830nm laser light for over 30 minutes, spectroscopic and histopathological analysis demonstrated that no sample degradation was observed. With heat transfer afforded by blood flow, it is likely that increased power levels will be possible for in vivo measurements, and this will enable a significant reduction in acquisition times. Moreover, in this study evidence has been provided that models constructed from high quality spectra (SNRs of 10 to 20) can be used to predict the histopathology of the sample measured with lower quality spectra (SNR < 5). Using the theoretical noise contributions discussed in Section 4.2.6 it can be estimated that employment of the same spectrometer configuration with lower acquisition times will result in the S/N ratios displayed in Table 6.1. Therefore in theory accurate prediction should still be possible with spectra measured in 2.5 seconds with a power density of 1.6kW mm^{-2} of 830nm light. Greater laser powers or further sensitivity improvements will reduce this time to below one second.

Studies published to date have not shown any significant thermal damage to tissue from high intensity laser illumination used during in vivo work.[16,134,146] Nevertheless, further studies into the effects of the excitation light on the probed tissue must be carried out prior to undertaking routine in vivo work. The effect of temperature rises on the tissue or photochemical reactions induced by the laser illumination may have unforeseen consequences.

Time / s	S/N Ratio
30	20
10	10.3
5	6.7
2.5	4.3
1	2.3

Table 6.1: Theoretical S/N ratios of Raman spectra from epithelial tissue using optimised spectrometer configuration.

The potential of NIR Raman spectroscopy to provide automated diagnosis for a number of medical conditions has been established. This can be achieved by employing diagnostic algorithms to distinguish between the differences in spectral features found in both normal and abnormal tissues. The simplest algorithms are based on empirically identified diagnostic features. These differences may be variations in intensity, intensity ratios and the number and location of peaks. However, it is minute changes in spectral shape that may indicate clinically significant biochemical changes that precede or accompany disease processes. High quality spectra are required to enable use of multivariate techniques that can analyse all the data in a spectrum and thus be more likely to provide an accurate test for the detection of disease. The use of multivariate linear discriminant models appears to provide the most repeatable method able to utilise most of the data contained within tissue spectra.

Assignments of Raman scattering peaks have been made tentatively from extensive study of the relevant literature. Glycogen has been demonstrated to be a significant component of the spectral variations in the Raman tissue spectra between healthy and diseased tissue. Both laryngeal and oesophageal tissue exhibit less glycogen peaks with increasing level of disease. This is likely to be due to the increased energy consumption by rapidly dividing neoplastic cells. This is in agreement with Raman spectral analysis in the cervix[84] and by other workers in the oesophagus,[132] although one investigation observed an increase in glycogen levels in lung cancers.[72] Distinct alterations in tissue biochemistry accompanying disease have been demonstrated in other principal components of the Raman spectra. However these changes are very complex combinations of increasing scattering from nucleic acids, alterations in protein secondary structure and lipid content. These transformations appear to be in line with current understanding of carcinogenesis in these tissues.

Low sample numbers and the lack of a thorough understanding of the shortcomings of histopathological analysis have restricted the accuracy of all of the tissue Raman studies published to date. The investigations have generally been limited to measuring spectral differences between two or three selected pathology types. However, it is important that samples covering the full spectrum of disease in each organ are studied; an achievement of this study. The spectral data from specimens covering all pathology types has been used to train the spectral diagnostic models. The work of calibrating the models with the current 'gold-standard' of histopathological analysis has required a great deal of collaboration with expert pathologists. High levels of discrepancy in tissue classification has made it vital that a number of pathologists, with expertise in the disease of interest, work together to provide a consensus of opinion on the tissue samples used to train and test the spectral models. In addition, tissue samples are commonly heterogeneous; therefore to enable an accurate calibration of the spectral diagnostic algorithms it was essential that tissue samples exhibiting only a single pathology were included for measurement.

The requirement for a consensus of histopathology opinion from three or more expert pathologists has been demonstrated in this study, not only for the calibration of spectroscopic diagnostic algorithms, but also for establishment of a reliable 'gold standard' diagnosis. Comparison of the oesophageal consensus and majority spectral discriminant models showed that the spectroscopic prediction of pathology was only as good as the training provided. This was demonstrated when samples were included in the training set with some discrepancy of histopathology opinion (i.e. only two out of three pathologists agreed on the diagnosis). The overlap in pathology groups occurred mostly between intestinal metaplasia, and low- and high-grade dysplasia. It is these groups that are the most clinically significant, but prove the most difficult for the pathologists to distinguish. The consensus models showed a small amount of overlap between these groups, although this was significantly lower than that found with the majority model where up to 50% of high-grade dysplasias were classified into other groups. Nevertheless, there is likely to be some overlap even in the best models due to the fact that the pathological groups have artificially defined boundaries. In fact the development of neoplastic tissue tends to follow a continuum of change, both biochemically and morphologically, from intestinal metaplasia to adenocarcinoma, and from squamous epithelium to squamous cell carcinoma.

6.1 Comparison with published work

Studies published demonstrating the separation of two or three pathology groups with Raman spectroscopy have tended to overstate the resulting sensitivities and specificities of the test. When the full spectrum of pathologies found in the tissue are included these outcome measures are almost invariably reduced. Other workers have demonstrated separation of samples by histopathologically defined group in the breast,[20] cervix,[84] colon,[86] skin[85] and most recently the oesophagus.[21] The number of spectral measurements used for construction of diagnostic algorithms have been between tens of measurements and a few hundred. These have been invariably from a restricted subset of the pathology groups found in the organ.

The most extensive breast tissue study to date, investigated samples covering three pathology groups: normal, benign and malignant tumours in 61 samples.[82] Timescales of

100 seconds were required to achieve sufficient S/N ratios. A linear discriminant model was trained with the PCs of the spectra from all 61 samples. Use of this prediction model to predict the histopathology of the samples produced results of 14/15, 13/15, 31/31 correctly predicted samples for normal, benign and cancerous samples respectively. However, the results have been significantly skewed by the fact that the same spectra used to train the model have been used to test it, i.e. neither cross-validation nor new samples have been used.

A Raman investigation in the cervix has demonstrated much improved experimental techniques, by studying five pathological groups (normal, metaplasia, inflammation, human papilloma virus and dysplasia), using a consensus of histopathology opinion from two-board certified clinical pathologists and the diagnostic algorithms were tested using cross-validation, or the leave-one-out method.[84] However, biopsies exhibiting mixed pathologies were included in the study by correlating the spectral results with the most severe pathological diagnosis. This will have introduced discrepancies when measurements were made from undefined regions of the sample. Both empirical and multivariate discriminant algorithms were tested using cross-validation for the separation of pre-cancers and all other tissues. The multivariate method discriminated between the two groups with sensitivities and specificities of 82% and 92% respectively. However, poor system sensitivities required spectra to be measured for up to 15 minutes for adequate S/N ratios to be achieved.

A number of authors have studied colon tissue samples without demonstrating the use of a discriminant model for separation of samples into their histopathological groups. The makeup of the colon, including a high lipid concentration does tend to produce spectra with S/N ratios of around 3 times greater than those exhibited by the oesophagus and larynx.[142,176] Therefore shorter acquisition times will be possible in this organ. Comparison between spectra has generally involved study of the visible differences between Raman peaks from abnormal and normal specimens from the same patient. Interesting variations in scattering bands attributable to lipids, proteins and nucleic acids have been demonstrated. However more work is required to calibrate and test diagnostic algorithms in the colon.

Two publications have demonstrated the use of Raman spectral models for the discrimination of histopathology in the oesophagus.[142,133] Both groups have used only a single pathologist to grade their samples and heterogeneous samples have been included in the studies. Shim et al included 260 biopsy samples from 17 patients in their study. Pathologies included normal (54), Barrett's (153), and dysplastic (53). An artificial neural network (ANN) was trained and used to predict the group membership of the samples. Differentiation between dysplasia and intestinal metaplasia was achieved with 77% sensitivity and 93% specificity.[142] Only three groups were included in the study and cross-validation testing was not mentioned. Wolthius et al measured 320 spectra (80 normal, 120 Barrett's, 120 adenocarcinoma) of excised tissue from three patients. Cross-validation of an optimised linear discriminant model enabled sensitivities and specificities of 97% and 98% to be achieved for the separation of adenocarcinoma and Barrett's oesophagus. The difficult groups of high- and low-grade dysplasia were not included in the study. This compares with 96% sensitivity and 84% specificity for

discrimination between intestinal metaplasia and neoplastic oesophagus tissue (including both dysplasia and adenocarcinoma) described in this study with a dataset including spectra from eight pathology groupings. The results in this study indicate a high degree of sensitivity to neoplasia, but a slightly lower level of specificity because the introduction of dysplastic samples, with both biochemical and histological similarities to IM samples, has caused some IM to be falsely predicted as cancerous/pre-cancerous. However from a medical perspective a false positive result is better than a false negative, i.e. where a cancerous lesion is predicted as normal.

Only one study to date has performed in vivo Raman measurements on the human oesophagus and colon.[142] These have been obtained from 20 patients. However to date no accompanying spectral analysis has been published. S/N ratios of 3-5 and 4-17 were achieved for oesophagus and colon respectively using 100mW of 785nm laser light integrated for 5 seconds and a multi-fibre Visionex® probe. The ability to obtain spectra of sufficient quality in short timescales has demonstrated the feasibility of transferring models constructed from in vitro measurements to the prediction of pathology in vivo.

The results - from the study outlined in this thesis - for discrimination between histopathology types in oesophageal and laryngeal tissue compare extremely favourably with those published on Raman spectroscopy in similar tissues. The number of groups used in this study has also provided a better representation of the tissue types likely to be encountered in a randomly selected biopsy sample. Furthermore, much more rigorous and repeatable experimental protocols have been used throughout.

6.2 Future prospects

In principle Raman spectroscopic classification of diseases that exhibit a significant biochemical modification should be feasible in any tissue of which a spectrum can be measured. The exploitation of this technique will require multi-disciplinary teams in many centres to begin work investigating the differences exhibited in diseased and normal samples of all relevant tissues. To enable a full understanding of the complex medical and technological problems a collaboration between surgeons, histopathologists, scientists and engineers will be necessary.

There is significant difficulty in employment of an imperfect 'gold standard' for calibration of novel diagnostic techniques. Classification algorithms can only be as good as the training they receive. Moreover considering that histopathology is regarded as the correct diagnosis, it will be very difficult to demonstrate that a new technique provides a more accurate representation of the true diagnosis. Improvements in detection and diagnosis of cancers and pre-cancers using new technologies will only be possible if histopathological results are carefully interpreted, with the proviso that the 'gold standard' diagnosis it not necessarily correct. Furthermore, future development of quantitative biochemical measurements of tissue state such as immunohistochemical markers, including p53 and telomerase are likely to provide a more accurate, objective, and repeatable diagnosis for calibration or evaluation of model performance.[25]

The greatest obstacle to automated medical diagnosis will most likely be the transferability and repeatability of Raman spectra acquired with different systems. If automated diagnostic

algorithms are to be used in clinical practice, it will be necessary to provide an 'off the shelf' spectral library and sort algorithm for a particular disease or tissue type. However this implies that spectra measured on all other systems will be identical. This will never be the case. However, variations can be minimised and spectra can be corrected to achieve the ideal that is used for calibration of these classification models. Methods of correction for spectrometer variations have been described elsewhere.[177,178] Pre-processing of spectra has been shown to reduce the effects caused by spectrometer variations, especially during the collection of the laryngeal spectral data. These include shift correction, energy sensitivity correction, wave number calibration and smoothing filters.

There are some additional technical problems that need to be solved to enable routine use of Raman spectroscopy as an in vivo clinical tool. The use of fibre-optic systems based upon near-infrared diode laser illumination, filtered probes and a single spectrometer/CCD detector arrangement appear to be the most promising, although radical new designs may be necessary to eradicate the silica Raman signal. With quick integration times, due to high sensitivity and low tissue fluorescence background signal the NIR system appears to offer the greatest benefits for use in a clinical environment. Current in vivo probe designs tend to sample from the first few 100μms. However, NIR photons are highly scattered in tissue, therefore with improved understanding of photon migration in tissue, imaging of subsurface lesions may become possible.

Raman spectroscopy can be applicable to many different cancers in the human body, including those found in solid organs. Future prospects for in vivo measurements may eventually enable interrogation of scattering properties using needle probes within solid organs, provided that probes can be miniaturised to enable insertion down a needle. However, the greatest impact of Raman spectroscopy will be in the assistance of biopsy targeting during surveillance in organs that develop cancer via pre-cancerous lesions, such as ulcerative colitis in the colon, Barrett's metaplasia in the oesophagus, and infection with human papilloma virus in the cervix. In many cancers the early cellular changes will be invisible and detection will rely upon a random biopsy targeting procedure. Evidently there will be a fair chance of missing abnormal lesions and large numbers of biopsy samples will be generated for histopathology departments to process. The use of a non-invasive spectroscopic targeting method to pre-select samples would be likely to significantly improve detection rates and reduce the unnecessary collection of normal tissue samples.

Additional likely benefits of in vivo spectroscopic diagnosis include:

- Non-invasive biopsy targeting of organs where excision biopsy would be potentially hazardous, such as the central nervous and vascular systems.
- The prospect of immediate diagnosis that could reduce patient anxiety, secondary procedures, and health service costs by enabling treatments to be performed as part of the same procedure.
- Validation of diagnosis prior to resection to provide a safety net for catching mis-diagnosed conditions prior to the irreversible removal of tissue.

- Identification of tumour margins during resection, to reduce the risk of leaving malignant tissue behind and maximise the normal tissue remaining, thus optimising healing and minimising recurrence.
- Objective measurement of tissue disease state in comparison to the subjective pattern recognition of the current 'gold standard' technique.

A complimentary approach may involve the use of Raman spectroscopy coupled to a confocal microscope as a histopathology tool. This may eventually lead to automated sample sorting, which could be achieved with minimal changes to the current sample preparation procedures. Samples could potentially be analysed prior to sectioning and staining for histopathological analysis to remove the huge number of normal samples produced in these procedures, leaving the histopathologists to deal with the samples of clinical significance. Moreover the most significant problem for histopathology is the high inter- and intra-observer discrepancy during sample classification. Provided inter-system repeatability is evaluated and extensive work on diagnostic algorithm training has been performed, then a Raman pathology tool would be likely to assist pathologists in providing a repeatable diagnosis from one hospital centre to the next and thus increase the chances of the adoption of screening and surveillance tests. Both prospects will take time for acceptance by the medical community and large multi-centre trials will be required to demonstrate efficacy.

7. Conclusions and Further Work

7.1 Conclusions

This study has demonstrated the facility of NIR-Raman spectroscopy to discriminate between normal and squamous neoplasias (in the larynx and the oesophagus), and normal and columnar neoplasias (in the oesophagus), in both fresh and formalin fixed tissues. The results compare extremely favourably with those published on Raman spectroscopy in similar tissues. Moreover, the number of groups used in this study has also provided a better representation of the pathologies likely to be encountered in a randomly selected biopsy sample; more rigorous and repeatable experimental protocols have been used throughout.

Cross-validation testing of spectral predictive models has demonstrated excellent results, although further evaluation and optimisation is required. Repeatable discrimination has been demonstrated between pathological groups using linear discriminant models fed with statistically significant principal components of the spectral data. In the larynx 100/112 normal, 34/38 dysplastic, and 42/49 laryngeal squamous cell carcinoma sample spectra were correctly predicted. In the oesophagus consensus trained models, 301/310 normal, 122/145 Barrett's and 152/162 neoplastic spectra have been correctly predicted in the three group models. Raman spectra of other epithelial tissues studied including tonsil, stomach, bladder, prostate, and endometrium exhibit similar features to the spectra from the larynx and oesophagus. It is expected that further study of specimens from these organs will enable spectral separation of normal and diseased states to be demonstrated.

There is a lack of understanding of the extremely complex biochemical processes preceding and accompanying carcinogenesis. Studies such as this one investigating essentially the differences in biochemistry between diseased and normal states can only enhance the knowledge base of medicine and science in this important area, as well as provide evidence of the potential of new tools for non-invasive optical diagnosis of cancer. Much of the work to date has demonstrated proof-of-principle, however the time has come for more extensive studies to push this exciting technology towards medical reality. The evidence provided by this study indicates that use of Raman spectroscopy for non-invasive detection and classification of disease is a distinct possibility. Potential difficulties in the transferability from in vitro to in vivo have been evaluated and no significant barriers have been observed. However, further in vivo probe development and optimisation will be required before 'optical biopsy' with Raman spectroscopy can become a reality.

7.2 Further Research

The following investigations would enhance and validate the results of the work performed in this thesis. A lack of time and tissue specimens has made these difficult to perform as part of this work.

- Validation of results with new homogeneous tissue samples with a consensus of histopathology opinion.
- Re-evaluation of tissue samples by histopathologists to improve consensus of opinion on discarded samples.

- Assessment of the outcome of measuring and predicting the pathology of samples exhibiting mixed histopathologies.
- Evaluation of the sample numbers required for optimum model construction, by increasing model sizes iteratively and evaluating performance at each stage.
- Evaluation of the effects on prediction model performance of low S/N ratio spectra, wavenumber shifts and changes to the spectral baseline shape. This would provide an understanding of the required tolerances of spectrometers for measurement of data for prediction against the spectral models.
- Evaluation of inter-spectrometer repeatability and methods of correction for the improvement of transferability.
- Model optimisation by utilisation of
    - Polarisation discrimination to selectively enhance or suppress spectral components.
    - Weighted algorithms to enhance the importance of particular pathology groups, such as adenocarcinoma or high-grade dysplasia, to reduce the chances of falsely predicting samples from these clinically significant groups as something more benign. Risk analysis would be required to provide the weights of risk of missing a particular condition. However different applications will require different algorithm architectures.
    - Staggered algorithms to reduce the reliance of the models on artificially created boundaries from one group to the next, which may have some detrimental effect on the separation. This could be achieved by making a decision between membership of between two to three groups at a time in stages to create a classification tree. For example a decision between squamous or columnar tissue, then if columnar, a decision between Barrett's or neoplasia, then if neoplasia, a decision between LGD, HGD or adenocarcinoma.
    - Spectral region selection may improve discrimination by removing irrelevant data. This will have to be carefully performed and may be detrimental to model specificity.
    - Pre-processing filtering using first and second order derivatives as well as smoothing functions may improve models by reducing the effects of poor spectrometer repeatability. This was demonstrated for the larynx model.

Of medical interest:

- Confocal Raman spectral mapping of tissue sections from different stages of carcinogenesis will enable a further understanding of the biochemical disease processes to be achieved. Co-registration of the spectral information with an image captured of the haemotoxylin and eosin stained sections would facilitate the use of multivariate image analysis to identify biochemical regions of interest in

the tissue. This technique will also identify whether different sampling volumes and depths may facilitate further improvements in discrimination between pathology states by demonstrating where in the tissue the most significnat biochemical changes occur.

- Retrospective studies, whereby tissue spectra measured from patients that have gone on to develop cancer could be used to identify which biochemical changes precede the development of morphological and architectural changes. For example samples that were wrongly predicted initially (in relation to histopathology) may have originated in samples from patients who were undergoing the biochemical development of cancer.

References

[1] *Cancer Statistics 1993 England and Wales*, Series MB1, **26**, TSO, Office for National Statistics, 29th November 1999.

[2] *Cancer Survival 1991-1998*, Office for National Statistics web page: 'http://www.ons.gov.uk', 31st March 2000.

[3] Virckow, R, *Cellular Pathology as Based on Histology*, 1850.

[4] Melville, DM, Jass, JR, Merson, BC, Pollock, Dj, Richman, PI, Shepherd, NA, Ritchie, JK, Love, SB, Lennard-Jones, JE, Observer Study of the Grading of Dysplasia in Ulcerative Colitis: Comparison with Clinical Outcome, *Hum. Pathol.*, **20**, 1008-1014, 1998.

[5] Jensen, P, Krogsgaard, MR, Christiansen, J, Braendstrup, O, Johansen, A, Olsen, J, Observer Variability in the Assessment of Type and Dysplasia of Colorectal Adenomas Analysed using Kappa Statistics, *Dis. Colon Rectum*, **38**, 195-198, 1995.

[6] Reid, BJ, Haggitt, RC, Rubin, CE, Roth, G, Surawicz, CM, Van Belle, G, Lewin, K, Weinstein, WM, Antonioli, DA, Goldman, H, MacDonald, W, Owen, D, Observer Variation in the Diagnosis of Dysplasia in Barrett's Oesophagus, *Human Pathology*, **19**, 2, 166-178, 1988.

[7] Blackwell, KE, Calcaterra, TC, Fu, Y-S, Laryngeal Dysplasia: Epidemiology and Treatment Outcome, *Ann Otol Rhinol Laryngol*, **104**, 596-602, 1995.

[8] Van Sandick, JW, van Lanshot, JJ, Kuiken, BW, Tytgat, GN, Offenhaus, GJ, Obertop, H, Impact of Endoscopic Biopsy Surveillance of Barrett's Oeophagus on Pathological Stage and Clinical Outcome of Barrett's Carcinoma, *Gut*, **43**, 216-222, 1998.

[9] Bohorfoush, AG, Tissue Spectroscopy for Gastrointestinal Diseases, *Endoscopy*, **28**, 372-380, 1996.

[10] Andrea M, Dias O, Santos A. Contact endoscopy during microlaryngeal surgery: a new technique for endoscopic examination of the larynx. *Ann Otol Rhinol Laryngol*, **104**, 5, 333-339, 1995.

[11] Alfano, RR, Tang, GC, Pradhan, A, Lam, W, Choy, DSJ, Opher, E, Fluorescence Spectra from Cancerous and Normal Human Breast and Lung Tissues, *IEEE Journal of Quantum Electronics*, **23**, 1806-1811, 1987.

[12] Andersson-Engels, S, Johansson, J, Svanberg, K, Svanberg, S, Fluorescence Imaging and Point Measurements of Tissue: Applications to the Demarcation of Malignant Tumours and Atherosclerotic Lesions, *Photochemistry and Photobiology*, **53**, 807-814, 1991.

[13] Panjehpour, M, Overholt, R, Vo-Dinh, T, Haggit, RC, Edwards, DH, Buckley, PF, Endoscopic Fluorescence Detection of High-Grade Dysplasia in Barrett's Oesophagus, *Gastroenterology*, **111**, 93-101, 1996.

[14] Redd, DCB, Feng, ZC, Yue, KT, Gansler, TS, Raman Spectrscopic Characterization of Human Breast Tissues: Implications for Breast Cancer Diagnosis, *Applied Spectroscopy*, **47**, 6, 787-791, 1993.

[15] Liu, CH, Das, BB, Glassman, WLS, Tang, GC, Yoo, KM, Zhu, HR, Akins, DL, Lubicz, SS, Cleary, J, Prudente, R, Celmere, E, Caron, A, Alfano, RR, Raman, Fluorescence, and Time-Resolved Light-Scattering as Optical Diagnostic-Techniques to Separate Diseased and Normal Biomedical Media, *Journal of Photochemistry and Photobiology B: Biology*, **16**, 2, 187-209, 1992.

[16] Mahadevan-Jansen A, Richards-Kortum R. Raman spectroscopy for the detection of cancers and precancers. *J Biomed Opt*, **1**, 31-70, 1996.

[17] Barr H, Dix T, Stone N. Optical spectroscopy for the early diagnosis of gastrointestinal malignancy. Review. *Lasers Med Sci*, **13**, 3-13, 1998.

[18] Williams KPJ, Pitt GD, Batchelder DN, Kip BJ. Confocal Raman microspectroscopy using a stigmatic spectrograph and CCD detector, *Applied Spectroscopy*, **48**(2), 232-235, 1994.

[19] Yazdi, Y, Ramanujam, N, Lotan, R, Mitchell, MF, Hittelman, W, Richards-Kortum, R, Resonance Raman Spectroscopy at 257nm Excitation of Normal and Malignant Cultured Breast and Cervical Cells, *Applied Spectroscopy*, **53**, 1, 82-85, 1999.

[20] Alfano, RR, Liu, CH, Sha, WL, Zhu, HR, Akins, DL, Cleary, J, Prudente, R, Cellmer, E, Human Breast Tissue Studied by IR Fourier Transform Raman Spectroscopy, *Lasers in the Life Sciences*, **4**, 1, 23-28, 1991.

[21] Bakker Schut TC, Stone N, Fulljames C, Barr H, Bruining HA, Puppels GJ. Progress in the detection of neoplastic progress and cancer by Raman spectroscopy. *Proc SPIE Biomedical Spectroscopy: Vibrational Spectroscopy and Other Novel Techniques*, **3918**, 2000.

[22] Hameetemaan, W, Tygat, GNJ, Houthoff, HJ, van den Tweel JG, Barrett's Oesophagus: Development of Dysplasia and Adenocarcinoma, *Gastroenterology*, 1989; **96**:1249.

[23] *Cancer Statistics Registrations: Registrations of Cancer Diagnosed in 1993, England and Wales.*, Office for National Statistics, Series MB1, 1999; **26**, 40-41, London: The Stationary Office.

[24] Tortora, GJ, Grabowski, SR, *Principles of Anatomy and Physiology*, 8th Edition, Biological Sciences Textbooks, Inc., HarperCollins, New York, 1996.

[25] Jankowski, JA, Harrison, RF, Perry, I, Balkwill, F, Tselepis, C, Barrett's Metaplasia, *Lancet*, **356**, 2079-2085, 2000.

[26] Winters, C, Jr., Spurling, TJ, Chobanian SJ, Curtis, DJ, Eposito, RL, Hacker, JF, 3rd., Johnson, DA, Cruess, DF, Coteligam, JD, Gurney, MS, Barrett's Oesophagus: A Prevalent, Occult Complication of Gastroesophageal Reflux Disease, *Gastroenterology*, **92**, 1, 118-124, 1987.

[27] Mann, NS, Tsai, MF, Nair, PK, Barrett's Esophagus in Pateints With Symptomatic Reflux Esophagitis, *Am J Gastroenterol*, **84**, 1494-1496, 1989.

[28] Paull, A, Trier, J, Dalton, M, Camp, R, Loeb, P, Goyal, R, The Histological Spectrum of Barrett's Oesophagus, *N Engl J Med*, **295**, 476-480, 1976.

[29] Hershfield NB, Line JF, Hildes, JA, McMorris, LS, Secretory Function of Barrett's Epithelium, *Gut*, **6**, 535-539, 1965.

[30] Naef AP, Savary M, Ozzelo L, Columnar-lined Lower Oesophagus: An Acquired Lesion With Malignant Predisposition, *J Thorac Cardiovasc Surg*, **70**, 826-835, 1975.

[31] Berenson MM, Riddell RH, Skinner DB, Freston JW, Malignant Transformation of Oesophageal Columnar Epithelium, *Cancer*, **41**, 554-561, 1978.

[32] Spechler SJ, Goyal RK, Barrett's Oesophagus, *N Engl J Med*, **315**, 362, 1986.

[33] Riddell RH, Dysplasia and Regression in Barrett's Epithelium. In: Spechler SJ, Goyal RK, eds. *Barrett's Esophagus: Pathophysiology, Diagnosis, and Management*. New York, Elsevier Science, 188-197, 1985.

[34] Cameron, AJ, Epidemiology of Columnar-Lined Esophagus and Adenocarcinoma, *Gastroenterology Clinics of North America*, **26**, 3, 487-494, 1997.

[35] Van der Veen, AH, Dees, J, Blankensteijn, JD, Van Blankensteijn, M, Adenocarcinoma in Barrett's Oesophagus: An Overrated Risk, *Gut*, **30**, 14-18, 1989.

[36] Gelfand GEJ, Finley, RJ, Nelems, B, et al, Transhiatal Esophagectomy For Carcinoma of the Esophagus and Cardia, *Arch Surg*, **127**, 1164, 1992.

[37] Ramamim, J, Cham, CW, Oesophagectomy for Carcinomma of the Oesophagus and Cardia, *Br J Surg*, **80**, 1305, 1993.

[38] Hesketh PJ, Clapp RW, Doos WG, Spechler SJ, The Increasing Frequency of Adenocarcinoma of the Oesophagus, *Cancer*, **64**, 526, 1989.

[39] Blot, WJ, Devesa, SS, Fraumeni, JF, Continued Climb in Rates of Esophageal Adenocarcinoma: An Update, *JAMA*, **270**, 1320, 1993.

[40] Sjögren RW, Johnson LF, Barrett's Esophagus: A Review, *Am J Med*, **74**, 3131, 1983.

[41] Haggitt RC, Dean PJ, Adenocarcinoma in Barrett's Epithelium, In: Spechler SJ, Goyal RK, eds. *Barrett's Esophagus: Pathophysiology, Diagnosis, and Management*, New York, Elsevier Science, 153-166, 1985.

[42] Sanfey, H, Hamilton, SR, Smith, RRL, Cameron JL, Carcinoma arising in Barrett's Oesophagus, *Surg Gynecol Obstet*, **161**, 570,1985.

[43] Reid, BJ, Rubin, CE, When is the Columnar-lined Esophagus Premalignant? (abstract), *Gastroenterology*, **88**, 1152, 1985.

[44] Smith RRL, Boitnott JK, Hamilton SR, Rogers EL, The Spectrum of Carcinoma Arising in Barrett's Esophagus, *Am J Surg Pathol*, **8**, 563-573, 1984.

[45] Miros M, Kerlin P, Walker N, Only Patients With Dysplasia Progress to Adenocarcinoma in Barrett's Oesophagus, *Gut*, **32**, 1441-1446, 1991.

[46] DeMeester TR, Atwood SEA, Smyrk TC, Therkildsen DH, Hinder RA, Surgical Therapy in Barrett's Esophagus, *Ann Surgery*, **212**, 528-542, 1990.

[47] Altorki NK, Sunagawa M, Little AG, Skinner DB, High-grade Dysplasia in Columnar-lined Esophagus, *Am J Surg*, **161**, 97-100, 1991.

[48] Petras, RE, Sivak Jr., MV, Rice TW, Barrett's Esophagus: A Review of the Pathologist's Role in Diagnosis and Management, *Pathol Am*, **26**, 1-32, 1991.

[49] Robertson, CS, Mayberry, JF, Nicholson, DA, et al., Value of Endoscopic Surveillance in the Detection of Neoplastic Change in Barrett's Oesophagus, *Br J Surg*, **75**, 760, 1988.

[50] Reid, BJ, Weinstein, WM, Lewin, KJ, et al. Endoscopic Biopsies Can Detect High-grade Dysplasia or Early Adenocarcinoma in Barrett's Oesophagus Without Grossly Recognizable Neoplastic Lesions, *Gastroenterology*, **94**, 81, 1988.

[51] Lee, RG, Dysplasia in Barrett's Oesophagus. A Clinicopathological Study of Six Patients, *Am J Surg Pathol*, **9**, 845, 1985.

[52] Reid BJ, Blount PL, Rubin CE, Levine DS, Haggitt RC, Rabinovich PS, Flow-cytometric and Histological Progression to Malignancy in Barrett's Esophagus: Prospective Endoscopic Surveillance of a Cohort, *Gastroenterology*, **102**, 1212-1219, 1992.

[53] Palmer, JM, *Anatomy for Speech and Hearing*, 4th Edition, Williams and Wilkins, Baltimore, USA, 119, 1993.

[54] Gabriel, CE, Jones, DG, The Importance of Chronic Laryngitis, *J Laryngol Otol*, **74**, 349-357, 1960.

[55] Ward PH, Berci, G, Observations on the Pathogenesis of Chronic Non-specific Pharyngitis and Laryngitis, *Laryngoscope*, **92**, 1377-1382, 1982.

[56] Robin PE, Reid A, Powell DJ, McConkey CC. The incidence of cancer of the larynx. *Clin Otolaryngol*, **16**, 198-201, 1991.

[57] Coleman, MP, Babb, P, Damiecki, P, Grosclaude, P, Honjo, S, Jones, J, Knerer, G, Pitard, A, Quin, M, Sloggett, A, De Stavola, B, *Cancer Survival Trends in England and Wales, 1971-1998: Deprivation and NHS Region*, Studies in medical and Population Subjects, **61**, Office for National Statistics, London: The Stationary Office.

[58] Muir C, Weiland L. Upper aerodigestive tract cancers. *Cancer*, **75**(suppl), 147-153, 1995.

[59] Hellquist, H, Lundgren, J, Olofsson, J, Hyperplasia, Keratosis, Dysplasia and Carcinoma In Situ of the Vocal Cords – A Follow-up Study., *Clin Otolaryngol*, **7**, 11-27, 1982.

[60] Silamniku, B, Bauer, W, Painter, C, Sessions, D, The Transformation of Laryngeal Keratosis Into Invasive Carcinoma, *Am J Otolaryngol*, **10**, 42-54, 1989.

[61] Crissman, JD, Laryngeal Keratosis and Subsequent Carcinoma, *Head Neck Surgery*, **1**, 386-391, 1979.

[62] Marchesini, R, Light Induced Fluorescenece Spectroscopy of Adenomas, Adenocarcinomas and Non-Neoplastic Mucosa in Human Colon, *Journal of Photochemistry and Photobiology B*, **14**, 219-230, 1992.

[63] Chung, W, Shwartz, J, Gardner, C, Sawaya, R, Jacques, SL, Fluorescence of Normal and Cancerous Brain Tissues: The Excitation/Emission Matrix, *Proc. SPIE:Advances in Laser and Light Spectroscopy to Diagnose Cancer and Other Diseases*, **2135**, 66-75, 1995.

[64] Sterenborg, HJCM, Motamedi, M, Wagner, RF, Duvic, M, Thomsen, S, Jacques, SL, In Vivo Fluorescnece Spectroscopy and Imaging of Human Skin Tumours, *Lasers in Medical Science*, **9**, 191-201, 1994.

[65] DaCosta, RS, Wilson, BC, Marcon, NE, Light-Induced Fluorescence Endoscopy of the Gastrointestinal Tract, *Gastrointestinal Endoscopy*, **10**, 1, 37-69, 2000.

[66] Mourant, JR, Bigio, IJ, Boyer, JD, Johnson, TM, Lacey, J, Bohorfoush, AG, Elastic Scattering Spectroscopy as a Diagnostic Tool for Differentiating Pathologies in the Gastrointestinal Tract, *Journal of Biomedical Optics*, **1**, 192-199, 1996.

[67] Backman, V, Wallace, MB, Perelman, LT, Arendt, JT, Gurjar, R, Muller, MG, Zhang, Q, Zonios, G, Kline, E, McGillican, Shapshay, S, Valdez, T, Badizadegan, K, Crawford, JM, Fitzmaurice, M, Kabani, S, Levin, HS, Seiler, M, Dasari, RR, Itzkan, I, Van Dam, J, Feld, MS, Detection of Pre-invasive Cancer Cells: Early-warning changes in precancerous epithelial cells can now be spotted in situ, *Nature*, **406**, 35-36, 2000.

[68] Tearney, GJ, Brezinski, ME, Bouma, BE, In Vivo Endoscopic Optical Biopsy with Optical Coherence Tomography, *Science*, **276**, 2037-2039, 1997.

[69] Kobayashi, K, Izatt, JA, Kulkarni, MD, Willis, J, Sivak, MV, High Resolution Cross-Sectional Imaging of the Gastrointestinal Tract Using Optical Coherence Tomography: Preliminary Results, *Gastrointestinal Endoscopy*, **47**, 515-523, 1998.

[70] Mantsch, HH, Eysel, H, Jackson, M, Liu, K-Z, Mansfield, JR, Schultz, C, Shaw, RA, Sowa, M, Emerging Medical Applications of Infrared Technologies, In: *Spectroscopy of Biological Molecules: Modern Trends*, Ed by Carmona, P, Navarro, R, Hernanz, A, Kluwer Academic Publishers, 421-424, 1997.

[71] Lasch, P, Naumann, D, FT-IR Microspectroscopic Imaging of Human Carcinoma Tissue Thin Sections, In: *Spectroscopy of Biological Molecules: Modern Trends*, Ed by Carmona, P, Navarro, R, Hernanz, A, Kluwer Academic Publishers, 441-442, 1997.

[72] Yano, K, Moriguchi, T, Ohoshima, S, Shimizu, Y, Katayama, H, Determination of Glycogen Levels in Human Lung Cancer and Normal Tissues by Fourier-Transform Infrared Spectroscopy, In: *Spectroscopy of Biological Molecules: Modern Trends*, Ed by Carmona, P, Navarro, R, Hernanz, A, Kluwer Academic Publishers, 443-444, 1997.

[73] Cooney, KM, Gossage, KW, McShane, MJ, Cote, GL, Motamedi, M, van der Breggen, WJ, Detection of Spectral Differences Between Normal and Cancerous Oral Tissue Using Near-infrared Spectroscopy, Proc. OSA TOPS: *Biomedical Optical Spectroscopy and Diagnostics / Therapeutic Laser Applications*, **22**, 96-98, 1998.

[74] McIntosh, LM, Jackson, M, Mantsch, HH, Stranc, MF, Pilavdzic, D, Crowson, AN, Infrared Spectra of Basal Cell Carcinomas Are Distinct From Non-Tumor-Bearing Skin Components, *Journal of Investigative Dermatology*, **112**, 951-956, 1999.

[75] Richards-Kortum, R, Sevick-Muraca, E, Quantitative Optical Spectroscopy for Tissue Diagnosis, *Annu. Rev. Phys. Chem.*, **47**, 555-606, 1996.

[76] Fulljames C, Stone N, Bennett D, Barr H. Beyond white light endoscopy – the prospect for endoscopic optical biopsy. *Italian Journal Gastroenterology and Hepatology*, **31**, 695-704, 1999.

[77] Mahadevan, A, Ramanujam, N, Mitchell, MF, Malpica, A, Thomsen, S, Richards-Kortum, R, Optical Techniques for the Diagnosis of Cervical Precancers: A Comparison of Raman and Fluorescence Spectroscopies, *Proc. SPIE: Advances in Fluorescence Sensing Technology II*, **2388**, 110-120, 1995.

[78] Halliday, K, Sillerud, L, Fenoglio-Preiser, C, Carbon^{13} and Proton Nuclear Magnetic Resonance Spectroscopy and Microscopy of Neoplasms, *Advanced Pathology*, **2**, 213-258, 1989.

[79] Puppels, GJ, van Aken, T, Wolthius, R, Caspers, PJ, Bakker Schut, TC, Bruining, HA, Romer, TJ, Buschman, HPJ, Wach, ML, Robinson, JS, Jr, In Vivo Tissue Characterisation by Raman Spectroscopy, *Proc. SPIE: Infrared Spectroscopy: New Tool in Medicine*, **3257**, 78-83, 1998.

[80] Shim, MG, Wilson, BC, Marple, E, Wach M. Study of fibre-optic probes for in vivo medical Raman spectroscopy. *Applied Spectroscopy*, **53**, 619-625, 1999.

[81] Feld, MS, Manoharan, R, Salenius, J, Orenstein-Carndona, J, Romer, TJ, Brennan, JF, Dasari, R, Wang, Y, Detection and Characterization of Human Tissue lesions with Near-Infrared Raman Spectroscopy, *Proc. SPIE: Advances in Fluorescence Sensing Technology II*, **2388**, 99-104, 1995.

[82] Manoharan, R, Shafer, K, Perelman, L, Wu, J, Chen, K, Deinum, G, Fitzmaurice, M, Myles, J, Crowe, J, Dasari, RR, Feld, MS, Raman Spectroscopy and Fluorescence Photon

Migration for Breast Cancer Diagnosis and Imaging, *Photochemistry and Photobiology*, **67**, 15-22, 1998.

[83] Mizuno A, Kitajima H, Kawauchi K, Muraishi S, Ozaki Y. Near-infrared Fourier transform Raman spectroscopic study of human brain tissues and tumors. *J Raman Spectrosc*, **25**, 25-29, 1994.

[84] Mahadevan-Jansen, A, Mitchell, MF, Ramanujam, N, Malpica, A, Thomsen, S, Utzinger, U, Richards-Kortum, R, Near-infrared Raman Spectroscopy for In Vitro Detection of Cervical Precancers, *Photochemistry and Photobiology*, **68**, 123-132, 1998.

[85] Gniadecka M, Wulf HC, Nielsen OF, Christensen DH, Hercogova J. Distinctive molecular abnormalities in benign and malignant skin lesions: studied by Raman spectroscopy. *Photochem Photobiol*, **66**, 418-423, 1991.

[86] Manoharan, R, Wang, Y, Dasari, RR, Singer, SS, Rava, RP, Feld, MS. Ultraviolet Resonance Raman Spectroscopy for Detection of Colon Cancer. *Lasers in the Life Sciences*, **6**, 4, 217-227, 1995.

[87] Raman, CV, Krishnan, KS, A New Type of Secondary Radiation, *Nature*, **121**, 501, 1928.

[88] Maiman, TH, *Nature*, **187**, 493, 1960.

[89] Yu NT, East EJ. Laser Raman spectroscopic studies of ocular lens and its isolated protein fractions. *J. Biol. Chem.*, **250**, 2196-2202, 1975.

[90] Wang SY, Hasty CE, Watson PA, Wicksted JP, Stith RD, March WF. Analysis of metabolites in aqueous solutions by using laser Raman spectroscopy. *Appl. Opt.*, **32**(6), 925-929, 1993.

[91] Manoharan R, Wang Y, Feld MS, Histochemical analysis of biological tissues using Raman spectroscopy. *Spectrochimica Acta Part A*, **52**, 215-249, 1996.

[92] Baraga JJ, Feld MS, Rava RP. Rapid Near-Infrared Raman Spectroscopy of Human Tissue with a Spectrograph and CCD Detector. *Appl. Spect.*, **46**(2), 187-190, 1992.

[93] Manoharan, R, Wang, Y, Boustany, N, Brennan III, JF, Baraga, JJ, Dasari, RR, Van Dam , J, Singer, S, Feld, MS, Raman Spectroscopy for Cancer Detection: Instrument Development and Tissue Diagnosis, *Proc. SPIE: Biomedical Optoelectronic Devices and Systems II*, **2328**, 128-132, 1994.

[94] Frank, CJ, Applications of Near-Infrared Raman Spectroscopy to the Study of Human Tissue Specimens, *PhD Thesis*, Ohio State University, 1994.

[95] Hendra, PJ, Ellis, G, Cutler, DJ, Use of Optical Fibres in Raman Spectroscopy, *Journal of Raman Spectroscopy*, **19**, 413-418, 1988.

[96] Lord, RC, Yu, N-T, Laser-Excited Raman Spectroscopy of Biomolecules I. Native Lysozyme and its Constituent Amino Acids, *Journal of Molecular Biology*, **50**, 509, 1970.

[97] Hartman, KA, Clayton, NW, Thomas, GJ, Jr., Studies of Virus Structure by Raman Spectroscopy, *Biochemical and Biophysical Research Communications*, **50**, 942, 1973.

[98] Carey, PR, Chapter 4: Protein Conformation from Raman and Resonance Raman Spectra, *Biochemical Applications of Raman and Resonance Raman Spectroscopies*, Academic Press, 1982.

[99] Miura, T, Thomas, GJ, Jr., Raman Spectroscopy of Proteins and Their Assemblies, Chapter 3 in *Subcellular Biochemistry, Volume 24. Proteins, Structure, and Engineering*, ed. by Biswas, BB, Roy, S, Plenum Press, New York, 1995.

[100] Adar, F, Erecinska, M, *Biochemistry*, **17**, 5484, 1978.

[101] O'Shea, DC, Bartlett, ML, Young, RA, *Arch. Oral Biol.*, **19**, 995, 1974.

[102] Tsuda, H, Arends, J, Raman Spectroscopy in Dental Research: A Short Review of Recent Studies, *Advances in Dental Research*, **11**, 4, 539-547, 1997.

[103] Yu, N-T, Jo, BH, Chang, RCC, Huber, JD, *Arch. Biochem. Biophys.*, **160**, 614, 1974.

[104] Larsson, K, Hellgren, L, A Study of the Combined Raman and Fluorescence Scattering from Human Blood Plasma, *Experientia*, **30**, 481-483, 1974.

[105] Plouvier, SR, Huong, PV, Microbial Chromophore Materials in Circulating Blood Identified by Laser Micro Raman Spectroscopy, *Biorheology*, **Suppl. I**, 345-347, 1984.

[106] Delhaye, M, Dhamelincourt, P, Raman Microprobe and Microscope with Laser Excitation, *Journal of Raman Spectroscopy*, **3**, 33-43, 1975.

[107] Abraham, JL, Etz, ES, Molecular Microanalysis of Pathological Specimens In Situ with a Laser Raman Microprobe, *Science*, **206**, 716-718, 1979.

[108] Buiteveld, H, De Mul, FFM, Mud, J, Greve, J, *Applied Spectroscopy*, **38**, 304, 1984.

[109] Ishida, H, Kamoto, R, Uchida, S, Ishitani, A, Ozaki, Y, Iriyama, K, Tsukie, E, Shibata, K, Ishihara, F, Kameda, H, *Applied Spectroscopy*, **41**, 407, 1987.

[110] Caille, J-P, Pigeon-Gosselin, M, Pezolet, *Biochim. Biophys. Acta*, **758**, 121, 1983.

[111] Hoey, S, Brown, DH, McConnell, AA, Smith, WE, Marabani, M, Sturrock, RD, Resonance Raman Spectroscopy of Hemoglobin in Intact Cells: A Probe of Oxygen Uptake by Erythrocytes in Rheumatoid Arthritis, *Journal of Inorganic Biochemistry*, **34**, 189-199, 1988.

[112] Williamson, JM, Bowling, RJ, McCreery, RL, Near-Infrared Raman Spectroscopy with a 783nm Diode Laser and CCD Array Detector, *Applied Spectroscopy*, **43**, 3, 372-375, 1989.

[113] Wang, Y, McCreery, RL, Evaluation of a Diode-Laser Charge Coupled Device Spectrometer for Near-Infrared Raman Spectroscopy, *Analytical Chemistry*, **61**, 2647-2651, 1989.

[114] Puppels, GJ, DeMul, FFM, Otto, C, Greve, J, Robert-Nicoud, M, Arndt-Jovin, DJ, Jovin, TM, Studying Living Cells and Chromosomes by Confocal Raman Microspectroscopy, *Nature*, **347**, 301-303, 1990.

[115] Puppels, GJ, Otto, C, Greve, J, Confocal Raman Microspectroscopy in Biology: Applications and Future Developments, *Trends in Analytical Chemistry*, **10**, 8, 249-253, 1991.

[116] Alfano, RR, Liu, CH, Glassman, WS, *US Patent* **5 261 410**, 1993.

[117] Frank CJ, McCreery RL, Redd DCB. Raman Spectroscopy of Normal and Diseased Human Breast Tissues. *Anal. Chem.*, **67**, 777-783, 1995.

[118] Redd, DCB, Frank, CJ, Feng, ZC, Gansler, TS, McCreery, RL, Raman Spectroscopic Characterization of Human Malignant Tissues: Implications for a Percutaneous Optical Biopsy Technique for In-Situ Tissue Diagnosis, *Proc SPIE: Optical Biopsy*, **2081**, 185-189, 1993.

[119] Frank, CJ, Redd, DCB, Gansler, TS, McCreery RL, Characterization of Human Breast Biopsy Specimens with Near-IR Raman Spectroscopy, *Anal. Chem.*, **66**, 319-326, 1994.

[120] McCreery, RL, Frank, CJ, Redd, DCB, Raman Spectroscopy of Human Biopsy Specimens, *Proc. SPIE: Advances in Fluorescence Sensing Technology II*, **2388**, 90-97, 1995.

[121] Lieber, CA, Molpus, K, Brader, K, Mahadevan-Jansen, A, Diagnostic Tool for Early Detection of Ovarian Cancers using Raman Spectroscopy, *Proc. SPIE: Biomedical Spectroscopy: Vibrational Spectroscopy and Other Novel Techniques*, **3918**, 129-134, 2000.

[122] Feld, MS, Manoharan, R, Wang, Y, Dasari, RR, UV Resonance and NIR Raman Scattering for Tissue Diagnosis and Optical Histochemistry, *Proceedings of the Fourteenth International Conference on Raman Spectroscopy*, Section 5: Biomedical Applications, 194-195, Hong Kong, 1994.

[123] Boustany, NN, Manoharan, R, Dasari, RR, Feld, MS, Analysis of Normal and Diseased Colon Mucosa Using Ultraviaolet Resonance Raman Spectroscopy, *Proc. SPIE:Advances in Laser and Light Spectroscopy to Diagnose Cancer and Other Diseases III: Optical Biopsy*, **2679**, 66-70, 1996.

[124] Boustany, NN, Manoharan, R, Dasari, RR, Feld, MS, Ultraviolet Resonance Raman Spectroscopy of Bulk and Microscopic Human Colon Tissue, *Applied Spectroscopy*, **54**, 24-30, 2000.

[125] Keller, S, Schrader, B, Hoffmann, A, Schrader, W, Metz, K, Rehlaender, A, Pahnke, J, Ruwe, M, Budach, Application of Near-Infrared-Fourier Transform Raman Spectroscopy in Medical Research, *Journal of Raman Spectroscopy*, **25**, 663-671, 1994.

[126] Hawi SR, Campbell WB, Kajdacsy-Balla A, Murphy R, Adar F, Nithipatikom K, Characterization of Normal and Malignant Human Hepatocytes by Raman Microspectroscopy, *Cancer Letters*, **110**, 35-40, 1996.

[127] Gniadecka, M, Wulf, HC, Mortensen, NN, Nielsen, OF, Christensen, DH, Diagnosis of Basal Cell Carcinoma by Raman Spectroscopy, *Journal of Raman Spectroscopy*, **28**, 2-3, 125-129, 1997.

[128] Gniadecka, M, Wulf, HC, Nielsen, OF, Christensen, DH, Hercogova, J, Potential of NIR-FT Raman Spectroscopy for Diagnosis of Malignant Melanoma, In: *Spectroscopy of Biological Molecules: Modern Trends*, Ed by Carmona, P, Navarro, R, Hernanz, A, Kluwer Academic Publishers, 449-450, 1997.

[129] Gniadecka, M, Nielsen, OF, Christensen, DH, Wulf, HC, Structure of Water, Proteins, and Lipids in Intact Human Skin, Hair, and Nail, *The Journal of Investigative Dermatology*, **110**, 4, 1998.

[130] Caspers, PJ, Lucassen, GW, Wolthuis, R, Bruining, HA, Puppels, GJ, In Vitro and In Vivo Raman Spectroscopy of Human Skin, *Biospectroscopy*, **4**, S31-S39, Supplement S, 1998.

[131] Sajid, J, Elhaddaoui, A, Turrell, S, Fourier Transform Vibrational Spectroscopic Analysis of Human Cerebral Tissue, *Journal of Raman Spectroscopy*, **28**, 165-169, 1997.

[132] Bakker Schut, TC, Van Dekken, H, Tilanus, HW, Bruining, HA, Puppels, GJ, NIR Raman Spectroscopy of Healthy and Diseased Oesophagus, In: *Spectroscopy of Biological Molecules: Modern Trends*, Ed by Carmona, P, Navarro, R, Hernanz, A, Kluwer Academic Publishers, 455-456, 1997.

[133] Wolthius, R, Bakker Schut, TC, Caspers, PJ, Buschman, HPJ, Romer, TJ, Bruining, HA, Puppels, GJ, Raman Spectroscopic Methods for In Vitro and In Vivo Tissue Characterization, In: *Fluorescent and Luminescent Probes*, 2nd edition, Edited by Mason, WT, Chapter 32, 433-455, 1999.

[134] Shim, MG, Song, L-MWK, Marcon, N, Hassaram, S, Wilson, BC, Assessment of Ex Vivo and In Vivo Near-Infrared Raman Spectroscopy for the Classification of Dysplasia Within Barrett's Esophagus, *Proc. SPIE: Biomedical Spectroscopy: Vibrational Spectroscopy and Other Novel Techniques*, **3918**, 114-119, 2000.

[135] Manfait, M, Lamaze, P, Lamfarraj, H, Pluot, M, Sockalingum, GD, Diagnosis and Prognosis of Tissue Pathologies by Raman Microspectroscopy: An Application to Human Thyroid Tumours, *Proc. SPIE: Biomedical Spectroscopy: Vibrational Spectroscopy and Other Novel Techniques*, **3918**, 153-160, 2000.

[136] Nie, S, Yu, N-T, Raman-Based Biomedical Diagnosis at the Molecular Level, *Proceedings of the Fourteenth International Conference on Raman Spectroscopy*, Section 5: Biomedical Applications, 198-199, Hong Kong, 1994.

[137] Myrick ML, Angel SM. Elimination of background in fibre-optic Raman measurements. *Appl. Spectro.* 1990, **44**, 565-570, 1990.

[138] Shim, MG, Wilson, BC, Development of an In Vivo Raman Spectroscopic System for Diagnostic Applications, *Journal of Raman Spectroscopy*, **28**, 131-142, 1997.

[139] Brennan, JF, Wang, Y, Dasari, RR, Feld, MS, Near-infrared Raman Spectrometer Systems for Human Tissue Studies, *Applied Spectroscopy*, **51**, 201-208, 1997.

[140] Zhang, G, Demos, SG, Alfano, RR, Raman Spectra of Biomedical Samples Using Optical Fibre Probes, *Proc. SPIE: Biomedical Sensing, Imaging, and Tracking Technologies II*, **2976**, 2-9, 1997.

[141] Shim, MG, Wilson, BC, Marple, E, Wach, M, Evaluation of Fibre Optic Probes for In Vivo Raman Spectroscopy, *Proc. SPIE: Infrared Spectroscopy: New Tool in Medicine*, **3257**, 208-217, 1998.

[142] Shim, MG, Song, LMWM, Marcon, NE, Wilson, BC, In Vivo Near-infrared Raman Spectroscopy: Demonstration of Feasibility During Clinical Gastrointestinal Endoscopy, *Photochemistry and Photobiology*, **72**, 146-150, 2000.

[143] Mahadevan-Jansen, A, Mitchell, WF, Ramanujam, N, Utzinger, U, Richards-Kortum, R, Development of a fiber Optic Probe to Measure NIR Raman Spectra of Cervical Tissues In Vivo, *Photochemistry and Photobiology*, **68**, 3, 427-431, 1998.

[144] Buschman, HP, Marple, ET, Wach, ML, Bennett, B, Bakker Schut, TC, Bruining, HA, Bruschke, AV, van der Laarse, A, Puppels, GJ, In Vivo Determination of the Molecular Composition of Artery Wall by Intravascular Raman Spectroscopy, *Analytical Chemistry*, **72**, 3771-3775, 2000.

[145] British Standards Institution (BSI), British Standard: Radiation safety of laser products and systems, Part 3: Guidance for Users, BS4803:Part3, London: BSI, 1983.

[146] Shim, M, Wilson, BC, The Effects of Ex Vivo Handling Procedures on the Near-Infrared Raman Spectra of Normal Mammalian Tissues, *Photochemistry and Photobiology*, **63**, 5, 662-671, 1996.

[147] Coohill, TP, Peak, MJ, Peak, JG, The Effects of the Ultraviolet Wavelengths of Radiation Present in Sunlight on Human Cells In Vitro, *Photochem. Photobiol.*, **46**, 6, 1043-1050, 1987.

[148] Szymanski HA. *Raman Spectroscopy Theory and Practice*, 1st edition. New York: Plenum Press, **2**, 1967.

[149] Banwell CN. *Fundamentals of Molecular Spectroscopy*, 2nd edition. London: McGraw Hill, 121, 1972.

[150] Carey PR, *Biochemical Applications of Raman and Resonance Raman Spectroscopies*, 1st edition. London: Academic Press inc, 6-47, 1982.

[151] Placzek, G, in *Handbuch der Radiologie*, Marx (Ed.), Akademische Verlagsgesellschaft, Leipzig, 1934.

[152] Dirac, PAM, The quantum theory of dispersion, *Proc. Royal Soc.*, **114**, 710, 1927.

[153] Kramers, HA, Heisenberg, W, Über die streuung von strahlung durch atome, *Z. Physik*, **31**, 681, 1925.

[154] Stevenson, CL, Vo-Dinh, T, Signal Expressions in Raman Spectroscopy, in *Modern Techniques in Raman Spectroscopy*, Laserna (Ed.), **1**, 1-38, John Wiley & Sons, Chichester, 1996.

[155] Blokhinstev, DI, Chapter 86: Emission, Absoption, and Scattering of Light by Atomic Systems, in *Principles of Quantum Mechanics*, Bjorklund (Ed.), Allyn and Bacon, Boston 1964.

[156] Hecht, E, p44, Chapter 3: Electromagnetic Theory, Photons and Light in *Optics*, 2nd edition, Addison-Wesley, Reading, Massachusetts, 1989.

[157] Yariv, A, p11, Chapter1: Electromagnetic Theory, in *Optical Electronics*, 4th edition, Saunders College, Orlando, 1991.

[158] Albrecht, AC, Hutley, MC, *J. Chem. Phys.*, **55**, 4438, 1971.

[159] Tang, J, Albrecht, AC, Developments in the Theories of Vibrational Raman Intensities, Chapter 2 in *Raman Spectroscopy*, Szymanski, HA, Ed., Vol. 2, Plenum Press, 1970.

[160] Shanmugaratriam, K, Sobin, LH, *Histological Typing of Tumours of the Upper Respiratory Tract and Ear*. Berlin: Springer-Verlag, 1991.

[161] *Model 3900S, CW Ti:Sapphire Laser Users Manual*, Spectra Physics, Mountain View, California, 1996.

[162] Kim, M, Owen, H, Carey, PR, High performance Raman spectroscopic system based on a single spectrograph, CCD, notch filters, and a Kr+ laser ranging from the near-IR to near-UV regions, *Applied Spectroscopy*, **47**, 1780-1783, 1993.

[163] Schoen, CL, Sharma, SK, Helsley, CE, Owen, H, Performance of a holographic supernotch filter, *Applied Spectroscopy*, **47**, 305-308, 1993.

[164] Bilhorn, RB, Scanning Multichannel Spectrometry Using a Charge-Coupled Device (CCD) in Time Delay Integration (TDI) Mode. US Patent 5173748, assigned to Eastman Kodak Company, 1992.

[165] Knoll, P, Singer, R, Keifer, W, Improving Spectroscopic Techniques by a Scanning Multichannel Method, *Applied Spectroscopy*, **44**, 776-782, 1990.

[166] Deckert, V, Keifer, W, Scanning Multichannel Technique For Improved Spectrochemical Measurements With a CCD Camera and Its Application to Raman Spectroscopy, *Applied Spectroscopy*, **46**, 322-328, 1992.

[167] Dyer, C, Smith BJE, Application of Continuous Extended Scanning Techniques to the Simultaneous Detection of Raman Scattering and Photoluminescence from Calcium Disilicates Using Visible and Near-Infrared Excitation, *Journal of Raman Spectroscopy*, **26**, 777-785, 1995.

[168] Hanlon, EB, Manoharan, R, Koo, T-W, Shafer, KE, Motz, JT, Fitzmaurice, M, Kramer, IR, Itzkan, I, Dasari, RR, Feld, MS, Propects for in vivo Raman spectroscopy, *Phys. Med. Biol.*, **45**, R1-R59, 2000.

[169] Hamaguchi, H, Calibrating Multichannel Raman Spectrometers, *Applied Spectroscopy Reviews*, **24**, 137-174, 1988.

[170] Stommen, D, Nakamoto, K, *Laboratory Raman Spectroscopy*, Wiley, New York, 1984.

[171] McCreery, RL, Instrumentation for Dispersive Raman Spectroscopy, Ch. 2, *Modern Techniques in Raman Spectroscopy*, Ed. by Laserna, JJ, John Wiley & Sons, Chichester, 64, 1996.

[172] Bass, M, Van Stryland, EW, Williams, DR, Wolfe, WL (Ed.s), *Handbook of Optics Volume 1, Fundamentals, Techniques and Design*, 2nd edition, McGraw-Hill, New York, 1995.

[173] Hair, JF, Anderson, RE, Tatham, Black WC. *Multivariate Data Analysis*. New York: Macmillan, Chapter 4, 1992.

[174] Fisher, LD, Van Belle, G, Biostatistics: A Methodology for the Health Sciences, Chapter 10 Analysis of Variance, 418-425, 1993.

[175] Ackroyd, R, Brown, NJ, Stephenson, TJ, Stoddard, CJ, Reed, MWR, Ablation Therapy for Barrett's Oesophagus: What Depth of Destruction is Needed?, *Journal of Clinical Pathology*, **52**, 7, 509-512, 1999.

[176] Boustany, NN, Crawford, JM, Manoharan, R, Dasari, RR, Feld, MS, Analysis of Nucleotides and Aromatic Amino Acids in Normal and Neoplastic Colon Mucosa by Ultraviolet Resonance Raman Spectroscopy, *Laboratory Investigation*, **79**, 1201-1214, 1999.

[177] Mann, CK, Vickers, TJ, Instrument-to-Instrument Transfer of Raman Spectra, *Applied Spectroscopy*, **53**, 7, 856-861, 1999.

[178] Mann, CK, Vickers, TJ, Chapter 6: The Quest for Accuracy in Raman Spectra, In: *Handbook of Raman Spectroscopy From the Research Laboratory to the Process Line*, 251-274, Ed. Lewis, IR, Edwards, HGM, New York, Marcel Dekker Inc., 2001.

Appendix 1: Histopathological Grading Criterion for Evaluation of Frozen Laryngeal Specimens

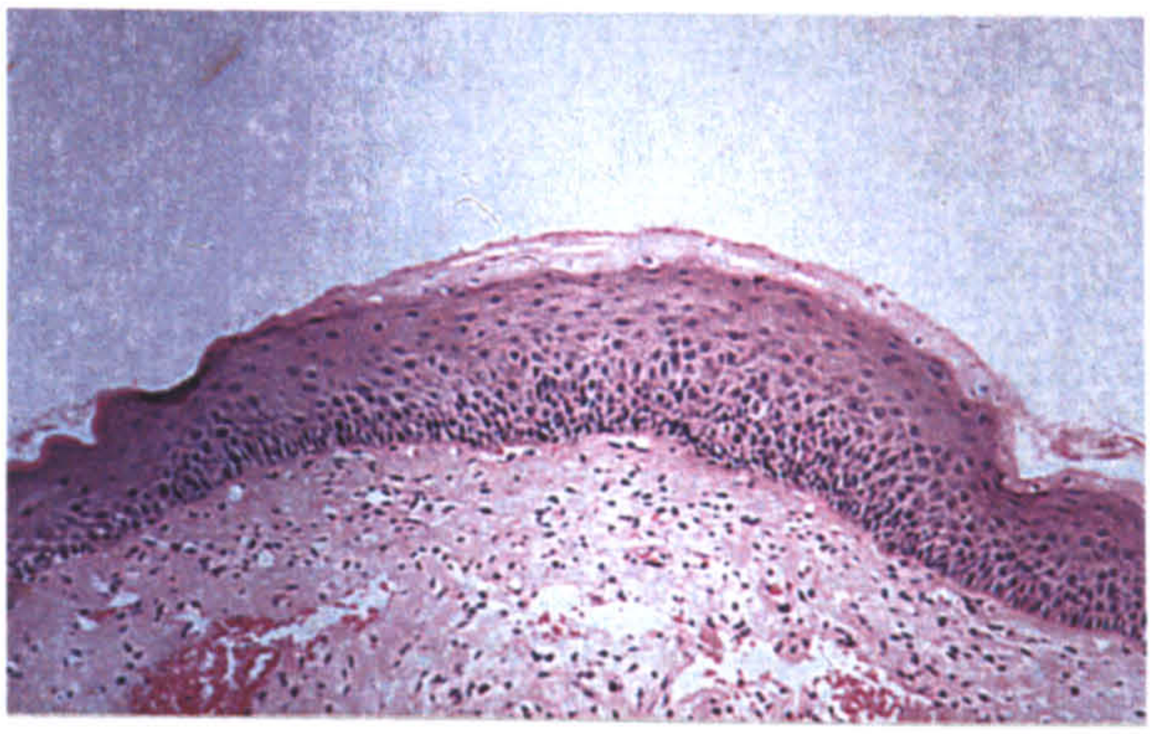

Normal Squamous Mucosa

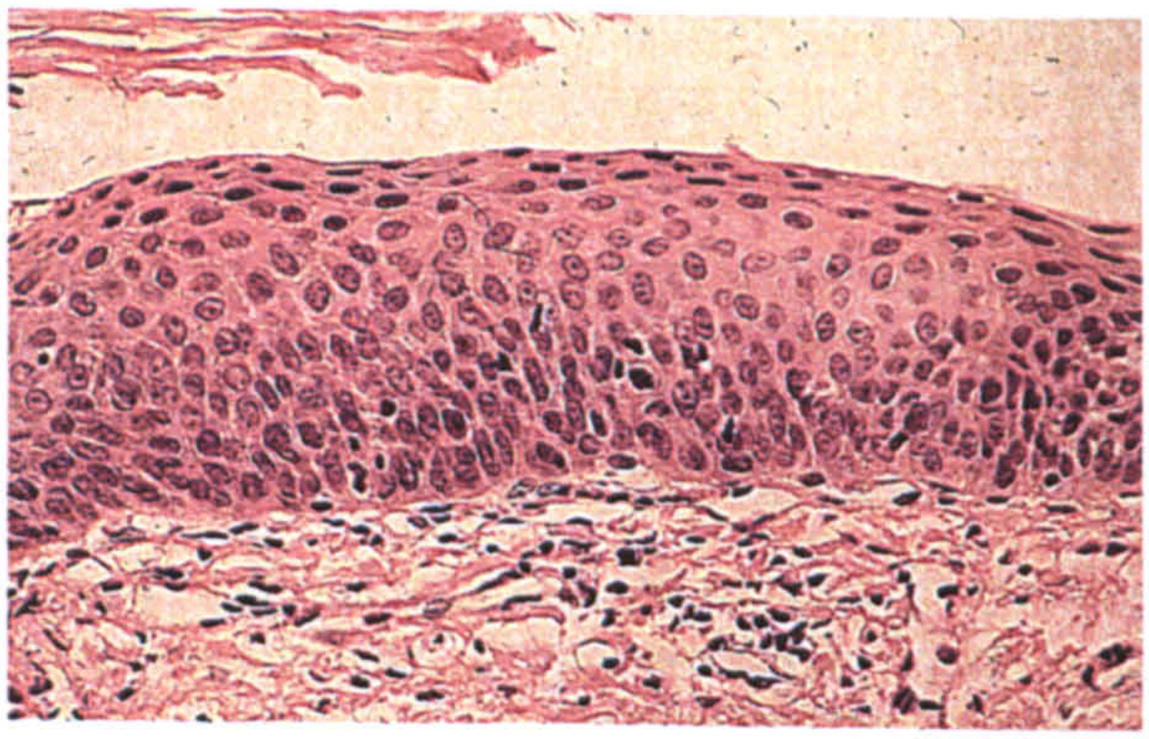

Squamous Dysplasia

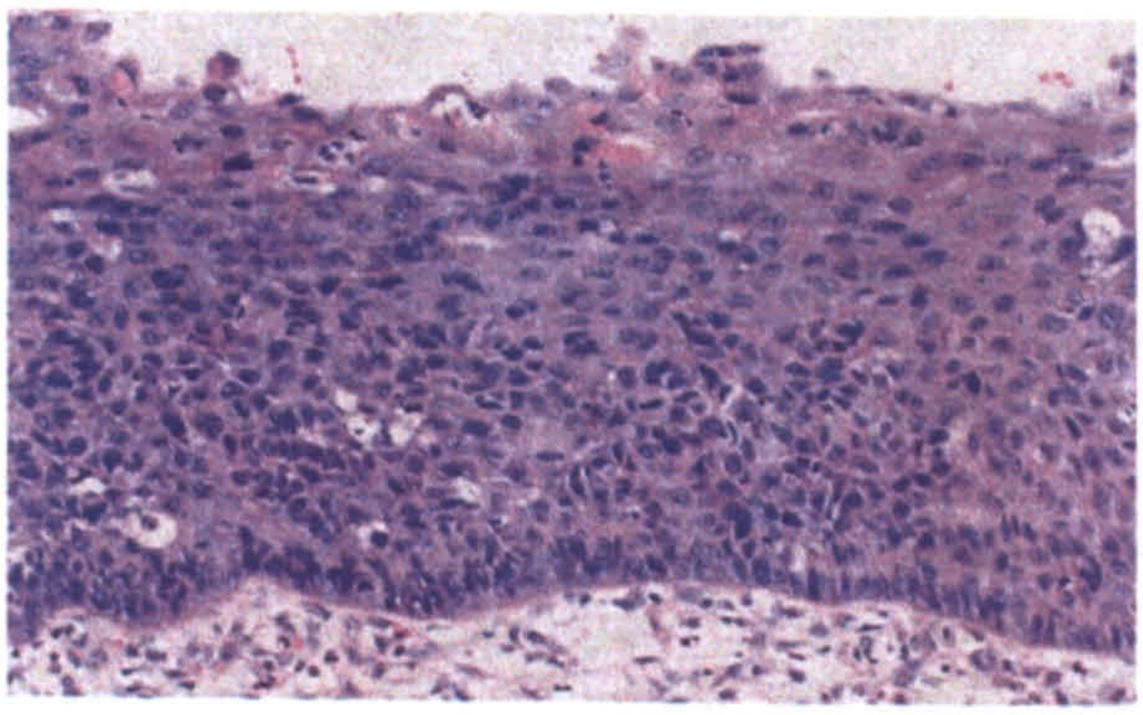

Squamous Cell Carcinoma

Figure A1.1: Microscopic images of histopathological sections larynx tissue, stained with haematoxilin and eosin (H & E). It can be seen from the images that morphological difference between normal squamous mucosa, squamous dysplasia and squamous cell carcinoma are subtle and subjective. This can lead to high levels of discrepancy (see Chapter 1).

Histopathology

A grading system was developed for this work utilising the commonly used criterion for distinguishing between pathological grades of laryngeal tissue tissue. The following categories have been used in this study:

1. Normal squamous mucosa.
2. Squamous Dysplasia.
3. Squamous cell carcinoma.

The pathological markers used to distinguish between the histopathological grades are outlined below (see Figure A1.1):

Squamous Cell Dysplasia is defined as a pre-cancerous lesion of squamous epithelium characterised by cellular atypia and loss of normal maturation and stratification.[1] In the larynx there are three grades of dysplasia. These are recognised on the basis of the degree of nuclear abnormalities and the proportion of epithelial thickness showing loss of normal stratification. Dysplasia and invasive carcinoma may be present in the same organ, with the potential for developing invasive carcinoma increasing with the severity of dysplasia.

Mild Dysplasia shows the characteristics of slight nuclear abnormalities, mainly in the basal third of the epithelial layer[1]. These abnormalities are minimal in the upper layers where the cells show normal maturation and stratification. Keratosis (the formation of a hard layer of keratin proteins) and chronic inflammation are usually present.

Moderate Dysplasia demonstrates more marked nuclear abnormalities than in mild dysplasia[1]. These changes are most marked in the lower two-thirds of the epithelial thickness. Moderate nuclear abnormalities may persist up to the surface, but cell maturation and stratification are evident in the upper layers. There are no abnormal mitoses (cell divisions). There can be associated keratosis.

Severe Dysplasia is reached when the epithelium shows marked nuclear abnormalities and loss of maturation involving more than two-thirds of the epithelial thickness with some stratification of the most superficial layers[1]. Nuclear pleomorphism (occurrence of more than one form in a life cycle) is common, and some of the cells may have bizarre nuclei. Mitoses are present high up in the epithelium, these may be abnormal. The cells are generally not crowded as in the classic carcinoma in situ and are usually more differentiated with intercellular bridges between the atypical cells. The distinction is made between severe dysplasia and carcinoma in situ by the presence of some maturation and stratification of the cells. The lesion is often associated with keratosis. Severe dysplasia has the same high risk for developing invasive carcinoma as carcinoma in situ and is therefore grouped with it for clinical purposes.

Carcinoma In Situ (Intraepithelial Carcinoma) is defined as a lesion which the full thickness of the squamous epithelium shows the cellular features of carcinoma without stromal invasion (progression below the basal membrane)[1]. It usually occurs with the epithelial cells having markedly abnormal hyperchromatic nuclei and variable cytoplasmic keratinisation; the appearance is very similar to severe dysplasia. In some

cases the cells are found to have little cytoplasm and no evidence of squamous differentiation. Cell division occurs high up in the epithelium with abnormal mitoses often present.

Laryngeal carcinoma in situ may occur as an isolated lesion or in association with invasive carcinoma; the absence of stromal invasion should therefore be confirmed by sampling the entire biopsy specimen.

Squamous Cell Carcinoma is a malignant epithelial tumour with squamous differentiation characterised by the formation of keratin and/or the presence of intercellular bridges. Squamous cell carcinomas of the upper respiratory tract produce the same range of histological appearances as those arising in other sites. The tumours are graded according to the degree of differentiation, cellular pleomorphism and mitotic activity. Well-differentiated carcinomas have a close resemblance to normal squamous epithelium and contain varying proportions of basal-type cells and squamous cells with intercellular bridges and full keratinisation; mitoses are rare. Moderately differentiated carcinomas have less keratinisation and more nuclear pleomorphism; there are more mitoses, including abnormal mitoses. Keratinisation and intercellular bridges are minimal and barely discernible in poorly differentiated carcinomas. Grading has been found to be of some value for predicting patient outcomes, although the assessment of the degree of differentiation is essentially subjective and influenced by variations in sampling.

---

[1] Shanmugaratnam K, *Histological typing of tumours of the upper respiratory tract and ear*, Springer-Verlag, Berlin, 1991.

Appendix 2: Histopathological Grading Criterion For Evaluation of Frozen Oesophageal Specimens

Endoscopic Detection of Oesophageal Malignancies

- Normal squamous mucosa is seen as a whitish region.
- Barrett's mucosa is red/pink and velvety.
- Unable to endoscopically distinguish Barrett's from dysplasia or early carcinomas.
- Can see tumour masses above a few mm in diameter.

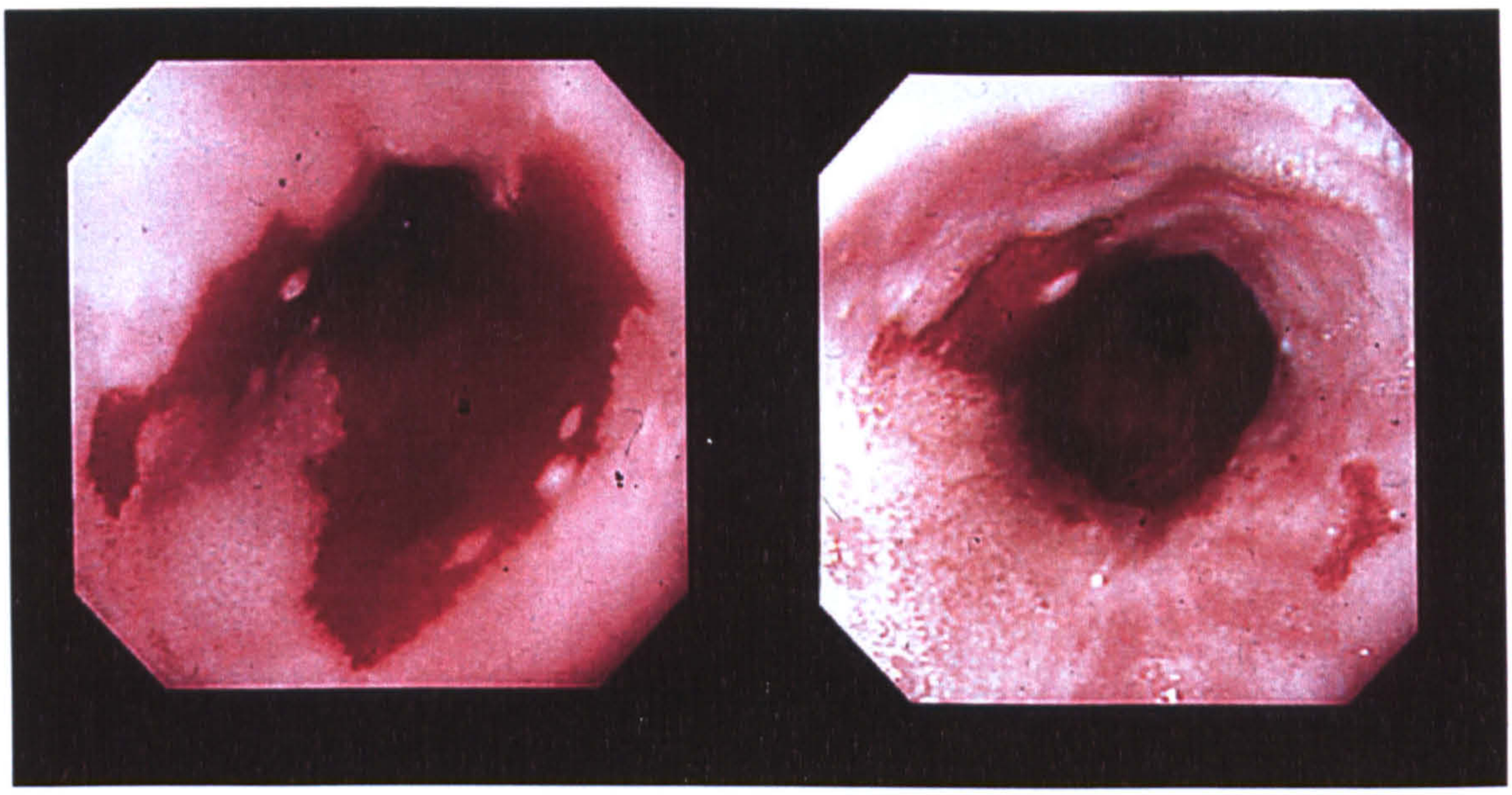

Figure A2.1: Endoscopic images down an oesophagus exhibiting Barrett's mucosa (red). The whiter regions are the normal squamous epithelial regions. The image on the left is before treatment with photodymnamic therapy. The image on the right is post-PDT treatment. It can be seen that the oesophagus has healed by regrowing mainly normal squamous mucosa.

It is not possible to distinguish between Barrett's mucosa (the benign pre-cursor to cancer) and early neoplastic change by visual inspection during endoscopy. It is therefore necessary to carry out surveillance biopsy following rigourous selection protocols. The most commonly accepted protocol involves the selection of excisional biospy samples from four quadrants, every two centimetres along the Barrett's mucosal region. Figure A2.1 displays a pair of images captured from one patient before and after a photodynamic therapy (PDT) treatment. The distinct difference between the Barrett's columnar and normal squamous mucosa can be seen. Figure A2.2 displays captured endscopic images from patients with invasive adenocarcinoma of the oesophagus. Prognosis for these patients is extremely poor.

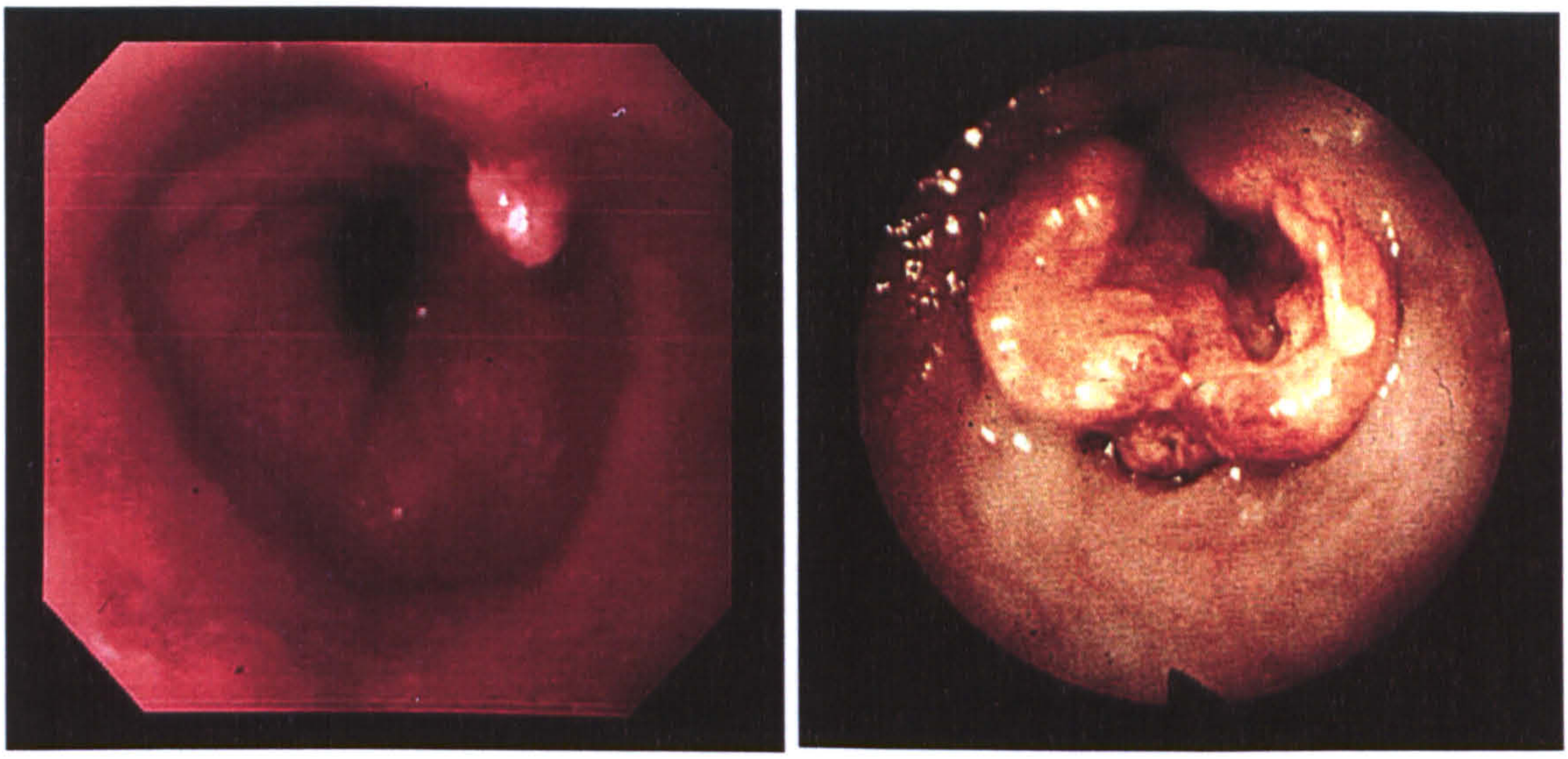

Figure A2.2: Endoscopic images exhibiting invasive adenocarcinomas, patient prognosis is extremely poor once the tumour begins invading deeper tissues.

Histopathology

A grading system was developed for this work utilising the commonly used criterion for distinguishing between pathological grades of oesophageal tissue. A panel of three internationally renowned pathologists on the gastrointestinal Registry for Barrett's dysplasia were consulted and used to develop a grading system to include a measurement of homogeneity. The resulting diagnosis for each sample were compared and majority and consensus opinion was used for predictive model construction and testing.

The following nine categories have been used in this study:

1. Normal squamous mucosa (Normal).
2. Cardiac type Barrett's mucosa (CB).
3. Fundic type Barrett's mucosa (FB).
4. Intestinal type Barrett's mucosa (IM).
5. Low-grade Barrett's dysplasia (LGD).
6. High-grade Barrett's dysplasia (HGD).
7. Adenocarcinoma (Adeno).
8. Squamous dysplasia (Sq Dys).
9. Squamous cell carcinoma (SCC).

The pathological markers used to distinguish between the histopathological grades are outlined below (see Figure A2.3):

Barrett's Oesophagus (columnar oesophageal epithelium) is defined as glandular metaplasia of the oesophageal mucosa, typically a sequel to chronic reflux oesophagitis. The Barrett's mucosa is in effect normal tissue, although it should not be in the oesophagus. There are three main types of glandular mucosa that are seen in Barrett's oesophagus: gastric, fundic and intestinal. Each type exhibits the architecture and biochemistry of tissue from the gastric and fundic stomach mucosa, or intestinal mucosa. It is the Barrett's intestinal mucosa that is known to increase the potential for developing adenocarcinoma by greater than 40 times.

Dysplasia in Barrett's Oesophagus is usually graded as mild, moderate or severe, the first two comprising low-grade and the last, high-grade dysplasia. Distinction between the later, adenocarcinoma in situ and intramucosal adenocarcinoma can be especially difficult on small, superficial endoscopic biopsies. Dysplasia is the most reliable marker for assessing the risk of adenocarcinoma in the lower oesophagus. In fact, most adenocarcinomas of the oesophagus arise in patients with Barrett's oesophagus. Dysplasia is thought to develop more or less exclusively in the intestinal type of mucosa. In low-grade dysplasia, the abnormal nuclei are limited to the lower half of the epithelial layer. In high-grade dysplasia more severe cytological change and architectural alterations are present. Hyperchromasia (excessive colour) and pleomorphism (occurance of more than one form in a life cycle) are more marked. Nuclear crowding and stratification are often present.

Adenocarcinoma is a malignant tumour composed of glandular epithelium, with papillary and/or tubular structures. The majority of oesophageal adenocarcinomas arise in metaplastic glandular mucosa of Barrett's oesophagus, a sequel to prolonged reflux oesophagitis. They occur in the lower portion of the oesophagus and may or may not be preceded by dysplasia. It may be difficult or impossible to determine whether an advanced adenocarcinoma of the lower oesophagus is the result of spread from a tumour of the stomach or is a true primary growth of the oesophagus.

Squamous Dysplasia is similar to the more extensively investigated lesion encountered in the uterine cervix. Nuclei are enlarged and hyperchromatic and show increased mitotic activity. In mild dysplasia such atypical nuclei are limited to the basal zone, and there is evidence of cytoplasmic maturation superficially. With increasing grades of dysplasia there is a progressive increase in the proportion of atypical basal cells until the entire thickness of the mucosa is replaced. This state is often described as carcinoma in situ.

Squamous Cell Carcinoma (SCC) is a malignant tumour composed of squamous-type epithelium. It is usually graded as well, moderately or poorly differentiated. Well differentiated tumours are those with abundant amounts of keratin, easily demonstrated intercellular bridges and cell layers undergoing differentiation. Poorly differentiated tumours are those with little or no keratin, intercellular bridges and differentiation of cell layers. Moderately differentiated tumours are those intermediate between well and poorly differentiated.

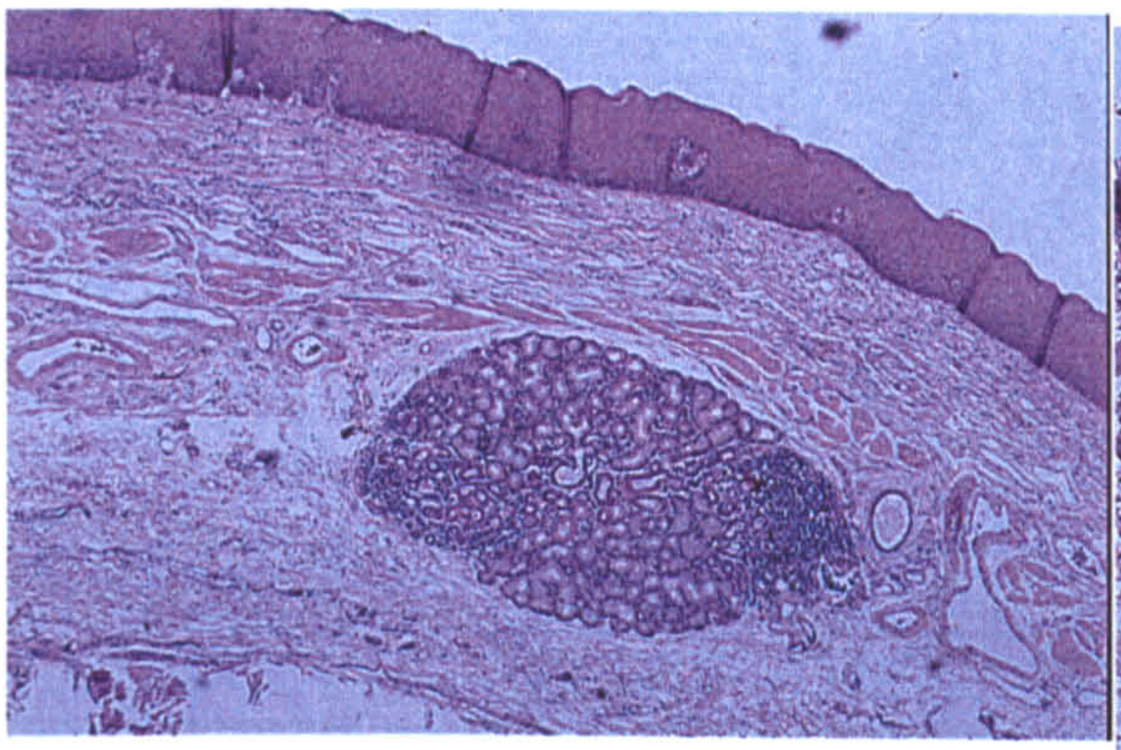

Normal Squamous Mucosa

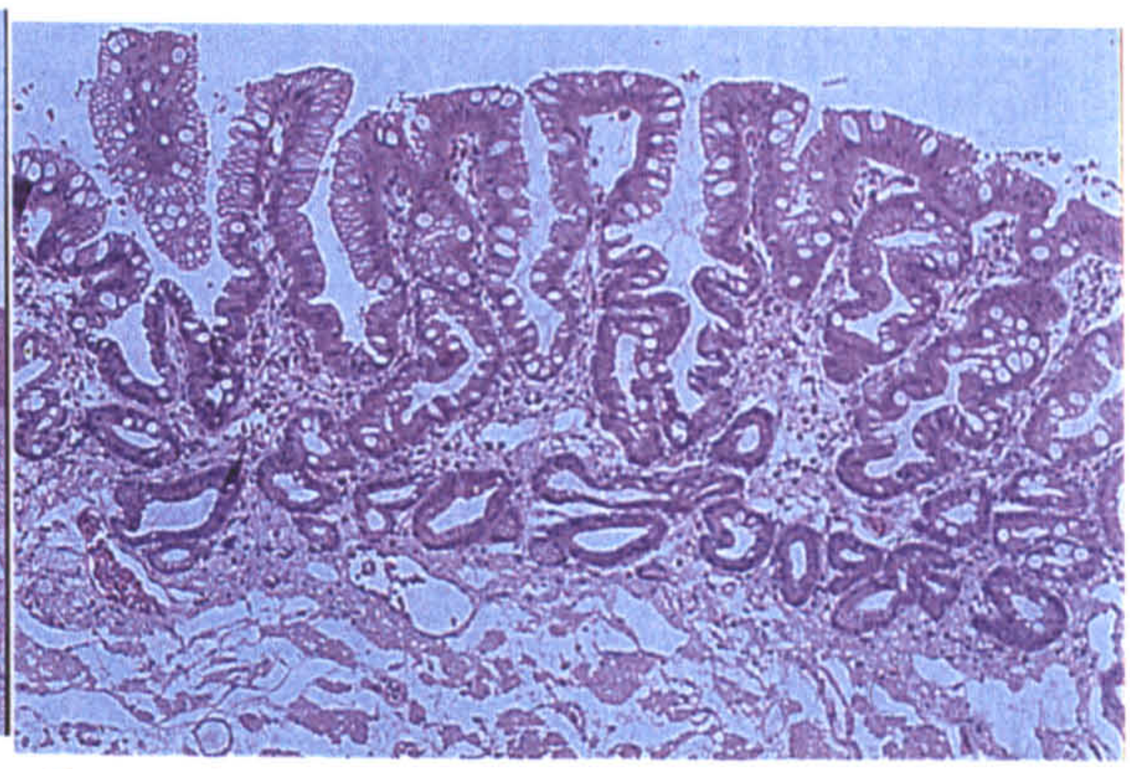

Barrett's Intestinal Metaplasia

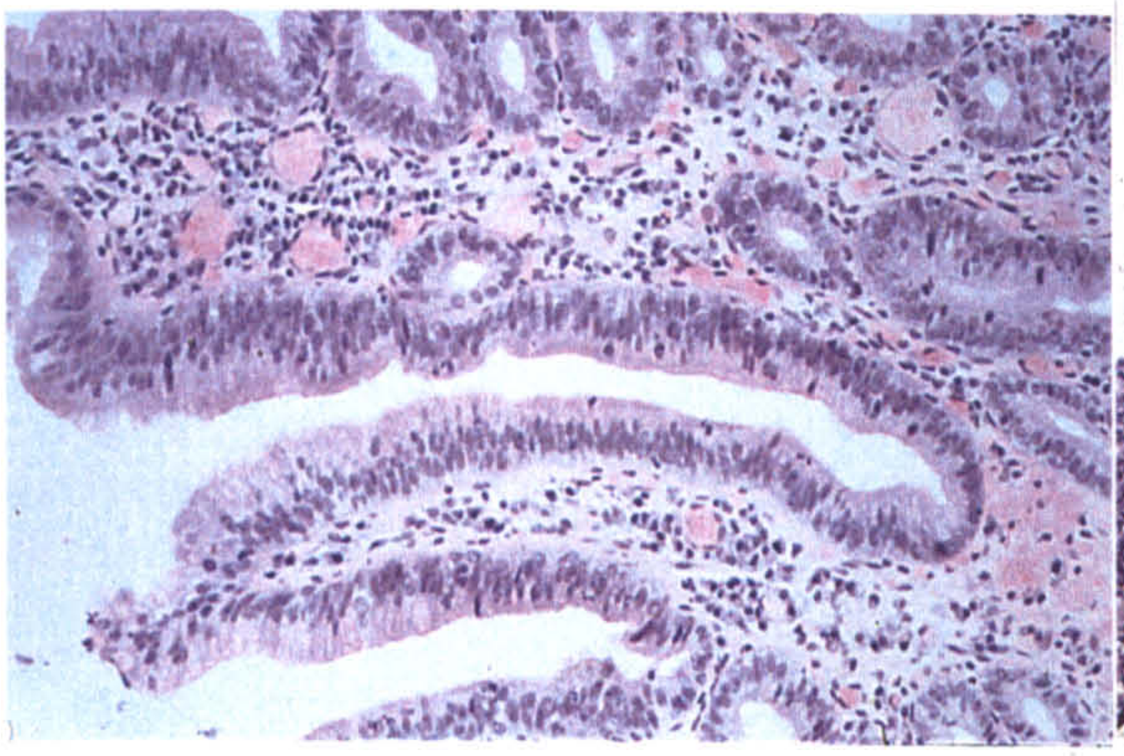

Low Grade Dysplasia

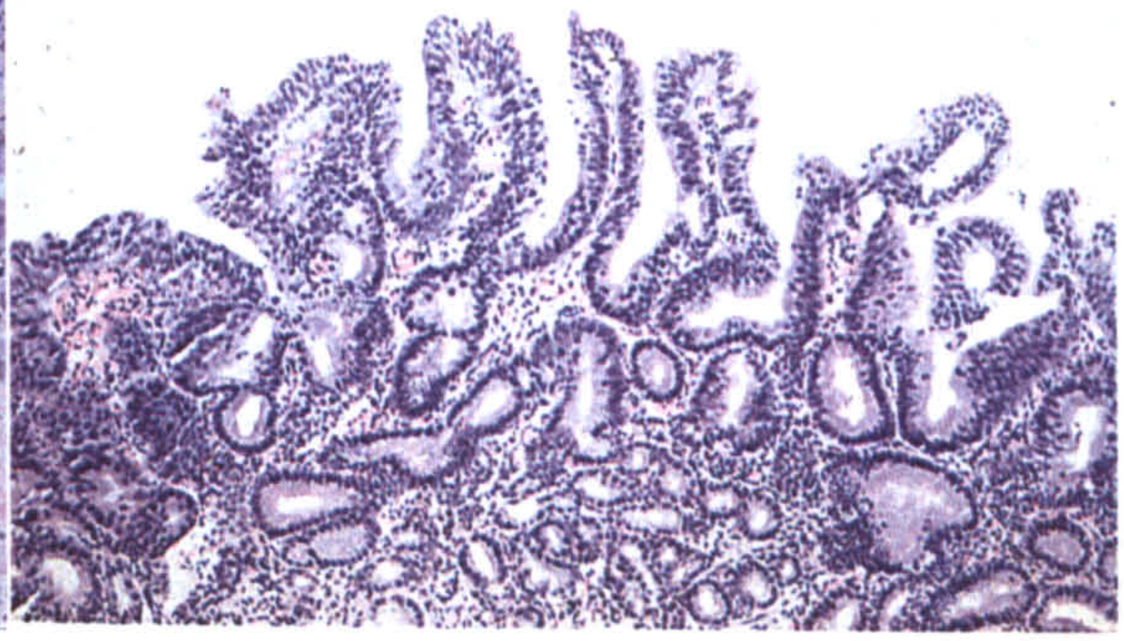

High Grade Dysplasia

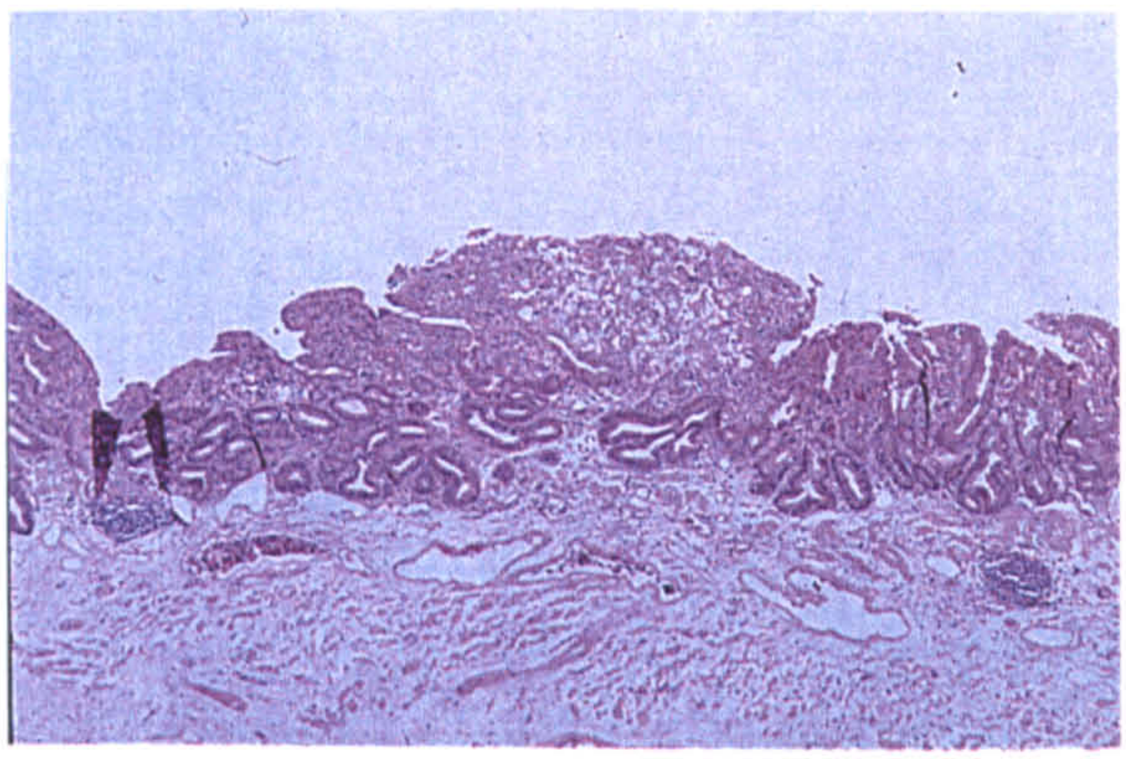

Adenocarcinoma

Figure A2.3: Microscopic images of histopathological sections of the oesophagus, stained with haematoxilin and eosin (H & E). It can be seen from the images that morphological difference between Barrett's intestinal metaplasia, low grade dysplasia and high grade dysplasia are very subtle and subjective. This leads to high levels of discrepancy (see Chapter 1).

Appendix 3: Multivariate Spectral Analysis

For analysis of spectra applied to medicine a number of authors have used empirical methods such as peak heights, peak areas and peak ratios to glean diagnostic information from highly complex spectra. In a small number of cases where there is a single molecular species that directly accompanies any abnormality this will be sufficient. However in the majority of cases biochemical changes preceding and accompanying morphological change are extremely complex. Methods of extracting information from Raman spectra should use as much information as possible to facilitate the most accurate prediction of histopathology. Multivariate techniques have been explored to enable utilisation of the maximum available information for prediction of diagnosis.

Statistical Measures

In order to evaluate the significance of an individual variable (either peak height, peak area, peak height ratio or principal component) to the separation of tissue samples into pathological groups, it is necessary to use statistical tests. The most simple of these being the Student t-test. The Student t-test procedure compares means for two groups, to evaluate whether they originate from the same population. Analysis of variance, an extension of the two-sample t-test, is used to test the hypothesis that several means are equal (i.e. drawn from populations with the same mean). In the use of ANOVA for the evaluation of variable significance, if the null hypothesis is rejected then the means of the variable are significantly different between each group.

ANOVA evaluates differences in group means by calculating the mean square of the variance between-groups and the mean square of the variance within-groups. The ratio of the mean squares gives the F-statistic. The greater the F-value, then the larger the differences between the group means. Use of look up tables for a particular level of significance provides us with a value for F_{crit}. This value is the cut-off for acceptance or rejection of the null hypothesis.[1,2,3]

An alternative for the evaluation of between group variable significance is the Wilks' Λ test. Wilks' Λ is the ratio of the within-group sum of squares to the total sum of squares. Where the sum of squares is the sum of the square of the variance of the variable from the mean value. This leads to Wilks' Λ values (no units) in the range of zero to one. A value of one means that there is no difference in the variables from one group to the next, whereas a value of zero means the variables tested are infinitely different from one group to the next.[4]

Principal Components Analysis

The calculation of principal components to describe the greatest variance in the spectra from the mean of the data set allows us to substantially reduce the number of data points in the analysis, thus enabling prediction algorithms to include effectively all the biochemical data that varies from one sample to the next. Principal components analysis (PCA) finds combinations of variables, called factors, which describe the major trends (sources of independent variation) in the data. Mathematically, PCA is an eigenvector decomposition of the variable correlation matrix. The principal components (PCs) are the

eigenvectors and the corresponding eigenvalues are the measure of the amount of spectral variance in the dataset (the mean of all the spectra in the dataset), the second is orthogonal to the first one, and in the direction of the largest residual variance, and so on. The last PCs, with the smallest eigenvalues, often only represent noise and can be omitted in further analysis. Pre-processing of data prior to PCA, such as mean or variance centring removes the mean spectrum of the dataset from the analysis and the first principal component will then describe the greatest variance from the mean.

PCA is an unsupervised data transformation procedure that creates new variables in the directions of maximal variation, but not necessarily in the directions that are most useful for diagnosis. In many cases further modelling is required to achieve the latter. The main advantages of using PCA prior to further analysis, apart from data compression, are the removal of all collinearity and the inherent signal averaging aspects. Because of the collinear nature of spectra, the amount of data reduction can be large; often a reduction of more than 95% can be achieved without loss of useful information. The data compression and the orthogonalty of the PCs can facilitate and speed up the consecutive steps in data analysis.

Linear Discriminant Analysis

Group membership for a particular spectrum can be predicted by comparing the spectrum to a number of reference spectra, by using some spectral distance measure, and classifying it to the most similar ones from a particular group. In many cases the principal components space is not optimal for the separation of the desired groupings. Further multivariate techniques can be applied that incorporate information about the origin of the samples in the model (supervised classification). This information can be used to find the directions in the spectral space that provide maximal distances between groups. The most often used method to achieve this is Linear Discrimant Analysis (LDA) or some derived form of this method. The linear discriminant function was originally derived by Fisher[5] as a technique for classifying an object or individual into one of two possible groups on the basis of a set of observations or measurements. LDA finds the direction in spectral space that is optimal for separating two groups. It selects the linear combination of vectors in spectral space that give the maximum value for the ratio between inter-group variance and intra-group variance. MDA is the multi-group analogue of LDA, it finds the (n-1) orthogonal directions that best separate n groups. LDA and MDA have the disadvantage that in order to obtain a reliable model the number of input variables (e.g. wavenumbers) should not exceed the number of samples. This problem is solved by performing discriminant analysis on the factors (PCs) extracted by PCA. This method has the advantage of the data compression and signal averaging aspects of PCA, while still using all the relevant information in the spectrum for the discriminant analysis.

Figures A3.1 and A3.2 are flow diagrams of the process of spectral diagnostic model building and cross-validation testing, and the process of prospective classification with a linear discriminant model respectively.

Diagnostic Model Build Process

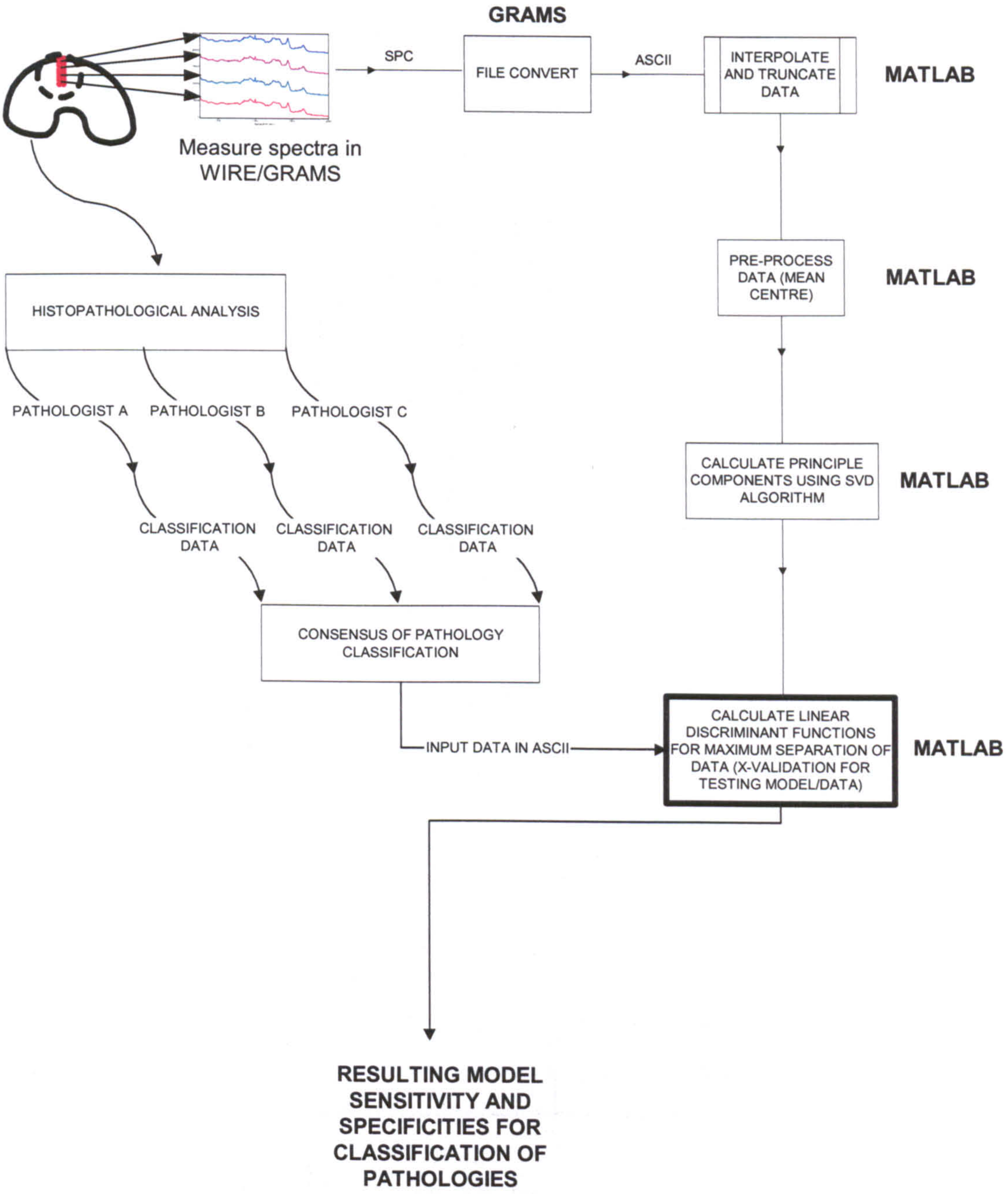

Figure A3.1: Flow diagram of the spectral diagnostic model building and cross-validation procedures.

Prospective Classification using Model

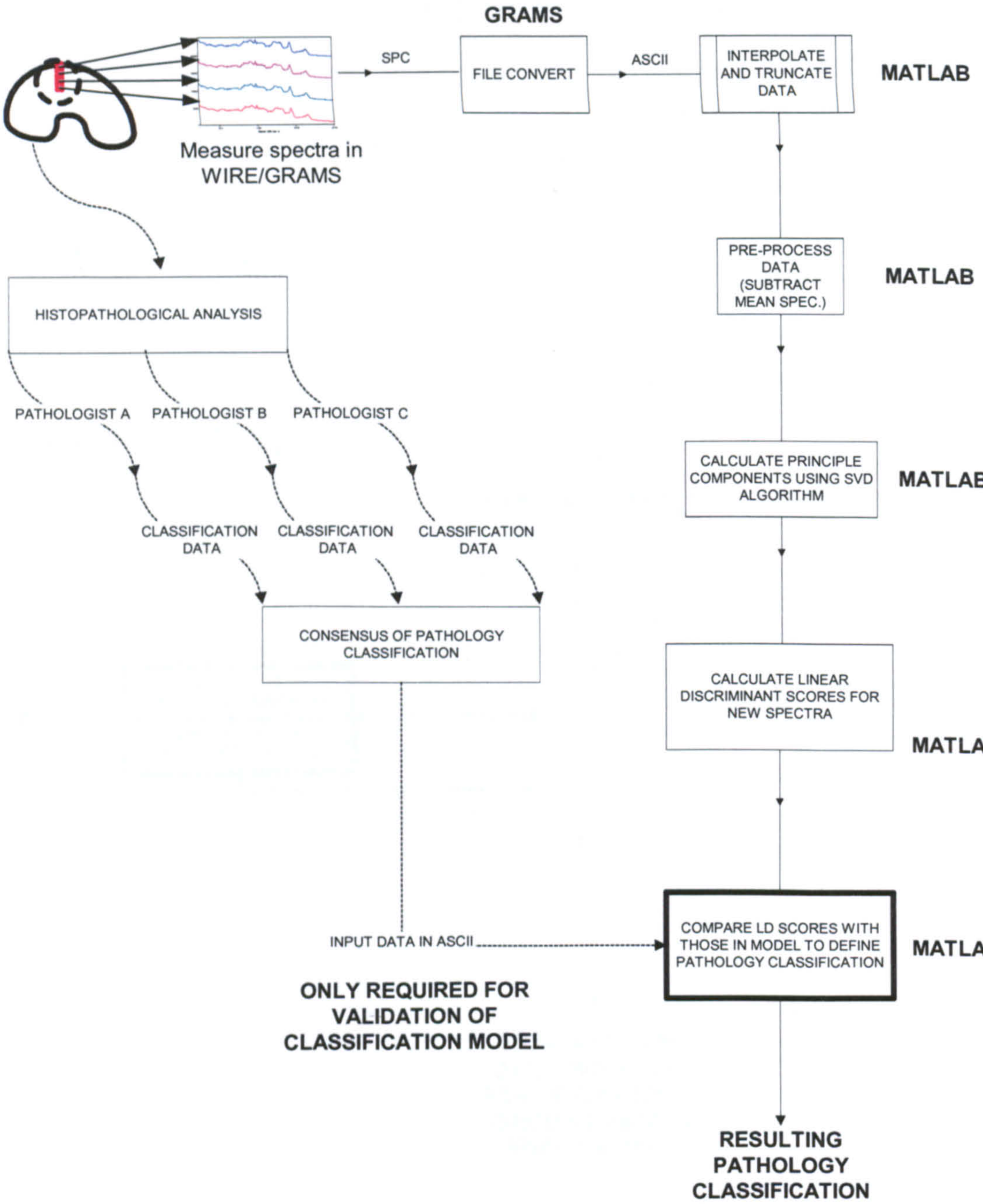

Figure A3.2: Flow diagram of the prospective classification procedure using the optimised linear discriminant model.

Diagnostic Outcome Measures

There are a number of measures of the power of a medical diagnostic test to correctly predict whether a patient has a particular condition. The most common of these are sensitivity and specificity. The sensitivity of a test is the percentage of individuals with disease who are classified as having disease. A test is sensitive to the disease if it is positive for most individuals having the disease. The specificity of a test is the percentage of individuals without the disease who are classified as not having the disease. A test is specific if it is positive for a small percentage of those without the disease.[6]

An example of results obtained from the Raman spectral prediction of laryngeal sample pathology is shown in Table A3.1. The resulting spectral prediction is classified as a true positive result if both the test and the 'gold standard' histopathology for a sample agree. True positive results are labelled in red. In the case of the test for normal samples the true negatives are coloured blue, i.e. those samples that are dysplastic or cancerous and are predicted to be not normal. The sensitivity can be calculated for all three test groups as the number of true positives (in red) divided by the sum of the true positives (in red) and false negatives (in green). The specificity for the normal case can be calculated by dividing the number of true negatives (in blue) by the sum of the true negatives (in blue) and false positives (in pink). The resulting values of sensitivities of the Raman prediction model for each of the three pathological groups are shown in Table A3.2.

Histopathology	Classification	Raman Predicted Group Membership: Normal	Dysplasia	Carcinoma	Total
No.	Normal	**100**	5	7	112
	Dysplasia	4	**34**	0	38
	Carcinoma	7	0	**42**	49

Table A3.1: Cross-validation classification results obtained using the discriminant functions calculated from the first 25 principal components of the larynx spectra. Each case was classified by the functions derived from all cases other than that case. 88.4 % of cross-validated grouped cases are correctly classified using this method.

	Normal	Dysplasia	Carcinoma
Sensitivity	89%	90%	86%
Specificity	87%	93%	95%

Table A3.2: Sensitivity and specificity of Raman spectroscopy as a diagnostic test to classify pathology in the larynx, calculated from the cross-validation classification results obtained from the linear discriminant model.

A further useful measure is the predictive value of a positive test. This is the percentage of subjects with a positive result who have the condition.

[1] Hair, JF, Jr., Anderson, RE, Tatham, RL, Black, WC, *Multivariate Data Analysis: With Readings*, 3rd Edition, Macmillan Publishing Company, New York, 153-155, 1992.
[2] Strike, PW, *Statistical Methods in Laboratory Medicine*, Butterworth-Heinmann Ltd., Oxford, 178-183, 1991.
[3] Fisher, LD, Van Belle, G, *Biostatistics: A Methodology for the Health Sciences*, John Wiley & Sons, New York, 418-450, 1993.
[4] Sharma, S, *Applied Multivariate Techniques*, John Wiley & Sons, New York, 246-253, 1996.
[5] Fisher, RA, The Use of Multiple Measurements on Taxonomic Problems, *Annals of Eugenics*, 7, 179-188, 1936.
[6] Fisher, LD, Van Belle, G, *Biostatistics: A Methodology for the Health Sciences*, John Wiley & Sons, New York, 206-207, 1993.

Appendix 4: Raman Peak Assignments for Biological Tissue

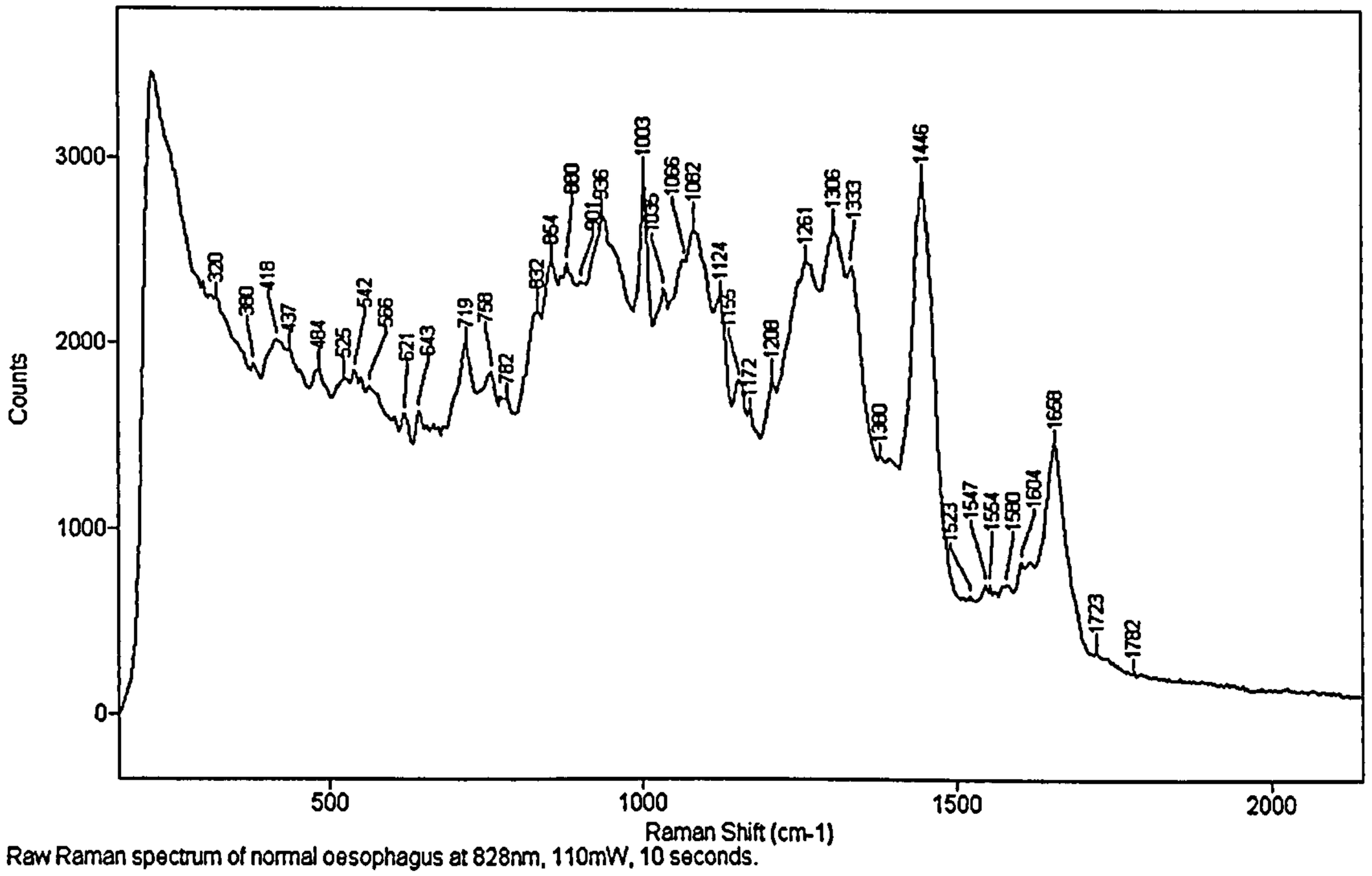

Raw Raman spectrum of normal oesophagus at 828nm, 110mW, 10 seconds.

Figure A4: Typical NIR-Raman of normal oesopaphageal mucosa.

Wavenumber / cm^{-1}	Assignments (for soft mammalian tissues)	Reference
350	Ribose, cytosine	1
385	Cytosine	1
429	Calcium hydroxyapatite	2
430	Cholesterol	2
435	Ribose	1
484	Glycogen (?)	
500	Guanine, cytosine + disulphide (protein)	1
500-550	Disulfide S-S stretch in proteins	3
505	S-S stretch (Bovine serum albumen, BSA)	4
508	Disulphide (S-S)	5
509	S-S disulphide bridges	6
510	Disulphide (C-S-S-C gauche-gauche-gauche)	3
518	Glucose	7
525	Disulphide (C-S-S-C gauche-gauche-trans)	3
528	Broad –S-S- stretch (protein)	2
533	COC deformation (glycosidic ring	8
540	Disulphide (C-S-S-C trans-gauche-trans)	3
547	Cholesterol	2
553	Glucose	9

556	S-S	10
574	Tryptophan	11
575	Cytosine, guanine + disul. (pr.)	1
587	Calcium hydroxyapatite	2
607	Cholesterol	2
622	Phenylalanine	5,12
626	Phenylalanine	13
620	Phenylalanine	2,14
637	Ribose + disulphide (protein)	1
643	Tyrosine	2
644-645	Tyrosine	11,12
665	Thiamine	15
668-669	C-S stretch (protein)	4,8
669	Thymine	12
670	Purine bases (A, G)	15
670	Guanine	1
670	Thymine and Guanine	16
681	Guanine ring breathing	12,16
682	Guanine	15
692	Creatine (O-C=O deformation)	17
700	Cholesterol	18
701	Cholesterol	2
710	Adenine	1
720	Nucleotide peak	19
720	C-N (membrane phospholipid head)	15
722	Adenine	1
725	C-S (Protein)	11
725	CH_2 rocking	8
727	=C-H in plane bend (breast lipid)	20
727	Adenine	15
729	Adenine ring breathing	12,16
730	Lactatic acid	21
746	P-O-P symmetric stretch (phospholipds)	22
748	Thiamine	15
749-750	Thymine ring breathing	8,12,16
759	Tryptophan	2,23
760	Tryptophan (protein)	1,6,11,24
770	Pyrimidine bases (C, T)	15
780	Nucleotide peak	19
780	Uracil ring	8
782	Cytosine ring breathing	12,15
787	Cytosine, uracil	1
787	Cytosine, uracil, thymine	25
788	DNA: O-P-O, cytosine, thymine	16
790	DNA:PO_2 symmetric stretch	12
790	Acetone (C-C-C stretch)	17
811	Nucleotide peak	19
814	DNA (PO_2)	10
815	Phosphate	1
817	C-C stretch, backbone	14

818	Ring breathing haemoglobin ??	13
825-842	O-P-O stretch (DNA)	15
830	Tyrosine (protein)	1,23,11,24,15
830	Lactatic acid (C-COOH stretch)	21,26
832-833	Tyrosine	6,12
832	DNA backbone	16
833	DNA:PO_2 asym. stretch	12
840-860	Polysaccharides	27,28
840	Glucose	9
847	Glucose	29
850	Tyrosine	15,24
853	Tyrosine	12,23
855	Tyrosine	6,11
856	Polysaccharides (?)	30
856	CC stretch, COC stretch, 1,4-glycosidic link	8
855-856	C-C stretch collagen backbone & proline ring	14,31,32,33
857	Tyrosine	2
860	Collagen (?)	34
860	Lactate (shifted from 830cm-1 due to alkalinity ?)	35
865	Ribose, TRP (protein)	1
866	Lactic acid	21
870	Proline	36
876	C-C stretch (hydroxyproline)	14
879	Tryptophan	23
880	Tryptophan	6,11
880	Tryptophan (ring deformation and NH displacement, sensitive to H-bond, 883cm-1 no H-bond, 871cm-1 strong H-bond)	24
885	Ribose, TRP (protein)	1
892	CH_2 rock, Collagen (hydroxyproline)	31
895-896	DNA backbone	12,16
915	Ribose	1
917	Deoxy-ribose (CH_2 deformation)	15
920	C-C stretch (proline ring)	14
920	Glucose	29
920	Lactic acid	21
925	DNA backbone	12
928	DNA backbone & Protein α-helix	16
928-940	C-C proline, valine	27,28
930	TRP (protein)	1
931	CH_3 rock, Collagen (proline)	31
932	Skeletal C-C: α-helix	12
935	Collagen (?)	34
935-945	Skeletal C-C: α-helix	15,
936	Hydroxyproline & C-C collagen backbone	32
936	C-C protein backbone	11
937-938	C-C stretch backbone	14,33
938	Peptide backbone stretch	2
939	C-C-N stretch	4
941	C-C protein skeletal stretch (muscle)	6
940	C-C stretch of proline and valine	37

950	Hydroxyproline	36
955	Heavily calcified aorta	38
956	Hydroxyapatite (standard sample)	38
956	Carotenoid	30
960	Hydroxyapatite phosphate stretch (calcified plaque)	2,39
960	Phosphate stretch in calcified aorta	40
960	Cholesterol	18
960	Phosphate symmetric stretch in calcified lesions, otherwise mainly cholesterol	5,30
961	P-O stretch of underlying bone	41
960-961	PO stretch (phosphate)	42,43
966	Hydroxyapatite	44
968	? Glucid C-OH	10
972	=C-H out of plane deformation (breast lipid)	20
975	Ribose	1
975	Deoxy-ribose (CH_2 deformation)	15
978	Phosphorylated proteins and nucleic acids	13
978	Phospholipids, glucose-1-phosphate	29
1000-1150	C-C skeletal (membrane hydrophobic tail)	15
1000-1001	Phenylalanine	10,36
1001-1004	Phenyl ring breathing mode	27
1002	Skeletal C-C: β-sheet	15
1002	Phenylalanine	2,11
1003	Urea	7,31,45
1004	Phenylalanine	8,12,16,14
1004	Phenylalanine & Tryptophan aromatic ring	4
1005	PHE (protein)	1
1005	β-carotene (breast)	20,46
1006	Phenylalanine (breathing mode)	15,22
1006	Carotenoids	30
1008	Carotenoids ?	34
1008	Urea C-N stretch	26,35
1010	C-N stretch	45
1013	Urea (N-C-N stretch)	17
1014	Tryptophan	15
1015	TRP (protein)	1
1016	Tryptophan	47
1017	DNA backbone C-O stretch	12
1031	Proline	2
1032	Phenylalanine	12
1035	Ribose, PHE (protein)	1
1035	C-C skeletal cis conformation	31
1040	? PHE ? increases in liver malignancy	48
1043	Hydroxyapatite (standard sample)	38
1043	Formalin artefact	14
1046	Lactic acid	21
1050	CO stretch or CCC trans conformational skeletal stretch	33
1057	DNA: backbone C-O stretch	12
1061-1062	Lipid (stratum corneum)	32,49
1064	Skeletal C-C stretch	50

1066	C-O, C-O-C stretch (phospholipds)	22
1066	C-C stretch	20
1066	Lipid in crystalline form	3
1069	Shifted hydroxyapatite band (i.e. tissue environment)	38
1070	Collagen/elastin ??	13,42
1070	Phosphate/carbonate	2,40,43
1070	Collagen, glucose-1-phosphate	29
1074	Adipose tissue	40, 51
1078	C-N stretch	52
1078-1090	C-C or C-O stretch (lipid), C-C or PO_2 stretch (nucleic acids)	27
1079	C-C stretch (lipid)	20
1082	C-C skeletal trans conformation	31
1082	Lipid (C-C & C-O stretch)	46
1082	Nonspecified protein vibrations ? PO_2^- in phospholipids and nucleic acids ?	37
1083	?PO_2^- DNA-backbone? Increases in liver cancer	48
1084	Lactic acid	21
1085	PHE (protein)	1
1085	Phospholipid	36
1085	Lipid C-C stretch	2
1086	C-C stretch, PO^{2-} stretch (phospholipids)	22
1086	Skeletal C-C stretch	50
1090-1091	PO_2^- (DNA)	10,15
1094	DNA: O-P-O^-	12,16
1095	CC stretch skeletal, COC stretch, 1,4-glycosidic link	8
1100	Phosphate PO_2^- stretch	1
1100	? formalin ?	18
1100-1110	Skeletal C-C: unordered	15
1100	Lipid (disorganised)	3
1104	Lipid C-C stretch	2
1119	C-C stretch (breast lipid)	20
1122	Lipid C-C stretch	2
1123	Glucose	29
1125	?	1
1125	Glucose	7
1126	Protein C-N stretch	12
1127-1128	Lipids (stratum corneum)	32,49
1128	Heme vibrational mode	53
1128	Skeletal C-C stretch	50
1129	C-C stretch (lipid)	33
1129	C-N (protein)	11
1130-1131	Glucose (C-O stretch)	17,54
1130	C-C stretch (lipid)	3,30
1131	Low density lipoproteins	2
1131	Lactic acid	21
1150	Carotenoids	39
1155	C-C stretch (carotenoids)	25
1155	C-C stretch, COH deformation	31
1156	C-N stretch (BSA)	4
1156	Urea	7

1156	Carotenoid	20,51
1157	β-carotene	46,30
1158	Carotenoids	34
1158	=C-C= carotenoid	55
1159	C-N (protein)	11
1162	Ribose	1
1175	C-O stretch (tyrosine/carbohydrates)	13
1176	Tyrosine, phenylalanine	12
1176	Carbonite substituted hydroxyapatite	38
1180	Tyrosine (exocyclic C-H and O-H bending in plane of ring)	24,47
1180	Cytosine, guanine, adenine	1
1182	??? greater in liver cancer than normal ???	48
1197	Carotenoid	20
1206	Hydoxyproline, tyrosine	14
1207	Tyrosine	23
1207	Tyrosine & Phenylalanine	4
1208	Thiamine	15
1210	TYR, PHE (protein)	1
1211	Thymine, tyrosine, phenylalanine	12
1227	Heme vibrational mode	53
1227-1247	Amide III: β-sheet	15
1230-1240	Amide III: β-sheet	56
1230-1245	Amide III: β-sheet	24
1230	Uracil in RNA	58
1235-1270	Amide III: unordered	15
1238	Uracil, cytosine, Amide III	1
1240	Amide III: β-sheet	18
1240	Pyrimidine bases (C, T)	15
1240	Thymine	12
1240-1260	Amide III: unordered	56,30
1243	Amide III: collagen	18
1245-1270	Amide III: irregular	24
1245	Amide III: keratin , disordered collagen (CH_2 wag, C-N stretch)	31
1246	Amide III (C-N stretch)	4,13
1246	Collagen, DNA	29
1247	Amide III: collagen	34,14
1247	Protein pk increases in brain sarcoma	18
1248	Amide III (one of pair of collagen amide III peaks)	57
1248	? PO_2^- in phospholipids and nucleic acids ?	37
1250	Cytosine, uracil, Amide III	1
1250	Cytosine	15
1253	Amide III: random coil (mouse breast adenocarc.)	19
1253	Heme proteins ? (liver)	48
1254	Adenine	16
1255	Cytosine	12
1258-1304	Amide III: α-helix	15
1259	Amide III (intensity less for benign breast than malignant tissue)	14
1260	Tyrosine (phenolic C-O stretch, width increases with degree of hydrogen bonding)	24
1260	Amide III	36

1260-1280	Amide III (BSA)	4,27
1260-1310	Amide III: α-helix	10,24,49
1261	Lipid	51
1264-1266	=C-H in plane bending (lipid)	27
1265	Glucose	7
1265	=C-H in plane deformation	20
1267	=C-H in plane deformation	18
1267	=C-H (membrane)	15
1267	Amide III	14
1268	Amide III	1
1271	Amide III (one of pair of collagen amide III peaks)	57
1271	Amide III: C-N stretch, N-H deform.	37
1272	Amide III: α-helix	22
1265-1300	Amide III: α-helix	56
1296	Lipids (stratum corneum)	32,49
1296	CH_2 deformation (ceramide, a lipid)	31
1297	CH_2 deformation	50
1297	Lipid	51
1300	C-C stretch	52
1300	Adenine, cytosine	1
1300-1336	CH_2 twisting and wagging (lipid)	27
1301	Lipid	18
1302	Lipid (CH_2 twist and =C-H bend)	46
1302	CH_2 twist and wagging (phospholipids)	22
1303	CH_2 twist (breast lipid)	20
1303	CH_3, CH_2 twisting	14
1303	Adipose tissue	40
1303	Adenine	16
1303	CH_2 chain deformation (membrane)	15
1303	CH_2 deformation (lipid)	2
1304	Adenine, cytosine	12
1306	Lipids	34
1309	CH_2 twist/wag (lipids)	37
1320	Guanine	1
1320	-CH_2 symmetric wagging (lipid)	2
1322	C-H (protein sidechains)	11
1325	Tryptophan (Alfano) / Nucleic acids (Feld)	13
1330	Phospholipids, DNA	29
1330	DNA nucleotide base	58
1333	Guanine	15
1334	CH deformation	8
1335	Nucleic acids	5,59
1335	Aromatic amino acids (?)	51
1336	UVRR Adenine & Guanine	60
1337	Nucleic acid purine bases (Guanine and adenine)	47
1338	Tryptophan	15
1339-1340	Adenine	12,15
1340	Nucleic acid mode in colon	57
1340	Tryptophan doublet	24
1340	Heme vibrational mode	53

1340	-CH_2 symmetric wagging (lipid)	2
1343	CH_3, CH_2 wagging	14
1343	Adenine, TRP (protein)	1
1350	Glucose	29
1358	Myoglobin peak in diseased breast tissue (downshifted and enhanced)	46
1358-1360	Haemoglobin (?) in liver, kidney & colon @407nm	34,18
1360	Tryptophan doublet	24
1361	Tryptophan	15
1365	Guanine, TRP (protein)	1
1370	Myoglobin (heme or pophyrin)	46
1370	-CH_3 symmetric deformation	2
1372	Lipids	34
1376-1377	Thymine, adenine, guanine	12,16
1380	Lactate (?)	35
1400	Uracil, adenine	1
1401	CH_3 symmetric bend	13
1421	Adenine, guanine	16
1427	UVRR Adenine & Guanine	60
1422	Adenine	12
1422-1441	Tryptophan (indole N-H in plane bend) shifts from 1422 (no H-bonding) to 1441 (strong H-bonding)	24
1438-1439	CH_2 deformation (lipid)	27
1438	CH_2 scissoring	50
1439	CH_2 scissoring deformation (normal breast lipid)	20, 61
1440	Lipid	51
1440	Shoulder lipid CH_2 scissor	2,31
1441	Lipid	34,18
1441	CH_2 in normal breast	36
1442	Lipid (C-H bend)	46
1442	CH_2 deformation (lipids and proteins)	22
1442	CH bend	51
1444	Adipose tissue	40
1445	CH_2 or CH_3 bending	52
1445-1452	CH_2, CH_3 deformation (protein)	27
1446	CH_2 or CH_3 bending (shifted for benign breast tumour)	14
1448	Deoxy-ribose (CH_2 deformation)	15
1449-1450	CH_2 or CH_3 bending (protein)	4,12,43
1449	CH-deformation	16
1450	C-H deformation	1,10
1450	CH_2 scissoring (shifted from 1439) (infiltrating ductal carcinoma)	61
1451	C-H bend	2,40
1451	CH_3 deform. asymmetric, CH_2 deform (protein)	31
1452	CH_2 deformation	8,36
1452	CH_2 scissor (lipid), CH_2/CH_3 protein	37
1454	CH_3 asymmetric bend	13
1454	Phospholipds, collagen	29
1455	CH_2 deformation (breast lipid)	20
1457	CH_3 deformation	50
1457	Lactic acid	21

1458	Nucleic acids (in colon)	57
1462	C-H deformation	1
1462	Deoxy-ribose (CH_2 deformation)	15
1466	Urea	7
1474	Altered lipid component in liver carcinoma	34
1480	Purine bases: Guanine, adenine	1,15,51,58
1484	UVRR Adenine & Guanine	60
1485	Nucleic acids	5,59
1485	Nucleic acid purine bases (Guanine and adenine)	47
1487	Guanine, adenine	12,16
1491	Formalin artefact	14
1509	Phenylalanine	4
1510-1511	Adenine	12,16
1514	C=C stretch (carotenoid, a cellular pigment)	25
1517	Carotenoid	20
1520	Carotenoid	6
1523	-C=C- Carotenoid	55
1523	β-carotene	46
1524	Carotenoid	30
1525	Low density lipoproteins	2
1528	Carotenoid (in liposarcoma)	51
1529	Carotenoid	34
1538	Carotenoid	39
1541	Typosine	11
1547	Tryptophan	23
1550	TRP (protein)	1,24
1552	Amide II (NH deform and CN stretch)	31
1553	Tryptophan	15
1554	Amide II (coronary thrombus)	2
1555	Amide II	10
1555	Tryptophan	47
1556	Tryptophan	4
1560	Heme vibrational mode	53
1570	Purine bases (A, G)	15
1573	Amide II (NH deform., CN stretch)	8
1575	Guanine, adenine, TRP (protein)	1
1576	Nucleic acids (colon)	57
1577-1578	Guanine, adenine	12,16
1578	Pyrimidine ring	62
1578	Heme protein	48
1579	UVRR Adenine & Guanine	60
1580	Nucleic acids	51,58
1585	Nucleic acids	59
1589-1590	Porphyrin (biliverdin, liver) C=C stretch	27
1593	Biliverdin / bilirubin	18
1593	Nucleic acid purine bases (Guanine and adenine)	47
1597	Urea	7
1600	?	1
1600	Tyrosine	24
1601	Pyrimidine ring	62

1601	Phenylalanine (BSA)	4
1602	Phenylalanine	11
1602	Tyrosine	47
1606	Phenylalnine, tyrosine	12
1610	Tyrosine (UVRR colon)	59
1612	Proteins and nucleic acid peaks ???	47
1616	Tyrosine (BSA)	4
1617	Tyrosine, phenylalanine	12
1618	Tyrosine	24
1618-1628	Porphyrin (lung) C=C stretch	27
1620	Uracil, TRP, TYR, PHE (pr.)	1
1620	Altered lipid component in liver cancer	34
1620	Heme vibrational mode	53
1620	Tryptophan (UVRR colon)	59
1622	Tryptophan	47
1637	Amide I (?)	14
1640	Intermolecular bending mode of water	45
1645-1655	Amide I: α-helix	24
1645-1660	Amide I: α-helix (???)	56,6
1650	C=C lipid band	59
1650-1651	Amide I (C=O stretch): α-helix	31,52
1651	Nucleic acid pyrimdine bases (cytosine & thymine)	47
1651	Keratin (C=O stretch Amide I)	33
1652	Lipid	34
1653	Lipid (C=C stretch)	46
1653-1657	Amide I	27,49
1654-1662	Amide I: α-helix	15
1645-1685	Amide I: unordered	15
1654	C=C stretch cis configuration (breast lipid)	20
1654	C=C stretch (lipid)	27
1655	Shoulder lipid C=C	2
1655	C=C	18
1655-1665	Amide I: irregular	24
1656	Unsaturated fat (C=C)	18
1656	Collagen	29
1656	Amide I: (C=O stretch) disordered, collagen triple helix	31
1656-1657	Amide I (C=O)	14,13
1657	C=C stretch (Lipids) (pre-resonance enhancement of this peak occurs at 250nm)	47
1657	Amide I (C=C lipid in normal breast)	36
1659	Amide I (BSA)	4
1660-1670	Amide I: unordered	56
1661	Amide I (C=O stretch)	37
1662	Nucleic acids (colon)	57
1664	Amide I: α-helix	22
1665	Amide I: collagen	18
1665	Uracil, guanine, cytosine, Am I	1
1665-1680	Amide I: β-sheet	15
1666	Urea	7
1667	C=C stretch (decreases with malignancy in liposarcoma)	51

1667	Amide I (disordered)	50
1668	Amide I (keratin: β-sheet, collagen)	31
1669	Lipid	51
1669	Amide I: random coil (mouse breast adenocarc.)	19
1665-1680	Amide I: β-sheet	24,56
1725	Lactate	26
1726	Lactate	7
1740	C=O stretch	18
1743	C=O stretch (breast lipid)	20
1743	C=O lipid ester	31
1745-1746	C=O stretch (lipid)	27
1768	COO stretch	31
2580	Sulphydryl (S-H)	5
2852	CH_2 sym-stretch (lipids/proteins)	37
2857	C-H stretch (-CH_2 sym) (breast lipid)	20
2875	C-H stretch (-CH_2 asym) (breast lipid)	20
2880	Aliphatic C-H stretch	1
2885	Lactate	45
2890	Glucose doublet	26,45
2890	Lactate triplet	35
2894	Lactate	7
2895	Glucose	7
2898	C-H stretch (-CH_3 sym) (breast lipid)	20
2929	C-H stretch (-CH_3 sym) (breast lipid)	20
2930	CH_2 anti-symmetric stretch	18
2935	C-H stretch	6
2942	Aliphatic C-H stretch	1
2942	CH_3 as-stretch (lipids/proteins)	37
2943	Glucose	7
2945	Lactate triplet	7,35,45
2950	Glucose doublet	26,45
2960	C-H stretch (-CH_3 asym) (breast lipid)	20
2975	Aliphatic C-H stretch	1
2990	Lactate triplet	35
2995	Lactate	7,45
3006	=C-H stretch (breast lipid)	20
3250	OH-stretch (bound and unbound water)	3
3390	OH-stretch	6

Proline and hydroxyproline make up 25% of the amino acids in collagen

1650-1675: *Amide I overlapping with C=C modes from lipids and/or ketone C=O from DNA bases.*

---

[1] Hartman, KA, Clayton, NW, Thomas, GJ, Jr., Studies of Virus Structure by Raman Spectroscopy, *Biochemical and Biophysical Research Communications*, **50**, 942, 1973.
[2] Yu, N-T, Li, X-Y, Kuck, JFR, Chapter 4: Biomedical Applications of Raman Spectroscopy: Eye Lens Research and Cardiovascular Diseases, In: *Biomedical Applications of Spectroscopy*, Ed. by Clark, RJH, Hester, RE, John Wiley & Sons, 1996.

[3] Gniadecka, M, Nielsen, OF, Christensen, DH, Wulf, HC, Structure of Water, Proteins, and Lipids in Intact Human Skin, Hair, and Nail, *The Journal of Investigative Dermatology*, **110**, 4, 1998.
[4] Fredericks, P, Virational Spectroscopy heads Towards Life, *Analysis*, S3-S8, 1995.
[5] Bergbauer, KL, Kuck, JFR, Su, KC, Yu, N-T, Raman Investigation of UV-Induced Eye Lens Damage and Its Prevention, *Proceedings of the Fourteenth International Conference on Raman Spectroscopy*, Section 5: Biomedical Applications, 188-189, Hong Kong, 1994.
[6] Ozaki, Y, Medical Application of Raman Spectroscopy, *Applied Spectroscopy Reviews*, **24**(3&4), 259-312, 1988.
[7] Goetz, MJ, Jr, Cote, GL, Erckens, R, March, W, Motamedi, M, Application of a Multivariate Technique to Raman Spectra for Quantification of Body Chemicals, *IEEE Transactions on Biomedical Engineering*, **42**, 7, 728-731, 1995.
[8] Maquelin, K, Choo-Smith, L-P, van Vreeswijk, T, Endtz, HP, Smith, B, Bennett, R, Bruining, HA, Puppels, GJ, Raman Spectroscopic Method for Identification of Clinically Relevant Microorganisms Growing on Solid Culture Medium, *Analalytical Chemistry*, **72**, 12-19, 2000.
[9] Chaiken, J, Finney, WF, Peterson, CM, Peterson, CP, Knudson, PE, Weinstock, RS, Lein, P, Noninvasive, In Vivo, Tissue Modulated Near Infrared Vibrational Spectroscopic Study of Mobile and Static Tissues: Blood Chemistry, *Proc. SPIE: Biomedical Spectroscopy: Vibrational Spectroscopy and Other Novel Techniques*, **3918**, 135-143, 2000.
[10] Manfait, M, Lamaze, P, Lamfarraj, H, Pluot, M, Sockalingum, GD, Diagnosis and Prognosis of Tissue Pathologies by Raman Microspectroscopy: An Application to Human Thyroid Tumours, *Proc. SPIE: Biomedical Spectroscopy: Vibrational Spectroscopy and Other Novel Techniques*, **3918**, 153-160, 2000.
[11] Siebinga, I, Vrensen, GFJM, Otto, K, Puppels, GJ, De Mul, FFM, Greve, J, Ageing and Changes in Protein Conformation in the Human Lens: A Raman Microspectroscopic Study, *Experimental Eye Research*, **54**, 759-767, 1992.
[12] Puppels, GJ, Confocal Raman Microspectroscopy, In: *Fluorescent and Luminescent Probes*, 2nd edition, Edited by Mason, WT, Chapter 29, 377-406, 1999.
[13] Mahadevan, A, Ramanujam, N, Mitchell, MF, Malpica, A, Thomsen, S, Richards-Kortum, R, Optical Techniques for the Diagnosis of Cervical Precancers: A Comparison of Raman and Fluorescence Spectroscopies, *Proc. SPIE: Advances in Fluorescence Sensing Technology II*, **2388**, 110-120, 1995.
[14] Frank, CJ, Applications of Near-Infrared Raman Spectroscopy to the Study of Human Tissue Specimens, *PhD Thesis*, Ohio State University, 1994.
[15] Mahadevan-Jansen, A, Richards-Kortum, R, Raman Spectroscopy for the Detection of Cancers and Precancers, *Journal of Biomedical Optics*, **1**, 1, 31-70, 1996.
[16] Puppels, GJ, Olminkhof, JHF, Segers-Nolten GMJ, Otto, C, DeMUl, FFM, Greve, J, Laser Irradiation and Raman Spectroscopy of Single Living Cells and Chromosomes: Sample Degredation Occurs with 514.5nm but not with 660nm Laser Light, *Experimental Cell Research*, **195**, 361-367, 1991.
[17] Dou, X, Yamaguchi, Y, Yamamoto, H, Doi, S, Ozaki, Y, Quantitative Analysis of Metabolites in Urine Using a Highly Precise, Compact Near-Infrared Raman Spectrometer, *Vibrational Spectroscopy*, **13**, 83-89, 1996.
[18] Keller, S, Schrader, B, Hoffmann, A, Schrader, W, Metz, K, Rehlaender, A, Pahnke, J, Ruwe, M, Budach, Application of Near-Infrared-Fourier Transform Raman Spectroscopy in Medical Research, *Journal of Raman Spectroscopy*, **25**, 663-671, 1994.
[19] Schrader, B, Keller, S, Lochte, T, Fendel, S, Moore, DS, Simon, A, Sawatzki, J, NIR FT Raman Spectroscopy in Medical Diagnosis, *Journal of Molecular Structure*, **348**, 293-296, 1995.
[20] Frank, CJ, Redd, DCB, Gansler, TS, McCreery RL, Characterization of Human Breast Biopsy Specimens with Near-IR Raman Spectroscopy, *Anal. Chem.*, **66**, 319-326, 1994.
[21] Pilotto, S, Pacheco, MTT, Silveira, L, Jr, Balbin Villaverde, A, Zangaro, RA, Analysis of Near-infrared Raman Spectroscopy as a New Technique for Transcutaneous Non-Invasive Diagnosis of Blood Components, *Lasers in Medical Science*, **16**, 2-9, 2001.
[22] Ozaki, Y, Sato, H, Borchman, D, Mizuno, A, Potential of Near-Infrared Raman Spectroscopy in Medical Science, *Proceedings of the Fourteenth International Conference on Raman Spectroscopy*, Section 5: Biomedical Applications, 201-203, Hong Kong, 1994.

[23] Nie, S, Berbauer, KL, Ho, JJ, Kuck, JFR, Jr., Yu, N-T, Applications of Near-Infrared Fourier Transform Raman Spectroscopy in Biology and Medicine, *Spectroscopy*, **5**, 7, 24-32, 1990.
[24] Miura, T, Thomas, GJ, Jr., Raman Spectroscopy of Proteins and Their Assemblies, Chapter 3 in *Subcellular Biochemistry, Volume 24. Proteins, Structure, and Engineering*, ed. by Biswas, BB, Roy, S, Plenum Press, New York, 1995.
[25] Naumann, Infrared and NIR Raman Spectroscopy in Medical Microbiology, *Proc. SPIE:Infrared Spectroscopy: New Tool in Medicine*, **3257**, 245-257, 1998.
[26] Wang, SY, Hasty, CE, Watson, PA, Wicksted, JP, Stith, RD, March, WF, Analysis of Metabolites in Aqueous Solutions by Using Laser Raman Spectroscopy, *Applied Optics*, **32**, 6, 925-929, 1993.
[27] Shim, M, Wilson, BC, The Effects of Ex Vivo Handling Procedures on the Near-Infrared Raman Spectra of Normal Mammalian Tissues, *Photochemistry and Photobiology*, **63**, 5, 662-671, 1996.
[28] Gniadecka, M, Wulf, HC, Mortensen, NN, Nielsen, OF, Christensen, DH, Diagnosis of Basal Cell Carcinoma by Raman Spectroscopy, *Journal of Raman Spectroscopy*, **28**, 2-3, 125-129, 1997.
[29] Mahadevan-Jansen, A, Mitchell, MF, Ramanujam, N, Malpica, A, Thomsen, S, Utzinger, U, Richards-Kortum, R, Near-infrared Raman Spectroscopy for In Vitro Detection of Cervical Precancers, *Photochemistry and Photobiology*, **68**, 123-132, 1998.
[30] Mizuno, A, Kitajima, H, Kawauchi, K, Muraishi, S, Ozaki, Y Near-Infrared Fourier-Transform Raman-Spectroscopic Study of Human Brain-Tissues and Tumours, *Journal of Raman Spectroscopy*, **25**, 1, 25-29, 1994.
[31] Lucassen, GW, Caspers, PJ, Puppels, GJ, In Vivo Infrared and Raman Spectroscopy of Human Stratum Corneum, *Proc. SPIE: Infrared Spectroscopy: New Tool in Medicine*, **3257**, 52-61, 1998.
[32] Caspers, PJ, Lucassen, GW, Wolthuis, R, Bruining, HA, Puppels, GJ, In Vitro and In Vivo Raman Spectroscopy of Human Skin, *Biospectroscopy*, **4**, S31-S39, Supplement S, 1998.
[33] Carter, EA, Williams, AC, Barry, BW, Edwards, HGM, Probing Diseased Skin with FT-Raman Spectroscopy, *Proc. SPIE: Infrared Spectroscopy: New Tool in Medicine*, **3257**, 72-77, 1998.
[34] Redd, DCB, Frank, CJ, Feng, ZC, Gansler, TS, McCreery, RL, Raman Spectroscopic Characterization of Human Malignant Tissues: Implications for a Percutaneous Optical Biopsy Technique for In-Situ Tissue Diagnosis, *Proc SPIE: Optical Biopsy*, **2081**, 185-189, 1993.
[35] Wicksted, JP, Erckens, RJ, Motamedi, M, March WF, Monitoring of Aqueous Humor Metabolites Using Raman Spectroscopy, *Proc SPIE: Advances in Laser and Light Spectroscopy to Diagnose Cancer and Other Diseases*, **2135**, 264-274, 1994.
[36] Feld, MS, Manoharan, R, Salenius, J, Orenstein-Carndona, J, Romer, TJ, Brennan, JF, Dasari, R, Wang, Y, Detection and Characterization of Human Tissue lesions with Near-Infrared Raman Spectroscopy, *Proc. SPIE: Advances in Fluorescence Sensing Technology II*, **2388**, 99-104, 1995.
[37] Gniadecka, M, Wulf, HC, Nielsen, OF, Christensen, DH, Hercogova, J, Distinctive Molecular Abnormalities in Benign and Malignant Skin Lesions: Studies by Raman Spectroscopy, *Photochemistry and Photobiology*, **66**, 4, 418-423, 1997.
[38] Klug, DD, Singleton, DL, Walley, VM, Laser Raman Spectrum of Calcified Human Aorta, *Lasers in Surgery and Medicine*, **12**, 13-17, 1992.
[39] Brennam, JF, III, Romer, TJ, Tercyak, AM, Wang, Y, Fitzmaurice, M, Lees, RS, Kramer, JR, Jr, Dasari, RR, feld, MS, In situ Histochemical Analysis of Human Coronary Artery By Raman Spectroscopy Compared with Biochemical Assay, *Proc. SPIE: Advances in Fluorescence Sensing Technology II*, **2388**, 105-109, 1995.
[40] Baraga, JJ, Feld, MS, Rava, RP, Rapid Near-Infrared Raman Spectroscopy of Human Tissue with a Spectrograph and CCD Detector, *Applied Spectroscopy*, **46**, 2, 187-190, 1992.
[41] Nie, S, Yu, N-T, Raman-Based Biomedical Diagnosis at the Molecular Level, *Proceedings of the Fourteenth International Conference on Raman Spectroscopy*, Section 5: Biomedical Applications, 198-199, Hong Kong, 1994.
[42] WentrupByrne, E, Armstrong, CA, Armstrong, RS, Collins, BM, Fourier Transform Raman Microscopic Mapping of the Molecular Components in a Human Tooth, *Journal of Raman Spectroscopy*, **28**, 151-158, 1997.
[43] Timlin, JA, Carden, A, Morris, MD, Chemical Microstructure of Cortical Bone Probed by Raman Transects, *Applied Spectroscopy*, **53**, 1429-1435, 1999.

[44] Clarke, RH, Hanlon, EB, Isner, JM, Brody, H, Laser Raman Spectroscopy of Calcified Atherosclerotic Lesions in Cardiovascular Tissue, *Applied Optics*, **26**, 3175-3177, 1987.
[45] Erckens, RJ, Motamedi, M, March, WF, Wicksted, JP, Raman Spectroscopy for Non-Invasive Characterization of Ocular Tissue: Potential for Detection of Biological Molecules, *Journal of Raman Spectroscopy*, **28**, 293-299, 1997.
[46] Redd, DCB, Feng, ZC, Yue, KT, Gansler, TS, Raman Spectrscopic Characterization of Human Breast Tissues: Implications for Breast Cancer Diagnosis, *Applied Spectroscopy*, **47**, 6, 787-791, 1993.
[47] Manoharan, R, Wang, Y, Dasari, RR, Singer, SS, Rava, RP, Feld, MS, Ultraviolet Resonance Raman Spectroscopy for Detection of Colon Cancer, *Lasers in the Life Sciences*, **6**, 4, 217-227, 1995.
[48] Hawi SR, Campbell WB, Kajdacsy-Balla A, Murphy R, Adar F, Nithipatikom K, Characterization of Normal and Malignant Human Hepatocytes by Raman Microspectroscopy, *Cancer Letters*, **110**, 35-40, 1996.
[49] Caspers, PJ, Dupont Toft Jacobsen, A, Lucassen, GW, Wolthius, R, Bruining, HA, Puppels, GJ, Raman Microspectrometry of Human Skin, In: *Spectroscopy of Biological Molecules: Modern Trends*, Ed by Carmona, P, Navarro, R, Hernanz, A, Kluwer Academic Publishers, 453-454, 1997.
[50] Sajid, J, Elhaddaoui, A, Turrell, S, Fourier Transform Vibrational Spectroscopic Analysis of Human Cerebral Tissue, *Journal of Raman Spectroscopy*, **28**, 165-169, 1997.
[51] Manoharan, R, Wang, Y, Boustany, N, Brennan III, JF, Baraga, JJ, Dasari, RR, Van Dam , J, Singer, S, Feld, MS, Raman Spectroscopy for Cancer Detection: Instrument Development and Tissue Diagnosis, *Proc. SPIE: Biomedical Optoelectronic Devices and Systems II*, **2328**, 128-132, 1994.
[52] Alfano, RR, Liu, CH, Sha, WL, Zhu, HR, Akins, DL, Cleary, J, Prudente, R, Cellmer, E, Human Breast Tissue Studied by IR Fourier Transform Raman Spectroscopy, *Lasers in the Life Sciences*, **4**, 1, 23-28, 1991.
[53] Shim, MG, Song, LMWM, Marcon, NE, Wilson, BC, In Vivo Near-infrared Raman Spectroscopy: Demonstration of Feasibility During Clinical Gastrointestinal Endoscopy, *Photochemistry and Photobiology*, **72**, 146-150, 2000.
[54] Dou, X, Yamaguchi, Y, Yamamoto, H, Doi, S, Ozaki, Y, A Highly Sensitive, CompactRaman System Without a Spectrometer for Quantitative Analysis of Biological Samples, *Vibrational Spectroscopy*, **14**, 199-205, 1997.
[55] Puppels, GJ, Otto, C, Greve, J, Confocal Raman Microspectroscopy in Biology: Applications and Future Developments, *Trends in Analytical Chemistry*, **10**, 8, 249-253, 1991.
[56] Carey, PR, Chapter 4: Protein Conformation from Raman and Resonance Raman Spectra, *Biochemical Applications of Raman and Resonance Raman Spectroscopies*, Academic Press, 1982.
[57] Manoharan, R, Wang, Y, Feld, MS, Histochemical analysis of biological tissues using Raman spectroscopy, *Spectrochim. Acta Part A*, **52**, 215-249, 1996.
[58] Yazdi, Y, Ramanujam, N, Lotan, R, Mitchell, MF, Hittelman, W, Richards-Kortum, R, Resonance Raman Spectroscopy at 257nm Excitation of Normal and Malignant Cultured Breast and Cervical Cells, *Applied Spectroscopy*, **53**, 1, 82-85, 1999.
[59] Boustany, NN, Manoharan, R, Dasari, RR, Feld, MS, Analysis of Normal and Diseased Colon Mucosa Using Ultraviaolet Resonance Raman Spectroscopy, *Proc. SPIE:Advances in Laser and Light Spectroscopy to Diagnose Cancer and Other Diseases III: Optical Biopsy*, **2679**, 66-70, 1996.
[60] Sureau, F, Chinsky, L, Amirand, C, Ballini, JP, Duquesne, M, Laigle, A, Turpin, PY, Vigny, P, An Ultraviolet Micro-Raman Spectrometer: Resonance Raman Spectroscopy within Single Living Cells, *Applied Spectroscopy*, **44**, 6, 1047-1051, 1990.
[61] Frank, CJ, McCreery, RL, Redd, DCB, Raman Spectroscopy of Normal and Diseased Human Breast Tissues, *Analytical Chemistry*, **67**, 777-783, 1995.
[62] Russel, MP, Vohnik, S, Thomas, GJ, Design and Performance of an Ultraviolet Resonance Raman Spectrometer for Proteins and Nucleic Acids, *Biophysical Journal*, **68**, 1607-1612, 1995.

Appendix 5: Relevant Publications by the Author

List of contents

Lasers Med Sci 1998, 13:3–13

REVIEW

Optical Spectroscopy for the Early Diagnosis of Gastrointestinal Malignancy

H. Barr, T. Dix and N. Stone
Gloucestershire Royal and Cranfield University Institute of Medical Sciences, Gloucestershire Royal Hospital, Gloucester, UK

Abstract. The early diagnosis of gastrointestinal malignancy will allow eradication of the disease prior to invasive cancer. At present, fluorescence spectroscopy offers the most realistic prospect of an early clinical system and is currently under evaluation. Optical coherence tomography can differentiate the layers of the oesophageal wall and has greater resolution than ultrasound. Although complicated, Raman spectroscopy offers the greatest information with possible development of a molecular endoscope.

Keywords: Biopsy; Fluorescence; Optical; Raman; Spectroscopy

INTRODUCTION

Virtually all gastrointestinal cancers present with surface abnormalities prior to becoming invasive tumours. These changes, invisible to white light illumination, have to be detected before the development of invasive cancer if eradication and prevention are to be possible. There may be a prolonged period of some years from the detection of early precancer of the gastrointestinal tract and the development of invasive cancer [1]. In addition there is a dramatic rise occurring in adenocarcinoma at the gastroesophageal junction [2]. The precancerous changes are currently detected using rigorous biopsy protocols [3], which are time consuming and cumbersome. Optical techniques may allow early diagnosis and permit screening protocols at endoscopy. Once detected there are now non-invasive endoscopic eradication methods available [4–7]. Over the next few years we are likely to see a revolution in endoscopic detection, and already the commercial possibilities are exciting industry [8].

Spectroscopic analysis of tissue depends on identifying a characteristic spectral emission that can be used to differentiate between normal and abnormal areas in real time. Optical biopsy is the term commonly used to describe this technique, but the term biopsy is a misnomer since no tissue is removed. The main goal in optical diagnostics is to identify early cancer or dysplasia [9]. Available methods include: fluorescence spectroscopy; elastic scattering spectroscopy; optical coherence tomography and Raman spectroscopy.

Correspondence to: Professor Hugh Barr, Gloucester Gastroenterology Group, Gloucestershire Royal and Cranfield University Institute of Medical Sciences, Gloucestershire Royal Hospital, Great Western Road, Gloucester GL1 3NN, UK.

FLUORESCENCE SPECTROSCOPY

Irradiation of a molecule by light can lead to its excitation and possible fluorescence emission. This emission is of a lower energy (longer wavelength) than the exciting photon. The ground and excited states of a molecule are broadened by vibrational motion and interactions with other surrounding molecules. Hence, the energies or wavelengths of light that the molecule will absorb are also broadened.

Absorption of the incident radiation by the atoms causes the electrons to be temporarily raised to higher energy orbits [9] in the singlet state. Once in this excited state, radiationless relaxation occurs on a picosecond time scale to the bottom of the excitation band [10] where the molecules remain for a few nanoseconds. From here, several competing processes can take place such as the broadband light emission in the form of fluorescence [10] or phosphorescence [11] via intersystem crossing

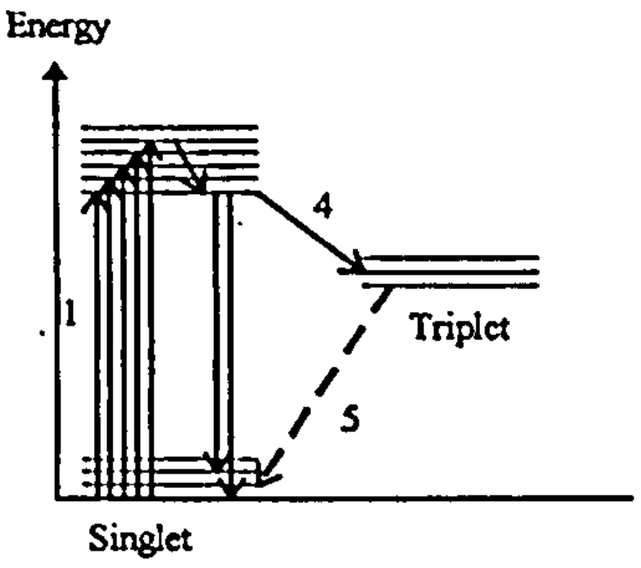

Fig. 1. Molecular absorption and emission of radiation.

[12] to the triplet state (Fig. 1). Alternatively, radiationless processes such as internal conversion and energy transfer to surrounding molecules can also take place.

A fluorophore has characteristic excitation and emission spectra, dependent on its microenvironment. Detection can be performed using a single excitation and emission wavelength, although to extract further information several excitation–emission pairs can be used. Fluorescence decay lifetimes and depolarisation can also provide important additional information.

Laser-Induced Tissue Autofluorescence

Naturally occurring fluorophores contribute to tissue autofluorescence in the near ultraviolet and visible region. Detailed interpretation of fluorescence signals is difficult because of the composite and unstructured nature of the spectra, their dependence on the microenvironment, and light re-absorption by tissue chromophores. One example is the green absorption band of haemoglobin.

Intrinsic fluorophores, such as collagen and porphyrins, have been used to characterise the physical state of many tissues including the colon, and upper aerodigestive tract [10–13]. The fluorescence signal provides information about the tissue microstructure and is strongly influenced by its chemical composition. A change in the state of the tissue towards cancer alters the autofluorescence of the tissue.

Some of the endogenous fluorophores responsible for tissue autofluorescence are listed in Table 1. Most useful are nicotinamide adenine dinucleotide, NADH, and the flavins which show changes in fluorescence spectra during metabolic transformation from the oxidised to the reduced state. They are, therefore, an important indicator of the level of metabolic activity in particular areas of tissue. When cellular metabolism is slowed and the redox potential is allowed to fully charge there is an abundance of reducing equivalents, i.e. NADH, NADPH, $FMNH_2$, $FADH_2$. When metabolism is stimulated and these reducing equivalents are oxidised, the redox potential is lowered, thus there is a shift to oxidised forms namely NAD^+, $NADP^+$, FMN, FAD. This process has been demonstrated using lactate to depress cellular metabolic activity and caffeine to increase metabolic activity [14].

We now know that oxidative species play an important role in the early molecular development of cancer [15]. The cell's defence against this oxidative stress includes NADH. Thus the fluorescence ratio of NADH to its oxidised form NAD^+ has the potential to discriminate between normal and precancerous tissue [14].

Table 1. Fluorescence lifetimes of naturally occurring fluorophores [16]

Fluorophor	Main excitation peak(s) (nm)	Main emission peak(s) (nm)	Fluorescence lifetime (ns)
Tryptophan	275	350	2.8, 1.5
Collagen	340, 270, 285	295, 395, 310	9.9, 5.0, 0.8
Elastin	460, 360, 425, 260	520, 410, 490, 410	6.7, 1.4, 7.8, 2.6, 0.5
NADH	350	460	0.6, 0.2
FNM	440	520	4.7
β-carotene		520	9.6, 2.0, 0.3
Endogenous porphyrins	400	610, 675	

This together with its high fluorescence yield make NADH a most promising fluorophore for investigation. The lack of fluorescence produced by the oxidised NAD^+ means that reduced fluorescence is seen in tumour tissue compared to the surrounding normal tissue. As the border of the tumour is approached, then the fluorescence increases. The low fluorescing centre and 'brighter' borders indicate the direction of the cancerous growth. The major exception to this rule are fibrous or schirrous cancers (breast) containing a high collagen content with high endogenous fluorescence.

Although autofluorescence has the attraction that no exogenous fluorophores are required, the fundamental problem is the broad structureless fluorescence emission caused by many non-specific fluorophores. This may be overcome by the administration of a specific exogenous fluorophore/photosensitiser that may accumulate or be retained in different concentrations by neoplastic and normal tissue.

Laser-Induced Photosensitiser Fluorescence

The administration of an exogenous fluorophore is complicated by the selection of an appropriate non-toxic agent and delivery vehicle. In addition, the biodistribution in tumour and normal tissue will vary with time. Also, these fluorescent agents often have associated photodynamic action, which restricts the administered patient dose. Autofluorescence emission from tissue porphyrins will reduce the contrast between tumour and normal tissue. One method of enhancing this restricted signal level is to ratio the red emission of the fluorophore with the blue-green tissue autofluorescence and thereby yield a dimensionless quantity [16].

The problem of targeting the mucosa and mucosal tumours directly may be achieved by using endogenous photosensitisation or immunophotodetection. The use of oral 5-aminolaevulinic acid may be very useful in the gastrointestinal tract and allow mucosal areas of dysplasia to generate excess fluorescence from protoporphyrin IX [4,17,18]. Anti-carcinoembryonic antigen monoclonal antibodies coupled to fluorescein have also been used for the immunophotodetection of human colon carcinomas in mice [19].

Fluorescence Polarisation Spectroscopy

The dependence of absorption on the polarisation of light and the depolarisation of fluorescence emission generated by polarised light have served as useful tools for identifying fluorophore electronic states and conformational structures in different environments [20]. It has been well established that the polarised spectroscopic properties of the fluorophores are highly dependent on polarity, pH and viscosity. Depolarisation studies of known fluorophores, extrinsic and intrinsic, can be used as probes to investigate their local environment. Extrinsic fluorescent dye molecules with known emission properties have been conjugated to non-emitting protein molecules in order to perform polarisation and lifetime studies that help elucidate protein structure, molecular dynamics, pathological state and characteristics of the local environment. Both rotational motions and energy-transferring mechanisms probably participate in depolarising the emission from the native fluorophores. One problem is that multiple scattering in tissue will destroy a large portion of the light polarisation.

All of the above techniques described have been based simply on the steady-state fluorescence intensity at a particular wavelength. This can be subject to significant measurement errors, due to the uncontrolled variation in excitation/tissue-detector geometry. Ratio based techniques using two or more excitation/emission wavelengths reduces, but cannot eliminate, these errors.

Time-Resolved Fluorescence Spectroscopy

Time-resolved detection can enhance the relative fluorescence emission of the dye [21,22], by removing the undesired short-lived background fluorescence. The simplest form of this is to gate the detection (introduce a time delay between the excitation pulse and signal detection). Time resolved detection has been used to study the uptake of haematoporphyrin derivative (HpD) and aluminium phthalocyanine (AlSPc) at the cellular level in a murine model [23].

An extension of the time-resolved technique is to use fluorescence lifetime imaging (FLIM). The fluorescence lifetimes of endogenous and exogenous fluorophores (Table 1) have a high information content and are sensitive to

numerous chemical and physical factors [24]. The measurement of fluorescence lifetime is unaffected by intensity-based measurement errors. Fluorescence lifetime is independent of fluorophore concentration and can be used to distinguish between tissues with different microenvironments, nucleic acid content, membrane permeability and enzymatic activity. For example, imaging of free versus protein bound NADH in cells is possible because of the differing lifetimes of the free and bound NADH (0.5 and 1.5 ns, respectively) [25]. FLIM is intrinsically more robust than steady-state measurements and if the technology can be made feasible for routine clinical use then combining spectral and lifetime information is likely to be very reliable.

Fluorescence Measuring Systems

Measurements can be performed either as a point by point measurement using an optical probe placed on or in the tissue or as a fluorescence image viewing the tissue surface. Both techniques can be used either directly or through a fibreoptic endoscope and can involve the postprocessing of the fluorescence signals (spectral ratios). Current systems vary from simple and relatively inexpensive fibreoptic fluorometers using a filtered lamp and photodiode detectors to highly complex and expensive multispectral imaging systems involving sophisticated laser sources, sensitive array detectors and computerised image processing to measure fluorescence decay lifetimes [26,27].

The common goal for all measuring systems is to obtain the maximum discrimination of the tumour fluorescence signal from the background fluorescence of normal tissue and to establish reliable limits for defining a positive fluorescent signal by comparative studies with histopathology. The most common technique is to ratio two or more fluorescence intensities. Bronchoscopic imaging systems are available for the detection of early squamous cell changes before the development of invasive lung cancer measuring the ratio of the red and green emission [28]. Digital background subtraction measuring a background level of autofluorescence at a shorter wavelength and extrapolating this to the red emission region of the exogenous dye [29,30], allows the contribution of the autofluorescence in the red to be removed from the digitised image. The fraction of the green image that is subtracted from the red is determined empirically by adjusting the video gain so that a black image is obtained when viewing a control site (normal tissue). The ratioing technique can be extended to four simultaneously imaged wavelengths [24,31]. Four individually spectrally filtered images formed on a matrix detector are processed by a computer pixel by pixel to produce an optimised contrast image. Another method of avoiding problems with intensity measurements is differential normalised fluorescence (DNF) which uses the difference in the normalised fluorescence spectra between the malignant and normal tissue [10,12]. Identification of an area of normal tissue in the patient is used to set a 'baseline curve'.

To utilise more of the spectral information and thus detect the early subtle changes in tissue a multivariate linear regression analysis (MVLR) technique has been developed [32]. Multiple excitation wavelengths were used and the resulting emission spectra were sampled at set intervals. By dividing the data into groups such as normal, dysplastic, and early carcinoma; the most 'diagnostic' excitation–emission pairs were selected. The encouraging results obtained could possibly be enhanced by the application of a neural network type learning system on fully sampled spectra.

Fluorescence lifetime measurements offer the most information for the detection of early precancerous changes. Unfortunately, the costly and complicated equipment required for these measurements does not lend itself to easy clinical use. In vitro measurements have been completed using the high frequency gain modulation of an image intensifier to preserve phase information with respect to an incident light source which is also intensity modulated at a high frequency [25]. To calculate the fluorescence lifetime a series of measurements were required to examine the detector phase angle dependence of the emission. Alternative systems have been used to complete measurements using a pulsed light source provided by either a mode-locked argon ion or nitrogen pumped dye laser [22,23]. The spectral and temporal content of the signal was preserved by using a streak camera as a detector coupled to a spectrograph.

Clinical Applications of Fluorescence Spectroscopy

For some time it has been known that tumours of the upper aerodigestive tract contained

endogenous porphyrins which allowed discrimination from the normal mucosa by autofluorescence [10,34]. Thus, most techniques are at present concentrating on laser induced fluorescence (LIF).

Panjepour et al. [10] have successfully identified high-grade dysplasia in Barrett's oesophagus using this technique. Thirty-six patients were studied and the area of Barrett's oesophagus interrogated using a nitrogen-pumped dye laser emitting 410 nm light in 5 ns pulses. This was used to excite tissue autofluorescence which was collected by a fibre bundle and analysed by a spectrograph. Both emitting and collecting fibres were included in a flexible fibreoptic probe (1.7 mm). The endoscopist passed this through the biopsy channel of the endoscope and placed the end touching the tissue. It must be noted that the fluorescence intensity is strongly affected by the probe placement against the tissue. Multiple measurements were taken and histological biopsy taken from the sites of spectral measurement. A mathematical model on differential normalised fluorescence was developed. Using this method, seven patients were detected to have high-grade dysplasia and all correlated completely with the biopsy samples. All patients with low-grade dysplasia were also correctly identified (six patients). Non-dysplastic Barrett's mucosa was identified in 16 of 23 patients (70%). An accompanying editorial [35] puts this paper in context, and suggests that a more user-friendly system is required. It would be preferable if it was incorporated directly into the endoscope with real-time imaging.

Another study of laser induced fluorescence for the detection of adenocarcinoma in Barrett's oesophagus adopted a different approach [36]. Patients with adenocarcinoma were pretreated with an intravenous photosensitiser and measurements performed immediately after resection of the oesophagus. Measurements were also taken during endoscopy in five patients to assess how applicable the technique was to clinical use. Fluorescence was excited using a nitrogen pumped dye laser connected to a 600 μm optical fibre. This fibre was used to collect light emitted from the tissue and connected to a charged coupled device camera. The fluorescence spectra from 450 to 750 nm were analysed. A tumour demarcation function was established in the form of a fluorescence ratio: the quotient of porphyrin fluorescence at 630 nm divided by autofluorescence at 500 nm. Normal oesophageal mucosa had a fluorescence ratio of 0.1 ± 0.058, gastric mucosa 0.16 ± 0.073, Barrett's oesophagus 0.205 ± 0.17, severe dysplasia 0.79 ± 0.54 and adenocarcinoma 0.78 ± 0.56. Thus, this technique can characterise different histological changes in the oesophagus, which were not macroscopically evident. Others have used hypercin for the fluorescence detection of stomach cancer [37].

Most work has concentrated on distinguishing between neoplastic and normal tissue in the colon [38–41]. This seems to be a proving ground for new detection techniques and systems. Fluorescence endoscope imaging of colonic adenomas has also been useful in identifying dysplasia in adenomatous polyps in the resected colons of three patients with familial adenomatous polyposis [42]. Although these techniques have concentrated on malignant disease, some inflammatory processes such as recurrent Crohn's disease, not evident macroscopically, can be detected using fluorescence endoscopy [43]. The ability of fluorescence techniques to distinguish between inflammation and neoplasia is therefore of current concern and a major challenge.

ELASTIC SCATTERING SPECTROSCOPY

In tissue the most likely mechanism of interaction for light photons is elastic scattering. Thus, the elastic scattering signal intensity is greater than all other signals and can be used to probe tissue characteristics [9,44]. Selected wavelengths of light, or white light, may be used to irradiate the tissue. The scattered light is collected by an optical fibre and an intensity spectrum is constructed. This comprises data from the elastic scattering and absorption of the tissue the light has passed through.

Light scattering is wavelength dependent, the greatest degree occurring in photons of wavelength similar to the size of the particles scattering them. This is predicted by Mie theory. Thus, the different morphological characteristics of precancer and cancer cells, as well as changes in tissue microstructure may be probed by this method. The depth to which the tissue can be probed is dependent on the penetration of the light and the geometry of the illuminating and collecting fibres. All the important scattering components of tissue have yet to be fully identified.

Its use for gastrointestinal neoplasia has been explored by the Los Alamos group [45]. Their approach has been to use different collecting and irradiating fibres in direct contact with the tissue to avoid specular reflectance. The advantages of elastic scattering are that the signals are large and information can be gathered rapidly and the equipment is relatively inexpensive. The diagnostic algorithms have yet to be fully evaluated and developed.

OPTICAL COHERENCE TOMOGRAPHY

Optical coherence tomography (OCT) examines fine tissue structure using light elastically backscattered from tissue layers and boundaries. Light from a monochromatic low coherence source (usually a superluminescent diode) is evenly split into two fibres. One fibre directs light to the tissue to be investigated and the other to a reference mirror. When the signals from the mirror and the tissue are recombined constructive interference occurs when the path lengths match to within the coherence length of the light. Thus, the optical path length of the reference arm controls the depth of measurement in the sample. Accurate cross-sectional images can be obtained from the backscattered light giving a two-dimensional image which can be displayed with false colour. The depth resolution depends on the light sources used and can vary from 50 μm to 2–4 μm if ultrashort pulsed lasers are used [46,47].

The use of this technique has been initially in vascular imaging [48] and skin diagnostics. It is analogous to ultrasound imaging, but with up to 10 times improved depth resolution OCT will give more detailed morphological information for the detection of early cancer. Both these techniques can be adapted for endoscopic use. The depth for OCT imaging in tissues is limited by the power of the superluminescent diode source. Images have been obtained in the gastrointestinal tract to a depth of 200–300 μm [49].

The most likely use for OCT will be to stage gastrointestinal neoplasms after they are discovered using other methods. This could be achieved using the technique to measure the depth of abnormal growth at a particular position within the gastrointestinal tract. A scan covering all regions would be likely to be too time consuming.

RAMAN SPECTROSCOPY

Raman spectroscopy is a very powerful technique, which has the potential to identify early molecular markers of malignant change. It can be used to probe the vibrational energy levels of tissue molecules. The detection of biochemical tissue changes via vibrational spectroscopy may provide a new methodology for the development of the molecular endoscope.

Raman Theory

If a monochromatic beam of photons passes through any medium a proportion will be scattered in all directions. These scattered photons will consist almost entirely of radiation of the incident frequency, ν. This is Rayleigh scattering, an elastic process, whereby no energy is lost from the interacting photon. However, a small number of photons will emerge with discrete frequencies above and below that of the incident beam ($\nu \pm \Delta\nu_i$). This is Raman scattering, and the energy shift is independent of the exciting frequency, ν, and is characteristic of the species of scattering molecule [50].

A Raman spectrum is a plot of scattered intensity as a function of energy difference between the incident and scattered photons. The units of energy are displayed in wavenumbers (1/wavelength). The loss (or gain) in photon energies corresponds to the difference in the final and initial vibrational energy levels of molecules participating in the interaction. A typical Raman peak is spectrally narrow, easy to resolve and sensitive to molecular structure and the surrounding environment. Vibrational spectroscopy techniques can thus provide specific histochemical information unparalleled by other optical methods.

The Raman effect can be induced by all frequencies of incident light. The energy change of the scattered photon is constant for a particular molecular species. As an example of this, the C=C stretching vibration of the benzene molecule always produces a Raman peak downshifted by 1612 cm^{-1} independent of the frequency of the excitation light [51]. The main factors that determine the choice of excitation wavelength are, the depth of penetration of the light through tissue; the intensity of the induced fluorescence signal at that wavelength; the availability of an intense source and a sensitive detector at the wavelength selected.

Raman scattering is an inherently weak process. The intensity of the Raman signal is typically 10^{-9} to 10^{-6} of the Rayleigh background [52]. Therefore, it is difficult to observe without intense monochromatic excitation and a sensitive detector. The Raman effect occurs without photon absorption by the molecule, but rather the molecule is perturbed by the photon and it is induced to undergo a vibrational or rotational transition. Hence the interaction process between the photon and molecule is very fast; of the order of picoseconds, whereas the time for absorption and fluorescence is of the order of 10 ns [53,54].

Raman Techniques

Visible

Early attempts to measure the Raman spectra of tissues were limited by two factors, the highly fluorescent nature of biological samples and the long integration times and high power densities required. The early Raman spectra of tissue were measured using visible laser excitation light; mainly from argon-ion laser lines [55,56]. Detection of the Raman scattered light involved using a monochromator to frequency disperse the collected light and a photomultiplier tube to detect the intensity of the photons in the frequency range of interest.

Infra-red Raman

Visible Raman spectroscopy has been superseded by the development of interferometers using Fourier transform Raman spectroscopy. This technique using infra-red excitation light, reduces tissue fluorescence. After modulation by the interferometer, the filtered Raman-scattered light is detected by means of a high sensitivity InGaAs detector. The Fourier transform IR-Raman technique produces adequate signal-to-noise, with moderately high power densities. However, acquisition times of about 30 min were required to obtain the spectra of highly fluorescent tissues [57,58].

Near Infra-red Raman

The development of diode lasers and CCD cameras, sensitive in the near infra-red, has made it possible to measure the tissue Raman spectra with near-infra-red (NIR) excitation. The major advantage of this technique is that NIR radiation does not generally induce electronic absorption. Therefore, most materials, including biological tissue, exhibit extremely weak fluorescence relative to visible excited Raman and relatively short integrations are possible [59,60].

The development of holographic notch filters has also played a major part in improving the practicality of Raman spectroscopy for medicine. The largest component of scattered light from tissue is the elastically scattered (Rayleigh) light. This must be filtered out before measurement. This was originally achieved with triple monochromators. However, the throughput of this type of system is very low, necessitating long acquisition times or high laser powers. However, with a holographic Rayleigh rejection filter, a single monochromator is required to separate the Raman spectra into its separate energies. Hence, a much greater throughput is achieved and much shorter acquisition times or reduced laser powers are possible.

Removal of Background Fluorescence

For biological tissue samples the optimal excitation wavelength range generally falls between 750 and 850 nm. The resulting tissue Raman spectra contain a large fluorescence background and they lie in the same spectral region.

A simple method to remove the fluorescence is polynomial subtraction; whereby the spectrum containing both Raman and fluorescence information is fit to a polynomial of high enough order to describe the fluorescence line shape but not the higher frequency Raman line shape. A fifth-order polynomial was found to be optimal by Mahadevan et al. [61]. The best fit polynomial was then subtracted from the spectrum to yield the Raman signal alone.

An alternative method is to vary the frequency of the excitation light over a narrow range (10–30 cm^{-1}). The Raman band positions vary directly with the excitation frequency, whereas the fluorescence emission remains fairly constant with such small changes in excitation frequency, allowing it to be efficiently subtracted out [60].

Time gating is another method to remove the fluorescence signal. This technique takes advantage of the short lifetimes of Raman scattering events (10^{-11}–10^{-13} s) compared with fluorescence lifetimes (10^{-9}–10^{-7} s) in biological samples to temporally differentiate between Raman and fluorescence signals.

Using a pulsed laser source, a time gate can be used to synchronise the detector with the laser pulse so that all the Raman signal is collected, while the majority of the fluorescence is rejected [54].

Resonance Raman Spectroscopy

An alternative strategy is to resonantly excite high-lying electronic states with ultraviolet light, a process known as UV resonance Raman spectroscopy (UVRR). In biological materials, quenching and non-radiative relaxation from these states often eliminates fluorescence or causes it to occur at much longer wavelengths, so that Raman spectra can be obtained without interference [51].

The principal advantage of UVRR in biomedical applications is that by selecting the appropriate excitation wavelength, Raman bands of disease markers can be selectively enhanced in the midst of overlapping vibrations from more abundant tissue components. UV excitation results in a tremendous increase in Raman intensity due to the Raman cross-section being proportional to the fourth power of the excitation frequency (ν^4). Hence, disease markers present in low concentration can be potentially observed. For example, nucleic acids are selectively enhanced with 251 nm laser light [51].

UVRR and NIR methods are complementary. UV light exhibits shallow penetration in tissue (20–50 μm), providing the ability to sample superficial lesions, such as dysplasia. NIR light has a relatively small extinction coefficient and hence penetrates deeply into tissues, providing the opportunity to sample large volumes and probe subsurface details.

Current Applications of Raman Spectroscopy

The majority of the work on Raman detection of malignancy has been for the detection of breast, brain, gynaecological and bladder cancer and some sarcomas [61–65]. There are some data on gastrointestinal cancer.

Redd et al. [64] produced Raman spectra of a number of normal and malignant colonic tissue samples in vitro. They demonstrated that Raman lines attributable to carotenoids and lipids have much greater intensities in adenocarcinoma. At an excitation wavelength of 514.5 nm carotenoid resonance enhancement is achieved. Whereas if near-IR excitation is used lipids provide the greater Raman component. They proposed an optical fibre probe design to measure the Raman spectra of tissues in situ.

Manoharan et al. [51,66] showed that the distinct biochemical differences between normal and neoplastic colonic tissues may be exploited spectrally using the technique of ultraviolet resonance Raman spectroscopy. In the histochemical detection of precancerous cells pathologists look for increases in the nuclear-to-cytoplasmic ratio. The study evaluated the use of UVRR to detect nucleic acid and protein changes in human colon adenocarcinoma and the surrounding normal colonic mucosa. The authors were the first to demonstrate Raman spectra from biological tissue using UV excitation light (239.6 nm). They showed that the ratio of nucleic acid to cytoplasmic content in the cells of colonic mucosa can be quantitatively determined from the intensity ratio of the nucleic acid bands to protein bands in the Raman spectra.

Feld et al. [63] used 830 nm excited CCD Raman spectroscopy to collect spectra from normal colon and colonic adenocarcinoma. Tissue samples from three patients were excited with 100 mW of laser power. Spectra were obtained with a collection time of 50 s. A comparison between the spectra of normal colonic mucosa and adenocarcinoma was made. Although the spectra were similar, small but significant differences were present. These were enhanced by producing difference spectra between normal and malignant tissue. Peaks were observed on the difference spectra at 1662, 1576, 1458 and 1340 cm^{-1}. These correspond to nucleic acid modes, indicating the nucleic acid content is higher in adenocarcinoma than in normal mucosa. This agrees with the histological method of grading malignancy by the nucleic acid to cytoplasmic ratio.

The majority of Raman studies have been carried out on excised samples. An unpublished study by Richards-Kortum et al. (1994), described by Mahadevan-Jansen et al. [54], showed that variations in Raman spectra between fixed and fresh tissues appeared to be minimal. Hence measurements in vitro should not affect the potential diagnostic capability of the spectra obtained. However, if the in vitro measurements are to be extrapolated to an in vivo tissue geometry, the biopsy specimens should be large enough to include all the layers

of tissue present in vivo that provide components of the Raman signal. Each tissue type will produce a different Raman signal due to its own biochemical and physiological makeup. Thus, in vitro measurements on thin samples of tissue may not provide the whole picture.

A number of authors have worked on the detection of metabolites in aqueous solution. This may have application in early detection of malignancy, as changes in cell biochemistry occur before any structural change. Examples of metabolites that have potential diagnostic significance include citrate in prostatic adenocarcinomas, glycogen in renal cell carcinomas, *N*-acetylaspartate in brain tumours, lactate and phospholipid metabolites in carcinomas of the prostate, colon and lung [63]. Cassanas et al. [67] demonstrated that lactic acid concentration could be measured, in aqueous solution, using Raman spectroscopy. Measuring lactate concentration in tissue using a Raman technique may be a useful diagnostic indicator for malignancy. Goetz et al. [68] and Berger et al. [69] also measured various metabolites using visible and NIR excitation Raman, respectively.

Practical Problems

Tissue is inhomogenous in composition and also highly scattering; the full analysis of Raman signals thus requires an understanding of tissue optical parameters and photon propagation in turbid media. Raman signals are inherently weak and, in addition, early diagnosis of disease requires detection of tissue molecular constituents present in low concentrations. This is accentuated by the fact that lasers with high intensity cannot be used to observe weak signals from tissues because of the potential for sample damage. Thirdly, the complex nature of tissue composition results in absorption of light throughout the entire UV–visible region, and subsequent intense fluorescence emission strongly interferes with weak Raman signals.

The major problem associated with Raman-fibre probes is that Raman signals are generated by the fibres themselves. The signal is proportional to the length of the fibre and to the excitation light intensity and can have magnitudes equal to and sometimes greater than that of the sample under study.

CONCLUSION

Clinical fluorescence detection of early precancer is still in its infancy. More and more work is concentrating on intrinsic fluorophores within the tissue rather than solely relying on the characteristic signal of an exogenous fluorophore. The technique which is expected to hold the most promise is the fluorescence lifetime imaging of the tissue's natural fluorophores, since this should yield most information.

Elastic scattering spectroscopy is possibly the cheapest and most accessible technique, but its lack of specificity may restrict its use for detecting precancerous lesions.

Optical coherence tomography has the potential to detect subtle structural changes within tissue. However, for the early detection of premalignancy, the measurement of biochemical rather than structural abnormalities may be necessary. The main potential in OCT lies in staging gastrointestinal neoplasms after they are discovered using other methods.

Raman spectroscopy has shown potential for the biomedical diagnosis of malignancy in localised sites. The most promising gastrointestinal malignancy for Raman detection is colon adenocarcinoma, where most work has been done. Techniques using ultraviolet, visible and near-infrared wavelengths of light have shown repeatable differences between normal and malignant Raman spectra in vitro. However, there are still a number of technical problems to be overcome to enable routine in vivo measurements.

More work is still required to understand how the various optical signatures of tissue are influenced by the local microenvironment and this then needs to be correlated with early pathological changes that the precancer undergoes.

REFERENCES

1. Hameeteman W, Tytgat GNJ, Houthoff HJ, Van Den Tweel JG. Barrett's esophagus: development of dysplasia and carcinoma. Gastroenterology 1989; 96:1249–56
2. Blot WJ, Devesa SS, Kneller RW, Fraumeni JF. Rising incidence of adenocarcinoma of the esophagus and gastric cardia. JAMA 1991; 265:1287–9
3. Levine DS, Haggitt RC, Blount PL, Rabinovitch PS, Rusch VW, Reid BJ. An endoscopic biopsy protocol can differentiate high-grade dysplasia from early adenocarcinoma in Barrett's esophagus. Gastroenterology 1993; 105:40–50
4. Barr H, Shepherd NA, Dix A, Roberts DJH, Tan WC, Krasner N. Eradication of high-grade dysplasia in

columnar-lined (Barrett's) oesophagus by photodynamic therapy with endogenously generated protoporphyrin IX. Lancet 1996; 348:584 5
5. Berenson MM, Johnson TD, Markowitz NR, Buchl KN, Samowitz WS. Restoration of squamous mucosa after ablation of Barrett's esophageal epithelium. Gastroenterology 1993; 104:1686 91
6. Regula J, MacRobert AJ, Gorchein A et al. Photosensitisation and photodynamic therapy of oesophageal, duodenal, and colorectal tumours using 5-aminolaevulinic acid induced protoporphyrin IX a pilot study. Gut 1995; 36:67–75
7. Overholt BF, Panjehpour M. Barrett's esophagus: photodynamic for ablation of dysplasia, reduction of specialized mucosa, and treatment of superficial esophageal cancer. Gastrointest Endosc 1995; 42:64–9
8. Pitt GD. A revolution in Raman spectroscopy. Physics Business, 1997:6 7
9. Bohorfoush AG. Tissue spectroscopy for gastrointestinal diseases. Endoscopy 1996; 28:372–80
10. Panjepour M, Overholt BF, Vo-Dinh T et al. Endoscopic fluorescence detection of high-grade dysplasia in Barrett's esophagus. Gastroenterology 1996; 111:93–101
11. Jacques SL. Mechanisms and limits of contrast in optical imaging of cancer, SPIE Proceedings of Conference on Advances in Lasers and Light Spectroscopy to Diagnose Cancer and Other Diseases II 1995; 2387.88 94
12. Vo-Dinh T, Panjehpour M, Overholt BF, Farris C, Buckley III FB, Sneed R. In vivo cancer diagnosis of the esophagus using differential normalised fluorescence (DNF) indices. Lasers Surg Med 1995; 16:41 -7
13. Savage HE, Kolli V, Ansley J, Chandawarker RY, Alfano RR, Schantz SP. Innate tissue fluorescence of the oral mucosa of controls. SPIE Proceedings of Conference on Advances in Lasers and Light Spectroscopy to Diagnose Cancer and Other Diseases II, 1995; 2387:2–14.
14. Svanberg K, Andersson-Engels S, Baert L et al. Tissue characterisation in some clinical specialities utilising laser-induced fluorescence. SPIE Proceedings of the Conference on Advances in Laser and Light Spectroscopy to Diagnose Cancer and Other Diseases, 1994; 2135.2 15
15. Irani K, Xia Y, Zweier JL et al. Mitogenic signaling mediated by oxidants in Ras-transformed fibroblasts. Science 1997; 275:1649 52
16. Stael von Holstein C, Nilsson AMK, Andersson-Engels S, Wilen R, Walther B, Svanberg K. Detection of adenocarcinoma in Barrett's oesophagus by means of laser induced fluorescence. Gut 1996; 39:711–6
17. Loh CS, Vernon D, MacRobert AJ, Bedwell J, Bown SG, Brown SB. Endogenous porphyrin distribution induced by 5-aminolaevulinic acid in the tissue layers of the gastrointestinal tract. J Photochem Photobiol B 1993; 20:47–54
18. Regula J, MacRobert AJ, Gorchein A et al. Photosensitisation and photodynamic therapy of oesophageal, duodenal, and colorectal tumours using 5-aminolaevulinic acid induced protoporphyrin IX - a pilot study. Gut 1995; 36.67 75
19. Folli S, Westermann P, Braichotte D et al. Antibody-indocyanin conjugates for immunophotodetection of human squamous cell carcinoma in nude mice. Cancer Res 1994; 54:2643 9
20. Tata DB, Foresti M, Cordero J, Tomashefsky P, Alfano MA, Alfano RR. Fluorescence polarisation spectroscopy and time-resolved fluorescence kinetics of native cancerous and normal rat kidney tissues. Biophys J 1986; 50.463 9
21. Andersson-Engels S, Berg R, Persson A, Svanberg S. Multispectral tissue characterisation with time resolved detection of diffusely scattered white light. Optics Lett 1993, 18.1697 9
22. Glanzmann T, Ballini J, Jichlinski P, van den Bergh H, Wagnieres G. Tissue characterisation by time-resolved spectroscopy of endogenous and exogenous fluorochromes: apparatus design and preliminary results. SPIE Proceedings on the Conference on Optical Biopsies and Microscopic techniques 1996; 2926:41–50
23. Cubeddu R, Canti G, Taroni P, Valentini G. Time-gated fluorescence spectroscopy and imaging of porphyrins and phthalocyanines. SPIE Proceedings of the Conference on Future Trends in Biomedical Applications of Lasers 1991; 1525:17 25
24. Andersson-Engels S, Wilson BC. In vivo fluorescence in clinical oncology: fundamental and practical issue. J Cell Pharmacol 1992; 3.66 79
25. Lakowicz JR, Szmacinski H, Nowaczyk K, Berndt KW, Johnson M. Fluorescence lifetime imaging. Anal Biochem 1992; 202:316 30
26. Andersson-Engels S, Ankerst S, Johansson J et al. Tumour marking properties of different hematoporphyrins and tetrasulphonated phthalocyanine – a comparison. Lasers Med Sci 1989; 4:115 23
27. Andersson-Engels S, Johansson J, Stenram U, Svanberg K, Svanberg S. Malignant tumour and atherosclerotic plaque diagnosis using laser-induced fluorescence. IEEE J Quantum Elect 1990; 26:2207 17
28. Qu J, MacAulay C, Lam S, Palcic B. Mechanisms of ratio fluorescence imaging of diseased tissue. SPIE 2387:71–9
29. Profio AE, Balchum OJ, Carstens F. Digital background subtraction for fluorescence imaging. Med Phys 1989; 5:717–21
30. Wagnieres G, Depeursinge Ch, Monnier Ph et al. Photodetection of early cancer by laser induced fluorescence of a tumour-selective dye: apparatus design and realization. Photodyn Ther Mechanisms II SPIE.1203, 1990
31. Andersson PS, Montan S, Svanberg S. Multispectral system for medical fluorescence imaging. IEEE J Quantum Elec 1987; 23:1798 805
32. Schomacker KT, Flotte TJ, Deutsch TF. Detection of chemically induced dysplasia in rat urinary bladder with laser-induced fluorescence. SPIE 1994; 2135:76 9
33. Andersson PS, Kjellen E, Montan S, Svanberg K, Svanberg S. Autofluorescence of various rodent tissues and human skin tumour samples. Lasers Med Sci 1987; 2:41 9
34. Andersson-Engels S, Elner A, Johansson J et al. Clinical recording of laser-induced fluorescence spectra for evaluation of tumour demarcation feasibility in selected clinical specialities. Lasers Med Sci 1989, 6:415–24
35. Van Dam J, Bjorkman DJ. Shedding some light on high-grade dysplasia. Gastroenterology 1996; 111:227 49
36. Stael von Holstein C, Nilsson AMK, Andersson-Engels S, Willen R, Walther B, Svanberg K. Detection of adenocarcinoma in Barrett's oesophagus by means of laser induced fluorescence. Gut 1996; 39:711 6
37. Dets SM, Buryi AN, Melnik IS, Joffe AY, Rusina TV. Laser-induced fluorescence detection of stomach

cancer using hypercin. SPIE Optical Biopsies Microscopic Techniques 1996; 2926.51–6
38. Kapadia C, Cutruzzola F, Obrian K, Stetz M, Enriquez R, Deckelbaum L. Laser induced fluorescence spectroscopy on human colonic mucosa. Gastroenterology 1990; 99.150–7
39. Cothren RM, Richards-Kortum R, Sivak M et al. Gastrointestinal tissue diagnostics by laser-induced fluorescence spectroscopy at endoscopy. Gastrointest Endosc 1990; 36:105–11
40. Schomacker K, Frisoli J, Compton C et al. Ultraviolet laser induced fluorescence of colonic tissue. Laser Surg Med 1992; 12:63–78
41. Zeng H, Weiss A, MacKinnon N, Cline R, MacAulay C. In vivo fluorescence spectroscopy of the gastrointestinal tract under multiple wavelength excitation. SPIE, Optical Biopsies Microsc Techniques 1996; 2926.4–8
42. Wang TD, Van Dam J, Crawford JM, Preisinger EA, Wang Y, Feld MS. Fluorescence endoscopic imaging of human colonic adenomas. Gastroenterology 1996; 111:1182 91
43. Manoury V, Mordon S, Klein O, Colombel J-F. Fluorescence endoscopic imaging study of anastomotic recurrence of Crohn's disease. Gastrointest Endosc 1996; 43:603 4
44. Mourant JR, Bigio IJ, Boyer J, Conn RL, Johnson T, Shimada T. Spectroscopic diagnosis of bladder cancer with elastic light scatering. Lasers Med Surg 1995; 17:350 7
45. Mourant JR, Boyer JD, Johnson TM et al. Detection of gastrointestinal cancer by elastic light scattering and absorption spectroscopies with the Los Alamos Optical Biopsy System. SPIE Proceedings of Conference on Advances in Lasers and Light Spectroscopy to Diagnose Cancer and Other Diseases II 1995; 2387:210–7
46. Fujimoto JG, Brezinski ME, Tearney GJ et al. Optical biopsy and imaging using optical coherence tomography. Nature Med 1995; 1:970–2
47 Bouma BE, Tearney GJ, Boppart SA, Hee MR, Brezinski MB, Fujimoto JG. High resolution optical coherence tomographic imaging using a modelocked TiAl203 laser source. Optics Lett 1995; 20:1486–8
48. Brezinski ME, Tearney GJ, Bouma BE et al. Optical coherence tomography for optical biopsy properties and demonstration of vascular pathology. Circulation 1996; 93:1206 13
49. Izatt JA, Wang H-W, Kulkarni M, Kobayashi K, Canto MI, Sivak MV. Optical coherence tomography and microscopy in gastrointestinal tissues. Advances in Optical Imaging and Photon Migration, Technical Digest, Washington, DC: Optical Society of America, 1996.24–6
50. Szymanski HA. Raman Spectroscopy Theory and Practice, 1st edn. New York: Plenum Press, 1967
51. Manoharan R, Wang Y, Dasari RR, Singer SS, Rava RP, Feld MS. Ultraviolet resonance Raman spectroscopy for detection of colon cancer. Lasers Life Sci 1995; 6:217 27
52. Banwell CN. Fundamentals of Molecular Spectroscopy, 2nd edn. London: McGraw Hill, 1972:121
53. Carey PR. Biochemical Applications of Raman and Resonance Raman Spectroscopies, 1st edn. London: Academic Press, 1982:6–47
54. Mahadevan-Jansen A, Richards-Kortum R. Raman spectroscopy for the detection of cancers and precancers. J Biomed Optics 1996; 1:31–70
55. Yu NT, East EJ. Laser Raman spectroscopic studies of ocular lens and its isolated protein fractions. J Biol Chem 1975; 250:2196–202
56. Wang SY, Hasty CE, Watson PA, Wicksted JP, Stith RD, March WF. Analysis of metabolites in aqueous solutions by using laser Raman spectroscopy. Appl Opt 1993; 32:925–9
57. Manaharan R, Wang Y, Feld MS. Histochemical analysis of biological tissues using Raman spectroscopy. Spectrochim Acta Part A 1996; 52.215 49
58. Alfano RR, Liu CH, Sha WL et al. Human breast tissues studied by IR Fourier transform Raman spectroscopy. Lasers Life Sci 1991; 4.23–8
59. Baraga JJ, Feld MS, Rava RP. Rapid near-infrared Raman spectroscopy of human tissue with a spectrograph and CCD detector. Appl Spect 1992; 46:187–90
60. Manoharan R, Wang Y, Boustany N et al. Raman spectroscopy for cancer detection: instrument development and tissue diagnosis. SPIE Proceedings of the Conference on Biomedical Optoelectronic Devices and Systems I 1994; 2328:129
61. Mahadevan A, Ramanujam N, Mitchell MF, Malpica A, Thomsen S, Richards-Kortum R. Optical techniques for the diagnosis of cervical precancers: a comparison of Raman and fluorescence spectroscopies. SPIE Proceedings of the Conference on Advances in Fluorescence Sensing Technology II 1995; 2388:110
62. Schader B, Keller S, Lochte T et al. NIR FT Raman spectroscopy in medical diagnosis. J Mol Struct 1995; 348:293–6
63. Feld MS, Manoharan R, Salenius J et al. Detection and characterisation of human tissue lesions with near infrared Raman spectroscopy. SPIE Proceedings of the Conference on Advances in Fluorescence Sensing Technology II 1995; 2388:110
64. Redd DCB, Frank CJ, Feng ZC, Gansler TS, McCreery RL. Raman spectroscopic characterisation of human malignant tissues: implications for a percutaneous optical biopsy technique for in-situ tissue diagnosis. SPIE Proceedings of the Conference on Optical Biopsy 1993; 2081:186
65. Special Issue: J Raman Spectrosc 19XX; 28:111-70
66. Halliday K, Sillerud L, Fenoglio-Preiser C. Carbon-13 and proton nuclear magnetic resonance spectroscopy and microscopy of neoplasms. Adv Pathol 1989; 2.213–58
67. Cassanas G, Morssli M, Fabregue E, Bardet L. Vibrational spectra of lactic acid and lactates. J Raman Spect 1991; 22:409–13
68. Goetz MJ Jr, Cote GL, Erckens R, March W, Motamedi M. Application of a multivariate technique to Raman spectra for quantification of body chemicals. IEEE Trans Biomed Engng 1995; 42:728 31
69. Berger AJ, Wang Y, Feld MS. Rapid, noninvasive concentration measurements of aqueous biological analytes by near-infrared Raman spectroscopy. Appl Opt 1996; 35:209–12

Paper received 4 June 1997;
accepted in revised form 11 September 1997.

PROGRESS REPORTS

OPERA MONOGRAFICA

Beyond white light endoscopy – the prospect for endoscopic optical biopsy

C. Fulljames, N. Stone, D. Bennett, H. Barr

The most important factor in the successful treatment of cancer is early detection. This will be more likely to facilitate eradication of abnormal cells prior to systemic invasion. White light endoscopy has been an essential tool in medical diagnosis for a number of years. Direct endoscopic inspection of gastrointestinal organs has revolutionised diagnostic techniques, improving the targeting of biopsies of macroscopic morphological abnormalities. Recent technological developments are threatening a further revolution enabling the instantaneous and non-invasive diagnosis of microscopic tissue abnormalities in vivo. This is made possible by improving the level of information that can be obtained from the tissue. As well as the two-dimensional surface morphology image, which the traditional endoscope can view, new techniques enable structure at depth, i.e., the third-dimension, to be imaged in high resolution. Other advances enable the detection of biochemical changes in tissue that precede any changes in morphology, thus enabling earlier diagnosis of tissue abnormalities. This review details recent advances that have the greatest potential, for use in partnership with endoscopy, for the diagnosis of malignancy and pre-malignancy.

Ital J Gastroenterol Hepatol 1999;31:695-704

Key words: fluorescence; Raman; spectroscopy

Introduction

The identification of many diseases and cancers in the gastrointestinal tract is by visual inspection at endoscopy, the diagnosis being confirmed by pathological analysis after biopsy. By the time a cancer is visible to white light endoscopy, it is often advanced, and when morphological pathological changes have occurred the disease is often invasive. Yet, almost all cancers in the gastrointestinal tract start as a subtle invisible mucosal change. In order to bring forward the diagnosis, interrogation of the surface changes prior to gross morphological transition is vital. There is great interest in optical techniques to go beyond our visual receptors (eyes) and detect the earliest transition to disease, prior to invasion. This would allow endoscopic minimally invasive destruction of these pre-invasive lesions.

The diagnosis of disease states and measurement of the extent of the disease process is often given by qualitative analysis of the biochemical changes within the tissue. For the detection of malignancy, however, tissue is removed as biopsy samples and examined histopathologically, looking for morphological changes rather than biochemical changes. There is delay in the diagnosis and the precise area in the tissue of a subtle change may not be evident when looked for at a subsequent endoscopy. Therefore, targeted local treatment may not be possible. The ideal would be to detect and treat at the same endoscopic examination. Non-invasive, rapid, histochemical and/or morphological analysis, potentially used in vivo, is possible using optical techniques. Biochemical information is obtained from fluorescence, absorption and Raman spectra, whereas morphological and structural information, such as nuclear size and density, is obtained from the elastic scattering properties of the tissue and optical coherence tomography measurements.

Light with wavelengths from 650 to 950 nm can propagate several millimetres through tissue, outside of this optical window absorption by haemoglobin and water predominate and the penetration is limited. Optical spectroscopy involves the excitation of tissue with photons and the identification of characteristic spectra. Tissue spectroscopy can, therefore, be used for the detection of ischaemia or inflammation but most interest in the technique lies in its ability to detect malignancy [1]. This has potential benefits for premalignant diseases of the gastrointestinal tract, such as Barrett's oesophagus, which have significant risks of developing into adenocarcinoma, through the development of high-grade dysplasia. At present, surveillance is carried out by taking random biopsies according to a rigorous protocol [2]. Tissue spectroscopy has advantages over more conventional methods used in histology and pathology in that

From: Gloucestershire Royal & Cranfield University Institute of Medical Sciences, Gloucestershire Royal Hospital, Gloucester, UK.

Address for correspondence: Miss C. Fulljames, Gloucestershire Royal & Cranfield University Institute of Medical Sciences, Gloucestershire Royal Hospital, Great Western Road, Gloucester, GL1 3NN, UK. Fax: +44-1452-394490.
E-mail: catherine@grhcranf.demon.co.uk

Invited Review, received July 19, 1999.

Table I. Major techniques for endoscopic optical biopsy (listed according to predominant information that will be elicited).

Morphology	Biochemical/Morphology	Molecular/Biochemical
Optical-coherence tomography	Laser-induced Fluorescence (Autofluorescence)	Raman
Elastic scattering	Laser-induced Fluorescence (Photosensitiser)	Resonance Raman
Multi-photon excitation		Infrared spectroscopy

it is non-invasive, allows rapid measurement and diagnosis, and guides the targeting of biopsies. The rapidity of spectroscopic measurements means that many more sites can be investigated than with pinch biopsies, thereby reducing sampling error. Also due to the non-invasive nature of spectroscopy multiple measurements can be taken without bleeding and tissue disruption with the potential for seeding abnormal cells. The subjective nature and the variation in the interpretation of morphological changes, so evident in the interpretation of gastrointestinal cancer [3], can be overcome by using standard mathematical techniques for interpretation of the data [4]. There are a number of spectroscopic methods available for the early diagnosis of gastrointestinal malignancy (Table I).

Fluorescence Spectroscopy

Scientific background

Light radiation absorbed by a molecule causes its excitation to a higher energy level. The molecule can return to its original energy level by emitting light of lower energy than the excitation light (longer wavelength). This is called fluorescence. The light wavelengths absorbed and emitted by a molecule are called the absorption and emission spectra and are highly specific of that species. Analysis of these spectra (spectroscopy) can indicate the molecules present. In complex biological tissue, there are many confounding factors related to the absorption, interaction with other molecules, distortion of the signal due to scattering in the tissue [5] and reabsorption by tissue other than chromophores (light absorbing molecules). Policard first studied fluorescence measurements for the detection of cancer and showed some cancers produced a bright red fluorescence [6]. This was later shown to be due to prophyrins produced by bacteria in necrotic areas of tumours [7].

The literature can be confusing since various techniques are used. It is, therefore, important to briefly describe some of the terms used. Excitation-emission spectroscopy uses multiple colour illumination in sequence, the fluorescence spectra being recorded for each wavelength, resulting in a contour type map. Different excitation wavelengths excite different chromophores in different ways giving more complex patterns with more biochemical information. This technique has been used for the diagnosis of brain and skin disease but most usefully for the detection of cervical cancer [8-11]. The technique of differential normalised fluorescence (DNF) is designed to amplify

Table II. Laser-induced fluorescence for detection of neoplastic change in gastrointestinal tract. Joffe et al. [82] used photosensitiser fluorescence, all others depended on auto fluorescence.

Tissue	Patients	Sensitivity	Specificity	Reference
Oesophageal cancer/normal	32	100	98	Panjehpour et al. [50] 1995
Barrett's oesophagus High grade/Low grade dysplasia	36	100	72	Panjehpour et al. [4] 1996
Colonic dysplastic adenomas/normal hyperplastic	57	90	95	Cothren [60] 1990
Colonic neoplastic polyp/hyperplastic polyp	61	86	77	Schomaker [62] 1992
Malignant gastric ulcer/benign ulcer+Gastritis	16	87.5		Joffe et al.[82] 1998

small spectral variations and enhance differences between normal and neoplastic tissue.[12] Normalisation is carried out by dividing the intensity at each wavelength by the integrated area under the spectrum and the difference between the normalised spectrum and the mean value from a normalised set of spectra. A baseline value can then be calculated.

Ratio fluorescence imaging uses two excitation wavelengths; the ratio of the two spectra is used to differentiate normal and malignant tissue [13]. In time domain fluorescence spectroscopy, the short-lived background fluorescence can be removed during time resolved fluorescence spectroscopy thus enhancing the relative fluorescence emissions. This method has been very useful for studying the uptake of photosensitisers such as haematoporphyrin derivative (HpD) and of aluminium phthalocyanine (AlSPc) [14]. Fluorescence lifetime imaging (FLIM) can be used to differentiate between endogenous and exogenous fluorophores. Such measurements are independent of the concentration of fluorescence molecules (fluorophores) and measurement intensity, but are sensitive to the microenvironment [15].

The most widely used method is laser-induced fluorescence (LIF) spectroscopy. This simply informs us of the method of applying light to the tissue [16-18]. A monochromatic laser source illuminates the sample tissue, causing fluorescence, which is detected with fibre optic bundles and delivered to a spectral analyser. Low power laser illumination can induce autofluorescence without causing tissue damage due to heating. Autofluorescence has spectral characteristics due to endogenous substances in the cells. These are molecules such as elastin, collagen, tryptophan, β-carotene, the reduced or oxidised form of nicotinamide adenine dinucleotide ($NADH/NAD^+$) and flavins, and are known as fluorophores. The fluorescence spectra of flavins are altered during metabolic changes from the oxidised to the reduced state, and can be good indicators of metabolic activity. NADH has a high fluorescence yield and, as an oxidative species, is important in the development of cancer. The ratio of NADH to NAD^+ has the potential of differentiating normal and precancerous tissue.

The use of LIFS to detect autofluorescence is preferable to the administration of an exogenous drug for routine screening, which is essentially an invasive procedure [12]. However, measurements of exogenous fluorophores have been made and used diagnostically in conjunction with intrinsic fluorescence, since tumour detection potential may be increased with the administration of these exogenous chromophores. Exogenous chromophores have been used for *in vivo* measurements of the brain and lung and *in vitro* measurements of prostate and bladder [16].

Laser induced autofluorescence can discriminate between normal and experimentally induced N-nitrosomethyl-benzylamine pre-malignant oesophageal tissue in rats [19]. It may also be a possible technique for the detection of neoplasia in the colon and oesophagus in patients [9 20]. A distinctive laser-induced autofluorescence has been reported in Barrett's adenocarcinoma [21]. In vivo results have also been published for tumour fluorescence detection in the urinary bladder and lungs.

Instead of depending entirely on autofluorescence, ex-

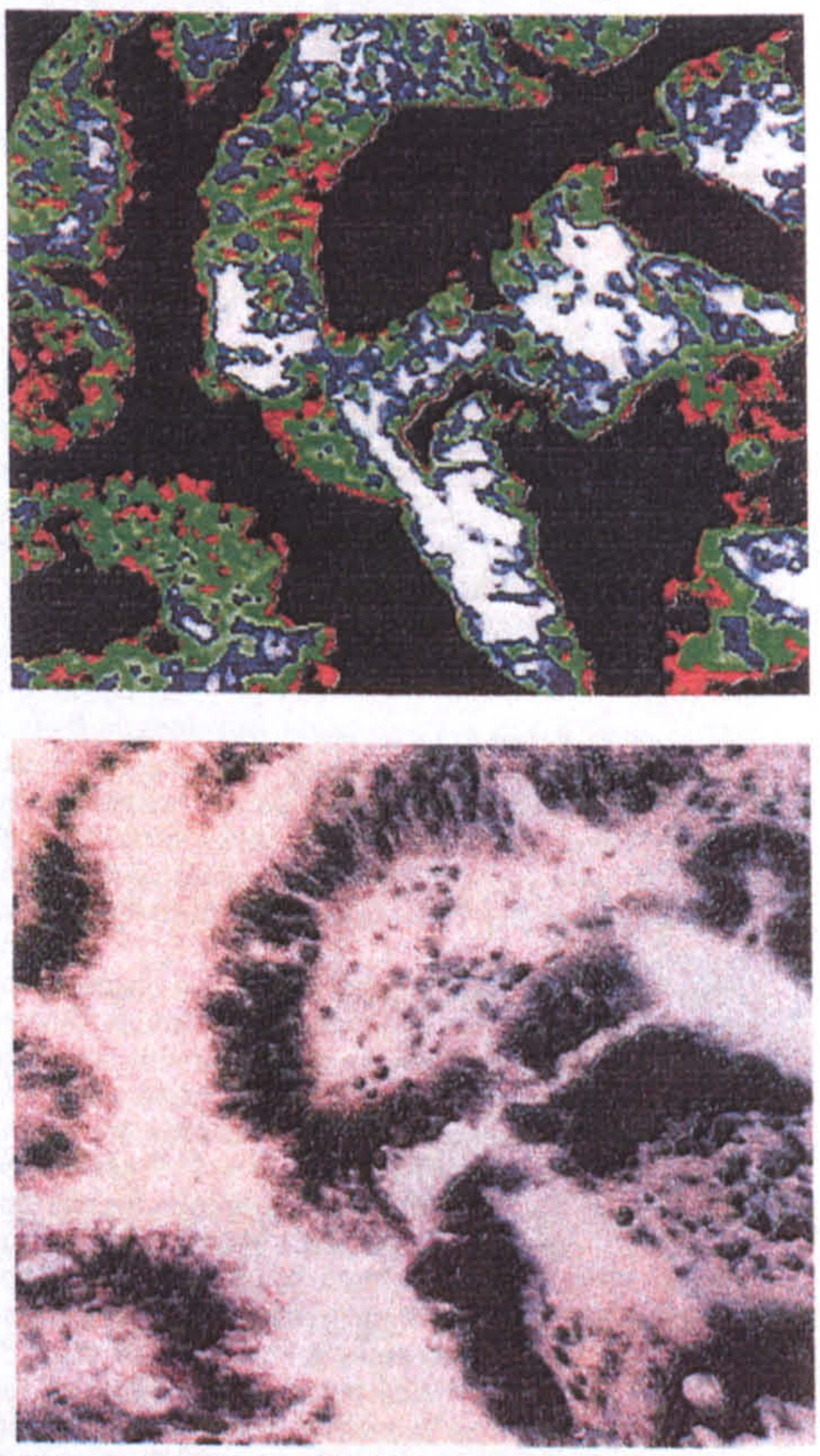

Fig. 1. Photomicrograph and fluorescence image of dysplastic columnar-lined oesophagus demonstrating accumulation of protoporphyrin IX in dysplastic epithelium compared with underlying stroma and adjacent cells. Fluorescence diagnosis is possible. High fluorescence is demonstrated by bright areas in upper picture corresponding to areas of dysplasia shown in the lower photomicrograph.

ogenous fluorophores have been administered in order to acheive targeting of neoplastic tissue. These exogenous fluorescence agents often have a photodynamic action thus limiting the administered dose. The heme precursor δ-amino levulinic acid (ALA) has been administered topically, orally or intravenously for the production of the photosensitiser protoporphyrin IX [18]. This selectively accumulates in dysplastic mucosa (Fig. 1) and can thus be used both for diagnosis and photodynamic therapy. Other studies have confirmed the usefulness of administering a low dose of the photosensitiser Photofrin [17 22 23]. It is retained in tumours to a greater extent than in normal tissue with a peak differential seen between 48 and 96 hours. This porphyrin fluoresces with a characteristic bimodal distribution with peaks at 630 and 690 nm.

Clinical Applications

General clinical experience

Laser-induced fluorescence spectroscopy has been used successfully in vivo for the characterisation of malignant tissue [24]. Ramanujam et al. [25 26] performed a clinical trial using LIFS for the diagnosis of cervical intraepithelial neoplasia, in 115 sites in 28 patients, using a nitrogen laser at 337 nm. Abnormal tissue was diagnosed with a sensitivity of 92% and specificity of 90% and CIN was diagnosed with a sensitivity of 87% and specificity of 73%. Lefell and Stetz [27] used a 325 nm excitation wavelength, from a helium-cadmium laser, to study photoaging of the skin. A correlation was found which is believed to be due to differences in the collagen and elastin content. It was also shown that the characteristic tissue fluorescence spectra are unrelated to age, pigmentation or skin thickness.

Lohmann et al. [28] has used LIFS for the diagnosis of melanoma in the skin. The ratio of maximum fluorescence outside the lesion to the minimum intensity within the lesion can be used to distinguish naevi and melanomas, but melanomas and dysplastic naevi cannot be distinguished. Sterenborg et al [11 29] have done similar work on in vivo autofluorescence for the detection of skin cancer. Results, however, were not found to be sufficiently reliable to be used for diagnosis, either in the shape of the spectra or the spatial distribution of the fluorescence intensity. Ebert et al. [30] carried out a study on fluorescence intensities of lesions and healthy skin by recording images rather than excitance. However, it was found that fluorescence images did not reveal any fluorescence pattern specific to the malignancy of the lesion.

Sartori et al. [31], Kitrell et al. [32] and Richards-Kortum et al. [33] have used LIFS for diagnosis with arterial tissue. The diagnosis of arterial plaque is important for laser angioplasty. Papazoglou et al. [24] and Deckelbaum et al. [34] have tested LIFS as a guidance tool for laser ablation. Perk et al. [35] have used LIFS for the detection of fibrotic endocardium and myocardium and study of conduction tissue in arrhythmia. Alfano et al. used LIFS for the diagnosis of cancer in breast and lung tissues [36-39]. Lam et al. used a novel bronchoscope to detect dysplasia and carcinoma in situ in the lung [40]. A total of 53 patients with known or suspected carcinoma and 41 volunteers were studied. Specificity was found to be 94% and sensitivity 72.5%.

Docchio [41] covers retinal vessel imaging and other established uses of fluorescence in ophthalmology. Zuclich et al. [42] studied the human eyes lens with a view to the diagnosis of cataracts and age-related changes. The onset of diabetes mellitus has been investigated by Eppstein and Bursell [43]. Piston has used fluorescence spectroscopy to monitor the metabolic state of the cornea [44].

Andersson-Engels et al. [45] and Bottiroli et al. [46] cite the presumed origin of the spectral signatures that correlate with pathologies such as cancer to be the concentration of NADH, or the redox state of flavin co-factors. Schomaker et al. [47] and Ramanujam et al. [48] suggest that some of the changes in the fluorescence are due to morphological changes.

Fluorescence diagnostics cannot replace biopsies and histopathology but can aid the endoscopist in the selection of biopsy sites. In addition to the classification of tissue as either benign or malignant in patients with cancer, the aim of LIF is to aid the detection of endoscopically 'invisible' premalignant pathology, such as dysplasia [49].

Upper gastrointestinal endoscopy

Lasers are ideal as endoscopic light sources to irradiate tissue since they can be passed down thin optical fibres. The spectra can also be collected by a similar or the same fibre. Usually, laser-induced fluorescence spectra are measured with a probe in contact with the tissue or as an image of the surface. Initially, Panjepour et al. [4 50] showed that LIFS has great potential differentiating benign and malignant disease and subsequently for the detection of high-grade dysplasia in columnar-lined (Barrett's) oesophagus. They used the DNF technique, with excitation at 410 nm. Normal and malignant tissues were found to have significant spectral differences at 480 and 660 nm, therefore, DNF_{480} and DNF_{660} were used to develop a discriminatory model. Using this technique, seven patients with high-grade dysplasia were successfully identified. There may be a problem in detecting focal areas of high-grade dysplasia in areas of low-grade dysplasia. This is not a problem confined to fluorescent tech-

niques. It is clearly a limitation of spectral analysis over an imaging method. Ideally, one would want to have a colour image with areas of dysplasia highlighted in colour. Thus allowing clear identification and targeted biopsy or destruction. The next stage must be direct incorporation into an endoscope with real-time imaging.

A nitrogen laser was used to pump a dye laser with an output at 405 nm. The radiation passed through a 600 μm core diameter quartz optical fibre to the tissue. Tissue fluorescence was collected by the same fibre and transmitted to a charge coupled device (CCD) connected to a polychromator. Broad tissue autofluorescence was seen at 500 nm due to endogenous tissue fluorophores and the porphyrin fluorescence at 630 and 690 nm. In malignant tissue, the porphyrin fluorescence is stronger and the auto-fluorescence is weaker. This has been exploited to examine the fluorescence spectral characteristics of normal mucosa, metaplastic and dysplastic columnar-lined (Barrett's) oesophagus and invasive carcinoma [51]. Fluorescence ratios were calculated as the quotient of the Photofrin fluorescence at 630 nm divided by the autofluorescence at 500 nm. Normal oesophageal mucosa had a ratio of 0.1, gastric mucosa 0.16, columnar-lined oesophagus 0.2, severe dysplasia 0.79, and adenocarcinoma 0.78. The important finding was that dysplasia was different from metaplasia. It is interesting to note that dysplasia and invasive cancer demonstrate similar fluorescence ratios, reflecting the morphological distinction that both appear as cancer cytologically. The only difference is invasion beyond the mucosa.

The problem of squamous dysplasia in the upper aerodigestive tract is increasing with surveillance of patients who have had previous therapy for cancer. Monnier et al. [52] used the detection of abnormal fluorescence signals for the diagnosis of superficial early mucosal cancers in endoscopically accessible areas. The early detection has allowed targeted endoscopic therapy avoiding the profound morbidity and mortality of radical surgical excision.

Early malignant ulceration of the stomach is difficult to distinguish from gastritis and benign disease. Chen et al. [53] evaluated the use of laser-induced autofluorescence spectroscopy for the detection of premalignant lesions of the human stomach in vivo and in vitro using a pulsed nitrogen laser. Laser-induced fluorescence detection can be improved by using an orally administered photosensitiser (encapsulated hyperflav 0.1-0.15 mg/kg body weight). Early gastric cancer and dysplasia was found in 87.5% of patients using endoscopic laser-induced fluorescence followed by targeted biopsy, compared with only 64.8% of patients having conventional endoscopy and biopsy [4]. Macroscopically invisible lesions were found.

Colonoscopy

The increasing recognition of flat adenomas and the need to differentiate hyperplastic from dysplastic adenomatous polyps with their potential for malignant change, means that a real-time imaging device is urgently required. Marchesini[54] measured the emission spectra of neoplastic and non-neoplastic colonic mucosa with fluorescence spectroscopy in an attempt to evaluate the possibility of differentiating malignancy from premalignancy and neoplastic from non-neoplastic tissue in vitro. Adenomatous tissue and non-neoplastic mucosa could be discriminated with a specificity of 93.2% and a sensitivity of 88.2%. Similarly, Kapadia et al. [20 55] used LIF with a helium-cadmium laser, at 325 nm, to differentiate adenomatous polyps from normal human colonic mucosa and hyperplastic polyps in vitro. Stepwise multivariate linear regression analysis was used to create a model comprising 35 resected adenomatous polyps and 35 normal human colonic mucosa specimens. Then 34 normal specimens, 16 adenomatous polyps and 16 hyperplastic polyps were classified with an accuracy, respectively, of 100%, 100% and 94%, indicating LIF to be a useful diagnostic tool for differentiating between normal and pre-cancerous tissue of the gastrointestinal tract.

Richards-Kortum et al. [56] used fluorescence spectroscopy for the diagnosis of colonic adenoma. Fluorescence excitation-emission matrices were used to identify the optimal excitation regions for differentiating normal and pathological tissues [57]. The excitation wavelength of 370 nm was shown to be optimal for in vitro discrimination of adenomas from normal tissue, but 330 and 430 nm can also be used. Romer et al. [58] used argon ion laser excitation of frozen sections of normal colonic mucosa and colonic adenomas and compared the tissue fluorescence with stained sections (H&E, Movat pentachrome, mucicarmine and oil red O). This was to identify the fluorophores or structures responsible for the LIF emission. Fluorescence in normal mucosa correlated with connective tissue fibres, principally collagen. Interestingly, cytoplasmic fluorescence increased with increasing grade of epithelial dysplasia. Yakshe et al. used LIF with an excitation at 325 or 337 nm for in vitro diagnosis of colonic adenocarcinoma and showed differences between carcinoma and normal tissue [59].

Cothren et al. [60] used a nitrogen pumped dye laser at 370 nm in 3 nsec at 20 Hz to examine 67 sites in 20 patients for the diagnosis of colon cancer during colonoscopy. Emitted tissue fluorescence is only collected from the surface area directly illuminated. LIF spectra were collected from 31 adenomas, 4 hyperplastic polyps and 32 samples of normal colonic mucosa. A 2D scatterplot of the fluorescence intensities

at 460 against 680 nm was used to distinguish premalignant colonic adenomas from normal mucosa and hyperplastic polyps with a sensitivity of 100% and specificity of 97%. Fluorescent emission intensity is consistently lower in adenoma than in normal tissue, which may be due to levels of connective tissue. In 1993, Cothren et al. [61] collected LIF spectra from the rectal mucosa of 16 patients with a history of previous adenomatous polyp in the last 18 months, and 16 age- and gender-matched patients with no similar history. Increased fluorescence was found at 680 nm for the polyp formers. The spectra differed only by a small extent. Therefore, LIFS cannot be used yet to predict the patients at risk of developing colorectal neoplasia.
Schomaker et al. [48] used a nitrogen laser at 337 nm in vivo and in vitro to examine 91 polyps and 86 normal colon tissue sites in 61 patients for the diagnosis of colon cancer, with a sensitivity of 86% and specificity of 77% for the separation of neoplastic and hyperplastic polyps using multivariate linear regression analysis. Neoplastic tissue and non-neoplastic tissue could be differentiated with a sensitivity of 80% and a specificity of 92%. In a similar study [62], looking at the changes in fluorescence post mortem, they showed that in vivo and in vitro fluorescence emissions are significantly different for adenomatous polyps, therefore, LIF spectra should be acquired in vivo.

Multi-photon excitation microscopy

Scientific background
Two-photon excitation microscopy has potential as an imaging tool for *in vivo* examination of deep tissue structure at a subcellular level [63]. Penetration depth can be optimised by using a near infrared excitation source. Two-photon absorption occurs at the focal point enabling optical sectioning to be used. Multi-photon excitation microscopy offers advantages over fluorescence imaging in highly scattering tissues. The principle behind the technique is the simultaneous absorption of two photons, which induce an electronic transition. Fluorophores generally have two photon absorption peaks at approximately two times their one-photon absorption wavelengths. Two-photon absorption can induce a fluorescence emission at much shorter wavelengths. It was first developed by Denk et al. for laser scanning microscopy and for the detection of fluorescence imaging in 1990 [64].

Clinical studies
Multi-photon excitation microscopy has been used to image human skin autofluorescence in vivo, from the surface to a depth of about 100 microns [63]. Results show the primary source of autofluorescence to be NAD(P)H with 730 nm excitation. It has also been used to study NAD(P)H metabolic imaging of a cornea *in vivo* [45]. With the use of ultraviolet light to excite chromophores, it has been observed that cell viability is compromised and considerable photobleaching occurs. However, this technique minimises the damaging effects of phototoxicity to the cells in the focal slice, rather than all the cells in the optical path. The two-photon scanning microscope, described by So et al. uses a femto second Ti-Sapphire laser at 730 nm [65].

Optical coherence tomography

Endoscopy is limited as it only visualises the superficial mucosal layer at low magnification. Magnification endoscopy enables greater detail to be seen but only observes the mucosal surface [66]. Endoscopic ultrasound allows evaluation of deeper tissue structure and is, therefore, used in the staging of cancer [67], however, the resolution is insufficient for the detection of subtle changes in the mucosa and sub-mucosa. Optical coherence tomography (OCT) offers a solution for imaging the superficial layers and detecting early invasion into the submucosa.

Scientific background
OCT is a technique for high resolution, cross-sectional tomographic imaging, giving morphological information on the tissue under investigation. OCT is similar to B-scan ultrasound except that reflected infrared light from tissue structures is measured as a function of depth rather than acoustic backscattering. In non-transparent tissues, optical scattering and attenuation make OCT more challenging, the use of the near infrared benefits from the reduced scattering at these wavelengths. OCT has the advantages of being compact and easily portable. Contact is not required during imaging, it can be performed in air without an intervening transducing media such as required for ultrasound.
The light for OCT comes from a short coherence length monochromatic source. It is split between two fibres, one of which illuminates the tissue to be studied and the other illuminates a mirror. On recombination of the signals from the tissue and the mirror, constructive interference is achieved when the path lengths match within the coherence length of the light. The mirror can be displaced thus changing the measurement depth in the sample. The depth resolution depends on the light sources used.

Clinical applications
OCT was first used for imaging the transparent structures in the eye. More recently, it has been used for

the early detection of glaucoma and to diagnose retinal macular disease with 10 μm resolution [68-71]. OCT has also been applied to the imaging of skin and blood vessels [72,73].

Tearney et al. carried out a study on OCT for in situ imaging of the gastrointestinal microstructure. Normal and diseased tissues were measured and compared with results from histology. The different tissue layers – mucosa, submucosa and muscularis – were identified using the technique [66]. The resolution of tissue structure down to 10 to 20 μm has the potential to improve the diagnostic limits of endoscopy. This is essential for the early staging of disease in the mucosa or sub-mucosa. Improvement in the acquisition times is required prior to clinical use. This may be achievable by using higher power light sources. A further study of the oesophagus was able to identify the microscopic structure of the mucosa and sub-mucosa, with crypts, blood vessels and oesophageal glands being clearly identifiable. OCT has the potential for the early detection and precise staging of small lesions [74]. As yet, OCT cannot resolve cellular and subcellular details. Therefore, mucosal dysplasia is only detectable once it has resulted in a gross morphological change, such as increase in surface thickness.

Raman spectroscopy

Scientific background

Raman spectroscopy is an inelastic scattering technique. It exploits the frequency shift, which occurs in the excitation light due to the excitation of vibrational and rotational states in illuminated molecules. The photons in the incident light beam undergo inelastic collisions with molecules, causing an exchange of energy. Thus the wavelength of the photon is subtly changed. Due to the conservation of energy, the energy gained or lost by the photon equals the energy change in the molecule and, therefore, molecular vibrations can be probed. The vibrational spectrum of a molecule reflects the arrangement of atomic nuclei and chemical bonds in the molecule. A precise molecular fingerprint is obtained.

The technique involves irradiating a sample of tissue with a monochromatic laser beam. The scattered light is collected and analysed for intensity and wavelength. The Raman effect is very weak, typically 10^{-9} to 10^{-6} of the enormous elastic (Rayleigh) scattered background. The interaction between the photon and the molecule is very fast (of the order of picoseconds). It should be regarded as a perturbation rather than an absorption reaction. In comparison, the time scale of absorption and fluorescence emission by a molecule is of the order of 10 ns.

The Raman shift is defined as the energy difference between the incoming and scattered photons. The zero point is set at the energy of the excitation photon. A larger shift indicates that more energy is required to bring about a vibrational motion, such as a bending or stretching motion of the molecule. The position of the Raman peaks is independent of the wavelength of excitation. Raman shift frequency is independent of the exciting frequency used. This means that the energy shift is constant for a particular molecular species. The units of energy used are displayed in wave numbers ($1/\lambda$ cm^{-1}). A very intense peak indicates that the corresponding vibrational state of the chemical bond or molecule is highly Raman active or more likely to be perturbed by incident photons.

When the energy of the excitation photon approaches that required to reach the higher electron state of a chromophore, the intensity of the Raman scattering increases greatly compared with normal Raman scattering conditions. This is called pre-resonance Raman. Once the excitation energy is sufficient to promote the chromophore into the higher electron energy state, absorption of a photon can occur. Following the almost instantaneous re-emission of a second photon, Resonance Raman (RR) can occur. This phenomenon produces an even greater Raman scattering intensity arising from pre-resonance conditions. These resonance techniques enable the vibrational spectra of individual chromophores to be probed in the midst of the myriad of others that are found in biological tissues. However, it must be noted that high energy photons are required to induce the Resonance Raman. These can have potentially damaging effects on biological tissue.

One of the major problems encountered in the Raman spectroscopy of biological tissues is that of fluorescence. A fairly recent development has been the use of Near Infrared (NIR) laser excitation and dispersive spectrometers to allow rapid detection of spectra with low background fluorescence. NIR radiation does not generally induce electronic absorption so fluorescence is weak relative to the Raman signal. Holographic notch filters are used to filter the elastically scattered (Rayleigh) light from the signal, combined with a single monochromator increases the output of the system compared with the triple monochromator used previously. The development of CCDs and diode lasers has enabled the development of portable NIR systems with short integration times [75,76].

Pre-clinical applications

Most biological molecules are Raman active with their own characteristic fingerprint. Proteins, nucleic acids, and cell membranes, single cells, cell cultures and tissues can all be studied. Most data on tissue Raman spec-

troscopy are in a pre-clinical stage. Raman spectroscopy has been used in the characterisation of brain, sarcomas, breast, colon, bladder and cervical cancers [76 77]. In the gastrointestinal tract, spectral analysis of colonic cancer and surrounding normal colon has demonstrated differences [78]. The Raman spectra were used (with ultraviolet excitation) to quantitatively measure the nucleic acid bands and cytoplasmic proteins. Their ratio was used to distinguish cancer from adjacent normal tissue. This allows a good comparison with the histological methods of identifying malignant cells by nuclear enlargement and staining. Raman spectroscopy has the potential for approaching the gold standard of histological assessment [79].

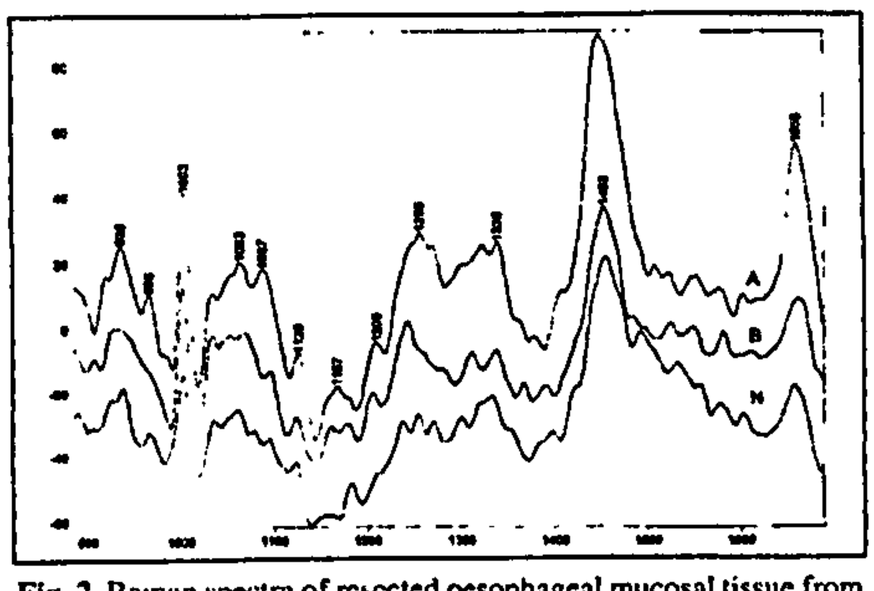

Fig. 2. Raman spectra of resected oesophageal mucosal tissue from one patient. Pathological diagnosis was adenocarcinoma (A), specialised intestinal metaplasia (B), and normal squamous epithelium (N). A Renishaw Raman microspectrometer was used to acquire the spectra with 633 nm excitation laser light.

Raman spectroscopy of columnar lined oesophagus may offer the opportunity to distinguish inflammation, metaplasia, dysplasia and cancer. Spectra have been collected (Fig. 2), but extensive work is required to develop this into a clinically useful model.

Elastic scattering spectroscopy

Scientific background

Light photons are most likely to interact with tissue by elastic scattering and absorption, therefore, the signals are strong and can be acquired rapidly. The mie theory states that light scattering is dependent on the wavelength of the incident light, with greater scattering occurring in photons of a similar wavelength to the size of the scattering particles (320-900 nm). The elastic scattering spectra are a representation of tissue morphology. The scattered signal varies depending on the sizes and shapes of the cell nuclei, cell crowding and shape. It provides similar information to the morphological analysis used in conventional histopathology, but can be used in vivo. The elastic scattering signal is sensitive to the illuminating wavelength.

Clinical studies

Elastic Scattering Spectroscopy has been used on the skin, eyes, bladder, prostate and gastrointestinal tract. Mourant et al. [80 81] tested Elastic Scattering Spectroscopy for the diagnosis of cancer in the gastrointestinal tract. A total of 60 sites in the colon and rectum of 16 patients were investigated and a spectral metric was developed, which was found to have a sensitivity of 100% and a specificity of 98%. Samples were taken from the lower gastrointestinal tract of a further 32 patients and from the stomach of 17 patients. The data suggested that elastic scattering spectroscopy was a promising tool for the detection of dysplasia.

Conclusions

Although the technology remains immature, the prospects for realistic optical diagnosis are clearly apparent. The advantages of real-time pathological, morphological, biochemical and molecular data on a sample of tissue is tantalising and exciting tremendous effort and interest. The requirements for a clinical instrument are demanding and set physics, optical engineering and medical instrumentation hard criteria. Endoscopic and histopathological diagnosis will not be a subjective opinion, but performed using optical instruments, mathematical algorithms and neural networks, leading to greater repeatability of results.

References

[1] Bohorfoush AG. Tissue spectroscopy for gastrointestinal diseases. [Review] [57 refs]. Endoscopy 1996;28:372-80.

[2] Levine DS, Haggit RC, Blount PL, Rabinovitch PS, Rusch VW, Reid BJ. An endoscopic protocol can differentiate high-grade dysplasia from early adenocarcinoma in Barrett's esophagus. Gastroenterology 1993;105:40-50.

[3] Schlemper RJ, Itabashi M, Kato Y, Lewin KJ, Riddell RH, Shimoda T. Differences in diagnostic criteria for gastric carcinoma between Japanese and Western pathologists. Lancet 1997;349:1725-9.

[4] Panjehpour M, Overholt R, Vo-Dinh T, Haggit RC, Edwards DH, Buckley PF. Endoscopic Fluorescence detection of High-grade dysplasia in Barrett's esophagus. Gastroenterology 1996;111:93-101.

[5] Cheong W, Prahl SA, Welch AJ. A review of the optical properties of biological tissues. IEEE J Quantum Electronics 1990;26:2166-85.

[6] Policard A. Etude sur les aspects offerts par des tumeurs experimentales examinées à la lumière de Wood. Compte-Rendus Soc Biol 1924;49:1423-4.

[7] Lam S, Hung J, Palcic B. Mechanism of photodetection of early lung cancer by ratio fluorometry. Laser Life Sci 1991;3:67-91.

[8] Chung W, Shwartz J, Gardner C, Sawaya R, Jacques SL. Fluorescence of normal and cancerous brain tissues: the excitation/emission matrix. Proc SPIE 1995;2135:66-75.

[9] Mahadevan A, Mitchell MF, Silva E, Thomsen S, Richards-Kortum R. Study of the fluorescence properties of normal and neoplastic human cervical tissue. Lasers Surg Med 1993;13:647-55.

[10] Richards-Kortum R, Mitchell MF, Ramanujam N, Mahadevan A, Thomsen S. In vivo fluorescence spectroscopy: potential for non-invasive automated diagnosis of cervical intraepithelial diagnosis of cervical inraepithelial neoplasia and use as a surrogate end-point biomarker. J Cell Biochem Suppl 1994;19:111-9.

[11] Sterenborg HJCM, Motamedi M, Wagner RF, Duvic M, Thomsen S, Jacques SL. In vivo fluorescence spectroscopy and imaging of human skin tumours. Lasers Med Sci 1994;9:191-201.

[12] Vo-Dinh T, Panjehpour M, Overholt R, Farris C, Buckley I, Sneed R. In vivo cancer diagnostics of the oesophagus using differential normalised fluorescence indices. Lasers Surg Med 1995;16:41-7.

[13] Lam S, Hung J, Palcic B. Detection of lung cancer by ratio fluorometry with and without Photofrin II. Proc SPIE 1990;1201:561-8.

[14] Cubbedu R. Time gated fluorescence spectroscopy and imaging of Porphyrins and phthalocyanines. Proc SPIE 1991;1525:17-25.

[15] Lakowicz JR, Szmacinski H, Nowacyzk K, Berndt KW, Johnson M. Fluorescence lifetime imaging. Anal Biochem 1992;202:316-30.

[16] Baert L, Berg R, van Damme D, Johansson J, Svanberg K, Svanberg S. Clinical fluorescence diagnosis of human bladder carcinoma following low-dose photofrin injection. Urology 1993;41:322-30.

[17] Svanberg K, Klinteberg C, Nilsson A, Wang I, Andersson-Engels S, Svanberg S. Laser based spectroscopic methods in tissue characterisation. Ann N Y Acad Sci 1998;838:123-9.

[18] Barr H, Shepherd NA, Dix A, Roberts DH, Tan WC, Krasner N. Eradication of high-grade dysplasia in columnar lined (Barrett's) oesophagus by photodynamic therapy with endogenously generated protoporphyrin IX. Lancet 1996;348:584-5.

[19] Glasgold R, Glasgold M, Savage H, Pinto J, Alfano R, Schantz S. Tissue autofluorescence as an intermediate endpoint in NMBA-induced oesophageal carcinogenesis. Cancer Lett 1994;82:33-41.

[20] Kapadia CR, Cutruzzola FW, O'Brien KM, Stetz ML, Enriques R, Deckelbaum LI. Laser induced fluorescence spectroscopy of human colonic mucosa: detection of adenomatous transformation. Gastroenterology 1990;99:150-7.

[21] Wang K, Gutta K, Laurkka M, Densmore J. Laser induced fluorescence in the detection of oesophageal carcinoma. Proc SPIE 1995;2324:14-8.

[22] Andersson-Engels S, Elner A, Johansson J, Karlson SE, Salford LG, Stromblad IG. Clinical recordings of laser-induced fluorescence spectra for evaluation of tumour demarcation feasibility in selected clinical specialities. Lasers Med Sci 1991;6:415-24.

[23] Lam S, Palcic B, McLean D, Hung J, Korblik M, Profio AE. Detection of early lung cancer using low dose Photofrin. Chest 1990;97:333-7.

[24] Papazoglou TG. Malignancies and atherselerotic plaque diagnosis – is laser induced fluorescence spectroscopy the ultimate solution? J Photochem Photobiol B 1995;28:3-11.

[25] Ramanujam N, Mitchell MF, Mahadevan A, Warren S, Thomsen S, Silva E, et al. In vivo diagnosis of cervical intraepithelial neoplasia using 337 nm excited laser induced fluorescence. Proc Natl Acad Sci USA 1998;91:193-7.

[26] Ramanujam N, Mitchell MF, Mahadevan A, Thomsen S, Silva E, Richards-Kortum R. Fluorescence Spectroscopy: A diagnostic tool for cervical intraepithelial neoplasia. Gynecol Oncol 1994;52:31-8.

[27] Lefell DJ, Stetz ML. In vivo fluorescence of human skin: a potential marker for photoaging. Arch Dermatol 1988;124:1514-8.

[28] Lohmann W, Nilles M, Bodeker RH. In situ differentiation of melanomas by fluorescence measurements. Naturwissenschaften 1991;78:456-7.

[29] Sterenborg HJCM, Motamedi M, Wagner RF, Thomsen S, Jacques SL. In vivo fluorescence spectroscopy for the diagnosis of skin diseases. Proc SPIE 1994;2324:32-7.

[30] Ebert B, Kohl M, Sukowski U, Rinneberg H, Winter H, Bellmann KP, et al. Fluorescence Imaging of cutaneous malignant melanomas and naevi. Lasers Med Sci 1998;13:204-8.

[31] Sartori M, Sauerbrey R, Kubodera S, Tittel FK, Roberts R, Henry PD. Autofluorescence of atherosclerotic human arteries – a new technique in medical imaging. IEEE J Quant Elec 1987;23:1794-7.

[32] Kitrell C, Willet RL, de las Santos-Pacheo C, Ratliff NB, Kramer JR, Malk EG, et al. Diagnosis of fibrous arterial atherosclerosis using fluorescence. Appl Optics 1985;24:2280-1.

[33] Richards-Kortum R, Mehta A, Hayes G, Cothren RM, Kolubayev T, Kitrell C, et al. Spectral diagnosis of atherosclerosis using an optical fiber laser catheter. Am Heart J 1989;118:381-91.

[34] Deckelbaum L, Stetz ML, O'Brien K, Cutruzola F. Fluorescence spectroscopy guidance of laser ablation of atherosclerotic plaque. Lasers Surg Med 1989;9:205-14.

[35] Perk M, Flynn GJ, Smith C, Bathgate B, Tulip J, Yue W, et al. LIF emission: 1. The spectroscopic identification of fibrotic endocardium and myocardium. Lasers Surg Med 1998;11:523-34.

[36] Alfano RR, Tang GC, Pradhan A, Bleich M, Choy DSJ, Opher E. Steady state and time resolved laser fluorescence from normal and tumour lung and breast tissues. J Tumour Marker Oncol 1988;3:165-74.

[37] Alfano RR, Pradhan A, Tang GC, Wahl SJ. Optical spectroscopic diagnosis of cancer and normal breast tissues. J Opt Soc Am B 1989,6:1015-23.

[38] Tang GC, Pradhan A, Alfano RR. Spectroscopic differences between human cancer and normal lung and breast tissues. Lasers Surg Med 1989;9:290-5.

[39] Alfano RR, Tang GC, Pradhan A, Lam W, Choy DSJ, Opher E. Fluorescence spectra from cancerous and normal human breast and lung tissues. IEEE J Quantum Electronics 1987;23:1806-11.

[40] Lam S, MacAulay C, Hung J, LeRiche J, Profio AE, Palcic BP. Detection of dysplasia and carcinoma in situ with a lung imaging fluorescence endoscope device. J Thorac Cardiovasc Surg 1993;105:1035-40.

[41] Docchio F. Ocular Fluorometry: principles, fluorophores, instrumentation and clinical applications. Lasers Surg Med 1989,9:515-32.

[42] Zuclich JA, Shimada T, Loree TR, Bigio IJ, Strobl K, Nie S. Rapid noninvasive optical characterisation of the human lens. Lasers Life Sci 1998;6:39-53.

[43] Eppstein J, Bursell SE. Non-invasive detection of diabetes mellitus. Proc SPIE 1992;1641:217-26.

[44] Piston DW, Masters BR, Webb WW. Three-dimensionally resolved NAD(P)H cellular metabolic redox imaging of the in situ cornea with two-photon excitation laser scanning microscopy. J Microsc 1995;178:20-7.

[45] Andersson-Engels S, Johansson J, Svanberg K, Svanberg S. Fluorescence imaging and point measurements of tissue: applications to the demarcation of malignant tumours and atherosclerotic lesions. Photochem Photobiol 1991;53:807-14.

[46] Botturoli G, Croce AC, Locatelli D, Marchesini R, Pignoli E, Toatis S, et al. Natural fluorescence of normal and neoplastic human colon: a comprehensive 'ex vivo' study. Lasers Surg Med 1995;16:48-60.

[47] Schomaker KT, Frisoli JK, Compton CC, Flotte TJ, Richter JM, Nishioka NS, et al. Ultraviolet laser-induced fluorescence of colonic tissue: Basic biology and diagnostic potential. Lasers Surg Med 1992;12:63-78.

[48] Ramanujam N, Mitchell MF, Mahadevan A, Warren S, Thomsen S, Silva E, et al. In vivo diagnosis of cervical intraepithelial neoplasia using 337 nm excited laser induce fluorescenec. Proc Natl Acad Sci 1994;91:10193-7.

[49] Van Dam J. Laser-induced fluorescence spectroscopy: somewhere over the rainbow. Gastroenterology 1996;110.643-4.

[50] Panjehpour M, Overholt R, Schmidhammer JL, Farris C, Buckley PF, Vo-Dinh T. Spectroscopic diagnosis of esophageal cancer, new classification model, improved measurement system. Gastrointest Endosc 1995;41:577-81.

[51] Stael von Holstein C, Nilssin AMK, Andersson-Engels S, Willen R, Walther B, Svanberg K. Detection of adenocarcinoma in Barrett's esophagus by means of laser induced fluorescence. Gut 1996;39:711-6.

[52] Monnier P, Savary C, Fontolliet G. Photodetection and PDT of early squamous call carcinomas of the pharynx, oesophagus and the trachco-bronchial tree. Lasers Med Sci 1990;5:149-69.

[53] Chen W, He B, Wei G. Ultraviolet laser-induced fluorescence (UV-LIF) spectroscopy diagnosis of human malignant tissues. Lasers Med Sci 1998;13:209-13.

[54] Marchesini R. Light induced fluorescence spectroscopy of adenomas, adenocarcinomas and non neoplastic mucosa in human colon. J Photochem Photobiol B 1992;14:219-30.

[55] Kapadia CR, Cutruzzola FW, O'Brien KM, Stetz ML, Enriquez R, Deckelbaum LI. Detection of adenomatous transformation of colonic mucosa by fiber optic laser-induced fluorescence (LIF) spectroscopy. Gastroenterology 1988;94:A216.

[56] Richards-Kortum R, Rava RP, Petras RE, Fitzmaurice M, Sivak M, Feld MS. Spectroscopic diagnosis of colonic dysplasia. Photochem Photobiol 1991;53:777-86.

[57] Richards-Kortum R, Tong L, Rava RP, Fitzmaurice M, Petras RE, Sivak M, et al. Spectral studies of GI tissues: optimizing excitation wavelengths for discrimination of normal and adenomatous tissues. Lasers Surg Med 1989;35:A184.

[58] Romer TJ, Fitzmaurice M, Cothren RM, Richards-Kortum R, Petras RE, Sivak M, et al. Laser induced fluorescence microscopy of normal colon and dysplasia in colonic adenomas; implications for spectroscopic diagnosis. Am J Gastroenterol 1995;90:81-7.

[59] Yakshe PN, Bonner RF, Patterson R, Leon MB, Fleischer DE. Laser induced fluorescence spectroscopy; can it be used in the diagnosis and treatment of colonic malignancy? Am J Gastroenterol 1989;84:1199(A).

[60] Cothren RM. Gastrointestinal tissue diagnosis by laser induced fluorescence spectroscopy at endoscopy. Gastrointest Endosc 1990;36:105-11.

[61] Cothren RM, Zhang K, Sivak MVJ, Gardner D, Narayan S, Zuccaro G. Autofluorescence spectroscopy as an indicator of potential for forming colonic adenomas. Gastrointest Endosc 1993;39:A294.

[62] Schomaker KT, Frisoli JK, Compton CC, Flotte TJ, Richter JM, Deutsch TF, et al. Ultraviolet laser-induced fluorescence of colonic polyps. Gastroenterology 1992;102:1155-60.

[63] Masters BR, So PTC, Gratton E. Optical biopsy of in vivo human skin: multi photon excitation microscopy. Lasers Med Sci 1998;13:196-203.

[64] Denk WJ, Strickler JH, Webb WW. Two photon laser scanning fluorescence microscopy. Science 1990;248:73-6.

[65] So PTC, French T, Yu WM. Time resolved fluorescence microscopy using two photon excitation. Bioimaging 1995;3:49-63.

[66] Tearney GJ, Brezinski ME, Bouma BE. In vivo endoscopic optical biopsy with optical coherence tomography. Science 1997;276:2037-9.

[67] Botet JF, Lightdale C. Endoscopic ultrasonography of the gastrointestinal tract. Gastroenterol Clin N Am 1995; 24:385-412.

[68] Fercher AF, Hitzenberger CK, Drexler W, Kamp G, Saffman H. In vivo optical coherence tomography. Am J Ophthalmol 1993;116:113-4.

[69] Hee MR, Izatt JR, Swanson EA. Optical coherence tomography of the human retina. Arch Ophthalmol 1995;113:325-32.

[70] Izatt JA, Hee MR, Swanson EA, Lin CP, Huang D, Schuman JS. Micrometer scale resolution imaging of the anterior eye with optical coherence tomography. Arch Ophthalmol 1994;112:1584-9.

[71] Puliafito CA, Hee MR, Lin CP. Imaging of macular diseases with optical coherence tomography. Ophthalmology 1995;102:217-29.

[72] Brezinski ME, Tearney GJ, Bouma BE, Izatt JA, Hee MR, Swanson EA. Optical coherence tomography for optical biopsy. Properties and demonstration of vascular pathology. Circulation 1996;93:1206-13.

[73] Schmitt JM, Yadlowsky MJ, Bonner RF. Subsurface imaging of living skin with optical coherence microscopy. Dermatology 1995;191:93-8.

[74] Kobayashi K, Izatt JA, Kulkarni MD, Willis J, Sivak MV. High resolution cross-sectional imaging of the gastrointestinal tract using optical coherence tomography: preliminary results. Gastrointest Endosc 1998;47:515-23.

[75] Pallister DM, Lui KL, Govil A, Morris MD, Owen H, Harrison TR. Raman microprobe with holographic beamsplitter for low-frequency operation. Appl Spectrosc 1992;46:1469-73.

[76] Mahadevan-Jansen A, Richards-Kortum R. Raman spectroscopy for the detection of cancers and pre-cancers. J Biomed Optics 1996;1:31-70.

[77] Mahadevan-Jansen A, Mitchell MF, Ramanujam N, Utzinger U, Richards-Kortum R. Near infrared Raman spectroscopy for in vitro detection of cervical precancers. Photochem Photobiol 1998;68:123-32.

[78] Manoharan W, Wang Y, Dasari RR, Singer SS, Rava RP, Feld MS. Ultraviolet resonance Raman spectroscopy for the detection of colon cancer. Lasers Life Sci 1995;6:217-27.

[79] Feld MS, Manoharan W, Salenius J, Ornstein-Cardona J, Romer TJ, Brennan III JF, et al. Detection and characterisation of human lesions with near infrared Raman spectroscopy. Proc SPIE 1995;2388:99-104.

[80] Mourant JR, Bigio IJ, Boyer JD, Johnson TM, Lacey J, Bohorfoush AG, et al. Elastic scattering spectroscopy as a diagnostic tool for differentiating pathologies in the gastrointestinal tract. J Biomed Optics 1996;1:192-9.

[81] Mourant JR, Boyer JD, Johnson TM. Detection of gastrointestinal cancer by elastic scattering and absorption spectroscopies with the Los Alamos Optical Biopsy System. SPIE Proc 1995;2387:210-7.

[82] Joffe AY, Sayenko VF, Denisov NA, Dets SM, Buryi AN. Early diagnosis of gastric cancer with laser-induced fluorescence. Proc SPIE 1998;3567:10-7.

ELSEVIER

www.elsevier.nl/locate/jphotobiol

J. Photochem. Photobiol. B: Biol. 53 (1999) 75–80

Journal of Photochemistry and Photobiology B:Biology

Photodynamic therapy using 5-aminolaevulinic acid for oesophageal adenocarcinoma associated with Barrett's metaplasia

W.C. Tan [a,d], C. Fulljames [b], N. Stone [b], A.J. Dix [b], N. Shepherd [b], D.J.H. Roberts [c], S.B. Brown [c], N. Krasner [a], H. Barr [b,*]

[a] *Department of Gastroenterology and Laser Unit, Aintree Hospital, Liverpool, UK*
[b] *Cranfield Postgraduate Medical School, Gloucestershire Royal Hospital, Great Western Road, Gloucester, UK*
[c] *Centre for Photobiology and Photodynamic Therapy, University of Leeds, Leeds, UK*
[d] *Department of Gastroenterology, Warrington Hospital, Warrington, UK*

Received 14 January 1999; accepted 21 October 1999

Abstract

Photodynamic therapy (PDT) is a novel technique for local endoscopic treatment of gastrointestinal neoplasia. Current photosensitisers for PDT may cause prolonged skin phototoxicity. 5-Aminolaevulinic acid (ALA), a precursor of the photosensitiser protoporphyrin IX (PpIX), is more acceptable because of its short half-life and preferential accumulation in mucosa and mucosal tumour. We have treated 12 patients, median age 73 years (range 55–88) with oesophageal adenocarcinoma arising from Barrett's metaplasia (two carcinomas-in-situ, grade 0; 10 carcinomas, grade I–IIA based on endoluminal ultrasound in two and CT scanning in 10 patients). ALA (60 and 75 mg/kg body weight) was given orally in two or five equally divided doses. The PpIX distribution in stomach, normal oesophagus, Barrett's mucosa and carcinoma was measured by quantitative fluorescence photometry. PDT was performed using laser light (630 nm) delivered via a cylindrical diffuser 4–6 h after the first dose of ALA. The patients received one to four sessions of PDT. PpIX accumulation in the mucosa was two to three times that in the lamina propria. The differential distribution between carcinomatous and normal oesophageal mucosa was less marked (carcinoma:normal mucosa ratio = 1.4). Higher doses of ALA increased PpIX accumulation in all tissues but did not increase the differential PpIX distribution between tumour and normal oesophageal mucosa. After PDT using ALA (ALA/PDT), all mucosa showed superficial white necrotic changes and the histology confirmed fibrinoid necrosis. One patient with carcinoma-in-situ had the tumour eradicated after one treatment with no recurrence at 28 months. Another patient with a small T1 tumour required four ALA/PDT treatments, and died of other disease after 36 months. There was no evidence of recurrence. The tumour bulk in the other carcinomas was not significantly reduced. ALA/PDT has a potential for the eradication of small tumours but careful patient selection with endoluminal ultrasound is needed when using ALA/PDT to treat oesophageal cancer.

Keywords: Photodynamic therapy; Laser; Protoporphyrin IX; Aminolaevulinic acid; Oesophageal cancer; Adenocarcinoma and fluorescence distribution

1. Introduction

Oesophageal adenocarcinoma carries a poor prognosis. Oesophagectomy, the only potentially curative treatment, has an operative mortality of 5–10% [1,2]. Recent data indicate that the incidence of this disease and of cancer of the gastric cardia is rising more rapidly than that of any other cancer [3,4]. This may be a reflection of the increase in the occurrence of Barrett's metaplasia of the oesophagus. Many patients presenting with frank oesophageal adenocarcinoma are too elderly and frail for surgery. Treatment options are further limited by this tumour's relative insensitivity to radiotherapy. The insertion of an oesophageal endoprosthesis and thermal laser ablation are the most widely used palliative therapies.

Photodynamic therapy (PDT) is a relatively new form of cancer treatment. It involves the administration of a photosensitising agent and subsequent local activation of the drug in the tumour by application of light of appropriate wavelength. PDT has been shown to cure some superficial malignancies [5,10]. For gastrointestinal cancer, it offers the possibility of local destruction of tumour cells. Also full thickness damage experimentally induced in the rat intestine did not reduce the colonic bursting pressure. Healing occurred by regeneration and scarring was less of a problem than following thermal treatment [6]. A recent experimental study

* Corresponding author. Tel.: +44-1452-394679; fax: +44-1452-394813; e-mail: Prof.Barr@themail.co.uk

1011-1344/99/$ - see front matter

in the rat stomach has shown that PDT using 5-aminolaevulinic acid (ALA/PDT) selectively causes mucosal necrosis without causing stenosis or perforation. Therefore it offers a promising technique for circumferential mucosal ablation [7].

One of the main disadvantages of PDT using conventional photosensitisers is generalised cutaneous photosensitivity. This can persist for 6–8 weeks, during which time the patient must avoid direct sunlight and strong artificial light [8]. A new technique using the haem precursor ALA largely avoids this problem. Administration of exogenous ALA induces the accumulation of protoporphyrin IX (PpIX) in a number of tissues, particularly epithelial surfaces [9]. PpIX, the immediate metabolic precursor of haem, is an effective photosensitiser. Cutaneous photosensitisation is mild and completely resolved in 24–48 h [11–13] because the biological half-life of PpIX is short.

We report the results of a study on the efficacy of ALA/PDT in 12 patients with frank oesophageal adenocarcinoma (stage I–IIA, $n=10$) or carcinoma-in-situ (stage 0, $n=2$) [14] associated with Barrett's metaplasia [15,16].

2. Patients and methods

Twelve patients (seven men and five women) of median age 73 years (range 55–88) with oesophageal adenocarcinoma arising from Barrett's metaplasia were treated. They were either considered unfit for ($n=7$), or had refused ($n=5$), surgery. Informed consent from the patients and approval from the local ethical committees were obtained. Endoscopic staging was performed to assess the visual appearance and where possible endoscopic ultrasound was used. All patients underwent preliminary endoscopic multiple random biopsy; a standard protocol was not always used. Patients treated in later years (eight patients) were biopsied according to a protocol. Biopsy of the four quadrants of the oesophagus at 2 cm intervals of the entire Barrett's segment was performed with multiple biopsy and brushing of suspicious areas. In two patients, there was only a minor abnormality in an area of Barrett's oesophagus, diagnosed as carcinoma-in-situ after biopsy. In six patients, the tumour was small, occupying 1 cm or less of the surface of the columnar lined oesophagus; two of these patients had endoscopic ultrasound that demonstrated a T2 N0 tumour in one and a T1 N0 lesion in the other. In the remaining four patients, the tumour was larger than 1 cm and nodular. All patients were free of lymph-node involvement and distant metastases on a combination of endoscopic ultrasound, chest X-ray and CT scan of thorax and abdomen. None of the frank carcinomas had invaded adjacent structures. None of the 12 patients had dysphagia at the time of treatment. The pathology was reviewed by an experienced gastrointestinal pathologist using the criteria of invasion for diagnosis of cancer. There may be a considerable difference between Western pathological assessment and that of the Japanese [21].

ALA was dissolved in lemonade or fruit juice and given orally 4–6 hours before laser-light exposure. We believe that the uptake of ALA was predominantly systemic although there may be a minimal local absorption. The contact time with the oesophageal mucosa is minimal and the mucosa is covered with mucus. ALA doses of 60 or 75 mg/kg body weight were given in two or five equally divided hourly doses. The patients were then kept in a darkened room for 24 h. Laser sources were an argon-pumped dye laser (Spectraphysics) or Laserscope KTP pumped dye laser system (600 Series Dye Module, Laserscope (UK) Ltd.), both emitting red light at 630 nm. The laser fibres were inserted into a cylindrical diffuser (length 1, 2 or 3 cm), which was placed intraluminally and the area of the tumour and surrounding Barrett's oesophagus irradiated. The power density of the laser ranged from 90 to 150 mW/cm^2 and the total energy levels were 100–200 J/cm^2. Each patient received between one and four treatments (Table 1). The patients were treated at endoscopy under sedation with Midazolam. Repeat endoscopy and biopsy was carried out one to seven days after

Table 1
Details of the patient's age, tumour, treatment dosimetry and outcome

Patient	Age	Tumour type/size	Reason for not having surgery	PDT sessions	ALA dose (mg/kg)	Light dose (J/cm^2)	Outcome
1	74	carcinoma-in-situ	ischaemic heart disease	1	75	100	complete eradication 28 months follow-up
2	63	carcinoma-in-situ	refusal	3	75	150	superficial necrosis
3	55	>1 cm	refusal	3	60	70	superficial necrosis
4	88	>1 cm	general frailty	2	60	100	superficial necrosis
5	62	>1 cm	refusal	4	60	70	superficial necrosis
6	75	>1 cm	general frailty	1	75	150	superficial necrosis
7	80	<1 cm	general frailty/cardiorespiratory disease	4	60	150	tumour eradicated, 36 months follow-up
8	80	<1 cm	general frailty	1	60	150	superficial necrosis
9	70	<1 cm	respiratory disease	2	60	150	superficial necrosis
10	73	<1 cm	respiratory disease	1	60	150	superficial necrosis
11	70	<1 cm	refusal	1	60	150	superficial necrosis
12	68	<1 cm	refusal	2	60	150	superficial necrosis

Table 2
PpIX fluorescence in tissue after oral administration of 60 mg/kg and 75 mg/kg of 5-aminolaevulinic acid

ALA dosage	Fluorescence intensity (unit/pixel)							
	Normal oesophagus (S.D.)		Oesophageal carcinoma (S.D.)		Barrett's oesophagus (S.D.)		Normal stomach (S.D.)	
	Mucosa	Lamina propria	Mucosa	Stroma	Mucosa	Lamina propria	Mucosa	Lamina propria
75 mg/kg	16027 (2674)		22271 (5623)	11482 (7863)	12205	5545	16535 (2433)	4301 (1644)
60 mg/kg	8255 (4440)		11112 (6365)	3002	9971 (1531)	3118 (985)	6500 (3101)	3257 (667)

treatment and at monthly intervals. Assessment of the treatment outcome was based on endoscopic and histological findings. All patients were treated with a proton pump inhibitor (20 mg bd. of omeprazole) after treatment.

PpIX distribution was studied in biopsies of tumour, normal and Barrett's oesophagus and stomach. Samples were taken immediately prior to treatment, snap-frozen in melting *iso*-pentane, and stored under liquid nitrogen until required. Frozen sections 10 μm thick (at least five per biopsy) were cut using a cryostat and allowed to dry for 30 min in the dark at room temperature. The sections were then examined using an epifluorescence microscope fitted with a cryogenic charge-coupled device camera (Astrocam N3200, Cambridge) and an XF46 fluorescence filter block (Omega Optical, VT, USA). Illumination was provided by a 1 mW helium–neon laser, and fluorescence was collected between 665 and 690 nm. All images were acquired over 5 min, using a ×40/1.40 oil-immersion fluorescence objective. Image processing was performed using the Imager 2 software suite (Astrocam, Cambridge). Sections were stained with haematoxylin and eosin, and re-photographed using a conventional 35 mm microscope camera, enabling correlation of the fluorescence distribution to histological structure. Tissue autofluorescence was measured in similar prepared sections from patients not pre-treated with ALA. The levels of PpIX fluorescence were calculated after correction for autofluorescence.

Patients often required repeated therapy in an attempt to eradicate malignant tissue. We found that after two to three weeks the necrosis in the oesophagus had separated and further treatment was possible. The timing was empirical and there are few data to indicate the best time for repeat therapy. The same drug–light regimen was used.

3. Results

3.1. Fluorescence distribution

PpIX fluorescence was higher in the tissues of patients who were given 75 mg/kg of ALA (in five divided doses) than in those receiving 60 kg/mg in two divided doses (Table 2). The PpIX fluorescence in oesophageal carcinoma was two to three times that of the surrounding lamina propria, The differential PpIX accumulation was no different between carcinoma and normal oesophageal mucosae (Table 3). Higher doses of ALA did not increase the differential accumulation of PpIX between normal mucosa and carcinoma.

Table 3
Fluorescence ratio between carcinoma and normal oesophageal mucosa and between carcinoma and its surrounding stroma

ALA dosage	Fluorescence ratio	
	75 mg/kg	60 mg/kg
Carcinoma/normal oesophagus (mucosa)	1.39	1.35
Carcinoma mucosa/stroma	1.94	3.70

3.2. Treatment outcome

All 12 patients showed response to the treatment with endoscopic evidence of superficial necrosis. Necrosis was evident within 24 h of treatment. Biopsy of the tumour confirmed fibrinoid necrosis. Assessment of the thickness of necrosis was not possible because of sloughing and angulation of the tissue biopsies. One patient with carcinoma-in-situ responded completely, repeat endoscopy and biopsy 28 months after treatment showing no recurrence. In this patient, the underlying Barrett's mucosa, which extended between 35 and 39 cm from the incisors, was replaced with pale looking squamous epithelium confirmed by histology, although unsuspected metaplastic glands remained buried under the neo-squamous mucosa. The other patient with carcinoma-in-situ was treated three times at intervals of two weeks. At this point it was appropriate to consider other treatment. The Barrett's epithelium showed similar squamous re-epithelisation but the carcinoma-in-situ was not completely eradicated. An elderly frail patient (unfit for surgery due to severe cardio-respiratory disease) with a T1 N0 tumour had the carcinoma eradicated after four PDT sessions over a period of four months. She died of her co-morbid disease 36 months after treatment without evidence of recurrent cancer. Other patients responded with superficial necrosis of mucosa but the tumour remained. Repeated treatment in some patients at two- to four-week intervals failed to improve on the outcome. The remaining nine patients in the frank carcinoma group needed thermal laser ablation to relieve or prevent dysphagia. Fig. 1 shows the endoscopic results of the treatment.

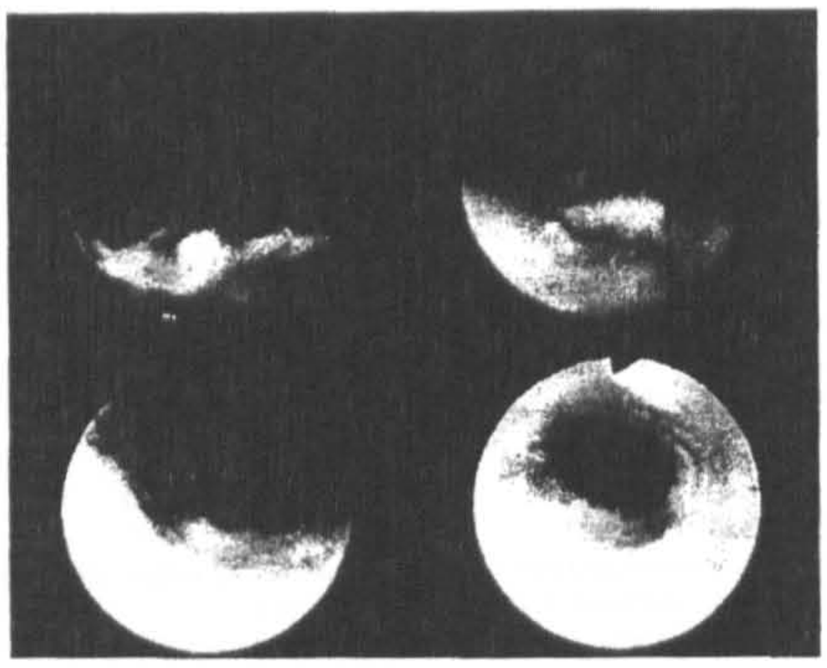

Fig. 1. Endoscopic outcome of patient 7 with small nodular tumour staged as T1 N0. Sequence shows nodule before treatment (upper left), superficial necrosis at one week (upper right), the result after two treatments (lower left) and the final result after four sessions of ALA/PDT at the 12 month follow-up (lower right) with neo-squamous epithelium in the area of the previous tumour.

3.3. Side-effects

Six patients had mild nausea, vomiting and retrosternal discomfort. Mild skin photosensitivity with erythema occurred in one patient who was inadvertently exposed to strong sunlight sitting by the window within 24 h of ALA ingestion. Aspartate transaminase (AST) and bilirubin were elevated in five patients (less than twice the normal range). Elevation of the liver enzymes was more marked when patients were exposed to the second dose of ALA. However, the enzymes always returned to normal after three to four days. No patients had any endoscopic complications.

3.4. Patient outcome

The two patients who had complete eradication continued to have surveillance endoscopy with multiple biopsy at six-monthly intervals until one died of other disease at 36 months. One patient remained well at 28 months follow up. The other patient with carcinoma-in-situ has had a successful oesophagectomy. Those patients with frank carcinoma received palliative thermal laser and other endoscopic therapy combined with chemotherapy and radiotherapy until death a mean of 16 months (range 6–26) later. Histological examination of treated areas has confirmed the presence of residual Barrett's metaplastic glands in the surviving patients. In our study, biopsies that were clearly identified as coming from a treated segment have shown residual glandular epithelium. This emphasises the impossibility of identifying cell type at endoscopy in areas of treatment. We have also commonly identified unsuspected buried glands [24].

4. Discussion

Initial attempts at treating oesophageal cancer with PDT relied on the use of photosensitisers such as haematoporphyrin derivative (HpD) and its more purified successor Photofrin. A complete response could be obtained in patients with small lesions. Sibille et al. [17] recently published the outcome of PDT of 123 patients with superficial oesophageal carcinoma using these photosensitisers between 1983 and 1991. They showed a complete response rate of 87% at six months. The actuarial five-year survival rate was 25%, but the disease specific survival rate was 74%. PDT-related complications were oesophageal stricture ($n=43$) and cutaneous photosensitisation ($n=16$). ALA is a new agent used in PDT. It is a 'pro-drug' and is converted in the body to PpIX, an effective photosensitiser. In vivo studies have shown that it can be given orally and that it has a short half-life with skin photosensitivity lasting only 24–48 h [11–13]. Other advantages of ALA are its preferential accumulation in mucosa and mucosal tumours. ALA/PDT has the potential benefit of eliminating the common complications of oesophageal PDT with conventional photosensitisers, i.e., prolonged cutaneous photosensitisation and oesophageal stricture [10,17]. In our study, none of the patients developed oesophageal stricture and only one patient had a very transient and mild cutaneous photosensitivity from inadvertent exposure to sunlight less than 24 h after treatment.

ALA/PDT has been used in the treatment of oral, gastrointestinal and skin cancer. Tissue necrosis was noted in oral and gastrointestinal cancers [12,13] and some skin cancers have been eradicated [18,19]. Regula et al. published [13] their pilot study on the efficacy of ALA/PDT and tissue PpIX distribution following oral administration of ALA; there were three oesophageal cancers among their 18 patients. They found that ALA/PDT was safe and tissue necrosis could be induced, but the disease was not eradicated.

Our study has concentrated on clinically small and superficial oesophageal adenocarcinomas that had arisen from Barrett's metaplasia. We studied the response of both the tumour and the metaplasia. In retrospect, four of the patients with tumours larger than 1 cm endoscopically were unsuitable for PDT. However the other eight patients were 'ideal' candidates for such treatment. Unfortunately, endoluminal ultrasound was not available for tumour staging in all patients. In one patient staged with endoluminal ultrasound, the tumour was deeper than the endoscopic appearance suggested. Clearly accurate staging is essential. A recent study of ALA/PDT has demonstrated that it is very effective for the eradication of dysplasia and for tumours that are less than 2 mm in depth [22]. It is clear that if the tumour is deeper, then ALA/PDT is not very effective. The alternative of photodynamic therapy with porfimer sodium (Photofrin) is very effective and can treat deeper tumours. This recently reported series is very informative, since 10 of 13 malignancies were ablated, but the oesophageal stricture rate was 34% [23]. These strictures appear to be because there is destruction of

the muscularis mucosa through into the submucosa. We now only use ALA/PDT for high-grade dysplasia and will use porfimer sodium for malignant lesions.

The fluorescence distribution study confirmed that PpIX accumulated in mucosa more than in the lamina propria or tumour stroma. The accumulation of PpIX after ALA administration by malignant oesophageal mucosa is little different from that by normal oesophageal mucosa. The lack of tumour selectivity may not be important, as the laser light is administered only to the oesophageal segment with tumour involvement. Higher doses of ALA increased PpIX accumulation but did not increase the differential distribution between normal and abnormal mucosa.

The main side-effects of ALA/PDT were nausea, vomiting and transient elevation of aspartate transaminase (AST) and bilirubin. The mechanism of the elevation of liver enzymes is not clear. It is interesting to note that patients with an acute attack of acute intermittent porphyria (AIP) also develop transient elevation of AST. None of the patients given ALA showed other symptoms of AIP. All the enzymes returned to normal after four to five days.

The reason why ALA/PDT only induced superficial necrosis is not obvious. It is possible, as suggested by Regula et al. [13], that photobleaching during PDT occurs more rapidly than with other photosensitisers. The alternative explanation is that the excitation wavelength of the light (630 nm) used is too far from the Soret band of PpIX, which is 405 nm. The reason for using longer-wavelength light is to improve tissue penetration.

Thermal laser [20] and PDT using haematoporphyrin have been used to treat Barrett's metaplasia and its associated early adenocarcinoma with encouraging results. However, some patients have developed oesophageal stricture after repeated treatment [10,23]. Our fluorescence distribution study confirmed the preferential accumulation of PpIX in the epithelium of abnormal and normal oesophagus, rather than the underlying stroma. This may make ALA an ideal agent for the treatment of widespread but very superficial lesions such as Barrett's dysplasia or carcinoma-in-situ. The surrounding Barrett's mucosa of our patients showed squamous re-epithelisation but with evidence of residual metaplastic glands at histology.

In conclusion, ALA/PDT can be effective in the treatment of oesophageal cancer confined to the mucosa, as shown in two patients. The adverse effects are minimal and the treatment can be repeated within a short period with no risk of oesophageal stricture. It is, however, not suitable for the treatment of established oesophageal carcinoma because of its superficial effect.

Acknowledgements

D.J.H.R. and S.B.B. are funded by the Yorkshire Cancer Research Campaign.

References

[1] S. Galandiuk, R.E. Hermann, D.M. Cosgrove, J.J. Gassman, Cancer of the esophagus: the Cleveland Clinic experience, Ann. Surg. 203 (1986) 101–108.
[2] T.R. DeMeester, G. Zantnott, K.E. Johansson, Selective therapeutic approach to cancer of the lower esophagus and cardia, J. Thorac. Cardiovasc. Surg. 95 (1988) 42–54.
[3] W.J. Blot, S.S. Devesa, R.W. Kneller, J.F.J. Fraumeni, Rising incidence of adenocarcinoma of the esophagus and gastric cardia, J. Am. Med. Assoc. 265 (1991) 1287–1289.
[4] T.R. DeMeester, S.E.A. Attwood, T.C. Smyrk, D.H. Theirkildsen, R.A. Hinder, Surgical therapy in Barrett's oesophagus, Ann. Surg. 212 (1990) 528–542.
[5] T.J. Dougherty, Yearly review — photodynamic therapy, J. Photochem. Photobiol. B: Biol. 58 (6) (1993) 895–900.
[6] H. Barr, C.J. Tralau, P.B. Boulos, A.J. MacRobert, R. Tilly, S G. Bown, The contrasting mechanisms of colonic collagen damage between photodynamic therapy and thermal injury, Photochem. Photobiol. 46 (1987) 795–800.
[7] C.S. Loh, A.J. MacRobert, G. Buonaccorsi, N. Krasner, S.G. Bown, Mucosal ablation using photodynamic therapy for the treatment of dysplasia: an experimental study in the normal rat stomach, Gut 38 (1996) 71–78.
[8] T.J. Dougherty, M.T. Cooper, T.S. Mang, Cutaneous phototoxic occurrences in patients receiving Photofrin, Lasers Surg. Med. 10 (1990) 485–488.
[9] C.S. Loh, D. Vernon, A.J. MacRobert, J. Bedwell, S.G. Bown, S.B. Brown, Endogenous porphyrin distribution induced by 5-aminolaevulinic acid in the tissue layers of the gastrointestinal tract, J. Photochem. Photobiol. B: Biol. 20 (1993) 47–54.
[10] B. Overholt, M. Panjehpour, E. Tefftteller, M. Rose, Photodynamic therapy for treatment of early adenocarcinoma in Barrett's oesophagus, Gastrointest. Endosc. 39 (1993) 73–76.
[11] J.C. Kennedy, R.H. Pottier, Endogenous protoporphyrin IX, a clinically useful photosensitizer for photodynamic therapy, J. Photochem. Photobiol. B: Biol. 14 (1992) 275–292.
[12] W.E. Grant, P.M. Speight, A.J. MacRobert, C. Hopper, S.G. Bown, Photodynamic therapy of normal rat arteries after photosensitisation using disulphonated aluminium phthalocyanine and 5-aminolaevulinic acid, Br. J. Cancer 70 (1994) 72–78.
[13] J. Regula, A.J. MacRobert, A. Gorchein, G A. Buonaccorsi, S.M. Thorpe, G.M. Spencer, A.R. Hatfield, S.G. Bown, Photosensitisation and photodynamic therapy of oesophageal, duodenal, and colorectal tumours using 5-aminolaevulinic acid induced protoporphyrin IX — a pilot study, Gut 36 (1995) 67–75.
[14] O H. Beahrs, D.E. Henson, R.V. Hutter (Eds.), Manual for Staging of Cancer, 3rd ed, American Joint Commitee on Cancer, J.B. Lippincot, Philadelphia, 1988, pp. 64–65.
[15] N. Barrett, Chronic peptic ulcer of the oesophagus and esophagitis, Br. J. Surg. 38 (1950) 175–182.
[16] P.R. Allison, A.S. Johnstone, The esophagus lined with gastric mucous membrane, Thorax 8 (1953) 87–101.
[17] A. Sibille, R. Lambert, J.C. Souquet, G. Sabben, F. Descos, Long-term survival after photodynamic therapy for esophageal cancer, Gastroenterology 108 (1995) 337–344.
[18] J.C. Kennedy, R.H. Pottier, D.C. Pross, Photodynamic therapy with endogenous protoporphyrin IX: basic principles and present clinical experience, J. Photochem. Photobiol. B: Biol. 6 (1990) 143–148.
[19] F. Cairnduff, M.R. Stringer, E.J. Hudson, D.V. Ash, S.B. Brown, Superficial photodynamic therapy with topical 5-aminolaevulinic acid for superficial primary and secondary skin cancer, Br. J. Cancer 69 (1994) 605–608.
[20] M.M. Berenson, T.D. Johnson, N.R. Markowitz, K.N. Buchi, W.S. Samowitz, Restoration of squamous mucosa after ablation of

Barrett's esophageal epithelium, Gastroenterology 104 (1993) 1686–1691.
[21] R.J. Schlemper, M. Itabashi, Y. Kato, R.H. Riddell, T. Shimoda, P. Sipporen, M. Stolte, H. Watanabe, H. Takahashi, R. Fujita, Differences in diagnostic criteria for gastric carcinoma between Japanese and Western pathologists, Lancet 349 (1997) 1725–1729.
[22] L. Gossner, M. Stolte, R. Stroka, K. Rick, E.G. Hahn, C. Ell, Photodynamic ablation of high grade dysplasia and early cancers in Barrett's esophagus by means of 5-aminolaevulinic acid, Gastroenterology 114 (1998) 447–455.
[23] B.F. Overholt, M. Panjepour, J.M. Haydek, Photodynamic therapy for Barrett's esophagus:follow-up in 100 patients, Gastrointest. Endosc. 49 (1999) 1–7.
[24] L.R. Biddlestone, C.P. Barham, S.P. Wilkinson, H. Barr, N A. Shepherd, The histopathology of treated Barrett's esophagus, Am. J. Surg. Pathol. 22 (1998) 239–244.

Progress in the detection of neoplastic progress and cancer by Raman spectroscopy

T.C. Bakker Schut[a] , N. Stone[b], C. Fulljames[b], H. Barr[b], HA. Bruining[a], G.J. Puppels[*a]

[a]Erasmus Medical Center Rotterdam, Dr. Molewaterplein 50, 3015 GE, Rotterdam, The Netherlands
[b]Gloucestershire Royal Hospital, Great Western Road, Gloucester, GL1 3NN, U.K.

ABSTRACT

Early detection of cancer is important because of the improved survival rates when the cancer is treated early. We study the application of NIR Raman spectroscopy for detection of dysplasia because this technique is sensitive to the small changes in molecular composition and conformation that occur during neoplastic progress, and because it can be used for minimally invasive *in vivo* detection using fiber-optic probes. The results of an *in vitro* study to detect neoplastic progress of esophageal Barrett's esophageal tissue will be presented. Using multivariate statistics, we developed three different linear discriminant analysis classification models to predict tissue type on the basis of the measured spectrum. Spectra of normal, metaplastic and dysplastic tissue could be discriminated with an accuracy of up to 88%. Therefore Raman spectroscopy seems to be a very suitable technique to detect dysplasia in Barrett's esophageal tissue.

Keywords: NIR Raman spectroscopy, dysplasia, multivariate spectral analysis

1. INTRODUCTION

A number of spectroscopic techniques is currently being investigated for *in vivo* detection of early cancer and especially of dysplasia, the first stage in the development of cancer.[1, 2] Early detection of cancer is important because of the improved chances in treating the cancer successfully. Detection of dysplasia is currently limited by the fact that it can only be done *ex vivo* by pathological grading of tissue biopsies. Therefore, the number of samples that can be investigated is limited. In most cases, dysplastic tissue cannot be discriminated *in vivo* from normal tissue by visual inspection, resulting in high numbers of unnecessary biopsies (i.e. of normal tissue) and a significant risk of missing areas of dysplastic tissue. Fast spectroscopic *in vivo* detection of dysplasia could be of use as a biopsy-guiding tool, enabling higher sampling rates and lower false positive rates by only taking biopsies from suspicious areas. If *in vivo* spectroscopy can be made specific and sensitive enough for the detection of dysplasia, it could ultimately reduce the need for taking biopsies.

In principle, Raman spectroscopy seems to be well suited for detection of dyplasia. It offers the detailed molecular information that is needed to detect neoplastic changes with high specificity and sensitivity, as was shown *in vitro* for detection of a number of cancers and pre-cancers.[2] Raman spectroscopy can be applied *in vivo* through the use of special fiber optic probes, which can be optimized for a particular application.[3] Applicability of *in vivo* Raman spectroscopy in a clinical setting depends on development of sensitive equipment and powerful spectral analysis to enable the extraction of clinically relevant parameters from spectra obtained with short collection times.

Our work focuses on detecting (pre)cancers in the Barrett's esophagus. A Barrett's esophagus is caused by gastric and duodenal refluxes, which changes the normal non-keratinized stratified squamous epithelium of the esophagus into columnar lined mucous producing epithelium, such as found in the intestines and stomach. This metaplastic state is now considered to be a pre-malignant state that increases the risk of development of adeno-carcinoma by a factor of 50.

Earlier work has proven that tumor tissue could be discriminated from normal and metaplastic esophageal tissue by Raman spectroscopy and multivariate statistical classification techniques.[4]. Here we investigated the possibilities for *in vitro* classification of normal, metaplastic and dysplastic esophageal tissue by NIR Raman spectroscopy. Using a Raman microspectrometer we obtained *in vitro* spectra of biopsy samples from a number of patients showing dysplasia in a Barrett's esophagus. Three different LDA models were evaluated to investigate the influence of different groupings on the classification results.

SPIE 3918-10
"Biomedical Spectroscopy: Vibrational Spectroscopy and Other Novel Techniques"
27th Jan 2000, San Jose.

2. MATERIAL AND METHODS

2.1 Tissue samples

For this *in vitro* study 10 different biopsies from 3 different patients with low and high grade dysplasia were used. All biopsies were graded by a pathologist in 4 different classes: 3 biopsies with Normal epithelium (N), 4 biopsies with Barrett's epithelium (B), 1 biopsy with Low Grade Dysplasisa (LGD), and 2 biopsies with High Grade Dysplasia (HGD). Raman spectra were taken from at least 20 different locations (about 100 μm apart) on the epithelial side of the biopsies.

2.2 Raman set-up

For all measurements 100 mW of 850 nm laser light from an Argon ion laser pumped Ti-Sapph laser (Spectra Physics, models 2020 and 3900S) was focused by a microscope objective (Nachet, magnification: 20 X, NA=0.4) on the sample. Raman light from the sample was collected by the same objective, filtered using a holographic notch filter and focused on the entrance of a fiber that was connected to the entrance of the spectrometer. An F/2 spectrometer, built-in-house, equipped with a liquid nitrogen cooled deep depletion CCD (Princeton Instruments), was used to record the spectra. All spectra were measured with a collection time of 30 seconds.[4]

2.3 Spectral analysis

All spectra were corrected for the wavelength dependent sensitivity of the set-up and for Raman light that was generated in the microscope objective. All spectra were then Savitzky-Golay differentiated to reduce the interference of slowly fluctuating background signal, and subsequently scaled to have zero mean and unit variance (auto-scaling).[4]

Multivariate statistical classification models were built as follows: The data were divided in a model set and a prediction set (for evaluation of the model). Two thirds of the full data set (evenly distributed) was used for modeling and 1 third was used for prediction. Clear outliers were removed from the data set. These were defined as spectra obtained from a biopsy sample that do not fall within a boundary of 10 times the standard deviation from the mean spectrum of that biopsy sample. Principal Component Analysis (PCA) was used on the model set to orthogonalise and reduce the number of parameters needed to represent the variance in the spectral dataset. A two-sided t-test was used to individually select those PC's that show the highest significance in discriminating the different classes. The scores of the model spectra on these PC's, which represent most of the useful variance in the dataset, were used as input for a Linear Discriminant Analysis (LDA) model. The number of PC's that were used as input was kept smaller than the number of spectra in the smallest model group to prevent overfitting in the LDA-model. LDA yields n-1 discriminants that best separate the n groups. Prediction spectra were first projected on the PCA model; the scores of these prediction spectra on the PC's were subsequently projected on the LDA-model to yield a classification

3. RESULTS

3.1 Model 1: Normal, Barrett's, Low Grade Dysplasia and High Grade Dysplasia

In the first model all 4 tissue types were included as different classes.

Figure 1 shows mean spectra for the 4 different types of tissue: Normal, Barrett's, Low Grade Dysplasia (LGD), and High Grade Dysplasia (HGD). Since the differences between the mean spectra are small, also the differences of the group means with the overall mean are shown.

Figure 2 shows the discriminants of this model. Since the model was developed on the basis of first derivative spectra, the discriminants were integrated to facilitate the interpretation of the spectral features, which is the subject of further analysis. The slowly fluctuating background in the discriminants is due to integration, and should be ignored. The discriminants show combinations of positive and negative features that coincide with specific Raman bands, and can be used to identify the differences between the two groups.

In figure 3 the LDA scores are shown for both the *in vitro* classification model (upper three plots) and prediction spectra (lower three plots). Normal samples (squares) have positive LD1 scores and negative LD2 scores; Barrett's samples (circles) have negative LD1 scores and positive LD2 scores; LGD samples (plus signs) have negative LD1 and LD3 scores and HGD samples (crosses) have negative LD1 and LD2 scores.

Evaluation of the model, gives a 89% correct classification of the model spectra, using a leave-one-out validation. The model was used to evaluate the independent test set of spectra. Table 1 shows the classification results for these test spectra. From these results, the sensitivity and specificity of Raman spectroscopy as a diagnostic test for the detection of the different tissue types, versus the standard method (pathology), were calculated. These parameters, and the prevalence of each tissue type, are given in table 2.

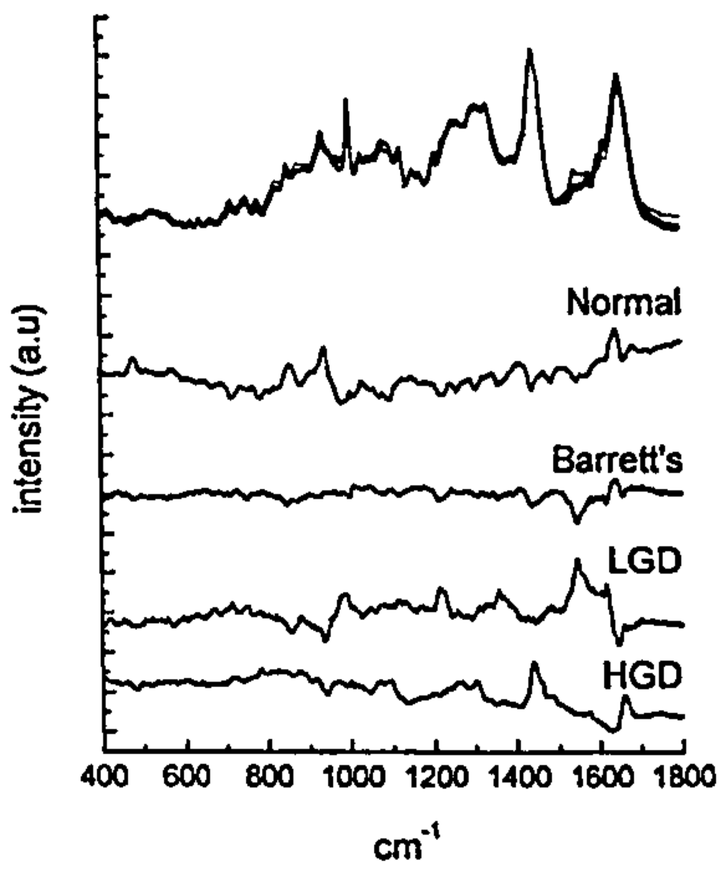

Figure 1: Above: Mean spectra of the 4 groups in model 1: Normal, Barrett's, Low Grade dysplasia (LGD) and High Grade Dysplasia (HGD). Below: Differences (times 4) of the four groups compared to their overall mean

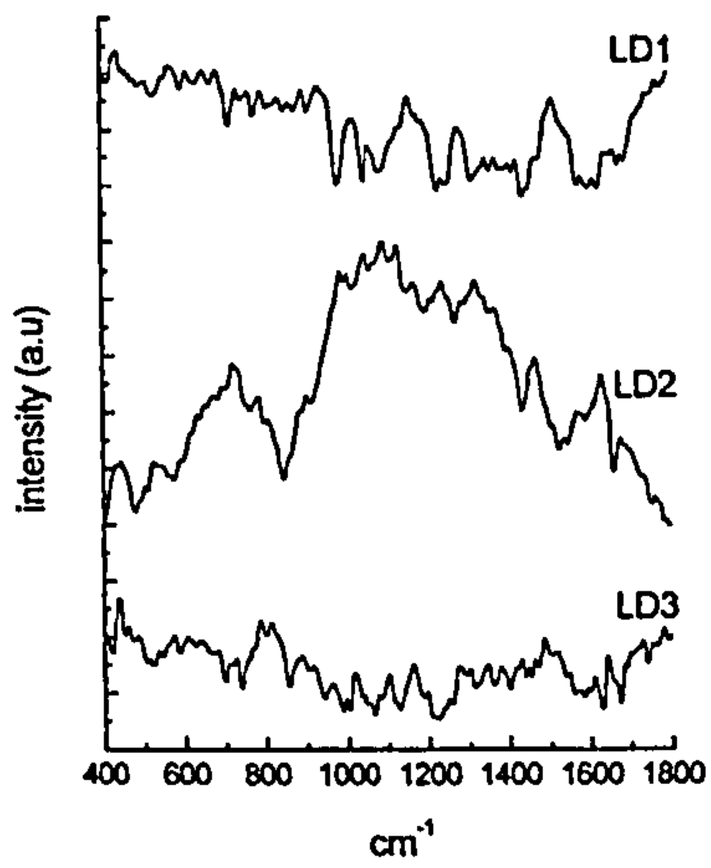

Figure 2: Linear Discriminants (LD) of model 1 to separate 4 groups of spectra: Normal, Barrett's, Low Grade Dysplasia and High Grade Dysplasia.

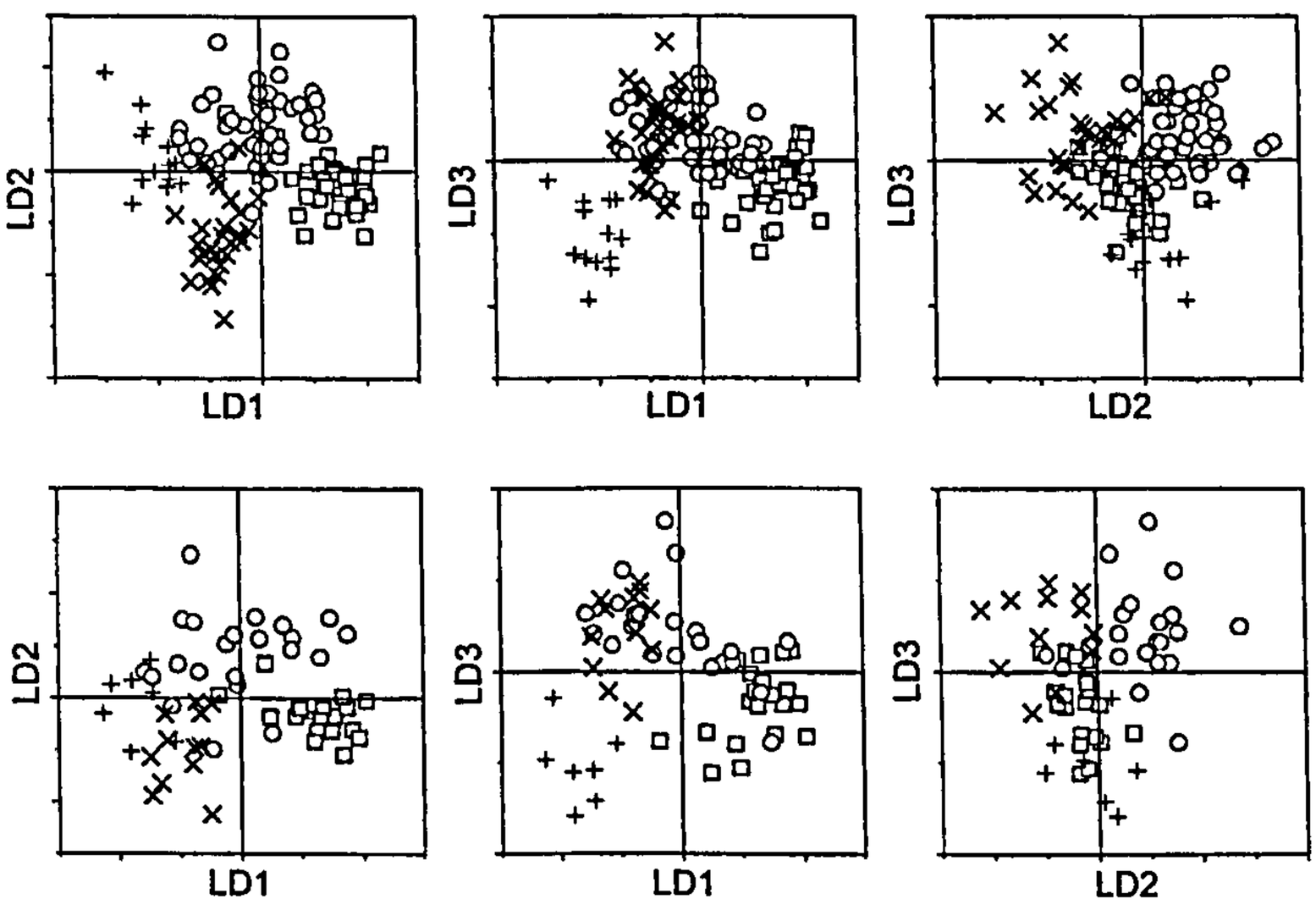

Figure 3: Scores of the model spectra (upper 3 plots) and prediction spectra (lower 3 plots) on the 3 discriminants of model 1, shown in figure 2. Each symbol denotes one spectrum. Symbols according to pathological grading: Squares denote normal, circles denote Barrett's, plus-signs denote low grade dysplasia, and crosses denote high grade dysplasia. The inner axes in the plots are the zero crossings of the score values.

Prediction set classification results for model 1						
		Pathology				
		HGD	LGD	Barrett's	Normal	Total
Raman	HGD	10	0	2	0	12
	LGD	0	7	0	1	8
	Barrett's	2	0	16	0	18
	Normal	0	0	4	19	23
	Total	12	7	22	20	61

Table 1:
Classification results of model 1 for the prediction spectra shown in figure 3: Raman classification (rows) versus Pathology classification (columns). Total number of misclassifications: 9 (14.75 %)

Raman spectroscopy for Barrett's tissue classification				
	HGD	LGD	Barrett's	Normal
Sensitivity	0.83	1,00	0.73	0.95
Specificity	0.96	0.98	0.95	0.90
Prevalence	0.20	0.11	0.36	0.33

Table 2:
Sensitivity and selectivity of Raman spectroscopy as a diagnostic test for classification of tissue types in Barrett's esophagus tissue using model 1. Numbers were calculated using the classification results of table 1.

3.2 Model 2: Normal, Barrett's, High Grade Dysplasia

In the second model we left out the Low Grade Dysplasia group. This group consists of only one biopsy sample that seems to be contaminated with blood, as can be seen from the peak at 1547 in the mean LGD spectrum in figure 1
Figure 4 shows the mean spectra for the remaining 3 types of tissue: Normal, Barrett's and High Grade Dysplasia (HGD), and their differences from the overall mean.
Figure 5 shows the (integrated) discriminants of this model. In figure 6 the LDA scores are shown for the classification (left plot) and prediction spectra (right plot). Normal samples (squares) have negative LD1 scores and positive LD2 scores; Barrett's samples (circles) have positive LD1 scores and HGD samples (crosses) have negative LD1 and LD2 scores.
Evaluation of the model, gives a 88% correct classification of the model spectra, using a leave-one-out validation. The model was used to evaluate the independent test set of spectra. Table 3 shows the classification results for these test spectra. From these results, the sensitivity and specificity of Raman spectroscopy as a diagnostic test for the detection of the different tissue types, versus the standard method (pathology), were calculated. These parameters, and the prevalence of each tissue type, are given in table 4.

3.3 Model 3: Normal, Barrett's and Dysplasia

In the third model we added the two dysplastic groups to form a new group called dysplasia. The difference between low and high grade dysplasia is somewhat ambiguous, and might cause artifacts in the model.
Figure 7 shows the mean spectra for the 3 types of tissue: Normal, Barrett's and Dysplasia, and their differences from the overall mean.
Figure 8 shows the (integrated) discriminants of this model. In figure 9 the LDA scores are shown for the classification (left plot) and prediction spectra (right plot). Normal samples (squares) have negative LD1 scores and positive LD2 scores; Barrett's samples (circles) have positive LD1 scores and Dysplasia samples (crosses) have negative LD1 and LD2 scores.
Evaluation of the model, gives a 91% correct classification of the model spectra, using a leave-one-out validation. The model was used to evaluate the independent test set of spectra. Table 5 shows the classification results for these test spectra. From these results, the sensitivity and specificity of Raman spectroscopy as a diagnostic test for the detection of the different tissue types, versus the standard method (pathology), were calculated. These parameters, and the prevalence of each tissue type, are given in table 6.

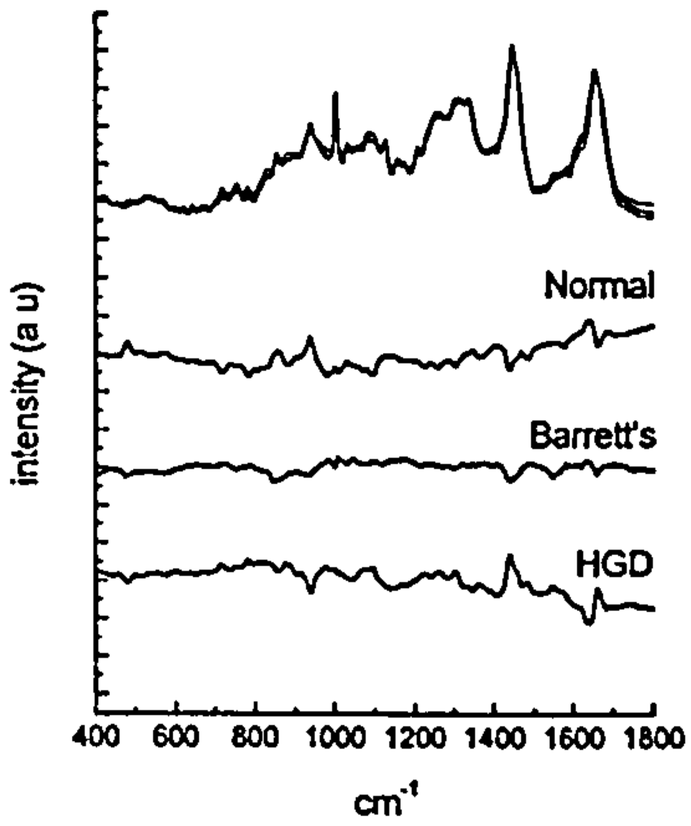

Figure 4: Above: Mean spectra of the 3 groups in model 2, Normal, Barrett's and High Grade Dysplasia (HGD). Below: Differences (times 4) of the four groups compared to their overall mean

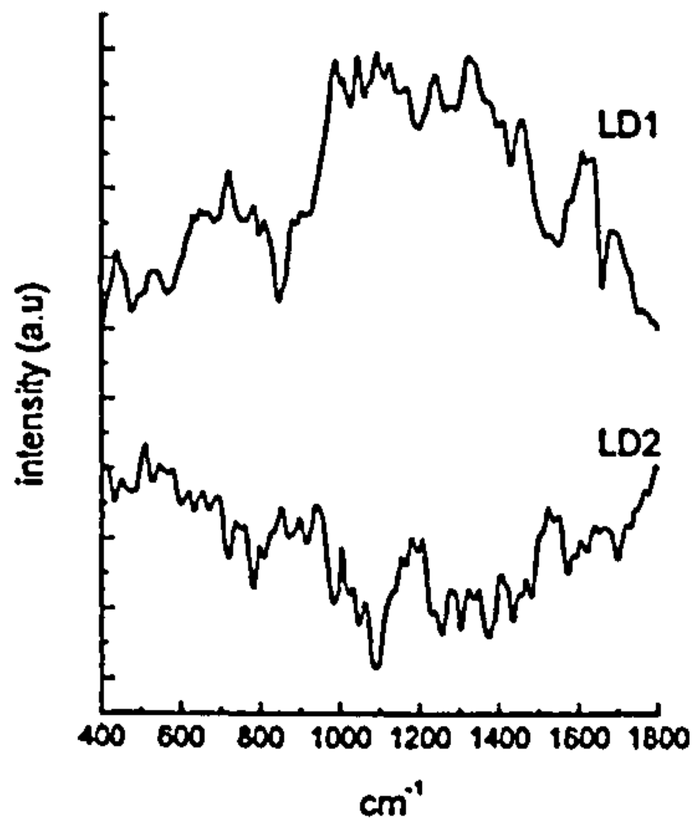

Figure 5: Linear Discriminants (LD) of model 2 to separate 3 groups of spectra: Normal, Barrett's and High Grade Dysplasia (HGD).

Figure 6: Scores of the model spectra (left plot) and prediction spectra (right plot) on the two discriminants of model 2, shown in figure 5. Each symbol denotes one spectrum. Symbols according to pathological grading: Squares denote normal, circles denote Barrett's, and crosses denote high grade dysplasia. The inner axes in the plots are the zero crossings of the score values.

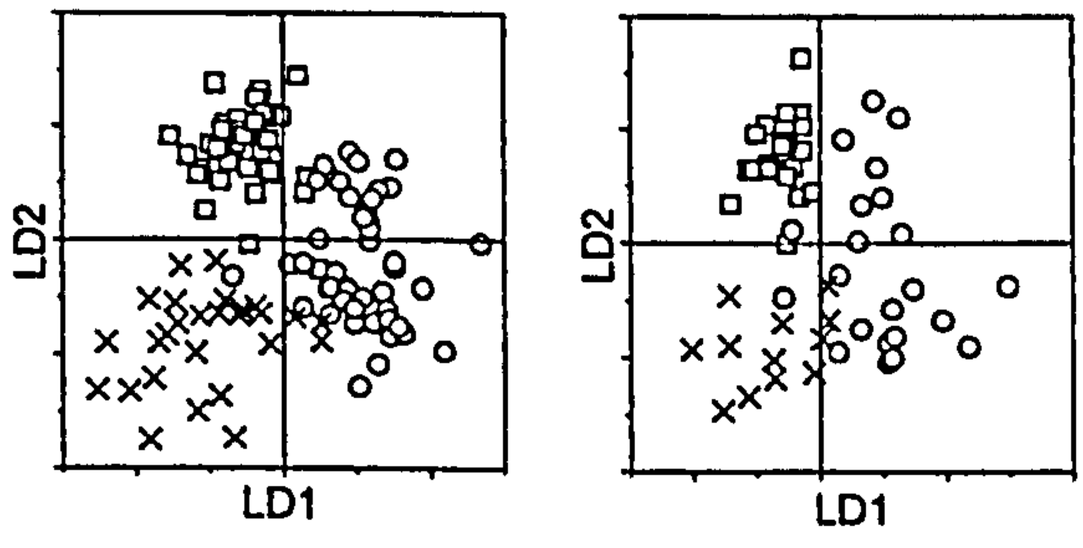

Table 3:
Classification results of model 2 for the prediction spectra shown in figure 6: Raman classification (rows) versus Pathology classification (columns). Total number of misclassifications: 6 (11.11 %)

Prediction set classification results for model 2

		Pathology			
		HGD	Barrett's	Normal	Total
Raman	HGD	10	1	0	11
	Barrett's	2	18	0	20
	Normal	0	3	20	23
	Total	12	22	20	54

Table 4:
Sensitivity and selectivity of Raman spectroscopy as a diagnostic test for classification of tissue types in Barrett's esophagus tissue using model 3. Numbers were calculated using the classification results of table 3.

Raman spectroscopy for Barrett's tissue classification

	HGD	Barrett's	Normal
Sensitivity	0.83	0.82	1.00
Specificity	0.98	0.94	0.91
Prevalence	0.22	0.41	0.37

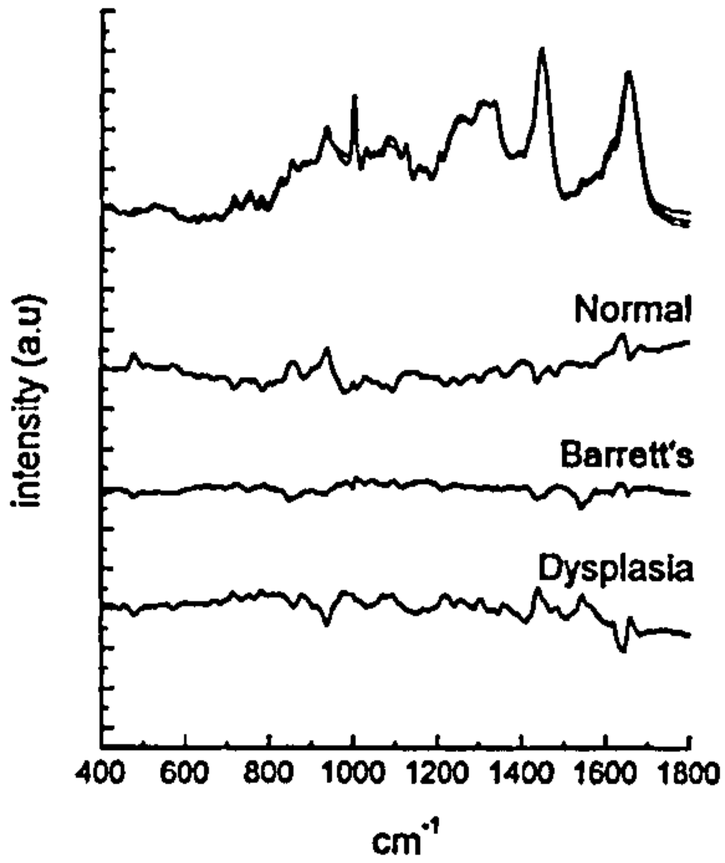

Figure 7: Above: Mean spectra of the 3 groups in model 3: Normal, Barrett's and Dysplasia. Below: Differences (times 4) of the four groups compared to their overall mean

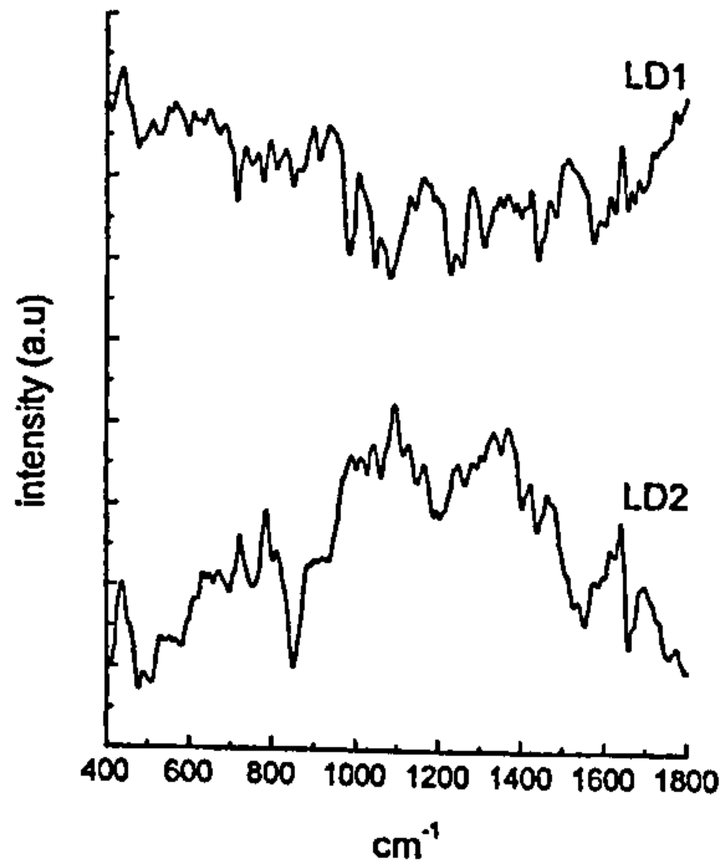

Figure 8: Two Linear Discriminants (LD) of model 3 to separate the three groups of spectra : Normal, Barrett's and Dysplasia.

Figure 9: Scores of the model spectra (left plot) and prediction spectra (right plot) on the two discriminants of model 3, shown in figure 8. Each symbol denotes one spectrum. Symbols according to pathological grading: Squares denote normal, circles denote Barrett's, and crosses denote dysplasia. The inner axes in the plots are the zero crossings of the score values.

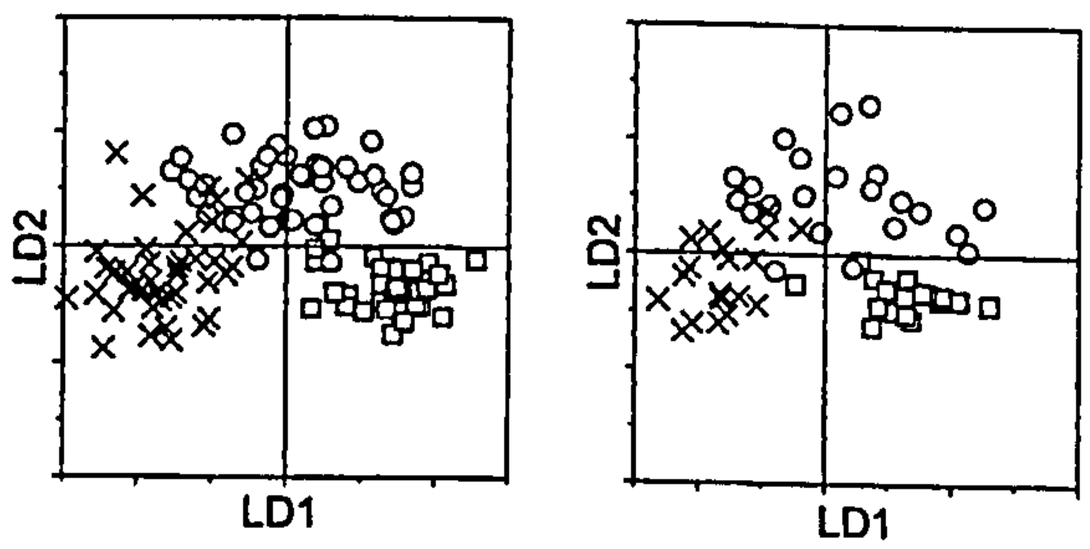

Table 5:
Classification results of model 3 for the prediction spectra shown in figure 9: Raman classification (rows) versus Pathology classification (columns). Total number of misclassifications: 8 (13.11 %)

Prediction set classification results for model 3

		Pathology			
		Dysplasia	Barrett's	Normal	Total
Raman	Dysplasia	17	1	1	19
	Barrett's	2	17	0	19
	Normal	0	4	19	23
	Total	19	22	20	61

Table 6:
Sensitivity and selectivity of Raman spectroscopy as a diagnostic test for classification of tissue types in Barrett's esophagus tissue using model 1. Numbers were calculated using the classification results of table 5.

Raman spectroscopy for Barrett's tissue classification

	Dysplasia	Barrett's	Normal
Sensitivity	0.89	0.77	0.95
Specificity	0.95	0.95	0.90
Prevalence	0.31	0.36	0.33

4. DISCUSSION

The data presented here clearly show that it possible to discriminate *in vitro* between normal, metaplastic and dysplastic tissue on the basis of their Raman spectra. The results of this *in vitro* study to detect dysplasia in biopsies from Barrett's esophagus show that there is some overlap in LDA-space between the four consecutive stages (Normal to Barrett's to LGD to HGD) in the progress towards carcinoma. This is probably due to problems with matching the Raman measurements with the pathology findings. First, it is difficult to exactly match the locations in the tissue sample where the spectra were measured with the location of pathological grading. Second, pathology does not give an exact composition of the tissue, but an overall grading. Samples graded as samples as HGD may contain some LGD and/or normal tissue. This will cause some misclassifications and overlap in the multivariate model that can only be prevented by using only samples with large areas of a single tissue type, which are hard to obtain. From figure 1A, it can be seen that the mean spectra of the four types of tissue are very similar. This can partly be caused by the contaminations in the model data set, but it can also be due to sample volume geometry: the axial resolution when using the 20X, Na=0.4 objective is somewhat larger than the thickness of the epithelial layer, where the main differences can be found, resulting in contributions from deeper tissue layers (lamina propria, muscle layer) which are similar for all tissues.

The model spectra of the first model, in which spectra of each type of tissue were grouped separately, were correctly classified in 89% of the cases using a leave-one-out validation, therefore the model is not ideal. The classification of the prediction spectra with this model is correct for 85% of the cases, similar to the model data set. As can be seen from figure 3, the distribution of the prediction set is similar to that of the model set, which indicates that there is no overfitting in the statistical model. Most of the misclassifications are made in the Barrett's group, which is not surprising since Barrett's tissue can be very heterogeneous and may also contain patches of normal tissue (model data sets also gave most misclassifications in Barrett's group).

In the second model we left out the LGD samples, which appeared to be contaminated with blood. It can be seen from the discriminants of model 1 (figure 2) that the blood contributions do not play a mayor role in the separation of the LGD group. Elimination of the LGD group did not have much effect on the sensitivity and specificity for the classification of the HGD samples, but improved the classification of the normal and Barrett's samples somewhat. This suggests that the interference of the LGD samples is mainly with the Barrett's samples and the normal samples, which is also indicated by the results of the classification of the spectra of model 1 (in the classification of the model spectra, one Barrett's sample and one normal sample but no HGD samples were classified as LGD).

In the third model we added the two dysplastic groups to form a new group called dysplasia. The difference between low and high grade dysplasia is somewhat ambiguous, and might cause artifacts in the model although the classification results of model 1 and model 2 suggest that these two groups hardly interfere. Adding LGD and HGD does not have an effect on the classification of the normal samples but it improves the separation between Barrett's samples and dysplastic samples somewhat. The blood present in the LGD spectra does not seem to cause problems in identifying the dysplastic samples as one group.

The sensitivity for detecting (high grade) dysplasia, as found by these LDA models, is not very high, but this limited study does indicate that it is possible to detect dysplasia in Barrett's tissue *in vitro*, using Raman spectroscopy. The specificity for detecting (high grade) dysplasia for the models developed here was in all cases higher than the sensitivity (specificity for detecting dysplasia >0.95). If a high sensitivity is required, the LDA models can easily be biased to yield a higher sensitivity, at the expense of having a lower specificity.

ACKNOWLEDGEMENTS

The authors wish to express their gratitude to the Dutch Foundation for Scientific Research (NWO, grant no. 910-38-055) and to RENISHAW, Inc (Wotton under Edge, UK) for funding of the work presented here.

REFERENCES

[1] Bohorfoush A.G., "Tissue spectroscopy for gastrointestinal diseases", *Endoscopy* 28, pp 372-380,1996

[2] Mahadevan-Jansen A. and R. Richards-Kortum,"Raman spectroscopy for the detection of cancers and precancers", *J. Biomed. Opt.* 1, pp 31-70, 1996.

[3] Shim M., Wilson, B.C., Marple, E. and M. Wach, "Study of fiber-optic probes for in vivo medical Raman spectroscopy", *Applied Spectroscopy* 53, pp 619-628, 1999

[4] Wolthuis R., Bakker Schut, T.C., Caspers, P.J., Buschman, H.P.J., Römer, T.J., Bruining, H.A. and G.J. Puppels,"Raman spectroscopic methods for *in vitro* and *in vivo* tissue characterization", *Fluorescent and luminescent probes for biological activity*, W.T..Mason (ed.), pp 433-454, Academic Press, London, 1999.

Raman Spectroscopy: A Diagnostic Tool for Detection of Early Malignant Changes in the Larynx

Nicholas Stone[a], Pela Stavroulaki[b], Catherine A. Fulljames[a], Martin Birchall[b], Hugh Barr[a]

[a]Institute of Medical Sciences, Gloucestershire Royal Hospital, Gloucester, GL1 3NN, U.K.

[b]Department of Otolaryngology, Head and Neck Surgery, University of Bristol, Southmead Hospital, Bristol BS10 5ND, U.K.

ABSTRACT

The incidence of laryngeal cancer has risen progressively over the last 25 years. Early diagnosis and treatment of pre-malignant lesions of the larynx is vital to prevent progression to invasive squamous cell carcinoma. In the larynx, it has long been recognised that histological evidence of maturation abnormality is associated with a higher risk of transformation to malignancy. Currently, it is extremely difficult if not impossible for the clinician to ascertain the level of abnormality present without removing a biopsy sample and sending it for histopathlogical analysis. Inherent risks with this technique include damage to vocal chords and loss of speech quality as well as possible selection of unrepresentative biopsy samples.

Raman spectroscopy, incorporated into an endoscopic system, has the potential to provide a real-time, non-invasive diagnostic technique able to detect biochemical changes that accompany abnormal pathology. Likely outcomes would be improved biopsy targeting and patient management by providing immediate results of tissue pathology. This paper demonstrates the capacity of near infrared Raman spectroscopy combined with statistical data analysis techniques to discriminate between normal, dysplastic and cancerous laryngeal tissue.

Keywords: Raman, Larynx, dysplasia, cancer, malignancy, biopsy, spectroscopy, detection, endoscopy.

1. INTRODUCTION

The incidence of laryngeal cancer has progressively risen over the last 25 years, with the most significant increase occurring in women[1]. It has been estimated that there has been no overall improvement in the mortality from laryngeal cancer over the last three decades. Delayed diagnosis leading to loco-regional failure and a high incidence of second primary malignancy in long-term survivors are the two main reasons for this poor outcome[2]. In addition, laryngeal cancer has the greatest effect on quality of life of any cancer, causing devastating lifestyle changes and resulting in permanent cosmetic and psychosocial disability. Therefore, the development of an automated diagnostic method allowing detection of premalignant and malignant lesions earlier, at a cellular level would facilitate faster, more effective patient management and potentially further reduce mortality.

The vast majority of laryngeal cancers originate on the surface. The standard method of detection is inspection of the organ with endoscopy and removal of a sample of tissue for histopathological analysis. This can be time consuming, costly and due to the random nature of biopsy selection stands a chance of missing any abnormal cells in the organ. In addition repeated biopsy procedures increase the risk of affecting the quality of the voice. The transformation from the normal state to carcinoma in the larynx involves an intermediate step, whereby the cells in the squamous epithelial layer begin to grow and mature abnormally. This state is called squamous dysplasia. It is known that lesions exhibiting mild dysplasia have a lower potential for malignant degeneration than those with severe dysplasia. If the tumour can be visually detected at endoscopy it may already be too late to initiate a full cure.

Raman spectroscopy has recently been proposed for early cancer diagnosis by a number of authors[3,4,5]. Although it has shown potential for early diagnosis of malignancy in a variety of organs (breast, brain, oesophagus[6], bladder, cervix)[7], it has yet to be demonstrated as a tool for detection of early laryngeal malignancies. Raman spectroscopy is the analysis of inelastic scattered photons following monochromatic laser excitation. It provides information about both the chemical and

morphological structure of tissue in near real time[8] and can be used as a non-invasive optical method of tissue characterization. Most biological molecules are Raman active with their own characteristic fingerprint. Proteins, nucleic acids, cell membranes, single cells and tissues can all be studied. The Raman spectrum is a plot of scattered intensity, as a function of energy difference between the incident and scattered photons. The loss (or gain) in photon energies corresponds to the difference in the final and initial vibrational energy levels of molecules participating in the interaction. The observed peaks (bands) in the Raman spectrum are relatively narrow, easy to resolve and sensitive to molecular structure, conformation and environment.

One of the primary obstacles encountered in the Raman spectroscopy of biological tissue is that of fluorescence. A fairly recent development has been the use of near infrared (NIR) laser excitation and dispersive spectrometers to allow rapid detection of spectra with low background fluorescence. NIR radiation generally does not induce electronic absorption in tissue chromophores so fluorescence is weak relative to the Raman signal. Holographic notch filters are used to filter the elastic (Rayleigh) scattered light from the signal, combined with a single monochromator the throughput of the system is increased compared with the triple monochromator used previously. The development of charge coupled device (CCD) detectors and solid state semiconductor lasers has enabled the development of portable NIR Raman systems providing spectra with high signal to noise with short integration times. Compatibility with fibre optics and the development of new probes is making in vivo diagnostics with Raman spectroscopy a real possibility.

The goal of this study was to assess the feasibility of using NIR Raman spectroscopy for the early diagnosis of laryngeal malignancy. As an initial step NIR Raman spectra of normal, dysplastic and squamous cell carcinoma were characterized and average spectra for each pathology were compared in order to determine its potential to differentiate between different pathologies. Multivariate analysis techniques were applied to test the separation of cancers, pre-cancers and normal tissue spectra by clusters.

2. MATERIALS AND METHODS

2.1 Subjects

Nineteen patients, ten men and nine women, participated in this preliminary study. Their ages ranged from 18 to 79 years, with a median of 53 years. Informed consent was obtained from each patient and the study was approved by the United Kingdom South and West Local Research Ethics Committee.

2.2 Tissue preparation

Biopsy specimens ($5x5x5mm^3$) were collected during routine surgical procedures (microlaryngoscopies) and snap frozen in liquid nitrogen. Histological sections were cut from each of the samples using a freezing-microtome (Figure 1a) and stained with hematoxylin and eosin (H&E). Remaining biopsy blocks were stored at – 85°C until spectroscopic studies could be carried out. The larynx sections were classified by a pathologist as normal, dysplastic and squamous cell carcinoma. For the purpose of this study, with limited numbers of samples, mild, moderate and severe dysplasia were grouped together[9]. Only homogenous samples with clearly defined pathologies were used in this study, those with mixed or indeterminate pathologies were discarded. Twenty-one samples were retained for study with Raman spectroscopy, including twelve histologically normal samples, four exhibiting dysplasia and five with squamous cell carcinoma. Before spectral measurements, the specimens were passively warmed to room temperature and rinsed with buffered isotonic saline solution (pH 7.4). No other sample pre-treatment of any kind was performed.

2.3 Instrumentation

Raman scattering measurements were obtained in vitro with a Renishaw System 1000 Raman micro-spectrometer. This system includes a tunable, argon ion pumped Ti:Sapphire laser (Spectra Physics 3900S), a high efficiency holographic spectrograph and a peltier cooled CCD detection system. Samples were orientated in the in vivo geometry (tissue surface upwards) and placed between two calcium fluoride slides (Figure 1b). A x80 ultra-long-working-distance lens was used to focus the excitation light onto the tissue and collect the scattered photons in non-confocal mode. At least four spectra were acquired from each sample (mean number = 7.3, range 4 to 12) with an excitation wavelength of 830nm. In this wavelength region, the absorption coefficients of water and tissue pigments are small and the effective penetration depth is large (typically a few mm). There was little contribution to the Raman signal from fluorescence. The laser power at the sample

was 36 ± 1.1 mW, focused to a spot size of approximately 5 μm at the tissue surface. The scattered Raman signal was integrated for 30 seconds and measured over a spectral range of 400-1800 cm^{-1} with respect to the excitation frequency.

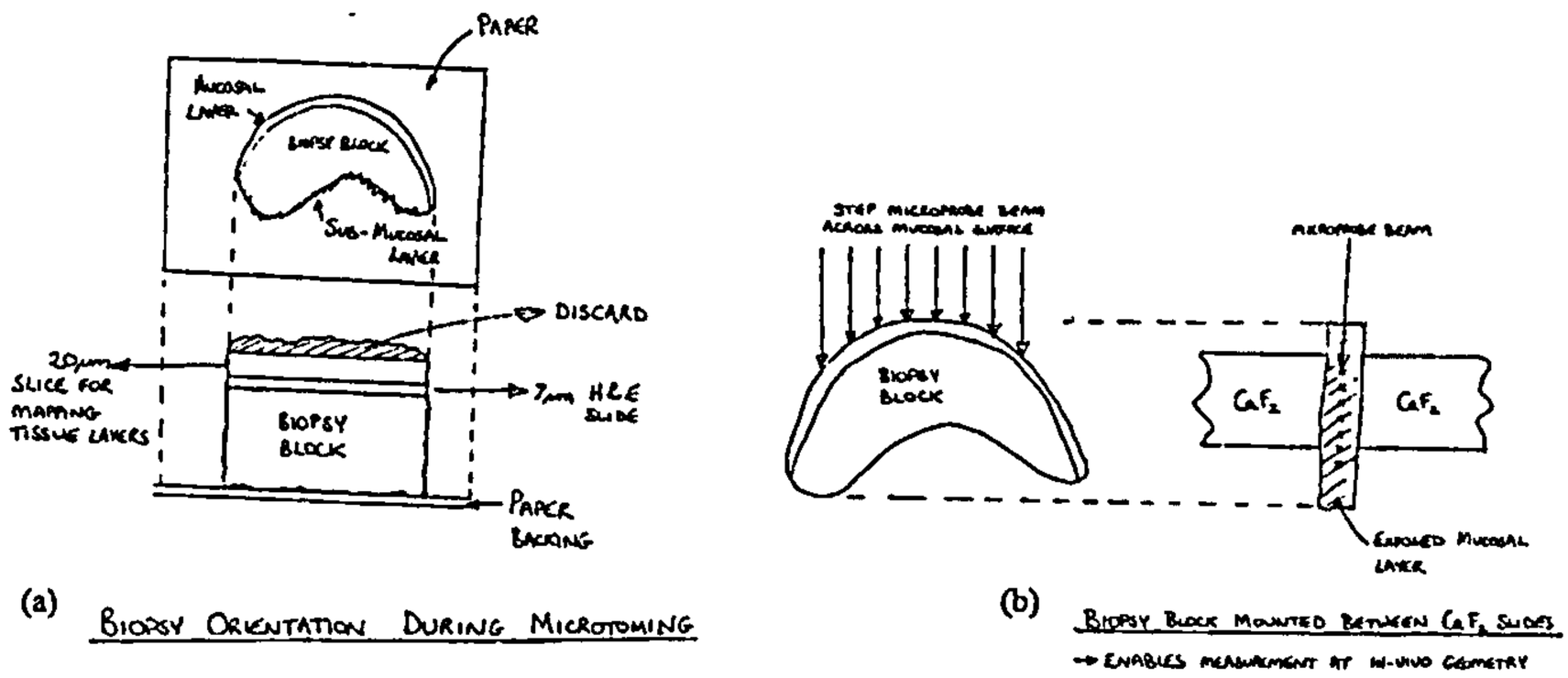

Figure 1. (a) Orientation of biopsy block for cutting with a freezing microtome. Sample was laid on acetate paper and sectioned. The histopathology of the section is studied and homogeneous samples are then investigated (b) with the Raman microspectrometer using an in vivo beam geometry.

2.4 Analysis

The system was calibrated for wavenumber shift using a neon lamp standard and Renishaw WIRE software. Tissue spectra were corrected for the energy dependent response of the system using a tungsten-filament lamp with a spectral output calibrated by the National Physical Laboratory, UK. No further manipulation of the tissue spectra was performed prior to analysis. Intra-sample repeatability was evaluated and mean spectra for each tissue pathology were obtained. Variations in the mean spectra with pathology were assessed using multiple analysis of variance (MANOVA)[10].

A large number of empirical methods have been employed in the literature to evaluate variations in the spectra with tissue pathologies. These usually involve absolute peak intensity or peak intensity ratio measurements. There is a disadvantage to this type of method in that only a tiny part of the huge amount of data, obtained on the histochemistry of the tissue, is used for analysis. Biological tissue is exceedingly complex and it is likely that there are many factors influencing pathology. Therefore a method that incorporates as much of the data as possible in the analysis is likely to provide a more rigorous method of separating spectra with pathology. One such method, principle component analysis (PCA) was performed on the tissue spectra using the Galactic GRAMS/32 PLS/IQ software suite. Of the 181 spectra acquired, 5 were discarded due to extremely poor signal to noise or an unusually large fluorescence background. The remaining spectra were compiled into a training data set, which was mean-centered. This involved calculating the average spectrum of all the spectra in the data set and subtracting this result from every spectrum. The data set was then subjected to a pre-processing filter, either none, a Savitsky-Golay 1st derivative, or a Savitsky-Golay 2nd derivative. Principle component analysis was used to describe the resulting spectra as a sum of a small orthogonal set (30) of linear combinations of the original variables. These are called principle components and they describe over 95% of the variance from the mean spectrum across the data set.

Multiple analysis of variance (MANOVA) was used on each principle component to identify the most diagnostically significant principle components for each experiment, i.e. those that show a significant difference in value for normal, dysplastic and cancerous larynx. The most significant components were plotted against one another to enable clustering with pathology to be visualized.

3. RESULTS

3.1 Spectral Analysis

The near infrared Raman spectra of normal laryngeal specimens showed little intra-sample variability (Figure 2). Visual inspection of the spectra show the peak shapes and positions to be repeatable, although overall spectral intensities can vary by 15% about the mean spectrum for each sample. The normal laryngeal spectra were dominated by several peaks shown in Figure 3. The Raman spectra have contributions from both proteins and nucleic acids. Amide I (at 1654 cm^{-1}) and amide III (at 1244-1262 cm^{-1}) bands originate from vibrations in the peptide modes of the proteins and reflect the secondary structure of the proteins, their arrangement in three dimensions (α-helix, β-pleated sheet, β-turn or random coil structure). The position of these two peaks indicated that the majority of proteins in the normal larynx are in the α-helix conformation[11]. The intense peak at 1336 cm^{-1} can be attributed to both collagen and nucleic acids (DNA) and more specifically to the purine bases guanine and adenine[12].

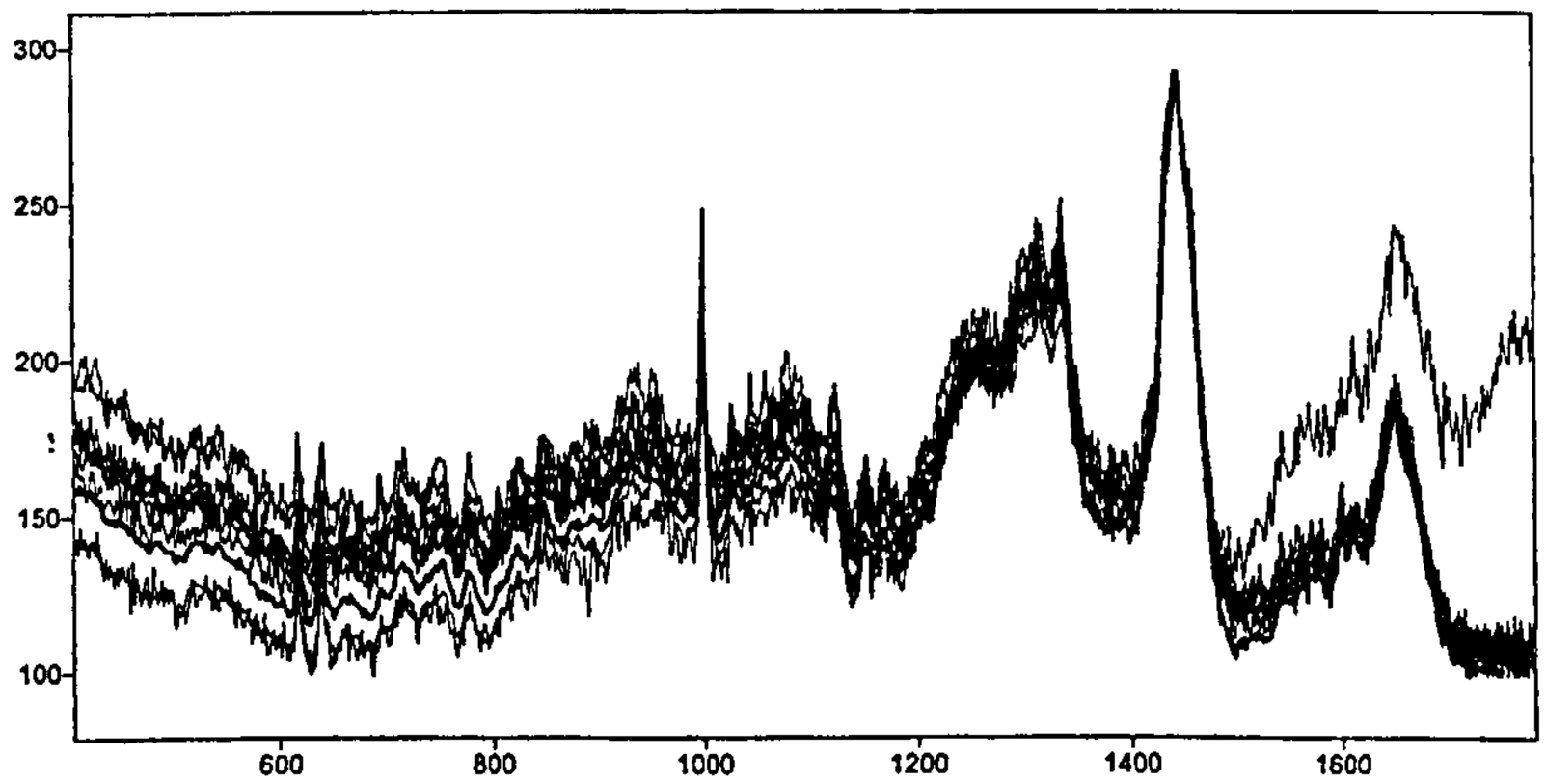

Figure 2. Spectra from one sample of normal larynx, showing the intra-sample variation. The mean spectrum is in bold.

Figure 4 shows the near infrared Raman spectra obtained from normal, dysplastic and malignant (squamous cell carcinoma) laryngeal specimens. For all neoplastic laryngeal specimens the overall intensity levels of the spectra are less than that for the normal larynx and that for dysplastic tissue is usually intermediate. The relative intensities of the nucleic acid (DNA) / collagen mode at 1336 cm^{-1} and the amide III mode at 1250 cm^{-1} was used as a diagnostic parameter to differentiate neoplastic lesions from normal samples. In the majority of malignant spectra the intensity ratio was greater with respect to the normal samples (Fig. 4 and Table 1), indicating increased collagen levels and/or cellular nuclear content in squamous cell carcinoma compared with that of normal laryngeal tissue. This is in agreement with the histological method of grading malignancy by the nucleic acid to cytoplasmatic ratio[13]. In dysplastic specimens this relative intensity ratio was between those of normal and malignant samples (Fig. 4 and Table 1).

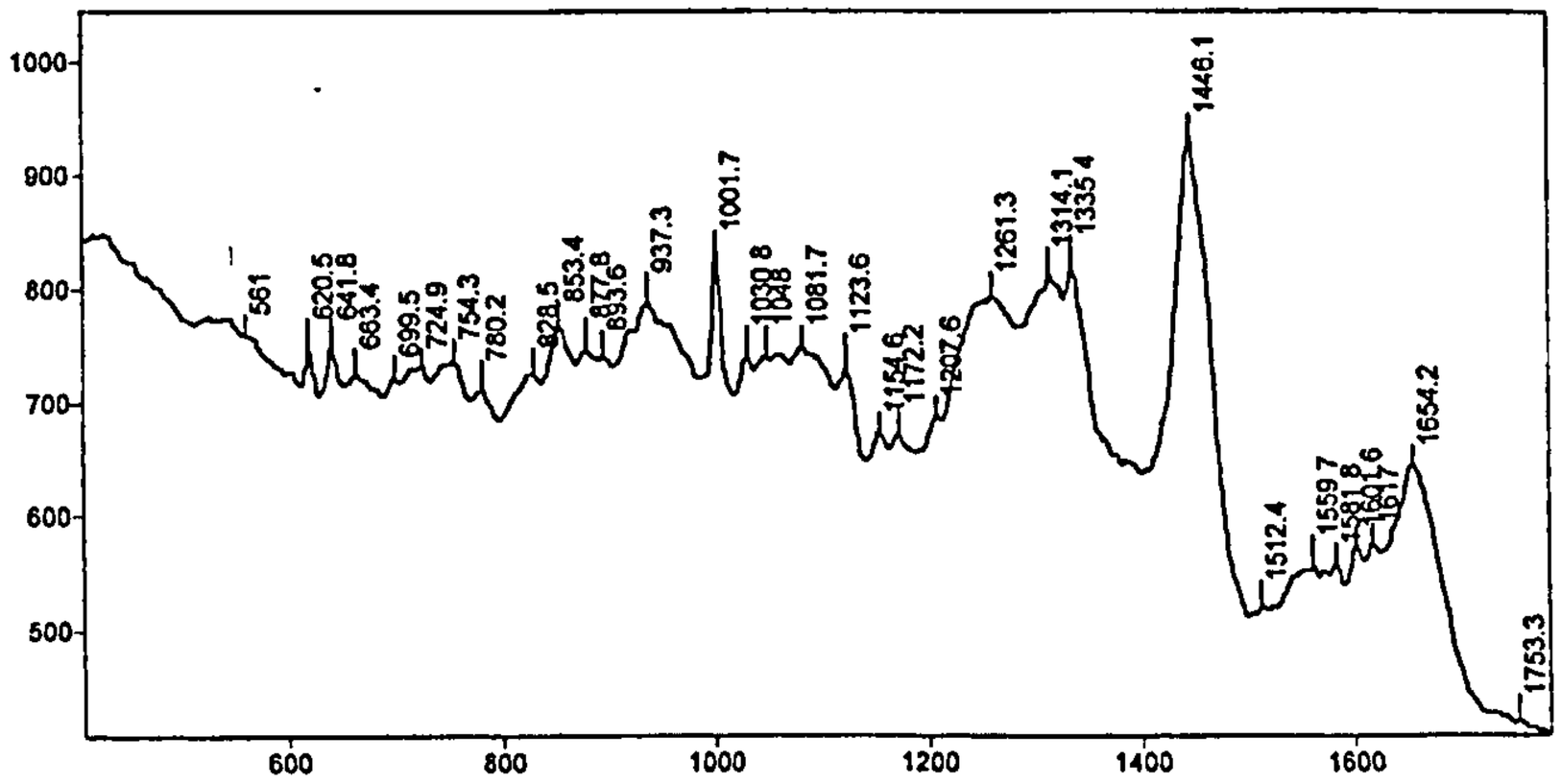

Counts / Raman Shift (cm-1)

Mean normal larynx spectrum from twelve biopsy samples (10 patients).

Figure 3: Mean normal larynx spectrum with peak positions labeled.

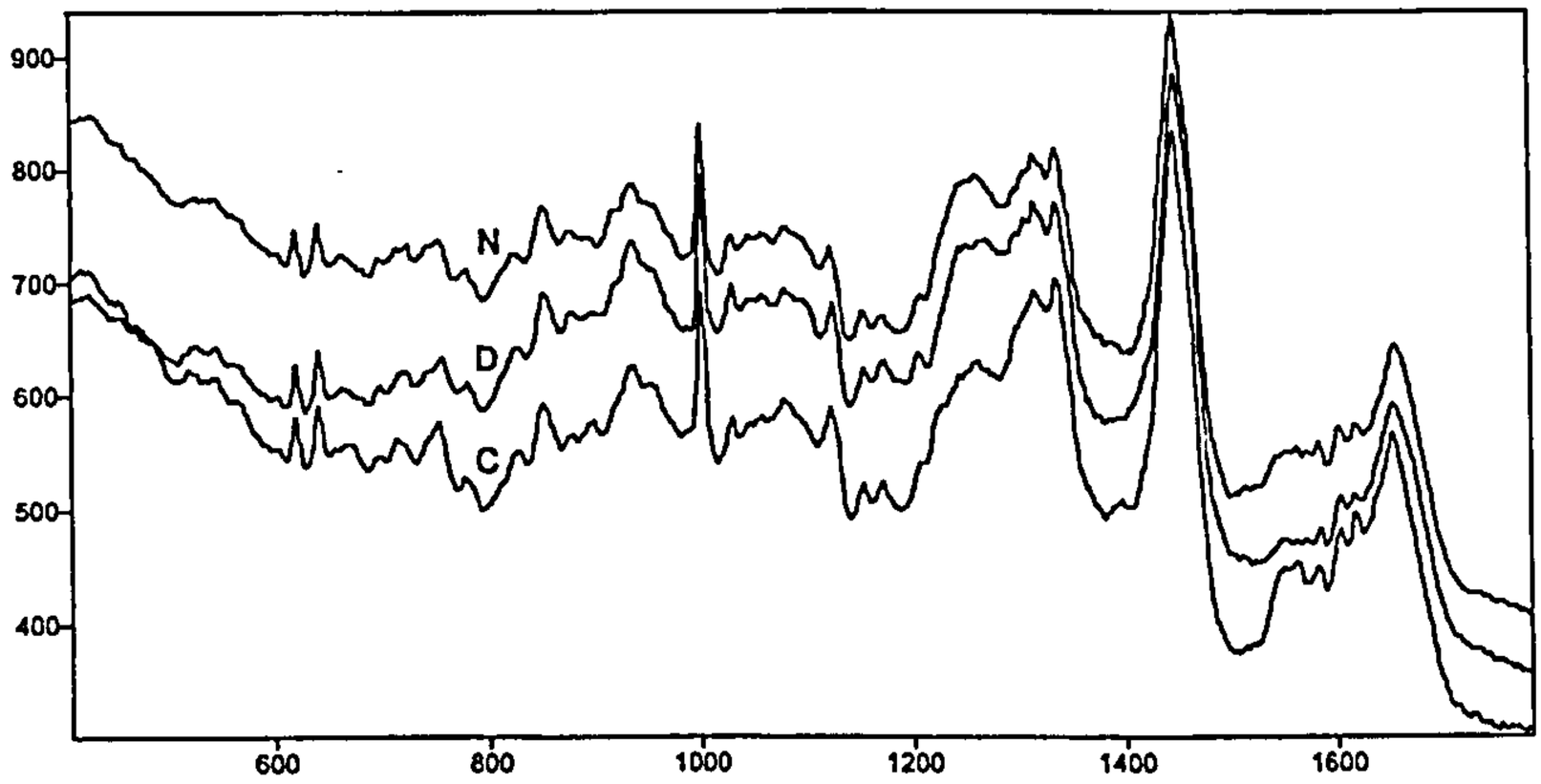

Counts / Raman Shift (cm-1)

Comparison of mean larynx spectra from each pathology.

N= normal larynx, D= dysplastic larynx, C= squamous cell carcinoma of the larynx.

Figure 4. Comparison of mean spectra from normal, dysplastic and squamous cell carcinoma of the larynx.

Pathology	No. of spectra	Sum of Peak Ratios	Mean Ratio of Peak Intensities (I_{1336}/I_{1250})	Variance
Normal	93	120.050	1.291	0.087
Dysplasia	29	38.189	1.317	0.118
Carcinoma	31	46.556	1.502	0.067

Table 1: summary of peak ratio analysis on raw larynx spectra

3.11 Significance of peak ratio method of analysis

Using multiple analysis of variance (MANOVA) to test the statistical significance of the empirical method of peak ratio analysis resulted in values: F=5.90, F_{crit}=3.06 and p=0.0034. Therefore using the intensity peak ratios at 1336 and 1250 cm^{-1} the set of spectra separate into different groups with pathology with greater than 99% significance.

3.2 Multivariate Analysis of Spectra

Multiple analysis of variance (MANOVA) was used on each principle component to identify the most diagnostically significant principle components for each experiment, i.e. those that show a significant difference in value for normal, dysplastic and cancerous larynx. These data are displayed in Table 2. The retained components exhibit a difference with pathology to a 95% significance level or above. The F-value is calculated from the sum of the squares of the variance of the mean principle component value between and within pathology groups. The larger the F-value the greater the effective grouping with pathology. F_{crit} is the cut-off value for 95% significance. The p-value is the probability that the principle components for all pathologies are statistically the same, i.e. that they do not correlate with histopathology of the sample.

(a) No pre-processing.

Principle Component	1	8	10	12	13	14
F-value	4.46	3.14	5.99	5.07	3.863	9.28
p-value	0.013	0.046	0.0031	0.007	0.023	0.00016

(b) Savitsky-Golay 1st derivative using a 7-point filter.

Principle Component	3	4	5	10
F-value	10.86	3.66	11.2	3.12
p-value	3.9×10^{-5}	0.028	2.9×10^{-5}	0.047

(c) Savitsky-Golay 1st derivative using a 21-point filter.

Principle Component	3	4	5	13
F-value	10.16	5.88	6.38	4.25
p-value	7.3×10^{-5}	0.003	0.002	0.016

(d) Savitsky-Golay 2nd derivative using a 7-point filter.

Principle Component	3	13
F-value	3.07	5.46
p-value	0.05	0.005

Tables 2(a) to 2(d) show the principle components displaying diagnostic significance and their corresponding MANOVA coefficients. F_{crit}=3.056 is the value of F for greater than 95% significance that the pathological groups are different.

The principle components describing the data set pre-processed using the Savitsky-Golay 7-point 1st derivative function were shown to be the most diagnostically significant. A two-dimensional plot of two diagnostically significant principle components from this data set is presented in Figure 5.

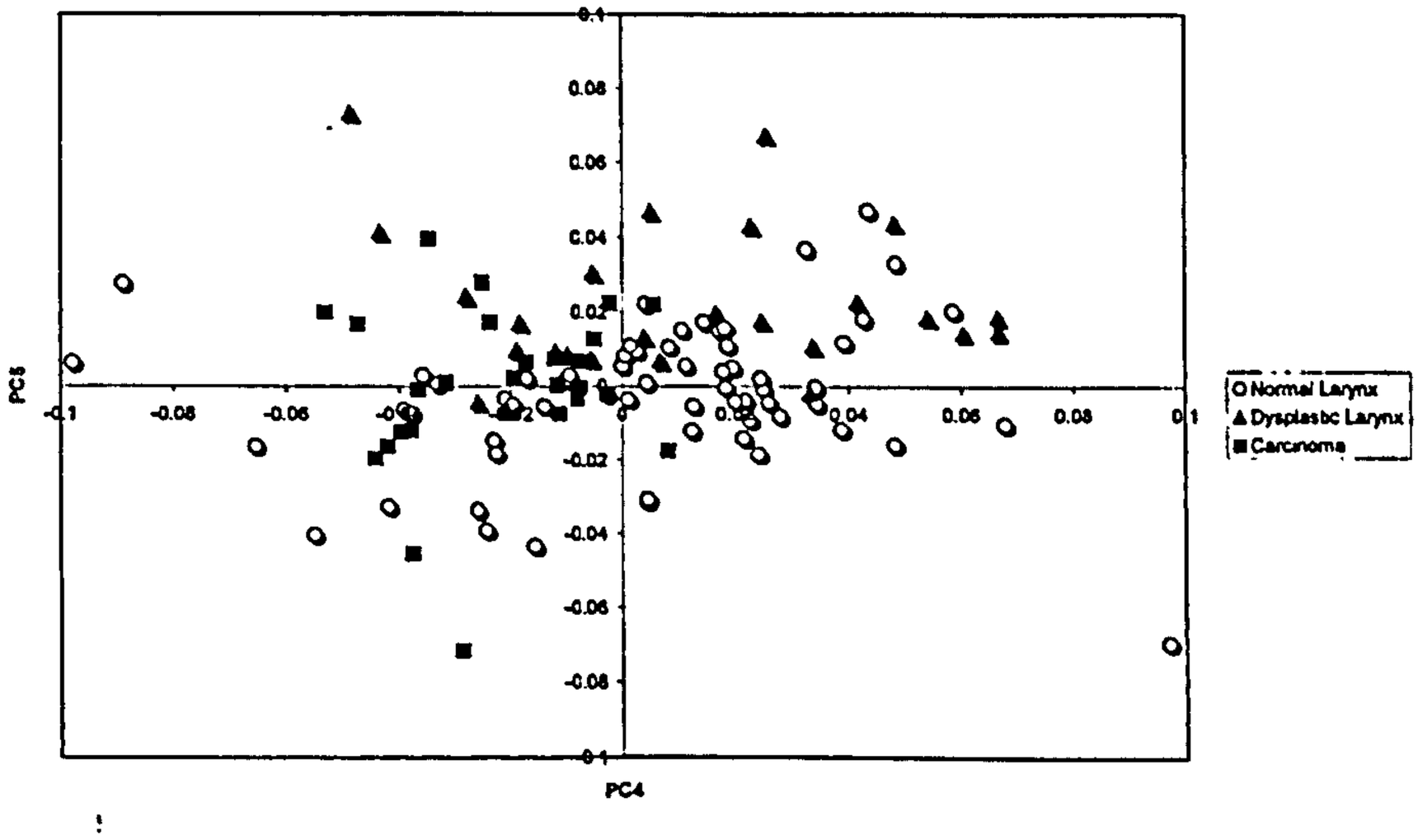

Figure 5 2D plot of diagnostically significant principle components derived from Larynx spectra acquired at 830nm.

4. DISCUSSIONS

Currently, histopathology is the gold standard of tissue diagnosis. However, histopathology requires tissue removal and it cannot provide immediate diagnostic feedback, while the accuracy of diagnosis can be limited by factors related to random sampling and handling of tissue. Furthermore, evaluation is based primarily on morphology rather than biochemistry. Therefore, the development of a non-invasive method of histochemical analysis with immediate diagnostic feedback, thus enabling detection of early dysplastic changes at the cellular level will be of great importance. Raman spectroscopy seems to hold a great deal of promise as it provides quantitative information about the biochemical (histochemical) differences between normal and neoplastic tissues. Most biological molecules are Raman-active, leading to distinctive spectral signatures (biochemical fingerprints) that represent a true form of optical histochemistry[7]. Suitable molecules for the study of neoplasia, as measured by Raman spectrospcopy, include proteins (hormones, oncofetal antigens, isoenzymes, immunoglobulins, carbohydrate antigens, keratins), nucleic acids (DNA, RNA), nucleosomes and cell membranes[3]. Indeed, recent studies have confirmed the feasibility of Raman spectroscopy for in vitro diagnosis of malignancy in skin, brain, breast, colon and cervix[14-18]. These studies relied on changes in relative protein-to-lipid content (breast, cervix) or changes in protein structure and hydrogen bonding of proteins and nucleic acids (skin, colon).

The present study is the first to demonstrate the spectral differences between normal and abnormal laryngeal tissue. Peak ratio analysis showed a significant difference between Raman spectra of normal, pre-malignant and malignant larynx. A possible diagnostic algorithm could be based on the relative intensities of two peaks, the nucleic acid (DNA) mode at 1336 cm^{-1} and the amide III mode at 1250 cm^{-1}. Our findings suggest that the relative intensity of the DNA mode and the amide III mode increases with progression to malignancy, indicating increased cellular nuclear content in precancerous-cancerous lesions, compared with that of normal laryngeal tissue. Based on our current understanding of the molecular origin of these Raman bands, our findings raise the possibility of changes in protein secondary structures (from α-helix to random coil conformation) and in C-H stretching bonds in nucleic acid bases. However, the present sample set from 19 patients is not large enough for a proper cross-validation study. We are currently gathering more data to increase the size of our database in order to enable both cross-validation and more importantly, prospective analysis.

Empirical methods have been employed in the literature to evaluate variations in the spectra with tissue pathologies. Of course this is a very simple method and results obtained are easy to interpret. However, the disadvantage is that only a tiny part of the histochemical data from the tissue is used for analysis. To take into account all the complexities of biological tissue a method incorporating as much of the data as possible in the analysis is likely to prove more rigorous at separating spectra with pathology. Principle component analysis was used in this study to reduce the data into a set of orthogonal linear combinations that describes the spectral variation from the mean. A statistical examination of the results show that using a 7-point Savitsky-Golay 1st derivative function to pre-process the data set provides the most diagnostically significant set of principle components. The probability of the spectra, from different pathologies, being from statistically the same group is as low as 0.000029 for component number 5. This is of the order of a hundred times less than that achieved by peak ratio analysis alone ($p=0.0034$). Principle components 3 and 5 were selected as two diagnostically significant components (Table 2(b)) and plotted against each an example of the separation obtained with the current set of larynx spectra.

The principle component analysis method has been tested using MANOVA and has shown diagnostic significance by grouping PCs with pathology. However with only small numbers of samples, outliers can have a greater affect on results. Therefore it is proposed that this study is continued to include greater sample numbers for each pathology. It may then be possible to separate individual sub-groups of dysplasia. Further work will involve building and optimising sort algorithms and spectral libraries and development of an in vivo Raman probe. This opens the real possibility of early cancer diagnosis, with a corresponding increased chance of cure by allowing assessment of adequacy of resection margins and directed or guided biopsies. This will be particularly useful in dysplasia and early glottic cancer where the repeated diagnostic biopsy procedures increase the risk of affecting the quality of voice. In addition, this "real-time" diagnosis may also mean that second procedures could be avoided, thus reducing cost.

The majority of Raman studies have been performed on excised samples. However, as variations in Raman spectra between fixed and fresh tissues appeared to be minimal[19], in vitro measurements should not affect the potential diagnostic capability of Near infrared Raman spectroscopy. So far successful in vivo applications have been confined to some exposed tissue areas such as in the eye[20], the nail[21], the artery, the skin and deeper tissues in animal models[4,5]. The most significant problem has been the signal generated by the fibres of the optic probes used (luminescence and Raman)[22-24]. The signal is proportional to the length of the fibers and to the excitation light intensity and can have magnitudes equal to and sometimes greater than that of the examined sample[6]. However, new fiber optic probes are being designed to deliver and collect signal more efficiently in order to enable routine in vivo measurements.

Although the spectral differences between normal and abnormal laryngeal tissue look promising, the obtained spectra are complex and their exact cellular and molecular basis is not completely understood yet. We believe that future microscopic and chemical studies will further clarify the molecular origins of these signals and will lead to the development of models correlating them to specific tissue changes.

Finally it must be noted that studies involving the comparison of any new diagnostic technique with the 'gold standard' technique have to rely on the assumption that the 'gold standard' provides diagnosis with 100% sensitivity and specificity, i.e. 0% false positives and false negatives. If this assumption is not valid then errors will be introduced into these studies.

5. CONCLUSIONS

High quality fluorescence-free Raman spectra of human laryngeal tissue can be obtained using near infrared excitation. Normal and neoplastic laryngeal tissues have distinct biochemical features, which can be exploited spectroscopically. The relative DNA-to-protein content could serve as possible diagnostic algorithm for spectral identification of malignancy and earlier dysplastic changes. However this paper has shown that multivariate analysis techniques have the ability to group spectra by sample pathology. With greater sample numbers it is likely that improvements in separation will be achieved. Therefore, the quality of the structural and compositional detail, which can be revealed by NIR Raman spectroscopy seems to make this new diagnostic modality a very attractive noninvasive tool for early detection of laryngeal cancer and precancer and could contribute significantly to understanding the underlying mechanisms of neoplasmatic transformation.

ACKNOWLEDGEMENTS

This work was partly funded and assisted by Renishaw plc spectroscopy division. The authors of this paper would like to thank the histology department at Gloucestershire Royal Hospital and especially Richard Allison for all their help and support with this project and others involving large amounts of tissue collection and storage. Neil Shepperd also deserves gratitude for all his work defining the pathologies of our samples.

REFERENCES

1. Robin PE, Reid A, Powell DJ, McConkey CC. 'The incidence of cancer of the larynx.' *Clin Otolaryngol*, 16 198-201, 1991.
2. Muir C, Weiland L. 'Upper aerodigestive tract cancers.', *Cancer*; 75(suppl):147-153, 1995.
3. Mahadevan-Jensen A, Richards-Kortum R. 'Raman spectroscopy for the detection of cancers and precancers.' *J Biomed Opt*; 1:31-70, 1996.
4. Puppels, GJ, van Aken, T, Wolthius, R, Caspers, PJ, Bakker Schut, TC, Bruining, HA, Romer, TJ, Buschman, HPJ, Wach, ML, Robinson, JS; 'In vivo tissue characterization by Raman spectroscopy' *Proc SPIE Infrared Spectroscopy:New Tool in Medicine*, 3257, p78-83, 1998.
5. Shim, MG, Wilson, BC, Marple, E, Wach M, 'Study of Fibre-Optic Probes for in Vivo Medical Raman Spectroscopy', *Applied Spectroscopy*, 53, 6:619-625, 1999
6. Fulljames, C, Stone, N, Bennett, D, Barr, H, 'Beyond white light endoscopy – the prospect for endoscopic optical biopsy', *Italian Journal Gastroenterology and Hepatolog*, awaiting publication.
7. Feld SM, Manoharan R, Salenius J, Orestein-Cardona J, Romer TJ, Brennan JF, Dasari R, Wang Y. 'Detection and characterisation of human tissue lesions with infrared Raman spectroscopy.' *Proc SPIE Biomed Soc*;2388:99-105, 1995.
8. Barr H, Dix T, Stone N. 'Optical spectroscopy for the early diagnosis of gastrointestinal malignancy. Review.' *Lasers Med Sci*,13:3-13, 1998.
9. Shanmugaratriam, K et al, *Histological Typing of Tumours of the Upper Respiratory Tract and Ear*, Springer-Verlag, Berlin 1991.
10. Hair, JF, Anderson, RE, Tatham, Black WC, *Multivariate Data Analysis*, Chapter 4, Macmillan, New York, 1992.
11. Tu AT. 'Peptide backbone conformation and microenvironment of protein side chains.' In: Clark RJH and Hester RE, ed. *Spectroscopy of biological systems*. New York: John Wiley & Sons Publishers; 13:47-112, 1986.
12. Perno JR, Grygon CA and Spiro TG. 'Raman excitation profiles for the nucleotides and for the nucleic acid duplexes poly(rA)-poly(rU) and poly(dG-dC).' *J Phys Chem*; 93:5672-78, 1989.
13. Naber SP. 'Molecular pathology: detection of neoplasia.' *N Engl J Med*; 331:1508-10, 1994.
14. Gniadecka M, Wulf HC, Nielsen OF, Christensen DH, Hercogova J. 'Distinctive molecular abnormalities in benign and malignant skin lesions: studied by Raman spectroscopy.' *Photochem Photobiol*; 66:418-23, 1997.
15. Mizuno A, Kitajima H, Kawauchi K, Muraishi S, Ozaki Y. 'Near-infrared Fourier transform Raman spectroscopic study of human brain. Tissues and tumors.' *J Raman Spectrosc*; 25:25-9, 1994.
16. Manoharan R, Shafer K, Perelman L, Wu J, Chen K, Deinum G, Fitzmaurice M, Myles J, Crowe J, Dasari RR, Feld MS. 'Raman spectroscopy and fluoresence photon migration for breast cancer diagnosis and imaging.' *Photochem Photobiol*; 67:15-22, 1998.
17. Rigas B, Morgello S, Goldman T, Wong PTT, 'Human colorectal cancers display abnormal Fourier-transform infrared spectra.' *Proc Natl Acad Sci USA 87*; 8140-8144, 1990.
18. Liu CH, Glassman WL Sha et al. 'Near-IR Raman spectroscopy of human aorta.' *Proc Soc Photo Opt Instr Eng*; 1599:77-80, 1991.
19. Shim MG, Wilson BC. 'The effects of ex vivo handling procedures on the Near-infrared Raman spectra of normal mammalian tissues.' *Photochem Photobiol*; 63:662-71, 1996.
20. Yu NT, Kuck JFR, Askren CC, 'Laser Raman spectroscopy of the lens in situ, measured in an anesthetized rabbit. *Current Eye Res*;1:615-18, 1982.
21. Schrader B, Keller S, Loechte T, Fendel S, Moore DS, Simon A, Sawatzki J, 'NIR FT Raman spectroscopy in medical diagnosis.' *J Mol Struct.*;348:293-96, 1995.
22. Myrick ML, Angel SM, Desiderio R, 'Comparison of some fiber optic configurations for measurement of luminescence and Raman scattering.' *Appl Opt*; 29:1333-1344, 1990.
23. Myrick ML, Angel SM, 'Elimination of background in fiber-optic Raman measurements.' *Appl Spectrosc*; 44:565-570, 1990.
24. Schwab SD, McCreery RL, 'Versatile, efficient Raman sampling with fiber optics.' *Anal Chem*; 56:2199-2204, 1984.

Raman spectroscopy for the diagnosis of dysplasia in columnar and squamous epithelium

Catherine Kendall*[a], Tom Bakker Schut[b], Nick Stone[a], Pela Stravroulaki[c], Gerwin Puppels[b], Hugh Barr[a]

[a]Cranfield Postgraduate Medical School, Gloucestershire Royal Hospital, Gloucester, GL1 3NN, UK,
[b]University Hospital Rotterdam Dijkzigt Surgery, NL-3015 GD Rotterdam, The Netherlands,
[c]Department of Otolaryngology, Head and Neck Surgery, Southmead Hospital, Bristol BS10 5ND, U.K

ABSTRACT

The incidence of oesophageal and laryngeal cancer has risen over past decades. The early detection of disease is vital for improved prognosis. The current gold standard method of tissue diagnosis is histopathology, which is invasive, costly and somewhat subjective. Raman spectroscopy however has potential for the non-invasive, early, in-vivo diagnosis of the biochemical changes associated with malignancy. Good quality Raman spectra have been measured in vitro using oesophageal and laryngeal tissue. Multivariate analysis has been implemented using principal component and linear discriminant analysis techniques. Sensitivity and specificity of more than 80% has been achieved for the discrimination of dysplasia and cancer, for both oesophageal and laryngeal tissue. On comparison with histopathology these results are seen to be an improvement, since pathology lacks sensitivity and specificity due to the subjective nature of the diagnosis. Thus illustrating that excellent discrimination between normal, dysplastic and cancerous tissue can be achieved using Raman Spectroscopy.

Keywords: Raman, larynx, oesophagus, malignancy, diagnosis, dysplasia, cancer, spectroscopy

1.INTRODUCTION

A number of spectroscopic techniques are currently being investigated for the *in vivo* detection of early dysplasia and cancer.[1, 2] Near infrared (NIR) Raman spectroscopy has been used to investigate the early detection of dysplasia in columnar and squamous epithelial tissue. Raman spectroscopy provides the detailed molecular information that is required to detect neoplastic changes with high specificity and sensitivity. It has been applied *in vitro* for the detection of a number of cancers and pre-cancers[3] and can be applied *in vivo* through the use of special fiber optic probes[4, 5, 6]. Previous work has shown that cancerous and dysplastic tissue can be distinguished from normal tissue by Raman spectroscopy in conjunction with statistical classification methods[7, 8].

The incidence of oesophageal cancer has been rising steadily in England and Wales since the 1960's. The incidence among men is average for men in Western Europe, where alcohol and tobacco consumption are the main risk factors. However women in England and Wales have a two to three fold higher risk than women in other European countries [9]. The increase of adenocarcinoma of the middle and lower thirds of the oesophagus has been unexplained. The survival rate of adults diagnosed in England and Wales during 1986-1990 was 23% at one year and only 7% at five years. Barrett's oesophagus, a condition in which the normal squamous oesophageal epithelium becomes more columnar in type, due to acid and bile reflux, is associated with the development of adenocarcinoma. It is suggested that patients with Barrett's have a fifty-fold increased risk of developing adenocarcinoma.[10]

The incidence of laryngeal cancer has progressively risen over the last 25 years, with the most significant increase being in women [11]. In England and Wales, where it is one of the more common cancers, incidence rates have been broadly stable and suggest a declining risk for successive generations of men [12]. Laryngeal cancer has the greatest effect on quality of life of any

* Correspondence: Email: catherine@grhcranf.demon.co.uk Telephone: +44-1452-395190

cancer, causing devastating lifestyle changes and resulting in permanent cosmetic and psychosocial disability. The transformation from normal tissue to squamous cell carcinoma in the larynx involves an intermediate step of squamous dysplasia, where the squamous epithelial cells mature and grow abnormally.

The majority of oesophageal and laryngeal cancers originate on the surface in the epithelial layer. At present diagnosis is undertaken *in vitro* by pathological grading of tissue biopsies taken at endoscopy. The number of samples that can be investigated is limited, so sampling is poor. In general dysplasia cannot be visually distinguished from normal tissue and once a tumour can be seen it may be too late to enable a full cure. In the case of laryngeal cancer repeated biopsies increase the risk of damage to vocal cords. Spectroscopic detection of dysplasia carried out *in vivo* would be fast and non-invasive, enabling more effective patient management, reduced mortality and improved prognosis. Spectroscopy could initially be used as a biopsy-guiding tool, enabling improved selection of biopsies, ultimately replacing the need for the excision of tissue biopsies.

The aim of this work was to develop the use of Raman spectroscopy in conjunction with multivariate statistical analysis for the early detection of dysplasia in oesophageal and laryngeal tissues.

2. MATERIALS AND METHODS

2.1 Tissue samples

41 homogeneous samples, from 7 patients with both low and high-grade dysplasia, were used for the oesophagus study. The pathologist graded them into 4 groups: 18 biopsies with Normal epithelium (NO), 13 biopsies with Barrett's epithelium (B), 5 biopsy with Low Grade Dysplasia (LGD), and 5 biopsies with High Grade Dysplasia (HGD).

32 samples, from 28 patients, were classified as homogenous and retained for the larynx study. They were graded into the following groups: 16 normal samples (NL), 7 dysplastic samples (DL) and 9 with squamous cell carcinoma (SCC).

Informed consent was obtained from each patient and the studies were approved by the United Kingdom South and West Local Research Ethics Committee.

2.2 Tissue preparation

Biopsy samples were collected during routine surgical procedures and snap frozen in liquid nitrogen. Frozen sections were cut using a freezing-microtome and the remaining biopsy block was stored at – 85°C until spectroscopic studies were carried out. The frozen sections were stained, with Haematoxylin and Eosin, for histopathological diagnosis by a consultant pathologist. Only homogenous samples with a clearly defined pathological diagnosis were used in this study.

2.3 Instrumentation

Oesophagus spectra were measured with a home built F/2 spectrometer, with an Argon ion pumped Ti: Sapphire laser (850 nm) and liquid nitrogen cooled deep depletion CCD. The laryngeal biopsy samples were measured using a Renishaw System 1000 Raman micro-spectrometer, with an argon ion pumped Ti: Sapphire laser (830 nm) and a peltier cooled CCD detection system. Raman spectra were taken from between 4 and 20 different locations (about 100 μm apart) on the epithelial side of the biopsies. All spectra were measured with a collection time of 30 seconds, over a spectral range of 400-1800 cm^{-1} with respect to the excitation frequency. In this wavelength region, the absorption coefficients of water and tissue pigments are small and the effective penetration depth is large, typically a few mm. There was little contribution to the Raman signal from fluorescence.

2.4 Spectral analysis

Spectra which were seen to have an abnormally large fluorescence background or extremely poor signal to noise ratio were excluded from the model. All the remaining spectra were used as a training dataset. These spectra were corrected for the wavelength dependent sensitivity of the Raman system, mean centered and a pre-processing filter applied, either none a

Savitsky-Golay 1st derivative, or a Savitsky-Golay 2nd derivative. Multivariate analysis techniques were implemented using principal component analysis (PCA) and linear discriminant analysis (LDA). PCA was performed using the Galactic GRAMS/32 PLS/IQ software suite on the measured spectra. This orthogonalises and reduces the number of parameters required to represent the variance in the spectral dataset. Twenty-five Principal Components (PC's) that describe over 99% of the variance from the mean spectrum across the data set were calculated. Multiple analysis of variance (MANOVA) was used on each principle component to identify the most diagnostically significant principle components from each model, those that show a significant difference in value for normal, dysplastic and cancerous tissue. The most significant components were plotted against one another to enable clustering with pathology to be visualized. The twenty-five PC's were used as input for an LDA model, created in SPSS, which maximises the variation between groups while minimising the variation within groups. The sensitivity and specificity of the generated models was calculated for comparison.

3. RESULTS

3.1 Oesophagus

Initially a four-pathology group model was investigated, the samples being classified into the following pathology groups; normal squamous, intestinal metaplasia, cardiac Barrett's and dysplasia. No pre-processing filter was used on the spectra after correction for the measurement set-up. Cross validation was used in the PCA and a prior probability of all groups equal, using the covariance matrix within groups gave the best results from the LDA.

Two of the discriminant functions from the LDA model are plotted in Figure 1, which illustrates the separation of the spectra with pathology.

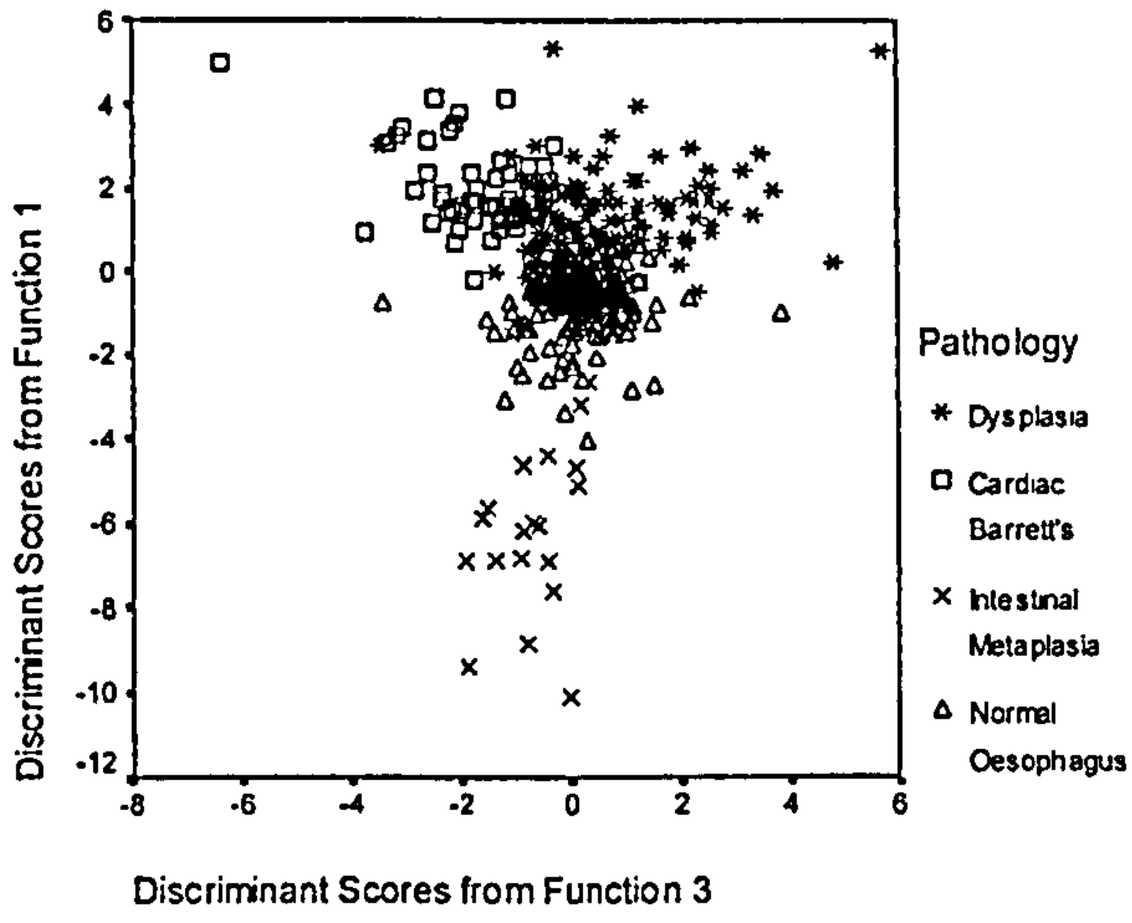

Figure 1. Discriminant scores from oesophagus LDA model.

A breakdown of these results can be seen in Table 1a, with the numbers of predicted cases in each group and the percentages both being displayed. Table 1b shows the sensitivity and specificity of this model for the correct diagnosis of that pathology group.

Pathology	Predicted Group Membership				
	Normal Oesophagus	Intestinal Metaplasia	Cardiac Barrett's	Dysplasia	Total
Normal Oesophagus	186	0	2	2	190
Intestinal Metaplasia	3	17	0	0	20
Cardiac Barrett's	3	0	54	3	60
Dysplasia	7	0	15	88	110
Normal Oesophagus	97.4	0 5	1.1	1.1	100
Intestinal Metaplasia	15.0	85.0	0.0	0.0	100
Cardiac Barrett's	5.0	0 0	90.0	5.0	100
Dysplasia	9.1	0 9	15.5	74.5	100

90.8 % of original grouped cases were correctly classified using this method.

Table 1a. Classification results of the four-pathology group model for the oesophagus.

	Normal Oesophagus	Intestinal Metaplasia	Cardiac Barrett's	Dysplasia
Sensitivity	98%	85%	90%	80%
Specificity	92%	100%	95%	98%

Table 1b. Sensitivity and specificity of the four-pathology group model for the oesophagus.

A five-pathology group model was then developed with the dysplasia samples being classified into two groups, low & high-grade dysplasia. A breakdown of the results can be seen in Table 2a, and the sensitivity & specificity in Table 2b.

Pathology	Predicted Group Membership					
	Normal Oesophagus	Intestinal Metaplasia	Cardiac Barrett's	Low Grade Dysplasia	High Grade Dysplasia	Total
Normal Oesophagus	174	1	1	9	5	190
Intestinal Metaplasia	1	19	0	0	0	20
Cardiac Barrett's	2	0	53	3	2	60
Low Grade Dysplasia	0	0	0	29	1	30
High Grade Dysplasia	0	0	13	18	49	80
Normal Oesophagus	91.6	0.5	0.5	4.7	2.6	100
Intestinal Metaplasia	5.0	95.0	0.0	0.0	0.0	100
Cardiac Barrett's	3.3	0.0	88.3	5.0	3.3	100
Low Grade Dysplasia	0.0	0.0	0.0	96.7	3.3	100
High Grade Dysplasia	0.0	0.0	16.3	22.5	61.3	100

85.3% of original grouped cases were correctly classified using this method.

Table 2a. Classification results of the five-group model for the oesophagus.

	Normal Oesophagus	Intestinal Metaplasia	Cardiac Barrett's	Low Grade Dysplasia	High Grade Dysplasia
Sensitivity	92%	95%	88%	97%	61%
Specificity	97%	100%	96%	91%	97%

Table 2b. Sensitivity and specificity of the five-group model for the oesophagus.

3.2 Larynx

The larynx provides a simpler model than the oesophagus in that there are only three pathology groups for classification, normal, dysplasia and cancerous. It should be noted that this group of larynx spectra were acquired with a range of measurement parameters. These included one and three pixel binning and variable power levels. Spectra were shift corrected, by alignment of all phenylalanine peaks at 1002 cm^{-1}, and smoothed using a 2nd order Savitsky-Golay filter. A 1st order Savitsky-Golay derivative pre-processing filter was used on the spectra. Self-prediction was used in the PCA and a prior probability of all groups equal, using the covariance matrix with separate groups gave the best results from the LDA. Two of the discriminant functions from the LDA model are plotted in Figure 2, which illustrates the separation of the spectra with pathology.

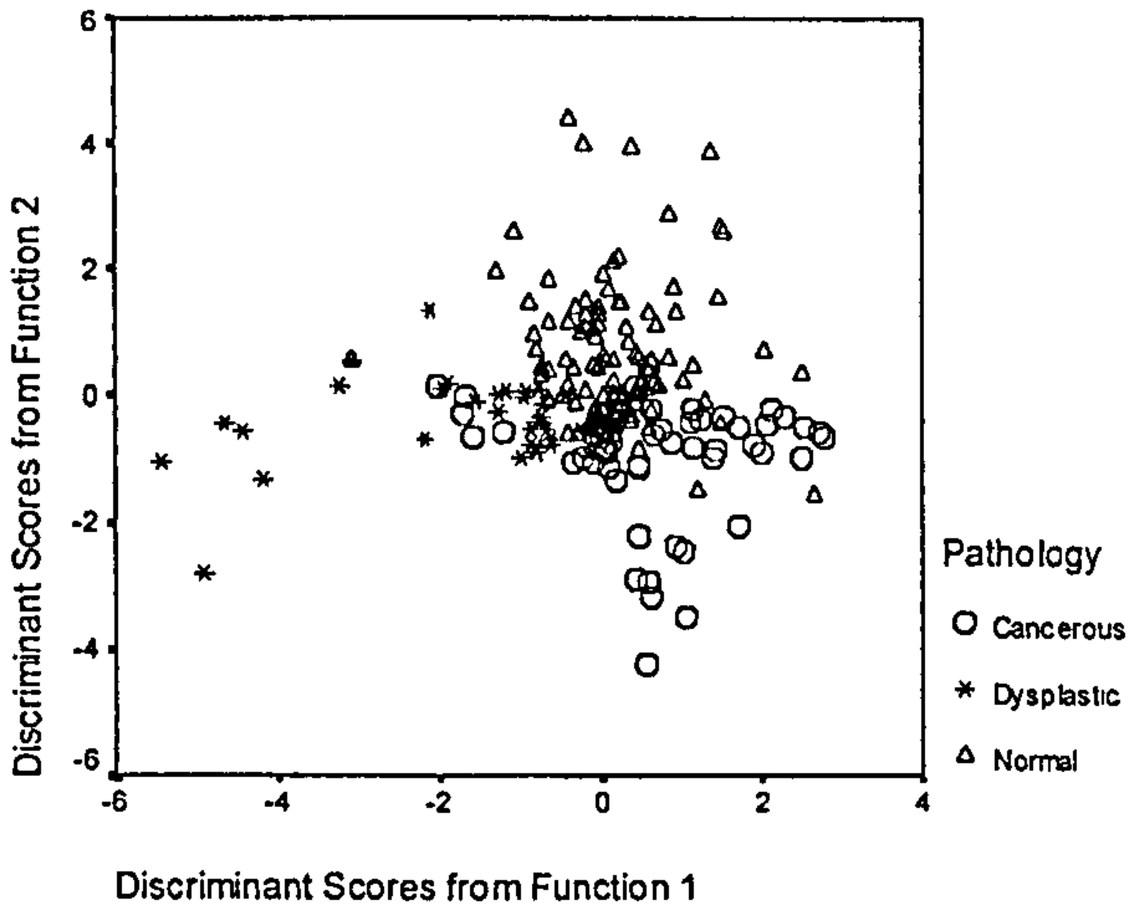

Figure 2. Discriminant scores from larynx LDA model.

A breakdown of these results can be seen in Table 3a, with the numbers of predicted cases in each group and the percentages both being displayed. Table 3b shows the sensitivity and specificity of this model for the correct diagnosis of that pathology group.

Pathology	Predicted Group Membership			
	Normal Larynx	Dysplasia	Cancerous	Total
Normal Larynx	96	4	12	112
Dysplasia	1	30	2	33
Cancerous	4	5	45	54
Normal Larynx	85.7	3.6	10.7	100
Dysplasia	3.0	90.9	6.1	100
Cancerous	7.4	9.3	83.3	100

85.9 % of original grouped cases were correctly classified using this method.

Table 3a. Classification results of the larynx model.

	Normal Larynx	Dysplasia	Cancerous
Sensitivity	86%	91%	83%
Specificity	94%	95%	90%

Table 3b. Sensitivity and specificity of the larynx model.

4. DISCUSSION

Near infrared Raman spectra with good signal to noise ratio and little fluorescence have been measured with oesophageal and laryngeal tissue, with little intra-sample variability seen in the measured spectra. Normal and neoplastic tissues have distinct biochemical features, which can be measured with Raman spectroscopy and analysed using statistical models. Multivariate analysis techniques have been shown to group the spectra by sample pathology with high sensitivity and specificity in vitro.

The statistical models are being developed to enable the early detection of dysplasia, therefore as few false negatives as possible for this group in particular are required, i.e. as high a sensitivity as possible. The four-pathology group oesophagus model correctly classifies over 90% of the spectra, combined with 80% sensitivity for the classification of dysplasia. Development of this model into the five-group model, may at first seem disappointing, with 85% of spectra being correctly classified. In particular the classification of high-grade dysplasia in the five-group model is lacking at 61%. However, on close inspection of the classification results, in Table 2a, it is seen that many of the high-grade dysplasia samples are misclassified as low-grade dysplasia. The statistical model will only be as good as the data it is built with, the spectra and the pathological diagnosis. We rely on the assumption that histopathology, as the gold standard method for tissue diagnosis, provides diagnosis with 100% sensitivity and specificity. However, pathological diagnosis is recognised as being somewhat subjective, especially when grading dysplasia, which may account for the misclassifications in this model[13, 14]. Histopathology is limited in other respects in that it is invasive, involves the random sampling of tissue, is costly and perhaps most importantly is based on morphological rather than biochemical analysis. The classification results obtained with the larynx model also gave good separation of the spectra with pathology, with more than 85% of the spectra being correctly classified. Dysplasia and cancer were correctly classified with a sensitivity of 91 and 83% respectively. It should be noted that the data collection parameters used with this data set were non-uniform.

The models developed in this work used a limited number of spectra. It is expected that the separation of the spectra will be improved with greater sample numbers. However these results continue to show that Raman spectroscopy has much potential for the early diagnosis of malignant change in the development of both oesophageal and laryngeal cancer.

ACKNOWLEDGEMENTS

This work was partially funded by Renishaw Plc. Spectroscopy division and the NHS South West Research & Development Unit. The authors would also like to thank the histology department at Gloucestershire Royal Hospital, in particular Prof. Neil Shepherd, Consultant Pathologist.

REFERENCES

1. Bohorfoush AG, "Tissue spectroscopy for gastrointestinal diseases", *Endoscopy* 28, pp 372-380, 1996
2. Fulljames C, Stone N, Bennett D, Barr H, "Beyond White Light Endoscopy - The Prospect for Endoscopic Optical Biopsy, *Ital. J. Gastroenterol. Hepatol.*31, pp 695-704, 1999

3. Mahadevan-Jansen A, Richards-Kortum R, "Raman spectroscopy for the detection of cancers and precancers", *J. Biomed. Opt.* 1, pp 31-70, 1996
4. Shim M, Wilson BC, Marple E, Wach M, "Study of fiber-optic probes for in vivo medical Raman spectroscopy", *Applied Spectroscopy* 53, pp 619-628, 1999
5. Puppels GJ, van Atken T, Wolthuis R, Caspers PJ, Bakker Schut TC, Bruining HA, Römer TJ, Buschman HPJ, Wach ML, Robinson JS, "In vivo tissue characterisation by Raman Spectroscopy", *Proc SPIE Infrared Spectroscopy: New Tool in Medicine*, 3257, pp 78-83, 1998
6. Wolthuis R., Bakker Schut TC, Caspers PJ, Buschman HPJ, Römer TJ, Bruining HA and GJ Puppels, "Raman spectroscopic methods for *in vitro* and *in vivo* tissue characterization", *Fluorescent and luminescent probes for biological activity*, Mason WT (ed.), pp 433-454, Academic Press, London, 1999
7. Bakker Schut TC, Stone N, Fulljames C, Barr H, Bruining HA, Puppels GJ, "Progress in the detection of neoplastic progress and cancer by Raman Spectroscopy", *Proc. SPIE* 3918, pp106-113, 2000
8. Stone N, Stravroulaki P, Fulljames C, Birchall M, Barr H, "Raman Spectroscopy: A Diagnostic Tool for Detection of Early Malignant Changes in the Larynx", *Proc. SPIE* 3918, pp120-128, 2000
9. Coleman MP, Babb P, Damiecki P, *Cancer Survival Trends in England & Wales 1971-1995: Deprivation and NHS Region. Chapter 12 163-172*, Office for National Statistics, 1999
10. Williamson WA, Ellis FH, Gibb SP, "Barrett's oesophagus. Prevalence and incidence of adenocarcinoma", *Arch Intern Med*, 151 pp 2212-2216, 1991
11. Robin PE, Reid A, Powell DJ, McConkey CC, "The incidence of cancer of the larynx", *Clin Otolaryngol*, 16 pp 198-201, 1991
12. Coleman MP, Babb P, Damiecki P, *Cancer Survival Trends in England & Wales 1971-1995: Deprivation and NHS Region, Chapter 21 269-276*, Office for National Statistics, 1999
13. Melville DM, Jass JR, Morson BC, "Observer study of the grading of ulcerative colitis: comparison with clinical outcome", *Hum Pathol* 20 pp1008-1014, 1989
14. Jensen P, Krogsgaard MR, Christiansen J, Braendstrup O, Johansen A, Olsen J, "Observer variability in the assessment of type and dysplasia of colorectal adenomas, analysed using Kappa statistics", *Dis. Colon Rectum* 38 pp195-198, 1995

Aliment Pharmacol Ther 2001; 15: 311–321.

Review article: the potential role for photodynamic therapy in the management of upper gastrointestinal disease

H. BARR, A. J. DIX, C. KENDALL & N. STONE
Cranfield Postgraduate Medical School in Gloucestershire, Gloucestershire Royal Hospital, Gloucester, UK

Accepted for publication 1 November 2000

SUMMARY

Photodynamic therapy involves the activation of an exogeneously administered, or an endogenously generated, photosensitizer with light to produce localized tissue destruction. It is an attractive, predominantly endosopic technique for the palliation of advanced upper gastrointestinal cancer and the eradication of early neoplastic and pre-neoplastic lesions. The nature of the biological response allowing safe healing and the exploitation of tissue threshold effects mean that adjacent tissue damage can be minimized.

This review used a database of 368 papers. The nature of the photosensitizer is critical to the depth of tissue damage and the risk of adjacent tissue damage and stricture formation. The generation of protoporphyrin IX following administration of 5-aminolaevulinic acid has proved useful for the treatment of high-grade dysplasia in Barrett's oesophagus. A double-blind randomized placebo controlled trial has confirmed that it is a safe and effective method for the ablation of low-grade dysplasia. The treatment of more advanced lesions requires exogeneously administered photosensitizers. However, recent data indicate that the neoplastic potential remains in some patients and continued follow-up is necessary.

Photodynamic therapy can be used to eradicate early neoplasia and palliate advanced cancer, but caution is required before a definitive cure can be claimed.

PHOTOBIOLOGY: THE PRINCIPLES OF PHOTODYNAMIC THERAPY

Photobiology is the basis of our survival on this planet. Without photosynthesis and the generation of oxidants and organic carbon (CH_2O) it is difficult to see how complex life could have developed.[1] Light is the necessary agent for the generation of these essential molecules. However, once oxygenic photosynthesis occurs, the organism is in a highly precarious state because a mechanism of protection from toxic highly reactive oxygen is vital. In plants photosynthesis occurs in highly specialized organelles, the chloroplasts. Light is essential for their biogenesis and allows the importation of protective oxygen quenching proteins.[2]

These light activated photosynthetic mechanisms are catalysed by molecules (photosensitizers/chlorophylls) within these complex photosystems.[1] The sudden and massive cellular destruction associated with autumnal senescence is associated with a loss of protection to generated toxic oxygen species and is an example of massive oxygenic photodestruction. Therapeutic exploitation of these basic biological mechanisms is the basis for the targeted photodestruction of photodynamic therapy.

Eukaryotic organisms, as large complex multicellular organisms, have a high degree of metabolic specialization, requiring oxygen for respiration and organic carbon as a fuel. The use of oxygen remains a paradox, because although necessary for life, it is reactive, potentially toxic and lethal to the cell. The generation

Correspondence to: Professor H. Barr, Cranfield Postgraduate Medical School in Gloucestershire, Gloucestershire Royal Hospital, Great Western Road, Gloucester GL1 3NN, UK.
E-mail: prof.barr@themail.co.uk

of reactive oxygen species is an initiator of apoptosis and is partly responsible for senescence. It appears that the defining moment for eukaryotic cells to overcome this problem occurred with the endosymbosis of mitochondria, a chloroplast-like energy complex derived from the cellular incorporation of primitive protobacteria, although it may have arisen at the same time as the cells nuclear component.[4] These organelles are essential for the safe use of oxygen during oxidative phosphorylation, and mammalian survival. They are the cells' energy complex and manufacture all the necessary molecules for safe oxygen electron transfer, similar to those in the chloroplast.[5, 6] These molecules are porphyrins, and are necessary for cytochrome and haem synthesis, but are natural endogeneous photosensitizers (Figure 1), able to absorb light and generate toxic oxygen species under certain circumstances (Figure 2).

Mammalian cells have protective mechanisms against toxic oxygen damage, similar to that of the chloroplast. Cell death will only occur if a critical threshold of toxic oxygen species is reached and the protective mechanisms associated with the mitochondria are overwhelmed.[4] Metabolic disorders that lead to an excessive accumulation of the endogeneous porphyrin photosensitizers can result in extreme cutaneous sensitivity to light. This is most evident in patients with acute intermittent porphyria who are deficient in porphobilinogen deaminase.[5] The therapeutic light activation of administered (exogeneous) or an endogeneously generated photosensitizer to destroy tissue is the basis of photodynamic therapy. The mechanism of cell death is by the generation of toxic oxygen species to overwhelm the cellular defence mechanisms. This technique has obvious attractions for the Gastroenterologist and Gastrointestinal Surgeon, whose trade is to illuminate and treat the dark regions of the gastrointestinal tract.

HISTORY OF CLINICAL PHOTODYNAMIC THERAPY

The discovery that an administered substance could cause photosensitivity is attributed to Oscar Raab. In the winter of 1887–1898, Professor von Tappeiner set his student Raab to study the toxicity of aniline dyes on paramecia. Raab recognized that the time to kill was related to the intensity of light in the laboratory. Von Tappeiner examined many other substances, including chlorophyll, and called the phenomenon 'photodynamic action/photodynamische Erscheinung'. He demonstrated that a photosensitizer, light and molecular oxygen were necessary.[7] He also suggested that tumours could be treated and some early clinical results were reported in 1905.[8]

There were sporadic reports of photodynamic therapy, but Dr T. J. Dougherty established the modern era at the Division of Radiation Biology at Roswell Park Memorial Institute, Buffalo, USA. He reported that a systemically injected porphyrin (haematoporphyrin), when activated by red light, caused complete eradication of transplanted experimental tumours. He also demonstrated the preferential accumulation of the photosensitizer in malignant tissue.[9] Endoscopists were quick to see the

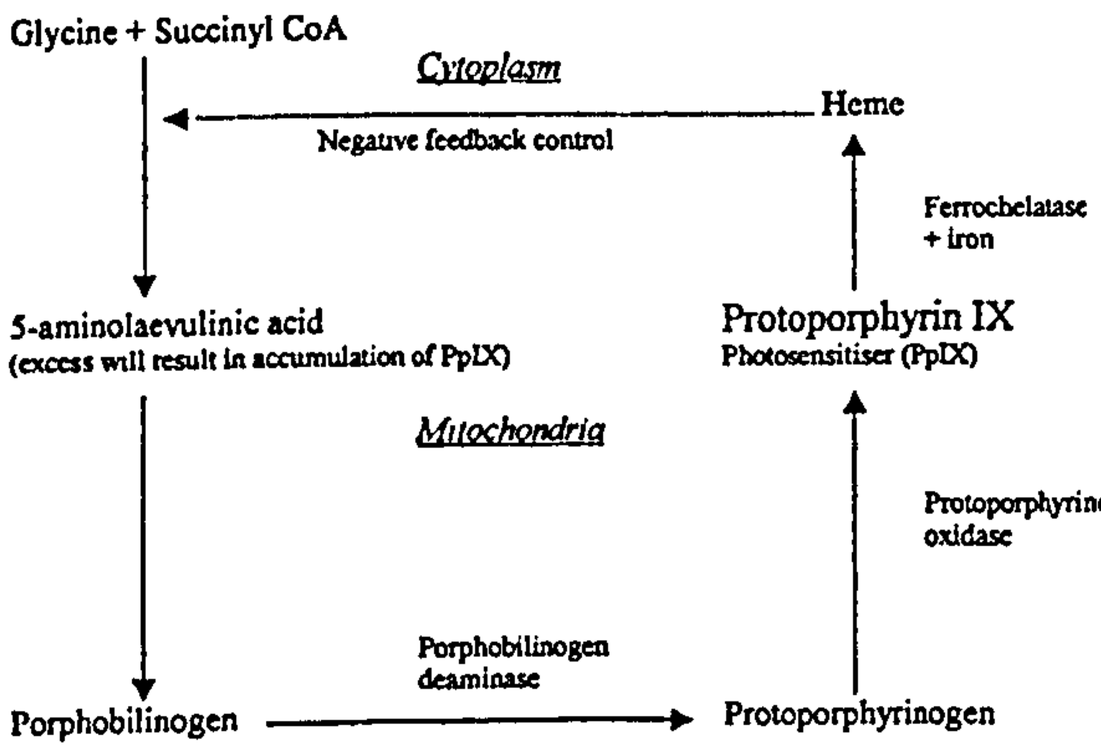

Figure 1. The mechanism for the generation of protoporphyrin IX following the excess administration of 5 aminolaevulinic acid.

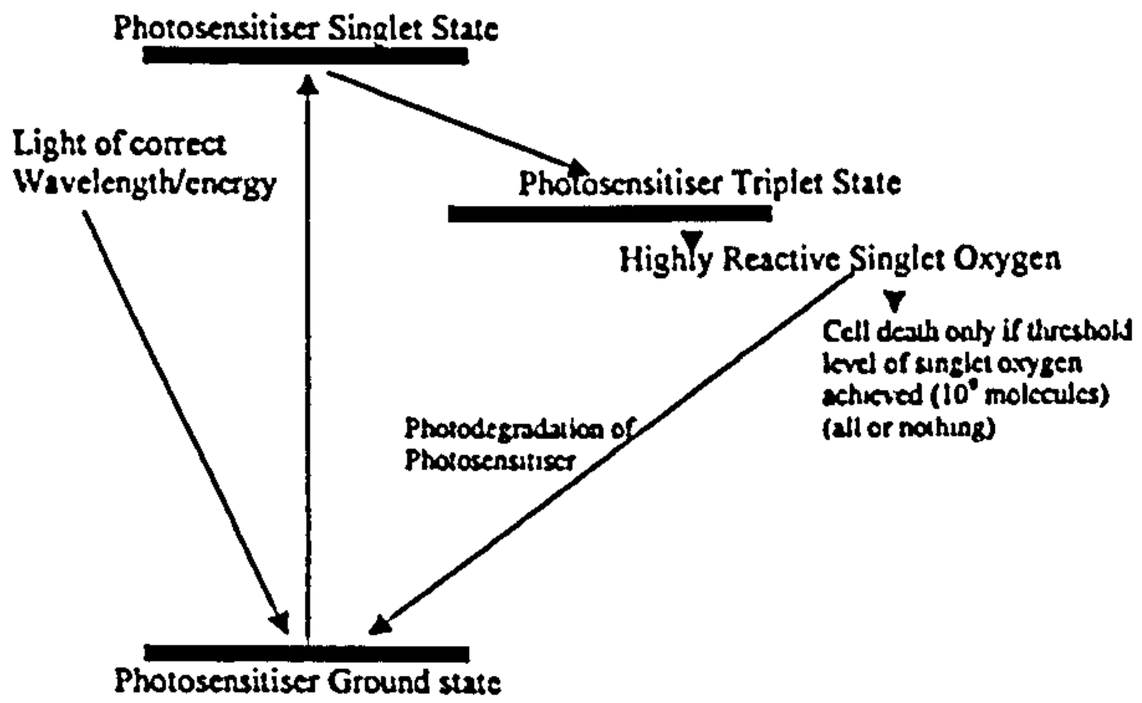

Figure 2. Diagram to illustrate the mechanism for the generation of singlet oxygen, the toxic photoproduct that is the necessary for photodynamic therapy.

potential of photodynamic therapy for the treatment of cancers accessible to the endoscope. A patient at the Tokyo Medical College with a small upper bronchial squamous cell tumour, treated in 1980 at bronchosopy with photodynamic therapy using a laser as the light source, had the tumour completely eradicated.[10] Large obstructing oesophageal cancers were similarly treated with photodynamic therapy with good relief of dysphagia and possible prolongation of survival.[11]

BIOLOGY AND PHOTOPHYSICS OF PHOTODYNAMIC THERAPY

The production of local tissue destruction after generating or administering a photosensitizer with the direct application of light forms the basis of photodynamic therapy. The most commonly used method of photodynamic therapy is to administer a photosensitizer, usually intravenously, and allow retention in the tissue for 48 h prior to irradiation with appropriate wavelength light, usually from a laser. The exogenously administered photosensitizers tend to accumulate in tumour stroma and in the submucosal layer of the gastrointestinal tract. This may be of little relevance if all the mucosa above is destroyed but does risk deeper damage.

The problem of targeting the photosensitizer to the mucosa, and avoiding systemic photosensitization may be overcome by using endogenous photosensitization. The metabolic activity of the mucosal cells, which have a rapid turnover, accumulate the endogeneous photosensitizer to a greater degree than the underlying stroma. The generated photosensitizer tends to stay within the cells in whose mitochondria it was synthesized.[4] The mechanism is shown in Figure 1. Following an excess administration of 5-aminolaevulinic acid (5-ALA), a precursor of haem, an intracellular accumulation of the photosensitizer protoporphyrin IX (PpIX) is induced. The synthesis of 5-ALA from glycine and succinyl-CoA is the first step in porphyrin biosynthesis and ultimately haem. This pathway is tightly regulated by end-product inhibition. If excess endogeneous 5-ALA is administered then this regulation is bypassed and an intracellular accumulation of the photosensitizer protoporphyrin IX (PpIX) is induced. The level of photosensitization is minimized to a few hours and the 5-ALA can be administered orally. The photosensitizer is activated in tissue using 633–635 nm laser light from an appropriate light source, such as a KTP pumped dye laser. The choice of photosensitizer is crucial to achieve the depth of necrosis that is required

It is important to examine the components of therapy and understand the photophysics (Figure 2) prior to examining the highly important biological response. Each photosensitizer has a specific action spectrum, which is the wavelengths of light that are absorbed to produce an excited electronic state. In this state the molecule has a higher energy and is generally much more reactive. The first excited state is normally the singlet and is short lived; it may decay to its ground state emitting fluorescence. This forms the basis of laser-induced photosensitizer fluorescence as a method of cancer detection.

If a low dose of photosensitizer is given to patients with cancer and fluorescence is specifically excited, the malignant tissue can be imaged or detected using spectral analysis by establishing a tumour demarcation function. This is calculated by dividing the photosensitizer fluorescence by the tissues' natural autofluorescence. For patients with oesophageal carcinoma, normal tissue has a fluorescence ratio of 0.1, Barrett's oesophagus 0.2, dysplastic columnar-lined epithelium 0.79 and carcinoma 0.78.[12] The natural autofluorescence occurring following irradiation of endogenous photosensitizer/fluorphores can also be used to detect cancer, and forms the basis of much instrument development for optical diagnosis.[13, 14] When the energy of the excited state is lost by fluorescence no photodynamic action occurs. However, the excited singlet molecule can undergo spin inversion to a metastable triplet state. This has a longer lifetime and is usually the reactive state involved in photodynamic action. Direct interaction with oxygen results in the generation of highly reactive singlet oxygen. One of the major targets for this molecule are membranes. They become peroxidized and are lysed, resulting in cell death.

As discussed previously, the cell has defences against oxidation and a certain threshold must be achieved for lethal injury to occur. The toxic photoproduct can also destroy the photosensitizer, a process called photodegradation. Several photosensitizers are retained in tumours longer than in their surrounding normal tissues. At certain times after administration there exists a concentration differential of 2–3 : 1 between the neoplastic tissue and adjacent normal structures. Selective tumour destruction can be achieved if the photosensitizer is administered in low dosage; the photosensitizer is photodegraded by light irradiation before a threshold photodynamic dose is reached. However, tumours that selectively retain a higher concentration of photosensitser are destroyed because a threshold photodynamic dose is achieved and cell death occurs. This selective effect is restricted to very low dose and is rarely clinically useful.

It is noticeable that some normal tissues are very resistant to photodynamic therapy. This is most apparent in the pancreas, where the normal cells contain many mitochondria and are resistant to oxidative stress; malignant pancreatic cells are much more sensitive to photodynamic therapy. Selective necrosis of tumour with sparing of normal pancreatic tissue can be demonstrated in experimentally induced tumours.[16, 17] Although differential damage between normal and malignant tissue can be difficult to achieve and requires very careful dosimetry, it is possible to spare surrounding stromal tissues using photodynamic therapy.

PHOTODYNAMIC THERAPY FOR ADVANCED UPPER GASTROINTESTINAL CANCER

The dreadful prognosis of oesophageal cancer is related in part to the fact that it remains undetected until the disease is far advanced. The patient presents with dysphagia and often only palliative treatment can be offered. The main aim of therapy is to open the oesophageal lumen, allowing the patient to swallow until death. Endoscopic photodynamic therapy is only one option, although alternatives including stent insertion, NdYAG laser photothermal therapy, thermal ablation and sclerosant or cytotoxic intratumoural injection are more frequently used.

Various methods are used for endoscopic photodynamic therapy. Most groups have used various derivatives of haematoporphyrin and Photofrin, at a dose of 2 mg/kg body weight, given by slow intravenous injection 48 h before irradiation with laser light in the red at 630 nm. The light can be delivered circumferentially using cylindrical diffusing quartz fibres: the length of the diffuser can be varied from 2 to 7 cm to treat various lengths of tumour. A total light dose of 150–300 J/cm is required to obtain up to 6 mm depth of necrosis. The depth of necrosis is highly dependent on the photosensitizer used. The depth of necrosis using exogenously administered photosensitizers is 6 mm, compared to 2 mm following the administration of 5 aminolaevulinic acid to generate the photosensitizer protoporphyrin IX.[21, 23, 37]

Treatment times of 10–20 min are required to deliver the light at a non-thermal fluence rate. It is important to note that some patients may have temporary worsening of dysphagia caused by oedema and tumour necrosis prior to necrotic tissue separation. This usually resolves after 5 days and may be associated with some blood loss. The duration of response is often quite prolonged, lasting for 10–15 weeks. This compares favourably with thermal ablation, which often requires monthly re-treatments. A large and important randomized comparison (236 patients) of Nd YAG laser therapy (108 patients) with photodynamic therapy (110 patients) showed that both treatments were equally effective. In this study, photodynamic therapy was

performed using the photosensitizer, porfimer sodium. The improvement in dysphagia and endoscopic tumour response was equal between the two groups. Photodynamic therapy was associated with temporary photosensitivity but was easier to perform and associated with less perforations (photodynamic therapy 1%, Nd YAG laser 7%).[18] Overall there appears to be no major benefit for photodynamic therapy over photothermal therapy. Modern expandable metal stents have become very easy to use and associated with relatively low morbidity, and are at present the most widely used method of palliation.[19] Photodynamic therapy is now considered to take a secondary place to other endoscopic methods for the palliation of advanced oesophageal cancer because it is less available, more complicated and requires quite expensive equipment. It should be considered for high oesophageal tumours, and for salvage therapy in patients whose stents have failed due to migration, overgrowth or in-growth. Because photodynamic therapy is non-thermal, there is no risk of damaging the stent.[20]

PHOTODYNAMIC THERAPY FOR EARLY UPPER GASTROINTESTINAL CANCER

There has been a renewed interest in endoscopic therapy for early gastrointestinal cancer since the advent of programmes that have detected pre-malignant and early neoplastic changes confined to the mucosa, or with early invasion of the lamina propria and submucosa. Radical surgical excision with the associated profound morbidity and indeed mortality is often a difficult dilemma for clinician and patient alike. These patients are often asymptomatic, and radical intervention is limited by co-morbidity.

SQUAMOUS CELL CARCINOMA

Patients who have had a previous squamous cell carcinoma in the head and neck or the upper aerodigestive tract are at increased risk of developing a second cancer. Screening of those populations is resulting in an increased detection of early tumours. As many as 15–20% of patients develop a second cancer.[24] The first treatment of early squamous cancers in the Far East was very successful, with 12 out of 13 patients treated showing no detected recurrence after 21–32 months follow-up.[25] The only complication was skin photosensitization.

Subsequently, other investigators have confirmed the effectiveness of photodynamic therapy for early oesophageal cancer (Table 2). In particular, a very important retrospective series indicated that long-term survival was possible after photodynamic therapy using haematoporphyrin derivative and laser light (630 nm) for early squamous and adenocarcinoma.[27] The patients were unsuitable for radical surgical resection and were staged using endoscopic ultrasound as uT1 or uT2. The 5-year cancer specific survival was 74%, but was associated with a high incidence of oesophageal stricture formation (43 out of 123 patients). The survival was not influenced by combination treatment with chemotherapy and radiotherapy.

There appears to be little difference between Photofrin (related to haematoporphyrin derivative) and the newer photosensitizer tetra(m-hydrxyphenyl) chlorin (mTHPC). Following treatment with Photofrin, 14 out of 17 patients with early cancer had a complete response, whereas 12 out of 14 patients treated with mTHPC had the tumour eradicated.[26] mTHPC is a very potent photosensitizer that can be administered in lower dosage and requires shorter irradiation times. The serious complication rate of oesophageal stricture and oesophagotracheal fistula is of concern. A method of limiting the depth of damage is possible by changing the photosensitizer to the endogeneously generated protoporphyrin IX after the oral administration of 5-ALA (Figure 1). The depth of damage of 2 mm is insufficient to ensure invasive cancer eradication.[21]

An alternative strategy is to limit the light penetration of the tissue by changing the wavelength of the activating light. A comparison of the more usually used red (630 nm) and green (517 nm) laser light for Photofrin photodynamic therapy has been performed in nine patients with early squamous cell carcinoma.[28] Green light will not penetrate tissue to the same depth as the more usually used red laser light. The results showed that green light was as effective in the eradication of *in situ* and intramucosal squamous cell carcinoma as red. The complete response rate was no different; some patients had oesophageal resection 6–36 months after photodynamic therapy. If the oesophagus had been treated using red light, there was trans-mural fibrosis with marked thinning of the wall. Green light produced only superficial fibrous scarring.

The use of green light with the photosensitizer mTHPC may reduce the rate of serious adverse events.[24] Of 19 patients with early squamous tumours treated with red

light and mTHPC photodynamic therapy, there were three complications: two possible perforations and one patient developed a tracheoesophageal fistula. One patient with a T1b tumour developed a recurrence 4 months after treatment. The use of green light with mTHPC photodynamic therapy was as effective but there were no serious complications.[29]

PHOTODYNAMIC THERAPY FOR BARRETT'S OESOPHAGUS AND CANCER

Adenocarcinoma of the lower oesophagus and the gastro-oesophageal junction is at present reaching epidemic proportions in the West. The rate of rise is now greatest in the UK. This is strongly associated with Barrett's or columnar lined oesophagus. Currently, adenocarcinoma in Barrett's oesophagus has an incidence of 800 per 100 000. This can be compared with lung cancer in men over 65 years, where the incidence is 500 per 100 000. Cancer incidence may be expressed as a percentage of a particular population developing cancer per year. For adults with Barrett's oesophagus the annual rate is 0.8%.[30] Carcinogenesis in Barrett's oesophagus is thought to follow a sequence from intestinal metaplasia through low- and high-grade dysplasia and finally to invasive cancer. The presence of dysplasia is regarded as the best marker for malignant transformation in the epithelium. Dysplasia is classified histologically into low- and high-grade, with indefinite used when dysplasia cannot be clearly differentiated from the reactive or regenerative changes associated with inflammation. This classification is a modification of histopathological classifications used in the rest of the gastrointestinal tract most notably for colonic dysplasia associated with inflammatory bowel disease.[11] High-grade dysplasia may be a marker for coexistent cancer and it is important that this is excluded prior to consideration of photodynamic therapy.[59, 68]

In order to eradicate dysplasia and Barrett's metaplasia, certain parameters must be understood to allow safe destruction and safe healing. There is one highly informative study which demonstrates that columnar-lined epithelium is minimally thicker (0.5 mm, range 0.39–0.59 mm) than normal squamous mucosa (0.49 mm, range 0.42–0.58 mm).[12] Initial measurements of snap frozen freshly excised oesophageal tissue using optical coherence tomography have recorded a depth of between 0.45 and 0.5 mm[13] Although this is the depth of metaplastic tissue, it is important to know whether dysplasia is thicker. There are no definite data on this but initial observations suggest that it is slightly thicker and it is certainly optically denser.[13] Table 1 indicates that ALA photodynamic therapy will be effective for dysplasia and metaplasia. If invasive cancer is present, and the patient is unsuitable for alternative treatment, exogenous photosensitization is necessary to ensure an adequate depth of necrosis.

Photodynamic therapy following endogeneous photosensitization with 5-ALA has been reported for the treatment of high-grade dysplasia and metaplasia in Barrett's oesophagus. There are extensive data on the uptake and distribution of photosensitizers in gastrointestinal mucosa. In experimental Barrett's-like oesophagus, protoporphyrin IX was generated in the epithelial cells whether squamous or columnar, with maximum levels occurring 3 h after oral or intravenous injection.

Table 1. Photodynamic therapy for upper gastrointestinal high-grade dysplasia and early cancer

	Stage	Eradication (%)	Follow-up (months)	Reference
ALA treatment of:				
Dysplastic Barrett's oesophagus		5/5 (100)	34	Barr, 1996[36]
		10/10 (100)	9.9	Gossner, 1998[37]
		7/7	28	Ackroyd, 1999[47]
Early oesophageal adenocarcinoma	T1	17/22 (77)	9.9	Gossner, 1998[37]
	T1–2	0/3 (0)	28	Ackroyd, 1999[47]
	T1–2	2/12 (16)	36	Tan, 1999[21]
Photofrin treatment of:				
Dysplastic Barrett's oesophagus		69/87 (79)	19	Overholt, 1999[43]
Early oesophageal carcinoma	T1–2	107/123 (87)	6	Sibille, 1995[47]
	T1–2	9/12 (75)	19	Overholt, 1999[43]
	T1	26/31 (84)	24	Savary, 1998[26]

The maximum photodynamic effect occurred 3–6 h after ALA administration.[69] The uptake in the mucosa was 3.5 times greater than in the muscularis, and there was little difference between oral or parenteral administration of the 5-ALA.[11, 15] These experimental studies have also supplied important reasons for the mucosal localization of PpIX. The muscularis contains more iron and has a reduced activity of one of the rate-controlling enzymes, porphobilinogen deaminase. Clinical studies of the PpIX distribution following oral 5-ALA have confirmed the mucosal accumulation relative to surrounding tissues.[16, 17]

Following the accumulation of PpIX, a photodynamic action will only occur following light irradiation. Initially all treatment parameters were empirically selected An elegant study in an experimental model of Barrett's-like oesophagus has confirmed that the most appropriate time for light irradiation is 2–3 h after 5-ALA administration. This time interval appears to be critical to achieve mucosal destruction while sparing oesophageal function.[18]

There have been two major clinical studies of 5-ALA photodynamic therapy for the ablation of high-grade dysplasia (Table 1). Both have demonstrated eradication of the dysplasia and one series demonstrated the successful eradication of T1 tumours that were less than 2 mm in depth.[16, 17] A prospective randomized trial of the treatment of low-grade dysplasia using ALA and irradiation with green light rather than the usual 630-nm red light has again confirmed how effective this treatment is in reversing dysplasia/metaplasia. Healing proceeded with the regeneration of neosquamous epithelium.[19, 70]

The healing of the treated epithelium and the prevention of cancer is vitally important. Neo-squamous epithelium was restored in 70% of patients, with eradication of dysplasia and intestinal metaplasia. However, in 30% the neo-squamous epithelium covered metaplastic glands.[71] This is similar to the results obtained when photothermal laser and argon plasma coagulator thermal therapy is used to eradicate dysplastic and metaplastic epithelium.[72, 73] In addition, following argon plasma coagulation, an intramucosal adenocarcinoma has arisen under the neo-squamous epithelium.[74] We have also recently reported a patient treated with photothermal laser therapy for low grade dysplasia who developed an adenocarcinoma, and a similar event has occurred in a patient treated with photodynamic therapy.[75]

It is clear that continued surveillance is necessary for patients after mucosal ablation therapy. Intriguingly, the recently reported randomized trial using ALA and green light records a very low incidence of residual and buried metaplasia.[70] Following photodynamic therapy, high-grade dysplasia can occur and despite phenotypic change there may be persistent genetic abnormalities.[76]

A variation of 5-ALA photodynamic therapy involves the direct endoscopic spraying of the agent combined with sodium bicarbonate as a mucolytic onto dysplastic Barrett's oesophagus. A period of time is allowed for local absorption and then the area is irradiated with light. The response following this technique was variable, with two out of nine patients failing to show any response.[10]

The use of exogeneous photodynamic therapy for early cancer and high-grade dysplasia has been examined in some detail. The development of optical biopsy techniques including optical coherence tomography is making accurate preoperative staging possible. There are now consistent data demonstrating the effectiveness of the Photofrin for the eradication of early adenocarcinoma arising from Barrett's oesophagus.[11] The method of treatment has been adapted from the treatment of large areas of Barrett's metaplasia with or without high-grade dysplasia. Forty-eight hours after the administration of 2 mg/kg of Photofrin, light from a laser at 630 nm is delivered at endoscopy to the oesophagus. A diffuser or a windowed centring balloon allows more accurate and even light dosimetry.[12] The length of the light delivering device can be 3, 5 or 7 cm. At present it is not recommended that more than 7 cm of Barrett's oesophagus is treated at one session. The power density used is 400 mW/cm^2 to provide an energy density of 100–250 J/cm^2 from the diffuser to the mucosa. Treatment can be performed on an outpatient basis and patients must all receive acid suppression with proton pump inhibitor therapy. There is now increasing evidence that proton pump inhibitor therapy only can improve various parameters of Barrett's oesophagus. The molecular evidence is that effective acid suppression favours differentiation and decreases proliferation.[77] There is also a decrease in the length of the Barrett's segment with an increase in the number of squamous islands, and a reduction in the proportion of sulphomucin-rich intestinal metaplasia.[78] A randomized double-blind study has confirmed that profound acid suppression with a proton pump inhibitor, leading to elimination of acid reflux, induces a partial regression of the columnar-lined segment.[79]

Following photodynamic therapy, direct sunlight must be avoided for a period of 4–6 weeks. This is clearly a more aggressive therapy than ALA photodynamic therapy: the level of damage is deeper and the surrounding tissues may be affected. Most patients develop small unilateral or bilateral pleural effusions. Occasionally the patient required a thoracentesis. Cutaneous photosensitivity can be a significant problem up to 2 months after photosensitization. The major concern has been the incidence of oesophageal stricture. Approximately 30% developed significant stenosis which responded to endoscopic oesophageal dilatation.

The results of Photofrin photodynamic therapy are very encouraging, with 75–80% of the Barrett's mucosa being converted to neosquamous mucosa. Complete eradication of all metaplastic epithelium occurred in 43 out of 100 patients. Dysplasia disappeared in 78 out of 100 patients, although 11 developed dysplasia during follow-up and required repeat treatment. Thirteen patients were treated for early cancer (T1–12 patients: T2–1 patient), and in 10 the tumour was eradicated. It is important to emphasize that the patients must remain under surveillance and repeated treatment will be necessary in some to treat residual or recurrent areas of dysplasia and metaplasia. Usually the areas are rather patchy and are best treated using thermal ablation using a thermal laser.[43]

PHOTODYNAMIC THERAPY FOR GASTRIC CANCER

The use of photodynamic therapy for the palliation of advanced gastric cancer appears to be of little advantage over alternative laser or thermal methods.[44] Early gastric cancer has a good prognosis but radical surgical excision carries significant morbidity. Local therapy of high-grade dysplasia and early cancer is possible because there is a low probability of lymph-node metastases. For small cancers (< 2 cm) of type I to IIa, the 5-year survival is between 80 and 95%.[48] Eastern Gastroenterologists and Surgeons have development methods of endoscopic mucosal resection, NdYAG laser therapy and photodynamic therapy to treat early gastric cancers after accurate staging with endosonography. A major advantage of endoscopic mucosal resection is the availability of a specimen for precise histopathological examination. However, thermal and endoscopic mucosal resection risks perforation and seeding tumour cells in the resection or thermal wound. Several first- and second-generation photosensitizers, including Photofrin, mTHPC and 5-ALA, have been assessed for photodynamic therapy of early gastric cancer.[45] The major disadvantage of ALA is that deep destruction is difficult, yet it is highly specific for the mucosa. Recently, mTHPC has been demonstrated to have a high photodynamic efficiency. Light irradiation doses can be reduced to 10–20 J/cm, allowing the treatment times to be reduced. Light fluences of 150–300 J/cm are required if Photofrin or ALA (PpIX) are used. This is particularly important in the stomach, where the geometry is difficult compared to that of the cylindrical oesophagus. Variations in the distance between light applicator and target can be reduced, allowing more precise dosimetry. Photodynamic therapy has proved to be effective for the treatment of type I, IIa and IIb cancers, if less than 2 cm in diameter.

PHOTODYNAMIC THERAPY FOR BILIARY AND PANCREATIC CANCER

Cholangiocarcinoma can be a relatively indolent tumour, but treatment with surgery, radiotherapy and chemotherapy is very difficult. Aggressive surgical therapy is only possible in a minority of patients with early cancers, and the median survival is between 13 and 20 months.[49] Survival of patients with T3 and T4 tumours is limited to between 300 and 420 days.[50] A recent study of photodynamic therapy in patients with non-resectable cholangiocarcinoma (type III and IV) who have failed endoprostheses insertion has proved to be highly informative. Twenty-two patients were photosensitized with Photofrin 2 days prior to intraluminal light irradiation of the obstructing tumour performed at cholangioscopy. There was no 30-day mortality and the median survival time was 439 days and one patient is alive at 739 days.[51, 52]

There are now some initial data on clinical photodynamic therapy for inoperable pancreatic cancer using mTHPC reported in abstract form.[53] The remarkable lack of serious complications associated with experimental photodynamic therapy to the pancreas has encouraged more detailed and clinical investigation.[54] Twelve patients have been treated with percutaneously inserted optical fibres and up to 6.5 cm of necrosis has been induced without major morbidity. Two patients are still alive at 16 and 17 months, and five patients have died of disease progression. There are also data on the treatment of carcinoma of the Ampulla of Vater with good local control of the disease.[55]

PHOTODYNAMIC THERAPY AND INFECTIOUS DISEASE

Helicobacter pylori is associated with upper gastrointestinal disease and can on occasion be difficult to eradicate. It is, however, very sensitive to photodynamic therapy.[56] *H. Pylori* on the surface of the gastric mucosa is accessible to topical photosensitizer application and to endoscopic light delivery. This technique has not yet entered the clinical arena.

CONCLUSION

Photodynamic therapy is very exciting and conceptually very attractive.[57] It has yet to enter into widespread routine clinical practice. This is partly because the technology has been expensive, in particular the lasers required are cumbersome and expensive. The newer diode lasers are smaller and much easier to use. The choice of photosensitizer is also important and can be confusing. The most developed area of clinical use is for the eradication of early neoplasia related to Barrett's oesophagus and previous squamous cell cancer. It is likely that large areas of field cancerization can be successfully ablated using photodynamic therapy.

REFERENCES

1 Nealson KH, Conrad PG. Life: past, present and future. Phil Trans R Soc Lond B 1999; 354: 1923–39.
2 Bauer J, Chen K, Hiltbunner A, *et al*. The major protein import receptor of plastids is essential for chloroplast biogenesis. Nature 2000; 403: 203–7.
3 Limburg J, Vrettos JS, Liable-Sands LM, Rheingold AL, Crabtree RH, Brudvig GW. A functional model for O–O bond formation by the O2-evolving complex in Photosystem II. Science 1999; 283: 1524–7.
4 Gray MW, Burger G, Lang BF. Mitochondral evolution. Science 1999; 283: 1476–81.
5 Thadani H, Deacon A, Peters T. Diagnosis and management of porphyria. Br Med J 2000; 320: 1647–51.
6 Moreira D, Le Guyader H, Phillippe H. The origin of red algae and the evolution of chloroplasts. Nature 2000; 405: 69–72.
7 Tappeiner H. Die photodynamische erscheinung. Ergebnisse der Physiologie 1909; 8: 698–741.
8 Jesionek A, Tappiener. Zur behandlung der hautcarcinoma mit fluorescierenden stoffen Arch. Klin Med 1905; 82: 223–7.
9 Dougherty TJ. Activated dyes as antitumor agents. J Natl Cancer Inst 1974; 52: 1333–6.
10 Hayata Y, Kato H, Konaka C, Ono J, Takizawa N. Hematoprphyrin derivative and laser photoradiation in the treatment of lung cancer. Chest 1982; 81: 269–77.
11 McCaughen JS, Hicks W, Laufman L, May E, Roach R. Palliation of esophageal malignancy with photoradiation therapy. Cancer 1984; 54: 2905–10.
12 Stael Holstein C, Nilsson AMK, Andersson-Engels S, Wilen R, Walther B, Svanberg K. Detection of adenocarcinoma in Barrett's oesophagus by means of laser-induced fluorescecence. Gut 1996; 39: 711–6.
13 Panjepour M, Overholt BF, Vo-Dinh T, *et al*. Endoscopic fluorescence detection of high-grade dysplasia in Barrett's oesophagus. Gastroenterology 1996; 111: 93–101.
14 Fuljames C, Stone N, Bennett D, Barr H. Beyond white light endoscopy: the prospects for endoscopic optical biopsy. Ital J Gastroenterol Hepatol 1999; 31: 695–704.
15 Barr H, Tralau CJ, Boulos PB, *et al*. Selective necrosis in dimethylhydrazine-induced rat colon tumors using phthalocyanine therapy. Gastroenterology 1990; 98: 1532–7.
16 Bown SG, Millson CE. Photodynamic therapy in Gastroenterology. Gut 1997; 41: 5–7.
17 Regula J, Ravi B, Bedwell J, MacRobert AJ, Bown SG. Photodynamic therapy using ALA induced PPIX for experimental pancreatic cancer-prolonged animal survival. Br J Cancer 1994; 70: 248–54.
18 Lightdale CJ, Heier SK, Marcon NE, *et al*. Photodynamic therapy with porfimer sodium versus thermal ablation therapy with Nd: YAG laser for palliation of esophageal cancer: a multicentre randomized trial. Gastrointest Endosc 1995; 42: 507–12.
19 Barr H. Endoscopic treatment of upper gastrointestinal cancer. Current medical literature. Gastroenterology 1999; 18: 61–6.
20 Lightdale CJ. Role of photodynamic therapy in the management of advanced esophageal cancer. Gastrointest Endosc Clin N Am 2000; 10: 397–408.
21 Heier SK, Rothman KA, Heier LM, Rosenthal WS. Photodynamic therapy for obstructing esophageal cancer: light dosimetry and a randomized comparison with Nd: YAG laser therapy. Gastroenterology 1995; 109: 63–72.
22 Barr H, Krasner N, Boulos PB, Chatlani PT, Bown SG. Photodynamic therapy for colorectal cancer: a quantitative pilot study. Br J Surg 1990; 77: 93–6.
23 Tan WC, Fuljames C, Stone N, *et al*. Photodynamic therapy using 5-aminolaevulinic acid for oesophageal adenocarcinoma associated with Barrett's metaplasia. J Photochem Photobiol, B: Biol 1999; 53: 75–80.
24 Radu A, Wagnieres G., van den Berg H, Monnier P. Photodynamic therapy of early squamous cell cancers of the esophagus. Gastrointest Endosc Clin N Am 2000; 10: 439–60.
25 Tian ME, Qui SL, Ji Q. Preliminary results of hematoporphyrin derivative-laser treatment for 13 cases of early esophageal carcinoma. Adv Exp Med Biol 1985; 193: 21–5.
26 Savary JF, Grosjean P, Monnier P, *et al*. Photodynamic therapy of early squamous cell carcinomas of the esophagus: a review of 31 cases. Endoscopy 1998; 30: 258–65.
27 Sibille A, Lambert R, Souquet J-C, Sabben G, Descos F. Long-term survival after photodynamic therapy for esophageal cancer. Gastroenterology 1995; 108: 337–44.
28 Grosjean P, Wagnieres G, Fontolliet C, *et al*. Clinical photodynamic therapy for superficial cancer in the oesophagus and

the bronchi: 514 nm compared with 630 nm light irradiation after sensitization with Photofrin II. Br J Cancer 1998; 77: 1989–95.
29 Grosjean P, Wagnieres G, Fontolliet C, Monnier P. Tetra (m-hydroxyphenyl) chlorin clinical photodynamic therapy of early bronchial and oesophageal cancers. Lasers Med Sci 1996; 11: 227–35.
30 Spechler SJ. Barrett's esophagus. Seminars Oncol 1994; 21: 431–7.
31 Haggitt RC. Barrett's esophagus, dysplasia, and adenocarcinoma. Hum Pathol 1988; 25: 982–93.
32 Ackroyd R, Brown NJ, Stephenson TJ, Stoddard CJ, Reed MW. Ablation treatment for Barrett's oesophagus: what depth of tissue destruction is needed? J Clin Pathol 1999; 52: 509–12.
33 Bamford K, James J, Barr H, Tatam R. Electromagnetic simulation of laser-induced fluorescence in bronchial tissue and predicted optical scattering behaviour. Opt Imaging Techn Biomonitoring IV 1998; 3567: 18–28.
34 Van den Boogert J, Houtsmuller AB, De Rooij FWM, De Bruin RWF, Van Siersema PD, Hillegersberg R. Kinetics, localization, and mechanism of 5-aminolaevulinic acid-induced porphyrin accumulation in normal and Barrett's-like rat esophagus. Lasers Surg Med 1999; 24: 3–13.
35 Barr H. Barrett's esophagus: Treatment with 5-aminolevulinic acid photodynamic therapy. Gastrointest Endo Clin N Am 2000; 10: 421–37.
36 Barr H, Shepherd NA, .Dix A, Roberts DJH, Tan WC, Krasner N. Eradication of high grade dysplasia in columnar-lined (Barrett's) oesophagus using photodynamic therapy with endogenously generated protoporphyrin IX. Lancet 1996; 348: 584–5.
37 Gossner L, May A, Stolte M, Seitz G, Hahn EG, Ell C. KTP laser destruction of dysplasia and early cancer in columnar-lined Barrett's esophagus. Gastrointest Endosc 1999; 49: 8–12.
38 Van den Boogert J, Hillegersberg R, Staveren HJ, De Bruin RWF, Siersema PD, Tilanus HW. Timing of illumination is essential for effective and safe photodynamic therapy: a study in the normal rat oesophagus. Br J Cancer 1999; 79: 825–30.
39 Ackroyd R, Davis MF, Stephenson TJ, *et al.* Photodynamic therapy for Barrett's oesophagus: a prospective randomised trial. Endoscopy 1997; 29: B17.
40 Ortner M, Zumbusch K, Liebetruth J, *et al.* Photodynamic therapy in Barrett's esophagus after local administration of 5-aminolaevulinic acid. Gastroenterology 1997; 112: A633(Abstract).
41 Overholt B, Panjehpour M, Tefftellar E. Photodynamic therapy for the treatment of early carcinoma in Barrett's esophagus. Gastrointest Endosc 1993; 39: 73–6.
42 Panjehpour M, Overholt BF, DeNovo R, Sneed R, Petersen MG. Centering balloon to improve esophageal photodynamic therapy. Lasers Surg Med 1992; 12: 631–8.
43 Overholt BF, Panjepour M, Haydek JM. Photodynamic therapy for Barrett's esophagus. Follow-up in 100 patients. Gastrointest Endosc 1999; 49: 1–7.
44 Gossner L, Ell C. Photodynamic therapy of gastric cancer. Gastrointest Endosc Clin N Am 2000; 10: 461–80.
45 Ell C, Gossner L, May A. Photodynamic ablation of early gastric cancers of the stomach by means of mTHPC and laser irradiation. Gut 1998; 43: 345–9.
46 Ell C, Gossner L. Photodynamic therapy and its potential for treatment of gastrointestinal malignancies and precancerous conditions. Endoscopy 1994; 26: 262–3.
47 Ackroyd R, Brown NJ, Davies MF, Stephenson TJ, Stoddard CJ, Reed MWR. Aminolaevulinic acid-induced photodynamic therapy in the treatment of dysplastic Barrett's oesophagus and adenocarcinoma. Lasers Med Sci 1999; 14: 278–85.
48 Toril A, Sakai M, Kajiyama T, *et al.* Endoscopic aspiration mucosectomy as curative endoscopic surgery: analysis of 24 early gastric cancers. Gastrointest Endosc 1995; 42: 475–9.
49 Pichlmayr R, Weimann A, Klempnauer J, *et al.* Surgical treatment in proximal bile duct cancer: Single-centre experience. Ann Surg 1996; 217: 20–5.
50 Burke EC, Jarnagin WR, Hochwald SN, *et al.* Hilar cholangiocarcinoma: patterns of spread, the importance of hepatic resection for curative operation, and a pre-surgical clinical staging system. Ann Surg 1998; 228: 385–9.
51 Ortner M, Liebetruth J, Schreiber ST, *et al.* Photodynamic therapy of nonresectable cholangiocarcinoma. Gastroenterology 1998; 114: 536–602.
52 Ortner M. Photodynamic therapy of cholangiocarcinoma cancer. Gastrointest Endosc Clin N Am 2000; 10: 481–6.
53 Rogowska A, Whitelaw DE, Lees WR, Bown SG. Photodynamic therapy for palliation of unresectable pancreatic cancer. Gastroenterology 1999; 116: A1159(Abstract).
54 Bown SG, Lovat LB. The biology of photodynamic therapy in the gastrointestinal tract. Gastrointest Endosc Clin N Am 2000; 10: 533–50.
55 Abulafi AM, Allardice JT, Van Williams NS, Someran N, Swain CP, Ainley CA. Photodynamic therapy for malignant tumours of the Ampulla of Vater. Gut 1995; 36: 853–6.
56 Millson CE, Wilson M, MacRobert AJ, bedwell J, Bown SG. The killing of *Helicobacter pylori* by low-power laser light in the presence of a photosensitiser. J Med Microbiol 1996; 44: 245–52.
57 Barr H. Gastrointestinal tumours: let there be light. Lancet 1998; 352: 1242–4.
58 Kennedy JC, Pottier RH. Endogenous protoporphyrin, a clinically useful photosensitiser for photodynamic therapy. J Photochem Photobiol B 1992; 14: 275–84.
59 Pera M, Trastek VF, Carpenter HA, Allen MS, Deschamps C, Pairolero PC. Barrett's esophagus with high-grade dysplasia: an indication for esophagectomy? Ann Thorac Surg 1992; 54: 199–204.
60 Rice TW, Falk GW, Achkar E, Petras RE. Surgical management of high-grade dysplasia in Barrett's esophagus. Am J Surg 1997; 174: 1832–6.
61 Steitz JM Jr, Andrews CW Jr, Ellis FH Jr Endoscopic surveillance of Barrett's oesophagus. Does it help? J Thorac Cardiovasc Surg 1993; 105: 383–8.
62 Levine DS, Haggitt RC, Blount PL, Rabinovitch PS, Rusch VW, Reid BJ. An endoscopic biopsy protocol can differentiate high-grade dysplasia from early adenocarcinoma in Barrett's esophagus. Gastroenterology 1993; 105: 40–50.

63 Peters JH, Clark GW, Ireland AP, Chandrasoma P, Smyrk TC, DeMeester DR. Outcome of adenocarcinoma in Barrett's esophagus in endoscopically surveyed and non-surveyed patients. J Thorac cardiovasc Surg 1994; 108: 813–21.
64 Edwards MJ, Gable DR, Lentsch AB, Richardson JD. The rationale for esophagectomy as the optimal therapy for Barrett's esophagus with high-grade dysplasia. Ann Surg 1996; 223: 585–9.
65 Collard JM, Romagnoli R., Hermans BP, Malaise J. Radical esophageal resection for adenocarcinoma arising in Barrett's esophagus. Am J Surg 1997; 174: 307–11.
66 Heitmeller RF, Redmond M, Hamilton SR. Barrett's esophagus with high-grade dysplasia. An indication for prophylactic esophagectomy. Ann Surg 1996; 224: 66–71.
67 Ferguson MK, Naunheim KS. Resection for Barrett's mucosa with high-grade dysplasia: implications for prophylactic photodynamic therapy. J Thorac Cardiovasc Surg 1997; 114: 824–9.
68 Cameron AJ, Carpenter HA. Barrett's esophagus, high-grade dysplasia, and early adenocarcinoma: a pathological study. Am J gastroenterol 1997; 92: 586–91.
69 Loh CS, Bedwell J, MacRobert AJ, Krasner N, Phillips D, Bown SG. Photodynamic therapy of the normal rat stomacha comparative study between disulfonated aluminium phthalocyanine and 5-aminolevulinic acid. Br J Cancer 1992; 66: 452–62.
70 Ackroyd R, Brown NJ, Davies MF, *et al.* Photodynamic therapy for dysplastic Barrett's oesophagus: a prospective, double blind, randomised, placebo controlled trial. Gut 2000; 47: 612–7.
71 Biddlestone LR, Barham CP, Wilkinson SP, Barr H, Shepherd NA. The histopathology of treated Barrett's esophagus. Am J Surg Pathol 1998; 22: 239–45.
72 Byrne JP, Armstrong GR, Attwood SEA. Restoration of the normal squamous lining in Barrett's esophagus by argon beam plasma coagulation. Am J Gastroenterol 1998; 93: 1810–5.
73 Barham CP, Jones RL, Biddlestone LR, Hardwick RH, Shepherd NA, Barr H. Photothermal laser ablation of Barrett's oesophagus: endoscopic and histological evidence of squamous re-epithelialisation. Gut 1997; 41: 281–384.
74 Van Laethem JL, Peny MO, Salmon I, Cremer M, Deviere J. Intramucosal adenocarcinoma arising under squamous re-epithellalisation of Barrett's oesophagus. Gut 2000; 46: 574–7.
75 Barr H. Barrett's esophagus: treatment with 5-aminolevulinic acid photodynamic therapy. Gastrointest Clin N Am 2000; 10: 421–37.
76 Krishnadath KK, Wang KK, Taniguchi K, *et al.* Persistent genetic abnormalities in Barrett's esophagus after photodynamic therapy. Gastroenterology 2000; 119: 624–30.
77 Ouata-Lascar R, Fitzgerald RC, Triadafilopoulos G. Differentiation and proliferation in Barrett's esophagus and the effects of acid suppression. Gastroenterology 1999; 117: 327–35.
78 Gore S, Healey CJ, Sutton R, *et al.* Regression of columnar lined (Barrett's) oesophagus with continuous omeprazole therapy. Aliment Pharmacol Ther 1993; 7: 623–8.
79 Peters FTM, Ganesh S, Kulpers EJ, *et al.* Endoscopic regression of Barrett's oesophagus during omeprazole treatment; a randomised double blind study. Gut 1999; 45: 489–94.